Materials Horizons: From Nature to Nanomaterials

Sarabjeet Singh Sidhu
Preetkanwal Singh Bains
Redouane Zitoune
Morteza Yazdani *Editors*

Futuristic Composites

Behavior, Characterization, and Manufacturing

Springer

Materials Horizons: From Nature to Nanomaterials

Series editor

Vijay Kumar Thakur, School of Aerospace, Transport and Manufacturing, Cranfield University, Bedford, UK

Materials are an indispensable part of human civilization since the inception of life on earth. With the passage of time, innumerable new materials have been explored as well as developed and the search for new innovative materials continues briskly. Keeping in mind the immense perspectives of various classes of materials, this series aims at providing a comprehensive collection of works across the breadth of materials research at cutting-edge interface of materials science with physics, chemistry, biology and engineering.

This series covers a galaxy of materials ranging from natural materials to nanomaterials. Some of the topics include but not limited to: biological materials, biomimetic materials, ceramics, composites, coatings, functional materials, glasses, inorganic materials, inorganic-organic hybrids, metals, membranes, magnetic materials, manufacturing of materials, nanomaterials, organic materials and pigments to name a few. The series provides most timely and comprehensive information on advanced synthesis, processing, characterization, manufacturing and applications in a broad range of interdisciplinary fields in science, engineering and technology.

This series accepts both authored and edited works, including textbooks, monographs, reference works, and professional books. The books in this series will provide a deep insight into the state-of-art of *Materials Horizons* and serve students, academic, government and industrial scientists involved in all aspects of materials research.

More information about this series at http://www.springer.com/series/16122

Sarabjeet Singh Sidhu · Preetkanwal Singh Bains
Redouane Zitoune · Morteza Yazdani
Editors

Futuristic Composites

Behavior, Characterization, and Manufacturing

Springer

Editors
Sarabjeet Singh Sidhu
Beant College of Engineering and Technology
Gurdaspur, Punjab, India

Preetkanwal Singh Bains
Beant College of Engineering and Technology
Gurdaspur, Punjab, India

Redouane Zitoune
Institut Clément Ader
Toulouse University
Toulouse, France

Morteza Yazdani
Department of Management
Universidad Loyola Andalucía
Sevilla, Spain

ISSN 2524-5384 ISSN 2524-5392 (electronic)
Materials Horizons: From Nature to Nanomaterials
ISBN 978-981-13-2416-1 ISBN 978-981-13-2417-8 (eBook)
https://doi.org/10.1007/978-981-13-2417-8

Library of Congress Control Number: 2018953293

This Springer imprint is published by the registered company Springer Nature Singapore Pte Ltd.
The registered company address is: 152 Beach Road, #21-01/04 Gateway East, Singapore 189721, Singapore

Contents

About the Editors

Dr. Sarabjeet Singh Sidhu is an assistant professor in the Department of Mechanical Engineering, Beant College of Engineering and Technology, Gurdaspur, Punjab, India. He received his Master of Technology from IKG Punjab Technical University, Jalandhar. His research interests include surface modification, residual stress analysis in metal matrix composites, biomaterials, and non-conventional machining processes. He has published more than 50 technical papers in reputed national and international journals/conferences and also served as a reviewer for various journals. Recently, he was awarded the Contribution Award by *Journal of Mechanical Science and Technology* (Springer).

Dr. Preetkanwal Singh Bains is a researcher in the Department of Mechanical Engineering, Beant College of Engineering and Technology, Gurdaspur, Punjab, India. His current research interests include materials engineering and advanced machining processes. He has contributed numerous innovative and novel manufacturing techniques, for which three patents have been filed in various fields of mechanical engineering. He is a life member of the Indian Society for Technical Education (ISTE) and American Society of Mechanical Engineers (ASME). He has also contributed many significant publications and served as a reviewer for prominent journals.

Dr. Redouane Zitoune is an associate professor in the Department of Mechanical Engineering, Paul Sabatier University (University of Toulouse), France. His doctoral work focused on the manufacturing and machining (drilling and milling) of composite materials. His current research interests include damage analysis during the drilling and milling of composite materials with conventional machining and abrasive water jet machining, and finite element analysis for machining. He is also interested in the thermal analysis of composite structures by means of optical fibers and finite element analysis. He has published more than 150 articles in national and international journals and conferences.

Dr. Morteza Yazdani is a researcher and adjunct professor, Universidad Europea de Madrid (UEM), Spain. He obtained his Ph.D. in business and economics at UEM and collaborated on the RUC-APS project during his postdoctoral work at the University of Toulouse, France. He has published more than 20 papers in leading international journals and is an active reviewer for many others, including *Sustainability, Applied Soft Computing*, and *Journal of Cleaner Production*.

Machining of FRP Composites: Surface Quality, Damage, and Material Integrity: Critical Review and Analysis

N. Nguyen-Dinh, A. Hejjaji, R. Zitoune, C. Bouvet and L. Crouzeix

Abstract Composite materials particularly fiber-reinforced plastics (FRPs) have brought remarkable advances in various engineering sectors because of their excellent mechanical properties. Ranging from space applications to consumer products, their demand is ever increasing, and to bridge this supply gap, constant endeavor is focused on optimizing their production rate. Numerous conventional and nonconventional processes are employed for manufacturing and machining these FRPs. Every day novel technologies are explored to make the production of FRPs much agile. FRPs are always manufactured to near net shape; however, functional assemblies demand minimal machining post manufacturing. The real challenge lies here as FRPs are difficult to machine due to their intrinsic anisotropy, fragility, and inhomogeneity. Abundant research done on conventional and nonconventional machining reveals that machining alters the surface characteristics and induces damage in FRPs. Researchers have demonstrated that machining parameters have great influence on the extent of surface degradation and damage, and have suggested several measures to improve the machining quality. Surface degradation and damage induced have a notable influence on the material integrity which may be inferior to the expected values, thus decreasing the reliability of the machined component. This chapter presents the readers a comprehensive review of various machining processes of FRPs focusing on the multilevel surface and damage characteristics, as well as their impact on the mechanical behavior. It shall help the designer of composite structures to understand the correlation between the machining processes, surface integrity, damage, and the mechanical properties induced in order to reduce the cost for the manufacturing during the design phase.

Keywords Fiber-reinforced composites (FRPs) · Composite machining
Surface quality · Machining damage · Material integrity

N. Nguyen-Dinh · A. Hejjaji · R. Zitoune (✉) · C. Bouvet · L. Crouzeix
Institute Clément Ader (ICA), CNRS UMR 5312, "INSA, UPS, Mines Albi, ISAE",
Université de Toulouse, 3 Rue Caroline Aigle, Toulouse, France
e-mail: redouane.zitoune@iut-tlse3.fr

S. S. Sidhu et al. (eds.), *Futuristic Composites*, Materials Horizons: From Nature to Nanomaterials, https://doi.org/10.1007/978-981-13-2417-8_1

1 Introduction

Fiber-reinforced plastics (FRPs) are a class of composite materials offering a very high strength-to-weight ratio/high modulus-to-weight ratio and corrosion resistance which makes them a widely used material in aerospace, marine, robotics, construction, transportation, sporting goods, and defense applications. Usage of composites in any of these applications needs a specific shape, size, load bearing capacity, geometrical, and damage tolerance. Hence, to obtain these attributes, they undergo series of processing operations starting from mold curing to machining for a final finish. Generally, the manufacturing of composite components is planned such that near net shape is obtained at the first step of molding itself. However, the final functional component will not be ready at this stage; it requires minimum basic machining operations like trimming, milling, grinding, and hole making to obtain a final component that will be used in the functional assembly. For example, current aircraft manufacturing employs machining operations like milling and grinding the edges of FRP panels after removing from molds, laser/abrasive waterjet cutting to make openings for ducts and windows, drilling to make holes for riveting of panels together or step milling to repair damaged sections. The real problem arises here, as FRPs are not easy to machine owing to their highly heterogeneous nature due to the presence of distinct phases of fiber reinforcements and a polymer matrix (specifically for the thermoset) having a huge variation in their mechanical, thermal, and physical properties. This makes machining of composites a complex phenomenon where cutting tool interaction is distinct from machining of metals [1].

The properties and machinability of fiber-reinforced plastics are governed by the type of reinforcement (e.g., carbon, glass, Kevlar, Basalt, etc.) and matrix (e.g., thermoset, thermoplastic, etc.) used to manufacture them. The combination of these two materials as a composite material throws the real challenge of machining them. The limited machinability of FRPs has challenged the scientific community to explore numerous technologies to machine FRPs successfully. Many studies have been performed on machining FRPs using conventional (Drilling, milling, trimming) and non-convectional technologies (Abrasive waterjet, laser, ultrasonic, and electrical discharge). Each machining technology has its own physics of material removal which modifies surface properties at the machined zone. The integrity of the new surface created may be inferior to that of the initial surface obtained after curing the FRPs. The newly modified surface contains microcracks and damages, and in some cases subsurface damages are also reported [2]. Numerous studies report various kinds of defects that arise during machining of FRPs, like delamination, fiber pullout, matrix cracking, matrix degradation and burnout in conventional machining, kerf taper, matrix recession, thermal damage in laser machining and delamination, grit embedment, striations, and craters in abrasive waterjet machining [3–10]. It was clearly established that every machining process has its own influence on the FRP composite which induces damage unique to that process. In addition, investigations prove that the extent of machining damage is greatly influenced by the machining parameters of the process, the nature and the orientation of the fibers (stacking

sequence), the nature of matrix, the process of manufacturing of the composite parts as well as the tool wear when the conventional process is considered. For example, in the work conducted by Zitoune et al. [5] on conventional drilling, it is seen that the delamination damage observed at the hole exit on the part manufactured by oven process is 20% superior compared to the part manufactured by autoclave process when the same machining parameters are used. This difference has been attributed to the interface quality between the plies which is affected by the process of manufacturing. In addition, it was mentioned by the authors that the size of the delamination at the hole exit is strongly influenced by the feed rate selected. In addition, these defects can be observed with the increase of the number of drilled holes or with the increase in the distance of machining even when machining is conducted with the optimal cutting parameters and optimal geometry of the cutting tool. This result can be explained by the local modification of the geometry of the cutting tool due to the wear phenomenon. In fact, several authors have shown that machining with inappropriate parameters increases the possibility of obtaining a poor quality machined component which can be responsible for the reduction of the endurance limit of the structure in service [11–22].

The kind of loads acting on a component varies with the application where the component is in service. For example, in aerospace structures, tensile, bending, and compressive loads (in static or fatigue) are common, whereas in sporting and aerospace applications impact loads are prevalent. Hence, every component has to be suitably designed to withstand loads in actual service conditions and loading specific to the intended application. The capability and extent of withstanding the applied functional loads by the FRP components are dependent on several factors like materials used, the geometry of the component, and stacking sequence; these factors are controllable and are taken into account during the design phase itself. However, several studies have shown that the strength of the FRP structure can be affected by the type of machining process employed to produce the component [11–22]. It is seen that the strength of the machined component is always less than the theoretical and ideal strength, the reasons for which is well established by several studies affirming that machined surface and machining-induced damage are the main factors. Arola et al. [12] have focused on the identification of the impact of the process of machining on the mechanical behavior during the impact loading. It was clearly observed that the FRPs' specimens trimmed by polycrystalline diamond (PCD) characterized by lower roughness parameter (R_a) compared to the specimens trimmed by abrasive waterjet (AWJ) process absorb more energy of impact compared to the AWJ specimens [12]. However, when only AWJ specimens were considered, it was seen that impact energy absorbed decreased with increase of roughness parameter (R_a). Similarly, when we look at studies conducted by Haddad et al. [21], it was seen that specimens machined with burr tool demonstrate better fatigue performance and also highest endurance limit when compared to specimens machined using other processes (Disc cut specimens with and without polishing) in spite of having the highest roughness values. Also, investigations on compressive strength of FRPs conducted by Ramulu et al. [17] show that apart from surface roughness the major factor for strength reduction is the extent of delamination caused by machining. This shows

that mechanical behavior is dependent on all three factors, i.e., surface characteristics, the extent of damage, and type of loading. As discussed earlier, for some cases of loading, the behavior is not directly dependent on surface parameters (R_a, R_v, R_z, etc.) and in some, it is solely dependent on surface characteristics. In fact, work carried out by Ghidossi et al. [16] establishes that average surface roughness (R_a), commonly used to characterize surfaces of metals and predict their mechanical behavior, does not hold good for composites. But industries have always used average surface roughness (R_a) as criterion for the characterization of the machined surface. However, if we refer to the results from the literature which focuses on the correlation of the mechanical behavior with surface characteristics based on the criteria used in industries (R_a, R_v, R_z, etc.), it is clear that there is an ambiguity. The damage generated by machining brings down the material integrity and increases stress concentration zones; this can be one of the reasons for the random evolution of mechanical behavior with surface roughness. Hence, it is necessary to evaluate the machined damage apart from surface roughness so as to predict the mechanical behavior of machined FRPs more accurately.

In the present chapter, an attempt has been made to compile and discuss the studies carried out on surface characterization and damage due to machining FRPs, and their influence on the mechanical behavior. The effects of different machining techniques like abrasive disc cutting, conventional milling (Burr Tool and PCD), drilling, laser machining, and abrasive waterjet machining are presented. The objective of this work is to help the readers untangle the complex and ambiguous link between machining, surface integrity, and damage with mechanical behavior. The characteristic of surfaces and damage generated by various conventional and nonconventional machining processes are discussed in the next section. It is then followed by a section on mechanical behavior under different types of static and dynamic loadings. By the end of the chapter, readers will be able to understand the effect of machining on the mechanical behavior of composites and the main cause of these behavioral changes. After the conclusion, recommendations for future works are presented briefly which advises the researchers about the research gaps present in this subject today.

2 Damage Analysis and Characterization in Function of the Process of Machining

Machining is a process of material removal from a component to get a specific shape and geometrical tolerance; in this course of action, a new surface is created and ideally in the case of FRPs the integrity of new surface created is inferior to that of the original one. The new surface will have two types of alterations: physical/geometrical alterations due to creation of micro-geometry and plastic deformation, and chemical alterations due to frictional heating and phase changes. Both kinds of alterations are due to the virtue of type of machining process and its principle of material removal. In this section, physics of material removal and the characteristics of the surface formed

are discussed for some conventional and nonconventional machining processes along with different types of machining damage induced in the component. Also, concise information is provided on the topic of effect of machining parameters on surface characteristics and induced damage.

2.1 Conventional Machining

Conventional machining techniques are the techniques involving direct physical interaction between a tool and workpiece where the material is removed from the workpiece by forceful plastic deformation. Cutting, trimming, drilling, and milling are some of the most basic operations performed traditionally using a physical tool. In this section, we shall discuss surface characteristics and common damage occurring due to cutting, drilling, and trimming.

Abrasive Cutters (Abrasive Disc/Diamond Saw) ADS or disc cutter is the easiest and least sophisticated technique available for cutting composites. The machining does not require prior preparations and is manually handled. The major defects generated by ADS cutting process are distinctly visible in the form of streaks as shown in Fig. 1. Studies and observations by Haddad et al. [21] on cutting CFRP laminates show that these streak marks represent wrenched zones and are all along the tool trajectory. These streak marks are caused by the abrasive action of diamond grains which are randomly distributed on the cutting face of the abrasive diamond cutter (ADS). The geometry of the streaks solely depends on the size and shape of the diamond grits. The fiber orientation to the cutting direction has no effect on the occurrence of these defects unlike other conventional machining techniques and is strictly dependent only on the tool trajectory. The studies also show that the defects are observed on the entire machined surface and are all identical owing to the fact that they are independent of the fiber orientations. The surface characterization results obtained show a high degree of deviation with an average depth of about 30 μm. The authors relate the huge deviations in geometrical and surface attributes of these damages to the fact that feed speed is not constant as the operation is manually controlled and also variations in shape and size of diamond grits used in the cutter.

Drilling Drilling is the most principle and extensively performed machining operation on composites, especially for the aerospace structures, due to the need of fastening and riveting. This conventional technique of machining process has been lasting for years in the industry, and plenty of research has been done to optimize the process to obtain best quality damage-free holes. Even though numerous new tool materials and tool designs are available for drilling FRPs, complete damage-free operation is unattainable. However, the extent of damage can be minimized using precisely optimized machining conditions and parameters. FRPs are highly abrasive in nature which advances the phenomenon of tool wear and hence inducing numerous defects. For example, work conducted by Hejjaji et al. [8] on drilling of CFRP

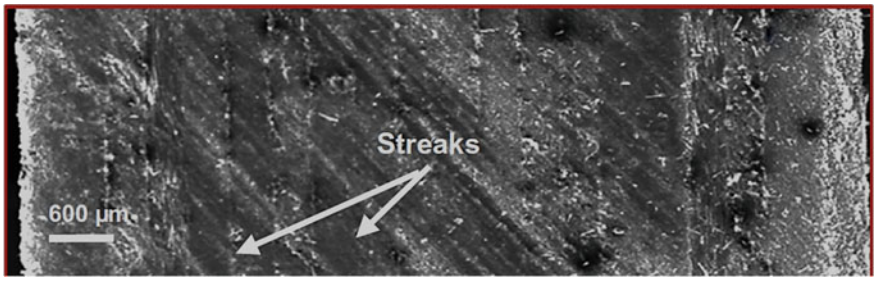

Fig. 1 SEM surface micrograph of CFRP machined by abrasive diamond saw showing streaks formed along the tool trajectory [21]

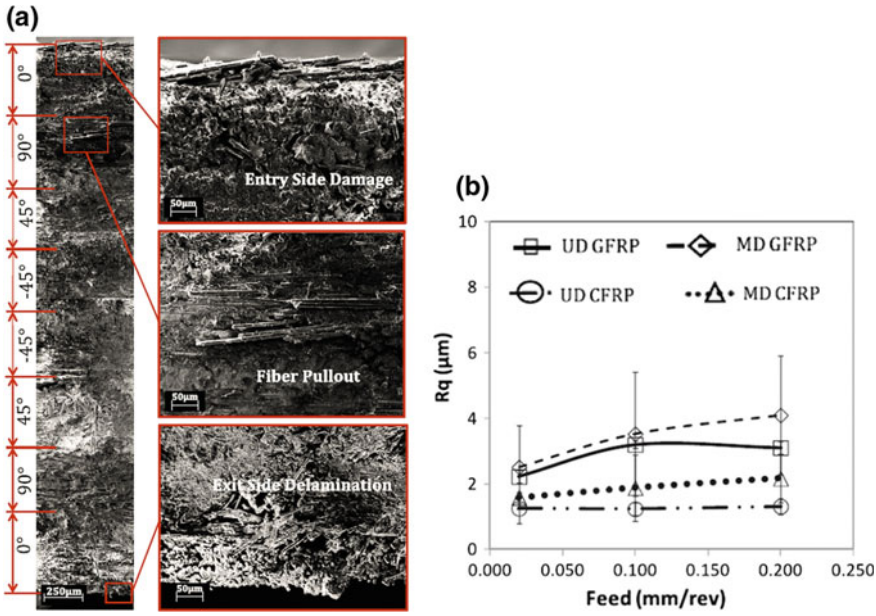

Fig. 2 **a** SEM image showing different types of damages in CFRP due to drilling. **b** Evolution of surface roughness with feed rate (mm/rev) [8]

and GFRP composites by polycrystalline diamond (PCD) drill bit reveals damages in the form of fiber peel up at the drill entry side, fiber pullouts in 45° and 90° plies, delamination at the drill bit exit side (cf. Fig. 2a), along with thermal effects like matrix degradation and smearing.

Drilling parameters, drill bit geometry, and cutting force were found to be the major factors that influence delamination and surface quality. Also, the surface roughness was measured for varying drilling parameters and it was found that roughness subsequently increased with increasing feed rate (mm/rev) (cf. Fig. 2b) which means that hole with good surface quality was obtained with a combination of lower feed

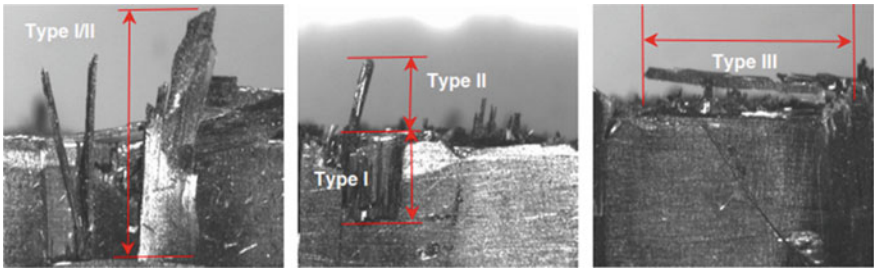

Fig. 3 Types of surface ply delamination [24]

rate and higher cutting speed, which is also acknowledged by other researchers like Eneyew et al. [7].

Trimming and Milling For conventional process like trimming and milling, the defects occurring can be classified into two categories, viz., defects occurring along the free edge and defects occurring on the machined surface.

Defects Occurring Along the Free Edge Delamination, a failure of the interface between consecutive plies, is typically observed on the top or bottom ply of FRP laminates because they are not supported from one side to pass the extreme machining forces. Layers of composite laminate are damaged by delamination under the action of forces induced in the axial direction by the cutting tool. As a result, delamination occurs in the form of fiber overhang and fiber breakout on the cut edges.

Colligan et al. [23] have classified delamination into three categories. Type I delamination is when fibers are broken and detached inward from the cut edge. Type II delamination is due to uncut fibers which protrude outward from the cut edge. Type III delamination is due to lose fibers partially fixed to the cut edge (Fig. 3). The combination of type I and II is frequently observed. The occurrence of delamination is highly affected by fiber orientation and this is reported by Colligan et al. for trimming CFRP (orientations PW, PX, 0°, 5°, 45°, 90°, 135°, 175° where PW and PX are plain weaves oriented at (0°/90°) and (45°/−45°), respectively) by measuring the depth of each type delamination. It is shown from Fig. 4 that the type I delamination is dominant in 90°, the type II in PX and 135°, and type III in 0° plies for PCD cutter. For the carbide cutter, type I delamination is commonly observed in 45° and 90° plies, while Type II is associated with PW, PX, 90° and 135. The Type III delamination is not noticed for carbide cutter. These results reveal that the extent of delamination depends on tool geometry, cutting forces, fiber orientation, and tool wear.

As discussed previously, the extent of delamination is expressed in the terms of length of the defect. The evolution of average delamination length varies based on the cutting conditions and machining length. An increase of cutting distance, an increase of feed rate, and a decrease of spindle speed give rise to increase in the average delamination length. Also, delamination length increases with an increase of theoretical chip thickness and tool wear, and both factors can be linked to raise

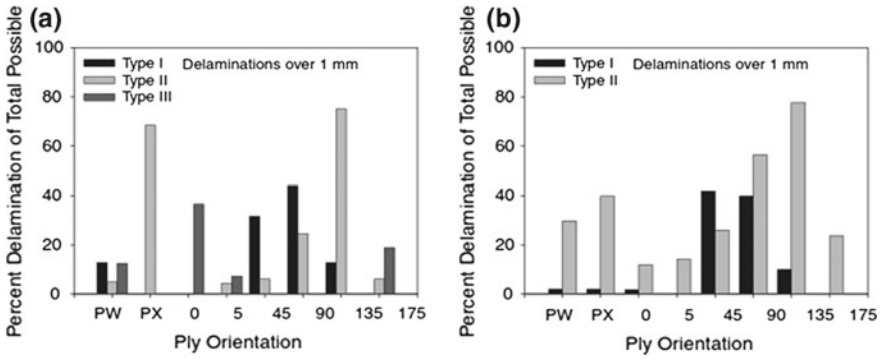

Fig. 4 Delamination frequency in relation to surface ply orientation for **a** PCD cutter and **b** carbide cutter [23]

cutting forces, which facilitates delamination. The influence of tool wear on the machining damage in the free edge of machined surface has been also reported in other studies [5, 16, 25, 26]. In addition to delamination, other defects observed on the machining edge are chipping, burrs, or uncut fibers. These defects are influenced by fiber orientations, tool wear, and cutting conditions.

Defects Occurring Along the Thickness of Machined Surface Trimming process of FRPs by cutting tools generates various kinds of flaws observed along thickness of machined surface. The occurrence of these defects is dependent on relative angle between the cutting and the fiber direction (θ), cutting parameters (cutting speed, feed rate, and depth of cut), tool wear, tool geometry (rake angle), and cutting configuration (down or up trimming/milling). In order to minimize these defects, the understanding of the mechanism of cutting is very important. The effect of fiber orientation on machining damage was found to be prime factor. Orthogonal machining of FRPs was carried out and to shed light on the chip formation [27–33]. Mechanism of material removal is categorized in three stages depending on fiber orientation. Figure 5 schematically shows the chip formation of unidirectional composite laminate. In case of fiber orientation $\theta = 0°$: if rake angle is positive, as cutting tool attacks the workpiece, an opening crack is created and propagating in the fiber/matrix interface (mode I fracture). The advancement of cutting tool (mode II) makes chip bending upward, and chips are completely formed when fractured. In the case of negative angle, chips are formed by buckling of the fiber under compressive load applied by the cutting edge. When cutting tool advances, chip is created without mode I fracture.

For positive fiber orientation larger than 0° and lower than 90°, the chip formation comprises fracture from compressive load induced shearing of fiber (mode II fracture) and sliding in the fiber/matrix interface (mode II fracture). Typically, surface finish in this stage is of superior quality because the fiber and matrix are sheared in the facilitated condition. For 90° fiber orientation and for negative orientations,

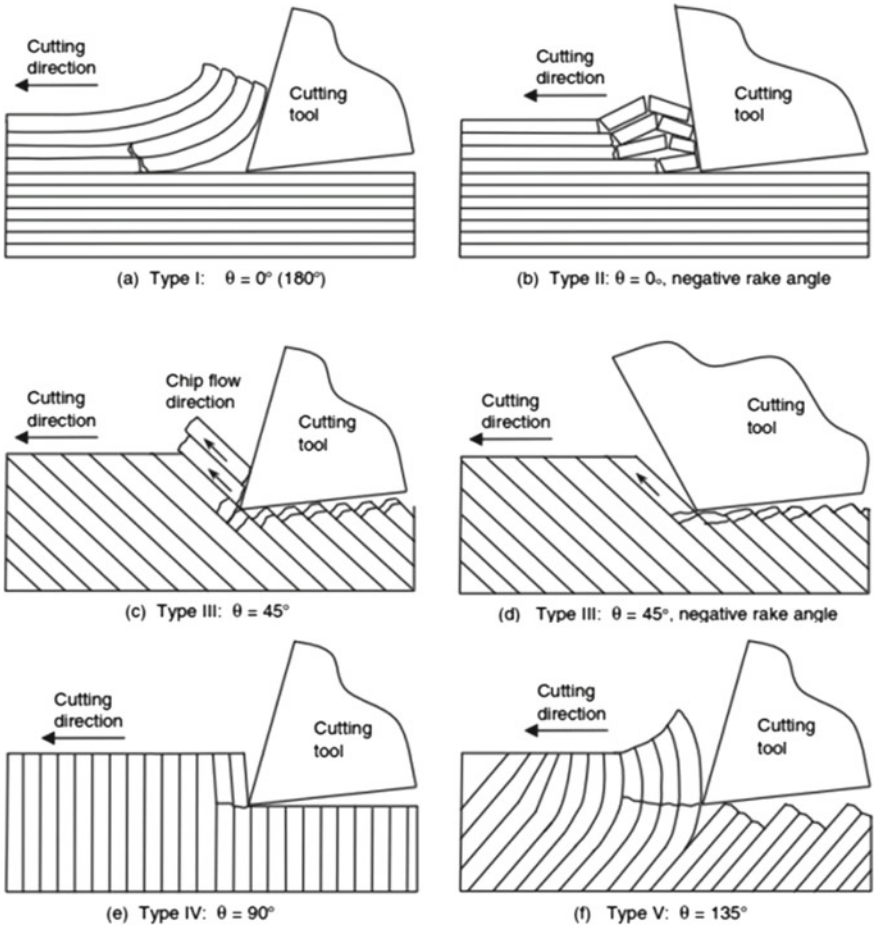

Fig. 5 Cutting mechanisms in the orthogonal machining of Graphite/Epoxy [28]

as cutting tools cut matrix and fibers (mode I fracture), a crack originates under tooltip, it penetrates into the subsurface along the fiber/matrix interface, followed by fiber shearing. Subsequently, chips are separated by the tool advancement (mode II fracture).

Scanning electron microscopy (SEM) images of PCD trimmed surface of unidirectional CFRP laminate describing chip formation as well as induced damage have been presented in series of research works [28, 30]. It is seen that the 0° orientation exposed fibers are visualized with a limited level of matrix covering. This is due to the lifting of fibers from matrix/fiber interface by shearing and buckling. For layers in which fiber orientation is larger than 0° and lower than 75°, the degree of redistributed matrix increases with increasing fiber orientation. Chip formation of multidirectional laminate is similar to that of unidirectional laminate which was

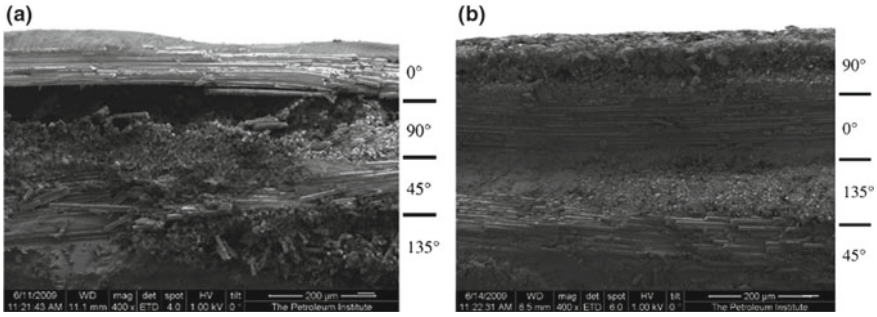

Fig. 6 SEM images of trimmed surface of multidirectional graphite/epoxy laminate, **a** V_c = 300 m/min, $V_f = 2.54$ m/min, **b** $V_c = 100$ m/min, $V_f = 10.16$ m/min [26]

documented in [29, 30]. However, machining defects occurring in 90° and 135° are less severe than on the trimmed surface of unidirectional material due to the support provided by adjacent plies.

It can be said that chip formation during machining FRPs subsequently depends on fiber orientations which is a critical factor having decisive effect on surface quality. Fiber orientations can be associated with other parameters to create many kinds of defects in both surface and subsurface. Figure 6 gives an example for effect of cutting conditions and the local fiber orientation on machining damage when multidirectional CFRP specimens were machined by burr tool [26]. It is apparent that machined surface obtained by trimming with low theoretical chip thickness [high cutting speed (V_c) and low feed rate (V_f)] offers small level of damage. Less machining damage is observed in locations of 0° and 45° layers, while defects in the shapes of pits, subsurface cracks due to out-of-plane displacement appear in the 90° and 135°. Regarding the microstructure of machined surface created by trimming at high theoretical chip thickness (low cutting speed and high feed rate), pitting, fuzzing, delaminating, and fiber pullout is extensively noted. Severe delamination and fiber pullout occur in 90° ply, and fuzzing is observed substantially in 135° ply.

Tool geometry also influences occurrence of machining defect during FRP trimming. The effect of rake angle on subsurface damage can be seen in Fig. 7. It is evident that the surfaces machined by cutting tool with negative and 0° rake angle exhibit more irregularity than those obtained by cutting tool with positive rake angle [34]. Significant pitting characterizes the machined surface in the first case; lower degree of irregularity is seen in the subsequent case. In addition to fiber orientations, the brittleness of matrix material and the bond strength between matrix and fiber are also important factors for occurrence of cracking and debonding defects.

As the trimming progresses, the contact between cutting edge and workpiece surface accelerates the friction and tool wear. The abrasiveness of fiber and low thermal conductivity of matrix material combined with low thermal conductivity of tool materials can make machining temperatures to rise rapidly. As a result, thermal damage is initiated in the machined surface. Mechanical and thermal surface

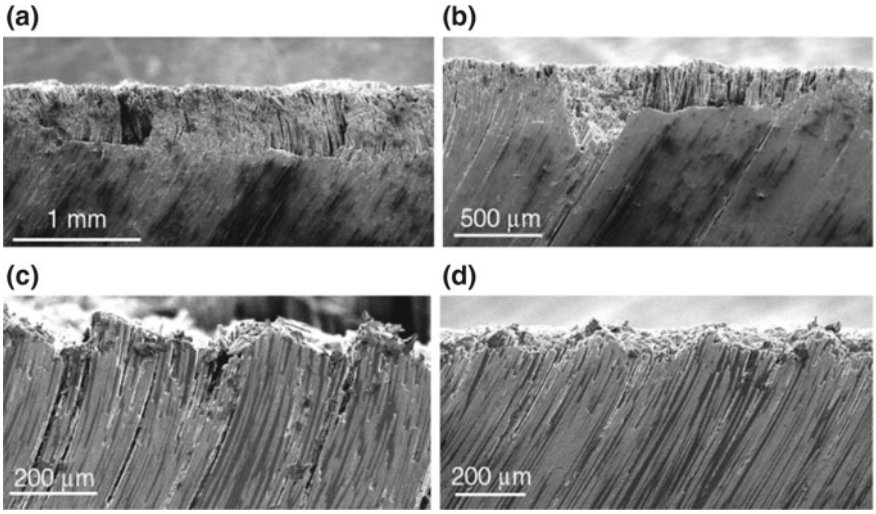

Fig. 7 Microstructure in the subsurface damage ($\theta = 120°$) with various rake angles, **a** rake angle = −20°, **b** rake angle = 0°, **c** rake angle = 20°, **d** rake angle = 40° [34]

defects are presented in Fig. 8 [35, 36]. Concerning the effect of tool wear on the creation of machining defects, minimum fiber pullout is visualized in Fig. 8a when cumulative cutting distance is 50 cm. In contrast, the higher level of fiber pullout is explicitly noted in whole thickness of machined surface at cutting distance of 2 m with the same cutting condition (cf. Fig. 8b). The increase of cutting distance corresponds to increase of cutting edge radius due to tool wear, which makes the trimming more difficult. However, at this cutting condition, mechanical defects dominate due to cutting temperature inferior to the glass transition temperature ($T_g = 187°$ for studied composite materials). When trimming is carried out with high cutting speed (V_c) and cutting distance is longer ($L_c = 2$ m), severe thermal damage occurs on the trimmed surface (Fig. 8c). At low feed speed (V_f), higher level of matrix degradation is observed (Fig. 8d). These defects are fiber pullout, matrix degradation, and wrenched areas. Machining temperature is a critical factor for initiation and propagation of machining damage in this stage. A low feed speed (125 mm/min) generates high friction, thereby raising the temperature above glass transition temperature. This initiates softening of the matrix material thus causing pitting and facilitating fiber pullout. Although at high cutting speed (1400 m/min) and low feed speed corresponding to small theoretical chip thickness, cutting edge radius and machining temperature become more important.

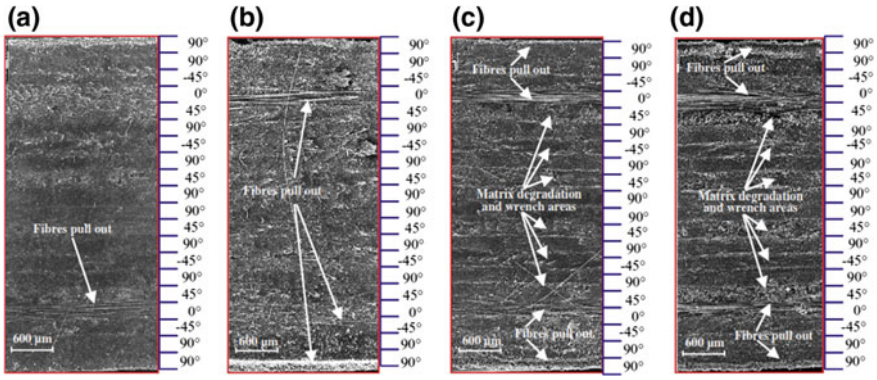

Fig. 8 SEM observation of surface damage for different cutting parameters **a** $V_c = 700$ m/min, $V_f = 500$ mm/min, $L_c = 50$ cm, **b** $V_c = 700$ m/min, $V_f = 500$ mm/min, $L_c = 2$ m, **c** $V_c = 1400$ m/min, $V_f = 500$ mm/min, $L_c = 2$ m, **d** $V_c = 1400$ m/min, $V_f = 125$ mm/min, $L_c = 2$ m [36]

2.1.1 Quality of Machined Surface

Damage makes machined surface rougher and affects the geometric precision of composite parts substantially. For this reason, the surface quality of machining composite needs to be characterized using reliable parameters. Additionally, the machined surface damage generated during machining creates stress concentration sites such as peaks, valleys, and microcracks, which are potentially degrading the mechanical performance [2]. To characterize the machined surface of composites, roughness criteria (Surface roughness, R_a) have been utilized commonly in industry.

Surface quality of machined FRPs is influenced by cutting parameters, fiber orientation, tool wear, and tool geometry as discussed earlier. The effect of cutting speed and feed speed on surface roughness can be seen in Fig. 9 [37]. An increase of feed speed and a decrease of cutting speed lead to augment surface roughness for both R_a and R_z. These can be explained by the fact that the increase of chip thickness due to augmentation of feed speed increases or lower cutting speed makes machining more difficult and as a result the rougher surface quality is obtained.

However, when studying the effect of cutting speed and feed rate on surface roughness of multidirectional CFRP at high cutting speed condition, Haddad et al. showed contrary results [36]. According to their results, machining CFRP at high cutting speed and low feed rate, more friction is generated which will accelerate the tool wear and causes cutting temperatures to increase giving rise to inferior surface quality (Fig. 10). If the temperature is greater than the glass transition temperature, the matrix is softened, which facilitates pitting and fiber pullout. This phenomenon is also observed in research work of Konig et al. [38] when cutting speed reaches over 1130 m/min.

Surface roughness increases with increasing the wear of cutting tool. This is described in the work of Ghidoshi et al. [16] when machining unidirectional carbon/epoxy (Fig. 11). Tool wear in this case is assumed that increase of cutting dis-

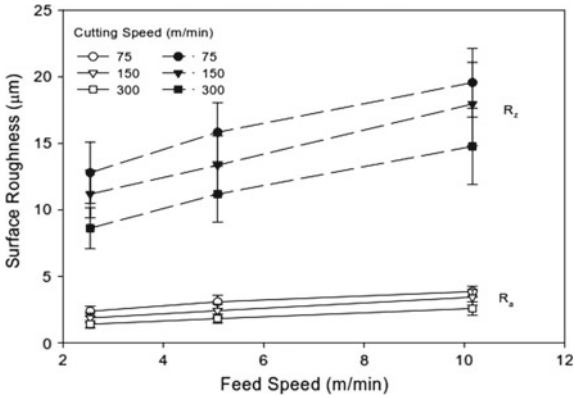

Fig. 9 Evolution of surface roughness versus feed speed when machining multidirectional CFRP [37]

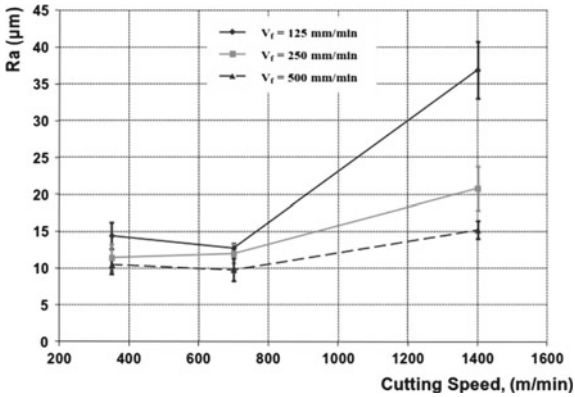

Fig. 10 Effect of cutting parameters on surface roughness (R_a) when machining CFRP at high cutting speed [36]

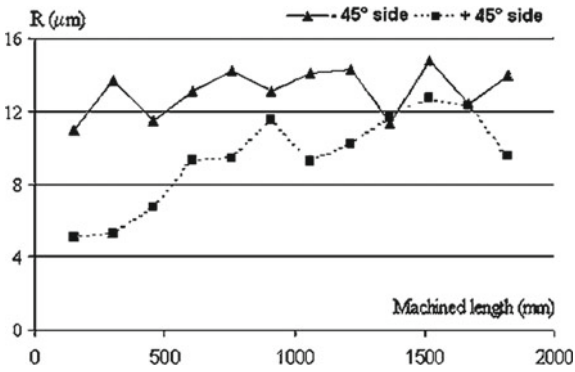

Fig. 11 Evolution of surface roughness as a function of machining distance for the −45° and +45° sides of the carbon/epoxy specimens [16]

tance leads to increase in cutting edge radius. As a result, machining is more difficult and a rougher machined surface is obtained. The effect of tool wear in terms of cutting distance has been also observed in research works of several authors such as Janardhan et al. [24] or Haddad et al. [36].

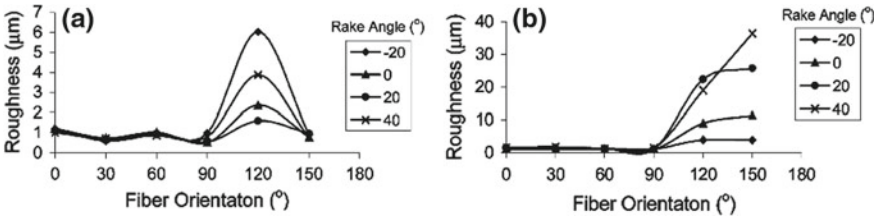

Fig. 12 Effect of fiber orientation on surface roughness. The depths of cut were **a** 0.001 mm and **b** 0.05 mm [34]

Janardhan et al. have reported that surface quality is also dependent on trimming configuration, which is demonstrated by machining CFRP by burr tool with cutting speed of 100 m/min combined with two values of feed rates (2.54 and 5.08 m/min). The surface quality obtained by down milling is poorer when compared to that of up milling. This difference can be linked directly to the mechanism of chip formation in which fiber and matrix are primarily sheared in up milling. Meanwhile, buckling and cracking occur in case of down milling [24]. The same results are also discussed for surface roughness when machining CFRP with straight flute PCD cutter [25].

Wang et al. [34] investigated the effect of tool geometry and depth of cut on the surface roughness when orthogonal machining of unidirectional laminate was carried out. Based on their research, surface roughness is similar in case of fiber orientation varying between 0° and 90° regardless of the value of depth of cut (0.001 and 0.05 mm). However, considering fiber orientation between 90° and 150°, the difference of surface roughness is clear when machining was carried out with previously mentioned depth of cut (Fig. 12).

Surface quality is one of the important factors utilized to examine the machinability of composite laminates. Surface roughness directly relates to tolerance of final dimension of composite parts in assembly systems. Hence, it also effects on the mechanical performance. In the next section, the impact of surface quality and induced damages on the mechanical behavior will be discussed.

2.1.2 Dust Generation During Conventional Processes

The generation of defects mentioned above is accompanied by the emission of fine dust particles of machined fiber and matrix with extremely small diameter and sharp edges. These particles are dispersed and suspended in the air and can be inhaled by machine operators. They have the potential to damage breathing system and cause toxic irritations, and are carcinogenic. The increasing usage of composite materials in industry leads to more frequent exposure of fine dust particles. It is necessary to minimize the emitted particles in the air to protect operators from the health problems mentioned. Surprisingly, these issues of dust particles resulting from machining of composite materials have been ignored from long time, and there are very few related

studies [39, 40]. Thus, further studies of dust generation during machining composite materials are imperative and should be earnestly considered by research communities.

Haddad et al. [39] have analyzed the influence of tool geometries and cutting parameters (cutting speed and feed speed) on dust particles generated during trimming laminated composite materials (CFRP) at two ranges of cutting speed, i.e., standard and high cutting speed. For standard cutting speed, three kinds of cutting tools including burr tools, coated and uncoated, and four flute end mills were utilized, while only uncoated burr tool was used at high cutting speed. The results showed that at standard cutting speed, tool geometries influence on number of harmful particles emitted, and the dust particles generated by four flutes end mills were superior to those generated while using both coated and uncoated burr tools. Moreover, it was found that coating has little impact on the generation of dust particles. Regarding the influence of cutting parameters, it was said that the number of harmful particles increases with decreasing feed speed and increasing cutting speed in both cases of cutting speed ranges. No explanations for phenomena previously mentioned were given by the authors.

Recently, Nguyen-Dinh et al. [40] have analyzed the impact of cutting parameters (cutting speed, feed rate, radial depth of cut) and tool wear on the number of harmful particles generated during trimming of CFRP specimens (using PCD tools). The results reveal that an increase in cutting speed and/or a decrease in feed rate leads to increase the level of number of harmful particles. This trend is similar to that documented by Haddad et al. [39]. Besides, the number of harmful particles also decreases with increasing cutting distance. It is found that the rougher surface is associated with the bigger size of dust particles. As known, dust particles generated during machining of composite can be inhaled by operators in the machining area. Hence, it is necessary to minimize dust particle emitted in the air. To do this, it is better to obtain particles of bigger size, as they drop off soon after getting detached from the composite specimen without dispersing into the air around. It was found that machining with high feed rate reduced number of particles in air. However, operating with these parameters to reduce dust emissions can give rise to much crucial problems like increased tool wear cutting forces, temperature, etc. To strike a balance, a fundamental study about the interacting influence between dust particle and machining damage should be more carefully conducted.

2.2 Nonconventional Processes

2.2.1 Abrasive WaterJet (AWJ) Machining (Trimming and Milling)

In this technique, pressurized water is mixed with abrasive particles of specific size and forced through a minute nozzle forming a high-velocity waterjet; this fine high-velocity waterjet carrying abrasive particles is directed on to the workpiece. The hard abrasive particles impact the workpiece surface, and material is removed by the mechanism of erosion, which varies accordingly for ductile and brittle workpiece

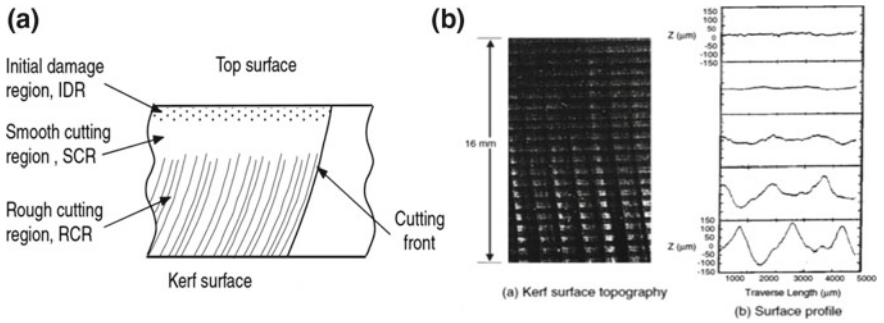

Fig. 13 **a** Schematic diagram showing different surface regions on the kerf wall of AWJ cut graphite/epoxy composite. **b** Kerf wall and corresponding roughness profiles [3]

materials. However, as FRPs are brittle, the material removal happens by erosion and brittle fracture. This process is widely used for trimming FRPs, and recently it is also used for controlled depth milling (pocket milling) of FRPs.

The AWJ trimming studies on graphite/epoxy composite by Arola et al. [3] demonstrate that cut surfaces have three distinct characteristic regions, viz., initial damage region (IDR), smooth cutting region (SCR), and a rough cutting region (RCR) as shown in Fig. 13. It is important to mention that the size and extent of these three regions are strongly influenced by the cutting parameters of the process as well as the nature of the machined material. Indeed, if we refer to the work of [3], it was mentioned that, for a particular material, the optimization of the AWJ machining parameters is done such a way that the smooth cutting region (SCR) extends to full thickness of the specimen. In fact, the creation of IDR at the top of the kerf is because of the low-density abrasive particle concentration at the boundary of the jet bombarding the surface. The surface is characterized by microscopic craters formed due to the impact of singular particles and abrasive wear tracks. Standoff distance is the most substantial parameter that favors the creation of IDR, while the other parameters have negligible effect. In general, machining with low standoff distance exhibits smaller IDR, whereas higher standoff distance favors the augmentation of the size of the damaged region. Surface waviness may appear haphazardly, due to irregularities in the jet traverse speed, dynamic oscillations of the nozzle, unstable jet pressure, and abrasive feed rate. Authors also mention that the surface roughness is mainly due to microscopic wear tracks initiated by the individual abrasive grits impacting the kerf wall. Hence, the size of the abrasive grit particles determines the size of the wear tracks, which means that larger particles give rise to higher surface roughness and waviness. The principal orientation direction of the wear tracks becomes more random with increasing depth of cut and a decreasing in abrasive mass flow rate. The rough cutting region is characterized by striations marks along the particle flow path. The study shows that extent of RCR can be reduced by higher jet pressure, lower cutting speeds, and larger abrasive particle size decreasing grit size as smaller particles have less cutting energy.

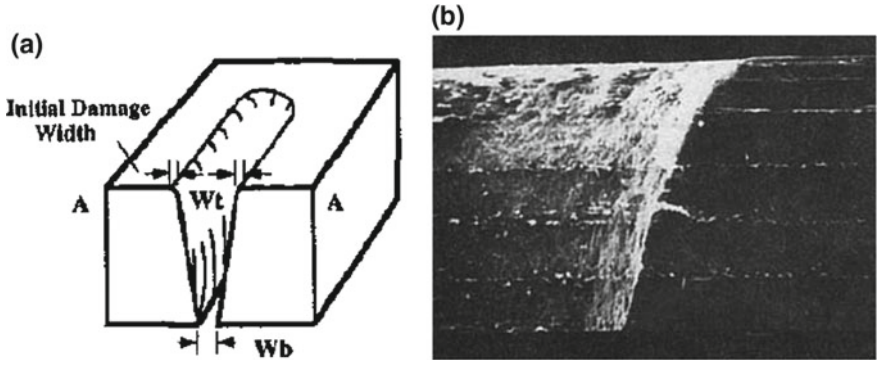

Fig. 14 **a** Diagram showing the geometry of a converging kerf taper. **b** Entrance kerf damage in graphite/epoxy specimens from Arola et al. [3]

As any other machining process, AWJ cutting and milling also has various induced defects, and following are the process-induced defects in FRPs machined by AWJ process.

Kerf Taper AWJ trimming can lead to create tapered edges on the kerf (Fig. 14). The kerf width and geometry is completely determined by the structure of the AWJ and the machinability of the workpiece. The structure of the AWJ depends on jet pressure, focusing tube diameter and nozzle diameter. The jet tends to spread out as it comes out of the focusing tube, and the velocity of the inner region of the jet is higher than the outer region and is always convergent, thus giving rise to a tapered cut. The radial jet velocity distribution is the main factor accounting for the kerf to taper. Studies conducted by Arola et al. [3] reveal that the prime factor generating the kerf taper is the Standoff distance, which is the distance from the nozzle to the surface of the workpiece. It is seen that as the distance increases, entrance kerf width also increases; it means that there is more material removed at the entrance than the later portions, hence, giving rise to a tapered edge. Kerf taper increases with jet traverse speed as cutting time decreases and reduces the amount of material removal. Using a high jet pressure, lower jet traverse speed and closer standoff distance can minimize kerf taper to a great extent.

Delamination It is one of the most frequently occurring defects when machining FRP composites. Abrasive waterjet machining is no spare of this defect. In studies conducted by Shanmugam et al. [4], it was found that the crack tips were generated due to the impact of shock wave of the waterjet at the initial cutting stage, while delamination is a result of water penetration into the crack tips that promotes water wedging and abrasive embedment. Once the crack tips are formed due to the shock waves, the crack propagation happens due to continuous stress acting on the crack tips. When the jet impinges on the workpiece, material removal occurs due to erosion phenomenon at the active region of a jet giving rise to a kerf. Apart from this, the jet expands in the eroded spaces on the kerf walls, thereby increasing secondary

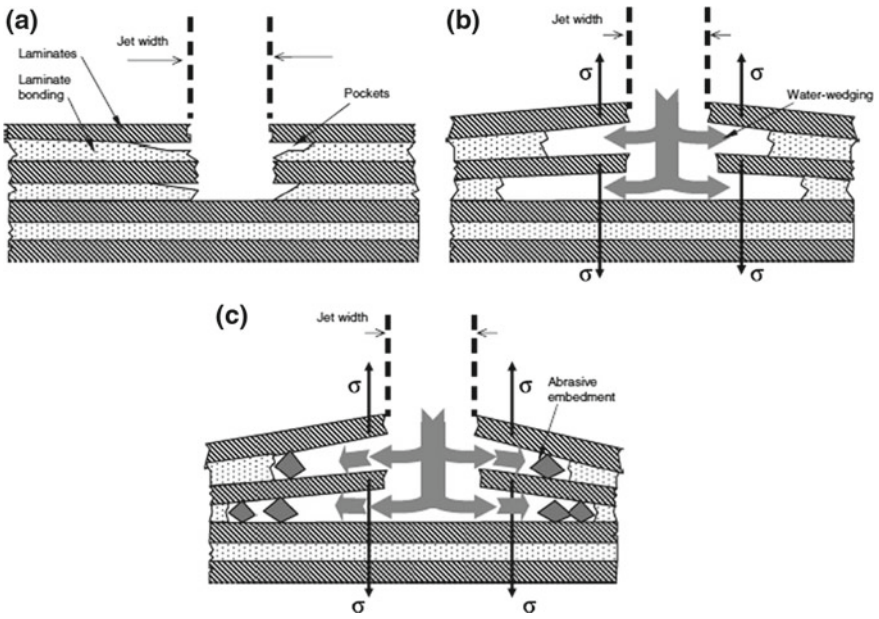

Fig. 15 Schematic view of the delamination mechanism during trimming with AWJ: **a** Damage initiation, **b** water wedging, **c** abrasive grit embedment between the plies [4]

stresses; this further opens up the crack. Finally, abrasive particles enter the crevices and their shearing action gives rise to delamination (Fig. 15).

The shearing action of the abrasive grits plays a dominant role in the material erosion mechanism. With the delay in introducing abrasive particles in jet stream (Fig. 16b), the workpiece is eroded mostly by the shockwave impact of the waterjet that results in an unclear cut with eroded spaces in between the plies of the laminate. The low material removal rate allows enough time for the cracks to initiate by the shock wave impact of the waterjet. The crack tips formed allow the penetration of water inside which develops a wedging action, triggering the propagation of the cracks. Later, the abrasive grit particles are introduced in the cracks which embed in between the plies and lead to further wedging action. The embedment of the abrasive particles also keeps the crack open [4].

Grit Embedment The hard abrasive particles hit the workpiece with a very high velocity, and if the workpiece is very soft compared to the abrasive, they get embedded on the surface. It has been reported that trimming and milling with AWJ favors the embedment of abrasive grits on the surface of the workpiece which can be responsible for the reduction in stiffness/strength of components in service [3, 4, 9] (Fig. 17).

The material removal in AWJ machining is due to the impact of numerous number of individual abrasive grits suspended in the pressurized water. Hence, this process

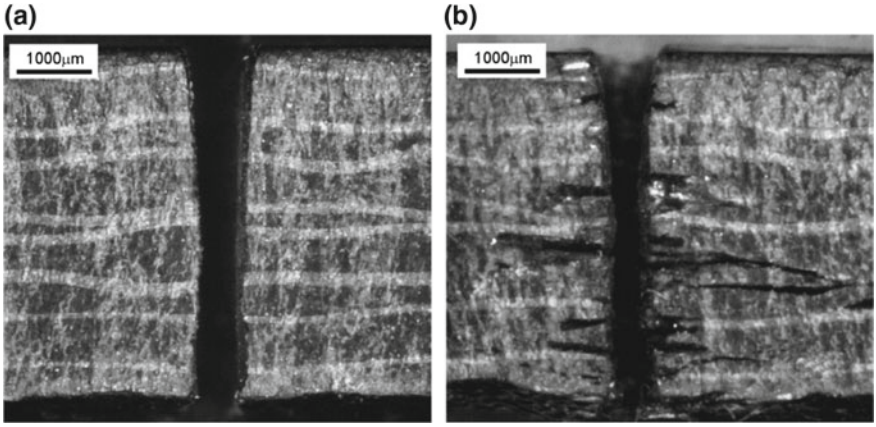

Fig. 16 Cross sections of workpieces machined at same jet pressure but **a** introducing abrasive particles without delay and **b** delay of 3 s [4]

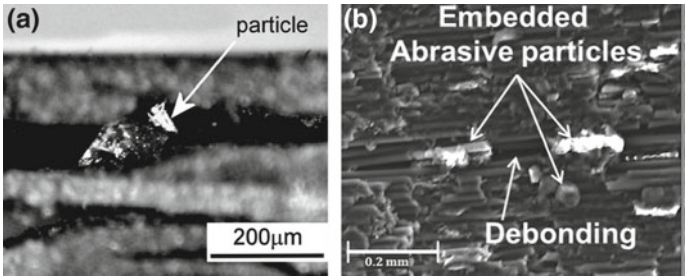

Fig. 17 Abrasive particle/s embedded in FRPs during **a** Trimming, Shanmugam et al. [4] and **b** Milling, Hejjaji et al. [9]

generally induces compressive residual stresses; theoretically, this would be expected to contribute to good fatigue behavior. However, in reality, the machined surface contains embedded abrasive grits and they act as stress concentration points; this phenomenon combined with high workpiece roughness significantly brings down the fatigue performance. Apart from this they also initiate crack growth by keeping the crack open leading to delamination in trimming or matrix/fiber debonding in milling.

The extent of abrasive particle embedment in milling depends on the configuration of milling. Studies by Fowler et al. [41] on AWJ milling of titanium alloy articulate that the high levels of abrasive particle embedment are seen during forward milling, whereas backward milling results in lower levels of abrasive particle embedment. However, high jet traverse speeds and milling direction have no strong influence on abrasive particle embedment. Also, slight rise in level of particle embedment is seen with increasing jet impingement angle.

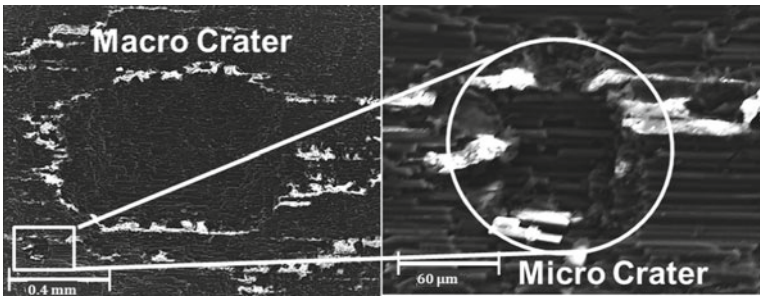

Fig. 18 AWJ milled surface showing macro- and micro-craters [9]

Craters and Striations During AWJ trimming of FRPs, satiation marks are seen at the exit side of the jet (cf. Fig. 13b); they are basically the wear tracks of slurry of thick abrasive particles, removed material, and water. The tracks become prominent at high traverse speeds [3]. 3D topography and microscopy observation conducted by Haddad et al. [21] indicate that striations appear at the exit of the machined surface; however, the craters are all over entire machined surface. According to Wang [42], the magnitude of striations decreases with the increase of the jet pressure and decreasing feed speed. The defects are equally spread across the machined surface; hence, AWJ specimens have least standard deviation of roughness.

In case of AWJ milling, periodic macro-craters are observed all over the machined surface when high jet pressure is employed and micro-craters are present in plentiful all over the surface (cf. Fig. 18). Micro-craters are formed due to the brittle failure during the impact of abrasive particles. Increasing jet pressure creates more of these micro-craters which in turn increase the surface roughness [9].

2.2.2 Laser Machining (Trimming and Milling)

Laser machining offers a high degree of flexibility and scope for automation along with low operation noise and dust levels, high cutting speeds. It can be used for almost any kind of materials. Particularly in the aerospace industry, laser machining is employed for trimming and hole making. This process uses intense heat to remove material by ablation where the material literally vaporizes or sublimates [6, 8]. We know that FRP composites comprises two different material systems, viz., matrix and fibers having dissimilar thermal properties. The effect of laser beam on matrix and fiber is different, which is the root cause of all defects in laser machining.

In the work of Hejjaji et al. [8], severe matrix recession (i.e., matrix loss due to vaporization) was observed wherein bare fibers were exposed in the case of CFRP laminates as shown in Fig. 19b. SEM analysis of machined specimens has shown that the fibers are cut by ablation and the matrix is evaporated near the hole wall surface for CFRP specimens. Matrix loss and degradation at beam entry and exit sides are

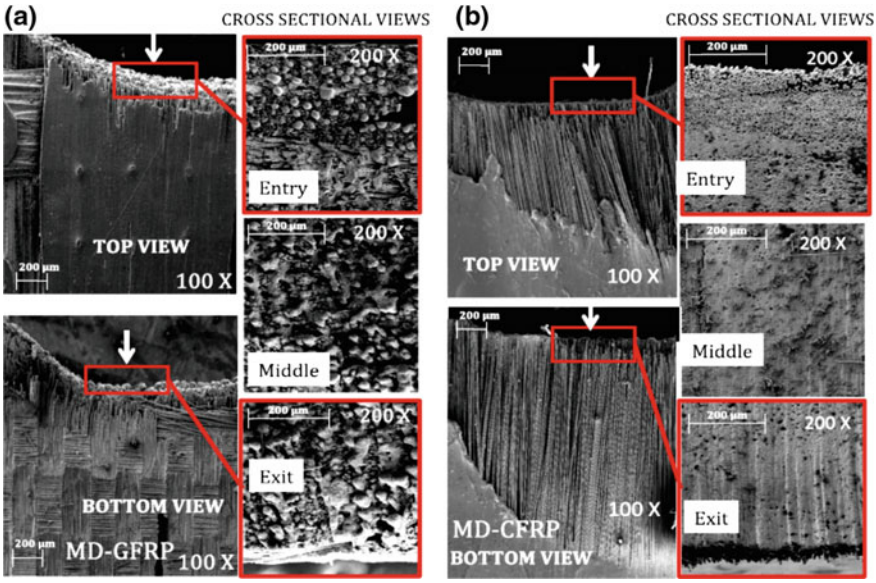

Fig. 19 SEM images for laser machined **a** MD-GFRP, **b** MD-CFRP [8]

also evident, and matrix loss is higher at the exit side of the beam. The extent of matrix loss is less in case of GFRP specimens as compared to CFRP specimens. In GFRP specimens, distinct globules due to re-solidification of melted glass can be identified along the hole walls (cf. Fig. 19a). No such solidification effect is seen in the CFRPs since C-fibers vaporize in the form of CO_2 without leaving any residue. The surface analysis shows that the GFRP laminates [both unidirectional (UD) and multidirectional (MD)] exhibit a rougher surface compared to CFRPs (both UD and MD), which is due to the phenomenon of re-solidification of melted glass fibers. Also, the layup sequence does not contribute to the variation of roughness. The study also reveals that there is a minute increase in the surface roughness which increases cutting velocity.

Leone et al. [6] have conducted milling operation on CFRP composites using laser machining. They demonstrate that the vicinity of the pocket wall and also the milled surface are affected by heat. Matrix burnout, uncut fibers, and charring defeats are shown in Fig. 20. The length of the heat-affected zone (HAZ) increases with decreasing beam traverse speed and increases with number of passes. The milling path strategy is equally important; overlapping of beam paths has shown severe matrix burnout and charred regions.

The work of Herzog et al. [18] describes the trimming quality in the terms of length of heat-affected zone (HAZ). The work revealed that the HAZ does not just depend on the process parameters but also the source and type of laser beam. It was concluded that pulsed Nd: YAG laser processing produced the best quality cuts with least HAZ for optimized machining parameters (cf. Fig. 21).

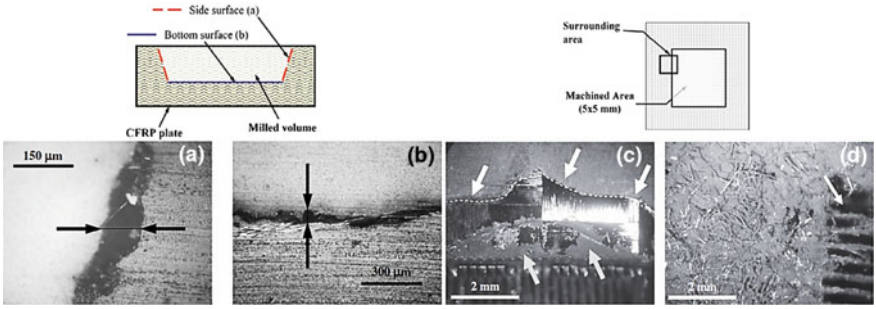

Fig. 20 Defects in laser milling of CFRP; Heat-affected zones **a** Side wall of the pocket. **b** Bottom of milled volume. **c** Matrix recession (white arrow) and charred plies (gray arrow). **d** Incoherent burnt matrix and fiber fragments, fiber pullout on the lateral machined surface (Arrow) [6]

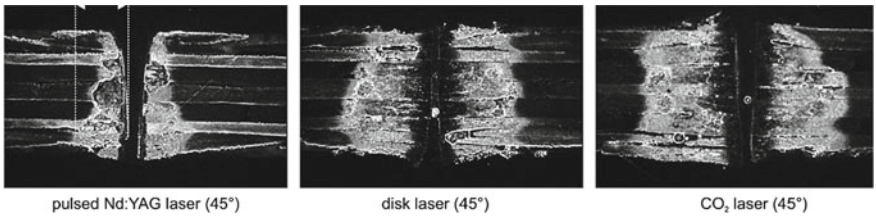

Fig. 21 Cross sections of CFRP samples processed using different kinds of laser beams [18]

3 Influences of Damage Induced on Mechanical Performance

Surface quality is one of the important factors utilized to examine the machinability of composite laminates. Surface roughness directly relates to tolerance of final dimension of composite parts in assembly systems. Hence, it also affects the mechanical performance during service. In this section, the impact of machining-induced damage characterized by surface roughness will be presented in relation to mechanical tests.

3.1 Tensile Test

Ghidossi et al. [25] had examined the impact of machining damage on tensile behavior of glass/epoxy unidirectional specimens obtained by side milling which is conducted in up (U) and down (D) milling configuration. The specimens were cut by polycrystalline diamond tool (PCD) and tested according to ASTM standards. Composite materials are inclined at 15° and 45° corresponding to four categories of each direction, e.g., $+\theta$°U, $-\theta$°U, $+\theta$°D, $-\theta$°D. SEM images of machined surfaces showed

that $+\theta°$U and $-\theta°$D fiber configurations exhibited very less damage induced. On the other hand, many kinds of surface and subsurface defects observed in SEM images in $-\theta°$U and $+\theta°$D fiber configurations such as uncut fibers, matrix cracking, and matrix/fiber debonding. In order to study the influence of damage, machined surface was characterized by average surface roughness (R_a). It was seen that the tensile strength decreases with increasing surface roughness of tested specimens for +15° fiber configuration. However, no effect of surface roughness on the tensile strength was seen in the case of other orientations. For the 45° layer orientations, influence of surface roughness on ultimate tensile strength exhibited arbitrary trend for all of the fiber configurations. From this, it is clear that the quantitative parameter, R_a, does not seem to relate qualitative investigation (SEM images) of surface quality. To interpret the independence of tensile strength on surface roughness, the authors gave two reasons. First, many small craters or any damage cannot be exactly reflected by the roughness stylus. Second, the incapability of detecting subsurface defects of roughness stylus is also one of the important reasons. Two reasons above give a conclusion that surface roughness is not suitable parameter for characterizing surface quality of composite machining.

In order to obtain good relationship between damage and the degradation of mechanical performance, the authors suggested two new damage criteria based on observed defects. The "percentage of damaged surface" and "depth of fiber/matrix debonding" criteria corresponding to +15°D and +45°D, −45°U, respectively. An increase of percentage of damaged surface leads to a decrease of ultimate stress. For the second criterion, the ultimate stress reduces substantially with the increase in the depth of subsurface cracking.

The influences of machining damage on tensile stress were also inspected by Sheikh-Ahmad et al. [37]. Multidirectional carbon fiber/epoxy laminate panels comprising 10 plies of plain weave fibers were trimmed by burr tools with up milling configuration. The trimming quality was characterized by ten-point mean surface roughness (R_z) and the maximum Type I delamination depth (TI_{max}). The classification of delamination and the definition of TI_{max} are presented in Sect. 2.1. It was seen that, with increase in TI_{max}, there was a reduction in failure. As a consequence of their study, it may be said that the proposed parameter "max Type I delamination depth" is quite successful to characterize machining damage and well correlates to the degradation of failure stress. Nevertheless, there are some types of observed delamination (Type II and III delamination) which also effect on the mechanical performance, while the proposed parameter has only taken into account the Type I delamination. This explains the high standard deviation failure stress with respect to TI_{max}. It is essential to take a different approach for this problem. The effect of ten-point mean roughness R_z, on the failure stress, exhibits the similar trend to that of TI_{max}. The standard deviation of failure stress in this case is also high. Besides, based on the description of tested specimen preparation, it is noted that the free length of tensile specimens was shorter than those recommended by standard.

3.2 Compressive Test

Squires et al. [43] conducted several experiments to study the effect of surface quality of machined unidirectional carbon/epoxy laminate on compressive stress. The specimens were machined using a diamond tipped blade with cutting conditions called method A and B. The difference between them is that common lubricant was mixed with water as the coolant in method A; meanwhile, common water from the main supply was used for method B. The dimensional precision values of method A and B were 0.05 and 0.5 mm, respectively. The specimens were machined and tested according to ASTM D 695M standards. Specimens machined by method A exhibit identical surface finish, a stable, and higher compressive strength. On the other hand, the surface roughness of specimens machined by method B drift between 3.5 and 22 μm. An increase in surface roughness leads to reduced compressive strength. For example, when surface roughness varies from 4 to 22 μm, the reduction of compressive strength is approximately 40%. Hence, according to these results, it can be concluded that surface roughness has significant influence on compressive strength of unidirectional composite laminates. However, it is noted that the use of water as coolant in this study is not a common procedure in industry, especially in aerospace field. Furthermore, unidirectional composite laminate is only used for studies and not in real applications. Both these conditions reduce the impact of this result. So, studying the effect of surface quality on the compressive properties of multidirectional laminate with dry trimming is necessary.

Haddad et al. [22] had investigated the effects of surface quality characterized by average surface roughness on compressive strength of CFRP composite T700/M21-GC with stacking sequence [90°/90°/−45°/0°/+45°/90°/−45°/90°/+45°/90°]s. The specimens were trimmed by burr tool to get the final dimension for compression test which was conducted according to the standard AFNOR NF T 51-120-3. The evolution of compressive strength versus surface roughness is shown in Fig. 22.

Altogether, a reduction of 29% of compressive strength was observed when surface roughness decreased from 4 to 29 μm. The compressive strength values obtained for different roughness values were categorized into three stages, where relation between compressive strength and surface roughness was associated with machining temperatures. In the first stage, specimens offer highest compressive strength when machining temperatures were lower than 130 °C. Compressive strength of specimens is not dependent on surface roughness when exhibiting stable trend in the second stage, where cutting temperatures varied from 130 °C to glass transition temperature ($T_g = 187$ °C). At the final stage, the compressive strength is lowest in which machining temperatures were higher than T_g. It can be said that surface quality characterized by average surface roughness significantly influences on the compressive strength of multidirectional composite laminates. This work suggests that apart from surface roughness, there is a significant influence of thermal damage that affects the compressive strength.

During trimming of FRPs, machining damage induced is typically different for each machining process as earlier in Sects. 2.1 and 2.2. Although machining defects

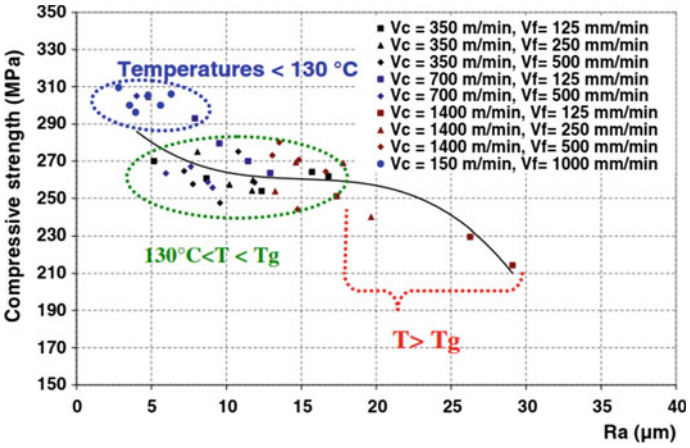

Fig. 22 Evolution of compressive strength versus surface roughness for various cutting conditions [22]

are different, machined surface of these processes is identically characterized by the same criterion (roughness criteria). Hence, comparing the influence of surface quality of each machining process is important. Haddad et al. [22] had conducted experiments to study the effect of surface roughness on compressive specimens which were machined by conventional cutting tool (burr tool), abrasive waterjet (AWJ), and abrasive diamond saw (ADS). The composite materials cut by three methods are the same to those trimmed by burr tool as described in previous paragraph. The influence of surface roughness on specimens machined by various machining processes is shown in Fig. 23. It is observed that with the same value of surface roughness, 6.4 μm, AWJ specimens with the small standard deviation exhibit higher, 21 and 15% of compressive strength than those of the burr tool and ADS specimens, respectively. Additionally, the compressive strengths of AWJ specimens decrease with increasing surface roughness. Nevertheless, those of burr tool specimens are not influenced by surface roughness.

3.3 Shear Test

In addition to compressive test, in the same research, Haddad et al. [22] also carried out interlaminar shear test to study the effect of surface roughness on specimens obtained by different machining processes. The cutting and material parameters are similar to those used for compression test. Figure 24 presents the evolution of interlaminar shear strength as a function of surface roughness in which specimens were trimmed by burr tools. The influence of surface roughness on interlaminar shear

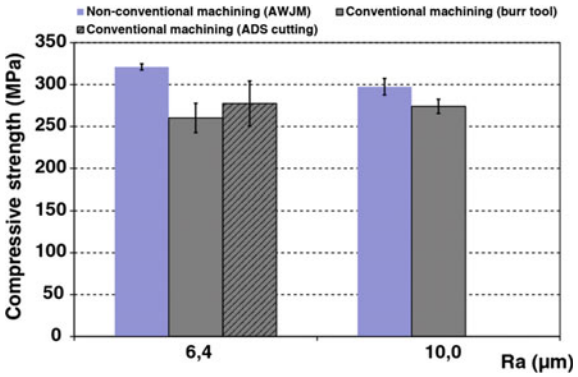

Fig. 23 Relation between surface roughness and compressive strength for different machining processes [22]

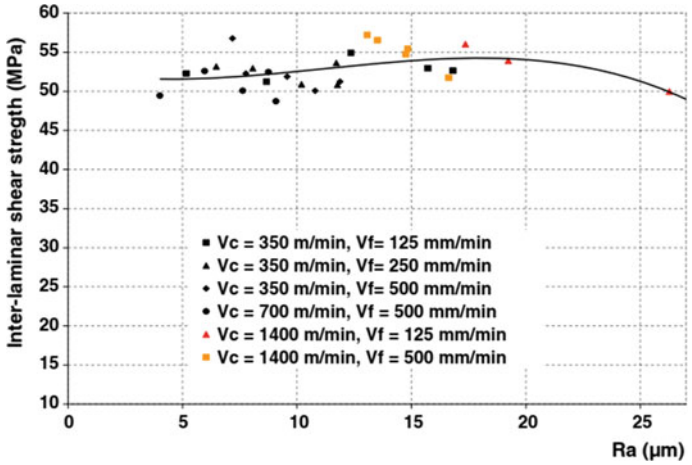

Fig. 24 Evolution of interlaminar shear strength versus surface roughness for various cutting conditions [22]

strength is rather small, and the interlaminar shear strength varies from 47 to 58 MPa irrespective of surface roughness.

The relation between surface roughness of specimens which were machined by various methods with their interlaminar shear strength is shown in Fig. 25 [22]. It is observed that the interlaminar shear strengths of ADS specimens are 6.5 and 6% higher than those of burr tool and AWJ specimens, respectively. The interlaminar shear strengths of AWJ specimens also degrade with the increase of surface roughness, and those of burr tool specimens are random. According to their result, the shapes of induced defects may cause the discrepancy in the interlaminar shear performance. Moreover, the mechanical properties are remarkably impacted by the mode of loading (tension/compression/bending/shear, etc.). The distinction of tool

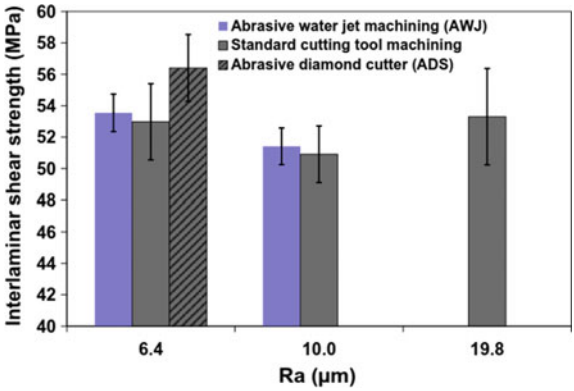

Fig. 25 The relation between surface roughness and interlaminar shear strength for different machining processes [21]

geometries in the case of burr tools also influences on the creation of residual stress in the cut surface, which leads to higher interlaminar strength when compared to other specimens.

An attempt to identify the impact of edge machining on shear strength of carbon/epoxy unidirectional laminates via Iosipescu shear test was carried out by Ghidossi et al. [16]. All layers of specimens were oriented at 0°, and trajectory of cutting tool created two grooves in both sides of specimens. When considering the effect of cutting speed on surface roughness, the authors realized that surface roughness increases with increasing cutting speed in +45° side, but cutting speed has no influence on surface roughness in −45° side. In the case of optical observation (SEM images), contradictory results were obtained. On the −45° side, trimming carried with high cutting speed created less surface damage than that with low cutting speed. In order to correlate the relation between cutting speed and failure stress (shear strength) of Iosipescu specimens, tests were conducted. It was seen that an increase of cutting speed leads to reduced failure stress. Surprisingly, the specimen having the highest failure stress was cut by low cutting speed which generated rougher surface observed by SEM images. This indicates that surface quality is to be replaced by other suitable parameter. The authors also believed that subsurface damage does play an important role in reducing mechanical properties of composite structures. This kind of damage should be subjected to X-ray analysis and quantified accordingly. However, it can be interpreted that in this case the cutting speed reaches the critical value which involves the increase of machining temperature close to the glass transition temperature of the polymer matrix, resulting in remarkable softening of the matrix. The variation of the matrix hardness changes the material behavior which affects cutting quality. The value of the critical cutting speed depends on fiber orientation, type of fiber, and matrix material and chip thickness [37].

3.4 Bending Test

Arola et al. [11] had conducted studies to find the influence of surface texture of specimens machined by different operations on flexural properties of multidirectional graphite/epoxy specimens. Machining processes used in this study were the abrasive waterjet (AWJ), circular diamond saw (DS), and conventional trimming by polycrystalline diamond tool. The machined quality was quantitatively characterized by measuring average surface roughness (R_a), peak-to-valley average (R_y) in both parallel and perpendicular to the machining directions. Furthermore, statistical parameters and SEM observation were also utilized to provide more information on surface texture. Flexural strength and modulus were obtained from four-point flexure loading to failure in which procedure of bending test was recommended by standard ASTM D790M. The quantitative results, R_a, R_y, showed that the surface roughness measured in longitudinal direction of DS specimens exhibited consistently and lowest. For instance, the result recorded in −45° ply was 0.3 μm and the minimum was 0.1 μm inlayer of +45°. Regarding the AWJ specimens, the surface quality was also consistent, although these values varied between 1.7 and 2.1 μm were higher than those of DS specimens. In the case of PCD trimmed specimens, it was clearly seen that surface roughness measured in the places of 0°, +45°, and 90° layers were small. However, in the positions of −45° layers, surface roughness was very significant, i.e., 11.3 and 10.1 μm at depth of 0.5 and 3.5 mm, respectively. The surface roughness measured in transverse direction was 0.5, 1.7, and 4.6 μm of DS, AWJ, and PCD specimens, respectively. The surface quality obtained by PCD specimens was lower than others due to severe damage occurring in −45° plies. The SEM images of machined specimens gave more information for this conclusion, in which matrix/fiber debonding, fiber pullout was obviously observed in machined surface of PCD specimens. Overall, it can be said that surface integrity of PCD specimen was lower than those of DS and AWJ specimens and this difference influenced on the mechanism of failure during pure bending test. Indeed, in progression of failure of the PCD specimens having less surface integrity, a high level of micro-cracking originating from the −45° ply damage was observed. In contrast, buckling of outermost layers occurred extensively as distinguished by the delamination between the 0° and 90° plies. However, the flexural properties including characteristics strength, Weibull modulus, and mean strength obtained by each group of three methods were similar. For instance, the characteristic strengths of all specimens vary between 704 and 717 MPa and mean strengths between 691 and 696 MPa which was small range. Hence, the authors have concluded that surface quality has no influence on flexural properties and the degree of damage induced in this study may significantly impact on other types of mechanical loading like fatigue or impact.

In order to examine the impact of surface roughness on the mechanical strength of composite parts, Eriksen [15] carried out bending test of short-fiber-reinforced thermoplastic (SFRTP) specimens machined at various degrees of surface roughness. The trimmed edges were classified into three groups denoted by low, medium, and high surface roughness. The SFRTPs selected were polyoxymethylene (POM) and

styrenearcylonitrile (SAN) whose fiber orientation was parallel and perpendicular loading direction. According to their study, it was noted that the bending strength was independent of surface roughness. In order to interpret this phenomenon, the author suggested two causes. First, the low bond strength between fiber and matrix may be insensitive to notches. This leads to reduced cracking during machining. Finally, the average surface roughness is insufficient to characterize surface damage as well as surface quality of machined composite parts. The effects of surface roughness on mechanical performances in fatigue and impact test are also conducted in their study and exhibit the similar trend.

3.5 Fatigue Test

Arola et al. [44] inspected the influence of surface quality on the dynamic behavior of graphite/bismaleimide (Gr/Bmi) multidirectional laminates by the performing fully reversed flexural fatigue test. The composite laminates tested had the stacking sequence $[(0°/45°/90°/-45°/)]_{6s}$ and were machined by ADS, and AWJ methods. The ADS specimens were cut to reach 0.2 μm of R_a; meanwhile, the AWJ machined specimens were machined to obtain R_a, 2 and 10 μm. Fatigue behavior was illustrated by the reduction in stiffness which was the ratio of instantaneous flexural modulus to that of initial state ratio, (E_N/E). Machining damage was characterized by a new parameter which was a combination of surface roughness and root radius following a math model proposed by Arola and Ramulu [14]. According to their results, the dependence of fatigue behavior on surface roughness is very clear. For instance, the specimens machined by ADS with 0.2 μm of R_a exhibited lowest reduction in stiffness and lasted highest number of cycles before to failure. Similarly, the AWJ specimens having 10 μm of R_a reduced the stiffness faster than specimen with 2 μm of R_a. It was observed that surface roughness was an important factor to examine the impact of surface quality on fatigue performance of Gr/Bmi laminates.

Haddad et al. [21] had conducted experiments to find the effect of damage induced on fatigue behavior of the CFRP composite T700/M21-GC specimens having stacking sequence [90°/90°/−45°/0°/+45°/90°/−45°/90°/+45°/90°]s. Three machining processes were used to trim, viz., abrasive diamond saw (ADS), burr tools, and abrasive waterjet (AWJ). The specimens trimmed by burr tools are cut to reach two levels of surface quality, good and poor. In order to examine the impact of defects induced, ADS machined specimens were rectified to get better surface quality. The machined surface was characterized by standard average surface roughness, R_a. The influence of damage on fatigue behavior is shown in Fig. 26.

The results obtained from the test also show that for the rectified ADS specimens, the endurance limit increases by 7.5% when compared to values of ADS specimens without rectification. The endurance limit of burr tool-good quality is highest; it is to be noted that these specimens have higher surface roughness than those of other specimens machined by ADS cutting and rectified. It can be said that surface roughness does not influence the endurance limit of burr tool specimens. For ADS specimens, an

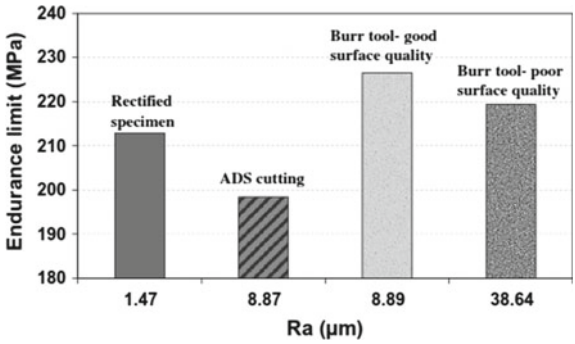

Fig. 26 Endurance limit versus surface roughness for different specimens [21]

increase of surface roughness leads to the reduction of endurance limit. The higher endurance limit of burr tool machined specimens might be linked to the residual stress which is caused by the crushing of machined surface by burr tools. Hence, the outmost layer of machined surface exhibits high stiffness, which reinforces these specimens. Additionally, it can be said that standard average surface roughness is the most dominant parameter used to characterize the surface quality of metal materials. The use of this parameter in inspecting surface quality of composite materials give rise to ambiguity in describing machining surface due to the irregularity of surface as well as many stress concentration factors. Hence, if these stress concentration factors are taken into account, the parameters used to characterize surface quality can significantly improve the prediction of changes in mechanical performances resulting due to induced damage.

3.6 Impact Test

In order to identify the influence of induced damage on impact loading behavior of composite laminates, Arola et al. [12] selected graphite/epoxy laminate and graphite/bismaleimide laminate with the stacking sequence $[X/+45°(-45°/45°/90°/0°)2/-45°/0°/-45°/-45°/90°/-45°/(0°/90°/45°/-45°)2/45°/X]_{6s}$ and $[0°/+45°/90°/-45°]_{6s}$, respectively. The composite specimens were machined by three machining methods, viz., abrasive diamond cutter (ADS), polycrystalline diamond (PCD), and abrasive waterjet (AWJ). AWJ process was carried out using three abrasive grit sizes to obtain specimens with different surface qualities. Surface quality was characterized by R_a, R_y, and statistical methods like probability density and cumulative height distribution. The ADS specimens exhibited highest surface quality, regardless of the characterization method. For AWJ specimens, the surface quality increased with the reduction of grain size. The surface quality of PCD specimens was lower than that of ADS specimen but higher than that of AWJ specimens. The surface roughness was measured in both parallel and perpendicular to machining direction of ADS and AWJ. Nevertheless, the

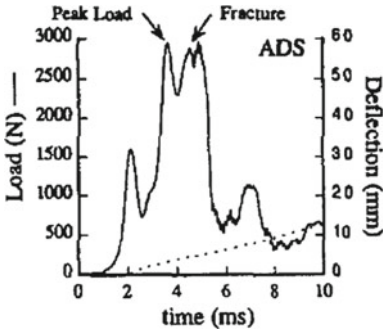

Fig. 27 Typical load-line displacement of the composite laminate machined with abrasive disc cutter, Impact velocity 2.25 m/s (Solid line = load, Dashed line = displacement) [12]

surface roughness measured in transverse direction of PCD specimens was higher than that of longitudinal direction. This is caused by the damage occurring in −45° ply. Impact behavior of composite laminate is described by parameters like peak load, fracture load, and energy at failure. It is observed that ADS specimens had the highest peak load, bending deflection, and absorbed energy for both kinds of FRPs (Fig. 27). The load and energy to fracture of the PCD specimens were inferior to those received from the other techniques used. An increase of surface roughness leads to inferior impact behavior and decreased peak load, deflection, and absorbed energy to failure.

4 Conclusion

A detailed study on machining of FRPs and its effects on surface quality and mechanical behavior has been presented in this work. The study considers both conventional (Trimming, disc cutting, milling, and drilling) and nonconventional (Abrasive water-jet, laser) machining processes. It is seen that every machining process used has a diverse effect on the FRPs and also nature of surface, and damage generated is dependent on the physics of material removal which is unique to the machining process employed. It is also seen that mechanical behavior is not just solely influenced by the surface characteristics (R_a, R_z) as assumed previously but also on the nature of loading configurations and extent of machining damage. The following are the critical observations that were made:

(a) **Surface Quality**—The quality of machined surfaces is characterized by average surface roughness, R_a. Abrasive disc cutting produces the best machined surface (Least R_a value) compared to any other method, the least R_a obtained is 0.2 μm; however, the quality is not consistent as the process is manually controlled. Conventional techniques like PCD or Burr tool machining produce surfaces that are close to ADS specimens; R_a ranges from 2 to 30 μm which is strictly dependent on the machining parameters. Cutting speed and tool wear (Cutting tool nose radius) are the most important factors which decide the sur-

face roughness. However, the surface roughness for conventional machining can be misleading sometimes as there are chances of obtaining low R_a values due to phenomenon of matrix smearing. The Surface roughness values for AWJ cut specimens have a huge variation (2–20 μm) which is dependent on machining parameters; however, the process repeatability is very high which is evident from consistent R_a values and least standard deviation. The value of R_a in the case of AWJ cutting is not uniform in transverse direction as three distinct zones with different surfaces qualities are formed (IDR, SCR, and RCR). In case of laser cutting, surface roughness is of the range 1–10 μm which is mainly dependent on thermal properties of the material systems and type of laser beam used; also significant influence of cutting velocity can be seen. In case of AWJ and laser milling, the surfaces are characterized by nearly repeatable and uniform R_a values and significant surface waviness is also evident which is dependent on the adopted milling strategy (scan pattern and scan step/transverse feed). The other factor deciding the value of R_a for conventional machining is stacking sequence; however, R_a is independent of stacking sequence in case of ADS cutting, AWJ, and laser cutting.

The average surface roughness, R_a, is highly localized measure of surface quality and it largely varies depending on direction of measurement (Longitudinal or transverse to machining direction), ply orientation, type of measurement (Contact and noncontact), and stylus tip radius (in case of contact measurement); also, it does not take into account the damages generated on the cutting surfaces; this explains the inconsistent and erratic evolution of mechanical behavior when seen as a function of R_a. Hence, the evolution of mechanical behavior with surface roughness is inconclusive.

(b) **Machining Damage/Defects**—The new/modified surface created after machining is normally of inferior quality compared to the initial surface and usually it comprises various defects which are due to the virtue of physics of machining process employed. Conventional techniques, namely, ADS/D cut specimens comprise streaks that are randomly distributed over the cut surface and follow the direction of disc rotation. In case of PCD/Burr tool cut/trimmed specimens, defects are classified based on position of their presence, namely, free edge defects consisting of chipping, peel up, spalling and surface defects consisting of delamination, matrix debonding and smearing, matrix degradation, fiber pullouts, etc. Feed rate, stacking sequence, tool geometry, tool material, and wear are the key factors which control the formation of these damages. In drilling, delamination is the most predominant damage, mostly occurring at last or last but one ply of drill bit exit side. At the entry side, fiber peel up and chipping can be seen, whereas the central plies along the hole wall are dominated with matrix cracking, debonding, thermal degradation, smearing, and fiber pullouts largely occurring around the plies oriented at 45° or −45°. In nonconventional machining with AWJ trimming, primary damage is the kerf wall taper and delamination due to water wedging. Surface defects consist of craters, streaks, or striations occurring at exit side of waterjet as a consequence of traverse speed and jet pressure. In AWJ milling, the defects are more or less of the same type as in

AWJ cutting and kerf taper; delamination occurs only for deep milled pocket walls, whereas craters and grit embedment are dominant on milled surface. Laser machining (both cutting and milling) is dominant with thermal defects like matrix degradation, matrix loss and excessive ablation, charred regions, and uncut fibers which is due to the huge variation in thermal properties of matrix and fiber materials; their extent of occurrence depends on type of laser system used, power output, and traverse speed. Kerf taper is also seen in laser cutting and milling but in case of milling wall taper is significant only when deep pockets are milled. Diverse studies have shown that this machining damage can be minimized with optimized machining parameters and employing suitable machining strategies.

(c) **Mechanical Behavior**—Post-machining material integrity of machined components are altered, and their strength diminishes with increasing machining-induced damage. The change in this mechanical behavior is attributed to the surface characteristics (R_a) and damage caused during machining; on the other hand, it is interesting to note that the mechanical performance of the machined component is influenced by type and configuration of loading too. Surface roughness has no complete effect on fatigue and bending behavior. However, for the compressive and interlaminar shear behavior, higher surface roughness leads to reduction of strength. In case of impact test and tensile test, the augmentation of surface roughness causes the reduction of strength. Hence, to conclude, mechanical behavior of machined parts is affected by surface roughness, the mode of machining process, and the type of loading (tension/compression/bending/shear/fatigue, etc.). So, it is to be kept in mind that surface roughness alone cannot ascertain the quality and performance of a machined FRP.

5 Recommendations and Future Work

The correlation of surface roughness with mechanical behavior has contradictory results; the possible reasons and recommendations to improve prediction of mechanical behavior can be one or more of the following:

- Exclusion of nature and extent of machining damage in prediction of mechanical behavior leads to ambiguous prediction of mechanical behavior. It is recommended to come up with a damage factor (F_d) which shall be the measure of damage and is unique for each machining process, for example, factors based on length of HAZ in laser machining, crater volume in AWJ milling, and delamination length in conventional milling. Correlation of the damage factor, $F_{d,}$ would provide better insight for prediction of mechanical behavior of the machined component.
- Considering residual stress is another aspect, which was not taken into account previously. For example, AWJ milling induces compressive residual stress on the component which can be beneficial in improving the fatigue life. Hence, this is one

aspect where future research can be conducted to predict the mechanical behavior of machined FRPs more precisely.

References

1. Sheikh Ahmad J (2009) Machining of polymer composites. Springer. ISBN 978-0-387-35539-9
2. Ramulu M (1999) Characterization of surface quality in machining of composites. In: Jahanmir S, Ramulu M, Koshy P (eds) Machining of ceramics and composites. Marcel Dekker, pp 575–648
3. Arola D, Ramulu M (1996) A study of kerf characteristics in abrasive waterjet machining of graphite/epoxy composite. J Eng Mater Technol 118:256–265
4. Shanmugam DK, Nguyen T, Wang J (2008) A study of delamination on graphite/epoxy composites in abrasive waterjet machining. Compos A 39:923–929
5. Zitoune R, Collombet F, Hernaiz Lopez G (2008) Experimental and analytical study of the influence of HexFit® glass fiber composite manufacturing process on delamination during drilling. Int J Mach Mach Mater 3(3/4):326–342
6. Leone C, Papa I, Tagliaferri F, Lopresto V (2013) Investigation of CFRP laser milling using a 30 W Q-switched Yb:YAG fiber laser: effect of process parameters on removal mechanisms and HAZ formation. Compos A 55:129–142
7. Eneyew ED, Ramulu M (2014) Experimental study of surface quality and damage when drilling unidirectional CFRP composites. J Mater Res Technolgy 3(4):354–362
8. Hejjaji A, Singh D, Kubher S, Kalyanasundaram D, Gururaja S (2016) Machining damage in FRPs: laser versus conventional drilling. Compos A 82:42–52
9. Hejjaji A, Zitoune R, Crouzeix L, Roux S Le, Collombet F (2017) Surface and machining induced damage characterization of abrasive water jet milled carbon/epoxy composite specimens and their impact on tensile behavior. Wear 376–377:1356–1364
10. Colligan K, Ramulu M, Arola D (1993) Investigation of edge quality and ply delamination in abrasive waterjet machining of graphite/epoxy. Mach Adv Compos ASME ASME Publ 66:167–186
11. Arola D, Ramulu M (1994) Machining induced surface texture effects on the flexural properties of graphite/epoxy laminates. Composites 25(8):822–834
12. Arola D, Ramulu M (1997) Net shape manufacturing and the performance of polymer composites under dynamic loads. Exp Mech 37(4):379–385
13. Arola D, Ramulu M (1998) Net shape machining and the process dependent failure of Fibre reinforced plastics under static loads. Exp Mech 20(4):210–220
14. Arola D, Ramulu M (1999) An examination of the effects from surface texture on the strength of fiber reinforced plastics. J Compos Mater 33(2):102–123
15. Eriksen E (2000) The influence of surface roughness on the mechanical strength properties of machined short-fibre-reinforced thermoplastics. Compos Sci Technol 60:107–113
16. Ghidossi P, El Mansori M, Pierron F (2004) Edge machining effects on the failure of polymer matrix composite coupons. Compos A 35:989–999
17. Ramulu M, Colligan K (2005) Edge finishing and delamination effects induced during abrasive waterjet machining on the compression strength of a graphite/epoxy composite. In: Paper Imece2005-82346, proceedings of IMECE: ASME international mechanical engineering congress & exposition Nov 5–11, 2005, Orlando, Florida
18. Herzog D, Jaeschke P, Meier O, Haferkamp H (2008) Investigations on the thermal effect caused by laser cutting with respect to static strength of CFRP. Int J Mach Tools Manuf 48:1464–1473
19. Zitoune R, Crouzeix L, Collombet F, Tamine T, Grunevald Y-H (2011) Behaviour of composite plates with drilled and moulded hole under tensile load. Compos Struct 93:2384–2391
20. Saleem M, Toubal L, Zitoune R, Bougherara H (2013) Investigating the effect of machining processes on the mechanical behavior of composite plates with circular holes. Compos A 55:169–177

21. Haddad M, Zitoune R, Bougherara H, Eyma F, Castanié B (2014) Study of trimming damages of CFRP structures in function of the machining processes and their impact on the mechanical behavior. Compos B 57:136–143
22. Haddad M, Zitoune R, Eyma F, Castanié B (2015) Influence of machining process and machining induced surface roughness on mechanical properties of continuous fiber composites. Exp Mech 55:519–528
23. Colligan K, Ramulu M (1991) Delamination in surface plies of graphite\epoxy caused by the edge trimming process. Process Manuf Compos Mater 27:113–125
24. Janardhan P, Sheikh-Ahmad J, Cheraghi H (2006) Edge trimming of CFRP with diamond interlocking tools. In: Aerospace manufacturing and automated fastening conference and exhibition
25. Ghidossi P, Mansori MEl, Pierron F (2006) Influence of specimen preparation by machining on the failure of polymer matrix off-axis tensile coupons. Compos Sci Technol 66:1857–1872
26. Sheikh-Ahmad J, Urban N, Cheraghi H (2012) Machining damage in edge trimming of CFRP. Mater Manuf Process 27:802–808
27. Koplev A, Lystrup A, Vorm T (1983) The cutting process, chips, and cutting forces in machining CFRP. Composites 14:371–376
28. Wang DH, Ramulu M, Arola D (1995) Orthogonal cutting mechanisms of graphite/epoxy composite. Part I: unidirectional laminate. Int J Mach Tools Manuf 35:1623–1638
29. Wang DH, Ramulu M, Arola D (1995) Orthogonal cutting mechanisms of graphite/epoxy composite. Part II: multi-directional laminate. Int J Mach Tools Manuf 35:1639–1648
30. Arola D, Ramulu M, Wang DH (1996) Chip formation in orthogonal trimming of graphite/epoxy composite. Compos Part A Appl Sci Manuf 27:121–133
31. Caprino G, Santo L, Nele L (1998) Interpretation of size effect in orthogonal machining of composite materials. Part I: unidirectional glass-fibre-reinforced plastics. Compos Part A Appl Sci Manuf 29:887–892
32. Zitoune R, Collombet F, Lachaud F, Piquet R, Pasquet P (2005) Experiment-calculation comparison of the cutting conditions representative of the long fiber composite drilling phase. Compos Sci Technol 65:455–466
33. Agarwal H, Amaranath A, Jamthe Y, Gururaja S (2015) An investigation of cutting mechanisms and strain fields during orthogonal cutting in CFRPs. Mach Sci Technol 19:416–439
34. Wang XM, Zhang LC (2003) An experimental investigation into the orthogonal cutting of unidirectional fibre reinforced plastics. Int J Mach Tools Manuf 43:1015–1022
35. Haddad M, Zitoune R, Eyma F, Castanié B, Bougherara H (2012) Surface quality and dust analysis in high speed trimming of CFRP. Appl Mech Mater 232:57–62
36. Haddad M, Zitoune R, Eyma F, Castanié B (2013) Machinability and surface quality during high speed trimming of multi directional CFRP. Int J Mach Mach Mater 13:289
37. Ahmad JS, Shahid AH (2013) Effect of edge trimming on failure stress of carbon fibre polymer composites. Int J Mach Mach Mater 13:331
38. König W, Wulf C, Grab P, Willerscheid H (1985) Machining of fibre reinforced plastics. CIRP Ann Manuf Technol 34:537–548
39. Haddad M, Zitoune R, Eyma F, Castanie B (2014) Study of the surface defects and dust generated during trimming of CFRP: Influence of tool geometry, machining parameters and cutting speed range. Compos Part A Appl Sci Manuf 66:142–154
40. Nguyen-Dinh N, Zitoune R, Bouvet C, Salem M (2017) Challenge in trimming of CFRP structures: multi-scale analysis of the generated damage. In: International conference on composite structures (ICCS 20), Paris, Sept 2017
41. Fowler G, Shipway PH, Pashby IR (2005) A technical note on grit embedment following abrasive water-jet milling of a titanium alloy. J Mater Process Technol 159:356–368
42. Wang J (1999) Abrasive water jet machining of polymer matrix composites—cutting performance, erosive process and predictive models. Int J Adv Manuf Technol 15(10):757–768
43. Squires CA, Netting KH, Chambers AR (2007) Understanding the factors affecting the compressive testing of unidirectional carbon fibre composites. Compos Part B Eng 38:481–487
44. Arola D, Williams CL (2002) Surface texture, fatigue, and the reduction in stiffness of fiber reinforced plastics. J Eng Mater Technol 124:160

Application of Atomic Force Microscopy to Study Metal–Organic Frameworks Materials and Composites

Amir Farokh Payam

Abstract Metal–organic frameworks (MOFs) also known as porous coordination polymers (PCP) are crystalline compounds including metal ion or cluster of metal ions coordinated to organic linkers. To provide more functionalities and enhance the MOFs properties, design and construction of MOFs composites have been proposed. MOF composites are materials that consist of combination of nanoparticles and MOFs. In this chapter, first a brief review of MOF materials and their synthesis approaches is presented. Then, MOF composites and their synthesis methods and applications are reviewed. Finally, the latest applications of advanced atomic force microscopy techniques to study the crystallization, morphology and structures of MOFs and their composites with nanomechanical characterization are reviewed.

Keywords Metal–organic frameworks (MOFs) · MOF composites
Synthesis methods · Atomic force microscopy (AFM)
Nanomechanical characterization · Crystal growth

1 Introduction

Metal–Organic Frameworks (MOFs) are crystalline compounds that consist of metal ions or clusters of metal ions coordinated to organic linkers. Significant properties of MOFs come from the moderate coordination bond energies which can control the reversibly self-correcting kinetic characteristics [1]. The main properties of MOFs are ultrahigh porosity, high internal surface areas, high thermal stability, single-site crystals, tunable and uniform pore structure, special confined nanopore, ability to tailor framework properties, and clearly defined crystal structure which exhibit an effective role in their applications include proton conduction, drug delivery, sensing, storage and separation [1–6]. However, limited electrical conductivity, poor chemical stability and lack in conventional catalytic active sites are the weak characteristics of

A. Farokh Payam (✉)
Department of Engineering, University of Bristol, Bristol, UK
e-mail: a.farokh-payam@bristol.ac.uk

S. S. Sidhu et al. (eds.), *Futuristic Composites*, Materials Horizons: From Nature to Nanomaterials, https://doi.org/10.1007/978-981-13-2417-8_2

MOFs [1, 2, 7, 8]. Recently, to introduce more functionalities, overcome MOFs limitations and improve the MOFs properties, combining MOFs and different functional nanomaterials has been suggested [7–11]. MOFs composites consist of one MOF and one or more constituent materials with different characteristics than each component. In MOF composite materials, the effective properties of MOFs and different types of functional materials can be combined and novel physical, chemical and mechanical characteristics can be obtained. So far, active species including quantum dots, polyoxometalates, metal nanoparticles/nanorods, carbon nanotubes, graphene, oxides, biomolecules and polymers are used to construct the MOF composites. MOF composites have considerable applications in biomedicine, protection of biomacromolecules, gas storage, separation, sensing and catalysis [1, 3, 4, 6–13].

To design and fabricate of the foregoing MOF's materials and composites, it is necessary to have comprehensive information about MOFs crystal growth, morphology, mechanical properties and especially understanding the details of MOF's mechanics, which rarely can be found [14, 15]. To develop the findings of mechanical properties of MOFs, there is a growing interest in the development of theoretical approaches, including density functional theory (DFT) [16, 17], application of group theory [18] and molecular dynamic simulations [19]. Although there is a significant growth of theoretical studies in this field, there is less effort to study the mechanical properties of MOFs experimentally.

High crystallinity of MOFs makes X-ray diffraction techniques promising to characterize the structure of MOFs [20]. Currently, some efforts have been performed to use the high-resolution transmission electron microscopy [21] and scanning electron microscopy [22] to study MOFs. However, due to the high complexity and variation of MOFs applications, development of new characterization methods for the understanding of the structures, crystal growth, morphology and properties of MOFs in their native functional environment is necessary [23]. Recently, the atomic force microscope (AFM) techniques have been received great attentions to image and characterize different materials at nanoscale in various mediums such as vacuum [24] and liquid environments [25–30] with atomic and angstrom resolution. So, there is a growing interest in the AFM application to study crystallization, morphology and characterize the structural and mechanical properties of MOFs.

In this chapter, first an introduction about the design and structure of MOFs is presented and the synthetic approaches of MOFs will be described. Second, the properties, synthesis approaches and applications of MOF composites are briefly reviewed. Finally, the recent techniques and methods in the application of AFM to study the MOFs materials and composites are reviewed. I should notice that the aim of this chapter is to provide general and comprehensive information for the readers who are not expert on chemistry but have interest in composites, nanotechnology and AFM applications.

2 Metal–Organic Framework

In the early 1990s, the fundamental concept of MOF was proposed by Hoskin and Robson [31]. By assembling of metal ions and organic molecules, they opened the way to produce the porous coordinated polymers [32]. Since then, several researches have been concentrated to the systematic design and fabrication of MOFs. Generally, metal–organic frameworks (MOFs) are crystalline compounds consist of metal ion-containing nodes or secondary building units (SBUs) coordinated to ligands organic linkers [33]. The main MOFs key properties are extraordinary topology, large internal surface area, ultrahigh porosity with rigidity and flexibility.

2.1 Design of MOFs

Generally, there are two methods to provide the desired surface chemistries and tune the pore size [34]. The first one is direct assembly of metal nodes and organic linkers to form new MOFs, and the second one is modification of pre-constructed precursor MOFs through post-synthesis. Recently, thousands of MOFs are synthesized by the flexible methods of producing MOFs [34]. Organic linkers' geometries and metal ions or clusters of metal ions coordination are the main factors in MOFs structures (Fig. 1) [2]. The process of metal ions and organic linkers' selection defines the type of MOFs [2]. Because it is difficult to obtain a priori synthesis structures from metal ions and organic linkers, there is a flexibility around the metal ions and a general lack of control of structure [35]. To solve this problem and obtain the robust framework and design directionality of MOFs, the concept of secondary building units (SBUs) consisting of metal ions and oxygen atoms is adopted. First time, to design of MOF-2 and MOF-5, the rigid framework is obtained based on such SBUs [35]. Since then, by selecting SBUs and link to control the shape, pore size and desired functionality, MOFs are adopted [5]. Factors such as solvent, ratio of precursors and temperature also can affect the morphology and structure of MOFs. Examples of different possible SBUs defined by Yaghi and his colleagues are shown in Fig. 2 [35]. Every year, varieties of MOFs are synthesized by attachment of organic linkers with SBUs in different ways [2].

There are different dimensionalities for MOF structure: 1D, 2D and 3D [36]. Bridging ligands' binding mode and metal ion geometry are the basic factors to form MOFs with different dimensionalities and topologies. Assembly of different metal ions with one linker or more than one linker (mixed linkers) can be used to build the framework. In comparison with MOFs composed of single linkers, MOFs consist of mixed linkers have more flexibility of surface area, modifiable pore size and chemical environment [36]. Generally, mixed linker frameworks are produced by connecting the metal ion or clusters with an anionic linker and a neutral linker [36]. Depending on binding modes, the framework can extend in different dimensions. At one-dimensional (1D) MOFs, coordination bonds are spread in one direction while

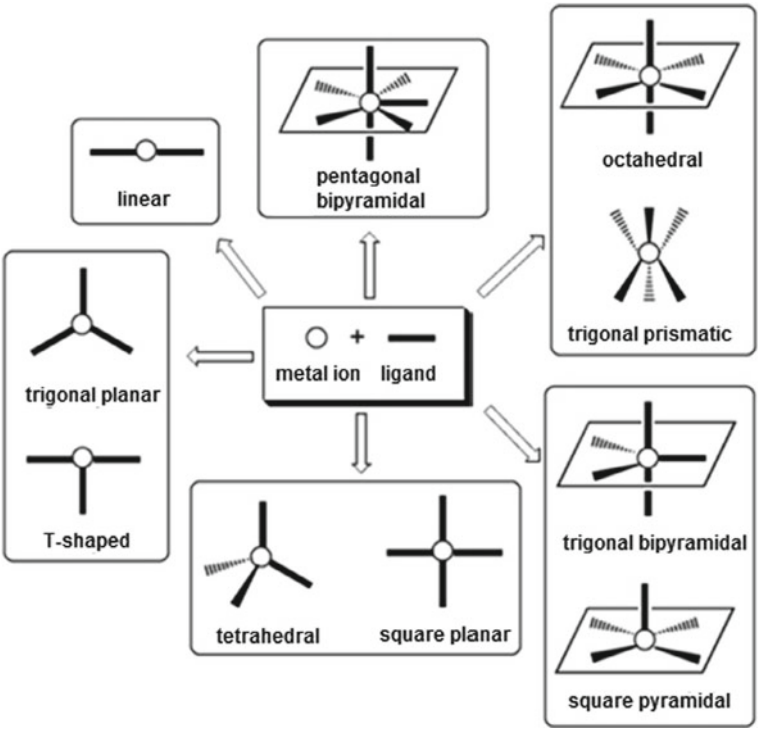

Fig. 1 Transition metal ions coordination geometries. Reprinted with permission from [2], Copyright from Elsevier

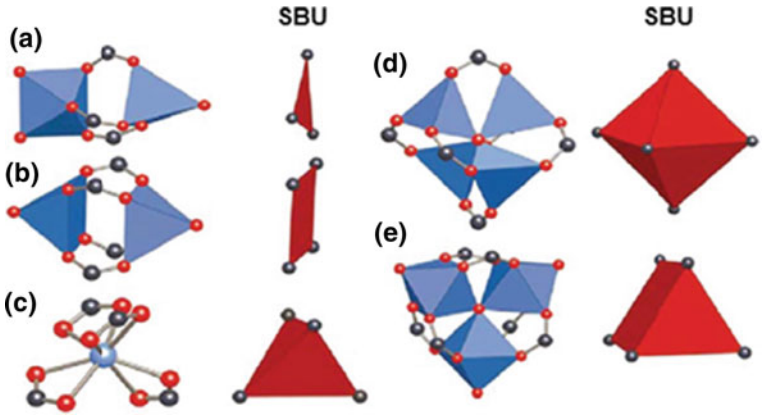

Fig. 2 Examples of different possible types of SBUs. Reprinted with permission from [2 and 35], Copyright from Elsevier and Springer Nature

at two- or three-dimensional MOFs, the coordination bonds are spread in two or three directions, respectively. In 3D MOFs, the high porosity and stability of frameworks come from spread of coordination bonds in three directions [36]. The neutral linkers' role is like the pillars and can increase the dimensionality [36]. Length of the linkers can control the porosity. Also, by functionalization of the linkers, the application of MOFs can be tuned.

2.2 Synthetic Approaches of MOF Materials

So far, different methods have been proposed to synthesis of MOFs to obtain permanent porosity and crystalline framework. In synthesis approaches, small changes in solvents, ratio of precursors and temperature can affect the MOFs performance and lead to the different properties or enhanced activity than desired [37]. Hence, synthetic methods of MOF materials have sufficiently great importance to obtain the desired properties and activities. In this section, the conventional synthesis approaches for MOFs construction are introduced.

2.2.1 Hydro (Solvo) Thermal Method

Hydrothermal synthesis is a technique to synthesis of single crystals and different chemical compounds which is dependent upon minerals solubility in hot water under high pressure. Crystal growth is carried out in an equipment with steel pressure vessel called an autoclave, in which a nutrient is supplied along with water [34]. There are two reasons which make the hydrothermal methods attractive for MOFs: Minimization of solubility of heavy organic molecules and rapid initiate of nucleation process for the generation of rare complex in the same experimental condition [2]. Solvothermal synthesis is a useful technique to grow crystals proper for structure determination, since the crystals growth takes from hours to days.

2.2.2 Microwave and Ultrasonic Methods

Microwave (MW) is an electromagnetic wave with a wavelength lies between 0.001 and 0.3 m [38]. Ionic conduction and dipole rotation are basic procedures for the energy transfer from microwaves to the material which is being heated [39]. In MW synthesis methods, best solvents are water or high dipole moment ionic liquids [40]. Nowadays, MW method is implemented in the synthesis of MOFs [40] and plays an important role in MOFs applications. Significant advantages of MW technique for the synthesis of MOFs are small crystals, morphology and phase control, short times of reaction, and distribution of particle size [2].

In ultrasonic (US) synthesis method, due to the application of ultrasonic waves between 20 kHz and 1 MHz, the reactant molecules are subjected to chemical

reactions [38]. The sonochemical mechanism at liquids which is principally based on production, rise and collapse of bubbles, is known as acoustic cavitation [41]. The advantages of ultrasonic method are the operation in normal conditions, simplicity and product selectively. Recently, due to low energy consumption, environmental friendly and affordable production cost, both MW and US techniques have been applied in the MOFs synthesis [40].

2.2.3 Electrochemical Synthesis

In the electrochemical synthesis method for MOFs, metal ions are placed at the anode while organic linkers are located at cathode and conducting salt fills the electrochemical cell [2]. Because there is no pressure, in comparison with hydrothermal method, there is more control on the concentration of reactant. Moreover, through control of the anodic oxidation, different rates of metal ions can be added to the solution [42]. The main advantages of electrochemical method are its rapidness at lower temperature, mild synthesis condition, crystal growth in short time and ease of scale-up besides its environmental friendly [43].

2.2.4 Mechanochemical Synthesis

The mechanochemical techniques are optimistic candidates in solvent-free synthesis [44]. Mechanochemical methods are based on chemical transformations induced by mechanical energy, such as compression, shear or friction [44]. In mechanochemical approach (grinding), the metal precursors and organic linkers are used to generate discrete coordination complexes with reorientation of intramolecular bonds which leads to the chemical reaction [2]. In mechanochemical techniques, metal oxides act as starting materials and water only will be byproduct [2]. Also, the mechanochemical reactions can be accelerated by the presence of liquid via amplification of the mobility of precursors [2]. The most advantages of this synthesis approach are reliability, its fastness and easiness, proper building blocks, environmentally friendly, offering quantitative yields, solvent-free access for the preparation of MOFs and high-quality materials [2]. Also, in comparison with other synthesis methods for MOFs, the mechanochemistry approach can provide adequate values of pure material for wide range testing [45]. This synthesis method can directly produce material in powder form. So, the materials can be used in diverse applications without any time-consuming treatments [46].

2.2.5 Diffusion Method

In diffusion method, larger crystal is produced by steady and slowly diffusion of two solutions. During the solvent–liquid diffusion, this grow occurs via the formation of three discrete layers. In this process, each layer has its specific role. The precipitant

solvent is in the first layer, the product solvent is in the second layer and these two layers are separated by third layer and permit slowly diffusion [2]. During movement of solvents from one layer to another layer, the actual crystals growth reveals at the layers interface. Other method is the slow rate reactants diffusion via gels [2, 47].

2.2.6 Solvent Evaporation and Ionothermal Synthesis

In solvent evaporation approach, via slow rise of the liquid concentration, the crystals are shaped. At first, until obtaining clear solution, with continuous stirring, the reactants are combined in suitable solvent [2]. After that, the reaction mixer is poured into beaker and with a parafilm is sealed. Through saturation of solution, removal of excess solvent or cooling of solution, the growth of crystal is initiated [2]. In ionothermal approach, the ionic liquids are used as solvent (instead of water in hydrothermal method) for the reaction because of their properties like poor coordination ability, high ionic conductivity, low volatility, high thermal stability and good dissolving capability [2].

2.2.7 Chemical Vapor Deposition

Chemical vapor deposition technique is the new development in solvent-free synthesis of MOF films and composites. For the first time, this two-step procedure, MOF-CVD [48], was proposed for ZIF-8. Initial step is related to the deposition of metal oxide precursor layers. Then to induce a phase transformation to the crystal lattice of MOF, the deposited layers are revealed to sublimed ligand molecules. During this reaction, water formation has an effective role for directing the transformation [48].

3 MOF Composites

To obtain new properties and improve the functional performance of MOFs, nanoparticles and MOFs can be combined into one construct which has the capability to exhibit new mechanical, physical and chemical characteristics different than individual components. The selection of suitable MOF can be performed by using the library of porous crystals or using simulation methods [49, 50]. Several active materials such as quantum dots (QDs), polyoxometalates (POMs), metal nanoparticles (NPs), oxides and carbon materials including graphene and carbon nanotubes (CNTs) and biomolecules are used to obtain properties unattainable by individual matters (Fig. 3) [8, 51–53].

When MOFs is a matrix, nanomaterials are usually used as functional species [54, 55]. Generally, there are two basic mechanisms to prepare nanoparticle/MOF composites when MOF acts as matrix. The first and common method employs techniques

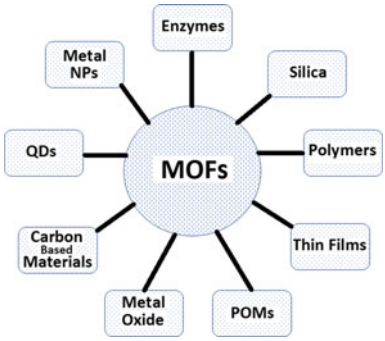

Fig. 3 Different types of MOFs composites

like liquid-phase infiltration [56], chemical vapor deposition [57] and solid grinding [58] to generate nanoparticles within the MOF channels. The second method, very recently developed, is direct introduction of pre-synthesized nanoparticles within MOF pores or combining nanoparticles within MOF precursors via solvothermal synthesis [10]. In the latter approach, the combination of nanoparticles and MOFs can be strengthened by decorating the nanoparticles with proper surface functional groups that usually happens in this method [59].

When MOFs consider as functional species, to build MOF composites, direct dispersion of MOF nanoparticles into meso/microporous materials and submerge of meso/microporous particles in MOF precursors under solvothermal synthesis are functional procedures [57, 60]. To strength the materials empathy and strong attachment to MOF nanoparticles, the meso/macroporous particles should have terminated group [7, 10]. In this section, the most common MOF composites, their preparation and applications are briefly reviewed.

3.1 MOF Composites

3.1.1 Enzyme–MOF Composites

Enzymes are biomacromolecules with mild reaction conditions, high selectivity and efficiency. Because of the capability to catalyse life-sustaining biological transformations efficiently, enzymes are very important for the life and industrial processes [61]. However, there are limitations in practical applications of enzymes like difficulty in the recovery, low thermal stabilities, loss of activity at operational conditions and narrow optimum pH ranges [61]. Also, enzymes generate contamination which leads to inevitable purification and separation steps [61]. With immobilization of enzymes at a solid support, their practical performance could be enhanced. Also, it facilitates the easiness of recovery and separation for reuse while keeping the selectivity and activity [62]. Tunability and uniformity of pore size plus functionality of pore walls make MOFs as an attractive candidate to accommodate enzymes for catalytic appli-

cations. Current improvements in mesoporous MOFs [63] facilitate the applications of enzymatic catalytic [8]. Typically, there are four types in synthesis approaches of MOF—enzyme composites: pore entrapment, covalent linkage, surface attachment and co-precipitation [61]. In addition of maintaining the activity and accessibility, the physical confinements provided by MOFs can lead to the denaturation of free enzymes.

3.1.2 MOF–Metal Nanoparticle

Due to the delocalization of free electrons, the physical, chemical and mechanical properties of metal nanoparticles are different than bulk metals [64]. For example, high ratio between surface area and volume of M-NPs leads to have many active sites. These properties provide wide range of potential and actual applications for M-NPs [54]. Shape and size control of M-NPs are critical points to get improved reactivity [65]. Since M-NPs possess high surface energies and tendency to aggregate and fuse, their thermodynamic stability is significantly reduced, which leads to difficulties in the control of shape and size with high uniformity [66]. So, the encapsulation of M-NPs in mesoporous and microporous solids can be an effective approach for preventing aggregation [8, 67]. Because of thermal robustness with capability of permanent nanoscale cavities, MOFs could be used as supports for M-NPs with controlled sizes within the pores, so the aggregation of NPs is prevented which provide the opportunities to use MOF/M-NPs composites for the applications like catalysis [8]. In general, the preparation of M-NP/MOF composites can be classified into four categories. The first one is the introduction of a MOF into a solution with a metal precursor or the mixing of a MOF with a metal precursor at the solid state, followed by the formation of M-NPs inside and/or on the external surface of the MOF. Second category associates to dispersion of M-NPs into a reaction solution for subsequent MOF synthesis, generally, to obtain M-NPs incorporated into MOFs. The third is step-by-step synthetic processes, for M-NPs/MOFs and sandwich-like structured MOF/M-NPs/MOFs. The last step is the simultaneous formation of the two components to afford M-NP/MOF composites [8].

3.1.3 MOF–Quantum Dot Composites

Quantum dots (QDs) are small particles or nanocrystals of a semiconducting material with diameters between 2 and 10 nm with distinctive electrical and optical characteristics. They possess advantages like broad absorption bands, low photobleaching, long lifetimes, narrow and symmetrical emission bands and high quantum yields [68]. QDs have the applications for light-emitting, biological imaging and solar photon conversion devices [69]. The characteristic UV–vis exciton peak of quantum dots is size dependent. Smaller QDs is associated with the shorter wavelengths and as a result fluorescence emission is tuneable [11]. Since QDs possess several desirable properties, inserting highly luminescent semiconductor QDs into the MOFs frame-

works leads to the extension of versatility of functional MOFs and stabilization of size-dependent optical and electronic characteristics of the QDs. The QD/MOF composites have extensive applications in gas storage, selective sensing of molecules, light harvesting and photocatalysis [8]. There are two methods to synthesis QD/MOF composites. The first one is based on "ship in bottle" approach. In this method, the QDs are located and distributed within the pores of the framework. It includes treatment by heating, hydrogenation or reduction. The MOF matrix should be stable under high-temperature condition. It is worthy to mention that if metal ions of the framework are vulnerable to variations of oxidation state, the network degradation may be happened. Also, this method has the potential to decrease the surface area of MOF matrix due to QDs insertion within the pores. The second approach for insertion of QDs within MOF framework is "bottle around ship" method. In this approach, a stabilized semiconductor nanoparticle is submerged in the solution containing building blocks of MOF and framework assembles around the QD [11]. There is an alternative technique for "bottle around the ship" approach to insert QDs within MOF matrices. The finding that demonstrates a class of nanostructured α-hopeite microparticles shows an outstanding capability to nucleate MOFs is the base of this approach [70]. Using these microparticles as seeds, MOFs can grow in solution at any flat surface and on complex 2D/3D surface morphologies. Moreover, the direct insertion of active species within the framework through the α-hopeite microparticles allows functionalization into the framework core, and not on its outer surface [70].

3.1.4 MOF–Carbon-Based Materials Composites

Carbon materials (including nanotubes, graphene, graphite and diamond) are 0D to 3D materials with different forms and degrees of graphitization. They encompass significant advantages including large surface area, porosity, mechanical strength, electrical conductivity and corrosion resistance [3, 71–73]. Especially, CNTs and graphene are used for several applications such as storage, separations, sensing and energy sector [73]. Graphene and CNTs possess distinctive electrical, thermal and mechanical properties which can be useful to combine with MOFs. For this purpose, several nanocarbon/MOF composites have been fabricated and offered extensive applications. There are different synthesis methods for carbon materials/MOF composites including in situ (one-pot and stepwise synthesis methods) and ex situ synthesis techniques [12].

In one-pot synthesis approach, the reactants are subjected to chemical reaction at only one reactor and a long-lasting separation and purification of the transitional chemicals are prevented. Because in some materials, one-pot synthesis causes difficulty for the modifications in the substrates without functional groups at surfaces, sometimes stepwise synthesis methods such as seeded growth are preferred. In this method, MOF crystals are first synthesized and deposited on the supports as seeds, which will greatly promote further MOF crystallization [74]. This process permits higher control of orientation and provides MOF membrane with a continuous, robust and defect-free properties. The layer-by-layer method (liquid-phase epitaxy)

is another stepwise synthesis method to mix MOFs with carbon nanomaterials such as carbon fibres [75].

However, in some conditions of in situ synthesis techniques, due to the possibility of interfere between unsuitable value of in situ carbon materials with the coordination reactions, a disgusting performance to destroy the structure of MOF/carbon-based composites may be occurred [12, 76]. Thus, in these situations, ex situ synthesis methods (integration of carbon materials with pre-synthesized MOFs) are used to produce the composites. In construction of MOF-based supercapacitor electrodes or carbon paste electrodes (CPEs), direct mixing techniques as an ex situ method are conventionally used. Here, the carbon-based materials behave as conductor to enhance electrical performance [12]. Self-assembly methods are the other ex situ method usually driven by electrostatic interactions, hydrogen bonding, π–π stacking and other forces. Whenever these techniques have been used for fabrication of MOF–carbon materials composites, all of the components are integrated [12].

3.1.5 MOF–Metal Oxide Composites

The main characteristics of metal oxide nanomaterials are their controllable functionality, crystallinity, size and shape which have extensive applications in catalysis, electronics, optics, electrochemical energy conversion and storage [77]. Integration of metal oxide nanoparticles with MOFs leads to the improvement of the properties of both metal oxide nanoparticles and MOFs. The synthesis methods of metal oxide NP/MOF composites are like M-NP/MOF materials. In one approach, through the decomposition process of preloaded precursors or oxidative annealing, the metal oxides are encapsulated inside the cavities of MOFs [78]. In the other technique, the pre-synthesized metal oxide NPs is introduced within the MOF matrices [79]. In this method, controlled crystal growth is promoted by decoration of NPs with proper surface functional groups (amine and carboxylic acid) [8, 80].

3.1.6 MOF–Silica Composites

Silica nanomaterials as porous, dielectric, stable, multifunctional materials recently find diverse applications in separation, drug release and catalysis [8, 81]. Combining the functionalities of silica nanomaterials and MOFs provide the distinctive characteristics and applications for both materials. There are two principle classes of MOF/silica composites. The first one is based on the inclusion of dispersed silica nanoparticles inside the pores of MOFs or MOF shell growth on a pre-created sphere of silica in MOF precursor solutions. In the second one, benefits of silica shell as a surface coating or the mesoporous characteristics and processability of silica supports to further the growth mechanism of microporous MOF particles in every part of the porous silica supports are used [8].

3.1.7 MOF–Polyoxometalate Composites

Polyoxometalates (POMs) have been described as metal–oxygen cluster anions, which cover diverse structures in terms of size, shape and principal composition. The terminal oxo-ligands are strong π-electron donors; so oxygen atoms strongly bind to main-group transition-metal ions in high oxidation state [82]. They have an effective role in several fields like catalysis, electrochemistry, photochromism, medicine and magnetism [8]. However, they possess low stability under catalytic conditions and low specific surface area. Stabilizing and optimization of MOFs catalytic performance can be obtained by immobilizing POMs in porous solid materials. The introduction of POMs into MOFs avoids the POMs from deactivating and conglomerating and increasing catalytic characteristics [8]. In one aspect, based on structural adaptivity and compositional diversity, POMs are flexible building blocks for coordination supramolecular fabrication [8, 83]. In these POM/MOFs composites, to link the metallic nodes covalently, the organic ligands of MOFs replace the oxo groups of POMs. Traditionally, there is a lack of predictability and controllability in their cluster assembly preparation [8]. In the other aspect, to produce POM/MOF composites, host–guest interactions can be used to introduce POMS in the pores of MOFs without sharing any covalent bonds between the two components [84]. Generally, there are two methods to synthesis POM/MOF host–guest composites. First one associates to the direct filling of POM moieties within pores of MOFs. However, in this approach, there are some drawbacks such as low homogeneity, leaching during reactions and a small loading value of POM [8]. In the second method, to construct the 3D MOFs, POMs behave as noncoordinating anionic templates. Using this one-pot approach which usually performed under hydrothermal conditions, POMs could be introduced into the MOFs framework in large amounts without the drawbacks of the first approach [8].

3.1.8 MOF Thin Films on Substrates

Nowadays, MOF thin films deposition with desired chemical functionality combined with porosity, at solid substrates, is demanded due to their potential application as catalytic coatings, smart membranes and chemical sensors [85]. There are two fabrication methods for direct growth/deposition of MOF thin films. First method is associated with adding the substrate to a MOF synthesis solution under ambient or solvothermal conditions [8, 86]. In this approach, simultaneously growth process occurs on the surface of the substrate surface and solution. This technique can be modified by using the aged precursor solutions containing MOF nuclei [87]. In this growth mechanism, polycrystalline films formation occurs where crystals are attached to the surface of substrate in approximate intergrown and continuous fashion [8]. Second approach associates to layer-by-layer approach proposed by [88], applied for MOF thin films synthesis on the substrates. The consecutive deposition of metal salts monolayers and organic linkers on a functionalized substrate are the base for this method [8]. Through rinsing with a suitable solvent, unreacted elements are

eliminated between successive deposition steps. Due to the separation of the two kinds of MOF building blocks, there is a self-limiting growth in each cycle. In the layer-by-layer method, growth of homogeneous and smooth MOF ultrathin films with nanometre-scale diameters is possible. Crystallographic orientation, accurate control of the thickness and interpenetration of the MOF multilayers are other benefits of this method [8].

3.1.9 MOF–Polymer Composites

Nowadays, composite materials of MOF-polymers such as MOF-based mixed-matrix membranes (MMMs), MOF-organic polymer and polymer supported MOF membranes are used significantly. Organic polymers have significant properties such as lightweight, easily production, good chemical and thermal stability, which are advantageous for the combination with other functional materials to fabricate composites [89]. Nanometre-scale polymers display extraordinary properties different than bulk states [55]. Although polymer membranes have been used extensively in gas separation, a trade-off between permeability and selectivity is the main constraint for their application. To solve this problem, polymers are combined with porous MOF materials with molecular sieve properties to enhance the gas separation capability of the membranes. There are three different approaches for synthesis of MOF-polymer composites [4, 8, 90, 91]. In the first one, the MOF crystals have been grown on a pre-synthesized polymer support. In the second method, the polymerization is carried out around the preformed MOF crystals and in the third method, polymerizable functional groups are used to modify copolymerizing monomers with MOF.

3.2 Application

In this section, some important applications of MOFs composites are reviewed.

3.2.1 Sensing

Surface-enhanced Raman scattering (SERS) provides a powerful non-destructive, high-resolution approach to detect very small amount of target molecules. The SERS effect is based on adsorption of detected molecules on metallic surface [8, 91, 92]. Encapsulating the metal nanostructures within porous MOFs offers some extraordinary improvements associated with the well-known properties of MOFs [8]. Thus, nanostructure MOFs composites can be employed to detect the specific molecules selectively. Because the MOF-5 has the potential to capture CO_2 from flue gas in a selective manner, the combination of MOF-5 and Au NPs into well-defined core–shell NPs with a single metal NP core coated with a uniform MOF shell is used for the selective detection of CO_2 in a gas mixture [8, 57].

3.2.2 Energy Applications

Recently, due to the serious problems and crisis in energy and environmental sectors, the development of nature-friendly sustainable energy storage and conversion technologies has attracted much attentions [93]. The MOFs and their composites are promising candidates for the energy conversion and storage. In this section, some important applications of MOFs composites in this filed are explained.

– **Hydrogen and Methane storage**

Microporous MOFs and their composites with high surface area are promising candidates for the storage of nature-friendly fuels like H_2 and CH_4. High value of pore volumes and coordinatively unsaturated metal sites are key factors in the increase of the capacity of hydrogen storage by enhancing of H_2 and MOFs interaction. However, instability of bare MOFs and low storage capacity are the main limitations of MOFs for hydrogen storage. Instead, using NP/MOF composites especially Pd/MOF composites can significantly enhance hydrogen storage capacity. This ability of Pd/MOF composite corresponds to spill over effect of Pd nanoparticles. It means the H_2 molecules are catalytically broken into monotonic units and inserted in the cavities of MOFs [10]. Pore volume and Brunauer–Emmett–Teller (BET) surface area under high pressure of MOFs composites make them as promising candidate for methane storage to satisfy the challenging U.S. DOE (263 cm^3 (STP) cm^{-3}) target [47, 93].

– **Fuel Cells**

Fuel cells are electrochemical equipment for conversion fuels to electrical energy for the applications such as electrical vehicles and portable electrical appliances [93]. The MOFs with high proton conduction and affordable syntheses are favourable for electrolytes in fuel cells. Proton conduction of MOFs can be performed in low-temperature (below 100 °C) and high-temperature (above 100 °C) regions. In the low-temperature region, the ability of MOF for proton conduction was reported in 2009 for the first time [94]. In this method, coordinated water, guest molecules and functional groups of ligands have a significant effect in proton conduction [93]. In the high-temperature method, non-volatile guests including triazole, imidazole, histamine and benzimidazole are embedded within the MOFs pores to set up easy proton delocalization path to stimulate the proton conduction at temperatures higher than 100 °C and in anhydrous conditions [93, 95].

– **Lithium-Based Batteries (LIB)**

The base of LIBs is the lithium ions, produced via the lithium-based anode oxidation, migration and return from cathode to anode during the process of charge and discharge, respectively [96]. Pristine MOFs are the alternatives for the common graphite anode materials. They possess large surface area and permanent pores for the storage and migration of Li + ion during charge and discharge mechanisms [93]. Although MOFs can be used as the anode for LIBs, developing stable MOFs with reversible regeneration or formation to obtain high-performance Li storage with distinctive cyclability is a challenge. Several MOF composites including metal oxides and porous carbons are used in LIB anode applications [97, 98].

3.2.3 Catalysis Applications

Because of high porosity and surface area with ordered crystalline structures, MOF composites demonstrate significant properties for catalytic applications [99]. The growth of active species and agglomeration can be limited by confined pore sizes, and transport of different substrate molecules for size-selective catalysis can be selectively performed [1].

– **Catalytic CO Oxidation**

Based on the study which has been performed in [1], NPs/MOF composites have considerable catalytic potential to oxidase CO at high temperatures. CO oxidation has diverse applications in the fields of polymer electrolyte fuel cells, automotive exhaust gas treatment and detection of trace amounts of CO in gas sensors [10].

– **Catalytic CO_2 Conversion**

The MOF-based composites can be used as active catalysts for CO_2 conversion. Metal or metal oxide NPs inserted in MOFs exhibit an effective role for CO_2 conversion to precious chemicals, including CO, CH_4, CH_3OH and light olefins [10]. To reduce the carbon emission, the solar energy can be utilized for the CO_2 conversion into precious products. So, photocatalysts such as Zn_2GeO_4, TiO_2, graphite-like carbon nitride (g–C_3N_4) and CdS are combined with MOFs to photocatalytically decrease CO_2 [1]. Also, recently growing numbers of MOFs are used as catalysts to form cyclic organic carbonate [10].

– **Catalytic Hydrogen Production**

- Catalytic Hydrogen Generation from Chemical Hydrides

High catalytic activities resulted from immobilization of metal NPs within MOFs can be used for hydrogen production from liquid chemical hybrids including ammonia borane (NH_3BH_3), hydrazine (N_2H_4) and aqueous formic acid (HCOOH) [1]. Tunable pore size with high specific surface area of NPs/MOFs composites provides the opportunity to the NPs size control in the confined cavities and generate monodispersed metal NPs with increased catalytic potential. Thus, several metal NPs such as mono-, bi- and trimetallic nanoparticles combined with different MOFs for the hydrogen generation [1].

- Catalytic Hydrogen Production from Water

Using solar energy and photocatalytic water splitting is a permissible approach to produce hydrogen. To enhance the charge transfer/separation efficiency of hydrogen production, development of new MOFs composites is a permissible strategy. For example, Pt NPs incorporate into MOFs to improve hydrogen evolution reaction (HER) activity [10]. Nowadays, various functional components, such as nickel particles [94], metal sulphides (e.g. MoxSy, NixSy, CdS), reduced graphene oxide (rGO), g-C_3N_4 and POMs [10], are used to substitute Pt and enhance the photocatalytic activity for HER [1].

– **Organic Reactions**

- Oxidation of Hydrocarbons

Specific properties of MOF composites like nanoconfinement offer the superior catalytic activity. Several active species in MOFs composites, such as Au, AuPd, PtPd alloy NPs, POMs and graphene oxide (GO), exhibited selective and active role in the oxidation process of hydrocarbons with molecular oxygen [1].

- Hydrogenation Reaction

Hydrogenation has extensively industrial applications. The Pd, Pt, Ru and Ni NPs, and their bimetallic NPs immobilized by MOFs are active catalysts in the hydrogenation of various substrates such as alkenes, alkynes, aromatics, nitro-aromatics, ketones, aldehydes and other compounds [1].

- Catalytic C–C Coupling

In organic synthesis, C–C coupling reactions are very important [1]. To further C–C coupling reactions, Pd is the most common catalyst, so MOF supported Pd NPs are developed as C–C coupling catalysts [1].

– **Catalytic Remediation of Pollutants**

Due to the flexibility of MOFs design by control of metal ions and organic linkers, MOF composites with graphite oxide (GO), metal NPs and metal oxide/sulphides are employed in the catalytic degradation of organic pollutants and Cr(VI) [1].

3.2.4 Adsorption of Harmful Gases

Unique properties of MOFs make them as suitable materials which extensively have been used to remove harmful gases (H_2S, NH_3, CO, NO, benzene and chlorinated hydrocarbons) from the environment.

Hydrogen sulphide (H_2S) is a flammable, poisonous gas with a characteristic odour of rotten eggs. It is commonly produced in petroleum and natural gas industries. Moreover, a sewer gas released from anaerobic decomposition. So, its removal from the environment is necessary. Adsorption of hydrogen sulphide on a porous support is a common way to remove H_2S. Recently, different MOFs are proposed for the H_2S adsorption such as MIL-100(Cr) MIL-53 (Al, Cr, Fe), MIL-47(V) and MIL-101(Cr) [18, 59]. Although these materials can adsorb hydrogen sulphide, only MIL-53(Al, Cr) and MIL-47(V) could provide the reversible adsorption with a total recovery of initial porosity. In [100], MOF composites combined with a copper-based MOF and GO have been used to remove hydrogen sulphide from the environment. In comparison with the parent materials, an improvement in hydrogen sulphide adsorption was observed. Also, in [100], it was exhibited that besides physisorption, reactive adsorption is the most effective factor in retention. They show that formation of copper sulphide is resulted from H_2S molecules bind to the copper centres of the MOF which react with the MOF units.

3.2.5 Drug Delivery

In order of the large surface areas and the ability of tuning, MOFs porous structures are promising candidate to improve drug loadings and interactions [101]. For the drug delivery, it is necessary to use biocompatible materials for porous solids application. The common MOFs which are toxic, have not been appropriate for drug delivery [101]. So, to use MOFs composites in drug delivery, it is necessary to synthesize biocompatible MOFs with endogenous linkers [101].

4 Atomic Force Microscopy Application

Recently, investigation of crystallization and control the crystal properties of MOFs has attracted extreme attentions [102, 103]. Real-time results of the different steps of MOFs crystallization process reveal the fascinating information on the processes occurring [104]. On other hand, accurate mechanical characterization of MOFs and their composites is very important to enhance their applications. Because of capability to image surface topography with an angstrom resolution and the potential to perform in situ studies, especially for MOFs materials and composites, atomic force microscope (AFM) is a powerful imaging method to interpret the crystallization mechanism of MOFs [3, 105–112]. Moreover, AFM has significant ability to characterize the nanomechanical properties of different samples from soft to hard stiffness with high accuracy. In this section, the recent applications of AFM to investigate the crystallization process of MOFs, study the morphology of MOFs and nanomechanical characterization of MOFs materials and composites are reviewed. Generally, the application of AFM for MOFs study can be classified into two categories:

1. Provide high spatial and time resolutions 2D and 3D images of MOFs materials and their real-time crystallization process.
2. Characterize nanomechanical properties of MOFs.

For the first time, Shoaee et al. [113] presented the high-resolution microscopic image of the surface of HKUST-1 using atomic force microscopy. They demonstrated types of defects, the aspects of the crystal form and the process of crystal growth for KHUST-1 [113]. As shown in Fig. 4, several dislocation growth spirals consisting of single- and multiple growth spirals are explored on the {111} facets. Authors of [106] using in situ AFM imaging could provide images of single-layer growth on the monolayer-supported low-defect HKUST-1 crystal. High-resolution real-time AFM maps of the growing {111} facet of an HKUST-1 crystal is presented in Fig. 5. The results of growth of triangular anisotropic steps and the ternary symmetry of the {111} face are presented in [106]. As it can be seen, 77 min after injection of the growth solution, a small area at the nucleation point related to nucleation of a fresh layer could be observed. This post-nucleation step does not appear in following images and grows rapidly into a bigger step with a triangular habit which is more

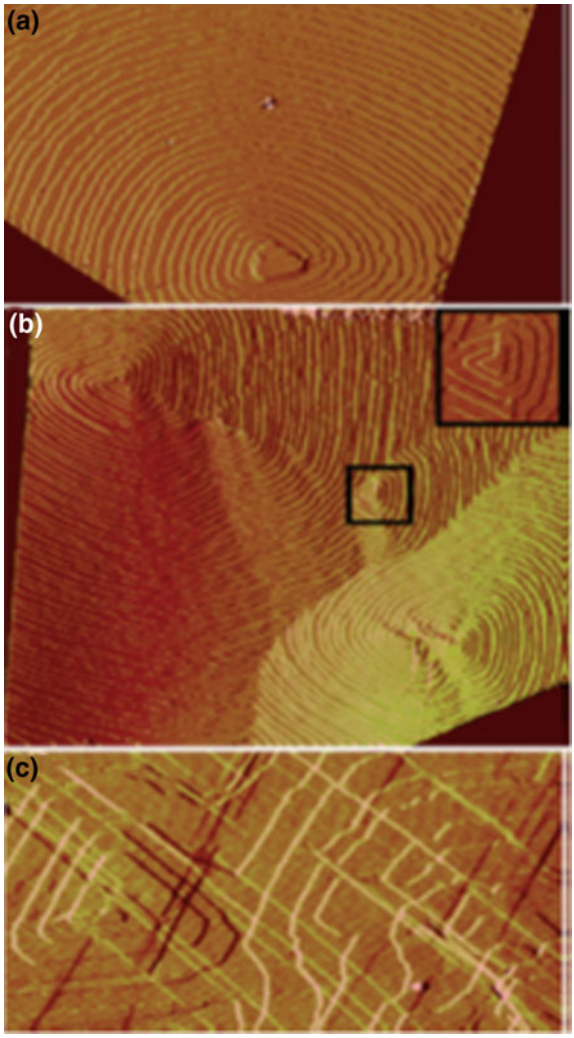

Fig. 4 AFM maps of {111} facets of HKUST-1, depicts **a** a double-growth spiral, **b** merging single- and multiple growth spirals **c** growth spirals overlaid with fractures primarily in the <110> directions. Reprinted with permission from [113], Copyright from Royal Society of Chemistry

stable. At 97 min of growth process, the abrupt drop in step speed corresponds to a sudden change in supersaturation [106].

The growth process of zeolitic imidazolate framework ZIF-8 MOF was studied in [107]. As the results shown in Fig. 6, in the growth process of ZIF-8, a two-dimensional surface nucleus appears at the growth terrace surface and spreads to form the surface growth step [107].

The first AFM investigation on MOF-5 crystal growth is performed by [104]. They could provide observation of the crystallization process of MOF-5 and the crystal surface morphology by exploring real-time 2D and spiral crystal growth. Their real-time AFM results provide opportunity to discover another mechanism of atomistic-level

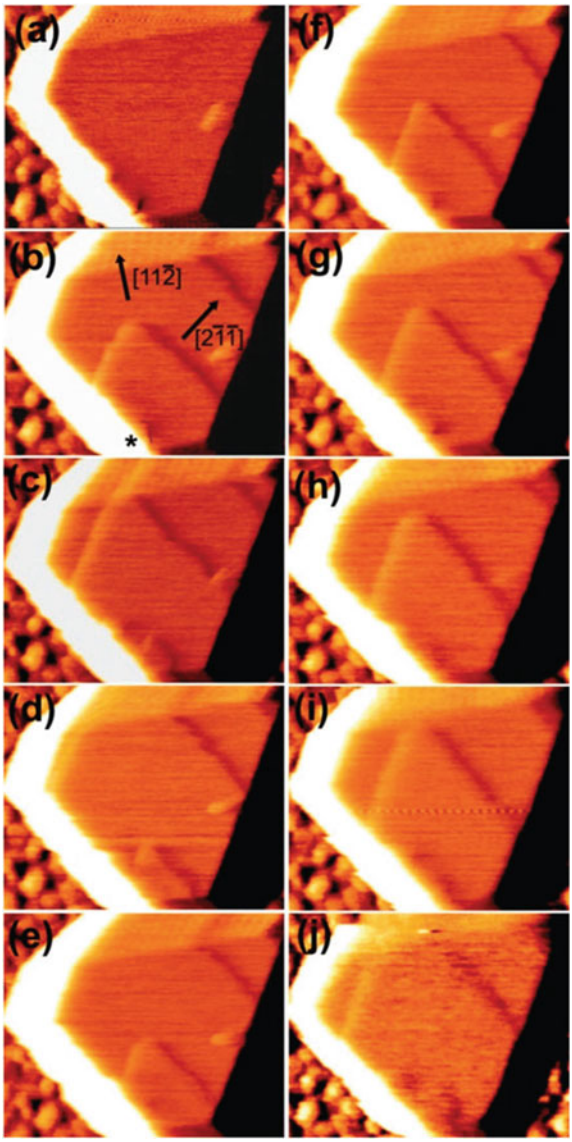

Fig. 5 Real-time atomic force microscopy maps of the {111} facet growth of an HKUST-1 crystal at **a** 56, **b** 77, **c** 79, **d** 82, **e** 85, **f** 88, **g** 91, **h** 94, **i** 97, **j** 108 mins after injection of the growth solution. Reprinted with permission from [106], Copyright from Royal Society of Chemistry

crystal growth of MOF-5 which depends on the ratio of growth solution Zn/H_2bdc and is denoted by variations in relative rates of growth and a stark transformation in terrace morphology [104]. In [114], high-resolution images of Cu_3(BTC)2 system (HKUST-1) MOF surface in both air and ultrahigh vacuum (UHV) mediums are obtained. From their results, direct growth of the surface structure of MOF crystal on the functionalized substrate is explored which can be used to the growth conditions optimization. By comparing their results with the ex situ AFM experiment which has

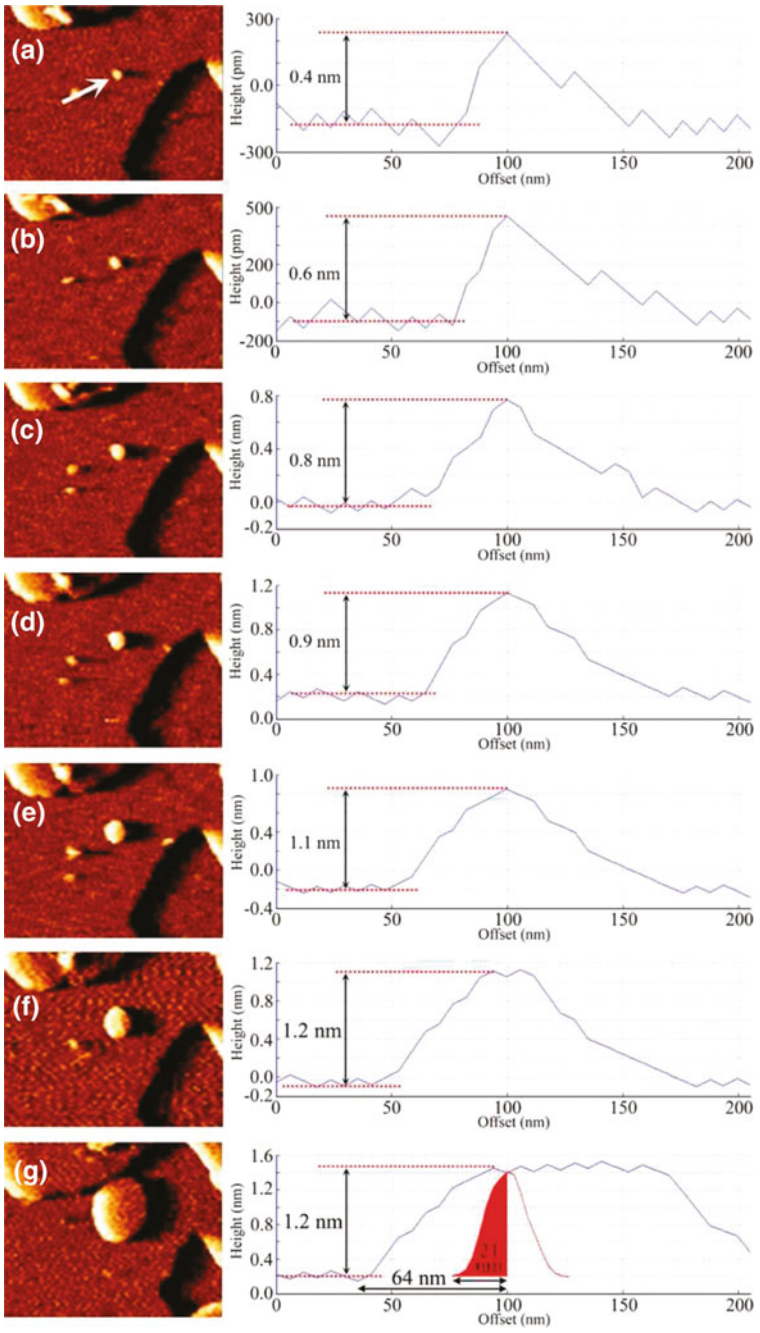
(a)
0.4 nm
Height (pm)
Offset (nm)
(b)
0.6 nm
Height (pm)
Offset (nm)
(c)
0.8 nm
Height (nm)
Offset (nm)
(d)
0.9 nm
Height (nm)
Offset (nm)
(e)
1.1 nm
Height (nm)
Offset (nm)
(f)
1.2 nm
Height (nm)
Offset (nm)
(g)
1.2 nm
64 nm
Height (nm)
Offset (nm)

◀**Fig. 6** Real-time atomic force microscopy maps and cross-sectional results of a developing growth step on the (110) face of a ZIF-8 crystal at 0 (**a**), 2.9 (**b**), 4.9 (**c**), 7.8 (**d**), 12.8 (**e**), 15.6 (**f**) and 40 (**g**) minutes after first observation of the 2D surface nuclei. Reprinted with permission from [107], Copyright © 2011, American Chemical Society

been carried out previously [113], they demonstrate that their presented approach has significant improvement of structural quality of MOF crystals grown on the substrate and it is a convenient way for in situ study of MOFs surface.

In [115], using AFM measurement the importance of ultrasonication as an efficient way to clean the MOF sample during the rinsing steps is demonstrated. It can noticeably improve the morphology and optical quality as shown in Fig. 7.

In [116], morphological behaviour of active channel material PDPP-TVT and its composite with electron-rich porous MOF using atomic force microscope are studied. Figure 8 shows the 2D and 3D maps of both PDPP-TVT and PDPP-TVT/MOF thin film composites. The results demonstrate that nodular ordered morphology with a larger grain size appears only in PDPP-TVT which is commonly observed for high molecular weight semi-crystalline conjugated polymer thin films. This property in thin films makes PDPP-TVT appropriate for charge transport route.

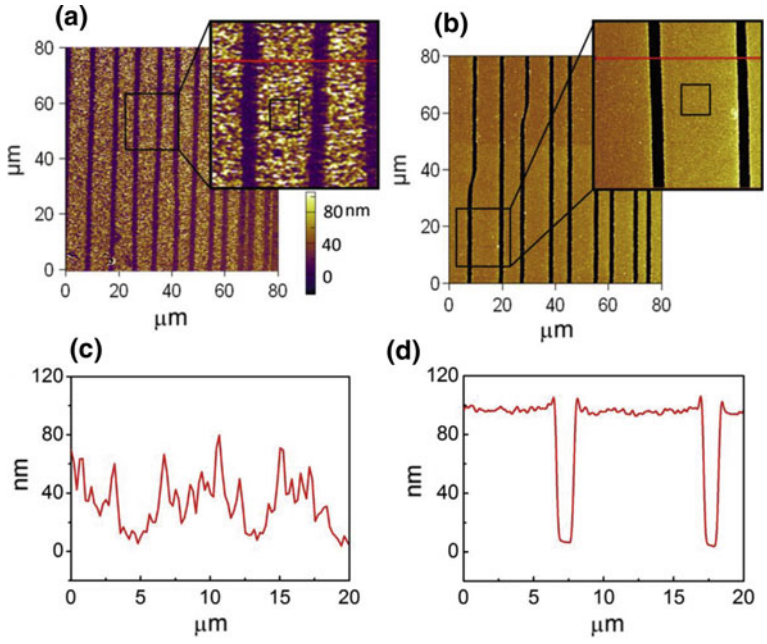

Fig. 7 AFM results with magnification of patterned HKUST-1 SURMOFs, prepared without (**a**) and with (**b**) ultrasonication. The cross-sectional results of (**a**) and (**b**) are shown in (**c**) and (**d**). Reprinted with permission from [115], Copyright from Elsevier

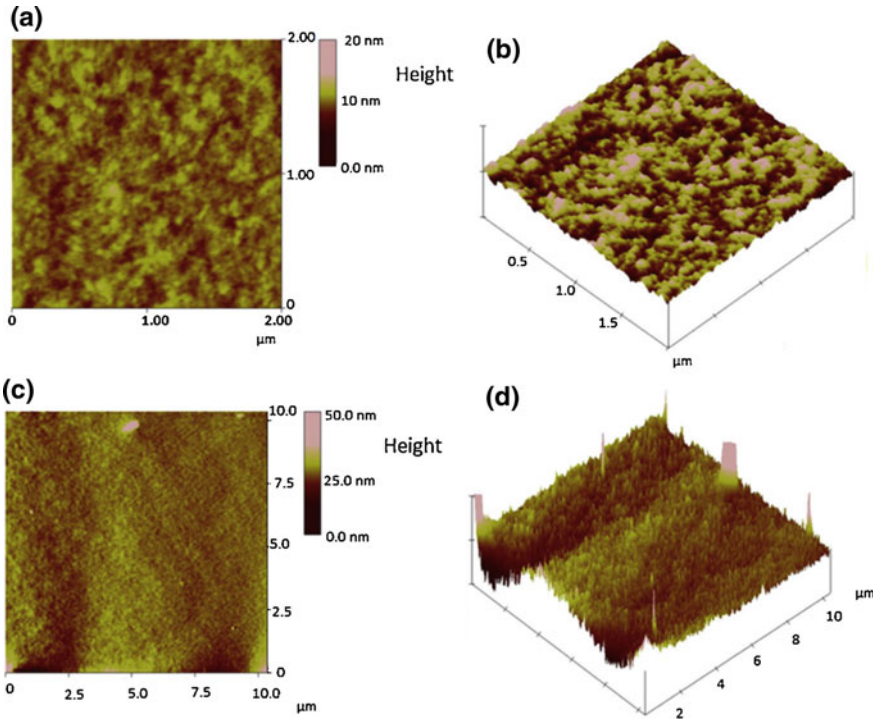

Fig. 8 Two-dimensional (left) and three-dimensional (right) AFM results of PDPP-TVT (**a**, **b**) and PDPP-TVT/MOF (**c**, **d**) thin films. Reprinted with permission from [116], Copyright from Elsevier

The maps of PDPP-TVT/MOF thin film composite show film texture with fine nodular morphological domains [116]. The introduction of MOF molecules with a heavy atom within the polymeric chains makes a slight interference of π–π stacking of polymeric chains, which may lead to fine thin film morphology of composite [116].

Two- and three-dimensional maps of MOF-5 and Au-MOF-5 are given in Fig. 9 [117]. There is a slight difference in the morphology of MOF-5 and Au-MOF-5. Average roughness of Au-MOF-5 film (98 nm) is higher than MOF-5 (86 nm). Although the enhance in roughness can be associated with several factors including degree of NPs coverage, size, etc., it is not explored exactly why the roughness in Au-MOF-5 is higher [117, 118].

In [119], for the first time it is revealed that MOF/thin film nanocomposite (TFN) membrane extremely improves the performance of water vapor transport from the mixture gas. Figure 10 shows surface morphologies of TFC and TFN/MOF composites membranes. Although there is ridge-and-valley structure in all the membrane's surface morphology, for TFN membranes it is sharper than TFC membrane. The root mean square (RMS) roughness (R_q), average surface roughness (R_a) and maximum surface roughness (R_{max}) of the TFC and TFN membranes are given in Table 1. Considerable variations were detected in the RMS surface roughness, R_{max} and R_a which

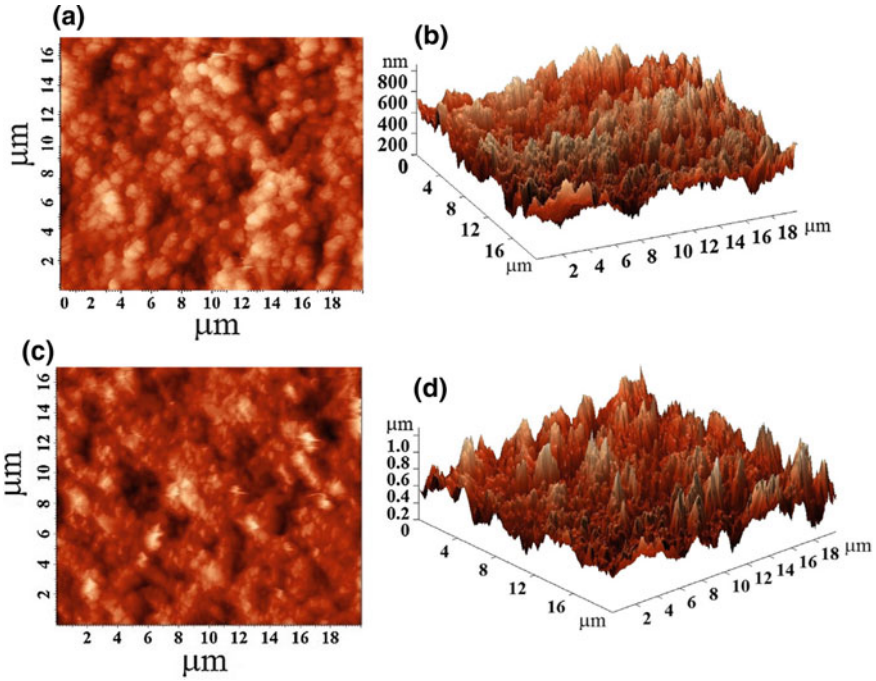

Fig. 9 2D (**a**, **c**) and 3D (**b**, **d**) atomic force microscopy maps of MOF-5 (**a**, **b**) and Au-MOF-5 (**c**, **d**). Reprinted with permission from [117], Copyright from Elsevier

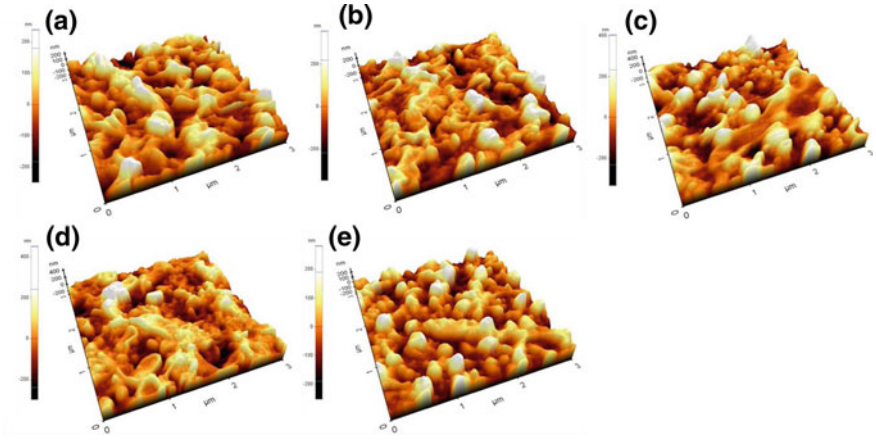

Fig. 10 Three-dimensional topographic images of **a** TFC, **b** MOF@TFN1 (0.01), **c** MOF@TFN2 (0.025), **d** MOF@TFN3 (0.05) and **e** MOF@TFN4 (0.1). Reprinted with permission from [119], Copyright from Elsevier

Table 1 Atomic force microscopy surface roughness values and water contact angle of TFC and MOF@TFN membranes

Membrane	R_q (nm)	R_{max} (nm)	R_a (nm)	Water contact angle (°)
TFC	75.05	238.63	59.77	56 ± 2
MOF@TFN1	92.1	354.67	72.47	42 ± 2
MOF@TFN2	98.8	403.06	78.37	39 ± 1
MOF@TFN3	97.33	450.1	75.79	37 ± 2
MOF@TFN4	80.01	281.39	65.17	44 ± 2

Reprinted with permission from [119], Copyright from Elsevier

Table 2 Mean surface roughness (R_a) and root mean square (rms) results of cross-linked asymmetric polyimide (P84) support, LS-P84, TFC, LS-TFN and conventional TFN membranes

	Cross-linked asymmetric polyimide (P84) support	LS-P84	TFC	LS-TFN	Conventional TFN
R_a (nm)	2.1 ± 0.0	56.6 ± 1.2	24.8 ± 1.7	47.0 ± 0.2	52.7 ± 0.6
R_{ms} (nm)	2.7 ± 0.1	62.8 ± 0.1	30.7 ± 1.2	57.5 ± 1.7	64.7 ± 0.2

Reprinted with permission from [120], Copyright © 2018, American Chemical Society

prove the MOF nanomaterials have an important effect in increasing the surface roughness parameter of the TFN membranes.

In [120], an approach for introducing a monolayer of hydrophilic MOF MIL-101(Cr) nanoparticles within thin film nanocomposite (TFN) membranes is proposed.

AFM results of LS-P84, TFC, LS-TFN and conventional TFN membranes have been presented in Figs. 11 and 12, and their R_a and R_{ms} values are given in Table 2. The topography of the bare cross-linked asymmetric polyimide (P84) support (Fig. 11a, b) measured with atomic force microscopy was considered as a reference for morphology and roughness variations characterization compared to other composite membranes, specifically with focus on MOF composites. In comparison with P84 support (R_a = ±2.1) (Fig. 11a, b), the ridge-and-valley characteristic of polyamide surface in TFC membranes enhances the roughness (R_a = ±24.8) (Fig. 12a), and the LS-MIL-101(Cr) film procedure in LS-P84 membranes (R_a = ±50.6) (Fig. 11c, d). By adding thin polyamide layer for formation of the LS-TFN membrane, the R_a value reduced to ±47.0 and its surface becomes smoother (Fig. 12b). Also, comparison between TFC with the two TFN membranes exhibits the increase in roughness that is enough to promote an increase in the membrane permeance. Comparison of R_a and root mean square values of LS-TFN and conventional TFN membranes (Table 2), demonstrates that the surface LS-TFN membrane is the smoothest [120].

AFM results of a conventional TFN membrane (Fig. 12c) depict a random distribution of MIL-101(Cr) NPs in the polyamide layer compared to LS-TFN membranes,

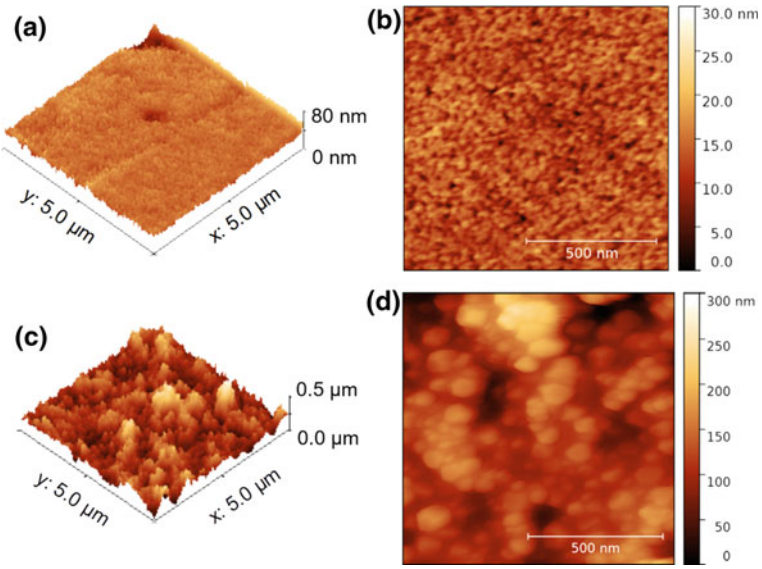

Fig. 11 **a** 3D and **b** 2D maps of the bare cross-linked asymmetric polyimide (P84) support. **c** 3D and **d** 2D maps of the LS film of MIL-101(Cr) NPs on the cross-linked asymmetric polyimide (P84) support (LSP84). Reprinted with permission from [120], Copyright © 2018, American Chemical Society

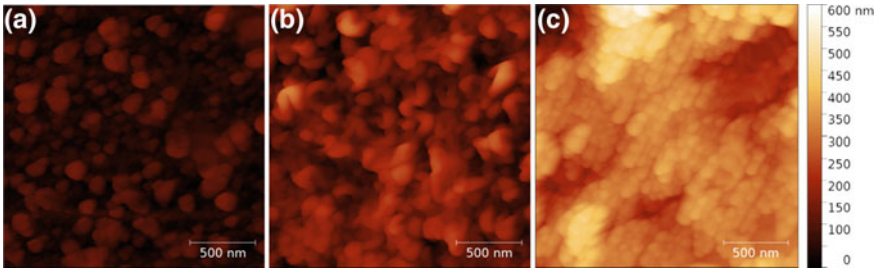

Fig. 12 AFM maps of the surface of **a** TFC membrane, **b** LS-TFN membrane and **c** conventional TFN membrane. Reprinted with permission from [120], Copyright © 2018, American Chemical Society

because of the absence of a well-formed MOF monolayer that it is clearly formed in the LS-TFN membrane.

The AFM images with angstrom resolution of the variations of a MOF surface immersed in liquid were presented in [23]. The results show that molecular species diffusion along the step edges of the open terraces characterizes the Ce-RPF-8 surfaces immersed in water and glycerol which experience a liquid dependent surface reconstruction process. While for water it occurs instinctively, in glycerol via applying an external force it is triggered [23]. These results demonstrate the ability of

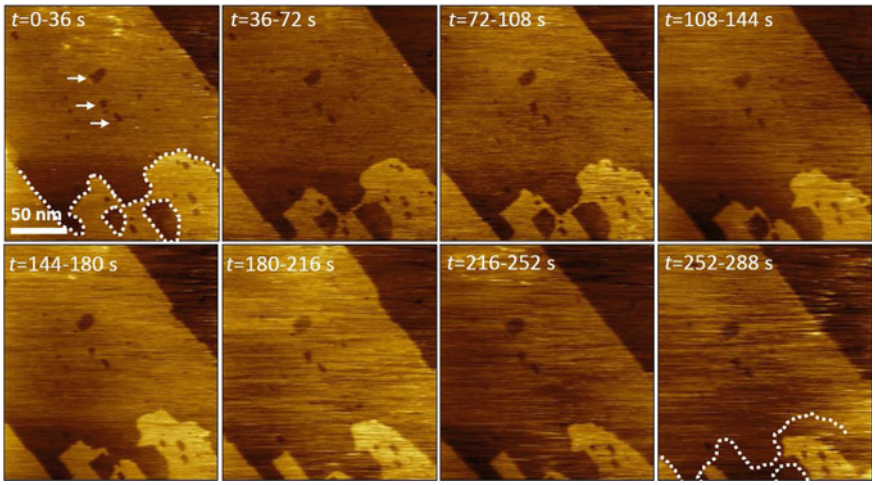

Fig. 13 Sequence of AM-AFM maps depicting MOF etching phenomena in water. Reprinted with permission from [23], Creative Commons Attribution 4.0 International License

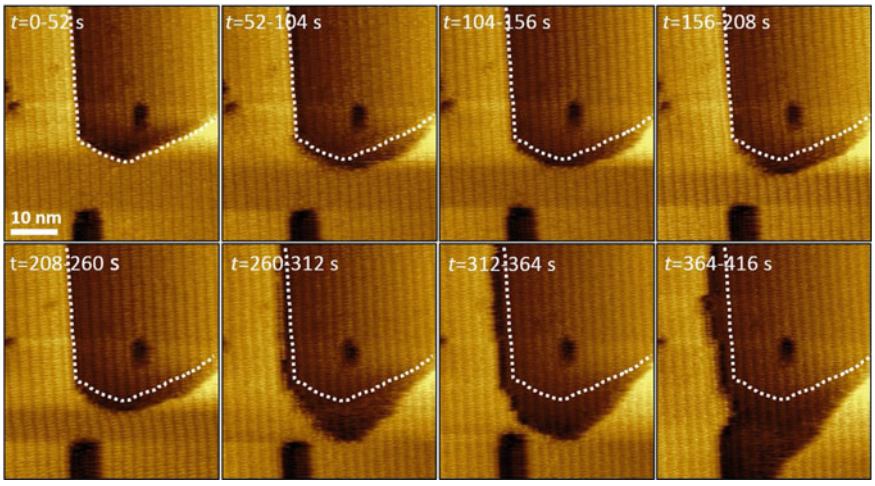

Fig. 14 Sequence of AM-AFM maps depicting MOF etching phenomena in glycerol. Reprinted with permission from [23], Creative Commons Attribution 4.0 International License

amplitude modulation mode of atomic force microscopy to observe the dynamics of the surface reconstruction mechanisms of MOF surfaces in aqueous environments with angstrom resolution [23]. The obtained results can be used for the optimization of MOF performance (Figs. 13 and 14).

In [121], a method to fabricate MOF films on the basis of soft-imprinting for the gas sensors application was proposed. The microporous MOF material [Zn2(bpdc)2(bpee)] was synthesized solvothermally and activated via remove of

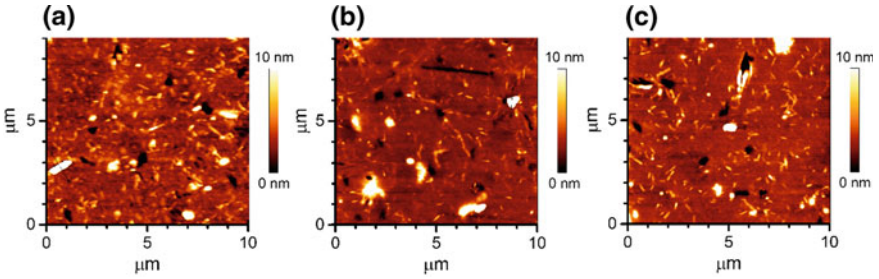

Fig. 15 AFM results of soft-imprinted [Zn2(bpdc)2(bpee)] powder on CA/quartz substrates prepared at **a** 2; **b** 4; and **c** 6 bar. Reprinted with permission from [121], Creative Commons Attribution 4.0 International License

occluded solvent molecules from its inner channels. Images of soft-imprinted films taken from atomic force microscope depicted MOF crystals were embedded partially into the CA. Using this method, films with mechanical stability were produced, with crystals protruding from the CA surface which are available for incoming gas molecules (Fig. 15).

AFM has been used to characterize the nanomechanical properties of MOFs and their composites. There are two ways proposed to characterize the nanomechanical properties of MOFs using AFM techniques. The first one is based on nanoindentation using tapping mode AFM and the second one is based on multifrequency operation of AFM especially bimodal AM-FM configuration [17, 30, 122]. The main advantage of bimodal AM-FM method is to provide simultaneous maps of topography and nanomechanical properties of the sample with high resolution in a very short time.

For the stiffness measurement of HKUST-1 thin films, Tan and his co-workers [122] performed multifrequency bimodal AM-FM AFM experiments. The values of elastic moduli (E) are calculated between 3 and 6 GPa. However, because they did not use appropriate reference material (they used Matrimid 5218 with 4 GPa elastic modulus) for MOFs, the proposed method should be modified to accurately determine the elastic modulus. By improving that technique, in [122], the nanomechanical properties of several metal ions and chemical functionalities have been characterized. By nanomechanical characterization of five types of zirconium (Zr) and hafnium (Hf) isostructural UiO-66-type MOFs, it was depicted that UiO-66(Hf)-type MOFs (46–104 GPa) is stiffer than UiO-66(Zr)-type MOFs (34–100 GPa). On other hand, both of them have higher stiffness than reported zinc/copper-based MOFs (3–10 GPa). Also, based on the experiments, it is revealed that the mechanical characteristics of MOFs are tunable through regulating the chemical functionalities of the ligands or using different metal nodes (Figs. 16, 17 and 18).

Also, recently in [30], the ability of AM-FM AFM not only to provide angstrom scale images but also to measure the Young's Modulus of MOF has been demonstrated [123]. The results of topography and elastic modulus are given in Fig. 19. The AM-FM AFM topography maps exhibit a periodic pattern and defects with angstrom spatial resolution. There is an agreement between the results of bimodal

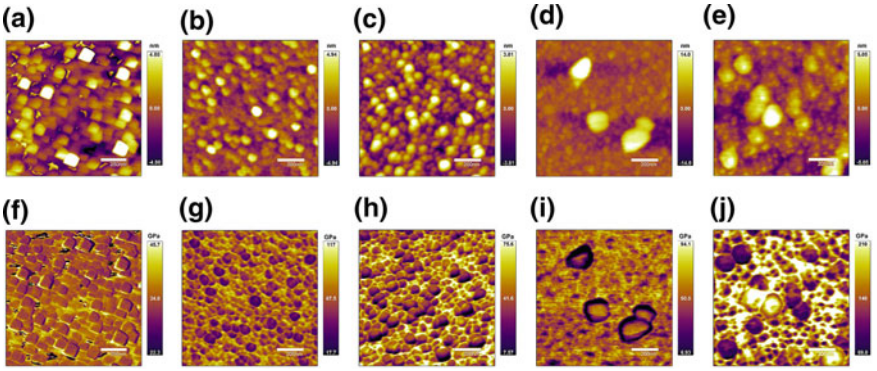

Fig. 16 Topography images of **a** UiO-66(Zr); **b** UiO-66(Zr)-$(OH)_2$; **c** UiO-66(Zr)-NH_2; **d** UiO-66(Zr)-$(COOH)_2$; **e** UiO-66(Zr)-$(F)_4$. Elastic modulus mapping of **f** UiO-66(Zr); **g** UiO-66(Zr)-$(OH)_2$; **h** UiO-66(Zr)-NH_2; **i** UiO-66(Zr)-$(COOH)_2$; **j** UiO-66(Zr)-$(F)_4$. Reprinted with permission from [122], Copyright © 2017, American Chemical Society

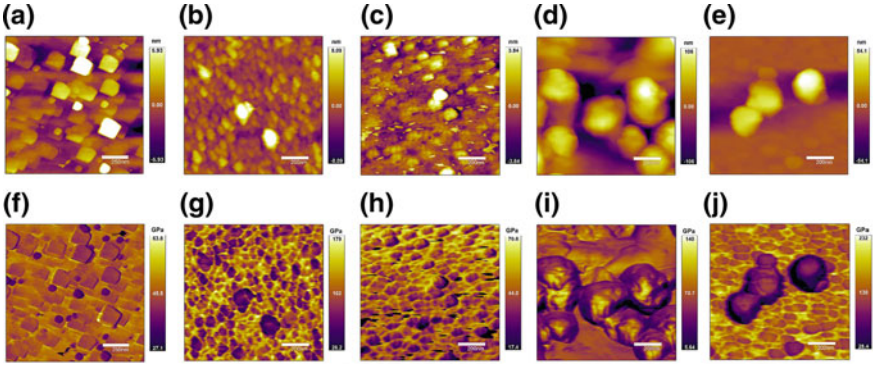

Fig. 17 Topography images of **a** UiO-66(Hf); **b** UiO-66(Hf)-$(OH)_2$; **c** UiO-66(Hf)-NH_2; **d** UiO-66(Hf)-$(COOH)_2$; **e** UiO-66(Hf)-$(F)_4$. Elastic modulus mapping of **f** UiO-66(Hf); **g** UiO-66(Hf)-$(OH)_2$; **h** UiO-66(Hf)-NH_2; **i** UiO-66(Hf)-$(COOH)_2$; **j** UiO-66(Hf)-$(F)_4$. Reprinted with permission from [122], Copyright © 2017, American Chemical Society

AM-FM AFM and X-ray crystallography (Fig. 19a). Bimodal AM-FM AFM could provide the stiffness maps in 26 s. There are four different areas in the map of elastic modulus (Fig. 19g).

The atomic structure comparison (Fig. 19b) demonstrates that Ce atoms are stiffer than carbon linkers. As illustrated in Fig. 20, the region (I) which is the softest region corresponds to the areas that lie between the two carbon rings. Region (II) is associated with the top of carbon rings. Regions (III) and (IV) are related to the Ce atoms. The difference between Elastic modulus of regions (III) and (IV) depicts the numbers and types of the atoms which surround the Ce atoms and determine their elastic response.

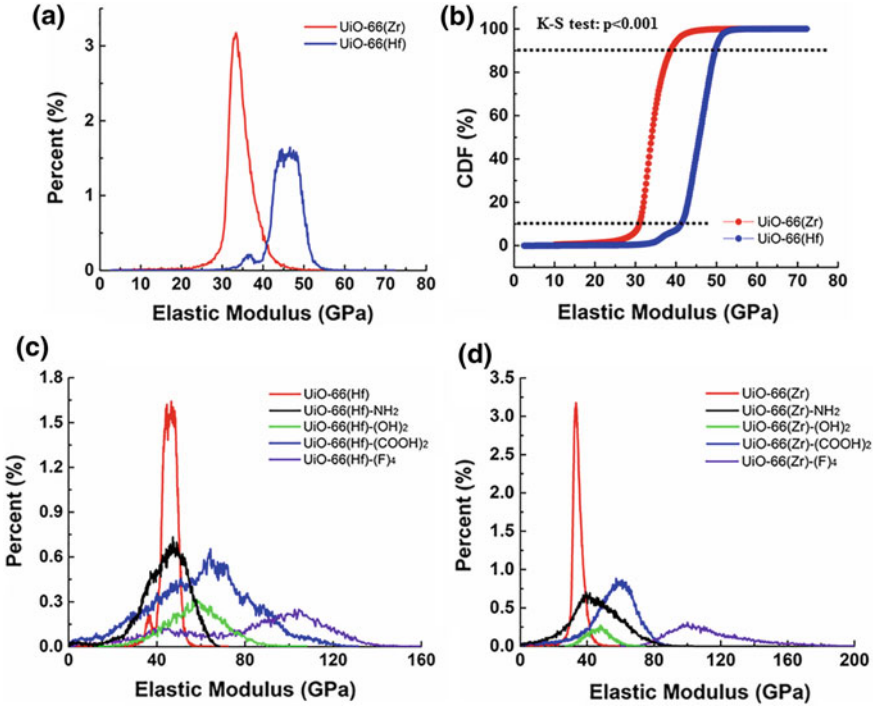

Fig. 18 Distribution curves of AM-FM elastic modulus mappings of **a** UiO-66(Hf/Zr). **b** CDF curves of the distribution curves presented in (**a**). **c** Distribution curves of UiO-66(Hf)-type MOFs. **d** Distribution curves of UiO-66(Zr)-type MOFs. Reprinted with permission from [122], Copyright © 2017, American Chemical Society

AFM nanoindentation also could map the surface topography and quantify the shape of the residual indents. In [17], for the first time, AFM nanoindentation has been used for quantitative nanomechanical characterization of ZIF-8. The measurements have been carried out on isolated micron-sized (~1 to 2 μm) and submicron (<500 nm) crystals of ZIF-8. By observation of AFM indenter tip strain rate in indentation procedure, they demonstrated that the method is valid for the quantification of Young's modulus and stiffness of nanoscale crystal samples (Fig. 21).

However, in contrast to multifrequency AM-FM AFM, quantitative analysis of AFM nanoindentation results is challengeable. The main challenges to mechanical quantification of MOFs using AFM nanoindentation are the possibility of tip damage or the intrinsic compliance of the AFM cantilever, accurate determination of contact area, reduced the resolution for three-dimensional mapping and indentation-triggered effects including the periphery of the indenter [17]. Moreover, when the indenter is loaded, creep, viscoelastic and adhesion interactions can affect the quality of data interpretation significantly [17].

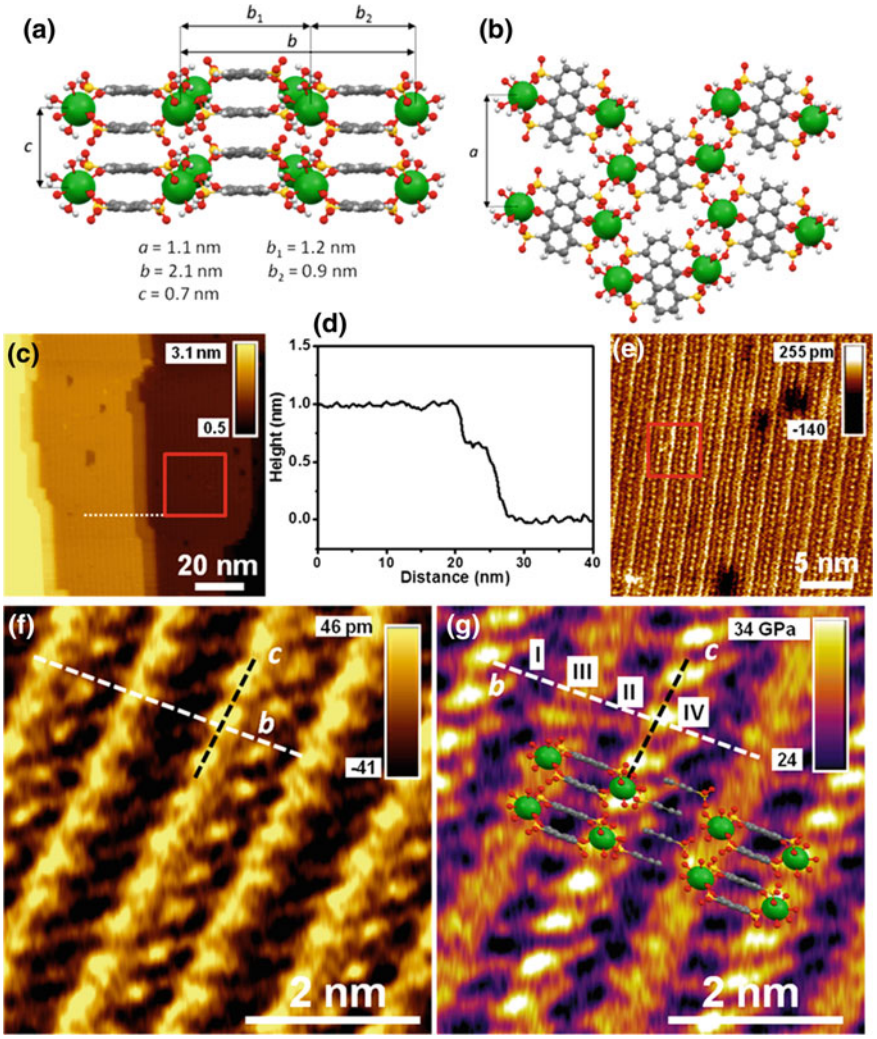

Fig. 19 MOF **a** top view, **b** side view structure. **c** Topography of a section of the MOF surface. **d** Height cross section along the line marked in **c**. **e** Sub-nanometre image of the part of MOF marked in **c**. **f** Angstrom bimodal (topographic) image of the part of MOF marked in **e**. **g** Elastic modulus map of the region shown in **f**. Reprinted with permission from [30], Copyright © 2017, American Chemical Society

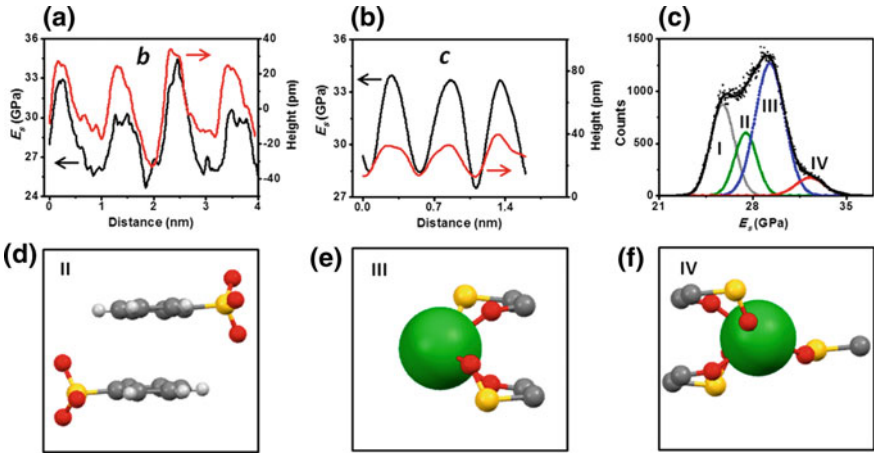

Fig. 20 Topography and Young's modulus cross sections along the dashed lines parallel to the **a** b lattice vector, **b** c lattice vector. **c** Statistic elastic modulus values obtained over the region shown in Fig. 19g. **d** Proposed atomic structure for the locations associated with a Young's modulus of (d0 27.5 GPa). **e** of 29.3 GPa. **f** 32.3 GPa. Atom colours: Ce, green; S, yellow; O, red; C, grey; H, white. Reprinted with permission from [30], Copyright © 2017, American Chemical Society

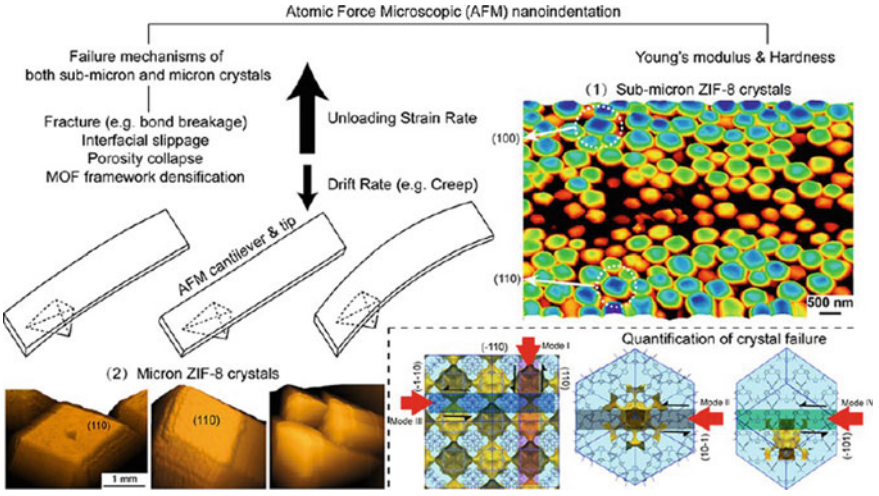

Fig. 21 Schematic of AFM indentation on ZIF-8. Reprinted with permission from [17], Copyright © 2017, American Chemical Society

References

1. Xiang W, Zhang Y, Lin H, Liu C (2017) Nanoparticle/metal–organic framework composites for catalytic applications: current status and perspective. Molecules 22(12):2103
2. Gangu KK, Maddila S, Mukkamala SB, Jonnalagadda SB (2016) A review on contemporary metal-organic framework materials. Inorganica Chim Acta 446:61–74
3. Bradshaw D, Garai A, Huo J (2012) Metal–organic framework growth at functional interfaces: thin films and composites for diverse applications. Chem Soc Rev 41(6):2344–2381
4. Kumar P, Vellingiri K, Kim KH, Brown RJC, Manos MJ (2016) Modern progress in metal-organic frameworks and their composites for diverse applications. Microporous Mesoporous Mater 253:251–265
5. Chen J, Li Y (2016) The road to MOF-related functional materials and beyond: desire, design, decoration, and development. Chem Rec 1456–1476
6. Stock N, Biswas S (2012) Synthesis of metal-organic frameworks (MOFs): routes to various MOF topologies, morphologies, and composites. Chem Rev 112(2):933–969
7. Li S, Huo F (2015) Metal–organic framework composites: from fundamentals to applications. Nanoscale 7(17):7482–7501
8. Zhu Q-L, Xu Q (2014) Metal–organic framework composites. Chem Soc Rev 43(16):5468–5512
9. Zhang Y, Feng X, Yuan S, Zhou J, Wang B (2016) Challenges and recent advances in MOF–polymer composite membranes for gas separation. Inorg Chem Front 3(7):896–909
10. Yu J et al (2017) Nanoparticle/MOF composites: preparations and applications. Mater Horiz 4(4):557–569
11. Aguilera-Sigalat J, Bradshaw D (2016) Synthesis and applications of metal-organic framework-quantum dot (QD at MOF) composites. Coord Chem Rev 307:267–291
12. Liu X-W, Sun T-J, Hu J-L, Wang S-D (2016) Composites of metal–organic frameworks and carbon-based materials: preparations, functionalities and applications. J Mater Chem A 4(10):3584–3616
13. Li W, Zhang Y, Li Q, Zhang G (2015) Metal-organic framework composite membranes: synthesis and separation applications. Chem Eng Sci 135:232–257
14. Li W, Henke S, Cheetham AK (2014) Research update: mechanical properties of metal-organic frameworks—influence of structure and chemical bonding. APL Mater 2(12)
15. Tan JC, Cheetham AK (2011) Mechanical properties of hybrid inorganic–organic framework materials: establishing fundamental structure–property relationships. Chem Soc Rev 40(2):1059
16. Ortiz AU, Boutin A, Fuchs AH, Coudert FX (2012) Anisotropic elastic properties of flexible metal-organic frameworks: how soft are soft porous crystals? Phys Rev Lett 109(19):1–5
17. Zeng Z, Tan JC (2017) afm nanoindentation to quantify mechanical properties of nano- and micron-sized crystals of a metal-organic framework material. ACS Appl Mater Interfaces 9(45):39839–39854
18. Marmier A, Evans KE (2016) Flexibility in MOFs: do scalar and group-theoretical counting rules work? Dalt. Trans. 45(10):4360–4369
19. Banlusan K, Antillon E, Strachan A (2015) Mechanisms of plastic deformation of metal-organic framework-5. J Phys Chem C 119(46):25845–25852
20. Øien-Ødegaard S, Shearer GC, Wragg DS, Lillerud KP (2017) Pitfalls in metal–organic framework crystallography: towards more accurate crystal structures. Chem Soc Rev 46(16):4867–4876
21. Wiktor C, Meledina M, Turner S, Lebedev OI, Fischer RA (2017) Transmission electron microscopy on metal–organic frameworks—a review. J Mater Chem A 5(29):14969–14989
22. Suga M et al (2014) Recent progress in scanning electron microscopy for the characterization of fine structural details of nano materials. Prog Solid State Chem 42(1–2):1–21
23. Chiodini S et al (2017) Angstrom-resolved metal-organic framework-liquid interfaces. Sci Rep 7(1):1–6

24. Dai Q, Vollmer R, Carpick RW, Ogletree DF, Salmeron M (1995) A variable temperature ultrahigh vacuum atomic force microscope. Rev Sci Instrum 66(11):5266–5271
25. Ortiz-Young D, Chiu H-C, Kim S, Voïtchovsky K, Riedo E (2013) The interplay between apparent viscosity and wettability in nanoconfined water. Nat Commun 4:2482
26. Kuna JJ et al (2009) The effect of nanometre-scale structure on interfacial energy. Nat Mater 8(10):837–842
27. Miller EJ, Trewby W, Farokh Payam A, Piantanida L, Cafolla C, Voïtchovsky K (2016) Sub-nanometer resolution imaging with amplitude-modulation atomic force microscopy in liquid. J Vis Exp 118:1–10
28. Payam AF, Ramos JR, Garcia R (2012) Molecular and nanoscale compositional contrast of soft matter in liquid: interplay between elastic and dissipative interactions. ACS Nano 6(6):4663–4670
29. Martin-Jimenez D, Chacon E, Tarazona P, Garcia R (2016) Atomically resolved three-dimensional structures of electrolyte aqueous solutions near a solid surface. Nat Commun 7:1–7
30. Amo CA, Perrino AP, Payam AF, Garcia R (2017) Mapping elastic properties of heterogeneous materials in liquid with angstrom-scale resolution. ACS Nano 11(9):8650–8659
31. Hoskins BF, Robson R (1990) Design and construction of a new class of scaffolding-like materials comprising infinite polymeric frameworks of 3D-linked molecular rods. a reappraisal of the Zn(CN)2 and Cd(CN)2 structures and the synthesis and structure of the diamond-related frameworks. J Am Chem Soc 112(4):1546–1554
32. Maji TK, Kitagawa S (2007) Chemistry of porous coordination polymers. Pure Appl Chem 79(12):2155–2177
33. Czaja AU, Trukhan N, Müller U (2009) Industrial applications of metal–organic frameworks. Chem Soc Rev 38(5):1284
34. Vakiti RK (2012) Hydro/solvothermal synthesis, structures and properties of metal-organic frameworks based on S-block metals. Western Kentucky University
35. Yaghi OM, Ockwig OKMNW, Chae HK, Eddaoudi M, Kim J (2003) Reticular synthesis and the design of new materials. Nature 423(6941):705–714
36. Haldar R, Maji TK (2013) Metal–organic frameworks (MOFs) based on mixed linker systems: structural diversities towards functional materials. Cryst Eng Comm 15(45):9276
37. Seetharaj R, Vandana PV, Arya P, Mathew S (2015) Dependence of solvents, pH, molar ratio and temperature in tuning metal organic framework architecture. Arab J Chem
38. Baig RBN, Varma RS (2012) Alternative energy input: mechanochemical, microwave and ultrasound-assisted organic synthesis. Chem Soc Rev 41(4):1559–1584
39. Surati MA, Jauhari SA, Desai KR (2012) A brief review: microwave assisted organic reaction. Arch Appl Sci Res. 4(1):645–661
40. Khan NA, Jhung SH (2015) Synthesis of metal-organic frameworks (MOFs) with microwave or ultrasound: rapid reaction, phase-selectivity, and size reduction. Coord Chem Rev 285:11–23
41. Xu H, Zeiger BW, Suslick KS (2013) Sonochemical synthesis of nanomaterials. Chem Soc Rev 42(7):2555–2567
42. Ameloot R, Stappers L, Fransaer J, Alaerts L, Sels BF, De Vos DE (2009) Patterned growth of metal-organic framework coatings by electrochemical synthesis. Chem Mater 21(13):2580–2582
43. Pirzadeh K, Ghoreyshi AA, Rahimnejad M, Mohammadi M (2018) Electrochemical synthesis, characterization and application of a microstructure Cu3(BTC)2 metal organic framework for CO2 and CH4 separation. Korean J Chem Eng 35(3):1–10
44. Achar TK, Bose A, Mal P (2017) Mechanochemical synthesis of small organic molecules. Beilstein J Org Chem 13:1907–1931
45. Kaupp G, Schmeyers J, Boy J (2001) Waste-free solid-state syntheses with quantitative yield. Chemosphere 43(1):55–61
46. Klimakow M, Klobes P, Thünemann AF, Rademann K, Emmerling F (2010) Mechanochemical synthesis of metal-organic frameworks: A fast and facile approach toward quantitative yields and high specific surface areas. Chem Mater 22(18):5216–5221

47. Fang QR et al (2007) Mesoporous metal-organic framework with rare ETB topology for hydrogen storage and dye assembly. Angew Chemie Int Ed 46(35):6638–6642
48. Stassen I et al (2016) Chemical vapour deposition of zeolitic imidazolate framework thin films. Nat Mater 15(3):304–310
49. Wilmer CE et al (2012) Large-scale screening of hypothetical metal-organic frameworks. Nat Chem 4(2):83–89
50. Dzubak AL et al (2012) Ab initio carbon capture in open-site metal-organic frameworks. Nat Chem 4(10):810–816
51. Liu Y et al (2014) Designable yolk-shell nanoparticle@MOF petalous heterostructures. Chem Mater 26(2):1119–1125
52. Li Z, Zeng HC (2013) Surface and bulk integrations of single-layered Au or Ag nanoparticles onto designated crystal planes 110 or 100 of ZIF-8. Chem Mater 25(9):1761–1768
53. Uemura T, Yanai N, Kitagawa S (2009) Polymerization reactions in porous coordination polymers. Chem Soc Rev 38(5):1228
54. You H, Yang S, Ding B, Yang H (2013) Synthesis of colloidal metal and metal alloy nanoparticles for electrochemical energy applications. Chem Soc Rev 42(7):2880–2904
55. Uemura T et al (2010) Unveiling thermal transitions of polymers in subnanometre pores. Nat Commun 1(7):1–8
56. Hwang YK et al (2008) Amine grafting on coordinatively unsaturated metal centers of MOFs: consequences for catalysis and metal encapsulation. Angew Chemie Int Ed 47(22):4144–4148
57. Kim H, Chun H, Kim G-H, Lee H-S, Kim K (2006) Vapor phase inclusion of ferrocene and its derivative in a microporous metal–organic porous material and its structural characterization by single crystal X-ray diffraction. Chem Commun 26:2759–2761
58. Ishida T, Nagaoka M, Akita T, Haruta M (2008) Deposition of gold clusters on porous coordination polymers by solid grinding and their catalytic activity in aerobic oxidation of alcohols. Chem A Eur J 14(28):8456–8460
59. Li Y, Zou B, Xiao A, Zhang H (2017) Advances of metal-organic frameworks in energy and environmental applications. Chinese J Chem 35(10):1501–1511
60. Bruce PG, Freunberger SA, Hardwick LJ, Tarascon J-M (2012) Li–O2 and Li–S batteries with high energy storage. Nat Mater 11(1):19–29
61. Lian X et al (2017) Enzyme–MOF (metal–organic framework) composites. Chem Soc Rev 46(11):3386–3401
62. Zhou Z, Hartmann M (2013) Progress in enzyme immobilization in ordered mesoporous materials and related applications. Chem Soc Rev 42(9):3894
63. Xuan W, Zhu C, Liu Y, Cui Y (2012) Mesoporous metal–organic framework materials. Chem Soc Rev 41(5):1677–1695
64. Lue JT (2001) A review of characterization and physical property studies of metallic nanoparticles. J Phys Chem Solids 62(9–10):1599–1612
65. Kelly KL, Coronado E, Zhao LL, Schatz GC (2003) The optical properties of metal nanoparticles: the influence of size, shape, and dielectric environment. J Phys Chem B 107(3):668–677
66. Moon HR, Lim D-W, Suh MP (2013) Fabrication of metal nanoparticles in metal–organic frameworks. Chem Soc Rev 42(4):1807–1824
67. White RJ, Luque R, Budarin VL, Clark JH, Macquarrie DJ (2009) Supported metal nanoparticles on porous materials. Methods and applications. Chem Soc Rev 38(2):481–494
68. Resch-Genger U, Grabolle M, Cavaliere-Jaricot S, Nitschke R, Nann T (2008) Quantum dots versus organic dyes as fluorescent labels. Nat Methods 5(9):763–775
69. Yang Z, Chen C-Y, Roy P, Chang H-T (2011) Quantum dot-sensitized solar cells incorporating nanomaterials. Chem Commun 47(34):9561
70. Falcaro P et al (2011) A new method to position and functionalize metal-organic framework crystals. Nat Commun 2(1)
71. Choi KM, Jeong HM, Park JH, Zhang YB, Kang JK, Yaghi OM (2014) Supercapacitors of nanocrystalline metal-organic frameworks. ACS Nano 8(7):7451–7457
72. Yue Y et al (2014) Multi-wall carbon nanotube@zeolite imidazolate framework composite from a nanoscale zinc oxide precursor. Microporous Mesoporous Mater 198:139–143

73. Klyamkin SN et al (2007) High-pressure hydrogen storage on modified MIL-101 metal–organic framework. Int J Energy Res (31):135–147
74. Qiu S, Xue M, Zhu G (2014) Metal–organic framework membranes: from synthesis to separation application. Chem Soc Rev 43(16):6116–6140
75. Shekhah O et al (2009) Controlling interpenetration in metal-organic frameworks by liquid-phase epitaxy. Nat Mater 8(6):481–484
76. Huang ZH, Liu G, Kang F (2012) Glucose-promoted Zn-based metal-organic framework/graphene oxide composites for hydrogen sulfide removal. ACS Appl Mater Interfaces 4(9):4942–4947
77. Vayssieres L (2004) On the design of advanced metal oxide nanomaterials. Int J Nanotechnol 1:1–41
78. Hermes S, Schröder F, Amirjalayer S, Schmid R, Fischer RA (2006) Loading of porous metal–organic open frameworks with organometallic CVD precursors: inclusion compounds of the type $[L_n M]_a$ @MOF-5. J Mater Chem 16(25):2464–2472
79. Lu G et al (2012) Imparting functionality to a metal-organic framework material by controlled nanoparticle encapsulation. Nat Chem 4(4):310–316
80. Ke F, Qiu L-G, Yuan Y-P, Jiang X, Zhu J-F (2012) Fe3O4@MOF core–shell magnetic microspheres with a designable metal–organic framework shell. J Mater Chem 22(19):9497
81. Slowing II, Trewyn BG, Giri S, Lin VSY (2007) Mesoporous silica nanoparticles for drug delivery and biosensing applications. Adv Funct Mater 17(8):1225–1236
82. Hutin M, Rosnes MH, Long DL, Cronin L (2013) Polyoxometalates: synthesis and structure—from building blocks to emergent materials, vol 2. Elsevier Ltd
83. Peng Z (2004) Rational synthesis of covalently bonded organic-inorganic hybrids. Angew Chemie Int Ed 43(8):930–935
84. Juan-Alcañiz J, Gascon J, Kapteijn F (2012) Metal–organic frameworks as scaffolds for the encapsulation of active species: state of the art and future perspectives. J Mater Chem 22(20):10102
85. Allendorf MD, Schwartzberg A, Stavila V, Talin AA (2011) A roadmap to implementing metal-organic frameworks in electronic devices: challenges and critical directions. Chem A Eur J 17(41):11372–11388
86. Guo H, Zhu G, Hewitt IJ, Qiu S (2009) 'Twin copper source' growth of metal–organic framework membrane: Cu 3 (BTC) 2 with high permeability and selectivity for recycling H2. J Am Chem Soc 131(5):1646–1647
87. Hermes S, Zacher D, Baunemann A, Wöll C, Fischer RA (2007) Selective growth and MOCVD loading of small single crystals of MOF-5 at alumina and silica surfaces modified with organic self-assembled monolayers. Chem Mater 19(9):2168–2173
88. Shekhah O et al (2007) Step-by-step route for the synthesis of metal-organic frameworks. J Am Chem Soc 129(49):15118–15119
89. Zou H, Wu S, Shen J (2008) Polymer/silica nanocomposites : preparation, polymer/silica nanocomposites : preparation, characterization, properties, and applications. 3893–3957
90. Le Calvez C, Zouboulaki M, Petit C, Peeva L, Shirshova N (2016) One step synthesis of MOF–polymer composites. RSC Adv 6(21):17314–17317
91. Chang S, Ko H, Singamaneni S, Gunawidjaja R, Tsukruk VV (2009) Nanoporous membranes with mixed nanoclusters for Raman-based label-free monitoring of peroxide compounds. Anal Chem 81(14):5740–5748
92. Panarin AY, Chirvony VS, Kholostov KI, Turpin PY, Terekhov SN (2009) Formation of SERS-active silver structures on the surface of mesoporous silicon. J Appl Spectrosc 76(2):280–287
93. Wang H, Zhu QL, Zou R, Xu Q (2017) Metal-organic frameworks for energy applications. Chem 2(1):52–80
94. Sadakiyo M, Yamada T, Kitagawa H (2009) Rational designs for highly proton-conductive metal—organic frameworks 789(10), 9906–9907
95. Ramaswamy P, Wong NE, Shimizu GKH (2014) MOFs as proton conductors—challenges and opportunities. Chem Soc Rev 43(16):5913–5932

96. Li S-L, Xu Q (2013) Metal–organic frameworks as platforms for clean energy. Energy Environ Sci 6(6):1656
97. Férey G et al (2007) Mixed-valence Li/Fe-based metal-organic frameworks with both reversible redox and sorption properties. Angew Chemie Int Ed 46(18):3259–3263
98. Zou F et al (2016) Metal organic frameworks derived hierarchical hollow NiO/Ni/graphene composites for lithium and sodium storage. ACS Nano 10(1):377–386
99. Deng H et al (2010) Multiple functional groups of varying ratios in metal-organic frameworks. 846–851
100. Petit C, Mendoza B, Bandosz TJ (2010) Hydrogen sulfide adsorption on MOFs and MOF/graphite oxide composites. Chem Phys Chem 11(17):3678–3684
101. Li H et al (2017) Composite CD-MOF nanocrystals-containing microspheres for sustained drug delivery. Nanoscale 9(22):7454–7463
102. Moh PY, Brenda M, Anderson MW, Attfield MP (2013) Crystallisation of solvothermally synthesised ZIF-8 investigated at the bulk, single crystal and surface level. Cryst Eng Comm 15(45):9672
103. Attfield MP, Cubillas P (2012) Crystal growth of nanoporous metal organic frameworks. Dalt Trans 41(14):3869–3878
104. Cubillas P, Anderson MW, Attfield MP (2012) Crystal growth mechanisms and morphological control of the prototypical metal-organic framework MOF-5 revealed by atomic force microscopy. Chem A Eur J 18(48):15406–15415
105. Brent R et al (2010) Unstitching the nanoscopic mystery of zeolite crystal formation. J Am Chem Soc 132(39):13858–13868
106. John NS, Scherb C, Shöâeè M, Anderson MW, Attfield MP, Bein T (2009) Single layer growth of sub-micron metal–organic framework crystals observed by in situ atomic force microscopy. Chem Commun 2(41):6294
107. Moh PY, Cubillas P, Anderson MW, Attfield MP (2011) Revelation of the molecular assembly of the nanoporous metal organic framework ZIF-8. J Am Chem Soc 133(34):13304–13307
108. McPherson A, Kuznetsov YG, Malkin A, Plomp M (2003) Macromolecular crystal growth as revealed by atomic force microscopy. J Struct Biol 142(1):32–46
109. Teng HH, Dove PM, De Yoreo JJ (2000) Kinetics of calcite growth: Surface processes and relationships to macroscopic rate laws. Geochim Cosmochim Acta 64(13):2255–2266
110. Holden MA, Cubillas P, Anderson MW (2010) In situ crystal growth of nanoporous zincophosphate observed by atomic force microscopy. Chem Commun 46(7):1047
111. Cubillas P, Holden MA, Anderson MW (2011) Crystal growth studies on microporous Zincophosphate-Faujasite using atomic force microscopy. Cryst Growth Des 11(7):3163–3171
112. Shoaee M, Anderson MW, Attfield MP (2008) Crystal growth of the nanoporous metal-organic framework HKUST-1 revealed by in situ atomic force microscopy. Angew Chemie Int Ed 47(44):8525–8528
113. Shöâeè M, Agger JR, Anderson MW, Attfield MP (2008) Crystal form, defects and growth of the metal organic framework HKUST-1 revealed by atomic force microscopy. Cryst Eng Comm 10(6):646
114. Szelagowska-Kunstman K et al (2008) Surface structure of metal–organic framework grown on self-assembled monolayers revealed by high-resolution atomic force microscopy. J Am Chem Soc 130(44):14446–14447
115. Gu ZG et al (2015) Transparent films of metal-organic frameworks for optical applications. Microporous Mesoporous Mater 211:82–87
116. Surya SG, Nagarkar SS, Ghosh SK, Sonar P, Ramgopal Rao V (2016) OFET based explosive sensors using diketopyrrolopyrrole and metal organic framework composite active channel material. Sens Actuators, B Chem 223:114–122
117. Yadav DK, Ganesan V, Sonkar PK, Gupta R, Rastogi PK (2016) Electrochemical investigation of gold nanoparticles incorporated zinc based metal-organic framework for selective recognition of nitrite and nitrobenzene. Electrochim Acta 200:276–282

118. Reznickova A, Novotna Z, Kasalkova N, Svorcik V (2013) Gold nanoparticles deposited on glass: physicochemical characterization and cytocompatibility. Nanoscale Res Lett 8(1):252
119. Ingole PG et al (2018) Water vapor separation from flue gas using MOF incorporated thin film nanocomposite hollow fiber membranes. Chem Eng J 334:2450–2458
120. Navarro M, Benito J, Paseta L, Gascón I, Coronas J, Téllez C (2018) Thin-Film nanocomposite membrane with the minimum amount of MOF by the Langmuir-Schaefer technique for nanofiltration. ACS Appl Mater Interfaces 10(1):1278–1287
121. Roales J et al (2017) Preparation of luminescent metal-organic framework films by soft-imprinting for 2,4-Dinitrotoluene sensing. Materials (Basel) 10(9)
122. Sun Y, Hu Z, Zhao D, Zeng K (2017) Mechanical properties of microcrystalline metal-organic frameworks (MOFs) measured by bimodal amplitude modulated-frequency modulated atomic force microscopy. ACS Appl Mater Interfaces 9(37):32202–32210
123. Gándara F et al (2012) Stable organic radical stacked by in situ coordination to rare earth cations in MOF materials. RSC Adv 2(3):949–955

Variability in Monolithic Composite Parts: From Data Collection to FE Analysis

Yves Davila, Laurent Crouzeix, Bernard Douchin, Francis Collombet, Yves-Henri Grunevald and Nathalie Rocher

Abstract A main challenge facing the structural applications of composite materials is related to the uncertainty in the material performance due to their inherent variabilities. Structural properties of composites are not only dependent on the manufacturing steps, but also on the constituent materials, reinforcement architecture and design choices. By introducing geometrical variabilities into finite element (FE) model through meta-models, the effect of variations in the composite structure can be studied at different scales. To assure that the FE results are in accordance with the real composite structure, the input parameters of the models must be in agreement with the actual material and its configuration in the structure. In this chapter, a methodology to study and introduce variabilities into a composite structure FE analysis is presented.

Keywords Composite · Variability · FE modelling CFRP · Fibre angle Thickness · Meta-models

1 Introduction

In this chapter, we discuss a methodology that offers a thorough approach to generate a database that allows to introduce material input data in finite element (FE) models [1] for the structural analysis. The variation of the input properties at each finite element is driven by changes in the geometry of the structure observed in a real composite structure. In our approach, mechanical properties are dependent on these geometry changes.

Y. Davila (✉) · L. Crouzeix · B. Douchin · F. Collombet · N. Rocher
INSA, UPS, Mines D'Albi, ISAE, ICA (Institut Clément Ader), Université de Toulouse, 3 rue Caroline Aigle, 31400 Toulouse, France
e-mail: yves.davila@iut-tlse3.fr

Y.-H. Grunevald
Composites, Expertise & Solutions, 131 Traverse de La Penne aux Camoins, 13821 La Penne Sur Huveaune, France

S. S. Sidhu et al. (eds.), *Futuristic Composites*, Materials Horizons: From Nature to Nanomaterials, https://doi.org/10.1007/978-981-13-2417-8_3

The proposed methodology has the advantage to give the designer a precise control over the property assignation for each element through the use of meta-models of property variations. The meta-models are mathematical expressions that are generated by the analysis of the structure morphology. The use of meta-models allows to control the gradient at which the properties of the composite change from one element to another without having a significant disparity in the material properties that is either unrealistic (e.g. a sudden change of 90° in the fibre direction along a UD ply) or characteristic of a major manufacturing defect (e.g. macroporosity). The input parameters for the meta-models are drawn from probabilistic distributions that are also obtained from the statistical analysis of data retrieved from the real composite structure.

In our FE models, the input parameters that control its mechanical behaviour include the mechanical properties of the constituent materials, the associated volume fractions, ply thicknesses, fibre orientation, etc.

The list of variables involved, and more importantly, their interactions between different scales of the composite material is infinite. In this chapter, two main sources of variability in composite structures are addressed. The first source is the in-plane variation of fibre orientations in a unidirectional ply lay-up [2]. The second source is the thickness variability for the plies and plate and the influence of these variations on the mechanical properties of the composite part [3]. Although other sources, such the surface area of the uncured prepreg, have been identified and measured [1, 4], the results obtained with this method are in agreement with the material configuration of the observed structure.

The resulting heterogeneous solution can suggest the probability of failure at a zone of the structure that was probably not considered when using classic homogeneous analysis and/or probability approaches.

2 Challenges in the Characterisation of the Variability at Different Scales of a Composite Structure

2.1 Overview

Variability in a composite structure can be traced back to variations in the constituent materials, its geometry and the employed manufacturing process. Therefore, the concept of variability cannot be separated from the final composite structure.

A general means to obtain the FE input parameters for the analysis of composite structures is to obtain the material properties from standardised tests and then determine the probability distribution function that provides the best fit of the experimental data [5–7]. It is very important to note that property distributions are obtained through normalised testing procedures using coupons with different standard geometries and different manufacturing conditions. This means that the information regarding the actual performance of particular arrangements may not be complete [8]. For this

reason, observation and measurements in the actual production structure should be performed in order to understand the effects that the geometry and manufacturing have in the final product. The information gathered over the observation phase is used to generate the input databases that will be used to feed into the FE models.

After the generation of the FE model, the solution may be found using Monte Carlo simulations. Other types of stochastic-based analysis can be performed to reduce the computation time and resources [9–11].

In order to produce results that are more representative of the reality of the material, we have developed an original methodology that introduces local variations into FE models with the same order of magnitude as the analysed structure [1]. The material properties are controlled through meta-models for each of the finite elements. The data introduced into the meta-models is issued from probability distribution functions of variables measured before, during and after the manufacturing of composite pieces.

2.2 Obtaining the Property Variations from Real Composite Parts

The study of the variability in composite materials is challenging concerning the data collection for the different properties due to interdependencies of variables at different composite scales. A major difficulty lies with the different methods employed in the characterisation of a certain property at two or more different composite scales. These methods may not be compatible with each other regarding its nature (destructive or non-destructive), specimen size, resolution of the measurement, etc.

To illustrate this premise, the relationship between the structure thickness and the fibre volume content is described. During the analysis phase, the thickness of the structure is determined by the sum of the ply thicknesses, or vice versa; the ply thickness is determined through the division of the section thickness by the number of layers. Provided that the geometry of the cross section of the structure does not change, both the ply thickness and the structure thickness are deemed as constant. However, in a real composite laminate, the plies do not have a constant thickness (cf. Fig. 1). Assuming an area density of the reinforcement as constant across the ply, and neglecting the porosity, the volume fractions of the constituent materials depend on the ply thickness.

To characterise the volume fractions, two different methods (cf. Fig. 2) are performed, one for the ply (mesoscale) and another for the whole plate (structure scale). In both cases, a specimen is acquired from a parent plate. To obtain the ply fibre ratio, a micrograph of the cross section of the specimen is taken and then by means of image analysis the volume fractions are determined. For the whole plate, the volume fractions of the composite constituents are determined by means of chemical digestion (normalised test NF EN 2564 [12] or ASTM D3171 [13]) of the composite specimen.

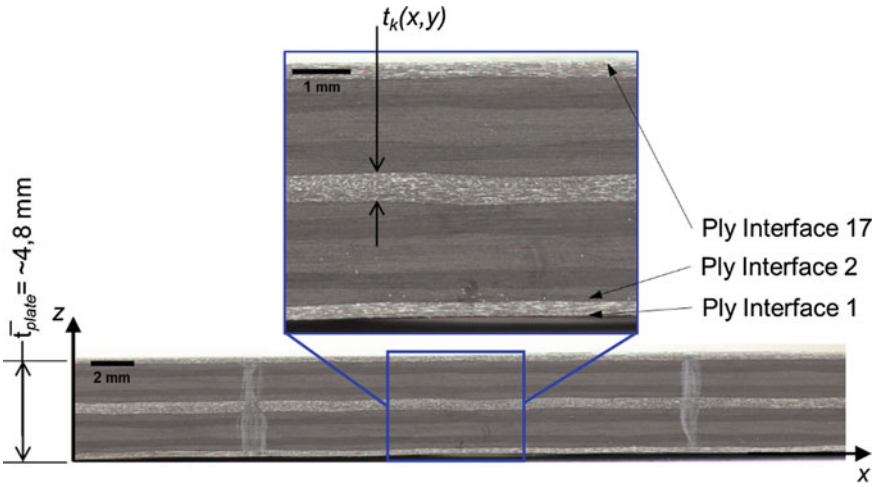

Fig. 1 Cross section of a UD composite plate (quasi-isotropic lay-up) exhibiting ply thickness variations

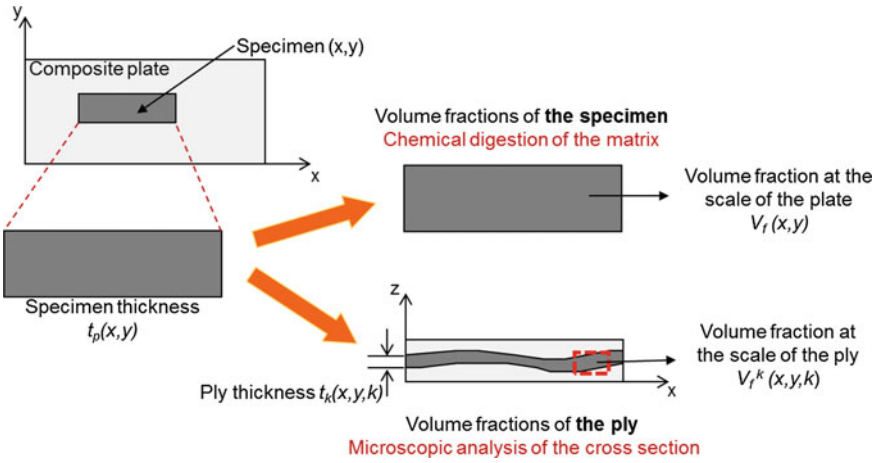

Fig. 2 Difference in techniques associated with the characterisation of the volume fractions at different scales of the composite

When comparing the volume fractions of the same specimen at these two different composite scales, they cannot be cross-checked within acceptable tolerances. On the one hand, the micrograph analysis requires the addition of material to the pre-existing composite specimen to facilitate the cross-sectional preparation of the specimen and its subsequent microscopic observation. The analysis is done at the cutting plane of the specimen. On the other hand, the method to determine the volume ratio of the complete specimen requires the destruction of the specimen and it determines the

average fibre volume content over the complete specimen. Also, each technique has its own accuracy and precision.

Although, more recently, a technique that can be used for obtaining the fibre volume fractions for both the plate and the ply scales is the micro X-ray computed tomography (CT) [14], where a complete 3D reconstruction of the specimen can be made. However, this technique is constrained by the size of the specimen, time of analysis, resolution of the CT scan machine, etc. It should also be noted that the use of a CT scan machine can be limited in terms of its availability and cost per hour.

2.3 FE Input from Geometrical and Material Variations

In order to have a light modelling technique, it is chosen to work with 2D shell elements. This allows a faster computation time. The inputs of the FE model are the material properties of Young's modulus and the shear modulus, the Poisson's ratio and the coefficient of thermal expansion along the principal directions of the lamina. The ply orientation, as well as the ply thickness are also introduced into the element definition. The calculations are done using the SAMCEF® (Siemens) FE software.

For each element, material properties are calculated along the principal directions in function of the local ply thicknesses and material properties of the fibre and resin using the law of mixtures. Figure 3 shows the modelling strategy. The volume fraction of the fibre V_f and the resin V_m can be calculated from the ply thickness t, an assumed porosity V_p and the area density of the reinforcement δ_{Af}. The latter parameter is considered as constant, while the ply thickness being variable from one point to another across the composite ply. With these parameters, the elastic properties of the local ply are calculated in the principal direction of the lamina. The reinforcement orientation is written into the composite lay-up definition of the element.

To assure that the properties introduced into the FE models are representative of actual material behaviour, the data must be acquired directly from the real composite structure. The data acquisition process must as extensive as possible in order to be able to obtain accurate trends.

3 Experimental Determination of Composite Variabilities

In order to study the variability of the composite structure during real manufacturing conditions, composite plates were fabricated with the HexPly® M10.1/38%/UD300/CHS unidirectional carbon/epoxy prepreg from Hexcel Composites. The plates are 600 mm long and 300 mm wide. The stratification is quasi-isotropic with 16 plies. The lay-up sequence is $[(90/-45/0/+45)_s]_s$. The composite plates are cured in autoclave. The cure cycle consists of two temperature dwells. The first one, at 90 °C during 15 min, is applied to homogenise the temperature material and to evacuate eventual porosities in the resin. The second dwell is applied at 120 °C

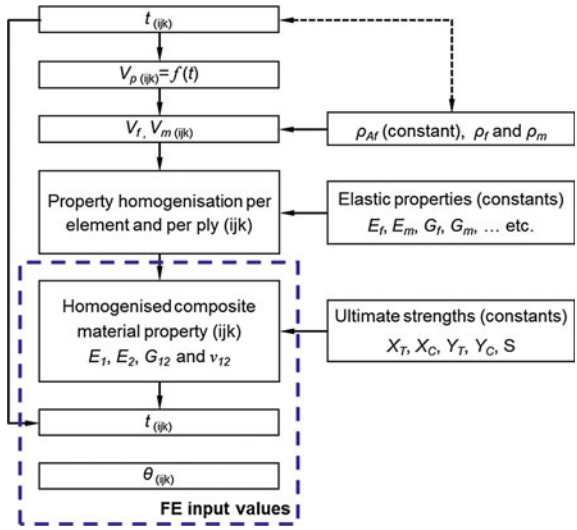

Fig. 3 Algorithm used to generate and assign individual element material properties for the FE model

during 60 min to allow a complete polymerisation of the matrix. The heating and cooling rates of the temperature cycle are 2 °C min^{-1}. A positive pressure of five bars is applied during the complete cure cycle.

Before, during and after the manufacturing, sources of variability are studied to find the probability distribution functions of the properties, as well as the mathematical representation (meta-models) of the continuous variations [1]. In this chapter, only the reinforcement orientation of a ply and plate thicknesses variation are presented; however, other sources have been studied [4].

3.1 Reinforcement Orientation

3.1.1 Experimental Determination

The first source of variability here presented is the determination of the in-plane reinforcement orientation [2]. During the lay-up procedure, series of images are taken using a Canon® EOS 550D digital camera with an EF 50 mm macro lens. The camera is placed directly above the working space at a distance of 1.7 m (cf. Fig. 4). To determine the reinforcement orientation, an in-house automatic image analysis program was developed. The method uses a Hough transform of the edges generated by the fibre bundles at the prepreg surface to measure the fibre angle of the reinforcement [15]. Figure 4 shows the different stages of the identification algorithm. The first step is to crop the image to exclude the ply edges from disrupting the cut-off values of pixel intensity (cf. Fig. 4a). Then, the image is segmented into a predefined number of elements (cf. Fig. 4b). Each segment of image is filtered by

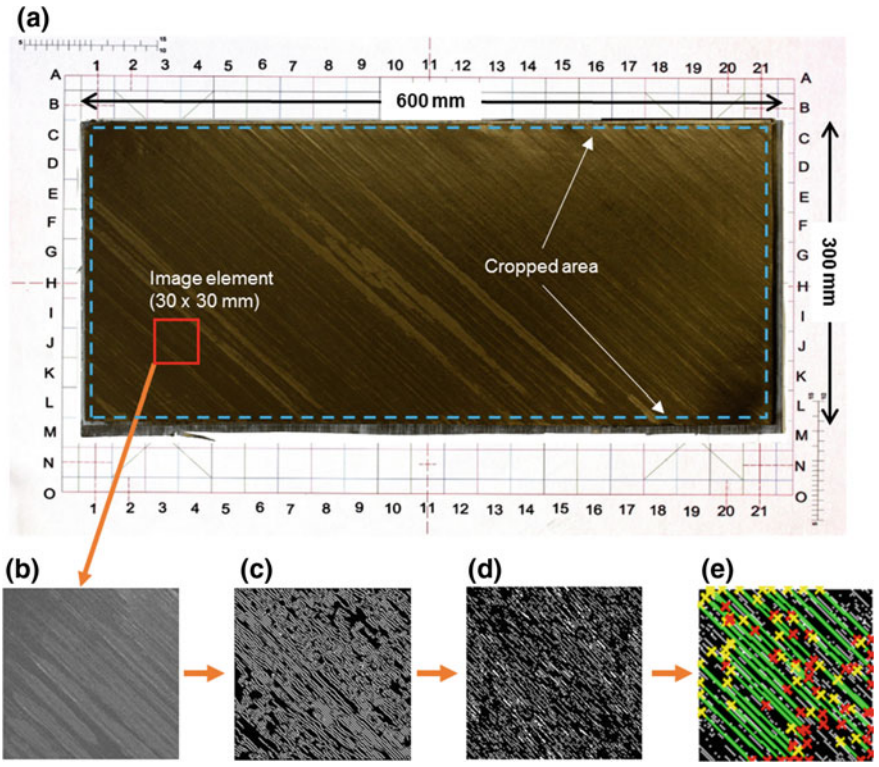

Fig. 4 Procedure of measurement of the fibre orientation of an uncured composite prepreg **a** uncured ply in the working zone, **b** segment of image, **c** filtering (LoG and convolution mask), **d** edge detection algorithm and **e** resulting Hugh lines following the reinforcement

a Laplacian of Gaussian kernel (LoG) and a series of convolution masks (Fig. 4c) [16]. Afterwards, to highlight the lines formed by the fibre bundles, an edge detection function is used [17]. Finally, to determine the angle formed by the fibre bundles, a Hough transform is performed (Fig. 4e).

The images are 5184 x 3456 px, with a resolution of 6.48 px/mm and a pixel aspect ratio of 1:1. In order to have a good compromise between the accuracy of the measurement and an acceptable image processing time, it was chosen to have a grid of 20 by 10 elements (30 mm per side).

Once the results from the image analysis are obtained, they are processed with an identification algorithm that fit the local angle perturbation into a 3D curve [2], where the amplitude of such curve is the fibre angle and its variation across the composite ply. The values obtained are then drawn to generate virtual plies with similar fibre orientation variations.

3.1.2 Fibre Orientation Meta-Models

The local variation in the fibre orientation θ_k is the result of the sum of the theoretical orientation θ_{th}, the global ply misalignment $\delta\theta$, the local fibre undulations θ_{wav} [18] and local perturbations done during the lay-up phase of the prepreg θ_{pert}.

The local fibre undulations θ_{wav} are expressed in function of the amplitude A_{wav} and the wavelength λ_{wav} of these undulations:

$$\theta_{\text{wav}}(\theta_{\text{th}}) = \frac{A_{\text{wav}}}{2} \sin\left(\frac{2\pi x \cos\theta_{\text{th}} + 2\pi x \sin\theta_{\text{th}}}{\lambda_{\text{wav}}}\right) \tag{1}$$

The local perturbations θ_{pert} distribution is introduced by the sum of 12 pseudo-Gaussian surfaces. The parameter B_i is the amplitude of the perturbation in degrees, X_i and Y_i are the coordinates of the origin of the perturbation and α_i and β_i are the length and width of the perturbation:

$$\theta_{\text{pert}}(x, y) = \sum_{i=1}^{12} B_i e^{-\left(\left(\frac{x-X_i}{\alpha_i}\right)^2 + \left(\frac{y-Y_i}{\beta_i}\right)^2\right)} \tag{2}$$

Figure 5 shows an example of a map of reinforcement orientation misalignments. The ply here represented has a $-45°$ orientation. The patterns shown in the figure are due to the periodic undulation in the reinforcement appearing perpendicular to the fibre direction. Also, the local perturbation makes that reinforcement angle at the centre right of the image is $-43°$, while in the lower left corner, the fibre orientation is $-47°$.

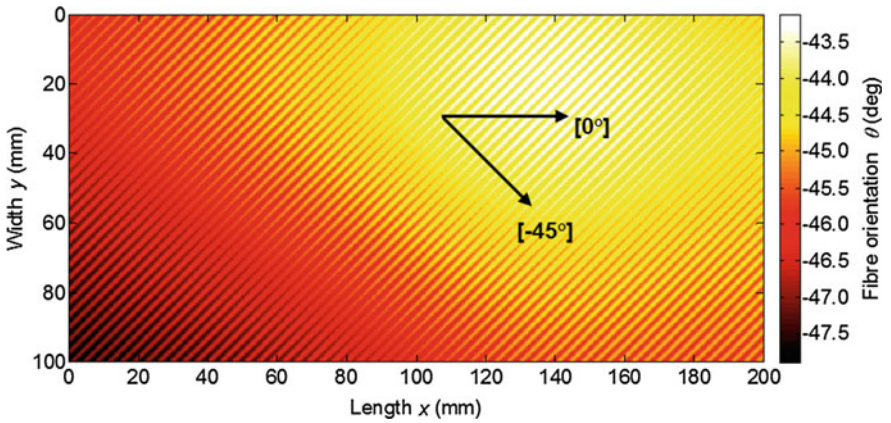

Fig. 5 Illustration of the resulting fibre misalignment in a ply at $-45°$ orientation

3.2 Ply Thickness

3.2.1 Experimental Determination

The second source of variability presented is the variation in ply and plate thicknesses of the cured composite plate.

After its manufacturing, the composite plates were placed into a 3D coordinate-measuring machine to determine the overall thickness of the plate. It was determined that the thickness is not constant across the plate. The thickest part of the plate was located at the centre of the plate while the thinnest were located at the corners of the plate. The difference between the thicknesses is up to 0.600 mm, which equals to the thickness of two plies.

The measurements were performed on a 45 x 45 mm sample. This specimen has an average plate thickness of 4.66 mm. The difference between the extreme thickness values of this sample is 0.310 mm, which corresponds to the thickness of a single ply.

This sample was used to obtain the ply thickness profiles. A series of micrographs of the cross section of the sample is taken using a portable optical microscope. The micrographs were assembled in order to have in a single image the complete cross section of the sample. Using an image analysis subroutine, the ply interfaces, as well as the thickness profile were determined for each ply in the lay-up. Then, each profile was analysed through a Fourier transform [3]. The coefficients obtained from the spectral analysis are used to generate a function that recreates a virtual ply with varying thicknesses.

3.2.2 Ply and Plate Thickness Variation Meta-Models

The meta-model used to control the element ply thickness t_{k} is the sum at each point of the plate of the average ply thickness $\bar{t}_{\mathrm{k}}$, the periodic variation of the ply thickness ξ_{tk} and the contribution to the ply thickness of the overall change in the plate thickness δ_{tplate}:

$$t_{\mathrm{k}}(x, y) = \overline{t_{\mathrm{k}}} + \xi t_{\mathrm{k}}(x, y) + \delta t_{\mathrm{plate}}(x, y) \tag{3}$$

where the expression of the periodic variation of the ply ξ_{tk} in two dimensions is:

$$\xi t_{\mathrm{k}}(x, y) = \sum_{i=1}^{10} \frac{A_i}{4}\left[\cos\left(\frac{2\pi x}{\lambda_i} + \phi_{\mathrm{k,i}}\right) + \cos\left(\frac{2\pi y}{\lambda_i} + \phi_{\mathrm{k,i}}\right)\right] \tag{4}$$

where the parameter A_i is the amplitude of the ith spectrum peak (retrieved by the Fourier transform) and λ_i is the wavelength. $\phi_{\mathrm{k,i}}$ is a pseudo-random phase shift introduced to control the coupling between the different plies.

Finally, the parameter δ_{tplate} that control the plate thickness variation is:

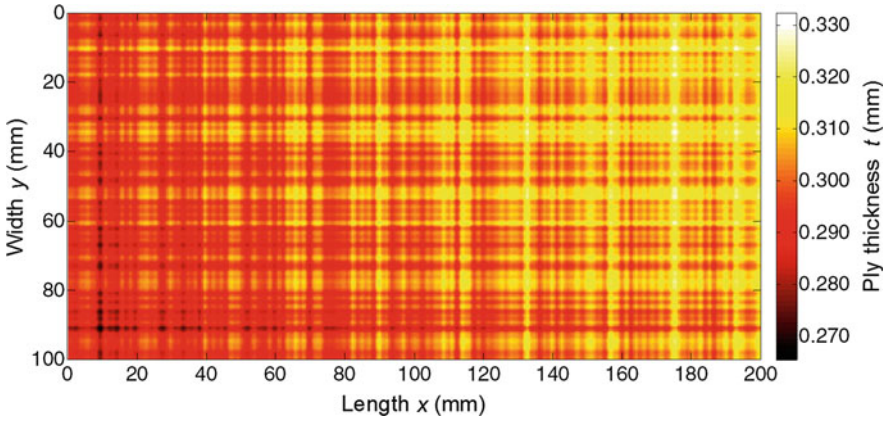

Fig. 6 Illustration of the generated ply thickness variation

$$\delta t_{\text{plate}}(x, y) = \frac{1}{16}\left[\frac{A_{\text{plate}}}{2}\left[\cos\left(\frac{2\pi}{\lambda_{\text{plate1}}}x + 300\right) + \cos\left(\frac{2\pi}{\lambda_{\text{plate2}}}y + 300\right)\right]\right] \tag{5}$$

It is noteworthy that at this stage the same parameters of amplitude and wavelength for the spectrum peaks are considered equal for both laminate x- and y-axes. Figure 6 shows the illustration of a generated ply thickness map. It is possible to see the local variations of the ply thickness, as well as the overall variation of the plate. On the lower left corner, the ply thickness is approximately 0.280 mm while in the upper right corner the thickness is 0.320 mm. Since the stratification of the composite plate is quasi-isotropic, it was considered that the magnitude of the amplitude and frequency parameters are equal in the principal axes of the laminate. However, this hypothesis makes appear a regular pattern of the generated ply thickness.

As explained before, the material properties are a function of the ply thickness. The first parameter to be considered is the porosity of the ply V_{pk}. This parameter does not only vary with the ply thickness but has a random variable ξ_{k} with zero mean and a nonzero standard deviation. The value of the porosity cannot be negative.

$$\begin{gathered} V_{\text{pk}}(x, y) \geq 0 \\ V_{\text{pk}}(x, y) = f(t_{\text{k}}, x, y) + \xi_{\text{k}}(x, y) \end{gathered} \tag{6}$$

To determine the volume fraction of the constituent materials, an equivalent fibre thickness is calculated. This thickness is obtained from the relationship of the density area of the fibres in the prepreg ρ_{Af} and the overall density of the carbon fibre δ_{f}. To simplify the calculations, these two values are considered constant. The area density of the fibre for the plates using the M10.1/38%/UD300/CHS prepreg was measured to be 305 g m^{-2}. The density of the fibres is considered to be 1800 g m^{-3}.

$$t_{\mathrm{f}} = \frac{\rho_{\mathrm{Af}}}{\rho_{\mathrm{f}}} \tag{7}$$

The volume fractions for the fibres $V_{\mathrm{fk}}(x, y)$ and for the matrix $V_{\mathrm{m}}(x, y)$ are calculated with:

$$V_{\mathrm{fk}}(x, y) = \frac{t_{\mathrm{f}}}{t_{\mathrm{k}}(x, y)} \tag{8}$$

$$V_{\mathrm{mk}}(x, y) = 1 - V_{\mathrm{fk}}(x, y) - V_{\mathrm{pk}}(x, y) \tag{9}$$

Once the local thickness and fibre orientation are calculated, the lamina Hooke's law in the main axes of the reinforcement $[S]_{\mathrm{lt}}$ is calculated using the law of mixtures. To apply the law of mixtures, the constituent materials' properties are considered as deterministic and constant. The Hooke's law for an orthotropic lamina in terms of compliance is:

$$\begin{Bmatrix} \varepsilon_x \\ \varepsilon_y \\ \gamma_{xy} \end{Bmatrix} = \begin{bmatrix} S_{11} & S_{21} & 0 \\ S_{12} & S_{22} & 0 \\ 0 & 0 & S_{66} \end{bmatrix} \begin{Bmatrix} \sigma_x \\ \sigma_y \\ \tau_{xy} \end{Bmatrix} \tag{10}$$

The compliance constants in terms of the engineering constants are expressed in Eq. (11). The Young's modulus E_x in the overall laminate xy-axes can be thus obtained for each element of the lamina at any ply orientation:

$$\begin{gathered} \overline{S}_{11} = \frac{1}{E_x} \quad \overline{S}_{22} = \frac{1}{E_y} \\ \overline{S}_{12} = \overline{S}_{21} = -\frac{\nu_{xy}}{E_x} = -\frac{\nu_{yx}}{E_y} \quad \overline{S}_{66} = \frac{1}{G_{xy}} \end{gathered} \tag{11}$$

The mechanical properties for the average ply of 0.300 mm of the HexPly® M10.1/38%/UD300/CHS composite system are expressed in Table 1.

Figure 7 shows the map of the Young's modulus in the x-axis E_x of a 200 × 100 mm ply having a reinforcement orientation of −45°. The variation in E_x is the result of variations in the thickness and fibre orientations.

The previous illustrations are the result of the use of the proposed meta-models with input parameters obtained through the measurement of the real composite plates (top section of the algorithm presented in Fig. 3). In the following section, the values produced by these meta-models will be introduced into FE models with variable material and geometrical properties (bottom section, FE inputs, of the algorithm presented in Fig. 3).

Table 1 Mechanical properties of the M10.1/38%/UD300/CHS for a 0.300-mm-thick ply and 55% fibre

Mechanical properties	Mean value	Standard deviation
Young's modulus E_1 (MPa)	106,500	6,000
Young's modulus E_2, E_3 (MPa)	9,300	660
Shear modulus G_{12}, G_{13} (MPa)	3,500	190
Shear modulus G_{23} (MPa)	2,500	150
Poisson's ratio ν_{12}, ν_{13}	0.336	0.003
Poisson's ratio ν_{23}	0.029	0.005
Coefficient of linear thermal expansion α_1 ($°C^{-1}$)	-0.6×10^{-6}	3.3×10^{-8}
Coefficient of linear thermal expansion α_2, α_3 ($°C^{-1}$)	14.3×10^{-6}	1×10^{-6}

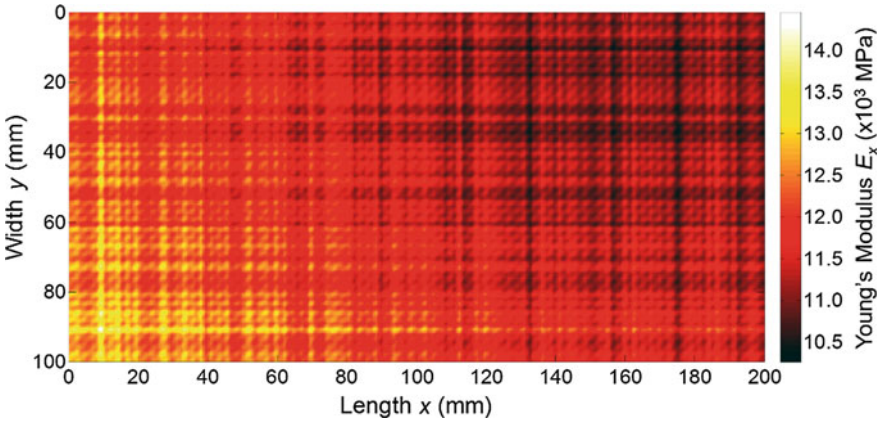

Fig. 7 Illustration of the resulting Young's modulus E_x distribution

4 Application of Finite Element Model with Variabilities

4.1 General FE Model Overview

The FE analysis is performed in SAMCEF®. All models use the 2D composite shell element. The main advantage of these elements is the possibility to introduce for each ply and each element the mechanical properties as well as the thickness and reinforcement orientation. It is thus possible to control the mechanical properties of the modelled composite individually from one point to another.

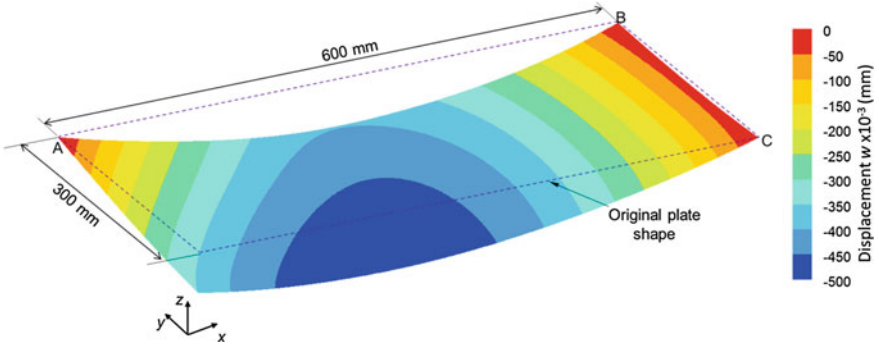

Fig. 8 Nodal displacements along the z-axis w

The meta-models are used to generate the FE geometries, and, to compute and assign the mechanical properties of the finite elements. Another script writes the information into the input file to be loaded into the FE software (cf. bottom part of the algorithm in Fig. 3) The meta-models as well as the input file writing code are written in MATLAB® to facilitate the generation of sets of different input files. The elements used in the presented FE models are linear elastic with or without geometric nonlinearity.

4.2 Analysis of the Strains Resulting from the Cooling Phase of the Polymerisation Cycle

The methodology can be used in the prediction of residual stresses produced during the cooling segment at the end of the cure cycle. The prepreg M10.1%/38%/UD300/CHS has a curing temperature of 120 °C. It is assumed that the composite plate is in a state of zero residual stress at the end of the curing segment [19]. Residual stresses are the result of the different thermal expansion properties of the fibre and matrix. In the following FE model, a perfect bonding at the interface of the fibres and matrix is assumed. The part–tool interaction, also cause of residual stresses, is not considered [20].

In this analysis, the 300×600 mm composite plate is modelled. The model has 180,000 elements and 1,100,000 degrees of freedom (DoF). The loading was a change of temperature $\Delta T = -120$ °C. The plate was constrained vertically (z-axis) in three of the four corners of the composite plate (Points A, B and C, Fig. 8). For point A, nodal displacements along the y-axis are constrained and for B and C points, and the displacements along the x-axis are constrained. Figure 8 shows the nodal displacements w (out-of-plane) along the z-axis.

A homogeneous model without the inclusion of material and geometrical variability shows an out-of-plane displacements w equal to zero. The model including mate-

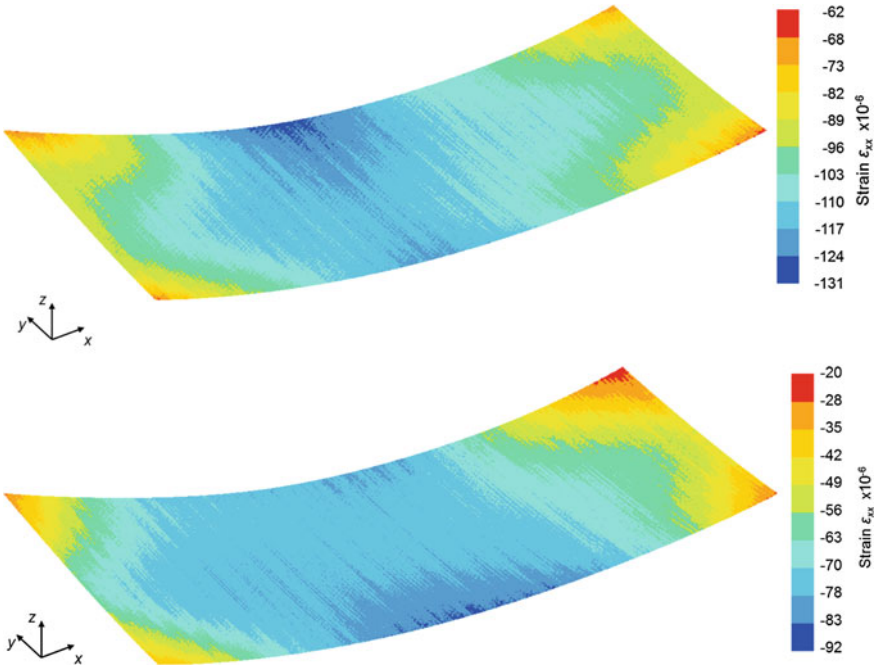

Fig. 9 FE strain field ε_{xx} of the top skin (top) and bottom skin (bottom) of the composite plate

rial and geometrical variabilities exhibits the out-of-plane displacements of −0.500 mm. These deflections are consistent with the values of out-of-plane displacements measured in the manufactured plates.

The resulting top and bottom skin strain fields ε_{xx} are shown in Fig. 9. Both skins are under compression. The difference in the strain field of 40×10^{-6} between the lower and the top skin is due to the warpage of the composite plate, made evidently by the out-of-plane displacements shown in Fig. 8. The difference in strains up to 70×10^{-6} at each single skin is due to the change in the plate thickness, with the thicker zone located at the centre of the plate and the thinner zones located at the four corners.

4.3 Four-Point Bending Test

The FE model with varying properties can be also used to correlate data obtained by mechanical tests. In this section, the comparison between the FE model and the experimental results of a four-point bending test is presented.

The lay-up in this test, as discussed previously, is $[(90/-45/0/+45)_s]_s$. The four-point bending test is done following the guidelines of the normalised test ISO 14125

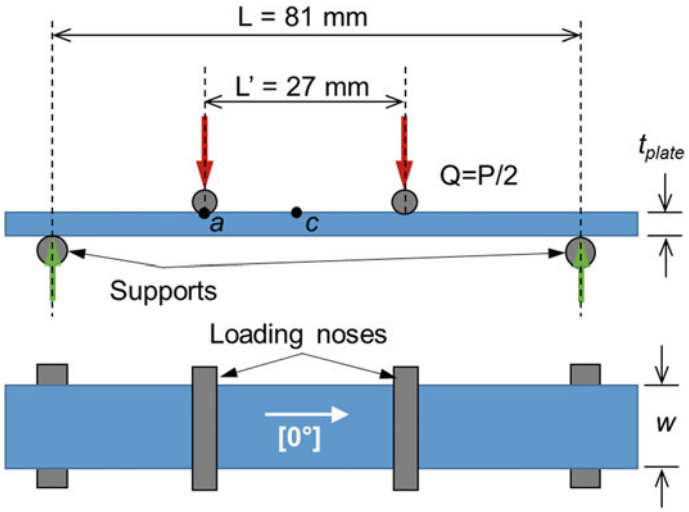

Fig. 10 Scheme of the four-point bend test setup

[21]. The dimensions and the testing setup are shown in Fig. 10. The specimen has for dimensions $w = 15$ mm and $L_{\text{spec}} = 100$ mm.

The displacement of the point 'a' (cf. Fig. 10) is used to determine the flexural modulus E_{fx} using Eq. (12).

$$E_{\text{fx}} = 0.185 \frac{L^3}{w \cdot t_{\text{plate}}^3} \left(\frac{\Delta P}{\Delta s_a} \right) \tag{12}$$

where L is the length between supports, ΔP is the load increment and Δs_a is the displacement of the point 'a'. Figure 11 shows the composite specimen at the end of the test after the failure of ply #14.

Figure 12 shows the calculated flexural modulus E_{fx} in function of the specimen thickness t_{plate}. The experimental data exhibits a significant scatter. However, the linear regression shows that the flexural modulus decreases with the augmentation in thickness of the plate. For reference, the average flexural modulus is 31250 MPa with a variation of 1.6% around the mean value.

The principal property that has an influence on the FE model is the ply thickness. In our models, the ply thicknesses range between 0.230 mm and 0.370 mm. The thickness is discretised every 0.050 mm. For each thickness value, the mechanical properties are calculated. Then, the corresponding values are assigned to each element. The plate material is still the HexPly® M10.1/38%/UD300/CHS whose mechanical properties are listed in Table 1.

The dimensions of the FE model are the same as the tested coupons. The element size is 1 x 1 mm. This size was selected in accordance with the wavelength used to describe the variation profile of the ply thickness. The FE model consists of

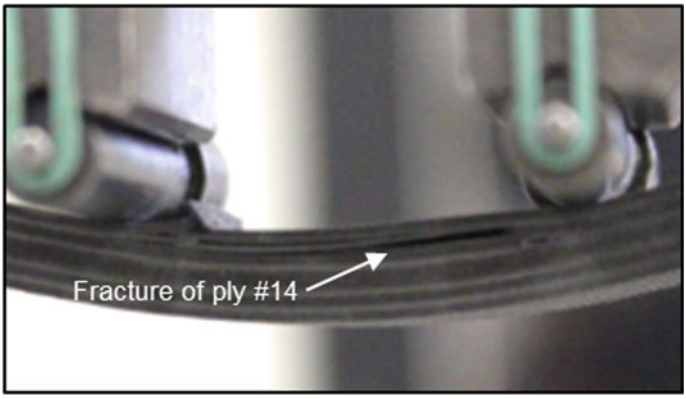

Fig. 11 Four-point bend test with failure at the ply #14 with 0° orientation plies

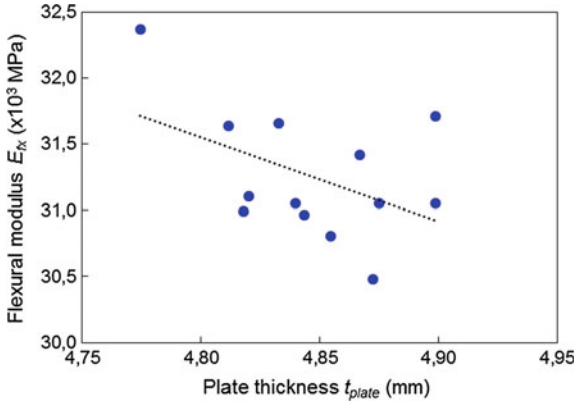

Fig. 12 Results of the flexural modulus E_{fx}

1500 elements with 9700 DoF. As per the experimental setup, the nodal displacement for the nodes placed on the machine supports is blocked along the z-direction. The load was applied through a nodal displacement of the nodes places below the loading noses along the z-direction of -3.5 mm.

Figure 13 shows the results' comparison between the model having a constant plate thickness, the FE model with property variations and the data acquired experimentally. In the model with constant thickness, the flexural modulus E_{fx} varies inversely to the thickness of the plate. Both the experimental data and the results from the FE models show a scatter around the E_{fx} variation having a constant ply thickness. These two sets, the experimental data and the one generated by means of the FE analysis, observe the same order of magnitude. These results prove indeed the interest of the proposed modelling strategy to recreate the variability of a macroscopy property like the flexural module of a composite laminate.

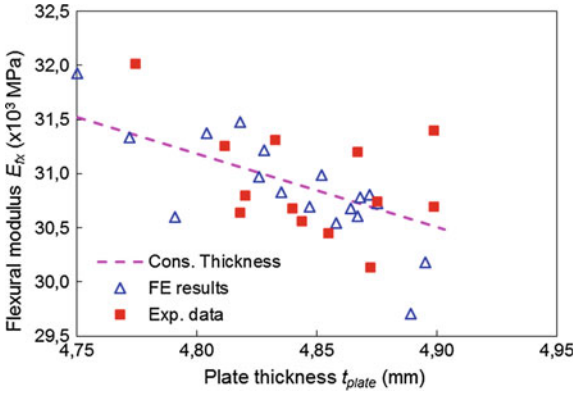

Fig. 13 Flexural modulus E_{fx} in function of plate thickness

4.4 FE Analysis of a Multi-instrumented Technological Evaluator

4.4.1 Overview of the Multi-instrumented Technological Evaluators (MITE) 'Toolbox'

The 'toolbox' named multi-instrumented technological evaluators [22] is a set of methodologies conceived to the study of complex composite structures. It was developed in conjunction with the Clément Ader Institute (Toulouse, France) and the SME Composites, Expertises & Solutions (La Penne-sur-Huveaune, France). This 'toolbox' consists of three main components. The first one is an original experimental setup that allows the application of compound loadings into a specific test coupon, also called multi-instrumented technological evaluator (MITE). The MITE is a composite structure in which the subjects of the study are incorporated in a representative situation. The MITE is instrumented for different analyses and measurement techniques. Finally, the third component of the 'toolbox' is the finite element models associated with the test machine and the MITE itself. The models are used to conceive the analysis, the loading path and the structure of the MITE. After the test, a refined model using the experimental boundary conditions is used to correlate the results between the experimental and FE model results [23, 24].

Figure 14 shows the original multi-axial testing machine. To generate a compound loading path, applied to the composite MITE by the mobile grip, it uses four electromechanical linear actuators that are independently controlled. These actuators are attached, on one end, to the frame of the testing machine structure, and on their other end, they are attached to a mobile steel rectangle. This rectangle is supported by an articulated arm to the floor of the testing machine structure. The movements allowed by the configuration of the arrangement of the actuators is a uniaxial tension–compression, three bending moments and any combination thereof (cf. Fig. 14). The MITE is placed between the frame and the mobile rectangle. This particular con-

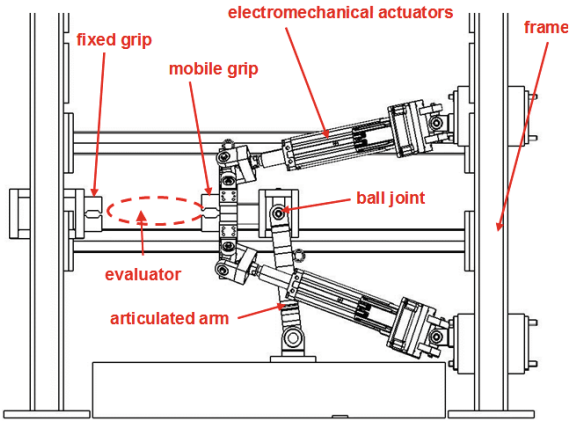

Fig. 14 Lateral view of the multi-axial testing machine

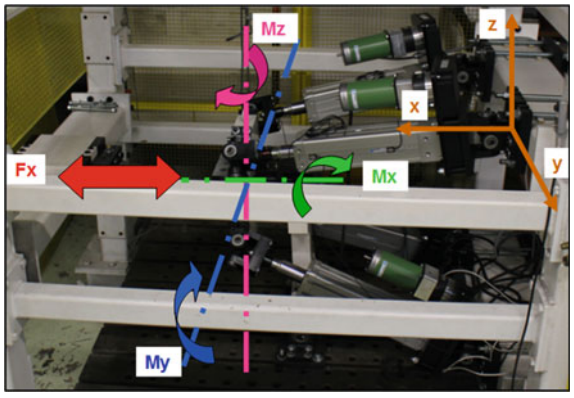

Fig. 15 Different possible loadings of the multi-axial testing machine

figuration offers the possibility of designing a particular sequence of uniaxial or compound displacements, putting the MITE under a chosen state of stress.

In its configuration, the maximal dimensions of the evaluators that can be tested in the testing machine are 600 mm by 300 mm. The maximum loading capacity of the machine in tension–compression is 140 kN, and in bending moments about the *x*-, *y*- and *z*-axes are 8, 30 and 40 kN m, respectively (Fig. 15).

In order to assure that the loadings are accurately transferred to the composite MITE, particularly bending moments, the MITE is provided with composite tabs. These tabs are tapered to avoid stress concentrations. The material of the tabs is the HexTOOL® M61, whose stiffness is similar to the testing coupon.

Figure 16 shows the 16 ply $[(90/-45/0/+45)_s]_s$ composite MITE. This evaluator consists of a composite plate of 600 x 130 mm. A black and white pattern is applied to the MITE to use digital image correlation (DIC). Additionally to the DIC, strain

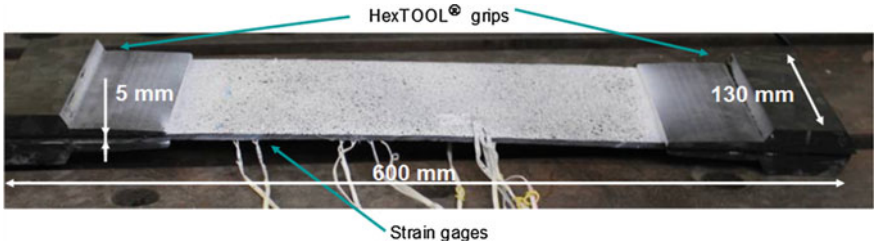

Fig. 16 View of the composite MITE

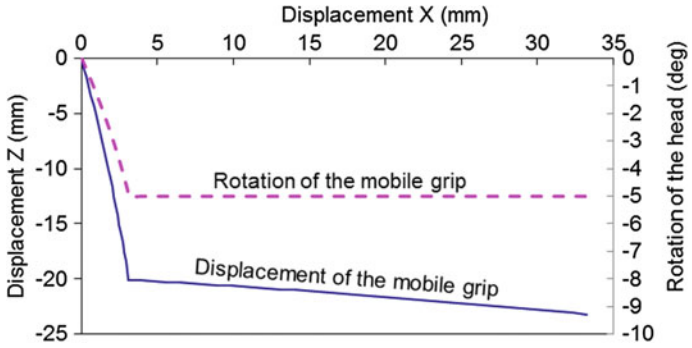

Fig. 17 Imposed displacements of the mobile grip

gauges are placed on different zones of relative interest to evaluate the variation in the strain field.

The load is applied through the displacement of the mobile grips. The imposed displacements are shown in Fig. 17. To induce the state of stress, two segments are employed. In the first one, a combined linear displacement of the machine head (mobile grip) along the x-axis and a rotation about the y-axis is used to put the ETMI in a pure bending state. Then, in the second segment, the rectangle is pushed by the mechanical actuators in the x-axis, applying a compression loading to the composite MITE. This combined movement effectively puts the ETMI in a buckling state. The durations of the segments are 4 and 6 minutes, respectively.

The failure point of the MITE was located few millimetres away from the fixed grip (cf. Fig. 18). The failure started at the fifth ply by compression of the 0° ply. The fracture triggered the delamination and the fracture of the four plies placed at the bottom of the evaluator.

4.4.2 FE Analysis of Composite MITE

In order to reduce the model complexity, only the working length of the MITE was analysed. The working length is the part of the MITE situated between the two

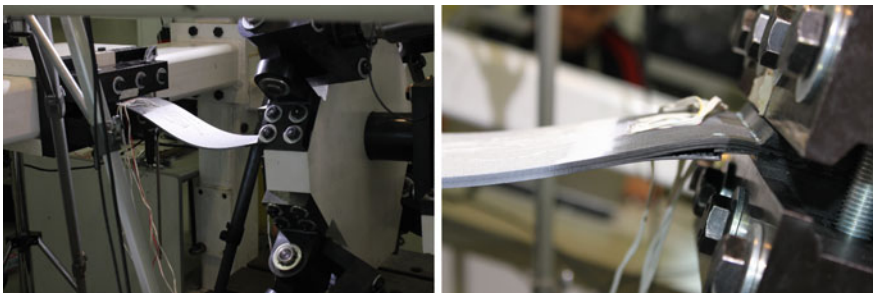

Fig. 18 Testing of the composite MITE: MITE in bucking before failure (right), after failure of the 0° ply near the clamp area

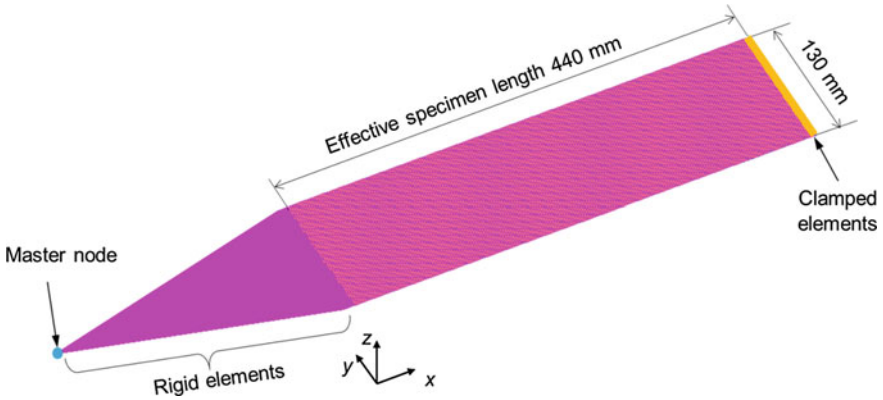

Fig. 19 FE representation of the ETMI and its boundary conditions

clamps and has a dimension of 440 mm. (cf. Fig. 19). The element size is 1×1 mm. The application of the loading displacement (same as the experimental setup shown in Fig. 17) is done through the use of a master node linked to the MITE by rigid elements (cf. Fig. 19). The MITE is clamped on the other end.

This analysis is performed by the nonlinear solver of SAMCEF performing an iterative solution as the buckling performance of the composite MITE is studied. The used elements are linear elastic with the nonlinear geometry activated. The FE calculations are done in 20 time steps.

Figure 20 shows the bottom skin strain field ε_{xx} of the MITE at the last time step. The strain field does not show a symmetry about the x-axis of the MITE, especially at the zone near the clamped end. Here, the difference in strain is 3000×10^{-6} between the right and left side of the MITE.

The resulting non-symmetric strain field is the product of local material and geometry variations introduced into the FE model. In a typical analysis, this difference would have been omitted as the strain field is symmetric in a homogeneous model. This result shows that this approach seems capable of restitution of certain local

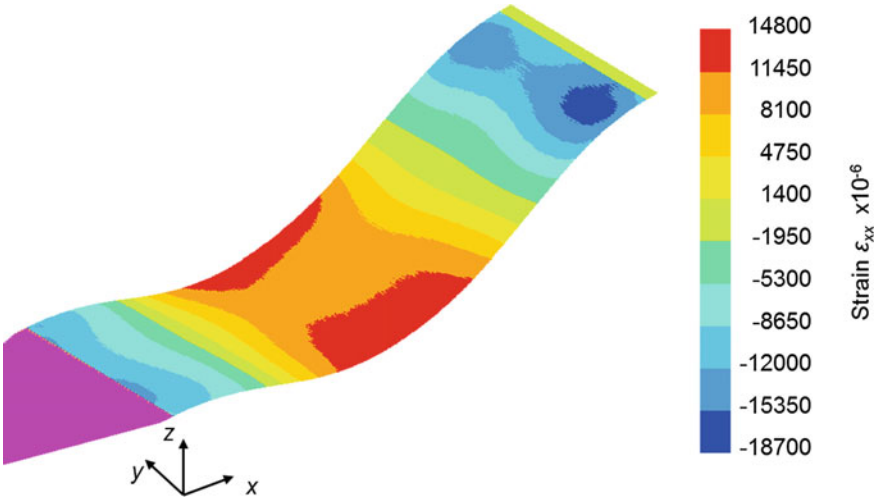

Fig. 20 FE strain field ε_{xx} of the bottom skin of the composite MITE

phenomena which can produce failure initiations outside the predicted zones from the analysis considering homogenous materials.

5 Conclusions

The aim of this chapter is to enrich the performance analysis of composite structures taking into account the inherent variability present in composites. The variation of its local properties is introduced through the study and analysis of morphological changes at meso- and macroscales of the composite structure. These variations are then incorporated into meta-models that control the spatial evolution of the mechanical and geometrical properties of the finite element composite models at different points of the model and between different models while respecting the orders of magnitude and the trends of said variations. Two main sources of variability have been presented, variations in the thickness of the laminate and the variation in the reinforcement orientation. These sources have a major impact on the mechanical properties of the composite structure. The FE modelling strategy has shown positive results in predicting structural variability.

The different cases here presented are not meant to be final solutions. They serve to show the feasibility FE models with variabilities with controlled gradients in certain mechanical and geometrical properties. Further development of models and hypotheses is required as well as the need to integrate other sources of variability related to structural features (ply drop-offs, stiffeners, etc.).

Acknowledgements The authors want to acknowledge the National Council of Science and Technology of Mexico (CONACYT) for providing the funding of the Ph.D. investigation of Yves Davila. This work benefits from the project called "Instrumentation with Multi-sensor for Composite Materials and structures (I2MC)" supported by the RTRA-STAE foundation (France). In memory of Prof. Robert Bazer-Bachi, co-leader of I2MC project.

References

1. Davila Y (2015) Multi-scale study of the material-processing coupling for the identification and modelling of variabilities in a composite structure, Ph.D. Thesis: (in English), Université Toulouse III Paul Sabatier," Université Toulouse 3 Paul Sabatier
2. Davila Y, Crouzeix L, Douchin B, Collombet F, Grunevald Y-H (2018) Identification and modelling of the in-plane reinforcement orientation variations in a CFRP laminate produced by manual lay-up. Appl Compos Mater 25(3):647–660
3. Davila Y, Crouzeix L, Douchin B, Collombet F, Grunevald Y-H (2017) Spatial evolution of the thickness variations over a cfrp laminated structure. Appl Compos Mater 24(5):1201–1215
4. Davila Y, Crouzeix L, Douchin B, Collombet F, Grunevald Y-H (2013) Quantification of sources of variability in CFRP plates cured in autoclave. In: 19th International conference on composite materials, 2013, pp 250–2567
5. Philippidis TP, Lekou DJ, Aggelis DG (1999) Mechanical property distribution of CFRP filament wound composites. Compos Struct 45:41–50
6. Lekou DJ, Philippidis TP (2008) Mechanical property variability in FRP laminates and its effect on failure prediction. Compos Part B Eng 39(7–8):1247–1256
7. Sriramula S, Chryssanthopoulos MK (2009) Quantification of uncertainty modelling in stochastic analysis of FRP composites. Compos Part A Appl Sci Manuf 40(11):1673–1684
8. Sutherland LS, Shenoi RA, Lewis SM (1999) Size and scale effects in composites: I. Literature review. Compos Sci Technol 59:209–220
9. Di Sciuva M, Lomario D (2003) A comparison between Monte Carlo and FORMs in calculating the reliability of a composite structure. Compos Struct 59(1):155–162
10. Bouhafs M, Sereir Z, Chateauneuf A (2012) Probabilistic analysis of the mechanical response of thick composite pipes under internal pressure. Int J Press Vessel Pip 95:7–15
11. Hyuk-Chun N (2011) Stochastic finite element analysis of composite plates considering spatial randomness of material properties and their correlations. Steel Compos Struct 11(2):115–130
12. AFNOR (1998) NF EN 2564: aerospace series. Carbon fibre laminates. Determination of the fibre, resin and void contents
13. ASTM International (2011) ASTM D3171: standard test methods for constituent content of composite materials
14. Wildenschild D, Vaz CMP, Rivers ML, Rikard D, Christensen BSB (2002) Using X-ray computed tomography in hydrology: systems, resolutions, and limitations. J Hydrol 267(3–4):285–297
15. Shi L, Wu S (2007) Automatic Fiber orientation detection for sewed carbon fibers. Tsinghua Sci Technol 12(4):447–452
16. Redon C, Chermant L, Chermant J, Coster M (1999) Automatic image analysis and morphology of fibre reinforced concrete. Cem Concret Compos 21:403–412
17. Canny J (1986) A computational approach to edge detection. IEEE Trans Pattern Anal Mach Intell 8(6):679–698
18. Potter KD, Khan B, Wisnom MR, Bell T, Stevens J (2008) Variability, fibre waviness and misalignment in the determination of the properties of composite materials and structures. Compos Part A Appl Sci Manuf 39(9):1343–1354
19. Mulle M, Collombet F, Olivier P, Zitoune R, Huchette C, Laurin F, Grunevald Y (2009) Assessment of cure-residual strains through the thickness of carbon–epoxy laminates using FBGs Part II: technological specimen. Compos Part A Appl Sci Manuf 40(10):1534–1544

20. Stefaniak D, Kappel E, Spröwitz T, Hühne C (2012) Experimental identification of process parameters inducing warpage of autoclave-processed CFRP parts. Compos Part A Appl Sci Manuf 43(7):1081–1091
21. AFNOR (1998) NF EN ISO 14125: fibre-reinforced plastic composites—determination of flexural properties
22. Collombet F, Grunevald Y-H, Crouzeix L, Douchin B, Zitoune R, Davila Y, Cerisier A, Thévenin R (2015) 10—Repairing composites. In: Advances in composites manufacturing and process design, Elsevier, pp 197–227
23. Crouzeix L, Davila Y, Collombet F, Douchin B, Grunevald Y, Zitoune R (2012) Study of double step lap composite repairs on CFRP evaluators. In: ECCM 15, 2012
24. Collombet F, Crouzeix L, Grunevald Y, Zeng H, Davila Y, Douchin B, Gillet A (2012) Primary principal composite structure repair with multi-instrumented technological evaluator tool box. In: ECCM 15, 2012

Selection of Optimal Aluminum-Based Composite Produced by Powder Metallurgy Process in Uncertain Environment

Razieh Abdoos, Ali Jahan and Hasan Abdoos

Abstract Powder metallurgy is one of the important processes in the production of aluminum composites, whose design is governed by optimal reinforcing properties such as type, volume fraction, and particle size. Given the variety of reinforcements in aluminum composites and different expected properties, Multi-Attributes Decision-Making (MADM) methods can be employed to find the best feasible option. The objective of the present study is to select an appropriate type of reinforcement in aluminum matrix composites (AA6061), made through mechanical milling and powder metallurgy processes. In this research, a combinative decision-making process including interval TOPSIS and fuzzy group weighing approaches was used for the selection of aluminum-based composite reinforced (for structural applications) by aluminum nitride, silicon nitride, zirconium boride, and carbon nanotubes, all of which have high tensile strength, elastic modulus and hardness, lightweight, and low cost. Integrated MADM method demonstrated that the silicon nitride is the optimal alternative for structural applications in such types of composite. The sensitivity analysis further indicated that the change in the weights of attributes did not change the preferred option order (silicon nitride), rather influencing the ranking orders of the second and third alternatives.

Keywords Material selection · Aluminum matrix composites
Structural application · Multi-attribute decision-making · Interval TOPSIS

R. Abdoos · A. Jahan (✉)
Department of Industrial Engineering, Islamic Azad University, Semnan Branch, Semnan, Iran
e-mail: iranalijahan@yahoo.com; a.jahan@semnaniau.ac.ir

H. Abdoos
Department of Nano Technology, Faculty of New Science and Technology, Semnan University, Semnan, Iran

S. S. Sidhu et al. (eds.), *Futuristic Composites*, Materials Horizons: From Nature to Nanomaterials, https://doi.org/10.1007/978-981-13-2417-8_4

1 Introduction

Aluminum-based composites are employed in many structural, nonstructural, and functional applications in various engineering fields. The production and use of aluminum-based composites will be inevitable in future years and in transportation sector because of the increase in the stringent environmental regulations and the emphasis on saving energy and fuel [1, 2]. Over the recent decades, various manufacturing processes have been used to produce metal-based composites, resulting in the production of composites with better properties and lower costs. Among various manufacturing methods, powder metallurgy process is able to produce aluminum-based composites with a variety of reinforcements, allowing for the design and determination of final properties through the facile control of reinforcement amount, size and distribution, a process involving powder mixing, compacting, and sintering. Mixing the matrix powder and reinforcement are crucial steps toward achieving a homogeneous distribution. High-energy ball milling is one of the most effective approaches to achieving a homogeneous distribution of reinforcement particles in a matrix. Over the recent years, high-energy ball milling has been widely utilized to produce advanced powder compounds. The mechanical milling method involves continuous collision of the balls with a mixture of the base powder and the reinforcement [3–6]. In this research, therefore, milling process was made use of with the aim of achieving a homogeneous distribution of reinforcement particles as one of the main steps in the production of aluminum-based composites. Research has shown that ultimate tensile strength (UTS), elastic modulus, fracture toughness, hardness, thermal conductivity, thermal expansion, and density are the most important factors in the selection of metal-based composites influenced by the characteristics of the matrix and reinforcement (Johnson [7]. In many cases, a combination of these features is needed, requiring the use of material selection procedure with the purpose of an optimal selection of matrix and reinforcement characteristics. Decision-making science deals with issues such as identification, categorization, and selection, particularly in uncertain environment [8]. The number of decision-making indicators, the variety of quantitative and qualitative criteria, and the necessity of their simultaneous consideration increase the complexity of decision-making processes [9].

For complex decisions, researchers have recently concentrated on Multiple Criteria Decision-Making (MCDM) which allows for many materials and design properties to be considered simultaneously [10], thereby precluding inappropriate use of materials [11]. In general, MCDM models can be categorized into two main categories:

- Multiple Objective Decision-Making (MODM)
- Multiple Attribute Decision-Making (MADM)

MODM has a lower level of transparency owing to the numerous and not explicitly defined alternatives (at least at the beginning of the evaluation process). This method assumes a simultaneous evaluation with regard to multiple objectives, searching for the best alternative. On the contrary, MADM is based on the evaluation of a relatively small number of alternatives characterized by attributes, with the evaluation

process determining how well the alternatives satisfy the objectives. Further taken into account are weighing the importance of criteria and assigning preferences to the alternatives. MODM models are used for designing, while MADM models are applied to the selection of the optimal alternative. TOPSIS is a major MADM method which considers the relative propinquity to the ideal solution and avoids anti-ideal answers as rating criteria, hence a suitable method for material selection [12]. Shanian and Savadogo [13, 14] presented models of material selection using an MADM method called ELECTRE and further employed TOPSIS in order to choose materials in metallic bipolar plates in polymer electrolytic fuel cells. In yet another study, they [15] proposed TOPSIS and VIKOR methods for selecting materials in high-reliability structural components in space and nuclear industries. Bahraminasab and Jahan [11] applied comprehensive VIKOR to the selection of materials suitable in knee prosthesis. In their selection of the best material to design a lighter wagon, Findik and Turan [16] utilized weighted property index method (WPIM). Maity and Chakraborty [17] proposed a fuzzy TOPSIS method to select a suitable abrasive material in a grinding wheel. Chauhan and Vaish [18] used several decision-making methods so as to choose hard-covering materials. The results of their research showed that carbon and magnesium oxide were, respectively, the most appropriate and inappropriate materials for hard coatings. Yazdani and Payam [19] used TOPSIS, VIKOR, and Ashby methods to select materials as operators in microelectromechanical systems. Milani et al. [20] investigated the effect of normalization methods on MADM and examined gear materials for use in power transmission applications, utilizing TOPSIS to rate the selected materials. In another study, Milani et al. [21] used a new MADM method for choosing composite materials with respect to their lifecycle in addition to reviewing recent experimental developments in the selection of the composites. Mansor et al. [22] employed TOPSIS for material selection and determination of the best thermoset matrix for binary composites used in car bumpers. Senthil et al. [23] optimized the machining variables of aluminum–copper composite reinforced with TiB_2 particles by the use of TOPSIS, a method also used by Khorshidi et al. [24] in their study of the optimal structure conditions to achieve maximum tensile properties in aluminum-based composites. In another study, Khorshidi and Hassani [25] compared TOPSIS and Preference Selection Index (PSI) as regards determining the appropriate combination of strength and workability in Al/SiC composites.

A significant point to be considered while choosing materials is the development and application of decision-making methods where interval data are used instead of exact values. Interval numbers are suitable in MADM models and uncertain conditions since in real applications, many quantities are reported in a range or interval [26]. Liao [27] used the two interval type 2 fuzzy TOPSIS methods to select the material used in the fuel injection nozzle in high-temperature oxygen-enriched environments. The main purpose of the present research is to use an interval TOPSIS decision-making method to select an aluminum-based composite reinforced with particles and prepared by powder metallurgy for structural applications.

2 Materials and Methods

2.1 Alternatives and Criteria

Many metal-based composites are used under stress conditions as components of machines or equipment employed in structural applications. In the present study, a suitable aluminum-based composite was selected for structural applications through the use of an integrated MADM method. It is further important to gather data associated with such factors as strength, elastic modulus, hardness, weight, and price, all playing crucial roles in structural applications.

In the current study, aluminum alloy 6061 was selected as a matrix, and aluminum nitride (AlN), silicon nitride (Si_3N_4), zirconium boride (ZrB_2), and carbon nanotubes (CNTs) were chosen as reinforcements. It is to be noted that aluminum-based composites reinforced with aluminum nitride particles [3, 6, 28–30], silicon nitride [6, 28, 31, 32], and zirconium boride [6, 33] have been previously studied. These composites were produced by powder metallurgy and mechanical milling. Further studied and compared was the effect of carbon nanotubes as relatively new reinforcements in aluminum matrix composites. Recent advances in metal-based composites reinforced with carbon nanotubes have shown a significant increase in the UTS and yield strength [4]. In this regard, the data pertaining to the UTS and hardness were obtained from empirical experiments of other researchers, and the density and elastic modulus of the composites were calculated using existing theoretical–empirical models. Density was specified via Eq. (1) [7]:

$$\rho_C = \Phi_M \rho_M + \Phi_R \rho_R \tag{1}$$

where ρ_C, ρ_M, and ρ_R are composite, matrix, and reinforcement density, and Φ_M and Φ_R are volume fractions of the matrix and reinforcement, respectively. Equation (2) was used to calculate the elastic modulus of the composite [7]:

$$E_C = (\Phi_M E_M + \Phi_R E_R)\rho_{fc}^{3.4} \tag{2}$$

where E_M and E_R are the elastic modulus of the matrix and the reinforcement, respectively, and ρ_{fc} is the fractional density of the composite. Weight fraction was converted to volume fraction based on the following:

$$V_R = \frac{W_R/\rho_R}{W_R/\rho_R + W_M/\rho_M} \tag{3}$$

where V_R is the volume fraction of the reinforcement, and W_R and W_M are the weights of the reinforcement and the matrix, respectively.

Table 1 illustrates the characteristics of aluminum-based composites reinforced with AlN, Si_3N_4, ZrB_2, and carbon nanotubes. As observed, all composites were subjected to mechanical milling for a homogenous distribution of the reinforcement.

Table 1 Characteristics of various reinforcements (decision matrix)

Reinforcement type	Tensile strength (MPa) [5, 6]	Hardness (HV) [6, 34]	Elastic module (GPa)	Density (g/cm^3)	Cost
AlN	[206, 402]	[63, 126]	[46.38, 67.17]	2.72	Medium
Si_3N_4	[214, 422]	[63, 119]	[45.47, 65.86]	2.73	Low
ZrB_2	[192, 320]	[59, 110]	[45.64, 66.09]	2.78	High
CNT	[416, 442]	[62, 74]	[59.47, 71.59]	2.69	High

Table 2 Linguistic variable corresponding to importance of criteria

	D_1	D_2	D_3	D_4	D_5
C_1	VH	VH	H	H	VH
C_2	MH	M	H	MH	M
C_3	VH	H	MH	VH	VH
C_4	H	VH	MH	M	VH
C_5	H	H	MH	M	MH

2.2 Weighting Strategy

A method based on Fuzzy logic was used in order to determine the importance of each criterion [34]. In this method, linguistic phrases have to be primarily converted to fuzzy numbers in order to obtain the weights.

The steps to determining the weights of the criteria are as follows [34, 35]:

- Using linguistic phrases, the importance of each index was determined by five people in the design team (Table 2). In Table 2, C_1 … C_5 show indicators (tensile strength, hardness, modulus, density, and price), and D_1 … D_5 represent the designers. The terms inside the table indicate the importance of each indicator from a designer viewpoint. H, VH, MH, and M refer to high importance, very high importance, moderate importance, and mean importance of the desired index, respectively.
- Each option in Table 2 is converted from the linguistic phrases into its corresponding fuzzy numbers.
- For each index, the corresponding weight is calculated and determined according to Eq. (4):

$$W_j = \{W_{J1}, W_{J2}, W_{J3}, W_{J4}\} \tag{4}$$

where

$$W_{J1} = \min_k \{W_{jk1}\}, \quad W_{J2} = \frac{1}{k} \sum W_{jk2},$$

$$W_{J3} = \frac{1}{k}\sum W_{jk3}, \quad W_{J4} = \max_k \{W_{jk4}\}$$

– The fuzzy values are de-fuzzed by Eq. (5), and, at the final stage, the weight of each index is normalized and the ultimate weights are obtained.

$$\begin{aligned}
\text{Defuzz}(W_j) &= \frac{\int \mu(w).w\mathrm{d}w}{\int \mu(w)\mathrm{d}w} \\
&= \frac{\int_{w_{j1}}^{w_{j2}} (\frac{w-w_{j1}}{w_{j2}-w_{j1}}).w\mathrm{d}w + \int_{w_{j2}}^{w_{j3}} w\mathrm{d}w + \int_{w_{j3}}^{w_{j4}} (\frac{w_{j4}-w}{w_{j4}-w_{j3}}).w\mathrm{d}w}{\int_{w_{j1}}^{w_{j2}} (\frac{w-w_{j1}}{w_{j2}-w_{j1}})\mathrm{d}w + \int_{w_{j2}}^{w_{j3}} \mathrm{d}w + \int_{w_{j3}}^{w_{j4}} (\frac{w_{j4}-w}{w_{j4}-w_{j3}})\mathrm{d}w} \\
&= \frac{-w_{j1}w_{j2} + w_{j3}w_{j4} + \frac{1}{3}(w_{j4}-w_{j3})^2 - \frac{1}{3}(w_{j2}-w_{j1})^2}{-w_{j1} - w_{j2} + w_{j3} + w_{j4}} \\
&= \frac{w_{j3}^2 + w_{j4}^2 + w_{j3}.w_{j4} - w_{j1}^2 - w_{j2}^2 - w_{j1}.w_{j2}}{3(-w_{j1} - w_{j2} + w_{j3} + w_{j4})}
\end{aligned} \tag{5}$$

2.3 Ranking via Interval TOPSIS Method

In this study, the steps to determining the best option by interval TOPSIS method [36] are as follows:

- Formation of an interval decision-making matrix consisting of m options, represented by $A_1, A_2, \ldots, A_m$ and n criteria, represented by $C_1, C_2, \ldots, C_n$ and $[x_{ij}] = [x_{ij}^{\mathrm{L}}, x_{ij}^{\mathrm{U}}]$ components, representing the specific interval values of the jth criterion for the ith alternative, in which x_{ij}^{L} and x_{ij}^{U} are the lower bound and the upper bound of the interval, respectively (Table 1).
- Formation of the normalized decision-making matrix using the Euclidean norm method (Eq. 6):

$$\begin{aligned}
r_{1j}^{\mathrm{L}} &= \frac{x_{1j}^{\mathrm{L}}}{\sqrt{\sum_{k=1}^{m}\left(\left(x_{kj}^{\mathrm{L}}\right)^2 + \left(x_{kj}^{\mathrm{U}}\right)^2\right)}} \quad i = 1, 2, \ldots, m, \\
r_{1j}^{\mathrm{U}} &= \frac{x_{1j}^{\mathrm{U}}}{\sqrt{\sum_{k=1}^{m}\left(\left(x_{kj}^{\mathrm{L}}\right)^2 + \left(x_{kj}^{\mathrm{U}}\right)^2\right)}} \quad j = 1, 2, \ldots, n
\end{aligned} \tag{6}$$

- Formation of a weighted normalized decision-making matrix (V) through the multiplication of the weights in the normalized decision-making matrix (Eq. 7):

$$V_{1j}^{\mathrm{L}} = W_j \times r_{1j}^{\mathrm{L}}, \quad V_{1j}^{\mathrm{U}} = W_j \times r_{1j}^{\mathrm{U}} \tag{7}$$

– Determining the positive and negative ideal alternatives by comparing larger or smaller intervals according to Eq. (8) and specifying positive and negative ideal options based on Eqs. (9) and (10):

$$\Delta_{A-B} = \left(\frac{1}{2}\left(a^{\mathrm{L}} + a^{\mathrm{U}}\right) - \frac{1}{2}\left(b^{\mathrm{L}} + b^{\mathrm{U}}\right)\right) \tag{8}$$

where $A = [a^{\mathrm{L}}, a^{\mathrm{U}}]$ and $B = [b^{\mathrm{L}}, b^{\mathrm{U}}]$ [36].

$$A^{+} = \left\{\left[v_1^{+\mathrm{L}}, v_1^{+\mathrm{U}}\right], \left[v_2^{+\mathrm{L}}, v_2^{+\mathrm{U}}\right], \ldots, \left[v_n^{+\mathrm{L}}, v_n^{+\mathrm{U}}\right]\right\} \tag{9}$$

$$A^{-} = \left\{\left[v_1^{-\mathrm{L}}, v_1^{-\mathrm{U}}\right], \left[v_2^{-\mathrm{L}}, v_2^{-\mathrm{U}}\right], \ldots, \left[v_n^{-\mathrm{L}}, v_n^{-\mathrm{U}}\right]\right\} \tag{10}$$

– Determining the distance of each option from the positive and negative ideal alternative:

$$S_i^{+} = \frac{1}{2}\sum_{j\in K_b}\left(\left(v_j^{+\mathrm{L}} + v_j^{+\mathrm{U}}\right) - \left(v_{1j}^{\mathrm{L}} + v_{1j}^{\mathrm{U}}\right)\right) + \frac{1}{2}\sum_{j\in K_c}\left(\left(v_{1j}^{\mathrm{L}} + v_{1j}^{\mathrm{U}}\right) - \left(v_j^{+\mathrm{L}} + v_j^{+\mathrm{U}}\right)\right) \tag{11}$$

$$S_i^{-} = \frac{1}{2}\sum_{j\in K_b}\left(\left(v_{1j}^{\mathrm{L}} + v_{1j}^{\mathrm{U}}\right) - \left(v_j^{-\mathrm{L}} + v_j^{-\mathrm{U}}\right)\right) + \frac{1}{2}\sum_{j\in K_c}\left(\left(v_j^{-\mathrm{L}} + v_j^{-\mathrm{U}}\right) - \left(v_{1j}^{\mathrm{L}} + v_{1j}^{\mathrm{U}}\right)\right) \tag{12}$$

where S_i^{+} is the distance of each option from the positive ideal option and S_i^{-} is related to the distance of each option from the ideal negative option.

– Calculation of the relative closeness of each option to the ideal option according to Eq. (13). After determining the RC_i value for each option, the one with the maximum value is the farthest from the negative ideal option or the closest to the positive ideal option.

$$\mathrm{RC}_i = \frac{S_i^{-}}{S_i^{-} + S_i^{+}}, \quad i = 1, 2, \ldots, m, \ 0 \le RC_i \le 1 \tag{13}$$

3 Results and Discussion

3.1 Weight of Criteria

The fuzzy numbers corresponding to the importance level of each indicator are demonstrated in Table 3. The fuzzy values of each index were calculated according to

Table 3 Importance weighting of material selection criteria assessed by designers (fuzzy set)

	D_1	D_2	D_3	D_4	D_5
C_1	(0.8, 0.9,1,1)	(0.8, 0.9,1,1)	(0.7, 0.8, 0.8, 0.9)	(0.7, 0.8, 0.8, 0.9)	(0.8, 0.9,1,1)
C_2	(0.5, 0.6, 0.7, 0.8)	(0.4, 0.5, 0.6, 0.7)	(0.7, 0.8, 0.8, 0.9)	(0.5, 0.6, 0.7, 0.8)	(0.4, 0.5, 0.6, 0.7)
C_3	(0.8, 0.9,1,1)	(0.7, 0.8, 0.8, 0.9)	(0.5, 0.6, 0.7, 0.8)	(0.8, 0.9,1,1)	(0.8, 0.9,1,1)
C_4	(0.7, 0.8, 0.8, 0.9)	(0.8, 0.9,1,1)	(0.5, 0.6, 0.7, 0.8)	(0.4, 0.5, 0.6, 0.7)	(0.8, 0.9,1,1)
C_5	(0.7, 0.8, 0.8, 0.9)	(0.7, 0.8, 0.8, 0.9)	(0.5, 0.6, 0.7, 0.8)	(0.4, 0.5, 0.6, 0.7)	(0.5, 0.6, 0.7, 0.8)

Table 4 Aggregated fuzzy values, defuzzified weighting, and final weighting of the criteria

Reinforcement type	Tensile strength (MPa)	Hardness (HV)	Elastic module (GPa)	Density (g/cm^3)	Cost
AlN	[0.051, 0.10]	[0045, 0.090]	[0061, 0.088]	[0.070, 0.070]	[0.052, 0.052]
Si_3N_4	[0053, 0.105]	[0.045, 0.085]	[0.060, 0.086]	[0.071, 0.071]	[0.031, 0.031]
ZrB_2	[0.048, 0.079]	[0.042, 0.079]	[0.060, 0.087]	[0.072, 0.072]	[0.073, 0.073]
CNT	[0.103, 0.110]	[0.045, 0.053]	[0.078, 0.094]	[0.070, 0.070]	[0.073, 0.073]

Eq. (4). Non-fuzzy weights were obtained based on Eq. (5) and the final (normalized) weights of the indices were further specified (Table 4).

The results of Table 4 show that according to the decision-makers' opinions and the determined weights, a final tensile strength index of 0.24 and price index of 0.17 resulted in the highest and lowest weights compared with other indicators, respectively. It is worth noting that the total weight of all indices equals 1.01, which approximates one.

3.2 Ranking

After specifying the weights pertaining to each indicator, the interval variables were rated through the use of TOPSIS where the existing interval matrix (Table 1) was converted into a normalized and weighted normalized matrix. Further calculated were the ideal positive and negative values, the interval between each option and the ideal option and, finally, the relative closeness of each option to the ideals. Equations (6)–(13) were used and the results are shown in Tables 5 and 6.

Considering that the first to third indices are positive and the fourth and fifth indices are negative, the ideal positive and negative options are

Table 5 Normalized decision matrix based on interval TOPSIS

Criteria	Calculated fuzzy value	Defuzzified weighting	Final weighting (Normalized)
Tensile strength	(0.70, 0.86, 0.92, 1)	0.87	0.24
Hardness	(0.40, 0.60, 0.64, 0.90)	0.64	0.18
Elastic module	(0.50, 0.82, 0.90, 1)	0.79	0.22
Density	(0.40, 0.74, 0.80, 1)	0.73	0.2
Cost	(0.40, 0.57, 0.63, 0.90)	0.63	0.17

Table 6 Normalized weighted decision matrix based on interval TOPSIS

Reinforcement type	Tensile strength (MPa)	Hardness (HV)	Elastic module (GPa)	Density (g/cm^3)	Cost
AlN	[0.213, 0.416]	[0.251, 0.502]	[0.276, 0.400]	[0.352, 0.352]	[0.308, 0.308]
Si_3N_4	[0.436, 0.221]	[0.251, 0.475]	[0.271, 0.392]	[0.354, 0.354]	[0.158, 0.158]
ZrB_2	[0.198, 0.331]	[0.235, 0.439]	[0.272, 0.394]	[0.360, 0.360]	[0.431, 0.431]
CNT	[0.430, 0.457]	[0.247, 0.295]	[0.354, 0.426]	[0.348, 0.348]	[0.431, 0.431]

Table 7 Ranking of alternatives according to interval TOPSIS

Ailternatives	S_i^+	S_i^-	RC_i
AlN	0.064	0.055	0.461
Si_3N_4	0.044	0.075	0.63
ZrB_2	0.107	0.012	0.102
CNT	0.061	0.058	0.489

$$A^+ = \left\{ \begin{matrix} [0.103, 0.110], [0.045, 0.090], [0.078, 0.094], \\ [0.070, 0.070], [0.031, 0.031] \end{matrix} \right\}$$

$$A^- = \left\{ \begin{matrix} [0.048, 0.079], [0.045, 0.053], [0.060, 0.086], \\ [0.072, 0.072], [0.073, 0.073] \end{matrix} \right\}$$

Table 7 demonstrates the distance between each option and the positive and negative ideals along with the relative closeness index.

According to the numbers obtained for the relative closeness index, Si_3N_4 (silicon nitrate), CNTs (carbon nanotube), AlN (Aluminum nitride), and ZrB_2 (Boride zirconium) were, respectively, the most effective reinforcements concerning aluminum-based composite (AA6061) produced by mechanical milling and powder metallurgy for structural applications with respect to properties such as UTS, elastic modulus, hardness, density, and price.

Table 8 Results of closeness index in sensitivity analysis

Alternatives	A	B	C	D	E	F
AlN	0.468	0.476	0.476	0.485	0.484	0.462
Si_3N_4	**0.64**	**0.644**	**0.631**	**0.648**	**0.651**	**0.662**
ZrB_2	0.105	0.114	0.118	0.122	0.12	0.09
CNT	0.47	0.462	0.479	0.455	0.448	0.445

3.3 Sensitivity Analysis

Sensitivity analysis is the study of the dependency of output variables on the input variables of a model. In other words, it is a way to change the inputs of a model in a systematic way, so that the effects of these changes can be predicted in the model output [37]. Sensitivity shows the amount of changes in a dependent variable caused by altering its corresponding independent variable in a given condition, assuming that other variables are constant. Sensitivity analysis specifies how a certain change in the importance of an indicator affects the selected options.

Since most data associated with MADM problem are inaccurate and modifiable, a post-problem sensitivity analysis can be conducive to a correct decision. Given the weight choice of different indicators with regard to decision-makers' opinions and the possibility of changing the data in a decision matrix, it is important to know the sensitivity of the indicators. Observing the changes in the results caused by the change in a parameter such as the weight of an indicator or the amount of an option in an indicator can help select the best option and make a more informed decision.

According to the results obtained in the ranking section, it is clear that the difference between the first and second choices is so high that the change in their weights cannot alter their priority. However, the second and third choices are less different, and hence the fact that it is more probable for their priorities to change with the alteration in their weights. Therefore, necessary changes were made for sensitivity analysis in the weights of the indices (Table 8). In this regard, the employed assumptions are as follows [38]:

(A) First index weight (C_1) is reduced by 10%.
(B) First index weight (C_1) is reduced by 10% and the second index weight (C_2) is increased by 10%.
(C) First index weight (C_1) and the fifth index weight ($C5$) are decreased by 10% and the second index weight (C_2) is increased by 10%.
(D) First index weight (C_1) is reduced by 10% and the second index weight (C_2) is increased by 20%.
(E) First index weight (C_1) is decreased by 15% and the second index weight (C_2) is increased by 15%.
(F) First index weight (C_1) and the second index weight (C_2) are reduced by 10% and the fifth index weight (C_5) is augmented by 20%.

In this section, we studied the effect of each indicator on the ranking and specified the results through analyzing the sensitivity to the effective factors. For this purpose, the desired parameters (tensile strength, hardness, and price) were analyzed by applying changes of 10, 15, and 20%. As shown in Table 8, decreasing the weights of indices C_1 and C_5, increasing the weight of index C_2, and calculating the new relative closeness index, silicon nitride (Si_3N_4) is still the optimal alternative and changes are only related to other ranks.

The changes of −10, +10, +15, and +20% in importance of hardness will result in swapping rank of the second and third options, which shows the significance of hardness in this study. Moreover, the 20% increase in importance of price along with a 10% reduction in tensile strength and hardness caused the exchanging of the second and third options.

According to certain research [4, 5, 39–41], carbon nanotubes generally have very high mechanical properties, including UTS, elastic modulus, and lightweight; therefore, its addition as a reinforcement to the aluminum matrix is expected to entail optimal conditions for structural applications. In the present study, however, aluminum nitride particles were ranked first regarding tensile strength, modulus, hardness, density, and low cost. One of the problems associated with adding carbon nanotubes to the metal matrix is the issues related to their uniform distribution in the matrix.

Uniform distribution (homogeneity) of carbon nanotubes in the matrix during processing is conducive to obtaining the predicted theoretical strength [42]. Efforts have been made to provide metal-based composites reinforced with carbon nanotubes using conventional metal casting or powder metallurgy processes [43–45]. Given the poor wettability of carbon nanotubes and molten aluminum and the difference in their densities, these carbon materials float rapidly on the melt surface without mixing. In powder metallurgy, carbon nanotubes cause significant residual stress in the aluminum matrix, reducing the tensile strength in non-annealed composites in contrast to pure aluminum. In addition, the bond between the matrix and the reinforcement is generally weak, leading to inefficient force transmission. The presence of adhesion forces among carbon nanotubes complicates the homogeneous distribution of nanotubes among matrix powders. Accordingly, solutions have been proposed to augment the homogeneity of the distribution of carbon nanostructured materials in metal matrixes; the functionalization and amount of the nanotubes, along with the matrix material and the mixing time can significantly affect the distribution of the nanotubes in the metal matrixes. Even a small number of nanotubes embedded in metal matrix can increase the composite hardness, since the micron-scale cavities of metal matrix are filled with nanotubes. Additional nanotubes, which are not able to fill the micron cavities, begin to form agglomerates along with aluminum particles, preventing the full sintering, causing defects, and gradually reducing composite hardness [46, 47]. Therefore, in most carbon nanotube-reinforced metal-based composites, the optimum amount of nanotubes is often between 1 and 2% by weight [40, 48], while there is no limitation for other ceramic reinforcement particles (such as nitrides and borides) where the amount of reinforcements can be up to 5% by weight [30–33]. Given the superiority of carbon nanotubes over ceramic particles, if the agglomeration-related

challenges are overcome and the number of nanotubes in metal matrix increased to more than 1–2 wt%, it can be expected that aluminum-based composite (AA6061) reinforced by nanotubes be ranked first regarding structural applications. The production and use of industrial nanotubes with good quality and low prices can also be useful in this regard.

4 Conclusion

The present study aimed to select the optimal aluminum-based composite reinforced with particulate materials such as aluminum nitride, silicon nitride, zirconium boride, and carbon nanotubes. The composites were processed by mechanical milling and powder metallurgy. The choice was made based on the use of composites in structural applications where interval TOPSIS decision-making method and fuzzy logic weighting procedure were combined. The conclusions of this research are as follows:

- The use of aluminum-based composites in structural applications requires properties such as UTS, hardness, and high elastic modulus with low density and low cost.
- Since the preponderance of data pertaining to the properties of composites is presented as a range or an interval in references, multi-criteria decision-making methods such as TOPSIS can successfully be used to select the preferred option.
- The results of TOPSIS decision-making process in the present study indicated that the reinforcement particles of silicon nitride, carbon nanotubes, aluminum nitride, and zirconium boride are the best alternatives for reinforcing AA6061 aluminum in structural applications.
- The sensitivity analysis showed that the increase and decrease in the weight of each indicator to a given value (10, 15, and 20%) cannot affect the selection of silicon nitride as the optimum alternative.
- Considering the remarkable characteristics of carbon nanotubes compared to other ceramic particles, it is anticipated that if we reduce the agglomeration and number of carbon nanotubes in the matrix, Al6061 composites reinforced with CNTs can be regarded as the best options for structural applications.

References

1. Surappa M (2003) Aluminium matrix composites: challenges and opportunities. Sadhana 28(1–2):319–334
2. Gökçe A, Fındık F, Kurt AO (2011) Microstructural examination and properties of premixed Al–Cu–Mg powder metallurgy alloy. Mater Charact 62(7):730–735
3. Firestein K et al (2017) High-strength aluminum-based composites reinforced with BN, AlB_2 and AlN particles fabricated via reactive spark plasma sintering of Al-BN powder mixtures. Mater Sci Eng, A 681:1–9

4. Wu Y, Kim G-Y, Russell AM (2012) Mechanical alloying of carbon nanotube and Al6061 powder for metal matrix composites. Mater Sci Eng, A 532:558–566
5. Najimi A, Shahverdi H (2017) Effect of milling methods on microstructures and mechanical properties of Al6061-CNT composite fabricated by spark plasma sintering. Mater Sci Eng, A 702:87–95
6. Fogagnolo J et al (2004) 6061 Al reinforced with zirconium diboride particles processed by conventional powder metallurgy and mechanical alloying. J Mater Sci 39(1):127–132
7. Johnson JL (2011) Opportunities for pm processing of metal matrix composites. Int J Powder Metall 47(2)
8. Azar A, Rjabzadeh A (2002) Applied decision making, knowledge perspectives. Negahe Danesh
9. Saaty TL (1985) Decision making for leaders. IEEE Trans Syst Man Cybern 3:450–452
10. Jahan A, Edwards KL (2015) A state-of-the-art survey on the influence of normalization techniques in ranking: improving the materials selection process in engineering design. Mater Des (1980–2015) 65:335–342
11. Bahraminasab M, Jahan A (2011) Material selection for femoral component of total knee replacement using comprehensive VIKOR. Mater Des 32(8–9):4471–4477
12. Shanian A, Savadogo O (2006) A material selection model based on the concept of multiple attribute decision making. Mater Des 27(4):329–337
13. Shanian A, Savadogo O (2006) A non-compensatory compromised solution for material selection of bipolar plates for polymer electrolyte membrane fuel cell (PEMFC) using ELECTRE IV. Electrochim Acta 51(25):5307–5315
14. Shanian A, Savadogo O (2006) TOPSIS multiple-criteria decision support analysis for material selection of metallic bipolar plates for polymer electrolyte fuel cell. J Power Sources 159(2):1095–1104
15. Shanian A, Savadogo O (2009) A methodological concept for material selection of highly sensitive components based on multiple criteria decision analysis. Expert Syst Appl 36(2):1362–1370
16. Findik F, Turan K (2012) Materials selection for lighter wagon design with a weighted property index method. Mater Des 37:470–477
17. Maity SR, Chakraborty S (2013) Grinding wheel abrasive material selection using fuzzy TOPSIS method. Mater Manuf Process 28(4):408–417
18. Chauhan A, Vaish R (2013) Hard coating material selection using multi-criteria decision making. Mater Des 44:240–245
19. Yazdani M, Payam AF (2015) A comparative study on material selection of microelectromechanical systems electrostatic actuators using Ashby, VIKOR and TOPSIS. Mater Des (1980–2015) 65:328–334
20. Milani A et al (2005) The effect of normalization norms in multiple attribute decision making models: a case study in gear material selection. Struct Multidiscipl Optim 29(4):312–318
21. Milani A et al (2011) Multiple criteria decision making with life cycle assessment for material selection of composites. Express Polym Lett 5(12)
22. Mansor M et al (2014) Materials selection of hybrid bio-composites thermoset matrix for automotive bumper beam application using TOPSIS method. Adv Environ Biol, 3138–3143
23. Senthil P, Vinodh S, Singh AK (2014) Parametric optimisation of EDM on Al-Cu/TiB_2 in-situ metal matrix composites using TOPSIS method. Int J Mach Mach Mater 16(1):80–94
24. Khorshidi R et al (2013) Selection of an optimal refinement condition to achieve maximum tensile properties of Al–15% Mg2Si composite based on TOPSIS method. Mater Des 46:442–450
25. Khorshidi R, Hassani A (2012) Comparative analysis between TOPSIS and PSI methods of materials selection to achieve a desirable combination of strength and workability in Al/SiC composite. Mater Des (1980–2015) 52:999–1010
26. Jahan A, Edwards K (2013) VIKOR method for material selection problems with interval numbers and target-based criteria. Mater Des 47:759–765
27. Liao TW (2015) Two interval type 2 fuzzy TOPSIS material selection methods. Mater Des 88:1088–1099

28. Fogagnolo J et al (2003) Effect of mechanical alloying on the morphology, microstructure and properties of aluminium matrix composite powders. Mater Sci Eng, A 342(1–2):131–143
29. Fogagnolo J, Robert M, Torralba J (2006) Mechanically alloyed AlN particle-reinforced Al-6061 matrix composites: powder processing, consolidation and mechanical strength and hardness of the as-extruded materials. Mater Sci Eng, A 426(1–2):85–94
30. Fogagnolo JB, Robert MH, Torralba JM (2003) The effects of mechanical alloying on the extrusion process of AA 6061 alloy reinforced with Si_3N_4. J Braz Soc Mech Sci Eng 25(2):201–206
31. Fogagnolo JB et al (2003) The effects of mechanical alloying on the compressibility of aluminium matrix composite powder. Mater Sci Eng, A 355(1–2):50–55
32. Fogagnolo J et al (2002) 6061 Al reinforced with silicon nitride particles processed by mechanical milling. Scripta Mater 47(4):243–248
33. Fogagnolo JB et al (2004) Aluminium matrix composites reinforced with Si_3N_4, AlN and ZrB_2, produced by conventional powder metallurgy and mechanical alloying. Kona Powder and Particle Journal 22:143–150
34. Girubha RJ, Vinodh S (2012) Application of fuzzy VIKOR and environmental impact analysis for material selection of an automotive component. Mater Des 37:478–486
35. Shemshadi A et al (2011) A fuzzy VIKOR method for supplier selection based on entropy measure for objective weighting. Expert Syst Appl 38(10):12160–12167
36. Dymova L, Sevastjanov P, Tikhonenko A (2013) A direct interval extension of TOPSIS method. Expert Syst Appl 40(12):4841–4847
37. Saltelli A et al (2008) Global sensitivity analysis: the primer. Wiley
38. Cables E, Lamata MT, Verdegay JL (2016) RIM-reference ideal method in multicriteria decision making. Inf Sci 337:1–10
39. Jeyasimman D et al (2014) Fabrication and consolidation behavior of Al 6061 nanocomposite powders reinforced by multi-walled carbon nanotubes. Powder Technol 258:189–197
40. Moghadam AD et al (2015) Mechanical and tribological properties of self-lubricating metal matrix nanocomposites reinforced by carbon nanotubes (CNTs) and graphene—a review. Compos B Eng 77:402–420
41. Yu M-F et al (2000) Strength and breaking mechanism of multiwalled carbon nanotubes under tensile load. Science 287(5453):637–640
42. Cha SI et al (2005) Extraordinary strengthening effect of carbon nanotubes in metal-matrix nanocomposites processed by molecular-level mixing. Adv Mater 17(11):1377–1381
43. Flahaut E et al (2000) Carbon nanotube–metal–oxide nanocomposites: microstructure, electrical conductivity and mechanical properties. Acta Mater 48(14):3803–3812
44. Wang X, Padture NP, Tanaka H (2004) Contact-damage-resistant ceramic/single-wall carbon nanotubes and ceramic/graphite composites. Nat Mater 3(8):539
45. Zhan G-D et al (2003) Single-wall carbon nanotubes as attractive toughening agents in alumina-based nanocomposites. Nat Mater 2(1):38
46. Clegg WJ (2000) Role of carbon in the sintering of boron-doped silicon carbide. J Am Ceram Soc 83(5):1039–1043
47. Wang LY et al (2003) Friction and wear behavior of electroless Ni-based CNT composite coatings. Wear 254(12):1289–1293
48. Tjong SC (2013) Recent progress in the development and properties of novel metal matrix nanocomposites reinforced with carbon nanotubes and graphene nanosheets. Mater Sci Eng R Rep 74(10):281–350

Intelligent Decision Making Tools in Manufacturing Technology Selection

Morteza Yazdani and Prasenjit Chatterjee

Abstract The importance of technology in modern companies is literally growing. Technology protects the natural environment and acts as catalyst toward a more productive economy. Technology development has been the most demanding activity in industrial sectors over years and technology selection and implementation is one of the acknowledged projects in many companies. There are many factors influencing the problem of evaluating and choosing a new technology. Therefore, manufacturing operation managers are involved in a decision-making system with conflicting elements in their selection process. In this condition, application of multi-attribute decision-making (MADM) tools is highly recommended. This study examines the utilization of analytic hierarchy process and an adopted MADM method named CoCoSo to simultaneously determine the importance of decision factors and obtain the optimal ranking. At the final stage, we configure a sensitivity analysis to check and examine the accuracy of the results and performance of the present decision system. The study corresponds to a case study of choosing best packaging technology for a dairy company.

Keywords Analytical hierarchy process · Combined compromise solution Multiple attribute decision-making · Technology selection

1 Introduction

Managing technological issues and the necessity to address them with the complex factors leads managers and decision makers (DMs) to confront with a process of

M. Yazdani (✉)
Department of Business and Management, Universidad Loyola Andalucia, Seville, Spain
e-mail: morteza_yazdani21@yahoo.com

P. Chatterjee
Department of Mechanical Engineering, MCKV Institute of Engineering, Howrah, West Bengal, India
e-mail: prasenjit2007@gmail.com

S. S. Sidhu et al. (eds.), *Futuristic Composites*, Materials Horizons: From Nature to Nanomaterials, https://doi.org/10.1007/978-981-13-2417-8_5

taking decision in various sectors such as manufacturing, business development, tourism, and agriculture [1]. Technology selection can be realized as a complex multidimensional decision problem containing both qualitative and quantitative factors, such as human resources, operational and financial dimensions with different orientations and conflicting attitudes [2]. Managers tend to adopt new technologies due to the benefits announced by other companies across the world or customer demand or change in taste of the clients. It is understood that managers must be aware of those change in the market and make a right decision of implementing such advanced technologies in their organizations processes and production technologies. It is very probable that the selection of inappropriate technology could lead to a destructive outcome both strategically and financially and irreversible harms [3].

Decision-making in the area of manufacturing is regarded mainly to integrated and intelligent approaches to supply chain. Most of applied approaches can be listed as mathematical programming; modeling, multi-variable, and multiple attribute decisionmaking (MADM) techniques. Techniques, such as Analytical Hierarchy Process, Analytical Network Process, Quality Function Deployment and TOPSIS (Technique for Order of Preference by Similarity to Ideal Solution), often merged with a fuzzy approach, have been extensively considered in many investigations [4]. In a supply chain management (SCM), structured procedures must be applied to all relevant supply chain activities and practices from product design, material purchasing, manufacturing processes, final product delivery, and logistics [5, 6]. Managers' final objective in sustainable SCM (SSCM) is to take care of the long-run improvement of the economic performance of their organization focusing on approaches to not just survive but also to prosper in the near and the distant future. It deals with undertaking activities and operations that can improve the economic performance avoiding catastrophic errors and eliminate risk of the whole system.

Within a supply chain, managing the operations, network design, performance measurement, supplier selection and development, modal and carrier selection, vehicle routing, location and packaging are the essential practices of managers in all levels [4, 7]. In a supply chain, experts and decision makers must be aware of the technology modernization, upgrade, configuration, and selection. So, it is imperative to figure out how this kind of decision can be made, what rules and philosophies must be considered and how to integrate them logically.

Pålsson et al. [8] conducted a study in automotive industry to compare the environmental and economic impacts of packaging systems in a specific supply chain. The proposed in their model factors like packaging fill rate, packaging material, transport, material handling, waste handling, and administration. Mohanty and Deshmukh [9] utilized an analytical hierarchy process tool to strategically select an advanced manufacturing technology for an Indian electronics manufacturing enterprise. In global companies, hiring advanced technologies is a very competitive and effective challenge. Kengpol and O'Brien [10] developed a decision support model to deal with rapid product development by employing AHP, Cost/Benefit, and statistical. Selecting the milling machines among many alternatives has been reported by an integrated approach which employs analytic hierarchy process and preference ranking organization method for enrichment evaluations (PROMETHEE) [11]. In

the same manner, Anand and Kodali [12] recognized the PROMETHEE method—an Analytical Network Process (ANP) as an illustrative analytical approach for selection of lean manufacturing technologies. Tavana et al. [13] indicated the beneficial and analytical framework of ANP through a hybrid model under the fuzzy environment for the utilization of advanced technology at NASA. The contribution of decision-making modeling is observed in technology selection in energy sector. For choosing the most sustainable electricity production technologies, a framework of multicriteria decision methods using MULTIMOORA and TOPSIS proposed by Streimikiene et al. [14]. The other study in this area has been verified using fuzzy multiple attributes and group decision-making algorithm by the principles of fusion of fuzzy information, 2-tuple linguistic representation model, and maximum entropy-ordered weighted averaging operator to direct RFID technology selection process [15]. Adopting MULTIMOORA tool by 2-tuple fuzzy linguistic model, Liu et al. [16] proposed a healthcare waste treatment technology assessment structure.

Although the literature on measuring performance of manufacturing and packaging systems has been mentioned above, it is a promising task to build analyses. An empirical study was directed at an aircraft manufacturer to support a technology selection decision for a typical medium complexity assembly investment project. The investigation carried out where experience-based decision support, fuzzy decision tree, and data mining were applied and structured [17]. In a growing supply chain, analytical hierarchy process approach combined with strategic assessment model (SAM) has been modeled to evaluate and select the manufacturing technologies [18]. In order to select the appropriate technologies in the presence of cardinal data, ordinal data, nondiscretionary factors, and weight restrictions, a new nondiscretionary factor-imprecise data envelopment analysis approach is designed [19]. A group of authors have intended to support manufacturing automation decision-making that addresses the risk of environment. For that goal, they created an approach which uses both the quality function deployment (QFD) technique and the failure mode and effects analysis (FMEA) techniques [20]. A fuzzy group decision-making analysis system aided a flexible manufacturing in the Taiwanese bicycle industry to demonstrate the best fitted advanced manufacturing technology for management policy [21]. It is confidentially declared as we mentioned before that the selection of manufacturing machine technology is a complex problem for firms due to qualitative and quantitative criteria involved. Therefore, Aloini et al. [22] preceded an intuitionistic fuzzy multicriteria group decision-making with TOPSIS method to a packaging machine selection problem in food packaging. It is a new performance measurement approach overlooking the need for a specific analysis of the elements. This covers and fills a considerable gap in the literature. So far, it is worthy to form a comprehensive framework and classify the methodologies which can aid readers and highlight information about. Operation research studies and specifically contribution of decision-making and intelligent theories remain as the highest interest among supply chain scientists.

This paper is organized as follows; Sect. 2 presents the required materials and tools in order to optimally select the best alternatives. Section 3 offers problem definition and results of the decision-making solution. Then conclusion is given as seen in Sect. 4.

Table 1 The ratio scale and definition of AHP

Intensity of importance	Definition
1	Equally important
3	Moderately important
5	Strongly more important
7	Very strong important
9	Extremely more important
2, 4, 6, 8	Intermediate more important

Saaty [25]

2 A Decision Framework for Manufacturing Technology Evaluation

In this section, the required methodologies to evaluate, analyze, and rank alternatives are presented step by step. The first method is AHP which assigns the importance of each criterion. Then CoCoSo a new burn multicriteria decision-making (MADM) tool forms a decision matrix including performance rating of alternatives respecting each criterion and weights of criteria in order to obtain relevant score of each alternative as we call it ranking.

2.1 AHP

MADM methods are utilized to analyze decision-making system, compare alternatives or decision factors and prioritize them. The method like AHP [23, 24] is invented to determine the importance of each decision factor and rank each alternative at the same time. Essential rule of AHP is that it acts based on decision experts judgment and pairwise comparison. AHP methodology follows the steps below to find relative importance degree of criteria:

Step 1: Prepare the pair wise comparison matrix A by utilizing the ratio scale in Table 1.
Step 2: Let $C_1, C_2, \ldots, C_n$ as the set of elements, although a_{ij} presents a quantified judgment on pair of elements $C_{i.}, C_{j.}$ the matrix A as follows;

$$A = [a_{ij}] = \begin{bmatrix} 1 & a_{12} & \ldots & a_{1n} \\ \frac{1}{a_{12}} & 1 & \ldots & a_{2n} \\ \vdots & \vdots & \vdots & \vdots \\ \frac{1}{a_{1n}} & \frac{1}{a_{2n}} & \ldots & 1 \end{bmatrix} \tag{1}$$

Table 2 AHP random index (R.I.) values

N	2	3	4	5	6	7	8
R.I.	0.00	0.52	0.9	1.12	1.24	1.32	1.41

where $a_{ij} = 1$ and $a_{ji} = \frac{1}{a_{ij}}$, $i.j = 1, 2, \ldots, n$.

In matrix A, the problem is on determining a set of numerical weights $W_1, W_2, \ldots, W_n$ in front of n element $C_1, C_2, \ldots, C_n$. If A is a consistency matrix, then the relation between weights and judgments are given by $a_{ij} = \frac{W_j}{W_i}$, for $(i, j = 1, 2, 3, \ldots, n)$. The largest Eigenvalue $\lambda_{\max}$ would be suggested by Saaty [25] as

$$\lambda_{\max} = \sum_{j=1}^{n} a_{ij} \frac{W_j}{W_i} \tag{2}$$

If A is a consistency matrix, then Eigenvector X can be obtained by

$$(A - \lambda_{\max} I)X = 0 \tag{3}$$

So, the consistency index (C.I.) and random index (R.I.) verify the consistency ratio (C.R.). The consistency index and consistency rate are as follows:

$$\text{C.I.} = \frac{\lambda_{\max} - n}{n - 1} \tag{4}$$

and

$$\text{C.R.} = \frac{\text{C.I.}}{\text{R.I.}} \tag{5}$$

The number 0.1 is the accepted upper limit of C.R. If the final consistency ration is higher this value, the evaluation process should be done again to improve consistency (Table 2).

2.2 Combined Compromise Solution (CoCoSo)

The growing trend in developing tools to aid complex decision systems forces investigators in this area to rethink and invent novel methodologies. Recently, a group of authors designed an algorithm to solve MADM problems using a combined approach. The method originates from some famous and applied tools like WASPAS and GRA. To solve a CoCoSo decision problem, after determining the alternatives and the related criteria, the following steps validated:

Step 1—Determining initial decision-making matrix as shown below:

$$x_{ij} = \begin{bmatrix} x_{11} & x_{12} & \dots & x_{1n} \\ x_{21} & x_{22} & \dots & x_{2n} \\ \dots & \dots & \dots & \dots \\ x_{m1} & x_{m2} & \dots & x_{mn} \end{bmatrix}; \quad i = 1, 2, \dots, m; \quad j = 1, 2, \dots, n. \tag{6}$$

Step 2—Normalization of criteria values is accomplished based on compromise normalization equation (see Zeleny [26]).

$$r_{ij} = \frac{x_{ij} - \min_i x_{ij}}{\max_i x_{ij} - \min_i x_{ij}}; \quad \text{for benefit criterion;} \tag{7}$$

$$r_{ij} = \frac{\max_i x_{ij} - x_{ij}}{\max_i x_{ij} - \min_i x_{ij}}; \quad \text{for cost criterion} \tag{8}$$

Step 3—Obtain the total of the weighted comparability sequence and the total of the power weight of comparability sequences for each alternative. Then sum of the weighted comparability sequence and also sum of the power weight of comparability sequences for each alternative are directed as S_i and P_i, respectively:

$$S_i = \sum_{j=1}^{n} (w_j r_{ij}) \tag{9}$$

This S_i value is achieved based on gray relational generation approach.

$$P_i = \sum_{j=1}^{n} (r_{ij})^{w_j} \tag{10}$$

This P_i value is also extracted according to the WASPAS multiplicative attitude.

Step 4—Compute relative weights of the alternatives using following aggregation strategies In this step, three appraisal score strategies to generate relative weights of alternatives, which are derived by formulas (6), (7), and (8), proposed.

$$\text{(A)} \quad k_{ia} = \frac{P_i + S_i}{\sum_{i=1}^{m} (P_i + S_i)} \tag{11}$$

$$\text{(B)} \quad k_{ib} = \frac{S_i}{\min_i S_i} + \frac{P_i}{\min_i P_i} \tag{12}$$

$$\text{(C)} \quad k_{ic} = \frac{\lambda(S_i) + (1 - \lambda)(P_i)}{(\lambda \max_i S_i + (1 - \lambda) \max_i P_i)}; \quad 0 \le \lambda \le 1 \tag{13}$$

In Eq. (8), λ (usually $\lambda = 0.5$) is chosen by decision makers. However, the flexibility and stability of the proposed CoCoSo can rely on other values.

Step 5—Final ranking of the alternatives are determined based on k_i, values (as bigger as better):

Table 3 Pairwise comparison matrix for decision attributes

	C_1	C_2	C_3	C_4	C_5	C_6	C_7
C_1	1	0.1111	0.5	0.143	0.333	0.5	0.166
C_2	0.333	1	2	0.333	2	3	2
C_3	0.2	0.5	1	2	1	0.25	0.5
C_4	0.5	3	0.5	1	3	0.333	2
C_5	3	0.5	1	0.333	1	3	0.333
C_6	2	0.333	0.166	3	0.333	1	0.333
C_7	6.00	0.5	0.2	0.5	3	3	1

$$k_i = (k_{ia}k_{ib}k_{ic})^{\frac{1}{3}} + \frac{1}{3}(k_{ia} + k_{ib} + k_{ic}) \tag{14}$$

3 Empirical Case and Results

This section practically is designated to inform the analytical steps toward solution of decision problem. To head the decision process and evaluate decision matrix, it must be mentioned decision attributes are listed as (1) Finance position; (2) Flexibility; (3) after sales service; (4) Design compatibility; (5) Quality; (6) Cost for company (cost); (7) Personnel training. In this study, we have objected to help and consult in a dairy company to optimally prioritize packaging companies under the above-mentioned factors. The available alternatives for our project can be counted: (1) Bemis company; (2) Tetrapack; (3) Liquibox; (4) ULMA packaging co.; (5) STANPAC co.; (6) AMCOR; (7) Smurfitkappa; (8) Dairypack.

First, with AHP method, we must perform pairwise comparison among decision-making attributes. The experts are asked to represent their evaluation and judgment using a 1–9 predefined scale, which is indicated in Table 3.

Then based on AHP algorithm, normalization is validated and the objective weights are calculated. Then, by the computation, we reach $\lambda_{\max} = 7.677$

$$\text{C.I.} = \frac{\lambda\text{max} - n}{n - 1} = \frac{7.677 - 7}{7 - 1} = 0.112839$$

For $n = 7$, R.I. = 1.32, Then

$$\text{C.R.} = \frac{\text{C.I.}}{\text{R.I.}} = \frac{0.112839}{1.32} = 0.085484$$

It is seen that C.R. < 0.1, and therefore the AHP results are consistent and we can rely on them for further actions. The weights are seen in the last column of Table 4.

Table 4 Normalized matrix and weights based on AHP

	C_1	C_2	C_3	C_4	C_5	C_6	C_7	Weight
C_1	0.0767	0.0187	0.0932	0.0195	0.0313	0.0451	0.0263	0.0444
C_2	0.0256	0.1682	0.3727	0.0456	0.1875	0.2707	0.3158	0.1980
C_3	0.0153	0.0841	0.1863	0.2736	0.0938	0.0226	0.0789	0.1078
C_4	0.0384	0.5047	0.0932	0.1368	0.2813	0.0301	0.3158	0.2000
C_5	0.2302	0.0841	0.1863	0.0456	0.0938	0.2707	0.0526	0.1376
C_6	0.1535	0.0561	0.0311	0.4104	0.0313	0.0902	0.0526	0.1179
C_7	0.4604	0.0841	0.0373	0.0684	0.2813	0.2707	0.1579	0.1943

Table 5 Performance matrix for packaging technology selection

Initial matrix	C_1	C_2	C_3	C_4	C_5	C_6	C_7
A_1	4	4	1	2	7	3	3
A_2	5	4	2	1	3	5	4
A_3	6	5	4	5	2	5	3
A_4	3	3	3	3	2	5	3
A_5	2	3	5	3	7	6	2
A_6	5	8	6	4	5	7	2
A_7	7	5	7	4	5	5	1
A_8	8	3	5	6	3	2	6

Next step is to drive process of formulating CoCoSo method to solve decision problem and obtain the overall ranking of alternative technologies. The initial step in the proposed algorithm is to form performance matrix of alternatives and criteria. To deal with that, we designed a 1–10 scale to rate alternatives regarding to each decision attribute. For example, if the financial position of alternative (packaging machinery company) 1 is very good, one can measure it as 7 or 8 and normally an average financial position for another alternative brings a value of 5. By this introduction, Table 5 presents the relative evaluation of alternatives under each factor. The normalized decision matrix is achieved using Eqs. (7) and (8). Table 6 is assigned to the normalized matrix.

In this stage, sum of the weighted comparability sequence and also sum of the power weight of comparability sequences for each alternative are computed as shown in Tables 7 and 8 in order (Table 9).

In final step of alternatives selection process, the algorithm allows us to test stability of the proposed method by three ranking strategy as formulas (11), (12), and (13) determine. Also λ value is considered 0.5 normally. The best alternative is A_8 (Dairy pack) in this example. All three ranking values remain similar to the final ranking which proves the stability and appropriate performance of the proposed CoCoSo method. Here, is the ranking order of decision alternatives:

Table 6 The normalized decision table

Normalized matrix	C_1	C_2	C_3	C_4	C_5	C_6	C_7
A_1	0.1	0.1143	0.0303	0.0714	0.2059	0.0789	0.125
A_2	0.125	0.1143	0.0606	0.0357	0.0882	0.1316	0.1667
A_3	0.15	0.1429	0.1212	0.1786	0.0588	0.1316	0.125
A_4	0.075	0.0857	0.0909	0.1071	0.0588	0.1316	0.125
A_5	0.05	0.0857	0.1515	0.1071	0.2059	0.1579	0.0833
A_6	0.125	0.2286	0.1818	0.1429	0.1471	0.1842	0.0833
A_7	0.175	0.1429	0.2121	0.1429	0.1471	0.1316	0.0417
A_8	0.2	0.0857	0.1515	0.2143	0.0882	0.0526	0.25

Table 7 Weighted comparability sequence

	C_1	C_2	C_3	C_4	C_5	C_6	C_7	S_i
A_1	0.0148	0.0396	0	0.04	0.1376	0.0943	0.0777	0.404
A_2	0.0222	0.0396	0.018	0	0.0275	0.0471	0.1166	0.271
A_3	0.0296	0.0792	0.054	0.16	0	0.0471	0.0777	0.4476
A_4	0.0074	0	0.036	0.08	0	0.0471	0.0777	0.2482
A_5	0	0	0.072	0.08	0.1376	0.0236	0.039	0.352
A_6	0.0222	0.198	0.089	0.12	0.0826	0	0.039	0.5515
A_7	0.037	0.0792	0.1078	0.12	0.0826	0.0471	0	0.4737
A_8	0.0444	0	0.072	0.2	0.0275	0.1179	0.1943	0.656

Table 8 Power weight of comparability sequences for alternatives

	C_1	C_2	C_3	C_4	C_5	C_6	C_7	P_i
A_1	0.9524	0.7271	0	0.7248	1	0.974	0.8369	5.2152
A_2	0.9697	0.7271	0.8243	0	0.8013	0.8976	0.9055	5.1256
A_3	0.9822	0.8341	0.928	0.9563	0	0.8976	0.8369	5.4351
A_4	0.9235	0	0.8883	0.8325	0	0.8976	0.8369	4.3789
A_5	0	0	0.9572	0.8325	1	0.8272	0.7315	4.3484
A_6	0.9697	1	0.9805	0.9029	0.9321	0	0.7315	5.5167
A_7	0.9919	0.8341	1	0.9029	0.9321	0.8976	0	5.5586
A_8	1	0	0.9572	1	0.8013	1	1	5.7586

Table 9 Final evaluation matrix and selection of best option

Alternatives	K_a	Ranking	K_b	Ranking	K_c	Ranking	K	Ranking
A_1	0.126	5	2.827	5	0.876	5	1.954	5
A_2	0.121	6	2.271	7	0.841	6	1.691	6
A_3	0.131	4	3.053	4	0.917	4	2.084	4
A_4	0.103	8	2.007	8	0.721	8	1.475	8
A_5	0.105	7	2.418	6	0.733	7	1.656	7
A_6	0.136	2	3.491	2	0.946	2	2.289	2
A_7	0.135	3	3.187	3	0.94	3	2.16	3
A_8	0.143	1	3.967	1	1	1	2.532	1

$$A_8 > A_6 > A_7 > A_3 > A_1 > A_2 > A_5 > A_4$$

Experts normally perform several strategies to test the performance of their proposed algorithm. One of those strategies is the utilization of sensitivity analysis. This approach clarifies affection of weight replacement to see ranking altering. Most of the decision-making problems can be confirmed by delivering such tests. In this study, we run a sensitivity analysis for the priority ranking of decision alternatives which is done using seven completely different and random tests. Table 10 shows the related tests and each corresponding ranking. In order to set the weight replacement, we did not follow any model or arrangement, since they have been produced randomly. The obtained output of the sensitivity tests obviously explains that A_8 remains as the best alternative and except than one test (test 1), the second best alternative also will remain similar as the original ranking. The same as the best option and based on Table 10, we confirm that the worst alternatives like A_4. Figure 1 schematically pictures the sensitivity analysis for better realization. To notice, A_4 and A_8 have the most stable ranking score. With a bit deviation, the stable ranking score of A_2 and A_5 can be claimed as well.

Table 10 Sensitivity analysis tests and priority of alternatives

	W_1	W_2	W_3	W_4	W_5	W_6	W_7	Ranking priority (k)
Test 1	0.044	0.198	0.194	0.118	0.138	0.108	0.2	$A_8 > A_6 > A_7 > A_3 > A_1 > A_5 > A_2 > A_4$
Test 2	0.194	0.108	0.044	0.138	0.2	0.118	0.198	$A_8 > A_7 > A_6 > A_1 > A_3 > A_2 > A_5 > A_4$
Test 3	0.2	0.108	0.138	0.118	0.198	0.044	0.194	$A_8 > A_7 > A_6 > A_3 > A_1 > A_2 > A_5 > A_4$
Test 4	0.2	0.138	0.044	0.118	0.198	0.194	0.108	$A_8 > A_7 > A_6 > A_1 > A_3 > A_2 > A_5 > A_4$
Test 5	0.198	0.2	0.194	0.044	0.108	0.138	0.118	$A_8 > A_7 > A_6 > A_1 > A_3 > A_2 > A_5 > A_5$
Test 6	0.194	0.044	0.138	0.108	0.2	0.198	0.118	$A_8 > A_7 > A_1 > A_6 > A_3 > A_2 > A_5 > A_4$
Test 7	0.138	0.194	0.044	0.198	0.118	0.2	0.108	$A_8 > A_7 > A_6 > A_1 > A_3 > A_2 > A_5 > A_5$

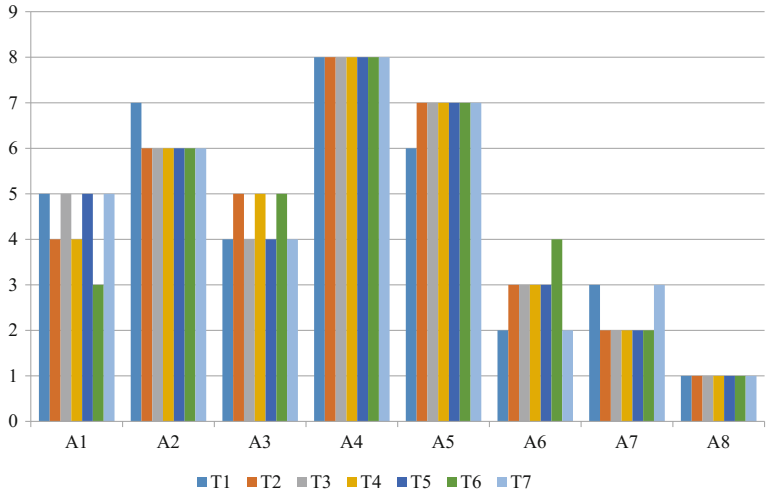

Fig. 1 Tests for sensitivity analysis results

4 Conclusion

Technology selection is a major milestone in transition toward the design, manufacturing and management. Among the studies in the literature, it was quite difficult to find research that considers relationship between various factors by implementing a real case study. We effectively defined a novel multiattribute decision-making structure to literally advice the optimal candidate for our case problem and offer a clear comprehension of the subject. In this paper, the application of analytical hierarchy process and combined compromise solution methods is demonstrated to a dairy company for selection of packaging technology. By the following criteria as financial position, flexibility, after sales service, design compatibility, quality, cost for company, and personnel training we have configured a hierarchical model and then computed the importance of each criteria using experts pairwise comparison. The AHP weights computation process was consistent enough and it has been validated. Thereafter, experts were asked to rate the performance of each candidate technology using a scale defined by the company. The CoCoSo method has been formulated and ranking of alternatives has been generated. This method can compete with the MADM methods and in future research projects the method can be used with high confidence. The best packaging technology must be purchased from A_8 (Dairy pack). It is the role of managers to negotiate for a reasonable price. The sensitivity analysis tests have been accomplished and the results guarantees that the optimal options are settled in a stable manner.

This study not only gets advantage of an integrated MADM structure to adopt a technology evaluation and selection problem in a manufacturing site, its generated outcomes have been tested and approved by series of sensitivity analysis. It is a very

important point to know that this model will be further applied in other applications but with justification and remodeling the variables and according to the case under study. It is highly appreciated and authors are invited to extend interval, fuzzy, and probabilistic model of CoCoSo and AHP.

References

1. Cetindamar D, Phaal R, Probert D (2016) Technology management: activities and tools. Palgrave Macmillan
2. Aliakbari Nouri F, Khalili Esbouei S, Antucheviciene J (2015) A hybrid MCDM approach based on fuzzy ANP and fuzzy TOPSIS for technology selection. Informatica 26(3):369–388
3. Farooq S, O'Brien C (2015) An action research methodology for manufacturing technology selection: a supply chain perspective. Prod Plann Control 26(6):467–488
4. Yazdani M, Zarate P, Coulibaly A, Zavadskas EK (2017) A group decision making support system in logistics and supply chain management. Expert Syst Appl 88:376–392
5. Brandenburg M, Govindan K, Sarkis J, Seuring S (2014) Quantitative models for sustainable supply chain management: developments and directions. Eur J Oper Res 233(2):299–312
6. Fahimnia B, Sarkis J, Davarzani H (2015) Green supply chain management: a review and bibliometric analysis. Int J Prod Econ 162:101–114
7. Tavana M, Yazdani M, Di Caprio D (2017) An application of an integrated ANP–QFD framework for sustainable supplier selection. Int J Logist Res Appl 20(3):254–275
8. Pålsson H, Finnsgård C, Wänström C (2013) Selection of packaging systems in supply chains from a sustainability perspective: the case of Volvo. Packag Technol Sci 26(5):289–310
9. Mohanty RP, Deshmukh SG (1998) Advanced manufacturing technology selection: a strategic model for learning and evaluation. Int J Prod Econ 55(3):295–307
10. Kengpol A, O'Brien C (2001) The development of a decision support tool for the selection of advanced technology to achieve rapid product development. Int J Prod Econ 69(2):177–191
11. Dağdeviren M (2008) Decision making in equipment selection: an integrated approach with AHP and PROMETHEE. J Intell Manuf 19(4):397–406
12. Anand G, Kodali R (2008) Selection of lean manufacturing systems using the PROMETHEE. J Model Manage 3(1):40–70
13. Tavana M, Khalili-Damghani K, Abtahi AR (2013) A hybrid fuzzy group decision support framework for advanced-technology prioritization at NASA. Expert Syst Appl 40(2):480–491
14. Streimikiene D, Balezentis T, Krisciukaitienė I, Balezentis A (2012) Prioritizing sustainable electricity production technologies: MCDM approach. Renew Sustain Energy Rev 16(5):3302–3311
15. Chuu S-J (2014) An investment evaluation of supply chain RFID technologies: a group decision-making model with multiple information sources. Knowl-Based Syst 66:210–220
16. Liu HC, You JX, Lu C, Shan MM (2014) Application of interval 2-tuple linguistic MULTIMOORA method for health-care waste treatment technology evaluation and selection. Waste Manag 34(11):2355–2364
17. Evans L, Lohse N, Summers M (2013) A fuzzy-decision-tree approach for manufacturing technology selection exploiting experience-based information. Expert Syst Appl 40(16):6412–6426
18. Farooq S, O'Brien C (2012) A technology selection framework for integrating manufacturing within a supply chain. Int J Prod Res 50(11):2987–3010
19. Saen RF (2009) Technology selection in the presence of imprecise data, weight restrictions, and nondiscretionary factors. Int J Adv Manuf Technol 41(7–8):827
20. Almannai B, Greenough R, Kay J (2008) A decision support tool based on QFD and FMEA for the selection of manufacturing automation technologies. Robot Comput Integr Manuf 24(4):501–507

21. Chuu SJ (2009) Selecting the advanced manufacturing technology using fuzzy multiple attributes group decision making with multiple fuzzy information. Comput Ind Eng 57(3):1033–1042
22. Aloini D, Dulmin R, Mininno V (2014) A peer IF-TOPSIS based decision support system for packaging machine selection. Expert Syst Appl 41(5):2157–2165
23. Mathiyazhagan K, Diabat A, Al-Refaie A, Xu L (2015) Application of analytical hierarchy process to evaluate pressures to implement green supply chain management. J Clean Prod 107:229–236
24. Govindan K, Kaliyan M, Kannan D, Haq AN (2014) Barriers analysis for green supply chain management implementation in Indian industries using analytic hierarchy process. Int J Prod Econ 147:555–568
25. Saaty TL (1977) A scaling method for priorities in hierarchical structures. J Math Psychol 15(3):234–281
26. Zeleny M (1973) Compromise programming. In: Cochrane JL, Zeleny M (eds) Multiple criteria decision making. University of South Carolina Press, Columbia, SC, pp 262–301

Application of MCDM Techniques on Nonconventional Machining of Composites

Sarabjeet Singh Sidhu, Preetkanwal Singh Bains, Morteza Yazdani and Sarfaraz Hashemkhani Zolfaniab

Abstract This study has been carried out to assess the impact of electrical discharge machining parameters on the SiC-reinforced aluminum metal matrix composites. The criteria in machining process including electrodes material, current, pulse time, and dielectric medium were diversified to evaluate their effect on material removal rate (MRR), surface roughness (SR), and residual stresses. The residual stresses induced due to subsequent heating and cooling shocks during the electric discharge process are of primary concern while machining process. The magnitude of residual stresses induced on the machined surface was estimated via X-ray diffraction method. The process conditions that influenced the responses were recognized and optimized synchronically using multiple criteria decision-making and statistical techniques. In this study, analytical hierarchy process (AHP) and a multi-objective optimization analysis (MOORA) will solve process condition problem. This approach confers the combination of process parameter settings suitable for the machining of such composites.

Keywords Residual stresses · Metal removal rate · Surface roughness
Analytical hierarchy process
Multi-objective optimization based on ratio analysis (MOORA)

S. S. Sidhu (✉) · P. S. Bains
Department of Mechanical Engineering, Beant College of Engineering & Technology, Gurdaspur 143521, Punjab, India
e-mail: sarabjeetsidhu@yahoo.com

P. S. Bains
e-mail: preetbains84@gmail.com

M. Yazdani
Department of Business Management,
Universidad Loyola Andalucia,, Seville, Spain
e-mail: morteza_yazdani21@yahoo.com

S. H. Zolfaniab
Department of Management, Science and Technology, Amirkabir University of Technology, Tehran, Iran
e-mail: sa.hashemkhani@gmail.com

S. S. Sidhu et al. (eds.), *Futuristic Composites*, Materials Horizons: From Nature to Nanomaterials, https://doi.org/10.1007/978-981-13-2417-8_6

1 Introduction

Today, advanced technology needs a material having excellent specific properties and capable of replacing high-cost alloy materials. Such properties are found in a composite material reinforced with whiskers/particles and are explored comprehensively for their applications in different fields of engineering. Such materials are achieved by prudent selection of two or more specific materials, and when they combined, it brings on a synergetic enhancement in properties. Metal matrix composites (MMCs) are categories as the composite materials made up of metal or alloy, which uniformly distribute the external load and form a percolating network to separate the reinforced fibers or particles [1]. These properties of MMCs make them suitable for the wide range of applications in automobile industries such as braking system, piston rods, piston pins, brake disc, etc. [2, 3]. Some problems such as high machining cost and degradation of surface material properties may arise due to the existence of hard ceramic pieces in MMCs; however, geometrical complexity and the reinforcement's distribution within composite matrix restrain the effectiveness of such machining processes. These constraints can be tackled by adopting such methods, which are capable of achieving the desired workpiece geometry along with minimum damage to the material properties [4, 5]. A method like this used for machining of MMCs is electrical discharge machining (EDM) process. EDM provides a potential manufacturing technique to machine composite materials with an intrinsic geometry besides better productivity, surface finish, and dimensional accuracy. In this technique, a tool electrode machines the material by the series of sparks plasma formed in a dielectric medium and generates a replica of the tool contour. The wide acceptance of this process is due to its capability to machine intricate shapes in hard-to-cut materials with negligible surface damage owing to the absence of physical contact between the tools and work material. However, some defects including cracks, spalling, porosity, residual stresses, and metallurgical transformation may occur on the machined surface and subsurface as a result of subsequent melting and cooling in EDM process [6–8].

Several studies have reported the EDM process aspects of particulate reinforced MMCs. Hocheng et al. [9] analyzed the material eroding rate of SiC/Al and correlation was developed between the spark energy and craters formation on the machined surface. One of the most recognized nonconventional machining techniques has been EDM that is an efficient technique in framing machine materials' difficulties [10]. Several optimization techniques were employed by various researchers to predict the effects of input process parameters on the MMCs [11, 12].

The role of multicriteria decision-making (MCDM) can be recognized in the optimization of EDM process. Gray relational analysis (GRA) was used to enhance process parameters of EDM while machining Al-10%SiC composites in research done by Singh et al. [13]. Kuriakose and Shunmugam [14] presented the multi-regression method to correlate input and output parameters of wire EDM process; further, these parameters were optimized adopting non-dominated sorting genetic algorithm method. Tzeng and Chen [15] coupled fuzzy-based model with Taguchi

method to study the multi-response characteristic of high-speed EDM process. Sidhu et al. [16] applied lexicographic goal programming approach to optimize the EDM parameters, while copper was utilized as a tool electrode in machining MMC. The effects of EDM process parameters on MRR, TWR, and surface integrity have been intensively reported in the literature. However, the residual stresses induced during EDM process are one of the important factors that may affect the service life of machined components. To analyze these residual stresses, a widely accepted X-ray diffraction technique method is explained in detail in the reference [17]. A review of the literature reports several studies that optimize the MRR, TWR, and surface roughness but very limited studies that globally optimize the response parameters including residual stresses MRR and SR for MMCs. Therefore, objectives of the study can be listed here:

- Influence of the parameters of machining process on the 65 vol% SiC/A356.2 (Sample I, solicited from Ceramic Process System, USA) and 10 vol% SiC-5 vol% quartz/Al composites (Sample II; Prepared by stir casting route [18]).
- Three response parameters such as MRR, SR, and residual stresses are evaluated using L_{18} Taguchi's experimental design.
- The response parameters are globally optimized using analytical hierarchy process (AHP) and multi-objective optimization based on ration analysis (MOORA) methods. This issue accounts as part of the contribution of this research due to the application of AHP-MOORA with real-world optimization problem.

Application of MCDM tools in the production and manufacturing area is tremendous. AHP is a method, which mostly is applied to weight decision factors and MOORA is a multi-objective method to select the best option. MOORA becomes popular in different research zones. Kalibatas and Turskis [19] to keep the quality of constructions for customers reported a framework for the evaluation of inner climate of new buildings. To help industrial engineering students in their future work career, fuzzy AHP and MOORA have been recommended to deliver optimal solutions [20]. Chakraborty [21] indicated the usage of AHP-MOORA different manufacturing decision problems as robot selection, machine tool, and prototype selections. Fuzzy AHP rather than AHP in uncertain environments is a key. In another study, fuzzy AHP and MOORA methods have been utilized to evaluate Indian technical educations [22].

2 Methodology

This part of the article introduces two MCDM methods as AHP and MOORA that are implemented in this work for EDM process evaluation (Fig. 1).

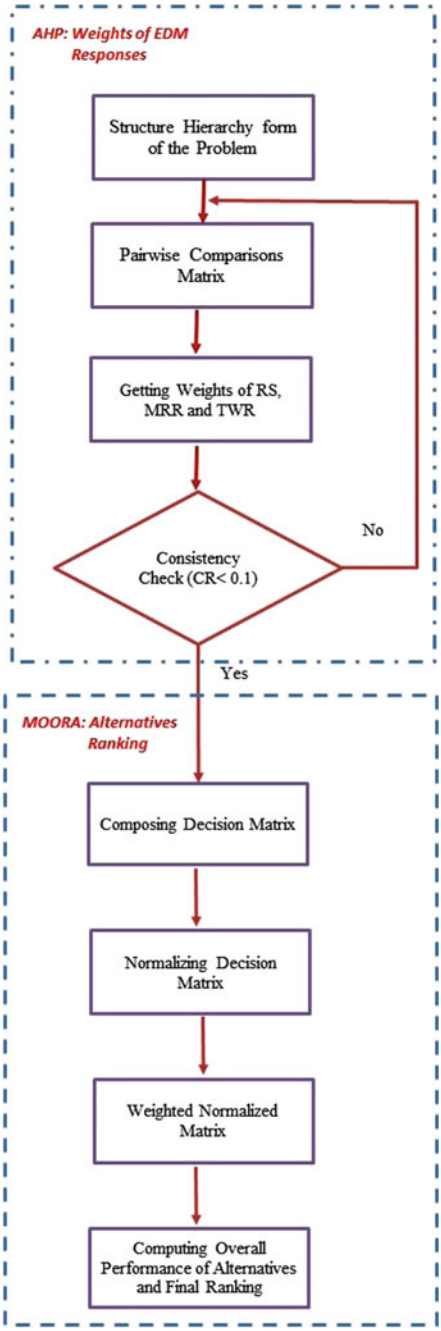

Fig. 1 Flowchart of AHP and MOORA methodology

Table 1 The ratio scale and definition of AHP [24]

Intensity of importance	Definition
1	Equally important
3	Moderately important
5	Strongly more important
7	Very strong important
9	Extremely more important
2, 4, 6, 8	Intermediately important

2.1 AHP

AHP addresses a quantitative structure of multistage, multicriteria, and multi-person hierarchical problem invented and developed by Saaty [23, 24]. The weights of criteria are obtained by following the below-mentioned steps in AHP methodology [25, 26]:

To obtain the weights of each factor, a goal and main problem must be defined. A hierarchy structure of all the variables and sub-variables based on complexity and level of decision-making is decided from the top to middle followed by the lowest priority. Then, experts should construct $(n \times n)$ pair-wise judgments tables regarding each level using defined scales in Table 1. Reciprocal automatically is produced based on previous judgments. Now, hierarchical synthesis is performed to weight the eigenvectors and the sum is taken over all weighted eigenvector entries relating to those in the lower level of the hierarchy. Ultimately, to assure the consistency of the process, a logical test must be done. The aforementioned tasks have to be repeated for all the levels.

2.2 MOORA

Multi-objective optimization is the process of considering several criteria (objectives) simultaneously considering predetermined constraints. MOORA [27, 28] allows experts to measure both beneficial and non-beneficial criteria in a process of selecting from a set of alternatives [29, 30]. This method has been implemented in optimization-based studies that are mainly connected to construction management, manufacturing decision-making, and material selection domain [30 32 33]. To solve a typical decision problem using MOORA [19] first, a decision matrix containing alternative information regarding each technical criterion is composed. Further to develop a comparable matrix with similar dimension for all the variables, a normalization process is implemented. As mentioned earlier, the weights of the criteria are achieved using AHP. Therefore, the weighted normalized matrix (WNM) is built by

multiplication of normalized matrix and criteria weights. Summations of WNM for benefit and non-benefit criteria are generated which are called overall rating (S_k^+) and (S_k^-), orderly. At the end, subtracting the overall ratings of (S_k^+) and (S_k^-) introduces prioritization of alternatives.

3 Experimental Details

3.1 Material Used in Experiments

The experiments were conducted on the Electrical Discharge Machine (model: *SD550 ZNC* of *OSCARMAX*) available in the Machine Tool Lab of the Institute. The workpieces with conventional polarity were machined using commercial grade EDM oil as a dielectric fluid, as well as two other combinations of a dielectric. In the first combination, the EDM oil was mixed with copper powder and in the second combination, the EDM oil was mixed with graphite powder particles. Three electrode materials, namely, (i) copper, (ii) graphite (Particle size 5.0 μm), and (iii) copper–graphite composite (50% Cu, Grade 673, resistivity 2.03 μΩ m) were used for the experimental study.

Three responses were measured after each experiment. The MRR was evaluated using a Chyo (MJ-300) weighing machine with an accuracy of 0.001 g. The surface roughness was measured with the help of Mitutoyo (SJ-400) surface roughness analyzer. The residual stresses induced while machining were measured by X-ray diffraction method on PANalytical's X'PertPro diffractometer using Cu-Kα1 characteristic X-rays. The diffractometer used in this study was a horizontal, fixed, laboratory-based system, and the maximum 2θ angle accessible was limited to 145°.

3.2 Experimentation

Based on preliminary pilot study, the process parameters that were varied during the experimental study were identified as workpiece material, dielectric medium, tool electrode material, pulse-on time, pulse-off time, and current. All these were listed as control factors and were varied during the study to measure MRR, SR, and residual stresses during various combinations of these factors. The parameters such as open circuit voltage (~135 V) and flushing pressure (0.6 kg/cm^2) were kept constant throughout the experimental study. The levels for these factors were chosen on the basis of the pilot study and the settings available on the machine. Table 2 represents the control factors and their levels for experimentation.

Since the factors chosen for study were a combination of two and three levels, a mixed experimental design (L_{18}) developed by Taguchi was used for this study [34]. The Taguchi's parametric design methodology drastically reduces the number

Table 2 Factors and their levels

Factors (symbol)	Levels		
	Level-1	Level-2	Level-3
Work piece (w)	65 vol% SiC/A356.2 (Sample I)	10 vol.% SiC-5vol% quartz/Al (Sample II)	–
Electrode (e)	Cu	Gr	Cu–Gr
Current (I) A	4	8	12
Pulse-on (t_{on}) µs	10	30	50
Pulse-off (t_{off}) µs	15	30	45
Dielectric (d)	EDM oil (D)	EDM oil (D) + Cu Powder	EDM oil (D) + Gr powder

of trials required to gather the necessary data without compromising with the quality of output data using orthogonal designed matrices. L_{18} denote 18 different trial conditions, which were conducted randomly to eliminate any undesirable bias in the study. The L_{18} is designed in a way that it accommodates the two-level factor in column 1 and the remaining three-level factors are assigned to other columns. The trial conditions after the assignment of factors to an L_{18} array are listed in Table 3. From the design matrix, the first column represents the types of workpiece materials used in the study. Thus, the first nine trials represent 65 vol% SiC/A356.2 MMC hereafter represented as Sample I and the remaining nine trials (trial 10–18) represent results for 10 vol% SiC-5 vol.% quartz in aluminum, hereafter referred to as Sample II. The assignment of other factors to remaining columns is listed in Table 3.

The 18 experimental trials with two repetitions were completed as per the Taguchi's design in a random order. The mean MRR, SR, and residual stress were measured at the end of each trial and are given in the second half of Table 2 under output responses. The MRR was evaluated by the weight difference of workpiece prior and after machining as given by Eq. (1):

$$\text{MRR} = \frac{(w_i - w_f)1000}{T} \text{ mg/min} \tag{1}$$

where w_i = weight of workpiece before machining (mg) and w_f = weight after machining (mg) (measured after cleaning the retained dielectric) and T = machining time (min). The SR was measured in terms of an arithmetic mean of absolute values R_a (µm). Each sample was examined at three different locations on the machined surface and was averaged for further analysis.

The residual stresses were evaluated with the help of X-ray diffraction classical procedure. The maximum observed peak diffracted from (422) plane was selected to measure the shift. In the sample, the change d-spacing between the crystallographic plane was clearly analyzed at the highest 2θ angle peak. The relation between d-spacing (Δd) with diffraction peak ($\Delta\theta$) is given by Eq. (2):

Table 3 Experimental layout ($L18$)

Trial No. $T(n)$ n: 1–18	Control factors						Output responses		
	(w)	(e)	(t_{off})	(t_{on})	(d)	(I)	Residual stress (MPa)	MRR (mg/min)	SR (μm)
1	Sample I	1	15	10	1	4	63.3	2.64	2.94
2	Sample I	1	30	30	2	8	74.6	14.275	2.05
3	Sample I	1	45	45	3	12	82.8	23.17	5.67
4	Sample I	2	15	45	2	8	36.3	23.38	2.09
5	Sample I	2	30	10	3	12	63.6	18.97	4.12
6	Sample I	2	45	30	1	4	110.3	3.04	3.00
7	Sample I	3	15	30	1	12	61.4	22.240	5.01
8	Sample I	3	30	45	2	4	78.5	9.860	2.06
9	Sample I	3	45	10	3	8	129	9.460	5.06
10	Sample II	1	15	30	3	8	70.4	20.90	6.69
11	Sample II	1	30	45	1	12	104	60.67	10.46
12	Sample II	1	45	10	2	4	78.1	10.860	4.69
13	Sample II	2	15	45	3	4	41.8	57.99	6.46
14	Sample II	2	30	10	1	8	149.3	18.86	8.44
15	Sample II	2	45	30	2	12	132.9	29.96	4.44
16	Sample II	3	15	10	2	12	77.7	65.5	6.76
17	Sample II	3	30	30	3	4	89.2	10.07	6.12
18	Sample II	3	45	45	1	8	231.5	45.72	7.95

$$\frac{\Delta d}{\Delta \theta} = (-)(\Delta\theta)\cot\theta \tag{2}$$

The X-ray data was obtained from built in software. The stresses were calculated by using $\sin^2\psi$ technique [35, 36], assuming unidirectional stress state. Equation (3) was used to calculate normal the residual stresses:

$$a^{+} = \frac{1}{2}\left(\in_{\varphi\psi+} + \in_{\varphi\psi-}\right) = \frac{1}{2}S_2 \sin^2\psi(\sigma_\varphi) + \in^{0}_{\varphi 0} \tag{3}$$

where parameters, a^{+} is the average of the lattice strain for positive ($\in_{\varphi\psi+}$) and negative ($\in_{\varphi\psi-}$) value tilt ψ (psi) for the given sample alignment {1/2 S_2 = (1 + ν)/E, 1/2 S_2}, are the X-ray elastic constants (XECs). The XEC's values, i.e., (1/2 S_2) for Samples I and II, are 6.98 T^{-1} Pa and 16.84 T^{-1} Pa, respectively. Equation (4) may be utilized to estimate the shear residual stress for further studied:

$$a^{-} = \frac{1}{2}\left(\in_{\varphi\psi+} - \in_{\varphi\psi-}\right) = \frac{1}{2}S_2 \sin(2\psi)(\tau_\varphi) \tag{4}$$

The sample calibration for the normal residual stress is represented below.

Calibration of residual stress for trial 2 (Sample I):

The machined sample was cut to a size of 25 × 25 mm using wire-cut EDM machine. To prevent alteration of machined surface by the heating of sample preparation process, it was ensured that the cutting edge is far away from the calibration area. The removal of re-solidified metal from surface was done by light etching process results in reduced measurement errors.

Residual stress analysis was performed in the aluminum matrix phase of the machined surface. The analysis was conducted on the isolated diffraction peaks detected at the highest value of 2θ. Figure 2 shows the X-ray spectra for trial 2. From the obtained spectra, the peak selected for residual stress measurement was at approx. 137.23°.

Table 4 represents the various parameters for trial 2 to measure residual stress at varying ψ-tilts (positive and negative). For exploring the surface residual stress, the regression equation generated from the plot of a^{+} versus $\sin^2\psi$ (Fig. 3) was compared with Eq. (3) [17] as it is illustrated below:

$$5.21E - 04 = \frac{1}{2}S_2\left(\sigma_\varphi\right)$$

where $1/2S_2 = 6.98\ T^{-1}$ Pa

Thus, the resulted residual stress induced during trial 2 was 74.6 MPa.

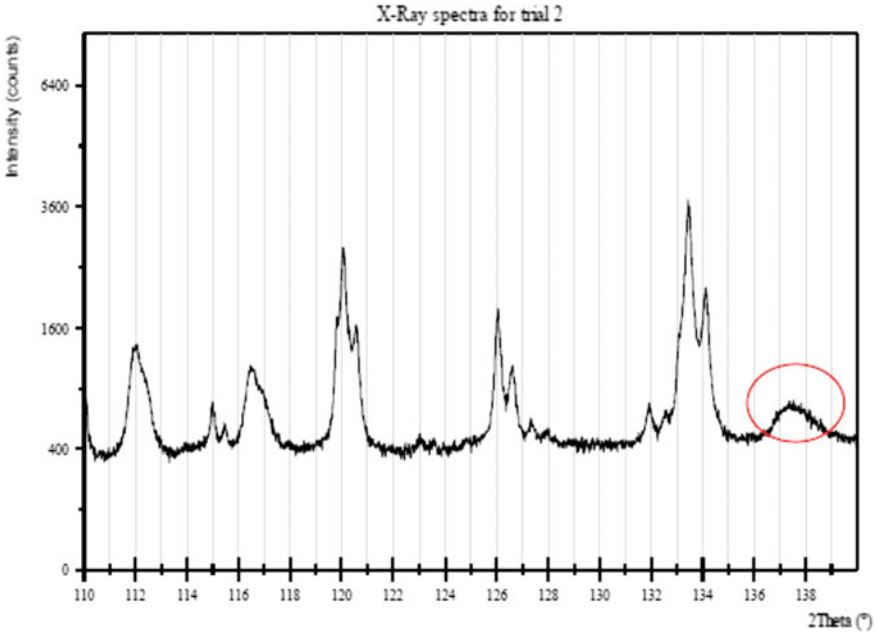

Fig. 2 X-ray spectra representing the selected peak for residual stress calibration (trial 2)

Table 4 Peak table and lattice strain for trial 2

Ψ	$\mathrm{Sin}^2\psi$	$d_{\varphi\psi+}$	$d_{\varphi\psi-}$	$\epsilon_{\psi\varphi-}$	$\epsilon_{\psi\varphi+}$	$a+$
12.92	0.05	0.827286	0.827336	0.0000205	0.00008099	0.0000508
18.44	0.1	0.827311	0.827199	0.0000506	−0.00008462	−0.000017
22.79	0.15	0.827472	0.827392	0.000245	0.00014868	0.000197
26.57	0.2	0.827425	0.827523	0.000189	0.00030703	0.000248
30.00	0.25	0.82745	0.827392	0.000219	0.00014868	0.000184
33.21	0.3	0.827499	0.827188	0.000278	−0.00009791	0.0000901
36.27	0.35	0.827564	0.827321	0.000357	0.00006286	0.00021
39.23	0.4	0.827434	0.827287	0.0002	0.00002176	0.000111
42.13	0.45	0.827673	0.827351	0.000488	0.00009912	0.000294
45	0.5	0.827543	0.827588	0.000331	0.00038561	0.000358

4 Results

4.1 ANOVA for MRR, SR, and Residual Stress

The experimental results obtained for MRR, SR, and residual stresses were examined using analysis of variance (ANOVA) and presented in Table 5. Comparing the data

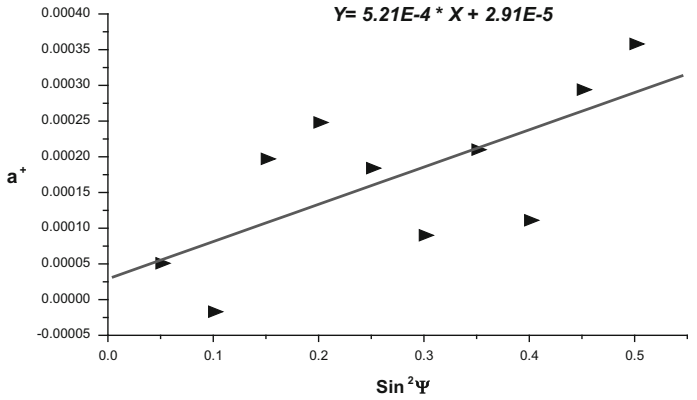

Fig. 3 Represents a^+ versus $\sin^2\psi$ plot for trail 2

F-values with the F critical at a confidence level of 95%, the significant factors were identified. The higher the F-value, the more is the effect of the parameter on the response.

4.1.1 MRR

Based on ANOVA, current and pulse-on time were recognized as significant factors affecting MRR response. Also, the change in workpiece reinforcement architecture resulted in the significant effect on MRR. The densely packed SiC particulate induced the shielding effect against the spark energy, and hence reduced material erosion. In relative comparison, dielectric, pulse-off time, and electrode material show the least effect on MRR. It was observed that the enhanced pulse-on time and current level increases the spark energy, thus resulting in higher melting or evaporation rate of the workpiece.

4.1.2 SR

Machining factors such as dielectric medium, current, and pulse-on time have shown significant effect on the surface roughness of the machined surface. In addition, the MMCs selected have shown significantly different SR profiles. The roughness enhanced with increase in current level, however, powder mixed dielectric medium improved the surface finish. On increasing, current or pulse-on time leads to the formation of bigger and deeper craters leading to rough machined surface. Addition of powder consistently improved the finish of the machined surface as suspended powder particles resulted in the uniform and widening of the plasma (spark) channel

Table 5 Analysis of variance for MRR, SR, residual stress

Factors	Dof	Sum of squares			Variance			*F*-value		
		MRR	SR	Residual stress	MRR	SR	Residual stress	MRR	SR	Residual stress
W/Pc	1	1977.26	50.0333	4204.4	1977.26	50.0333	4204.4	10.50*	80.99*	9.13*
Electrode	2	62.5	1.959	3284	31.25	0.9795	1641.98	0.17	1.59	3.57*
Pulse-off	2	435.5	0.9768	14262.5	217.75	0.4884	7131.27	1.16	0.79	15.49*
Pulse-on	2	1448.53	4.652	110.5	724.26	2.326	55.26	3.85*	3.77*	0.12
Dielectric	2	10.67	22.5037	6526.1	5.33	11.2519	3263.04	0.03	18.21*	7.09*
Current	2	1494.86	10.6571	4725.5	747.43	5.3286	2362.75	3.97*	8.63*	5.13*
Error	6	1129.73	3.7064	2762.6	188.29	0.6177	460.44			
Total	17	6559.04	94.4886	35875.7						

*Significant factor

between the electrodes. This reduces the magnitude of impact force resulting in small and shallow craters lowering the surface roughness.

4.1.3 Residual Stress

ANOVA for residual stress shows that pulse-off time, dielectric medium, and current significantly affected the residual stresses. It is observed that pulse-on time showed effects on MRR, SR but had least effect on residual stresses formation. However, pulse-off time contributed significantly to the development of residual stress. The presence of suspended particles in dielectric facilitates easy formation of plasma channel between electrode and the workpiece, and hence, resulted in lower SR and residual stress. The conductivity of suspended particle plays the major role in determining the SR but has no impact in the development of residual stresses. The main effect plots of the three responses are given in Fig. 4. Figure 4 shows the variation in the responses plotted on y-axis with change in parameter settings.

4.2 Implementation of AHP and MOORA in EDM Process

The AHP is a decision-aiding tool that involves defining the goal, quantifying the relative importance (priorities), and attributing the relevance between the criteria [37]. The advantage of this tool is that it combines both qualitative and quantitative parameters. AHP is designed to reflect the way in which decision-maker thinks and chooses the alternatives based on weighted values. It can effectively organize both tangible (objective) and intangible (subjective) factors in a systematic way and provides reliable results using simple calculations [38]. This decision-making tool was applied to solve various problems related to manufacturing, project management, and mining industries [39].

It was observed that extremely different results would have obtained if each single response optimized separately. For example, if MRR is optimized individually it would have resulted in the identification of some parameters of the process that increase MRR (as MRR is a higher the better function). These parameters may not have resulted in reduced SR as roughness was not considered during optimization. The vice versa would have been true if SR was optimized individually. Same thing applies for residual stresses. In order to get a more useful and global optimization result, it is important that all the responses are optimized together. AHP is simply structured and widely used to deal in multiple goal decision-making techniques under certainty, i.e., the data is deterministic [40].

In this step, AHP is applied to identify the weights of three criteria for EDM process. In experimental design layout, nine trials are conducted for each type of MMCs and the orthogonality was maintained by selecting L_{18} experimental design. In the present design given in Table 2, trials 1–9 are the available alternative for Sample I and trials 10–18 for Sample II. The MMCs used in the present study are

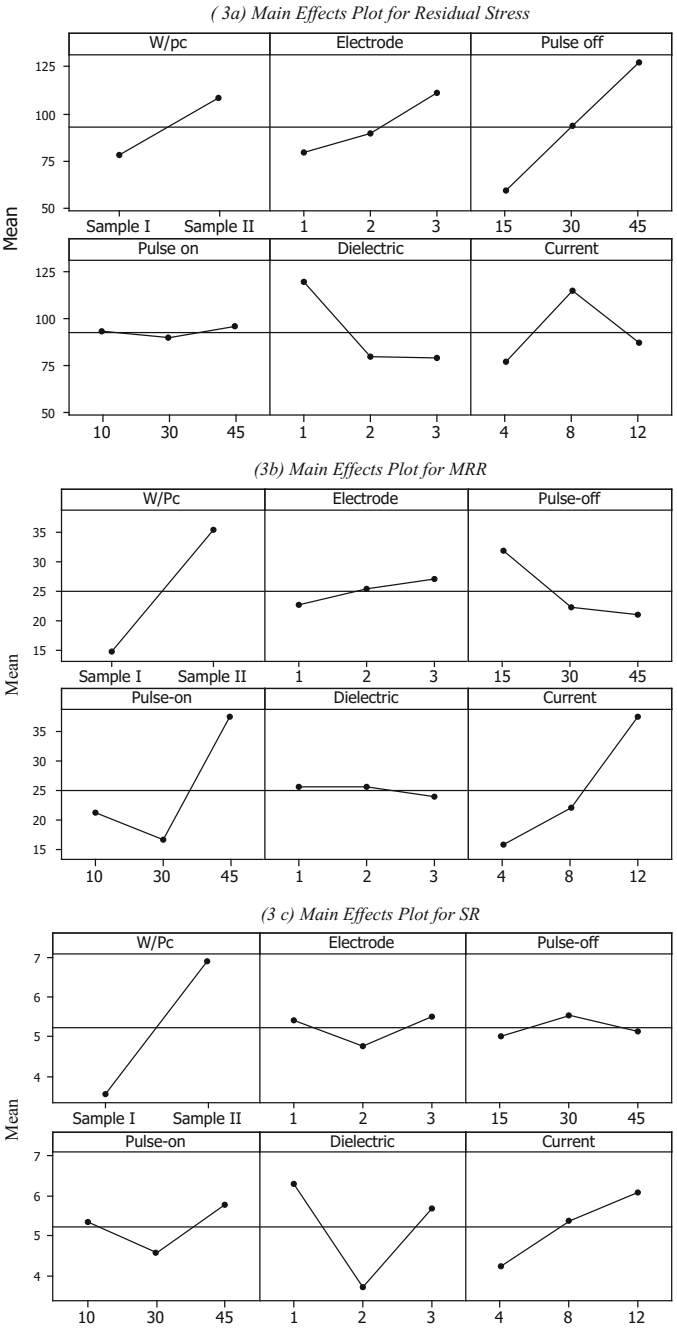

Fig. 4 Main effect plots of responses. **a** Residual stresses, **b** MRR, **c** SR

Table 6 Pairwise comparison of criteria to weight criteria

	Residual stress	MRR	SR	Priority vector
Residual stress	1	5	2	0.5954
MRR	1/5	1	1/2	0.1283
SR	1/2	2	1	0.2764

$\lambda_{max} = 3.0054$, CI = 0.0027

Table 7 Ranking of trials for Sample I based on MOORA method

Trials	Residual stress	MRR	SR	Benefit	Cost	MOORA ranking
	0.5954	0.1283	0.2764	S_k^+	S_k^-	
T_1	63.3	2.64	2.94	0.00699	0.22436	6
T_2	74.6	14.275	2.05	0.03782	0.23016	2
T_3	82.8	23.17	5.67	0.06138	0.33765	7
T_4	36.3	23.38	2.09	0.06193	0.13845	1
T_5	63.6	18.97	4.12	0.05025	0.25366	3
T_6	110.3	3.04	3	0.00805	0.33955	8
T_7	61.4	22.24	5.01	0.05891	0.26988	4
T_8	78.5	9.86	2.06	0.02612	0.23984	5
T_9	129	9.46	5.06	0.02506	0.43468	9

used for high-end applications in automobile, aerospace, and electronic industries. Hence, the residual stresses and surface roughness (SR) developed during the EDM process affect the service life of these materials products. Considering the severity of induced residual stress, it was assigned with maximum weight followed by surface roughness and material removal rate. Using assigned weights to residual stress, MRR, and SR, a (3×3) weight column matrix shown in Table 6 was established for pair-wise comparison. The comparison was based on the design requirement of the machined component. First, the residual stresses induced during the EDM is the main problem and it needs to be considered more seriously; hence, it was *five times* important factors as compared to the MRR and *two times* important than its surface finish. Furthermore, in this problem, we also emphasized the surface finish to avoid the cost of secondary operation, i.e., SR was *two times* more important than MRR.

The AHP weights assigned are stable as well as consistent (CR > 0). Thus, they were used in MOORA process as the main input to find the favorite trial for both samples. The criteria used were to minimize the residual stress and SR and maximize the MRR. The results of MOORA are shown in Tables 7 and 8.

It was observed that trial 4 is the best alternative for Sample I according to AHP-MOORA method. Also, the second option in this category is trial 2. For Sample II, it is reported that trial 13 and trial 16 can be recommended as the first and second top alternatives.

Table 8 Ranking of trials for Sample II based on MOORA method

Trials	Residual stress	MRR	SR	Benefit	Cost	MOORA ranking
	0.5954	0.1283	0.2764	S_k^+	S_k^-	
T_{10}	70.4	20.9	6.69	0.02165	0.20239	4
T_{11}	104	60.67	10.46	0.06285	0.30646	6
T_{12}	78.1	10.86	4.69	0.01125	0.18914	3
T_{13}	41.8	57.99	6.46	0.06007	0.15239	1
T_{14}	149.3	18.86	8.44	0.01954	0.35477	8
T_{15}	132.9	29.96	4.44	0.03103	0.27599	7
T_{16}	77.7	65.5	6.76	0.06785	0.21530	2
T_{17}	89.2	10.07	6.12	0.01043	0.22591	5
T_{18}	231.5	45.72	7.95	0.04736	0.48355	9

For the Sample I, the machining performed with graphite tool electrode in the presence of Cu powder mixed with dielectric medium at pulse-off and pulse-on time of 15 and 45 μs, respectively, coupled with current at intermediate setting, i.e., 8 A is the best option for the desired machined surface. For the Sample II, the best machining option reports in the dielectric mixed with graphite powder with a lowest current setting, i.e., 4 A. Thus, for desired machining characteristics, the spark energy (i.e., pulse-on time and current) may be adjusted according to the reinforcement architecture of MMCs. However, for superior surface integrity and higher MRR, the MMCs can be machined with fine-grained graphite electrode at reduced pulse-off time setting in the presence of suspended additive in the dielectric medium, thus resulted in reduced re-solidified layer.

5 Conclusion

The process conditions that affect the three responses, namely, residual stresses, MRR, and SR, are identified for the two different types of MMCs. Current and pulse-on time are the significant parameters affecting MRR and SR of MMCs. The surface finish of the MMCs depends upon the conductivity of suspended powder in the dielectric medium. On the other hand, pulse-off time significantly influenced the induced residual stresses followed by dielectric medium, current, and the electrode material used. The three criteria weights are achieved using AHP methodology that is further adopted by MOORA method to rank process parameters combination for both the MMCs. The optimal conditions for both types of MMCs are identified. The overall process setting for both the samples reveals that machining of MMCs with graphite material electrode at the higher setting of pulse-on time and machining in the presence of suspended particulates dielectric medium gives superior surface

integrity with desired MRR. It is witnessed that for the machining of MMCs, the SiC reinforcement architecture in matrix phase significantly affects the current level and dielectric medium selection. The addition of powder in the dielectric medium reduces its insulating strength, thus enhanced the MRR that is reported.

References

1. Callister WD (2004) Composites. Materials science and engineering an introduction, 6th edn. Wiley, New York, pp 527–560
2. Ahamed AR, Asokan P, Aravindan S (2009) EDM of hybrid Al–SiCp–B4Cp and Al–SiCp—Glassp MMCs. Int J Adv Manuf Technol 44(5–6):520–528
3. Bains PS, Sidhu SS, Payal HS (2016) Fabrication and machining of metal matrix composites: a review. Mater Manuf Processes 31(5):553–573
4. Schachra A, Lenz E (1976) LBM and EDM—a comparison on crack behavior. Ann CIRP 25:121–123
5. Sidhu SS, Batish A, Kumar S (2014) Study of surface properties in particulate-reinforced metal matrix composites (MMCs) using powder-mixed electrical discharge machining (EDM). Mater Manuf Process 29(1):46–52
6. Feng X, Wong YS, Hong GS (2016) Characterization and geometric modeling of single and overlapping craters in micro-EDM. Mach Sci Technol Int J 20(1):79–98
7. Gill AS, Kumar S (2016) Surface roughness and microhardness evaluation for EDM with Cu–Mn powder metallurgy tool. Mater Manuf Processes 31(4):514–521
8. Pal VK, Choudhury SK (2016) Fabrication and analysis of complex-shape tool for EDM by AWJM process. Adv Mater Process Technol 1(3–4):444–452
9. Hocheng H, Lei WT, Hsu HS (1997) Preliminary study of material removal in electrical-discharge machining of SiC/Al. J Mater Process Technol 63(1):813–818
10. Singh PN, Raghukandan K, Pai BC (2004) Optimization by grey relational analysis of EDM parameters on machining Al–10% SiC P composites. J Mater Process Technol 155:1658–1661
11. Garg RK, Singh KK, Sachdeva A, Sharma VS, Ojha K, Singh S (2010) Review of research work in sinking EDM and WEDM on metal matrix composite materials. Int J Adv Manuf Technol 50(5–8):611–624
12. Majumder A, Das PK, Majumder A, Debnath M (2014) An approach to optimize the EDM process parameters using desirability-based multi-objective PSO. Prod Manuf Res 2(1):228–240
13. Singh PN, Raghukandan K, Rathinasabapathi M, Pai BC (2004) Electric discharge machining of Al–10% SiC p as-cast metal matrix composites. J Mater Process Technol 155:1653–1657
14. Kuriakose S, Shunmugam MS (2005) Multi-objective optimization of wire-electro discharge machining process by non-dominated sorting genetic algorithm. J Mater Process Technol 170(1):133–141
15. Tzeng YF, Chen FC (2007) Multi-objective optimisation of high-speed electrical discharge machining process using a Taguchi fuzzy-based approach. Mater Des 28(4):1159–1168
16. Sidhu SS, Batish A, Kumar S (2013) EDM of metal matrix composite for parameter design using lexicographic goal programming. Mater Manuf Processes 28(4):495–500
17. Withers PJ, Bhadeshia HKDH (2001) Residual stress. Part 1–measurement techniques. Mater Sci Technol 17(4):355–365
18. Sidhu SS, Batish A, Kumar S (2013) Fabrication and electrical discharge machining of metal–matrix composites: a review. J Reinf Plast Compos 32(17):1310–1320
19. Kalibatas D, Turskis Z (2008) Multicriteria evaluation of inner climate by using MOORA method. Inf Technol Control 37:79–83
20. Akkaya G, Turanoğlu B, Öztaş S (2015) An integrated fuzzy AHP and fuzzy MOORA approach to the problem of industrial engineering sector choosing. Expert Syst Appl 42(24):9565–9573

21. Chakraborty S (2011) Applications of the MOORA method for decision making in manufacturing environment. Int J Adv Manuf Technol 54(9–12):1155–1166
22. Das MC, Sarkar B, Ray S (2012) Comparative evaluation of Indian technical institutions using fuzzy AHP and MOORA. Int J Multicriteria Decis Making 2(1):74–93
23. Saaty TL (1977) A scaling method for priorities in hierarchical structures. J Math Psychol 15(3):234–281
24. Saaty TL (1988) What is the analytic hierarchy process?. Springer, Berlin, pp 109–121
25. Amiri MP (2010) Project selection for oil-fields development by using the AHP and fuzzy TOPSIS methods. Expert Syst Appl 37(9):6218–6224
26. Triantaphyllou E (2000) Multi-criteria decision making methods: a comparative study. Springer, US, pp 5–21
27. Brauers WKM, Zavadskas EK (2006) The MOORA method and its application to privatization in a transition economy. Control Cybern 35(2):445
28. Zavadskas EK, Turskis Z, Kildienė S (2014) State of art surveys of overviews on MCDM/MADM methods. Technol Econ Dev Econ 20(1):165–179
29. Balezentis T, Balezentis A (2014) A survey on development and applications of the multi-criteria decision making method MULTIMOORA. J Multi-Criteria Decis Anal 21(3–4):209–222
30. Stanujkic D (2016) An extension of the ratio system approach of MOORA method for group decision-making based on interval-valued triangular fuzzy numbers. Technol Econ Dev Econ 22(1):122–141
31. Brauers WKM, Ginevičius R, Podvezko V (2010) Regional development in Lithuania considering multiple objectives by the MOORA method. Technol Econ Dev Econ 16(4):613–640
32. Karande P, Chakraborty S (2012) Application of multi-objective optimization on the basis of ratio analysis (MOORA) method for materials selection. Mater Des 37:317–324
33. Lazauskas M et al (2015) Multicriteria assessment of unfinished construction projects. Gradevinar 67(4):319–328
34. Ross PJ (1998) Taguchi techniques for quality engineering. McGraw Hill Book Company, New York, p 228
35. Sidhu SS, Batish A, Kumar S (2015) Analysis of residual stresses in particulate reinforced aluminum matrix composite after EDM. J Mater Sci Technol 31(15):1850–1859
36. Welzel U, Ligot J, Lamparter P, Vermeulen AC, Mittemeijer EJ (2005) Stress analysis of polycrystalline thin films and surface regions by X-ray diffraction. J Appl Crystallogr 38(1):1–29
37. Saaty TL (2001) Fundamentals of the analytic hierarchy process. Springer, Netherlands, pp 15–35
38. Al-Harbi KMAS (2001) Application of the AHP in project management. Int J Project Manage 19(1):19–27
39. Whitaker R (2007) Validation examples of the analytic hierarchy process and analytic network process. Math Comput Model 46(7):840–859
40. Taha AH (2008) Decision analysis and games. Operation research an introduction, 9th edn. Pearson education, India, pp 503–511

Multi-objective Optimization of MWCNT Mixed Electric Discharge Machining of Al–30SiC$_p$ MMC Using Particle Swarm Optimization

Chander Prakash, Sunpreet Singh, Manjeet Singh, Parvesh Antil, Abdul Azeez Abdu Aliyu, A. M. Abdul-Rani and Sarabjeet S. Sidhu

Abstract In the present research work, the multi-walled carbon nanotube (MWCNT) mixed electric discharge machining of Al–SiC$_p$-based MMC has been proposed. The effect on MWCNT concentration, peak current, pulse duration, and duty cycle on the surface roughness and material removal rate has been investigated and multi-objective optimization of MWCNT mixed-EDM process parameters has been carried out for the machining of Al–30SiC$_p$ substrate using particle swarm optimization (PSO) technique. The SR and MRR increased with peak current and pulse duration in the case of EDM, but SR decreased and MRR increased with the dispersion of MWCNTs in EDM dielectric fluid. The empirical model has been developed by response surface methodology to interpret the relation between input parameters and output characteristics such as SR and MRR. However, the impacts of MWCNT mixed-EDM parameters on SR and MRR are clashing in nature; there is no single condition of machining parameters, which gives the best machining quality. Multi-objective particle swarm optimization technique was used to find the best optimal condition of MWCNT mixed-EDM parameters to minimize the SR and maximize the MRR. The best global solution where, maximum MRR (1.134 mm^3/min) and minimum SR (1.097 μm) obtained from the Pareto optimal front is at peak current = 15.59 A, pulse-on = 169.61 μs, duty cycle = 65.17%, and MWCNT powder concentration = 4.08 g/l. The MRR and SR are increased by 14.89 and 15.94%,

C. Prakash (✉) · S. Singh · M. Singh
School of Mechanical Engineering, Lovely Professional University, Phagwara 144411, Punjab, India
e-mail: chander.mechengg@gmail.com

P. Antil
Department of Mechanical Engineering, Northern India Engineering College, New Delhi, India

A. A. A. Aliyu · A. M. Abdul-Rani
Department of Mechanical Engineering, Institute of Technology Petronas Sdn. Bhd., Perak Tengah, Malaysia

S. S. Sidhu
Department of Mechanical Engineering, Beant College of Engineering & Technology, Gurdaspur 143521, Punjab, India

S. S. Sidhu et al. (eds.), *Futuristic Composites*, Materials Horizons: From Nature to Nanomaterials, https://doi.org/10.1007/978-981-13-2417-8_7

respectively, after mixing 4.08 g/l MWCNT concentration in dielectric fluid. From the above study, it is recommended for the process engineer to use the proposed optimal setting to achieve maximum MRR and minimum SR.

Keywords EDM · Al–SiC_p · MMC · SR · MRR · Nanofinishing
Process parameters · Optimization

1 Introduction

Al–SiC_p metal matrix composites (MMCs) have gained plentiful application in various industries, for instance, in automotive and aerospace sectors, owing to their one of a kind blend of mechanical properties, wear resistance, and retention of strength at elevated temperatures [1–5]. However, it has been witnessed that their full potential use is not escalating and hindered due to lack of machinability, with most of the conventional machining processes, often results into high tool wear, poor surface roughness, and high machining cost [6]. In this context, numerous researchers studied and investigated the suitability of advanced and nonconventional machining processes (such as electric discharge machining, abrasive jet machining, electron beam machining, and laser beam machining) to overcome the aforesaid bottlenecks [7, 8]. Among these, electric discharge machining (EDM) has been found as one of the best-suited machining technologies for machining Al–SiC_p MMC [9]. EDM is a thermomechanical process widely used to machine the hard and tough material with the ease [10]. The heat energy librated from the electrical sparks melts the workpiece surface and removed the material in the form of micron-size debris [11]. Prakash et al. reported the mechanism of material removal during EDM process in details, as illustrated in Fig. 1 [12]. In EDM, countless electrical sparks have been generated within fraction of seconds, which induced heat energy causing removal of material from workpiece surface [13]. In the presence of dielectric fluid, this librated heat energy thermally affected the top surface layer of workpiece material due to sudden quenching. Thus, various surface deformities like high surface roughness, high surface cracks, and micron size pits/dimples were shaped on the machined surface which breaks down the surface quality [14]. Keeping in mind the end objective to reduce the generation of surface flaws like micro-cracks, high ridges of re-disposition of molten pool, and high roughness, numerous modifications and progressions in EDM process has been carried out by numerous analysts [15, 16]. In the as-adopted modifications and progressions, the machining mechanisms of one or more process have been superimposed to take advantage of one process over other and called as hybridization. These hybridizations are such as electro-discharge diamond grinding (EDDG), ultrasonic vibration-assisted EDM (UVA-EDM), rotary-assisted EDM (RAEDM), HyFlex EDM, electro-discharge coating/surface modification by composite or green tool electrode, near dry EDM and powder mixed-EDM (PM-EDM) [17–25]. In comparison to all, the PM-EDM has been accepted and used as the most encouraging hybridized process to deal with reduction of surface defects and to enhance the sur-

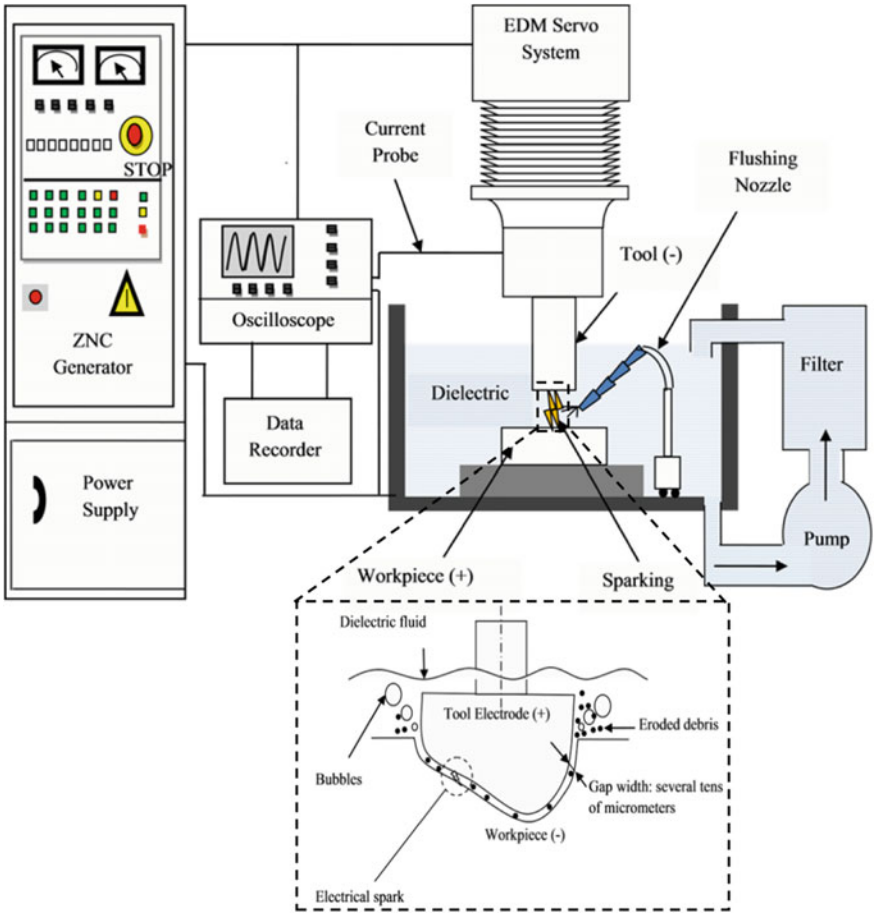

Fig. 1 Schematic illustrated the mechanism of material removal in EDM process [12]

face quality [26–30]. Prakash et al. [31] investigate the capability of PM-EDM not only to enhance the surface quality but also to improve the machining performance. It has been reported that with the dispersion of powder particles in the dielectric fluid, the uniformity and sparking area increased but the increased discharge gap which reduced the thermal energy resulted from the electrical sparks. As a result of this, small and tiny discharge craters were developed on the machined surface and lead to decrease in the SR value of the machined surface. On the other hand, with the dispersion of powder particles, the sparking area increased. As a consequence the top layer of workpiece is expelled in the form of micron debris from large locations; thus increased the MRR value.

Singh et al. studied the capability of PM-EDM to enhance the SR, MRR, and TWR characteristics by using tungsten powder particles as dielectric solvent [32–34]. It has been reported that tungsten powder in dielectric fluid enhanced the machining

gap and increased the machining contact area, as a result the material was removed in micron and sub-micron sized in large proportion with small pit size. Mohan et al. reported the application of PM-EDM for drilling the hole in Al–SiC MMCs and studied the effect of tool polarity along with other machining parameters on the machined hole surface quality [35]. Sidhu et al. investigated the efficacy of PM-EDM process to enhance the surface characteristics, machining performance, and surface properties of Al–SiC_p MMC and it has been reported that microhardness of the substrate surface was enhanced by the PM-EDM process using material migration method [36, 37]. Pecas and Henriques [38] reported the potential of PM-EDM for the finishing of workpiece material. Recently, Prakash et al. [39] explored the capability of PM-EDM as finishing process and studied the effect of surface finish achieved by PM-EDM process on the fatigue performance of Ti-based implant material. A number of researchers used PM-EDM process to enhance the machining performance, surface characteristics, and surface properties using micron-sized powder particles in the dielectric fluid [40–45]. The application of nonmetallic powder particles as a dielectric solvent has been used for the machining the work material with the aim of producing nanofinished part [46–48]. Miao et al. explored the capability of MWCNT mixedEDM process for the finishing of workpiece using miniature tool electrode. It was reported that with the use of MWCNT in EDM dielectric fluid, the machined surface quality and machining efficiency was improved by 70 and 66%, respectively [49]. Izman et al. [50] used the potential of MWCNT mixed-EDM for the reducing the recast layer thickness, improving the MRR and surface finish. It was reported that MRR and surface was improved by 7 and 9%, respectively. Prabhu and Vinayagam [51] reported that nanolevel surface finish ~75 nm was achieved on AISI-D2 steel substrate by MWCNT mixed-EDM process. Further, the utility of MWCNT-mixed-EDM for the finishing of Inconel 825 has been reported [52]. It was reported that surface finish of the components was enhanced by 34% than EDMed substrate. Sari et al. reported the nanofinishing of AISI H-13 tool by EDM using MWCNT mixed additive in dielectric fluid. The effect of MWCNT concentration on the re-deposition layer was studied and it was reported that the thickness of re-deposited layer was significantly. MWCNTs minimize the thickness of recast layer due to larger heat absorption [53]. When MWCNTs is added in to dielectric of EDM, produces 20% improvement in SR of AISI D2 tool steel [54]. Recently, Shabgard and Khosrozadeh [55] investigated the effect of MWCNT in dielectric fluid on SR, MRR, and TWR and it has been reported that the TWR and SR were significantly reduced by the use of MWCNT in dielectric fluid.

Optimization is very imperative to determine the best possible setting of input-process parameters to maximize the response characteristics. A number of single/conventional techniques such as Taguchi, response surface methodology, Grey relation have been adopted in the past to optimize the process parameters of EDM and PM-EDM process [56–61]. These techniques are only applicable for optimizing single parameter and are usually not favorable for multiparametric objectives, since outcomes get clashed. Non-dominated sorted genetic algorithm (NSGA)-II was found suitable for the multiobjective optimization of EDM and PM-EDM process parameters to maximize the machine efficiency and to obtain quality surface

[62, 63]. Padhee et al. [64] implemented the application of NSGA-II to determine the optimal setting of PM-EDM process parameters to maximize MRR and to minimize SR for EN-32 steel. Recently, Mohanty et al. [65] used the capability of particle swarm optimization (PSO) for the optimization of nano-Al_2O_3-mixed-EDM process parameters for maximizing MRR and minimizing SR and TWR. Kennedy and Eberhart presented PSO first time in 1995 as an effective transformative computational procedure to optimize the response characteristics [66]. The PSO is developed to solve the consistent nonlinear streamlining issues after identifying the behavior of natural swarm bird coming back to perch and observed in numerous types of winged creatures [67–69]. The PSO method can produce top notch arrangements inside short computation time and stable merging attributes [70–72]. Because of the great execution of the PSO system, numerous process engineers/scientists discover the PSO as a productive option over other inquiry calculations particularly when managing multi-target streamlining issues [73].

The surface quality and the machining performance of Al–30SiCp MMC is a challenging issue in the machining process. However, there is no study available on the machining of Al–30SiCp MMC using MWCNT-mixed-EDM. In this way, the current study investigated the effect of MWCNT concentration on SR and MRR, further more multiobjective particle swarm optimization has been carried out to determine the optimal best setting to maximize the MRR and minimize SR. Till date no research study is available, which considered implication of PSO for multiobjective optimization of NPM-EDM process for Al-30SiCp MMC by using CNTs as powder additive.

2 Experimental Planning and Optimization

2.1 Materials and Experimentation

Widely used Al–305SiC_p MMC was used as workpiece for machining using powder mixed electric discharge machining process. The surface of Al–305SiC_p MMC was well grounded and cleaned with ethanol followed by drying at room temperature. The machining of Al–30SiC_p workpiece was carried out by using multi-walled carbon nanotube (MWCNT) mixed-EDM process. The MWCNTS powder particles were used as dielectric solvent and mixed in dielectric fluid. The SEM micrograph of MWCNT powder particles are shown in Fig. 2. The experimental setup for the surface modification was in-house developed and called as nanopowder-mixed electric discharge machining (NPM-EDM), as shown in Fig. 3. In order to perform a NPM-EDM process, a separate tank of the dielectric capacity of 5 L was designed and MWCNT powder was mixed in the dielectric fluid at various concentrations 0, 2, 4, 6, 8 g/l. The die-sinking EDM machine (ELECTRONICA model 5535) has been utilized to conduct the experiments. A circular shape copper alloy rod of size ϕ

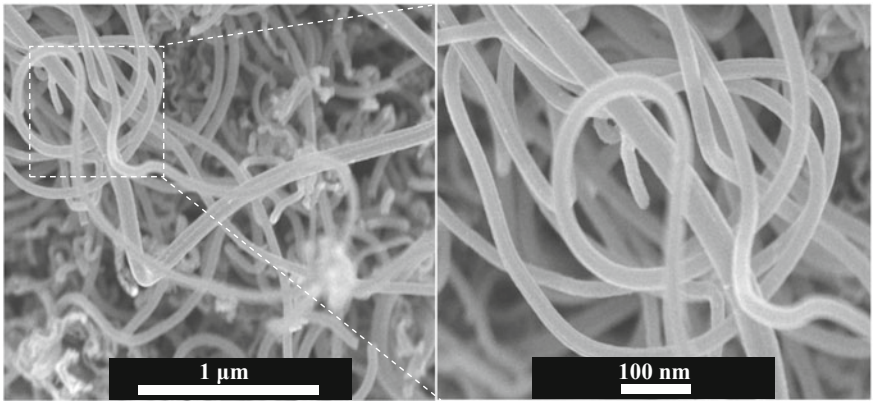

Fig. 2 SEM micrograph showing the morphology and size of MWCNT particles

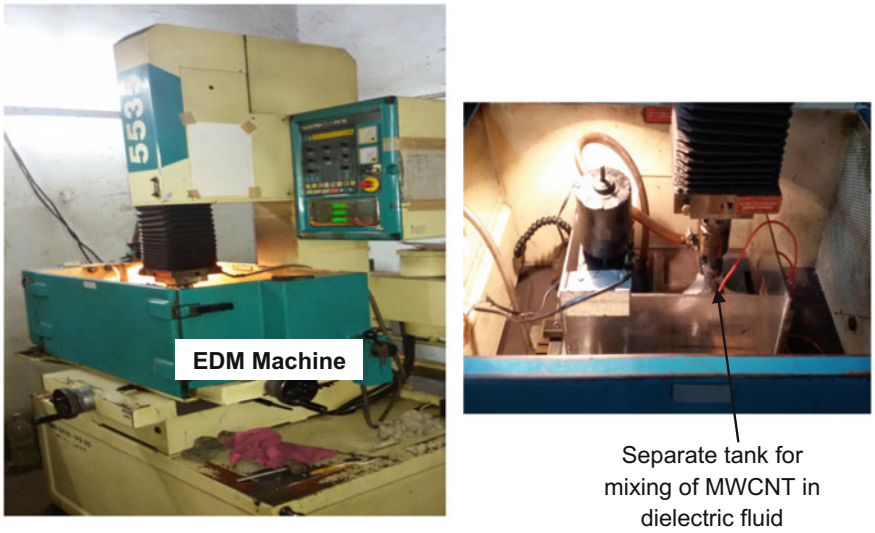

Fig. 3 Experimental setup of HA mixed electric discharge machining process

10 × 50 mm was used as an electrode for the machining process. Table 1 shows the detailed experimental conditions for the NPM-EDM process. From the initial trials, four input-process parameters were chosen for the examination. Table 1 presents the process parameters and their level.

Table 1 Process parameters and their levels

Working parameters	Description and levels
Tool electrode	Copper
Workpiece	Al–30SiC$_p$
Polarity	Tool (+), Workpiece (−)
Pulse current (A)	5 10 15 20 25
Pulse duration (μs)	50 100 150 200 250
Duty cycle (%)	8 24 40 56 80
MWCNT powder concentration (g/l)	0 2 4 6 8

2.2 Materials Characterization

The surface roughness (SR) and material removal rate (MRR) are considered as output response characteristics. The surface roughness was measured by Mitutoyo surface roughness tester. The MRR was computed by dividing the material removal per unit time, as per the procedure adopted previously [32]. In experimentation, central composite rotatable design (CCRD) has been used as a module of response surface methodology. Table 2 shows the design of experiment and obtained value of MRR and SR.

2.3 Optimization Using MO-PSO

Because of clashing nature of output characteristics as MRR and SR, the single optimal settings of process parameter is not fulfilling the goals. In such circumstances, MO-PSO gives better execution when contrasted with the customary improvement strategy because of their heartiness, independency of slope data, and utilization of inborn parallelism in looking through the plan space. The algorithm flowchart of MO-PSO algorithm is shown in Fig. 4.

3 Results and Discussions

3.1 Effect of Process Parameter on MRR and SR

Figure 5 shows the 3D response surface plot for the material removal rate (MRR) with respect to process parameters. Figure 5a shows the effect of interaction of peak current (I_p) and pulse duration (T_{on}) on MRR. The MRR increased with peak current (I_p), this is because when I_p increased, a large amount of heat is liberated

Table 2 Experimental design with response characteristics values of MRR and SR

S. No.	I_p	T_{on}	T_{au}	P_c	MRR	SR
1	10	100	24	2	1.001	1.412
2	20	100	24	2	1.105	1.589
3	10	200	24	2	0.985	1.514
4	20	200	24	2	1.164	1.721
5	10	100	56	2	1.155	1.529
6	20	100	56	2	1.230	1.758
7	10	200	56	2	1.149	1.65
8	20	200	56	2	1.345	1.862
9	10	100	24	6	1.159	1.487
10	20	100	24	6	1.229	1.839
11	10	200	24	6	1.230	1.625
12	20	200	24	6	1.450	1.987
13	10	100	56	6	1.215	1.419
14	20	100	56	6	1.307	1.731
15	10	200	56	6	1.234	1.645
16	20	200	56	6	1.424	1.928
17	5	150	40	4	1.072	1.305
18	25	150	40	4	1.195	1.899
19	15	50	40	4	1.201	1.456
20	15	250	40	4	1.299	1.678
21	15	150	8	4	1.051	1.467
22	15	150	72	4	1.262	1.607
23	15	150	40	0	1.132	1.89
24	15	150	40	8	1.425	1.939
25	15	150	40	4	1.165	1.551
26	15	150	40	4	1.176	1.529
27	15	150	40	4	1.138	1.489
28	15	150	40	4	1.161	1.549
29	15	150	40	4	1.145	1.512
30	15	150	40	4	1.175	1.512

and sunk into the workpiece. As a consequence, the size and shape of pits/craters on the modified surface increases, which further increases the MRR. The MRR value increased from 1.05 to 1.28 mm^3/min when peak current increased from 5 to 25 A. The MRR value first decreased with the pulse duration but, after certain value of pulse duration (150 μs), it starts increasing and goes on. This is due to the fact that discharge energy is proportional to pulse duration, thus an increase in the later enlarged the depth and width of craters [21, 74]. The MRR value increased from 1.03 to 1.55 mm^3/min when pulse duration increased from 150 to 250 μs at peak current and duty cycle of 5 A and 8%, respectively. The highest MRR (1.55 mm^3/min) is achieved at high level of peak current and high level of pulse duration. Figure 5b

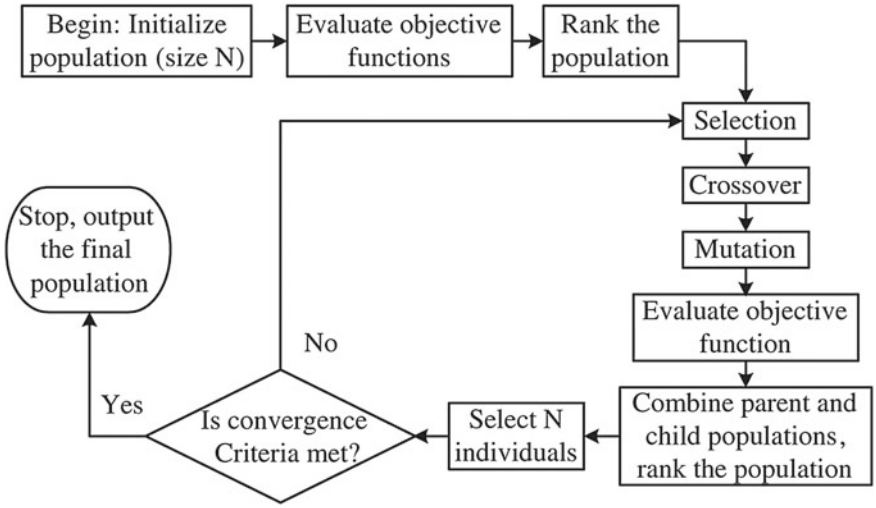

Fig. 4 Algorithm flowchart of MO-PSO

shows the effect of interaction of pulse duration (T_{on}) and powder concentration (P_c). The MRR increases with the MWCNT concentration in the dielectric fluid at any value of I_p and T_{on}. This is because, with the dispersion of MWCNT powder particles in the dielectric fluid, the spark locations increases and removed the material in larger proportion form the workpiece surface As a consequence, the top layer of workpiece is expelled in the form of micron-debris from large locations; thus, increased the MRR value. The MRR value increased from 1.15 to 1.38 mm^3/min, when MWCNT concentration increased from 0 to 6 g/l at pulse duration and duty cycle of 50 μs and 8%, respectively. The highest MRR (1.66 mm^3/min) is achieved at high level of peak current and high level of MWCNT concentration.

The MRR value is high in all cases of MWCNT mixed-EDM as compared to EDM. Figure 5c shows the variation of MRR value with respect to MWCNT concentration and duty factor. The MRR value increased with the duty factor at any value of peak current and pulse duration. This is due to the fact that as the duty cycle increases the pulse interval decreases and pulse duration increases. As a result, large amount of discharge energy sank into the workpiece material and causing removal of material in the form of deep and large craters. The MRR value increased from 0.90 to 1.35 mm^3/min, when duty cycle increased from 8 to 80% at peak current and pulse duration of 5 A and 50 μs, respectively. The highest MRR (1.35 mm^3/min) is achieved at high level of duty factor and high level of MWCNT concentration. The MRR increased very rapidly in combination with MWCNT concentration and pulse duration. The maximum MRR value has been obtained at high value of peak current, pulse duration, duty cycle, and MWCNT concentration. The best optimal condition where high MRR was obtained is $A3$, $B3$, $C3$, and $D3$. Table 3 presents the analysis of variance (ANOVA) for the MRR and showing all of the input-process parameters

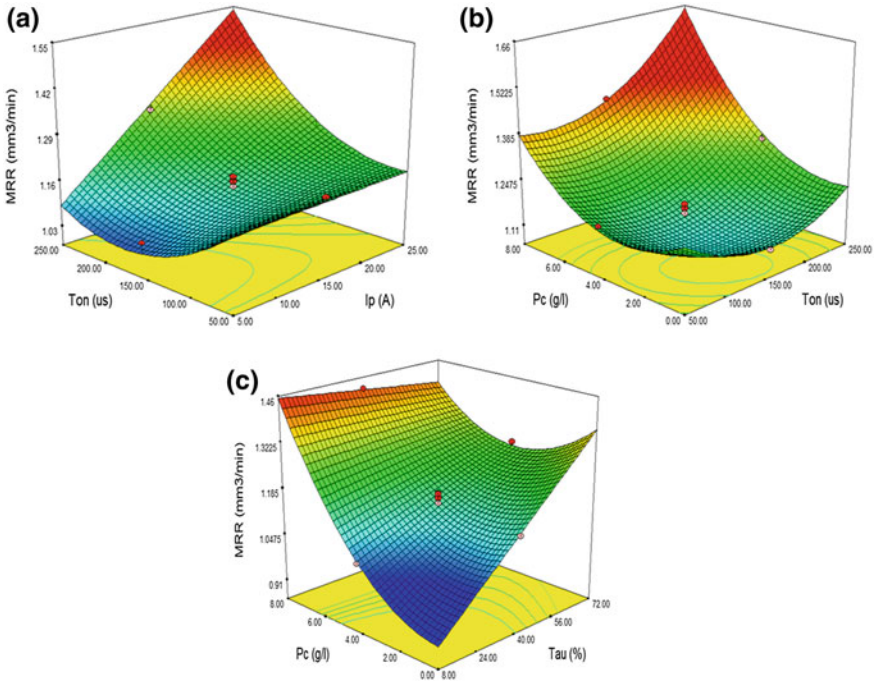

Fig. 5 3D response surface plot of MRR with respect to input-process parameters and their interaction

have significant contribution toward increasing the MRR. The mathematical model for the perdition of MRR was computed and represented in Eq. (3.1).

$$\begin{aligned}\text{MRR} = {} & 1.16243 - 5.27625\text{E}{-}003 * A - 4.62664\text{E}{-}003 * B \\ & + 7.01198\text{E}{-}003 * C - 0.013202 * D + 1.11325\text{E}{-}004 * A * B \\ & + 1.72313\text{E}{-}004 * B * D - 1.00059\text{E}{-}003 * C * D \\ & + 9.71031\text{E}{-}006 * B2 + 7.85020\text{E}{-}003 * D2 \end{aligned} \tag{3.1}$$

Figure 6 shows the 3D response surface plot for the surface roughness (SR) with respect to process parameters and their interactions. Figure 6a shows the effect of interaction of peak current (I_p) and pulse duration (T_{on}) on SR. As the peak current increases the SR increases, this is because when peak current increases, a large amount of heat is liberated and sunk into the workpiece. As a consequence, the increase in the size and shape of pits/craters increases the SR value from 1.22 to 1.80 μm. Similar trend was observed for the case of pulse duration parameter, as evidently. The SR value increases with the increase in pulse duration, because the discharge energy increased with the increase in pulse duration; thus deep and wide craters were developed on the machined surface. The SR value increased from 1.22

Table 3 ANOVA table for MRR

Source	Sum of squares	df	Mean square	F value	p-value (prob > F)
Model	0.353	9	0.0392	48.836	<0.0001 (significant)
I_p	0.078	1	0.0782	97.351	<0.0001
T_{on}	0.025	1	0.0250	31.097	<0.0001
T_{au}	0.055	1	0.0556	69.206	<0.0001
P_c	0.120	1	0.1204	149.799	<0.0001
$I_p * T_{on}$	0.012	1	0.0123	15.411	0.0008
$T_{on} * T_{au}$	0.004	1	0.0047	5.907	0.0246
$T_{au} * P_c$	0.016	1	0.0164	20.398	0.0002
T_{on}^2	0.017	1	0.0167	20.845	0.0002
P_c^2	0.028	1	0.0280	34.877	<0.0001
Residual	0.016	20	0.0008		
Lack of fit	0.014866711	15	0.0009	4.075	0.0643 (not significant)
Pure error	0.001216	5	0.0002		
Cor. total	0.369522252	29			
Std. dev. = 0.028357					R-squared = 0.956477
Mean = 1.19936					Adj R-squared = 0.936892
C.V. % = 2.364368					Pred R-squared = 0.901096
PRESS = 0.036547					Adeq Precision = 27.01855

to 1.50 μm when pulse duration increased from 50 to 250 μs. The lowest value of SR (1.22 μm) is obtained at low level of peak current and pulse duration.

Figure 6b shows the effect of interaction of MWCNT concentration (P_c) and pulse duration (T_{on}) on SR at any value of I_p and T_{on}. The SR value first decreases with MWCNT powder concentration but it starts increasing when the MWCNT powder concentration increases beyond 4 g/l. By the dispersion of MWCNT powder particles in the deionised water, the uniformity and sparking area increased but the increased discharge gap reduced the thermal energy resulted from the electrical sparks. As a result of this, small and tiny discharge craters were developed on the machined surface and lead to a decrease in the SR value of the machined surface [21]. The MWCNT powder concentration increased beyond 4 g/l, the powder particle get stuck with the plasma and get deposited on the machined surface. The SR value decreased from 1.79

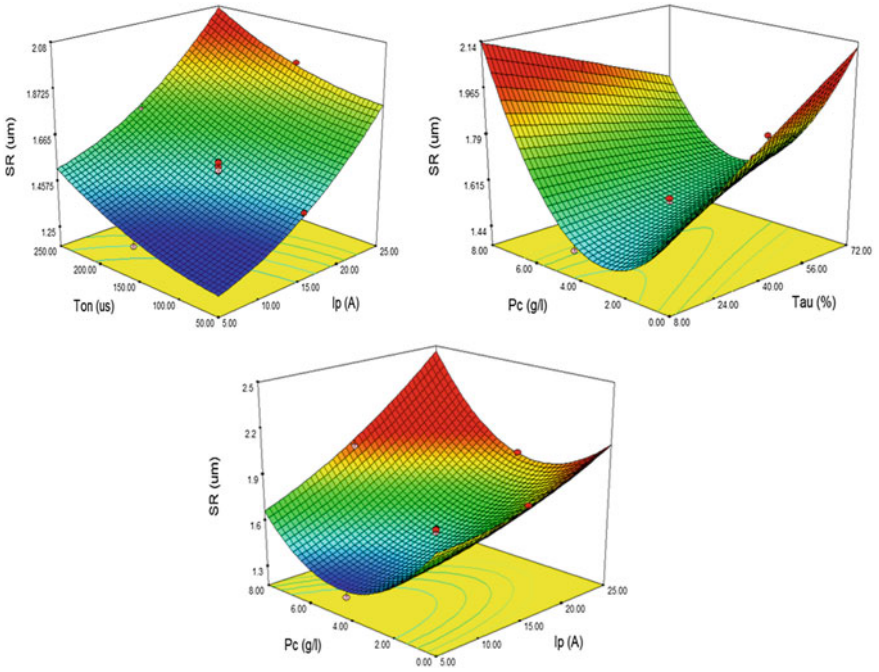

Fig. 6 3D response surface plot of SR with respect to input-process parameters and their interaction

to 1.35 μm, when MWCNT powder concentration increased from 0 to 4 g/l and it start increases from 1.35 to 2.14 μm when powder concentration increased from 6 to 8 g/l. The SR value increased with respect with the increase in duty cycle, due to the fact that as the duty cycle increased the pulse interval decreased and pulse duration increased. As a result, large amount of discharge energy sinked into the workpiece material and causing removal of material in the form of deep and large craters. The SR value increased from 1.79 to 2.12 μm, when duty cycle increased from 8 to 72%. The SR decreased very rapidly in combination with low peak current and 4 g/l MWCNT powder concentration. The minimum SR value was obtained at low value of peak current, pulse duration, duty cycle, and high level of MWCNT concentration. The best optimal condition where low SR was obtained is $A1$, $B1$, $C1$, and $D3$. Table 4 presents the analysis of variance (ANOVA) for the SR and showing all input-process parameters has significant contribution toward the SR. The mathematical model for the perdition of SR is computed, as represented in Eq. (3.2).

$$\begin{aligned} \mathrm{SR} = {} & 1.30396 - 7.79792\mathrm{E}{-}003 * A + 1.34333\mathrm{E}{-}003 * B \\ & + 7.71354\mathrm{E}{-}003 * C - 0.16473 * D + 3.02500\mathrm{E}{-}003 * A * D \\ & - 1.51953\mathrm{E}{-}003 * C * D + 7.79375\mathrm{E}{-}004 * A2 + 0.024402 * D2 \end{aligned} \quad (3.2)$$

Table 4 ANOVA table for SR

Source	Sum of squares	df	Mean square	F value	p-value (prob > F)
Model	0.931993779	8	0.116499	95.860887	<0.0001 (significant)
I_p	0.459820167	1	0.45982	378.36106	<0.0001
T_{on}	0.108272667	1	0.108273	89.091701	<0.0001
T_{au}	0.016432667	1	0.016433	13.521549	0.0014
P_c	0.021840667	1	0.021841	17.971499	0.0004
$I_p * P_c$	0.014641	1	0.014641	12.047284	0.0023
$T_{au} * P_c$	0.03783025	1	0.03783	31.128459	<0.0001
T_{on}^2	0.010798674	1	0.010799	8.8856424	0.0071
P_c^2	0.271007007	1	0.271007	222.99696	<0.0001
Residual	0.025521188	21	0.001215		
Lack of fit	0.022629854	16	0.001414	2.4458714	0.1643 (not significant)
Pure error	0.002891333	5	0.000578		
Cor. total	0.957514967	29			
Std. dev. = 0.035					R-squared = 0.9733
Mean = 1.64					Adj R-squared=0.9632
C.V. % = 2.13					Pred R-squared=0.9328
PRESS = 0.064					Adeq precision = 34.024

3.2 Multiobjective Optimization Using MO-PSO

It is noticed that when SR reduced, the MRR reduces. The MRR requires to be maximized while regulating the SR. Because of clashing nature of MRR and SR, it is important to locate the optimal set of conditions of input-process parameters that yield high MRR and least SR. Accordingly, the function MRR is changed over into minimization type and the objective functions are altered as below:

Objective 1 = Minimize (1/MRR);
Objective 2 = Minimize (SR).

With a specific end goal to perform such multiobjective optimization, a source code of the proposed algorithm MO-PSO was executed utilizing MATLAB. Figure 7 shows the spread of Pareto front which contains the 100 optimal set of conditions where both functions were optimized. In this way, the choice of a result against

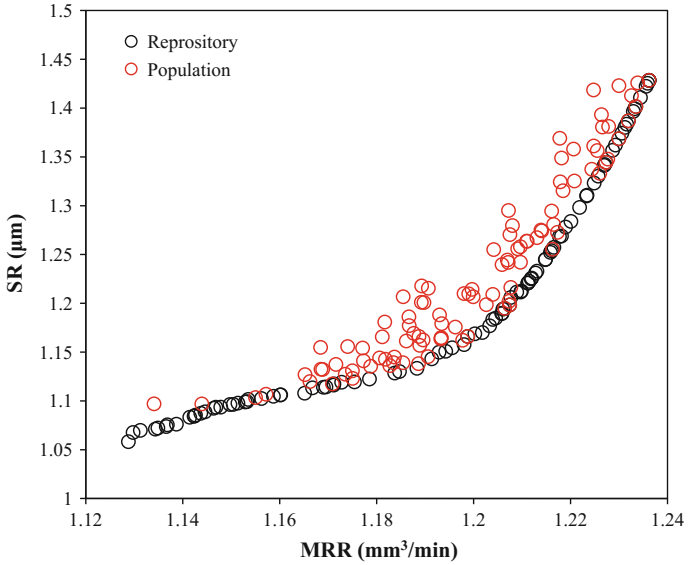

Fig. 7 Pareto optimal front of the MRR and SR using MO-PSO

Table 5 Optimal solutions obtained from MO-PSO with confirmation test

Solution No.	I_p (A)	T_{on} (µs)	τ (%)	P_c (g/l)	MRR (mm^3/min)	SR (µm)
1	25	250	80	0	1.23	1.428
2	15.59	169.61	65.17	4.08	1.13	1.097
3	24.27	242.75	77.08	0	1.23	1.423
4	21.85	221.51	68.19	2.43	1.17	1.14
5	19.24	199.86	72.30	2.41	1.16	1.13

different relies on item necessity as well as decision of process designer/engineer. It has been observed that MO-PSO predicted the best results within boundaries. Out of 100 global best solutions, the first 5 solutions are presented in Table 5.

3.2.1 Comparison of Experimental and Optimal MRR

In the investigation and comparing of experiential results of MRR with Pareto front, it is observed that the maximum MRR is 1.45 mm^3/min at peak current = 20 A, pulse-on = 200 µs, duty cycle = 24%, and MWCNT powder concentration = 6 g/l, corresponding to experiment no. 24 in Table 2. On the other hand, the maximum MRR obtained from the Pareto optimal front is 1.23 mm^3/min at peak current = 25 A, pulse-on = 250 µs, duty cycle = 80%, and MWCNT powder concentration = 0 g/l as shown in Table 2 (serial no. 1). The MRR predicted obtained from the optimal solution is

slightly lower than the experimental value. Moreover, from the 3D response of MRR (Fig. 5), it can be clearly seen that the MRR decreases if the pulse duration and duty cycle increases. So, it indicates that proper selection of process parameter level gives the maximum MRR. From Table 2 (experimental results no. 1), the minimum MRR is 0.987 mm^3/min at peak current = 20 A, pulse-on = 200 μs, duty cycle = 24%, and MWCNT powder concentration = 6 g/l. On the other hand, the minimum MRR obtained from the Pareto optimal front is 1.134 mm^3/min at peak current = 15.59 A, pulse-on = 169.61 μs, duty cycle = 65.17%, and MWCNT powder concentration = 4.08 g/l. The results show that the lower MRR obtained from optimal solution is much higher (about more than 1.7 times) as compared to the experimental value. This is because the MRR increases with increase of MWCNT powder concentration as more stable spark is generated in the machining zone.

3.2.2 Comparison of Experimental and Optimal SR

In the investigation and comparing of experiential results of SR with Pareto front, it is observed that the maximum SR is 1.987 μm at peak current = 20 A, pulse-on = 200 μs, duty cycle = 24%, and MWCNT powder concentration = 6 g/l corresponding to experiment no. 12 in Table 2. On the other hand, the maximum SR obtained from the Pareto optimal front is 1.4285 μm at peak current = 25 A, pulse-on = 250 μs, duty cycle = 80%, and MWCNT powder concentration = 0 g/l corresponding as shown in Table 2 (serial no. 1). The predicted SR value obtained from the optimal solution is very much lower than the experimental. Moreover, from the 3D response of SR (Fig. 6), it can be clearly seen that the SR decreases if the pulse duration decreases. So, it indicates that proper selection of process parameter level gives the maximum SR. From the Table 2 (experimental results no. 17), the minimum SR is 1.305 μm at peak current = 5 A, pulse-on = 150 μs, duty cycle = 40%, and MWCNT powder concentration = 4 g/l corresponding. On the other hand, the minimum SR obtained from the Pareto optimal front is 1.097 μm at peak current = 15.59 A, pulse-on = 169.61 μs, duty cycle = 65.17%, and MWCNT powder concentration = 4.08 g/l corresponding. The results show that the lower SR obtained from optimal solution is much higher (about more than 2.66 times) as compared to the experimental value. This is because the SR decreases with increase of MWCNT powder concentration as more stable spark is generated in the machining zone.

4 Conclusions

In this chapter, particle swarm optimization (PSO) is used for the multi-objective optimization of process parameters of MWCNT mixed-EDM process. The following conclusions are drawn after the critical observation of the results obtained:

1. The MRR increases with peak current, pulse duration, duty factor, and MWCNT powder concentration. The addition of MWCNT in dielectric fluid increases the uniformity and spark locations, as a result, more materials is removed from workpiece surface in comparison to EDM only.
2. The SR increases with peak current, pulse duration, and duty factor. It decreases with increase of MWCNT powder concentration, but, after 4 g/l, it starts increasing. The addition of MWCNT in dielectric fluid increases the discharge gap; as a result the reduced level of thermal energy caused the formation of micron and sub-micron debris, thereby improved the surface finish.
3. The MO-PSO provides a number of combinations of process parameters in comparison to experimental values, which indicates that proper selection of process parameters enhances machining efficiency.
4. The combinations of high peak current, pulse duration, duty factor, powder concentration are more suitable for getting higher value of MRR.
5. The combination of low peak current, moderate pulse duration, high duty factor, and 2–4 g/l MWCNT powder concentration are more suitable for the better surface finish.
6. The MO-PSO provides set of optimal solutions as presented in Pareto front. The optimum solutions facilitate for process engineer to select the optimal value of control parameters depending upon product requirement.

References

1. Buschmann R (2006) Preforms for the reinforcement of light metals—manufacture, applications and potential. In: Kainer KU (ed) Metal matrix composites: custom-made materials for automotive and aerospace engineering. Wiley-VCH Verlag GmbH & Co. KGaA, Weinheim, pp 77–94
2. Pai BC, Pillai RM, Satyanarayana KG (1998) Light metal matrix composites—present status and future strategies. NML, Jamshedpur, pp 26–40
3. Antil P, Singh S, Manna A (2017) Glass fibers/SiC_p reinforced epoxy composites: effect of environmental conditions. J Compos Mater 52(9):1253–1264
4. Antil P, Singh S, Manna A (2018) Effect of reinforced SiC particulates of different grit size on mechanical and tribological properties of hybrid PMCs. Mater Today Proc 5(2):8073–8079
5. Antil P, Singh S, Manna A (2018) Analysis on effect of electroless coated SiC_p on mechanical properties of polymer matrix composites. Part Sci Technol. https://doi.org/10.1080/02726351.2018.1444691 (In press)
6. Weinert K, Lange M, Petzoldt V (2002) Machining of metal matrix composites. In: Proceedings of ESDA2002: 6th Biennial conference on engineering systems, design and analysis, Istanbul, Turkey, 8–11 July 2002. ASME, New York
7. Muthuramalingam T, Mohan B (2015) A review on influence of electrical process parameters in EDM process. Arch Civil Mech Eng 15:87–94
8. Antil P, Singh S, Manna A (2017) Electrochemical discharge drilling of sic reinforced polymer matrix composite using Taguchi's grey relational analysis. Arab J Sci Eng 43(3):1257–1266
9. Muller F, Monaghan J (2000) Non-conventional machining of particle reinforced metal matrix composite. Int J Mach Tools Manuf 40(9):1351–1366
10. Rajurkar KP (1994) Nontraditional manufacturing processes (Chap. 13). In: Handbook of design manufacturing and automation. Wiley, USA

11. Abbas NM, Solomon DG, Bahari MF (2007) A review on current research trends in electrical discharge machining (EDM). Int J Mach Tools Manuf 47:1214–1228
12. Prakash C, Kansal HK, Pabla BS, Puri S, Aggarwal A (2016) Electric discharge machining a potential choice for surface modification of metallic implants for orthopedics applications: a review. Proc Inst Mech Eng Part B J Eng Manuf 230(2):331–353. https://doi.org/10.1177/0954405415579113
13. Prakash C, Kansal HK, Pabla BS, Puri S (2015) Processing and characterization of novel biomimetic nanoporous bioceramic surface on β-Ti implant by powder mixed electric discharge machining. J Mater Eng Perform 24:3622–3633. https://doi.org/10.1007/s11665-015-1619-6
14. Prakash C, Uddin MS (2017) Surface modification of β-phase Ti implant by hydroxyapatite mixed electric discharge machining to enhance the corrosion resistance and in-vitro bioactivity. Surf Coat Technol 236(Part A):134–145. https://doi.org/10.1016/j.surfcoat.2017.07.040
15. Kumar S, Singh R, Singh TP, Sethi BL (2009) Surface modification by electrical discharge machining: a review. J Mater Process Technol 209:3675–3687
16. Garg RK, Singh KK, Sachdeva A, Sharma VS, Ojha K, Singh S (2010) Review of research work in sinking EDM and WEDM on metal matrix composite materials. Int J Adv Manuf Technol 50:611–624
17. Agrawal SS, Yadava V (2016) Development and experimental study of surface-electrical discharge diamond grinding of Al–10 wt%SiC composite. J Inst Eng India Ser C 97:1. https://doi.org/10.1007/s40032-015-0183-z
18. Shabgard MR, Alenabi H (2015) Ultrasonic assisted electrical discharge machining of Ti–6Al–4V alloy. Mater Manuf Process 30(8):991–1000. https://doi.org/10.1080/10426914.2015.1004686
19. Dwivedi AP, Choudhury SK (2016) Effect of tool rotation on MRR, TWR and surface integrity of AISI-D3 steel using rotary EDM process. Mater Manuf Process. https://doi.org/10.1080/10426914.2016.1140198
20. Pirani C, Iacono F, Generali L, Sassatelli P, Nucci C, Lusvarghi L, Gandolfi MG, Prati C (2015) HyFlex EDM: superficial features, metallurgical analysis and fatigue resistance of innovative electro discharge machined NiTi rotary instruments. Int Endod J. https://doi.org/10.1111/iej.12470
21. Krishna ME, Patowari PK (2014) Parametric study of electric discharge coating using powder metallurgical green compact electrodes. Mater Manuf Process 29(9):1131–1138. https://doi.org/10.1080/10426914.2014.930887
22. Muthuramalingam T, Mohan B, Jothilingam A (2014) Effect of tool electrode resolidification on surface hardness in electrical discharge machining. Mater Manuf Process 29(11–12):1374–1380
23. Gill AS, Kumar S (2016) Surface roughness and microhardness evaluation for EDM with Cu–Mn powder metallurgy tool. Mater Manuf Processes 31(4):514–521. https://doi.org/10.1080/10426914.2015.1070412
24. Shen Y, Liu Y, Zhang Y, Dong H, Sun P, Wang X, Zheng C, Ji R (2016) Effects of an electrode material on a novel compound machining of Inconel 718. Mater Manuf Process 31(7):845–851. https://doi.org/10.1080/10426914.2015.1019133
25. Ahmed A (2016) Deposition and analysis of composite coating on aluminum using Ti–B4C powder metallurgy tools in EDM. Mater Manuf Process 31(6):467–474. https://doi.org/10.1080/10426914.2015.1025967
26. Pecas P, Henriques E (2008) Effect of the powder concentration and dielectric flow in the surface morphology in electrical discharge machining with powder-mixed dielectric (PMD-EDM). Int J Adv Manuf Technol 37:1120–1132
27. Pecas P, Henriques E (2008) Electrical discharge machining using simple and powder mixed dielectric: the effect of the electrode area on the surface roughness and topography. J Mater Process Technol 200:250–258
28. Prakash C, Kansal HK, Pabla BS, Puri S (2015) Potential of powder mixed electric discharge machining to enhance the wear and tribological performance of β-Ti implant for orthopedic applications. J Nanoeng Nanomanuf 5(4):261–269. https://doi.org/10.1166/jnan.2015.1245

29. Prakash C, Kansal HK, Pabla BS, Puri S (2016) Multi-objective optimization of powder mixed electric discharge machining parameters for fabrication of biocompatible layer on β-Ti alloy using NSGA-II coupled with Taguchi based response surface methodology. J Mech Sci Technol 30(9):4195–4204. https://doi.org/10.1007/s12206-016-0831-0
30. Prakash C, Kansal HK, Pabla BS, Puri S (2016) Effect of surface nano-porosities fabricated by powder mixed electric discharge machining on bone-implant interface: an experimental and finite element study. Nanosci Nanotechnol Lett 8(10):815–826. https://doi.org/10.1166/nnl.2016.2255
31. Prakash C, Kansal HK, Pabla BS, Puri S (2017) Experimental investigations in powder mixed electrical discharge machining of Ti–35Nb–7Ta–5Zr β–Ti alloy. Mater Manuf Process 32(3):274–285. https://doi.org/10.1080/10426914.2016.1198018
32. Singh B, Kumar J, Kumar S (2016) Investigation of the tool wear rate in tungsten powder-mixed electric discharge machining of AA6061/10%SiCp composite. Mater Manuf Process 31(4)
33. Singh B, Kumar J, Kumar S (2015) Influences of process parameters on MRR improvement in simple and powder-mixed EDM of AA6061/10%SiC composite. Mater Manuf Process 30(3)
34. Singh B, Kumar J, Kumar S (2014) Experimental investigation on surface characteristics in powder-mixed electrodischarge machining of AA6061/10%SiC composite. Mater Manuf Process 29(3)
35. Mohan B, Rajadurai A, Satyanarayana KG (2002) Effect of SiC and rotation of electrode on electric discharge machining of Al-SiC composite. J Mater Process Technol 124:297–304
36. Sidhu SS, Batish A, Kumar S (2013) Neural network-based modeling to predict residual stresses during electric discharge machining of Al/SiC metal matrix composites. Proc Inst Mech Eng Part B J Eng Manuf 227(11), 1679–1692
37. Sidhu SS, Batish A, Kumar S (2014) Study of surface properties in particulate-reinforced metal matrix composites (MMCs) using powder-mixed electrical discharge machining (EDM). Mater Manuf Process 29(1)
38. Pecas P, Henriques E (2003) Influence of silicon powder-mixed dielectric on conventional electrical discharge machining. Int J Mach Tools Manuf 43(14):1465–1471
39. Prakash C, Kansal HK, Pabla BS, Puri S (2015) Powder mixed electric discharge machining an innovative surface modification technique to enhance fatigue performance and bioactivity of β-Ti implant for orthopaedics application. J Comput Inf Sci Eng 14(4):1–9. https://doi.org/10.1115/1.4033901
40. Talla G, Gangopadhayay S, Biswas CK (2017) State of the art in powder-mixed electric discharge machining: a review. Proc Inst Mech Eng Part B J Eng Manuf 231(14):2511–2526
41. Ojha K, Garg RK, Singh KK (2011) Parametric optimization of PMEDM process using chromium powder mixed dielectric and triangular shape electrodes. J Miner Mater Charact Eng 10(11):1087–1102
42. Singh S, Yeh MF (2012) Optimization of abrasive powder mixed EDM of aluminum matrix composites with multiple responses using gray relational analysis. J Mater Eng Perform 21(4):481–491
43. Kumar S, Singh R, Singh TP, Sethi BL (2009) Comparison of material transfer in electrical discharge machining of AISI H13 die steel. J Mech Eng Sci 223(7):1733–1740
44. Kumar S, Batra U (2012) Surface modification of die steel materials by EDM method using tungsten powder mixed dielectric. J Manuf Process 14:35–40
45. Hu FQ, Cao FY, Song BY, Hou PJ, Zhang Y, Chen K, Wei JQ (2013) Surface properties of SiCp/Al composite by powder-mixed EDM. Procedia CIRP 6:101–106
46. Jahan MP, Rahman M, Wong YS (2011) Study on the nano-powder-mixed sinking and milling micro-EDM of WC-Co. Int J Adv Manuf Technol 53:167–180
47. Prihandana GS, Mahardika M, Hamdi M, Wong YS, Mitsui K (2011) Accuracy improvement in nanographite powder-suspended dielectric fluid for micro-electrical discharge machining processes. Int J Adv Manuf Technol 56:143–149
48. Baseri H, Sadeghian S (2016) Effects of nanopowder TiO_2-mixed dielectric and rotary tool on EDM. Int J Adv Manuf Technol 83(1–4):519–528

49. Mai C, Hocheng H, Huang S (2012) Advantages of carbon nano tubes in electrical discharge machining. Int J Adv Manuf Technol 59(1–4):111–117
50. Izman S, GHodsiyeh D, Hamed T, Rosliza R, Rezazadeh M (2012) Effects of adding multiwalled carbon nanotube into dielectric when EDMing titanium alloy. Adv Mater Res 463–464:1445–1449
51. Prabhu S, Vinayagam BK (2010) Analysis of surface characteristics of AISI D2 tool steel material using EDM process with Single wall carbon nano tubes. Int J Eng Technol 2(1):35–41
52. Prabhu S, Vinayagam BK (2012) Modeling the machining parameters of AISI D2 tool steel material with multi wall carbon nano tube in electrical discharge machining process using response surface methodology. Int J Phys Sci 7(2):297–305
53. Prabhu S, Vinayagam BK (2009) Effect of graphite electrode material on EDM of AISI D2 tool steel with multiwall Carbon Nanotube using regression analysis. Int J Eng Stud 1(2):93–104
54. Sari MM, Noordin MY, Brusa S (2013) Role of multi-wall carbon nanotubes on the main parameters of the electrical discharge machining (EDM) process. Int J Adv Manuf Technol 68(5–8):1095–1102
55. Shabgard M, Khosrozadeh B (2017) Investigation of carbon nanotube added dielectric on the surface characteristics and machining performance of Ti–6Al–4V alloy in EDM process. J Manuf Process 25:212–219
56. Ikram A, Mufti NA, Saleem MQ, Khan AR (2013) Parametric optimization for surface roughness, kerf and MRR in wire electrical discharge machining (WEDM) using Taguchi design of experiment. J Mech Sci Technol 27(7):2133–2141
57. Dao TP, Huang SC (2015) Robust design for a flexible bearing with 1-DOF translation using the Taguchi method and the utility concept. J Mech Sci Technol 29(8):3309–3320
58. Jung JH, Kwon WT (2010) Optimization of EDM process for multiple performance characteristics using Taguchi method and Grey relational analysis. J Mech Sci Technol 24(5):1083–1090
59. Santhanakumar M, Adalarasan R, Rajmohan M (2016) Parameter design for cut surface characteristics in abrasive waterjet cutting of Al/SiC/Al_2O_3 composite using grey theory based RSM. J Mech Sci Technol 30(1):371–379
60. Gopalakannan S, Senthilvelan T (2014) Optimization of machining parameters for EDM operations based on central composite design and desirability approach. J Mech Sci Technol 28(3):1045–1053
61. Tao Z, Yaoyao S, Xiaojun L, Tianran H (2016) Optimization of abrasive flow polishing process parameters for static blade ring based on response surface methodology. J Mech Sci Technol 30(3):1085–1093
62. Yadav RN, Yadava V, Singh GK (2014) Application of non-dominated sorting genetic algorithm for multi-objective optimization of electrical discharge diamond face grinding process. J Mech Sci Technol 28(6):2299–2306
63. Bharti PS, Maheshwari S, Sharma C (2012) Multi-objective optimization of electric-discharge machining process using controlled elitist NSGA-II. J Mech Sci Technol 26(6):1875–1883
64. Padhee S, Nayak N, Panda SK, Dhal PR, Mahapatra SS (2012) Multi-objective parametric optimization of powder mixed electro-discharge machining using response surface methodology and non-dominated sorting genetic algorithm. Sadhana 37(2):223–240
65. Mohanty S, Mishra A, Nanda BK, Routara BC (2017) Multi-objective parametric optimization of nano powder mixed electrical discharge machining of AlSiCp using response surface methodology and particle swarm optimization. Alexandria Eng J
66. Kennedy J, Eberhart R (1995) Particle swarm optimization. In: Proceedings of the IEEE international conference on neural networks, vol 4, pp 1942–1948. IEEE
67. Kalayci CB, Gupta SM (2013) A particle swarm optimization algorithm with neighborhood-based mutation for sequence dependent disassembly line balancing problem. Int J Adv Manuf Technol 69(1–4):197–209
68. Jia Q, Seo Y (2013) An improved particle swarm optimization for the resource-constrained project scheduling problem. Int J Adv Manuf Technol 67(9–12):2627–2638
69. Li X, Gao L, Wen X (2012) Application of an efficient modified particle swarm optimization algorithm for process planning. Int J Adv Manuf Technol 67(5–8):1355–1369

70. Yildiz AR, Solanki KN (2012) Multi-objective optimization of vehicle crashworthiness using a new particle swarm based approach. Int J Adv Manuf Technol 59(1–4):367–376
71. Yang WA, Guo Y, Liao WH (2011) Optimization of multi-pass face milling using a fuzzy particle swarm optimization algorithm. Int J Adv Manuf Technol 54(1–4):45–57
72. Costa A, Celano G, Fichera S (2011) Optimization of multi-pass turning economies through a hybrid particle swarm optimization technique. Int J Adv Manuf Technol 53(5–8):421–433
73. Srinivas J, Giri R, Yang SH (2009) Optimization of multi-pass turning using particle swarm intelligence. Int J Adv Manuf Technol 40(1–2):56–66
74. Aliyu AAA, Abdul-Rani AM, Ginta TL, Prakash C, Axinte E, Razak MA, Ali S (2017) A review of additive mixed-electric discharge machining: current status and future perspectives for surface modification of biomedical implants. Adv Mater Sci Eng

Investigating the Polymeric Composites for Online Repair and Maintenance

Ranvijay Kumar, Rupinder Singh and I. P. S. Ahuja

Abstract Polymers are one of the most commonly used materials in engineering applications (such as structure, pipelines, etc.). Infield practices, whenever a crack/leakage develops in polymeric pipelines, there is need of quick online repair/maintenance. In such cases, replacement of the whole pipeline section can lead to high downtime and cost. The online repair/maintenance of those cracks/leakages can be performed with the application of friction/friction stir welding but it needs the development of polymeric composite material that is compatible with substrate (pipeline) materials. This study outlines the development of such polymeric composites on the basis of maintaining rheological properties. In this chapter, an experimental investigations have been reported for two differently characterized polymers (namely, acrylonitrile butadiene styrene (ABS) polyamide (PA)6), which were reinforced with Al metal powder by twin screw extrusion process. The results suggested that ABS reinforced with 15% Al metal powder by weight (ABS–15Al) and PA6 with 50% Al (PA6–50Al) resulted in similar range of melt flow index (MFI) as 11.57 g/10 min and 11.97 g/10 min, respectively, and confirmed the compatibility for joining of both polymer by friction/friction stir welding. The functional prototypes have been printed on commercial fused deposition modeling (FDM)-based 3D printer, (by using feedstock filament prepared with standard twin screw extrusion process). The mechanical properties of composite feedstock filaments were investigated for optimization of extrusion parameters. Additionally, friction stir welding has been performed to check the feasibility of joining of developed composite parts (prepared as functional prototypes) on FDM.

R. Kumar · I. P. S. Ahuja
Department of Mechanical Engineering, Punjabi University, Patiala, India
e-mail: ranvijayk12@gmail.com

I. P. S. Ahuja
e-mail: ahujaips@gmail.com

R. Kumar · R. Singh (✉)
Department of Production Engineering, Guru Nanak Dev Engineering College, Ludhiana, India
e-mail: rupindersingh78@yahoo.com

S. S. Sidhu et al. (eds.), *Futuristic Composites*, Materials Horizons: From Nature to Nanomaterials, https://doi.org/10.1007/978-981-13-2417-8_8

Keywords Friction stir welding · Twin screw extrusion · ABS · PA6 · DSC · MFI Tensile strength · Rapid tooling · Dissimilar thermoplastic

1 Brief of Composite Materials, Processing, Rapid Tooling, and Welding Applications

Polymeric composites are commercially prepared by extrusion or molding (e.g., injection molding, single screw extrusion, multi-screw extrusion, and casting processes) for its applicability in the engineering fields like automobile, structural, maintenance, etc. Previous studies have outlined that single screw and double screw extrusion are most widely used for polymer composite preparations. Twin screw extrusion has emerged as one of the advanced techniques which provide the better mixing, morphology, and mechanical characteristics over conventional extrusion process for composite preparations [1]. Different destructive or nondestructive testing (like X-ray diffraction (XRD), tensile properties, microhardness, differential scanning calorimetry (DSC), scanning electron microscopy (SEM), small-Angle X-ray scattering (SAXS) and transmission electron microscopy (TEM), etc.) have suggested significant improvement of polymeric composite as compared to virgin polymers [2]. Injection molding process has been widely accepted for the development of multi-functional components with improved material properties. Some of the recent studies highlighted the cross-linking of PA6 polymer chain with the use of diamond Nanoparticles in PA6 matrix, effect of inducing water in PA6, and potential of PA6 for various industrial applications. While using the twin screw extrusion for feedstock production, the proper time should be given for the heating so that heat zone should be properly formed inside the heater [3]. This will help the blend to heat uniformly and then, it could be extruded easily through screws. Overheating of the material should be avoided otherwise it can seriously damage the blend and later this can affect the mechanical properties of the blend [4–6].

The FDM is one of the cost-effective additive manufacturing processes, which is mostly applicable for the preparations of functional/nonfunctional prototypes. This has now revolutionized the engineering field for preparing rapid tooling. The rapid tools prepared by FDM applied in the friction/friction stir welding concept can be applied as repair/maintenance tool [7–12]. As per prospective of repair maintenance of pipelines, welding/joining of two similar materials is quite common and various studies have been reported as welding of ABS–ABS, PA–PA, LDPE (Low-density polyethylene)–LDPE, HDPE (High-density polyethylene)–HDPE, etc., as these materials possessed the same characteristics [13–15]. But, while joining/welding of two dissimilar polymeric materials, it is not that easy to join/weld because both polymer exhibit different properties (such as melt flow index, melting point, molecular weight, etc.) [16–18]. Some studies have reported that by maintaining melt flow index of two different polymers (such as ABS and PA6) by metal powder reinforcement (in the close range), there is high possibility of joining [19–24]. As the literature

reported, it was found that specimen sheet of PMMA (Poly methyl methacrylate) with dimensions of $100 \times 25 \times 3$ mm needs 500–200 rpm, 5.5–12 s welding time, three bars pressure, and insert depth of 3.5–4 mm [16, 17]. Friction-based injection clinching joining technique (F-ICJ) for joining of PEI-AA6082-T6 sheets needs the rotational speed of 7500–20,000 rpm, 0.2–0. MPa axial pressure, and 2500–5000 ms welding time [25]. Welding/joining of 2 mm sheets of PA6 laminates reinforced by carbon molecules through friction welding concept needs 1000–3000 rpm of rotational speed, 1.8–2.2 mm insert depth, and 3.6–7.5 s frictional welding time [14]. It has been reported that friction welding for sheets of 10 mm PMMA needs 700 rpm, transverse speed of 25 mm/min, 15–35 mm shoulder dimensions, and 5–6 mm insert diameters [16]. Similarly, for sheets of $100 \times 100 \times 3$ mm having curvature of 2.7 mm radius of AA6082-PP (polypropylene) sheets need 1000 rpm, 100 mm/min transverse speed, 3000 N thrust, and 3–7 mm insert diameter [18]. While joining/welding of polycarbonate (PC)–PC of $90 \times 20 \times 3$ mm through friction stir welding, it has been reported that tool plunge rate between 8 and 46 mm/min, tool rotation 1500–5400 rpm, preheating time 0–20 s, dwell time 0–20 s, and waiting time of 0–20 s are required [15]. As most of the studies have suggested that similar material joining is possible but dissimilar material needs to be made compatible for possible joining/welding application. In the present study, efforts are going to be made to develop the rapid tool for prospective of repair/maintenance of pipelines by the twin screw extrusion and FDM. Additionally, welding practices have been conducted to check the feasibility of the joining of metal powder reinforced polymeric composites.

2 Preparations of Feedstock Filaments of Polymeric Composites

The friction/friction stir welding of two virgin dissimilar polymers during pilot experimentations was failed. In the present study, the processing of polymeric composite has been discussed for the preparations of feedstock filaments. Feedstock filaments of FDM have been used for the production of rapid tooling, which was finally applied in welding/joining applications for repair/maintenance.

2.1 Materials

The primary aim of this study is to establish the compatibility of two dissimilarly characterized polymeric materials by preparations of polymeric composite. ABS and PA6 have different melt flow index (MFI), melting point, peak load, peak strength, and hardness properties (see Table 1).

Table 1 Materials property of commercially pure ABS and PA6

Material	Melting point (°C)	Melt flow index (g/10 min)	Shore *D* hardness	Peak load (N)	Peak strength (MPa)
ABS	201.22	8.76	73.0	59.2	23.40
PA6	219.35	23.27	71.5	203.0	94.90

Al metal powder of commercially pure grade (99.9% purity) has been taken of 50 μm grains size for the reinforcement in polymeric matrix. The polymeric composites have been prepared by incorporating the Al metal powders in the ABS and PA6 matrix by the twin screw extrusion.

2.2 MFI Evaluation

As per material testing data of ABS and PA6 (see Table 1), joining of ABS and PA6 were not possible through friction welding (during pilot experimentation stage). In particular application of pipeline repair/maintenance by friction/friction stir welding, it is must to have the compatibility between two dissimilar polymeric materials. The MFI of polymeric material can be modified by preparations of polymers composites, i.e., polymer and metal powder in some definite proportion. MFI is one of the rheological properties which can be determined by a melt flow tester. The material deposited through the heating outlet can be considered as their MFI in 10 min [20–22]. The unit of MFI is g/10 min. Figure 1 shows the experimental view of a MFI tester used in the present study. MFI was performed under the ASTM D1238 as applying 3.8 kg weight and 230 °C temperature.

The MFI results of Al reinforced ABS and PA6 polymeric composites are shown in Fig. 2.

The results suggested that MFI of ABS with 15% Al powder (ABS–15Al) and PA6 with 50% (PA6–50Al) obtained in very close range of MFI as 11.57 g/10 min and 11.97 g/min, respectively. These Al reinforcement levels have been selected for composite preparations by twin screw extrusion for development of rapid tooling.

2.3 DSC Analysis

DSC is an analytical setup for thermal properties determination. Initially, the material has undergone a heating up to 250 °C to remove the thermal histories associated with material. For this study, melting point of ABS, PA6, ABS–15Al, and PA6–50Al were evaluated under the continuous heating and continuous cooling as endothermic and exothermic reactions.

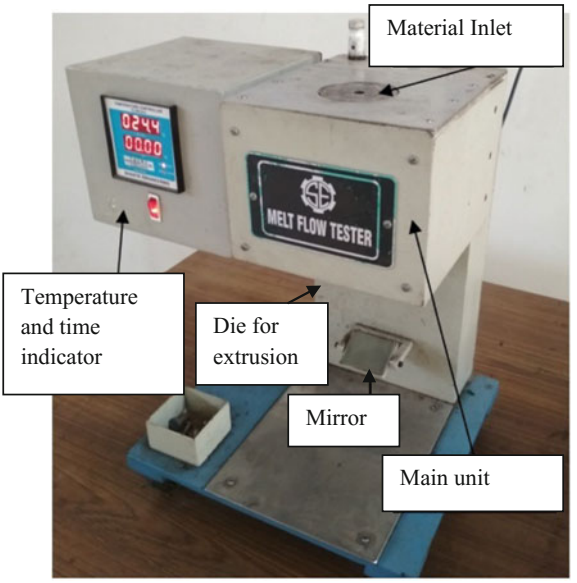

Fig. 1 MFI tester (as per ASTM D1238)

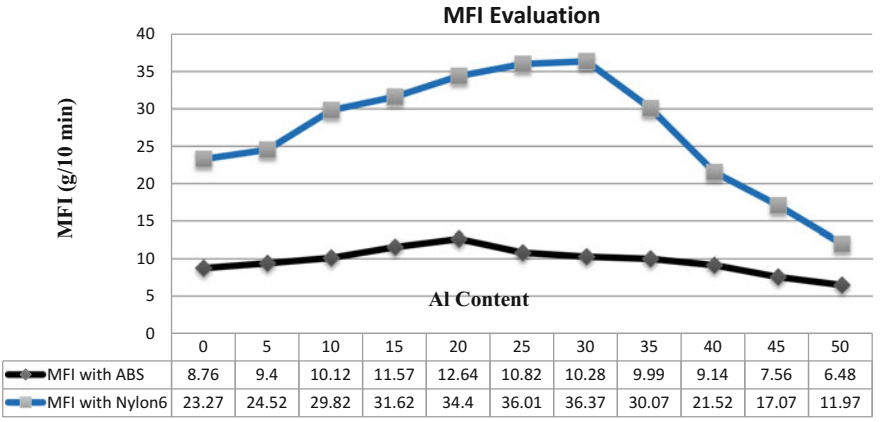

	0	5	10	15	20	25	30	35	40	45	50
MFI with ABS	8.76	9.4	10.12	11.57	12.64	10.82	10.28	9.99	9.14	7.56	6.48
MFI with Nylon6	23.27	24.52	29.82	31.62	34.4	36.01	36.37	30.07	21.52	17.07	11.97

Fig. 2 MFI trends for Al reinforced ABS and PA6 composites

Endothermic changes: Under continuous heating of 30–250 °C at 10 °C/min and N_2 gas flow of 50 ml/min, exothermic reactions were performed to check the melting points of the materials.

Exothermic reactions: Under continuous cooling of 250–30 °C at −10 °C/10 min and gas flow of 50 ml/min, exothermic reactions were performed to solidify the material for next thermal cycles.

Figure 3 shows DSC thermographs for virgin PA6. Finally, the melting points of the mentioned materials were evaluated (see Table 2). The DSC results suggested

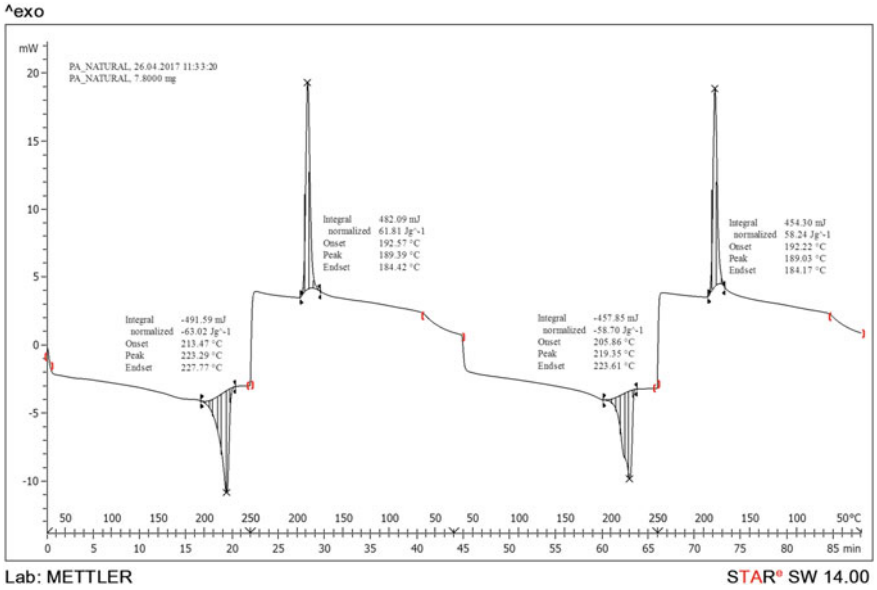

Fig. 3 DSC-based thermographs for virgin PA6

Table 2 Melting point of ABS, PA6, ABS–15Al, and PA6–50Al

Material	ABS	PA6	ABS–15Al	PA6–50Al
Melting point	201.22	219.35	218.11	218.27

that PA6 was appeared as more thermally stable than ABS as the melting point of PA6 was not changed largely after 50% Al reinforcement to it. Incorporating 15% Al content to the ABS was resulted in the melting point of 218.11 °C which was almost closer to the melting of PA6–50Al having 218.27 °C. From here, it resulted in an interesting fact that maintaining melt flow by Al reinforcement also contributed in the similar melting points.

2.4 Feedstock Filament Preparations

In commercial practices, screw extrusion processes are employed for the preparation of the feedstock composites for FDM. There are some of the classifications which are available for the preparations of polymeric composite as feedstock. The detailed classification of extrusion processes is given in Fig. 4.

For the current study, twin screw extrusion with intermeshing and corotating screws have been used to form feedstock polymeric composite.

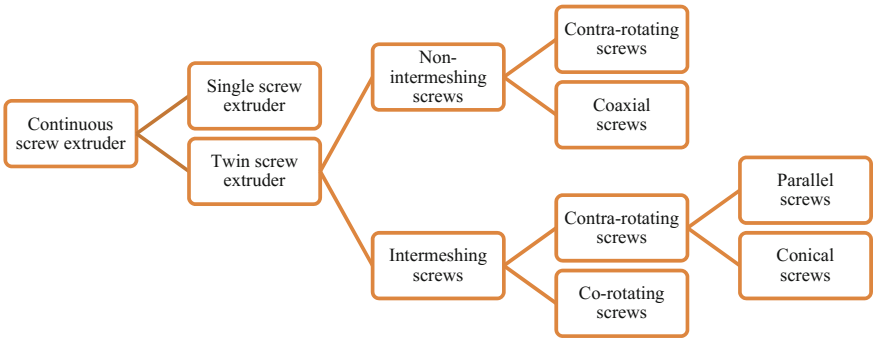

Fig. 4 Detailed classification of extrusion process

Table 3 Processing conditions of ABS–15Al and PA–50Al for feedstock preparations

Materials/factors	Temperature (°C)	Applied load (kg)	Screw speed (rpm)
ABS–15Al	220, 225, 230	10, 15, 20	20, 25, 30
PA6–50Al	240, 245, 250	10, 15, 20	15, 20, 30

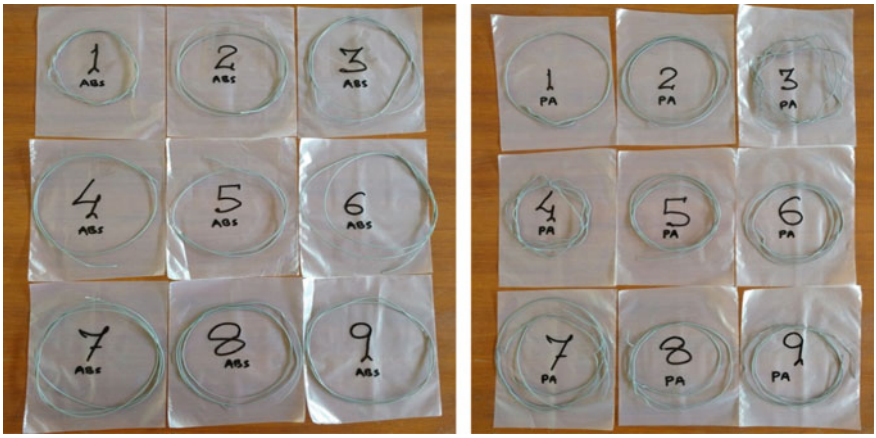

Fig. 5 Feedstock filaments of ABS–15Al and PA6–50Al

Based upon the pilot experimentation, it was found that uniform feedstock was obtained under the given range of input process parameters (see Table 3). So, level of temperature, applied load, and screw speed have been selected based upon pilot experimentations.

Based upon Table 3, Taguchi L9 orthogonal array as design of experiment technique has been used to optimize the mechanical properties for feedstock filaments of 1.75 mm diameter. Figure 5 shows the prepared feedstock filament of ABS–15Al and PA6–50Al.

Table 4 Mechanical properties of ABS–15Al feedstock filaments as per Taguchi L9 OA

Exp. No.	Temperature (°C)	Applied load (kg)	Screw speed (rpm)	Break load (N)	Break strength (MPa)
1	220	10	20	35.21	15.63
2	220	15	25	36.58	16.16
3	220	20	30	44.13	19.27
4	225	10	25	33.85	15.76
5	225	15	30	39.67	18.21
6	225	20	20	27.20	15.01
7	230	10	30	35.21	15.77
8	230	15	20	21.47	12.10
9	230	20	25	22.84	12.83

Table 5 Mechanical properties of PA6–50Al feedstock filaments as per Taguchi L9 OA

Exp. No.	Temperature (°C)	Applied load (kg)	Screw speed (rpm)	Break load (N)	Break strength (MPa)
1	240	10	15	29.84	10.14
2	240	15	20	36.58	12.40
3	240	20	25	45.41	15.36
4	245	10	20	36.13	15.30
5	245	15	25	42.95	18.71
6	245	20	15	58.42	22.79
7	250	10	25	26.39	11.81
8	250	15	15	33.12	14.38
9	250	20	20	35.28	15.63

A Taguchi-based design of L9 orthogonal array has been developed separately for ABS–15Al and PA6–50Al as per Table 3. Tables 4 and 5 show evaluated mechanical properties of feedstock filaments under different experimental runs.

3 Results and Discussions

The "Larger is better" case has been selected for break load as well as break strength as the desired maximum always for feedstock filaments. The signal-to-noise (SN) ratios have been determined by the given expressions:

For properties which desired Larger is better, the SN ratios can be calculated as

$$\eta = -10 \log\left[\frac{1}{n}\sum_{k=1}^{n}\frac{1}{y^2}\right]$$

Table 6 SN ratio for feedstock properties at different experimental conditions

	ABS–15Al		PA6–50Al	
Exp. No.	SN ratio of break load	SN ratio break strength	SN ratio of break load	SN ratio break strength
1	30.93	23.87	29.49	20.12
2	31.26	24.16	31.26	21.86
3	32.89	25.69	33.14	23.72
4	30.59	23.95	31.15	23.69
5	31.96	25.20	32.65	25.44
6	28.69	23.52	35.33	27.15
7	30.93	23.95	28.42	21.44
8	26.63	21.65	30.40	23.15
9	27.17	22.16	30.95	23.87

For properties which desired Smaller is better, the SN ratios can be calculated as

$$\eta = -10 \log\left[\frac{1}{n}\sum_{k=1}^{n} y^2\right]$$

where η is SN ratio, n is the No. of experiment, and y is the material properties at experiment No. k. Table 6 shows the variation of SN ratios over input process variable for break load and break strength in case of ABS–15Al and PA6–50Al.

The calculation of SN ratio has suggested that for break load and break strength of ABS–15Al filaments temperature of 230 °C, 10 kg applied load, and 30 rpm of screw speed contributed mostly for the changes in the output parameter. Similarly, in case of break load and break strength of PA6–50Al, 245 °C temperature, applied load of 20 kg, and screw speed of 15 rpm have been mostly contributed for changes over output properties (see Fig. 6).

The analysis of variance (ANOVA) table has been developed through Minitab analysis software. Therefore, considering the case of break load of ABS–15Al, the ANOVA table has been developed (see Table 7). Table suggested that P-value was evaluated lesser than 0.05 for temperature and screw speed. As P-value was appeared lesser than 0.05, so that temperature and screw speed were significant factors for experimentation.

Delta value is the difference between the maximum and minimum value of SN ratio. As delta value was achieved maximum in case of temperature, so it was ranked 1 and minimum in case of applied load, it was ranked 3 for the contribution of SN ratio during experimentation (see Table 8).

The optimum value of SN ratio of break load for ABS–15Al can be predicted by using the following equation:

$$\eta_{\text{opt}} = m + (m_{\text{A1}} - m) + (m_{\text{B1}} - m) + (m_{\text{C3}} - m) \quad (1)$$

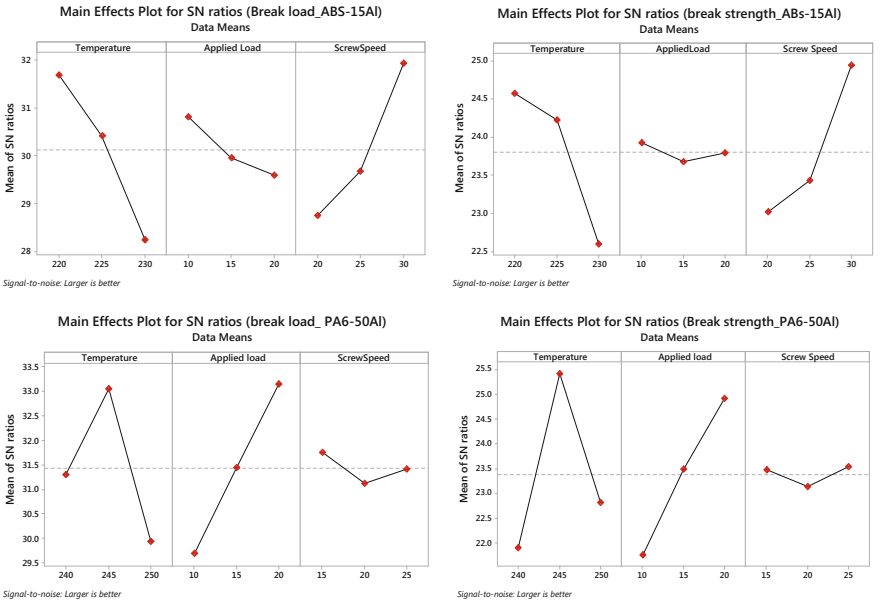

Fig. 6 Linear graphical model of SN ratio for ABS–15Al and PA6–50Al

Table 7 Analysis of variance for SN ratios

Source	DF	Seq SS	Adj SS	Adj MS	*F*	*P*
Temperature	2	18.2454	18.2454	9.12269	131.19	0.008
Applied load	2	2.4001	2.4001	1.20004	17.26	0.055
Screw speed	2	16.0439	16.0439	8.02193	115.36	0.009
Residual error	2	0.1391	0.1391	0.06954		
Total	8	36.8284				

Table 8 Response table for signal-to-noise ratios

Level	Temperature	Applied load	Screw speed
1	31.70	30.82	28.75
2	30.42	29.96	29.68
3	28.25	29.59	31.93
Delta	3.45	1.23	3.18
Rank	1	3	2

where "m" is the overall mean of SN ratio, m_{A1} is the mean of SN ratio for temperature at level 1, m_{B1} is the mean of SN ratio for the applied load at level 1, and m_{C3} is the mean of SN data for RPM at level 3.

Table 9 Predicted versus experimental value at optimized setup

Properties	ABS–15Al	PA6–50Al
Break load (N) (predicted/actual)	49.15/49.72	56.82/57.03
Break strength (MPa) (predicted/actual)	21.87/22.01	22.72/22.87

Now, for lesser is better by type case

$$y_{\text{opt}}^2 = (1/10)^{\eta\text{opt}/10} \tag{2}$$

for properties, larger is better type case

$$y_{\text{opt}}^2 = (10)^{\eta\text{opt}/10} \tag{3}$$

Calculation:

The overall mean of SN ratio (m) was taken from Table 6

$$m = 30.31 \text{ dB}$$

Now, from response table of signal-to-noise ratio, $m_{\text{A1}} = 31.70$, $m_{\text{B1}} = 30.82$, and $m_{\text{C3}} = 31.93$, (from Table 8).

Now taking Eq. (1), putting the values

$$\eta_{\text{opt}} = 30.31 + (31.70 - 30.31) + (30.82 - 30.31) + (31.93 - 30.31)$$
$$\eta_{\text{opt}} = 33.83$$

From Eq. (3), $y_{\text{opt}}^2 = (10)^{\eta\text{opt}/10}$

$$y_{\text{opt}}^2 = (10)^{33.83/10}$$
$$y_{\text{opt}} = 49.15 \text{ N}$$

The predicted optimum value for break load for ABS–15Al = 49.15 N.

In this way, by applying the abovementioned equation, predicted value can be determined towards optimization of process parameters. The break load and break strength values in the cases of ABS–15Al and PA–50Al have been predicted similarly (see Table 9).

Based upon Tables 7, 8 and 9; Fig. 7 shows the SEM-based photomicrographs for ABS–15% Al and PA6–50% Al samples at best setting suggested. As shown in Fig. 7, a uniform distribution of metallic powder was observed.

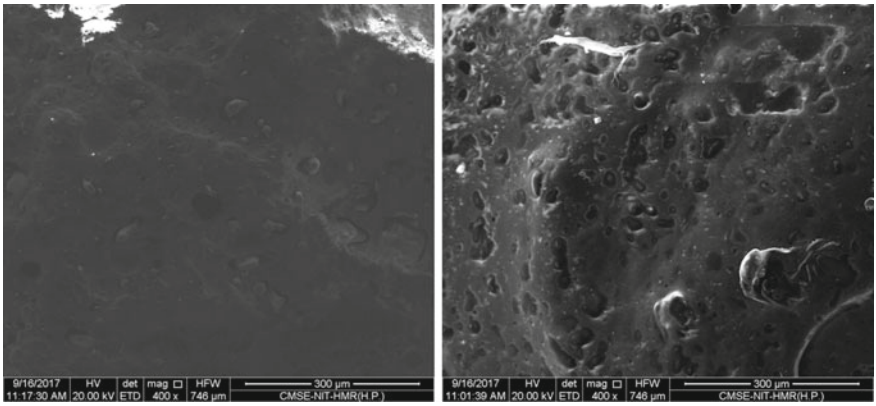

(a) ABS-15%Al (by weight) (b) PA6-50%Al (by weight)

Fig. 7 SEM of polymeric composites

Table 10 Properties of friction stir weld joints using rapid tool

Properties	Peak load (N)	Break load (N)	Elongation at peak (mm)	Elongation at break (mm)	Peak strength (MPa)	Break strength (MPa)
Values	49.9	44.9	2.85	2.85	4.16	3.75

4 Friction Stir Welding of Developed Polymeric Composite Material by Rapid Tooling

The FDM process has been used to print the rectangular sheets of $50 \times 30 \times 4$ mm and pin as rapid tool of 9 mm diameter. FDM processed these parts under maintaining some input process parameters. Under infill density of 0.8, 6 number of perimeter, deposition angle of 60°, nozzle diameter of 0.3 mm, filament diameter of 1.75 mm, honeycomb fill pattern, perimeter speed of 30 mm/s, infill speed of 60 mm/s, travel speed of 130 mm/s, extruder temperature of 250 °C, and bed temperature of 55 °C parts were prepared. Rectangular sheet was prepared with ABS–15Al, whereas PA6–50Al was used to fabricate the pin profile under the same processing conditions.

Friction stir welding on vertical milling setup with rotational speed of 1400 rpm, transverse speed of 30 mm/min, and taking 9 mm semi-consumable pin have been performed (see Fig. 8).

Table 10 shows the evaluated joint characteristic made by sheets of ABS–15Al with the application of semi-consumable rapid tool of PA6–50Al. The load versus deflection plot has been prepared using the evaluated mechanical properties (see Fig. 9). The load versus deflection explains that load-bearing capacity of joint was obtained as 4.99 Kgf and elongation of 2.85 m at breaking point.

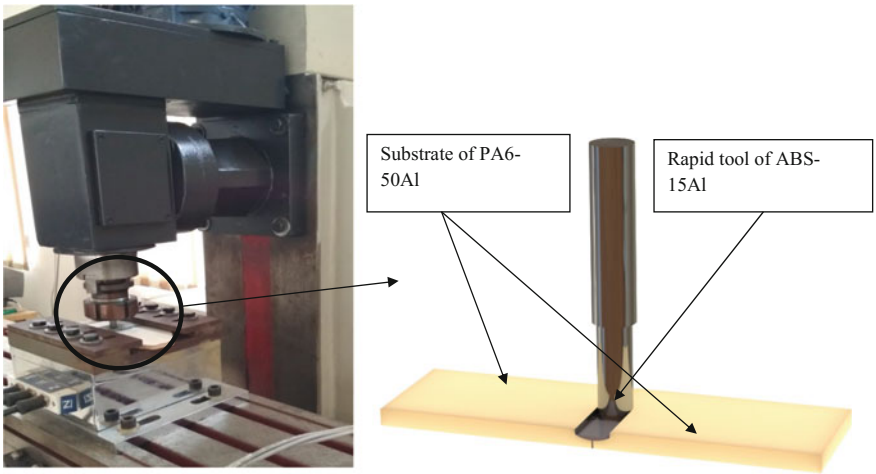

Fig. 8 Actual experimental view of the welding process with rapid tool

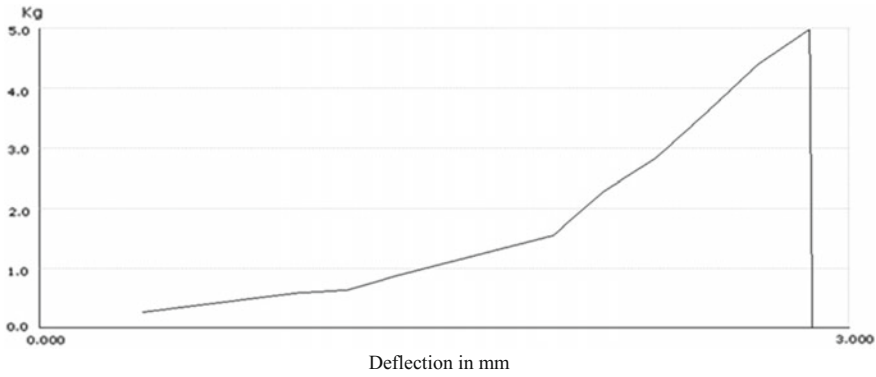

Fig. 9 Load versus deflection curve of joint made by friction stir welding

Figure 10 shows the photomicrograph of the weld zone, which ensures uniform dispersion of metallic reinforcement in polymeric matrix.

5 Summary

The following observations have been noted from our study for development of polymeric composite for its application in repair/maintenance of pipelines.

- Since friction/friction stir welding is an established process of joining of polymeric composite material, so it can be potentially applied in the repair/maintenance of leakages/cracks of pipelines those are generally made up of polymeric materials.

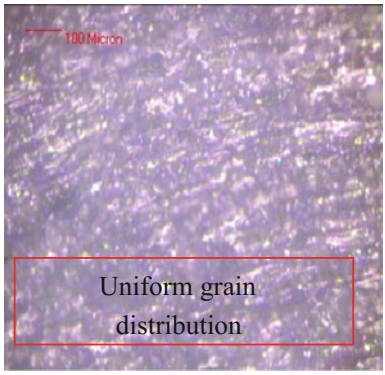

Fig. 10 Optical micrographs of welded pieces at 100×

- The repair/maintenance of pipeline can be performed by friction stir welding by developing the rapid tool of dissimilar polymeric composite material with maintained MFI.
- In the present case, ABS–15Al and PA6–50Al resulted in the similar MFI. The welding of ABS–15Al sheets by the rapid tool of PA6–50Al resulted in excellent weld characteristics of peak load of 49.9 N, break load of 44.9 N, 2.85 mm elongation, 4.16 MPa peak strength, and 3.75 MPa break strength.

Acknowledgements The authors are highly thankful to Board of research in nuclear science (BRNS) No: 34/14/10/2016-BRNS/34036 and University grant commission (UGC) F.30-66/2016 (SA-II) for providing financial assistance to carry out the research work.

References

1. Wagner JR Jr, Mount EM III, Giles HF Jr (2014) Extrusion: the definitive processing guide and handbook, 2nd edn
2. Process E twin-screw extrusion and applications. https://doi.org/10.3139/9781569906064.006
3. Singh R, Kumar R, Ranjan N (2018) Sustainability of recycled ABS and PA6 by banana fiber reinforcement: thermal, mechanical and morphological properties. J Inst Eng Ser C. https://doi.org/10.1007/s40032-017-0435-1
4. Ray S, Easteal AJ (2007) Advances in polymer-filler composites: macro to nano. Mater Manuf Process 22:741–749. https://doi.org/10.1080/10426910701385366
5. Olakanmi EO, Thompson OM, Vunain E et al (2016) Effects of *Daniellia oliveri* wood flour characteristics on the processing and functional properties of wood polymer composites. Mater Manuf Process 31:1073–1084. https://doi.org/10.1080/10426914.2015.1037895
6. Chaitanya S, Singh I (2017) Processing of PLA/sisal fiber biocomposites using direct- and extrusion-injection molding. Mater Manuf Process 32:468–474. https://doi.org/10.1080/10426914.2016.1198034
7. Singh R, Kumar R, Ranjan N et al (2018) On the recyclability of polyamide for sustainable composite structures in civil engineering. Compos Struct 184. https://doi.org/10.1016/j.compstruct.2017.10.036

8. Kumar R, Singh R, Ahuja IPS et al (2018) Friction welding for the manufacturing of PA6 and ABS structures reinforced with Fe particles. Compos Part B Eng 132:244–257. https://doi.org/10.1016/j.compositesb.2017.08.018
9. Singh R, Kumar R, Mascolo I, Modano M (2018) On the applicability of composite PA6-TiO2 filaments for the rapid prototyping of innovative materials and structures. Compos Part B Eng 143:132–140. https://doi.org/10.1016/J.COMPOSITESB.2018.01.032
10. Kumar R, Singh R, Hui D et al (2018) Graphene as biomedical sensing element: state of art review and potential engineering applications. Compos Part B Eng 134. https://doi.org/10.1016/j.compositesb.2017.09.049
11. Kumar R, Singh R, Ahuja IPS et al (2018) Weldability of thermoplastic materials for friction stir welding—a state of art review and future applications. Compos Part B Eng 137. https://doi.org/10.1016/j.compositesb.2017.10.039
12. Singh R, Kumar R, Feo L, Fraternali F (2016) Friction welding of dissimilar plastic/polymer materials with metal powder reinforcement for engineering applications. Compos Part B Eng 101. https://doi.org/10.1016/j.compositesb.2016.06.082
13. Squeo EA, Bruno G, Guglielmotti A, Quadrini F (2009) Friction stir welding of polyethylene sheets. The Annals of DUNANjREA DE JOS University of Galati Fascicle V. Technologies in Machine Building, ISSN. 1221–4566
14. Gonçalves J, Dos Santos JF, Canto LB, Amancio-Filho ST (2015) Friction spot welding of carbon fiber-reinforced polyamide 66 laminate. Mater Lett 159:506–509
15. Paoletti A, Lambiase F, Di Ilio A (2015) Optimization of friction stir welding of thermoplastics. Procedia CIRP 33:563–568
16. Simões F, Rodrigues DM (2014) Material flow and thermo-mechanical conditions during friction stir welding of polymers: literature review, experimental results and empirical analysis. Mater Des 59:344–351
17. Oliveira PHF, Amancio-Filho ST, Santos JF, Hage E Jr (2010) Preliminary study on the feasibility of friction spot welding in PMMA. Mater Lett 64:2098–2101
18. Buffa G, Baffari D, Campanella D, Fratini L (2016) An innovative friction stir welding based technique to produce dissimilar light alloys to thermoplastic matrix composite joints. Procedia Manuf 5:319–331. https://doi.org/10.1016/j.promfg.2016.08.028
19. Kumar R, Singh R, Ahuja IPS (2018) Investigations of mechanical, thermal and morphological properties of FDM fabricated parts for friction welding applications. Measurement 120:11–20
20. Singh R, Kumar R, Kumar S (2017) Polymer waste as fused deposition modeling feed stock filament for industrial applications. Ref Modul Mater Sci Mater Eng 1–12. https://doi.org/10.1016/b978-0-12-803581-8.04153-9
21. Singh R, Kumar R, Hashmi MSJ (2017) Friction welding of dissimilar plastic-based material by metal powder reinforcement. Elsevier Ltd
22. Singh R, Kumar R (2017) Development of low-cost graphene-polymer blended in-house filament for fused deposition modeling. Elsevier Ltd
23. Kumar R, Singh R (2018) Prospect of graphene for use as sensors in miniaturized and biomedical sensing devices. Ref Modul Mater Sci Mater Eng 1–13. https://doi.org/10.1016/b978-0-12-803581-8.10334-0
24. Singh R, Kumar R, Ahuja IS (2017) Thermal analysis for joining of dissimilar polymeric materials through friction stir welding BT. Ref Modul Mater Sci Mater Eng
25. Abibe AB, Sônego M, dos Santos JF et al (2016) On the feasibility of a friction-based staking joining method for polymer-metal hybrid structures. Mater Des 92:632–642

Investigation of Surface Properties of Al–SiC Composites in Hybrid Electrical Discharge Machining

Preetkanwal Singh Bains, Sanbir Singh, Sarabjeet Singh Sidhu, Sandeep Kaur and T. R. Ablyaz

Abstract In this research study, hybrid AJEDM (abrasive jet-assisted EDM) had been employed on the aluminum–silicon carbide composite (Al–SiC) material with an aim to attain high surface finish along with the higher material removal rate and lower tool wear rate. SiC abrasive particulates mixed EDM oil was used as a dielectric medium for flushing from the center of the tool electrode. The input parameters, for instance current, pulse-on/off, dielectric medium, and tool hole diameter were considered. It has been observed in the research work that MRR is significantly affected by the machining parameters such as peak current, pulse-on/off as well as type of flushing conditions and MRR enhanced significantly with the increase in spark energy at lower pulse-off time whereas the flushing by dielectric mixed with SiC particulates lead to sharp reduction in MRR. However, surface finish improved steeply in SiC-assisted dielectric flushing conditions. But surprisingly, the tool erosion rate drastically reduced with SiC-assisted flushing of dielectric fluid along with thinner recast layer. The selected parameters like current, hole diameter, and pulse-on/off time showed insignificant effect on the TER and SR. Furthermore, the results were advocated with various SEM and EDS images.

P. S. Bains (✉) · S. Singh · S. S. Sidhu
Department of Mechanical Engineering, Beant College of Engineering & Technology, Gurdaspur, Punjab, India
e-mail: preetbains84@gmail.com

S. Singh
e-mail: singhsanbir@gmail.com

S. S. Sidhu
e-mail: sarabjeetsidhu@yahoo.com

S. Kaur
GNDU (RC), Gurdaspur, Punjab, India
e-mail: sandeep.kaur18@gmail.com

T. R. Ablyaz
Faculty of Mechanical Engineering, Perm National Research Polytechnic University (PNIPU), Perm, Russia
e-mail: lowrider11-13-11@mail.ru

S. S. Sidhu et al. (eds.), *Futuristic Composites*, Materials Horizons: From Nature to Nanomaterials, https://doi.org/10.1007/978-981-13-2417-8_9

Keywords EDM · TER · AJEDM · MMC · MRR · TAGUCHI

Abbreviations

Adj MS	Adjusted mean square
Adj SS	Adjusted sums of squares
AJEDM	Abrasive jet-assisted electrical discharge machining
Al–SiC	Aluminum–silicon carbide
dB	Decibels
DF	Degrees of freedom
DOE	Design of experiment
EDM	Electrical discharge machining
EDS	Energy-dispersive X-ray spectroscopy
I (A)	Current (amperes)
MH (HV)	Microhardness (Vickers pyramid number)
MMC	Metal matrix composite
MRR	Material removal rate
P-value	Probability
SEM	Scanning electron microscope
Seq SS	Sequential sums of squares
SiC	Silicon carbide
S/*N*	Signal to noise ratio
TWR	Tool wear rate
ZNC	*Z*-axis numeric control

1 Introduction

In today's technological era, manufacturing industries are facing a major challenge from the materials that are very difficult to cut/machine such as ceramics, super alloys, and composites along with precise requirements of the design like high surface quality, complex shapes, high bending stiffness, high strength, good damping capacity, better fatigue characteristics, and machining costs. The engineering challenges posed by the rapid growth in the development of such materials owed to the emergence of new and advanced machining processes, also known as "Unconventional Machining Methods". The word "unconventional" is used because metals like tungsten, hardened stainless steel, tantalum, and some high strength alloys, composites cannot be worked or processed upon by conventional methods. Nowadays, the nonconventional machining routes are more commonly used in the manufacturing industries in place of the traditional tools for machining. For the last few years, Electric Discharge Machine (EDM) is used to deal with the machining of such category of materials in the desired size and shape as well as for the required accuracy [1].

Electrical Discharge Machining is an example of advanced unconventional machining method (Fig. 1), wherein, material erosion takes place by the repeated action of spark between tool and workpiece in the presence of dielectric; so it becomes important to select machining parameters to achieving optimal machining performance [2]. Though, EDM possesses a major drawback of its reluctance to be used for large-scale production because of low MRR and poor surface finish, an attempt was made to enhance the surface properties of workpiece by mixing various types of powder in dielectric fluid. Favorable results were witnessed along with decrease in thickness of the recast layer as compared to conventional EDM [3]. Re-deposition of the eroded material back into machined surface came out to be one of the extreme difficulties in the way of high metal removal rate. Under high temperature and rapid cooling phenomenon, the hydroxides and melting metal debris solidify to form a recast layer [4]. Hence, a more efficient and convenient flushing system was proposed in order to improve process performance that made use of a abrasive particles mixed dielectric fluid jet [5]. MRR of EDM largely depends on the flushing conditions and to enhance the flushing conditions of EDM tube electrodes of different diameters were fabricated and then after surface quality and machining efficiency were investigated. Results showed that increase in internal diameter enhanced the surface finish and material removal rate [4]. Further, to improve the flushing conditions different shaped diameter electrodes were fabricated. The double-hole tube electrode was conformed as to have the optimal structure for relevant higher MRR [6]. The conventional EDM could be improved in terms of machining characteristics by combining various mechanisms jointly ("Hybridizing EDM") during machining to attain preferred surface integrity and stability of process. The development of hybrid machining is intended to utilize of the combined benefits of individual process and to avoid or plunge their limitations at the same time exhibited by the individual constituents [7, 8].

Abrasive jet machining (AJM) is one of the suitable options for machining of brittle and hard materials efficiently in surface finishing, deburring, and cleaning of surfaces, and is the focus of concern for many researchers for fabricating micro holes, slits etc. [9]. Tsai et al. [10] employed AJM to enhance the surface finish of tungsten carbide and SKD 61 steel machined by EDM. The results indicated the improvement in surface roughness from 1.3 to 0.7 mm within short time interval. Lin et al. [11] used the hybrid process of EDM and AJM under several parameters and concluded that abrasive particles used in the hybrid process not only improved the surface finish but material removal rate of SKD 61 steel as well.

The main motive behind this study is to analyze the performance of abrasive particles assisted EDM operation on machining characteristics, for instance, MRR, TWR, and SR and recast layer formation. The prominent process parameters such as current, pulse-on, pulse-off, tube electrode inner diameter, and type of dielectric were chosen to analyze their effects on performance of process. Moreover, to develop a mathematical model for machine parameters and machining characteristics, Taguchi's design approach (DOE) was selected. Finally, process parameters were optimized to get the desired surface finish, material removal rate, and tool erosion rate.

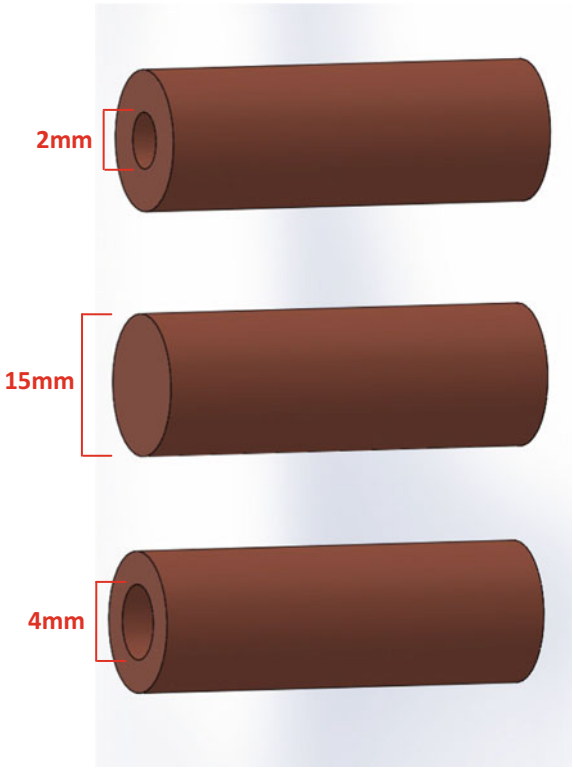

Fig. 1 Copper electrodes with variable hole diameter

2 Materials and Methods

2.1 Material

Two hollow electrodes of electrolytic copper having an outer diameter of 15 mm and internal diameters of 2 and 4 mm, respectively, were used for the abrasive mixed dielectric to flow through the tool, as shown in Fig. 1. Al–SiC MMC workpiece in a rectangular shape (2 mm × 2 mm) had been procured from CPS Technologies, USA (Fig. 2). The properties of the workpiece material are tabulated in Table 1 and selected process parameters in Table 2. Commercial grade EDM oil was used as the dielectric medium and abrasive particles of SiC having size of 220 mesh were used in 30 gm/L for abrasive-assisted machining.

Table 1 The properties of Al–SiC MMC

Aluminum alloy 356 (matrix)	Silicon carbide (reinforcement)	Density (g/cm)	Thermal conductivity (W/m K) @ 25 °C	Specific heat (J/g K) @ 25 °C	Young's modulus (GPa)	Strength (MPa)	Electrical resistance (μOhm cm)
63 vol%	37 vol%	2.89	180 typical (170 W/m K min)	0.808	167	471	20.7

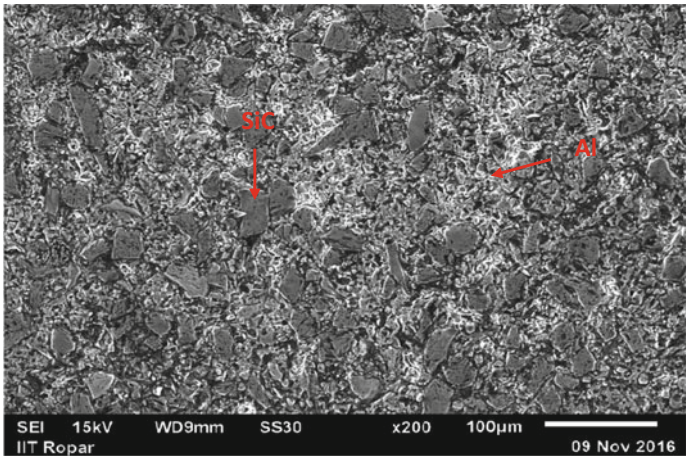

Fig. 2 SEM of unmachined Al–SiC (37 vol%SiC/A356)

2.2 DOE–Taguchi Approach

In this experimental work, two replications are performed at random order to find out the *S*/*N* ratio for more accurate output. The *S*/*N* ratio is considered as measure of performance in terms of the ratio of amount of preferred signal power to the unwanted noise which is symbolized as:

- "larger is better": when aim is to maximize the response

$$S/N = -10 * \log\left(\sum \left(1/Y^2\right)/n\right)$$

- "smaller is better": when aim is to minimize the response

$$S/N = -10 * \log\left(\sum \left(Y^2\right)/n\right)$$

Considering Y = output variable; n = experiments

Table 2 Input parameters and their levels

Variables	Level	
	1	2
Current (A)	6	12
Pulse-on (μs)	45	90
Pulse-off (μs)	45	90
Electrode hole diameter (mm)	2	4
Flushing type	Nonabrasive fluid	Abrasive fluid

In Taguchi designed experimentation, higher values of the *S*/*N* ratio identify the eminent process parameter settings that minimize the impact of the noise factors. The DOE procedure was implemented to identify and scrutinize the prominent parameters systematically, which was then verified with the Taguchi-based method. Taguchi's L_{16} orthogonal experimental design was framed to draw valid conclusions during abrasive-assisted ED machining of Al–SiC MMC and the factors assignment was done using Minitab 15.

The results of the investigations have been represented graphically for the critical discussion on MRR, TWR and SR of the electrical discharge machining process for the various investigations. The experiments were planned as per Taguchi's L_{16} array in the design of experiments which helped in reducing the number of experiments (Table 3).

2.3 Experimentation

The series of experiments were carried out on EDM (OSCARMAX, S645, ZNC), wherein a specially fabricated tank with a pump, for homogeneous mixing of suspended abrasive particles was mounted. The SiC particulates (220 mesh) were mixed in EDM oil of commercial grade as dielectric media with dilution of 30 gm/L and were continuously stirred to avoid settling down. The scheme of designed setup along with a brief illustration of the layout is shown in Fig. 3. The various trails were conducted using L_{16} orthogonal array by varying the various input factors at their respective levels.

For comparative analysis, experiments were conducted with jet through the electrode hole under a pressure of 1 bar for both, nonabrasive and abrasive fluids. The polarity of the tool was positive. To reveal the particular micrographic structure, the specimen was grounded using grinding machine and electrode tips were polished using emery paper. The workpiece was designated negative and tool as positive polarity. A precision electronic balance (0.001 g precision) was employed to measure workpiece and electrode weights prior and after machining. Sixteen different experiments were performed to determine the MRR, TWR, and SR of Al–SiC MMC

Fig. 3 EDM used for experimentation and abrasive jet machining setup

Table 3 Experimental results

Trials	Hole diameter	Current	Pulse-on	Pulse-off	Electrode type	MRR (mg/min)	TWR (mg/min)	SR (μm)
1	2	6	45	45	1	18.815	3.318	0.1366
2	2	6	45	90	2	11.320	1.698	0.0867
3	2	6	90	45	2	21.739	1.739	0.1067
4	2	6	90	90	1	16.012	0.942	0.55
5	2	12	45	45	2	24.284	2.857	0.1567
6	2	12	45	90	1	22.702	4.870	0.44
7	2	12	90	45	1	46.135	0.439	0.11
8	2	12	90	90	2	32.0	2.0	0.1867
9	4	6	45	45	2	11.196	1.967	0.1367
10	4	6	45	90	1	13.670	3.039	0.15
11	4	6	90	45	1	31.613	4.918	0.37
12	4	6	90	90	2	13.031	1.629	0.3734
13	4	12	45	45	1	59.553	6.976	0.38
14	4	12	45	90	2	20.625	0.938	0.0867
15	4	12	90	45	2	39.850	1.409	0.1634
16	4	12	90	90	1	49.411	4.705	0.34

by using different parameters as shown in Table 3. SEMs and EDS were carried out to examine the microstructure of machined specimen.

3 Results and Discussions

3.1 Influences on MRR

Table 3 demonstrates the planned experimental design and results obtained thereafter. The various outcomes were analyzed through ANOVA by using Design Expert software to test the significance of the model adopted (Table 4). From the table, it is clear that MRR is the function of peak current, pulse-on, flushing type, and pulse-off. It has been exhibited in Fig. 4 (main effects plot) and Table 4 for material removal rate that the peak current was the most significant factor augmenting the MMR steeply apart from pulse-on duration being other factor affecting the concerned response significantly.

The material removal mechanism has been elaborated in scanning electron microscope (SEM) analysis as well. The enhanced MRR can be attributed to the high spark energy that mechanically improved the erosion volume through the melt pool from the surface of workpiece. On the contrary, it is witnessed that the MRR decreased steeply when flushing was done with SiC abrasive particulates mixed dielectric medium for

Table 4 Analysis of variance (ANOVA) for material removal rate

S. No.	Source	DF	Seq SS	Adj SS	*F*-value	*P*-value
1.	Hole diameter	1	130.1	130.1	2.39	0.153
2.	Current	1	1150.1	1150.1	28.48	0.0000[a]
3.	Pulse-on	1	288.5	288.5	5.30	0.044[b]
4.	Pulse-off	1	349.1	349.1	6.41	0.030[b]
5.	Flushing	1	436.6	436.6	8.02	0.018[b]
6.	Residual errors	10	544.3	544.3		

[a]Most significant, [b]significant

Table 5 Analysis of variance (ANOVA) for TWR

S. No.	Source	DF	Seq SS	Adj SS	*F*-value	*P*-value
1.	Hole diameter	1	3.7143	3.7143	1.46	0.255
2.	Current	1	1.5221	1.5221	0.60	0.457
3.	Pulse-on	1	3.8740	3.8740	1.52	0.246
4.	Pulse-off	1	0.8992	0.8992	0.35	0.565
5.	Flushing type	1	13.9895	13.9895	5.50	0.0441[a]
6.	Residual errors	10	25.4506	25.4506		

[a]Significant

the enhanced pulse-off time. The reason for lower MRR (with abrasive) was due to entrapment of molten material in the machining zone and the subsequent deposition of SiC abrasive particles on the workpiece surface (Fig. 5). It is also observed that perhaps the selected SiC particulates must have demonstrated a shielding effect while abrasive jet-assisted ED machining of MMC.

3.2 Influences on TWR

Various machining parameter like current, hole diameter of tool, and pulse-on/off duration do not have considerable effect on TWR, as shown in Table 5, except the type of flushing which is the most significant factor affecting the wear of tool while ED machining of MMC. It is clear from the graph (Fig. 6) that SiC particulates mixed flushing dielectric resulted in the lowest tool erosion. This is due to the reason that the SiC particulates used as the abrasive particles is mixed in the dielectric re-deposited on the surface of the copper tool, thereby reducing the tool wear rate.

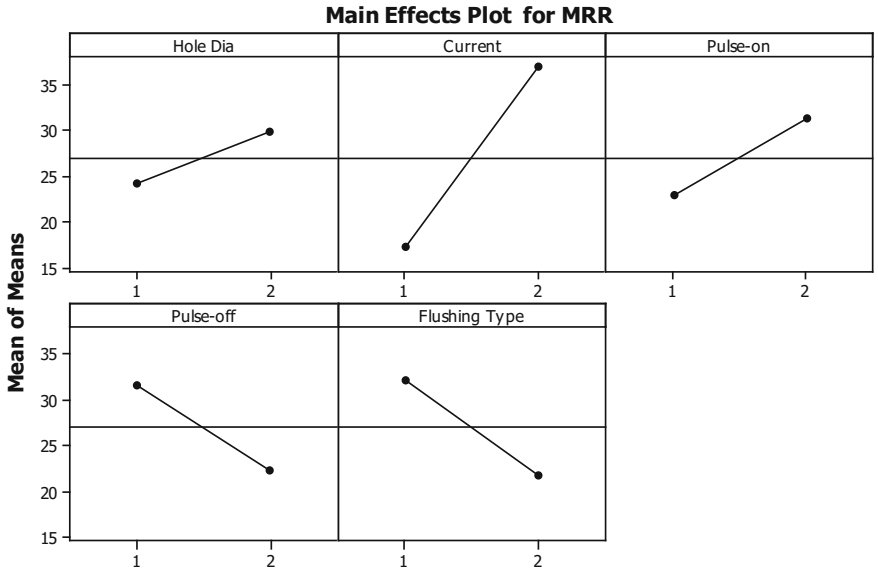

Fig. 4 Main effect plot for material removal rate (MRR)

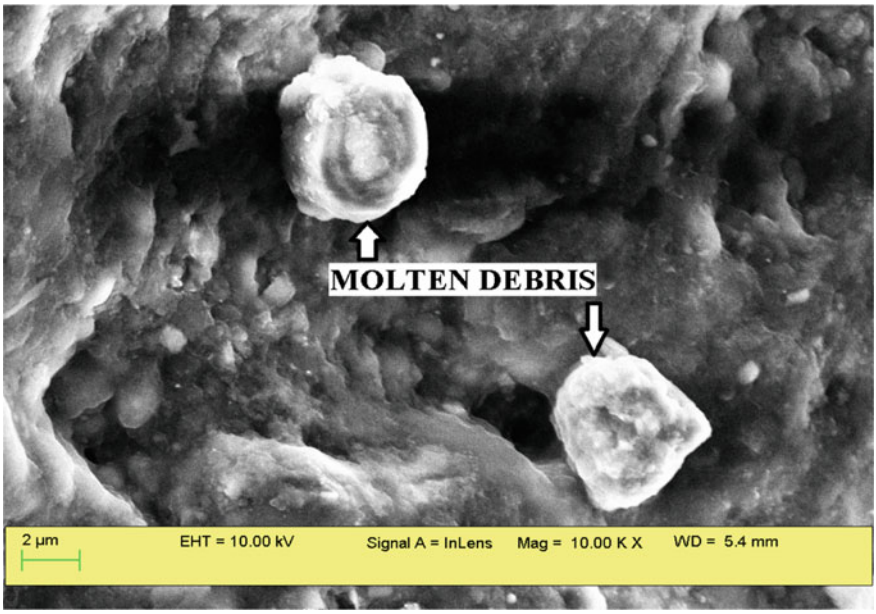

Fig. 5 Scanning electron microscope (SEM) analysis of workpiece

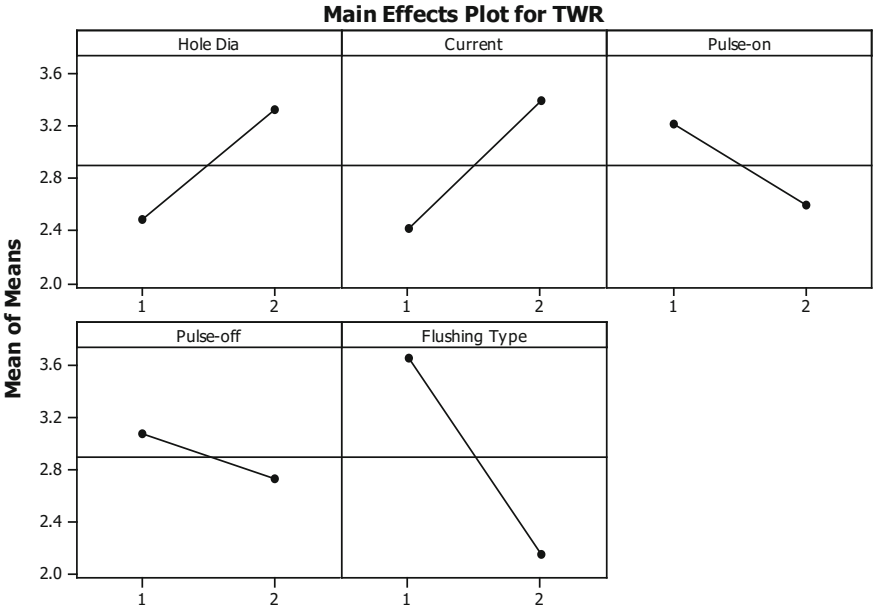

Fig. 6 Main effects plot for means for TWR

Table 6 Analysis of variance (ANOVA) for surface roughness

S. No.	Source	DF	Seq SS	Adj SS	*F*-value	*P*-value
1.	Hole diameter	1	0.003215	0.003215	0.17	0.686
2.	Current	1	0.000136	0.000136	0.01	0.933
3.	Pulse-on	1	0.024555	0.024555	1.32	0.277
4.	Pulse-off	1	0.026683	0.026683	1.44	0.258
5.	Flushing type	1	0.086966	0.086966	4.69	0.056[a]
6.	Residual errors	10	0.185346	0.185346		

[a]Significant

3.3 Influences on SR

The surface roughness is significantly influenced by flushing type, wherein flushing was done with pure dielectric and with abrasive mixed dielectric. The relations of surface roughness (SR) with current, hole diameter, pulse-on, flushing type, and pulse-off are shown in Fig. 7. The machining with SiC mixed dielectric resulted in the higher surface finish whereas comparatively, a rougher surface is achieved when machining is executed in pure dielectric (Table 6).

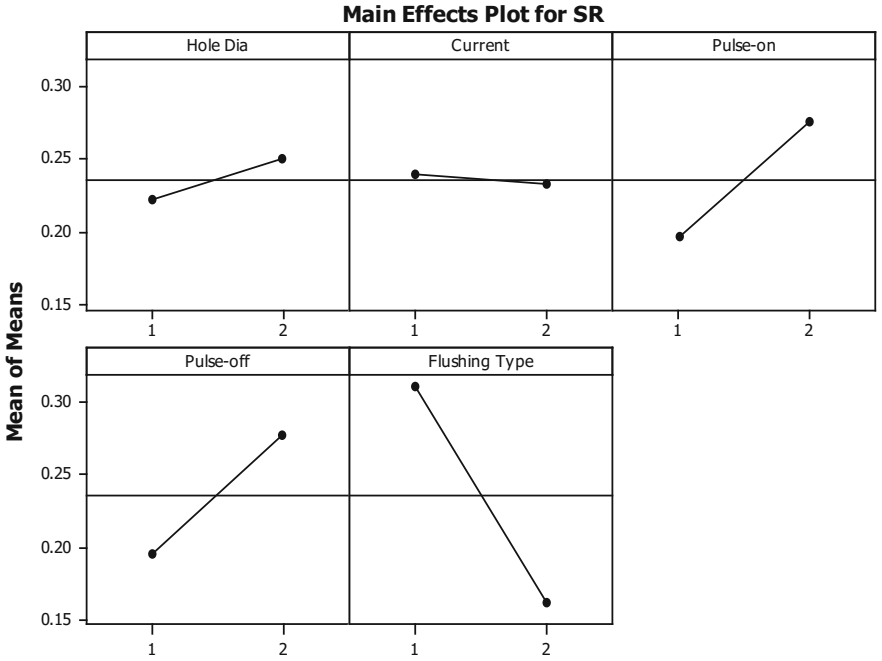

Fig. 7 Main effects plot for surface roughness

From the scanning electron microscope (SEM) analysis (Fig. 8a), it can be observed that large and deep holes or pits are visible on the surface prominently during machining in pure dielectric oil. Surface topology is witnessed to be quite rough which resulted in higher surface roughness. On the obverse, when SiC-assisted dielectric is used for the machining process (Fig. 8b), the surface is smooth and comparatively lesser deep or large pits were formed which indicates low value of surface roughness.

3.4 Surface Characteristics

In order to study the results of the experiments in an elaborative manner in terms of constituent elements, the EDS (Energy-dispersive X-ray spectroscopy) was performed on both types of samples machined with the conventional EDM as well as with the abrasive-assisted EDM. Figure 9 exhibits the EDS of the sample in trial 7 ED machined with the conventional EDM, i.e., flushing with the pure dielectric oil.

The EDS spectrum shown in Fig. 9 shows the traces of copper (electrode material) deposited on the machined surface of workpiece. The EDS of the sample in trail 13 machined with the abrasive-assisted hybrid EDM was also performed (Fig. 10).

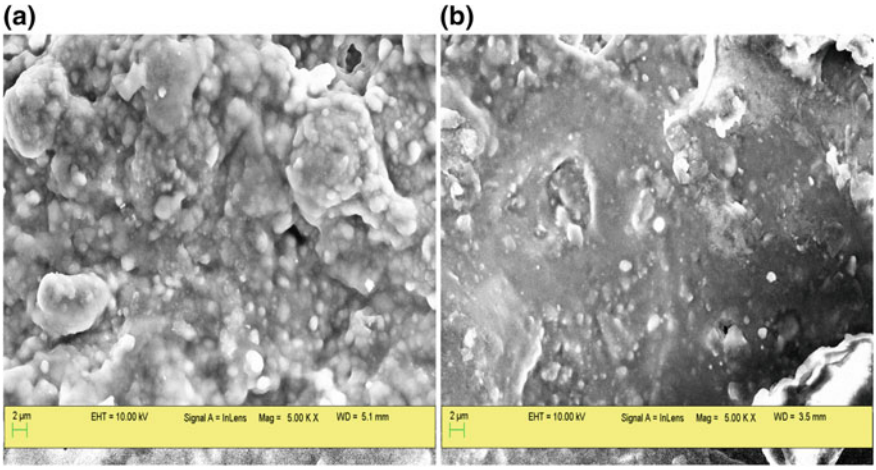

Fig. 8 SEM analysis of workpiece **a** without abrasives **b** with abrasives

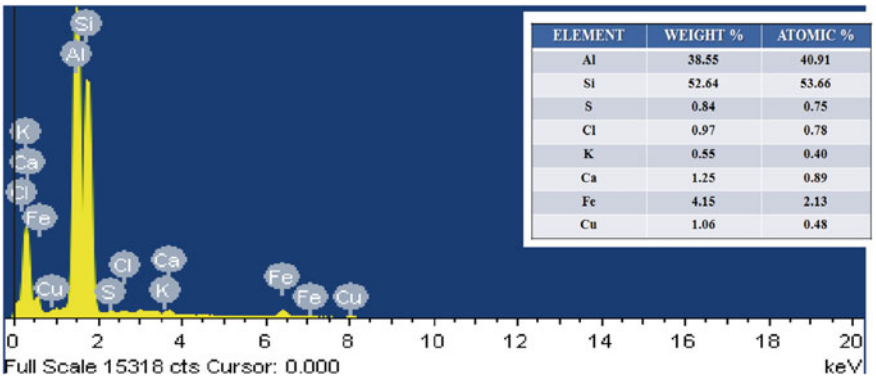

ELEMENT	WEIGHT %	ATOMIC %
Al	38.55	40.91
Si	52.64	53.66
S	0.84	0.75
Cl	0.97	0.78
K	0.55	0.40
Ca	1.25	0.89
Fe	4.15	2.13
Cu	1.06	0.48

Fig. 9 EDS spectrum of trial 7

The formation of oxides on the surface of the machined workpiece can be witnessed in the EDS spectrum shown in Fig. 10 that eventually led to the increase of surface hardness of the workpiece.

3.5 Recast Layer Formation

The material eroded in conventional EDM by thermo-physical behavior often results in certain damaging impacts in the form of re-deposited layer (recast layer). It has been evident through SEM images that AJEDM in SiC particulates mixed dielectric fluid has resulted in the reduction of recast layer thickness. On the other hand, nonho-

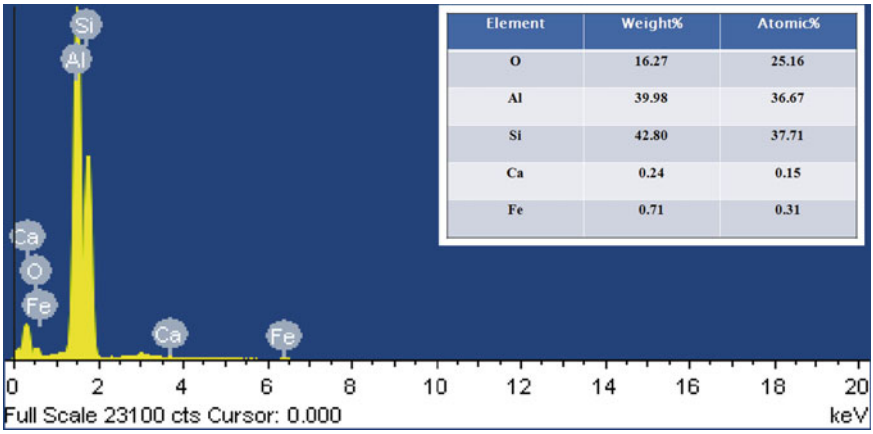

Element	Weight%	Atomic%
O	16.27	25.16
Al	39.98	36.67
Si	42.80	37.71
Ca	0.24	0.15
Fe	0.71	0.31

Fig. 10 EDS spectrum of trial 13

mogeneous metallurgical phases were witnessed in the thermally influenced region in terms of micro-cracks within the hard and brittle layer. Mostly, these micro-cracks are developed perpendicular to the machined surface and layers underneath remain unaffected by these surface alterations. The thickest recast layer has been recorded (52.428 μm) in trial 6 at high spark energy and higher pause time without abrasive jet-assisted EDM. It can be quantified to the fact that, at higher peak current, continuous sparking takes place at lowest pulse-on and high-end pulse-off duration settings causing an enormous quantity of molten debris to re-solidifies and result in a thicker recast layer at the end (Fig. 11).

However, in AJEDM, almost 62% decrease in thickness of recast layer (19.763 μm) has been witnessed in trial 8 in the same set of operating parameters. The recast layer is minimized due to effectual flushing of molten debris from the electrode-workpiece gap resulting in uniformity of the recast layer.

4 Conclusions

The study was carried out on EDM of MMC with and without abrasive-assisted jet flushing conditions. The following observations are enlisted.

1. MRR is significantly affected by the machining parameters such as peak current, pulse-on/off as well as type of flushing conditions. It was observed that MRR enhanced significantly with the increase in spark energy at lower pulse-off time. The flushing by dielectric mixed with SiC particulates leads to sharp reduction in MRR.
2. The surface finish improved steeply in SiC-assisted dielectric flushing conditions.

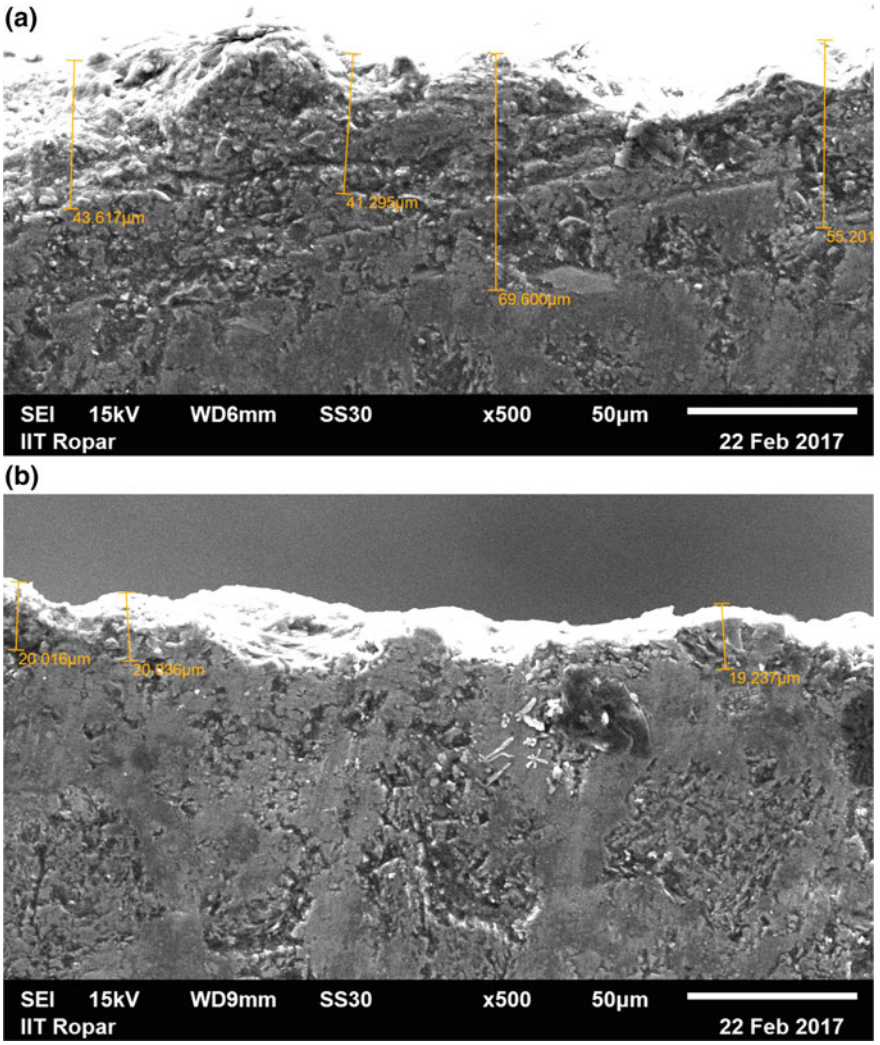

Fig. 11 SEM depicting recast layer formation for **a** trial 6 and **b** trial 8

3. The tool wear rate drastically reduced with SiC-assisted flushing of dielectric fluid.
4. The selected parameters for instance, current, hole diameter, pulse-on/off time shows insignificant effect on the TWR and SR.
5. Thinner recast layer was observed with AJEDM as compared to conventional EDM process.

References

1. Bains PS, Sidhu SS, Payal HS (2016) Fabrication and machining of metal matrix composites: a review. Mater Manuf Process 31(5):553–573
2. Patel KM, Pandey PM, Venkateswara Rao P (2009) Determination of an optimum parametric combination using a surface roughness prediction model for EDM of Al_2O_3/SiC_w/TiC ceramic composite. Mater Manuf Process 24(6):675–682
3. Sidhu SS, Batish A, Kumar S (2014) Study of surface properties in particulate-reinforced metal matrix composites (MMCs) using powder-mixed electrical discharge machining (EDM). Mater Manuf Process 29(1):46–52
4. Zhang Y, Xu Z, Xing J, Zhu D (2016) Effect of tube-electrode inner diameter on electrochemical discharge machining of nickel-based superalloy. Chin J Aeronaut 29(4):1103–1110
5. Arantes LJ, da Silva ER, dos Santos RF, Sales WF, Raslan AA (2016) The electrical discharge machining process aided by abrasive jet. Int J Adv Manuf Technol 1–10
6. Zhang Y, Xu Z, Zhu Y, Zhu D (2016) Effect of tube-electrode inner structure on machining performance in tube-electrode high-speed electrochemical discharge drilling. J Mater Process Technol 231:38–49
7. Rajurkar KP, Zhu D, Mcgeough JA, Kozak J, De Silva A (1999) New developments in electrochemical machining. CIRP Ann 48(2):569–579
8. Pajak PT, Silva AKM, Harrison DK, Mcgeough JA (2004) Modeling the aspects of precision and efficiency in laser-assisted jet electrochemical machining (LAJECM). J Mater Process Technol 149:512–518
9. Qu J, Shih AJ, Scattergood RO, Luo J (2005) Abrasive micro-blasting to improve surface integrity of electrical discharge machined WC–Co composite. J Mater Process Technol 166(3):440–448
10. Tsai FC, Yan BH, Kuan CY, Huang FY (2008) A Taguchi and experimental investigation into the optimal processing conditions for the abrasive jet polishing of SKD61 mold steel. Int J Mach Tools Manuf 48(7):932–945
11. Lin Y-C, Chen Y-F, Wang A-C, Sei W-L (2012) Machining performance on hybrid process of abrasive jet machining and electrical discharge machining. Trans Nonferrous Met Soc China 22:s775–s780

Development of Various Industrial Lime Sludge Waste-Filled Hybrid Polymeric Composites for Environmental Sustainability

Satadru Kashyap and Dilip Datta

Abstract A potentially hazardous industrial waste material in our society is lime sludge which is sourced mainly from various industries (fertilizer, paper, sugar and soda ash) and generally disposed off in dumpyards or used in unauthorized land filling—both causing pollution. Hence, an alternative idea of environmental sustainability is by reusing lime sludge as reinforcing agent in polymeric composites. In this line of thought, lime sludge waste is used as filler in HDPE and epoxy matrices in order to investigate the effects of lime sludge on its composite properties. This would ultimately, throw light on the feasibility and commercial viability of lime sludge reuse in polymeric composites. Mechanical properties of HDPE composites are studied with maleic anhydride-grafted polyethylene (MAPE) as compatibilizer for effective adhesion at the filler/matrix boundary. Lime sludge waste was also used as filler in conjunction with randomly dispersed short coir fibre reinforced HDPE composites along with 5 wt% MAPE as compatibilizer. It is observed the properties such as flexural strength and mechanical rigidity (tensile and flexural) of the lime sludge infused composites improved with filler addition. The tensile strength increased up to 20 wt% filler addition due to effective reinforcement; however, beyond that the tensile strength decreased due to particle agglomeration. Additionally, lime sludge is used as filler in short and long coir fibre added epoxy composites. It is found that lime sludge content of 6 wt% results in superior tensile strength in coir fibre reinforced epoxy composites. In general, lime sludge is found to improve the bending strength and mechanical rigidity (tensile and flexural modulus) with increasing filler weight fraction. Thus, the reuse of lime sludge filler in polymeric composites not only results in the enhancement of various mechanical properties, but also reduces pollution, decreases the cost of the composites and improves the commercial viability of lime sludge waste.

S. Kashyap (✉) · D. Datta
Department of Mechanical Engineering, Tezpur University, Napaam 784028, Assam, India
e-mail: satadru@tezu.ernet.in

D. Datta
e-mail: ddatta@tezu.ernet.in

S. S. Sidhu et al. (eds.), *Futuristic Composites*, Materials Horizons: From Nature to Nanomaterials, https://doi.org/10.1007/978-981-13-2417-8_10

1 Introduction

Industrial lime sludge predominantly consists of calcium carbonate ($CaCO_3$) in the form of lime in addition to trace amounts of compounds (Al_2O_3 and SiO_2) [1]. As per the report of the Central Pollution Control Board (Govt. of India) [1], industrial lime sludge waste produced from the fertilizer, paper, soda ash, carbide and sugar industries in India, is usually used in illogical land filling or disposed off in different dumpyards, which is potentially hazardous for the environment. Due to this pressing need to develop ecologically pleasant waste recycling methods, Wiegand and Unwin [2] suggested a few alternative techniques of lime sludge waste utilization—such as brick production, developing building materials and ceramics, revival of raw components from sludge, making feedstock for ethanol production, pelletization of sludge used in alternative fuel and finally, as possible composts. Recently, Torkashvand et al. [3] revealed that 2% lime sludge addition in *Sorghum vulgaris* plant surprisingly improved its shoot dry matter and micronutrient uptake. Evanylo and Daniels [4] used de-watered paper sludge as a potential potting soil replacement and found that sludge from paper mill worked as steady fertilizer which may be used as a nutrient supplement source and for soil modification, along with a potting medium.

One of the most extensively used fillers in the manufacturing of polymeric composites is $CaCO_3$. It is also used as a reinforcing filler [5], for improving the toughness (impact toughness) of HDPE and polypropylene [6, 7], to increase the elastic rigidity, impact strength and hardness of composites [7], for enhancing the viscosity of thermoplastics [8]; and most importantly, to reduce cost and increase economic viability [5–7]. Since lime sludge mainly consists of $CaCO_3$, this research investigates the feasibility of employing lime sludge as a reinforcing filler in polymeric composites. Lime sludge-filled polymeric composite is a novel idea which would focus on integrating three advantages, (i) reusing industrial lime sludge waste for environmental sustainability, (ii) development of a novel set of composites and (iii) decreasing the manufacturing cost.

However, the outright hindrance in using virgin particulate fillers in polymeric composites is low compatibility at the filler-matrix interfacial boundary. This is due to the fact that the polar filler is hydrophilic in nature, while the non-polar polymeric matrix is hydrophobic in nature [9, 10]. Hence, inorganic fillers are immiscible in thermoplastic polymers such as polyolefins (HDPE, PP, LDPE, etc.) and do not disperse easily. Inorganic fillers have the tendency to agglomerate while mixing with a thermoplastic polymer, as they possess strong intermolecular bonding. This has been earlier observed in the case of raw lime sludge-filled HDPE composites [11, 12]. Thus, deterioration in thermal and mechanical properties of the polymeric composites is observed on account of this filler-matrix incompatibility and low interfacial adhesion [13–15]. Hence, in the last few years, numerous techniques have been proposed for improving the interfacial adhesion and compatibility at the filler-matrix interface. This leads to the enhancement of the properties of the composites.

These methods include use of compatibilizers, viz. maleic anhydride grafting on polyolefins (such as HDPE and PP) [9, 10], the addition of coupling agents such as silanes [16], modifying the filler surface chemically [13, 14, 17], a hydrophilic functional group being grafted on the matrix [15], etc. The use of maleic anhydride-grafted polymer is a very effective as a compatibilizing agent at the filler-matrix interface and has been employed commonly in case of polymeric composites—so that it would improve their properties by enhancing the filler-matrix adhesion at the interface [9].

Of late, it has also been proved that solid particulate fillers incorporated in a fibre reinforced composites yielded advantageous results in terms of increased rigidity (modulus) and reduced product costs along with certain shortcomings such as lower strength and impact toughness [18, 19]. Gracia et al. [20] were among the first researchers to propose the concept of hybrid composites for improved characteristics of fibre reinforced composites. Subsequently, Liau et al. [21] observed that the impact toughness significantly improved upon the addition of ceramic whiskers or particulates in the hybrid composites. Similar researches have been attempted in the recent past in order to determine the physico-mechanical as well as wear behaviour of hybrid composites [22, 23].

An industrial waste which should be employed as a filler or reinforcement in composites needs to be versatile in its applications. Needless to say, it is a mandatory requirement for lime sludge waste to be resourceful enough to be used in a variety of polymeric matrices and along with other reinforcing agents in hybrid composites. In this study, lime sludge industrial waste is used as reinforcing filler in various hybrid composites, viz. HDPE, MAPE-added HDPE, coir-HDPE-MAPE, epoxy and coir fibre epoxy. This would throw some light on the versatility and feasibility of lime sludge waste as reinforcing filler and its effects on the properties of composites when used with various polymeric matrices.

2 Materials and Methods

Materials used in the fabrication of lime sludge-filled polymeric composites; experimental procedures involved and the instrumentation used in the characterization of the composites are described under this section.

2.1 Materials

Haldia Petrochemicals Ltd. supplied HDPE polymer (grade 5108L) in the form of pellets with a melt flow index of 1.9 g/min (@190 °C, 2.16 kg) and 0.95 g/cm^3 density. 1.2% maleic anhydride-grafted HDPE (OPTIM-E156) was obtained from Pluss Polymers Pvt. Ltd., Gurgaon (India). It has a melt flow index of 7 g/min (@190 °C, 2.16 kg) and 0.953 g/cm^3 density.

(a) Raw lime sludge (b) Coir fibre

Fig. 1 Raw lime sludge and coir fibre used in the fabrication of composites

Reliance Polymers provided PP (grade AM120N) having a melt flow index of 1.2 g/min (@230 °C, 2.16 kg). Epoxy (Lapox-12) and hardener are obtained from Perfect Trading Company, Kolkata (India). Raw lime sludge (Fig. 1) is obtained from Hindustan Paper Corporation Limited (HPCL) paper mill at Jagiroad, Assam (India). Raw lime sludge is manually ground for 10 min and the particles are passed through a sieve size of number 170 in order to control the particle size. Subsequently, before blending with polymeric matrix, any remaining moisture content is removed by heating it to 110 °C for 2 h in a hot air oven (model: 114/14, make: Reico). Stearic acid is supplied by HiMedia Laboratories Pvt. Ltd., Mumbai, India. Ethanol is provided by Merck Specialities Pvt. Ltd., Mumbai, India.

Coir fibre (Fig. 1b) is obtained locally and is surface treated with 5% NaOH solution to remove any lignin from its surface. Coir fibres are washed with water in order to remove any dusts and contaminants and subsequently, dried for 48 h at room temperature. The mercerization process consisted of immersing coir fibre (200 g) in a 5% (w/v) NaOH aqueous solution (2 L) at room temperature for 1 h. Subsequently, it is washed 10 times with distilled water so that the adsorbed alkali is leached away from the fibres. Afterwards, the fibres are dried for 48 h at room temperature and for 8 h at 50 °C in an oven. The dried fibres are sealed in a container prior to composite fabrication to avoid atmospheric contamination [24, 25].

2.2 Sample Preparation

Lime sludge is used as filler in two types of polymeric matrices, viz. HDPE and epoxy. Additionally, lime sludge is also used as filler in coir fibre reinforced HDPE and epoxy composites. MAPE is used as a compatibilizing agent in lime sludge-filled HDPE and coir-HDPE composites.

Table 1 HDPE-MAPE composites filled with lime sludge along with their weight fractions

Description	Lime sludge (wt%)	HDPE (wt%)	MAPE (wt%)
HDPE/LS/MAPE (89/10/1)	10	89	1
HDPE/LS/MAPE (79/20/1)	20	79	1
HDPE/LS/MAPE (69/30/1)	30	69	1
HDPE/LS/MAPE (87/10/3)	10	87	3
HDPE/LS/MAPE (77/20/3)	20	77	3
HDPE/LS/MAPE (67/30/3)	30	67	3
HDPE/LS/MAPE (85/10/5)	10	85	5
HDPE/LS/MAPE (75/20/5)	20	75	5
HDPE/LS/MAPE (65/30/5)	30	65	5

2.2.1 Lime Sludge-Filled HDPE-MAPE Composites

HDPE-MAPE composites filled with lime sludge are mixed together in a twin screw extruder (model: Voltam EX100). The blended polymeric composites in the form of wires are cooled and cut into pellets. Finally, test specimens are moulded (as per tensile, flexure and impact testing requirements) from the blended pellets by means of an injection moulding machine (model: Voltam IM100). The test specimens prepared with different weight % of the constituents—lime sludge, HDPE and MAPE are shown in Table 1.

2.2.2 Lime Sludge-Filled Coir-HDPE Composites

Moreover, randomly dispersed short coir fibre (8 mm long) reinforced HDPE and HDPE-MAPE composites are blended and fabricated using twin screw extruder and injection moulding techniques as mentioned above, in order to study the effects of adding 5 wt% MAPE compatibilizer to varying weight fractions of coir and HDPE in the composites. Subsequently, test specimens were fabricated by incorporating varying weight fractions of lime sludge in 20 wt% coir fibre reinforced HDPE-MAPE composites. It is found that 20 wt% of coir fibre addition provided the highest tensile strength in coir-HDPE-MAPE composites. Hence, lime sludge content is varied keeping the coir fibre content fixed at 20 wt%. The variation of constituting components in these composites is provided in Table 2.

Table 2 Lime sludge-filled coir reinforced HDPE and HDPE-MAPE composites along with their weight %

Description	Lime sludge (wt%)	Coir (wt%)	HDPE (wt%)	MAPE (wt%)
HDPE/CF (90/10)	–	10	90	–
HDPE/CF (80/20)	–	20	80	–
HDPE/CF (70/30)	–	30	70	–
HDPE/CF/MAPE (85/10/5)	–	10	85	5
HDPE/CF/MAPE (75/20/5)	–	20	75	5
HDPE/CF/MAPE (65/30/5)	–	30	65	5
HDPE/LS/CF/MAPE (65/10/20/5)	10	20	65	5
HDPE/LS/CF/MAPE (60/15/20/5)	15	20	60	5
HDPE/LS/CF/MAPE (55/20/20/5)	20	20	55	5

2.2.3 Lime Sludge-Filled Coir-Epoxy Composites

Lime sludge-filled short coir fibre reinforced epoxy composites are fabricated by randomly dispersing 30 wt% of 8 mm long coir fibres in an epoxy matrix. Lime sludge in these coir-epoxy composites is incorporated in weight fractions of 3, 6, 9 and 12 wt%, respectively.

The composites are fabricated by using a compression moulding machine (make: SANTEC) at a pressure of 10 kg/cm^2 for 24 h (curing time). The epoxy and hardener are used in the ratio of 10:1. For fabrication of composite, a handmade mould of dimension $120 \times 80 \times 5$ mm^3 is fabricated with mild steel. For trouble-free removal of the composites, a silicon-based spray is applied to mould. Epoxy resin with its corresponding hardener is thoroughly mixed. The chopped fibres mixed with the resin and gently poured inside the mould. The closed mould is then compressed using compression moulding for curing time of 24 h at lab temperature. Additionally, lime sludge-filled long coir fibre (120 mm, 30 wt%, uniaxially aligned) reinforced epoxy composites are also fabricated in similar fashion with varying contents of lime sludge, viz. 3, 6, 9 and 12 wt%, respectively. The lime sludge-filled coir epoxy composites and their weight fractions are tabulated in Table 3.

Table 3 Coir-epoxy composites filled with lime sludge along with their weight %

Description	Lime sludge (wt%)	Epoxy (wt%)	Coir (wt%)
Pure Epoxy	–	100	–
3LS–97 Epoxy	3	97	–
6LS–94 Epoxy	6	94	–
9LS–91 Epoxy	9	91	–
12LS–88 Epoxy	12	88	–
30 Coir-Epoxy (8 mm)	–	70	30
3LS–30 Coir-Epoxy (8 mm)	3	67	30
6LS–30 Coir-Epoxy (8 mm)	6	64	30
9LS–30 Coir-Epoxy (8 mm)	9	61	30
12LS–30 Coir-Epoxy (8 mm)	12	58	30
30 Coir-Epoxy (long)	–	70	30
3LS–30 Coir-Epoxy (long)	3	67	30
6LS–30 Coir-Epoxy (long)	6	64	30
9LS–30 Coir-Epoxy (long)	9	61	30
12LS–30 Coir-Epoxy (long)	12	58	30

2.3 Mechanical Testing

The mechanical properties of the injection moulded composites are measured using a UTM (model: Hounsfield H100K-S) of capacity 100 kN. Testing (tensile and bending tests) is done by means of a 250 N load cell at a crosshead speed of 1 mm/min. For each designated composite, a total of five specimens are fabricated and tested as per ASTM and ISO standards. The average value of the five composite samples is computed for each composite. The notched Izod impact test, for the lime sludge—HDPE composite system is conducted by means of a pendulum impact testing machine (model: CEAST Spa Italy, P/N0963.000). All the mechanical testing of the samples are conducted according to ASTM standards, i.e. tensile testing—D638 (specimen V), flexure testing—ASTM D7264 and impact testing—ASTM D256 standards respectively. Injection moulded test specimens are shown in Fig. 2. Additionally, tensile and flexural properties of compression moulded lime sludge-coir-epoxy composites are determined by means of a UTM (Make: Zwick Z010) according to ISO 527 and ISO 178, respectively. This is done at a crosshead speed of 2 mm/min. Compression moulded tensile and flexure test specimens before and after their testing as per ISO standards are shown in Fig. 3.

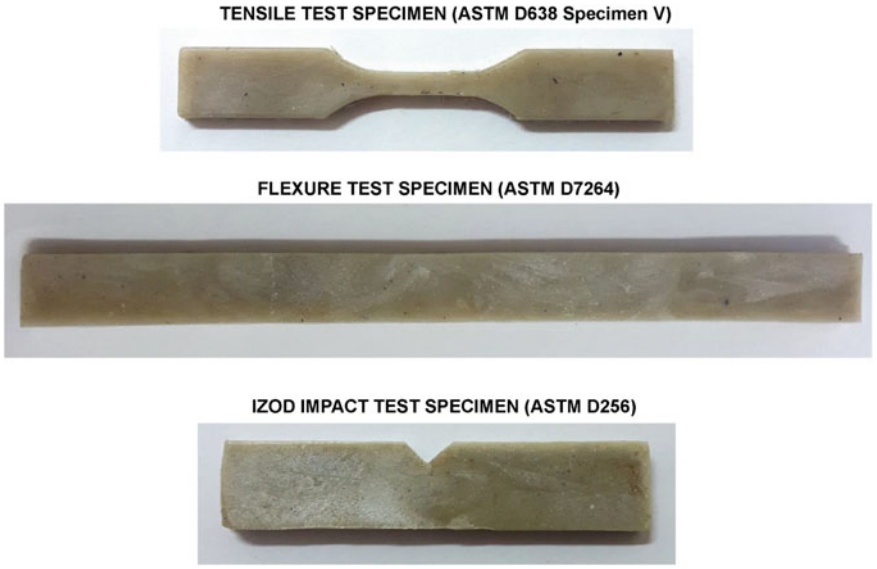

Fig. 2 Injection moulded test specimens fabricated as per ASTM standards (lime sludge-filled HDPE composites)

Fig. 3 Compression moulded tensile and flexure test specimens (lime sludge-filled coir-epoxy composite) before and after testing as per ISO standards

2.4 SEM Analysis

A scanning electron microscope (SEM) (model: JEOL, JSM6390LV) in its secondary electron mode is used to study the morphology at the fractured surfaces of the composites that are developed upon tensile testing. The samples used are HDPE/LS

(70/30) and HDPE/LS/MAPE (65/30/5), respectively. In order to avoid electrical charging, the specimens surfaces are sputter coated with Pt before their examination under the microscope.

3 Results and Discussions

3.1 Lime Sludge-Filled HDPE-MAPE Composites

In the present study, lime sludge is used as a reinforcing filler in HDPE-MAPE blends in varying weight fractions in order to investigate the effects of lime sludge and maleic anhydride compatibilizer on the properties of the composites. Mechanical tests are carried out for three sets of lime sludge-filled HDPE composites. Subsequently, composites are tested with MAPE content varying as 1, 3 and 5 wt% and lime sludge content varying as 10, 20 and 30 wt% for each MAPE content, respectively. Thus, this is done in order to study the effect of increasing content of MAPE compatibilizer on lime sludge-filled HDPE composites in conjunction with raw lime sludge-filled HDPE composites.

It is imperative to mention that the whole motivation behind using an industrial waste (lime sludge) as a reinforcing agent in thermoplastic composites is low cost of the composites and reusing a material that causes environmental pollution. Since MAPE is a costly material when compared with pure HDPE; hence, the ultimate goal is to use MAPE in smaller quantities which would enhance the characteristics of the samples without affecting the commercial viability of the product. Hence, the characteristic features of lime sludge reinforced HDPE-MAPE blends are illustrated in this segment with a focus on the outcome of lime sludge and MAPE in the composites.

The test results of the composites are measured and shown in Table 4.

3.1.1 Tensile Properties

The tensile strengths of lime sludge-MAPE blends showed higher values when compared to raw lime sludge composites for all filler weight %. Higher tensile strengths of lime sludge-HDPE-MAPE composites indicate better physical interaction at the filler-matrix boundary due to the maleic anhydride compatibilizer grafted on the HDPE chains and resistance is exerted by lime sludge particles to the propagation of the cracks. Lime sludge particles are hydrophilic in nature while the HDPE chains are hydrophobic which causes fragile adhesion at the filler-matrix boundary. Maleic anhydride-grafting modifies the interface, thus providing effective bonding (adhesion) at the interface along with the appropriate distribution of the filler in the matrix. This results in the improvement of the tensile strength. However, at higher concentrations above 20 wt% lime sludge, the tensile strength decreases due to filler particle

Table 4 Lime sludge reinforced HDPE-MAPE composites and their properties

Description	Tensile strength (MPa)	Tensile modulus (MPa)	Elongation at break (%)	Flexural strength (MPa)	Flexural modulus (MPa)	Impact strength (J/m)
HDPE/LS (90/10)	13.67 ± 0.14	152.8 ± 6.2	629 ± 9	8.84 ± 0.72	493.4 ± 9.9	7.94 ± 0.5
HDPE/LS (80/20)	11.32 ± 0.45	170.8 ± 7.9	34.4 ± 9	10.53 ± 0.49	589.2 ± 7.4	7.75 ± 0.2
HDPE/LS (70/30)	11.09 ± 0.24	215.2 ± 13	32.8 ± 9	12.19 ± 0.72	635.0 ± 10.9	7.36 ± 0.7
HDPE/LS/MAPE (89/10/1)	16.24 ± 0.19	196.2 ± 11.6	252 ± 19.6	13.64 ± 0.25	512 ± 9.6	31.79 ± 2.3
HDPE/LS/MAPE (79/20/1)	16.99 ± 0.15	210.5 ± 9.9	40 ± 11.0	14.47 ± 0.20	595 ± 11.1	40.26 ± 1.4
HDPE/LS/MAPE (69/30/1)	16.54 ± 0.24	219.2 ± 8.8	28 ± 5.2	14.83 ± 0.11	646 ± 12.5	41.24 ± 0.4
HDPE/LS/MAPE (87/10/3)	16.58 ± 0.25	198.5 ± 8.5	210 ± 11.8	14.09 ± 0.18	521 ± 13.7	39.14 ± 0.7
HDPE/LS/MAPE (77/20/3)	17.71 ± 0.16	221.3 ± 9.1	29 ± 5.5	14.85 ± 0.16	612 ± 13.0	42.18 ± 0.6
HDPE/LS/MAPE (67/30/3)	16.91 ± 0.30	260.3 ± 12	27 ± 4.7	15.89 ± 0.19	683 ± 7.1	44.36 ± 0.4
HDPE/LS/MAPE (85/10/5)	17.92 ± 0.22	232 ± 13.5	151 ± 11.4	15.01 ± 0.14	598 ± 12.3	43.79 ± 0.5
HDPE/LS/MAPE (75/20/5)	18.59 ± 0.26	257 ± 11.4	23 ± 4.8	15.14 ± 0.09	652 ± 13.0	44.34 ± 0.2
HDPE/LS/MAPE (65/30/5)	18.04 ± 0.16	275.5 ± 13.3	21 ± 5.1	16.24 ± 0.14	693 ± 4.9	46.84 ± 0.4

Fig. 4 A lime sludge-HDPE composite samples after tensile test having higher and lower ductility

agglomeration which creates stress concentration sites leading to crack initiation at these locations upon loading. Similar behaviour in the tensile properties of $CaCO_3$-based filler (kaolin) in a polymer matrix modified by maleic anhydride was also reported earlier [26].

The tensile modulus of lime sludge-HDPE-MAPE composites showed a considerable increase with rising filler weight fraction, when compared with raw and stearic acid coated lime sludge composites. This is due to—(1) substitution of a tough matrix with rigid particles, thus restricting the chain mobility hindering deformation within the elastic limit; and (2) effective adhesion at the filler-matrix boundary resulting in successful stress transfer within the elastic limit.

A considerable decrement in the ductility (elongation at break) is observed with the increment in lime sludge loading in the composites. This is a characteristic feature shown by generally most of the particulate composites. The samples of filled composites after tensile test exhibiting higher and lower ductility based on their lime sludge weight content is shown in Fig. 4. Modification with maleic anhydride as a coupling agent improved the strength and rigidity of the composites with a consequential reduction in the ductility; due to the fact that MAPE improved the adhesion at the filler-matrix boundary [26]. Thus, modification with MAPE as the coupling agent is advantageous as it improved certain properties such as the strength and rigidity of the composites.

The evidence in the improvement in the properties of the MAPE-added lime sludge-filled HDPE composites are further shown by the Fig. 5. It is observed in Fig. 5a that without the presence of a compatibilizer, the fractured surface revealed loose lime sludge particles which dissociate from the polymeric matrix upon loading due to low bonding at the interface; thus ensuring poorer composite properties. However, in case of MAPE-added composites (refer Fig. 5b), it is observed at the fractured surface that the lime sludge particles stay implanted in the matrix representing efficient adhesion at the interface between filler and matrix. Hence, it is morphologically evident that improved bonding ensures enhancement of mechanical properties of the MAPE-added composites.

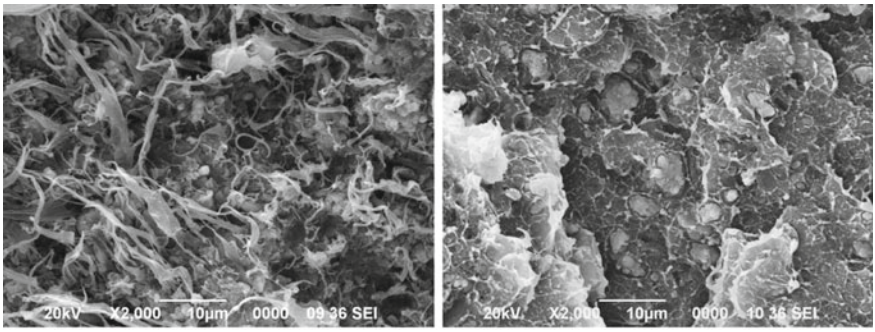

(a) HDPE/LS (70/30) (b) HDPE/LS/MAPE (65/30/5)

Fig. 5 SEM micrographs at the fractured surface of lime sludge-filled HDPE and MAPE-added lime sludge-filled HDPE

3.1.2 Flexural Properties

A sample lime sludge-HDPE composite before and after flexural test is shown in Fig. 6. The improvement in the bending strength may be due to the fact that the rough and rigid filler particles provided enhanced anchorage mechanically. This resulted in the improved transfer of stress from the matrix to the rigid filler particles in composite samples under the influence of bending stresses. Additionally, upon moulding, it is noticed that the surface of the polymeric composite is rendered smooth due to the restriction provided by the mould walls throughout moulding of the composites. This smooth surface rich in polymer hampers the production of cracks at the specimen surfaces (bottom and top surfaces experiencing maximum stress) during flexural loading. Superior entanglement between HDPE chains, lime sludge particles and the maleic anhydride (MA) modified HDPE chains and physical interaction under bending stresses lead to better flexural strengths for HDPE-MAPE composites. In order to resist higher amounts of stress for the identical amount of deformation within the elastic limit, the composites must exhibit higher rigidity. This is achieved by the introduction of rigid lime sludge particles and thus, flexural modulus is also observed to be an improvement with increasing filler loading in the composites.

3.1.3 Impact Properties

Lime sludge-filled HDPE composite before and after impact test is depicted in Fig. 7. Table 4 shows that the impact strength of lime sludge-HDPE-MAPE composites improved with increasing weight fraction of lime sludge filler. MAPE improved interfacial compatibility of lime sludge with the polymeric matrix as a result of which it could deliver more impact energy upon fracture.

MAPE assumed the function of bridge among the filler and HDPE matrix and improved the surface condition among each component. Hence, the impact strength

Fig. 6 A lime sludge-filled HDPE composite before and after flexural (bending) test

Fig. 7 A lime sludge-filled HDPE composite before and after impact testing

of composites improved much more than that observed for raw and stearic acid coated lime sludge-HDPE composites. Similar observations in the increase in the flexural and impact properties was reported earlier by Zhou et al. [27] where MAPE was used as the compatibilizer in carbon fibre/wood plastic composites.

It is also remarkable to note that out of all three MAPE contents (i.e. 1, 3 and 5 wt%), a MAPE content of 5 wt% proved to be the optimum weight fraction of MAPE in the composites which would result in the best mechanical properties among all the three sets of composites. This suggests that a weight fraction of 5 wt% MAPE provides the most effective interfacial adhesion at the filler-matrix boundary, thereby improving the mechanical properties.

3.2 *Lime Sludge-Filled Coir-HDPE-MAPE Hybrid Composites*

In this study, short coir fibres (8 mm long) and lime sludge were chosen as fillers in HDPE matrix. Additionally, 5 wt% MAPE is also employed as a compatibilizing agent in order to increase the bonding at the interfacial boundary. Since for lime sludge-filled HDPE composites, a weight fraction of 5 wt% provides the most superior properties of the composites, hence, a 5 wt% MAPE is also used in lime sludge-coir-HDPE-MAPE composites. Coir fibre is utilized because, in addition to mitigating environmental issues of using hazardous and non-biodegradable synthetic materials, natural fibres also offer advantages, viz. less costly, versatility, lightweight, biodegradable, renewability, high specific strength and specific modulus, lower equipment abrasion and energy consumption during processing [28]. Coir fibre (CF) has low cellulose content, high microfibrillar angle, not as brittle as glass fibre, can be chemically surface modified, is non-toxic (no waste disposal issues), waterproof, resistant to salt water and has lower tensile strength and high elongation compared to other ligno-cellulosic fibres [29, 30].

Thus, incorporation of lime sludge waste into fibre reinforced polymeric composites can propose some routes towards exploring alternatives for developing an industry for lime sludge waste, thus, in turn increasing its economic value. Hence, this study would throw some light on the effects of lime sludge on the properties of the coir-HDPE-MAPE composites.

The test outcomes of these composites are measured and tabulated in Table 5. Initially, the effects of coir and MAPE on HDPE matrix are discussed with the intention of assessing the outcome of adding coir on the characteristics of the hybrid composites. This is done in order to first determine the effective coir content in the composite which would exhibit superior properties. The coir content which shows optimum properties is then selected for fabrication of lime sludge-coir-HDPE composites with varying lime sludge content. Moreover, the variation in mechanical properties as a result of 5 wt% MAPE addition as a compatibilizer in the lime sludge-coir-HDPE is also presented.

3.2.1 Effect of Coir Fibre Content on Coir-HDPE Composites

The mechanical features of coir-HDPE composites with varying fibre contents (10, 20 and 30 wt%) are depicted in Table 5. It is seen that the tensile strength of coir-HDPE composites improved by 19.8% when coir weight fraction improved from 10 to 20 wt%. This initial increase may be attributed to the effective reinforcement offered by randomly distributed short coir fibres in HDPE matrix. However, the tensile strength decreased upon addition of more coir fibres (at 30 wt%) due to dewetting at the fibre-matrix boundary, thereby resulting in crack initiation at these locations upon loading. Similar trend in the tensile strength was reported earlier during testing of bagasse fibre [31] and rice straw fibre [32]. However, stiffness

Table 5 Tensile properties of lime sludge—coir-HDPE-MAPE composites

Designation	Tensile strength (MPa)	Tensile modulus (MPa)	Elongation at break (%)	Flexural strength (MPa)	Flexural modulus (MPa)	Impact strength (J/m)
HDPE/CF (90/10)	15.1 ± 0.8	236.5 ± 20.2	63.1 ± 14	11.5 ± 0.3	311.2 ± 13.2	20.6 ± 1.7
HDPE/CF (80/20)	18.8 ± 0.5	258.2 ± 21.6	22.7 ± 6.2	12.3 ± 0.3	375.3 ± 15.7	18.1 ± 1.1
HDPE/CF (70/30)	15.9 ± 0.5	275.8 ± 17.7	10.8 ± 2.0	12.7 ± 0.4	391.6 ± 14.1	17.5 ± 0.4
HDPE/CF/MAPE (85/10/5)	22.6 ± 0.3	311.2 ± 18.1	78.1 ± 10	12.1 ± 0.2	311.3 ± 12.3	22.9 ± 0.8
HDPE/CF/MAPE (75/20/5)	29.6 ± 0.4	336.9 ± 17.8	48.7 ± 6.3	12.8 ± 0.4	338.5 ± 13.3	20.9 ± 0.7
HDPE/CF/MAPE (65/30/5)	22.4 ± 0.3	364.2 ± 25.3	34.4 ± 4.8	14.5 ± 0.3	405.3 ± 10.6	19.3 ± 0.5
HDPE/LS/CF/MAPE (65/10/20/5)	24.1 ± 0.3	321.5 ± 14.8	52.4 ± 6.6	17.6 ± 0.4	437.4 ± 10.7	20.7 ± 0.6
HDPE/LS/CF/MAPE (60/15/20/5)	34.5 ± 0.3	345.1 ± 17.4	35.6 ± 5.2	19.4 ± 0.2	453.7 ± 15.3	19.5 ± 0.3
HDPE/LS/CF/MAPE (55/20/20/5)	25.4 ± 0.4	378.6 ± 14.9	14.9 ± 4.9	21.5 ± 0.4	475.8 ± 13.8	18.1 ± 0.4

and rigidity of the composites increased upon fibre loading as the tensile modulus increased by 14% when coir fibre content increased from 10 to 30 wt%. The increase in stiffness upon coir loading is due to the high stiffness of the fibres [33]. Needless to mention that with the improvement in the stiffness and tensile strength of the samples, the ductility of composites is bound to decrease significantly which is shown in Table 5. This significant reduction in the ductility (82.8%) with increasing coir weight fraction can be attributed to the destruction of structural integrity upon loading due to interfacial dewetting, increasing stiffness and fibre bundling at higher fibre content [34].

The flexural properties also improved with rising fibre loading in the coir-HDPE composites. However, the difference in increase of flexural strength was not significant, i.e. 11.55 MPa for 10 wt% to 12.71 MPa for 30 wt%. The flexural modulus increased significantly from 311.2 MPa for 10 wt% to 391.6 MPa for 30 wt% coir fibre loading. A similar trend in the flexural behaviour was reported earlier by Bettini et al. [35] for coir fibres reinforced PP composites. In this case, the mobility of the amorphous polymeric phase is largely hindered due to the existence of coir fibres in it. This results in the increase in the stiffness of the composites during bending.

Addition of coir fibre caused a decrement in the Izod impact strength when evaluated against pure HDPE, i.e. 30.33 J/m for pure HDPE to 17.53 J/m for 30 wt% coir fibre loading. The reduction in the impact strength is on account of the presence of coir fibres in the polymeric composites. As a result, the energy absorbed upon impact loading is reduced to a great extent, which subsequently decreased impact toughness. In related research reported earlier by various researchers, a decrease in the impact strength of polymeric composites was noticed upon addition of natural fibres which was attributed to poor interfacial adhesion at the fibre-matrix boundary [31, 32].

3.3 Effect of MAPE on Coir-HDPE Composites

The properties of coir-HDPE composites with 5 wt% of MAPE as compatibilizer and varying fibre content (10, 20 and 30 wt%) are shown in Table 5. Use of MAPE as a compatibilizer in coir-HDPE composites significantly improved almost all properties of the composites. This is in harmony with the outcomes reported earlier by other researchers in the case of maleic anhydride-based compatibilizer added composites [31, 36].

Although similar trends in the increase or decrease in the mechanical properties are shown by MAPE compatibilized composites when compared to neat coir-HDPE composites, the values obtained are far superior for MAPE compatibilized composites. This increase in the mechanical properties with the incorporation of 5 wt% MAPE compatibilizer, is due to the reaction between the hydroxyl groups of the coir fibres and the anhydride groups of the compatibilizer resulting in the formation of an ester linkage at the interface [37]. Additionally, the flexible polyethylene chains of MAPE can diffuse into the HDPE matrix and coir fibre bundles, improving the

continuity of the system. This would decrease the void content between the fibres and matrix, thereby increasing the interfacial adhesion at the filler-matrix boundary resulting in the increase in the mechanical properties [38, 39].

3.4 Effect of Lime Sludge on Coir-HDPE-MAPE Composites

Since the coir-HDPE composites showed optimum properties at 20 wt% fibre content, this fibre content is chosen for fabrication of lime sludge added coir-HDPE-MAPE composites with varying content of lime sludge (10, 15 and 20 wt%) in them. 5 wt% of MAPE is used as the compatibilizer. The lime sludge-coir-HDPE-MAPE composite properties are tabularized in Table 5.

Experimental results depicted that the tensile strength improved from 24.16 to 34.48 MPa when the lime sludge loading increased from 10 to 15 wt%, owing to successful reinforcement and distribution of filler particles in the matrix [40]. Upon further increment in filler weight fraction to 20 wt%, the strength reduced to 25.39 MPa indicating agglomeration of lime sludge particles, thus resulting in higher stress concentration sites and filler–filler interaction being more dominant than filler–matrix interaction [41]. Moreover, the addition of rigid lime sludge particles increased the tensile modulus from 321.5 to 378.6 MPa when lime sludge weight fraction improved from 10 to 20 wt%; thus increasing the rigidity of the specimens. Enhancement in the rigidity and strength, led to the reduction in ductility as it decreased from 52.43% to 24.93% with increase in lime sludge loading. The reasons for this trend in the properties of the composites are—particle agglomeration at higher filler content, filler–filler interaction rather than filler–matrix interaction and low ductility of the filler particles [41].

The flexural properties also improved upon lime sludge addition to the hybrid composites. The bending strength improved from 17.55 to 21.56 MPa while the bending modulus enhanced from 437.3 to 475.7 MPa as lime sludge loading rose up to 20 wt% from 10 wt%. The strength and rigidity of the coir-HDPE-MAPE composites subjected to bending increased when rigid filler particles are added to the matrix. The increment in rigidity may be due to the fact that under flexural loading conditions, the rigid lime sludge particles restrict the mobility of the polymer chains upon its addition [42, 43].

The Izod impact strength decreased from 20.69 to 18.14 J/m upon addition of lime sludge particles to the coir-HDPE-MAPE composites (as lime sludge loading rose up to 20 wt% from 10 wt%). Presence of rigid particles resulted in brittle failure of the composites. Due to this reason, the composite fails yielding comparatively much lower energy upon impact loading. Although MAPE provides good interfacial adhesion resulting in better impact properties compared to the composites fabricated without any coupling agent; yet the impact strengths of MAPE composites are still lower than the virgin polymer [44].

It is remarkable to observe that addition of lime sludge improved all the mechanical properties (viz. tensile strength and modulus, flexural strength and modulus) of the

coir-HDPE-MAPE composites, barring the elongation at break and impact strength, when compared with coir-HDPE-MAPE composites without any lime sludge addition. This suggests that rigid lime sludge particles had converted the coir-HDPE-MAPE composites into more rigid and less ductile material which resulted in decrease in the elongation and impact strength. This indicates that lime sludge proves to be an effective reinforcing agent in enhancing the rigidity and strength of the hybrid composite samples under both tensile and bending loading conditions.

3.5 Lime Sludge-Filled Coir Fibre-Epoxy Composites

It may be stated that generally the overall properties of lime sludge-filled epoxy composites are observed to be poor for its commercial use in diverse applications. Hence, of late, a substantial amount of research on hybrid composites with a variety of filler-fibre combinations have been conducted, viz. bio particles-coir [45], crab carapace-coir [46], powdered hazelnut shells jute [47], etc., in various polymer matrices. This is done in order to reap the benefits of both the reinforcing agents which would improve the properties of the composites in entirety. In this section, lime sludge is used as a potential reinforcing agent in coir-epoxy composites, in order to determine whether lime sludge addition in these composites offer a positive gain on the already existing counterparts. Two sets of coir-epoxy composites are tested—(i) 30 wt% of short coir fibre (8 mm long) and (ii) 30 wt% of long coir fibre uniaxially aligned (120 mm long); with lime sludge weight fraction varying as 0, 3, 6, 9 and 12 wt% in the composites.

3.5.1 Mechanical Properties

It is a known fact that the tensile properties of long fibre composites exhibit significantly higher properties when the fibres are aligned in the direction of tensile loading due to effective stress transfer from the matrix to the fibres and the continuity of the fibres throughout the composites. Thus, in the present study, it is observed that all the long coir fibre composites exhibit better properties than the corresponding short fibre (randomly oriented) composites with correspondingly identical lime sludge filler and fibre loading. The tensile and flexural properties of lime sludge-filled short and long coir fibre reinforced epoxy composites are tabulated in Table 6.

Tensile Properties

The properties of lime sludge-filled short and long coir fibre reinforced epoxy composites under tensile and flexural loading conditions are depicted in Figs. 8 and 9, respectively. It is observed that initially the tensile strength increased upon addition of lime sludge for both 30 wt% short and long coir-epoxy composites up to a lime sludge

Table 6 Tensile properties of lime sludge-filled coir epoxy composites

Designation	Tensile strength (MPa)	Tensile modulus (MPa)	Elongation at break (%)	Flexural strength (MPa)	Flexural modulus (MPa)
30 Coir-Epoxy (8 mm)	16.27 ± 0.12	411.4 ± 15.3	10.14 ± 0.14	30.6 ± 0.27	312.2 ± 10.3
3LS–30 Coir-Epoxy (8 mm)	12.33 ± 0.11	451.6 ± 13.6	9.18 ± 0.16	32.3 ± 0.24	353.4 ± 11.1
6LS–30 Coir-Epoxy (8 mm)	16.19 ± 0.17	496.0 ± 14.6	8.55 ± 0.25	36.3 ± 0.22	379.8 ± 12.3
9LS–30 Coir-Epoxy (8 mm)	13.76 ± 0.26	521.0 ± 12.8	6.74 ± 0.21	38.6 ± 0.19	434.2 ± 8.5
12LS–30 Coir-Epoxy (8 mm)	12.91 ± 0.15	543.4 ± 11.9	6.17 ± 0.18	45.9 ± 0.31	460.4 ± 10.9
30 Coir-Epoxy (long)	28.91 ± 0.75	501.6 ± 14.6	21.26 ± 0.23	42.7 ± 0.20	484.0 ± 12.5
3LS–30 Coir-Epoxy (long)	20.41 ± 0.43	524.0 ± 18.8	18.76 ± 0.18	44.5 ± 0.15	507.8 ± 13.3
6LS–30 Coir-Epoxy (long)	25.42 ± 0.39	552.6 ± 10.1	12.88 ± 0.29	51.7 ± 0.22	528.4 ± 13.5
9LS–30 Coir-Epoxy (long)	22.95 ± 0.77	587.4 ± 18.7	10.11 ± 0.15	57.5 ± 0.19	572.4 ± 8.6
12LS–30 Coir-Epoxy (long)	19.72 ± 0.23	613.2 ± 12.0	7.56 ± 0.38	60.4 ± 0.21	581.4 ± 11.9

content of 6 wt%, suggesting that lime sludge acts as an effective reinforcement, i.e. rigid filler particles resist the propagation of cracks upon loading up to 6 wt%. This can be credited to better dispersion of coir fibres and lime sludge particles in the matrix; thus guaranteeing efficient transfer of stress from the epoxy matrix to the reinforcing agents (fibres and particles). Appropriate dispersion and better bonding at the interface of filler and matrix causes an improvement in the tensile strength. However, as the lime sludge content increases beyond 6 wt%, the tensile strength starts to reduce. This is due to particle agglomeration, non-uniform dispersion of fillers, coir fibre bundling and low interfacial adhesion. This is in conformation with the outcomes achieved by Aldousiri et al. [48] where it was reported that the strength of coir reinforced HDPE composites under tensile loading, depended on factors such

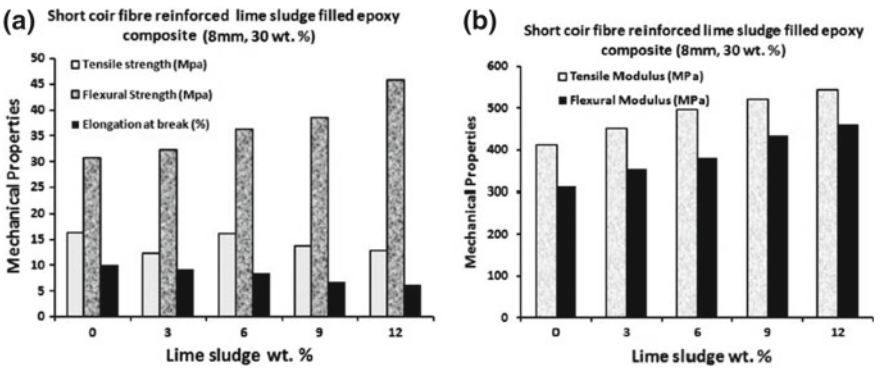

Fig. 8 Mechanical properties of lime sludge-filled short coir fibre reinforced epoxy composite

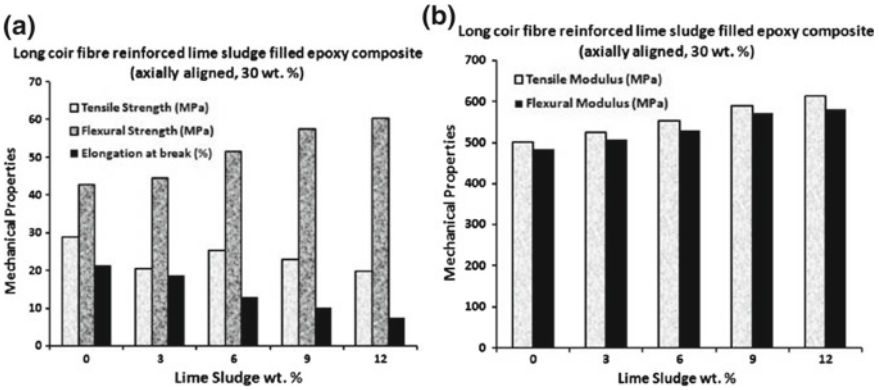

Fig. 9 Mechanical properties of lime sludge-filled long coir fibre reinforced epoxy composite

as filler loading and interfacial adhesion at the filler-matrix boundary. Additionally, it is natural that the long coir fibre composites exhibit superior tensile properties when compared with short fibre composites. This is due to the fact that the long coir fibres are aligned in the direction of tensile loading which ensures efficient transfer of stress from the matrix to the fibres.

Addition of rigid lime sludge particles and fibres in a softer matrix led to the improvement in the rigidity (Young's modulus) with increasing lime sludge weight %. Thus, the tensile modulus increased from 411.3 MPa for 0 wt% to 543.2 MPa for 12 wt% lime sludge loading for short coir fibre composites and 501.4 MPa for 0 wt% to 613.2 MPa for 12 wt% lime sludge loading for long coir fibre composites. Needless to say, the rigidity of long fibre reinforced composites are observed to be superior than that of short fibre composites owing to the fact that long, continuous and uniaxially aligned fibres are stiffer and stronger than short randomly distributed coir fibre in the epoxy matrix which provided efficient transfer of stress from epoxy to the coir fibres.

Ductility decreased with rising lime sludge weight fraction in case of both short and long coir fibre reinforced epoxy composites. The elongation at break (%) decreased from 10.14% for 0 wt% to 6.17% for 12 wt% lime sludge loading for short coir fibre composites and 21.26% for 0 wt% to 7.55% for 12 wt% lime sludge loading for long coir fibre composites. This decline in the ductility of composites is a characteristic of reinforced thermoplastic composites which is a result of low elongation of fibres. Additionally, the mobility of polymer molecules past each other is reduced to a great extent due to the presence of rigid lime sludge particles resulting in reduced ductility. Such trend in reduced ductility with increasing filler content was also reported earlier by Yao et al. [49]. Thus, tensile characteristics of lime sludge reinforced coir-epoxy hybrid composites are found to be much better than pure epoxy or lime sludge-epoxy composites. This is due to the added benefits of incorporating both lime sludge and coir fibres as reinforcements in the epoxy matrix.

At higher lime sludge content, particle agglomeration could result in the development of microvoids acting as stress concentration sites; thus decreasing the tensile properties. Such trend in the tensile behaviour of clay-filled coir reinforced polymeric composites was reported earlier by Muthu et al. [50]

Flexural Properties

The flexural strength increased from 30.66 MPa for 0 wt% to 45.88 MPa for 12 wt% lime sludge loading for short coir fibre composites and 42.68 MPa for 0 wt% to 60.42 MPa for 12 wt% lime sludge loading for long coir fibre composites. Lime sludge waste particles acted as efficient reinforcing agents along with coir fibres in the matrix. Moreover, upon moulding, it is noticed that the surface of the polymeric composite are rendered smooth due to the restriction provided by the mould walls throughout moulding of the composites. This smooth surface (rich in polymer) hampers the production of cracks at the specimen surfaces (bottom and top surfaces experiencing maximum stress) during flexural loading. Additionally, earlier studies reported that the improvement in the bending strength may be due to the fact that the rough and rigid filler particles provided enhanced anchorage mechanically. This resulted in improved transfer of stress from the matrix to the rigid filler particles in composite samples under the influence of bending stresses [51–53].

Flexural modulus improved with rising lime sludge weight fraction in the composites. The increase in flexural modulus follows a similar trend to tensile modulus which also rose due to increased brittleness and rigidity of the composites. Lime sludge particles are rigid particles and results in improving the stiffness and rigidity of the composites upon their incorporation in the polymeric matrix. Moreover, resisting higher amounts of stress for the identical amount of deformation within the elastic limit requires highly rigid composites. Since the composites show high rigidity, it means their flexural modulus has also improved, as observed from the experimental data. The improvement in bending strength and modulus with rising filler content loading was earlier also observed in various studies [51–53]. However, it is observed that both bending strength and modulus of continuous (long) fibre

composites are much superior to short fibre composites for the same filler loading as continuous fibres provided effective reinforcement and effective transfer of stress from the matrix to the fibres upon loading.

4 Conclusion

In order to be commercially viable and structurally feasible as a filler in polymeric composites, an industrial waste must be versatile enough to improve properties of composites with a variety of polymeric matrices and reinforcing agents. Hence, lime sludge waste is used as filler in a variety of matrices, viz. HDPE and epoxy and used alongside coir fibres in a polymeric matrix. MAPE is used as a compatibilizing agent in lime sludge-filled HDPE composites so as to improve their interfacial bonding at the junction of filler and matrix. It is observed that lime sludge acts an effective reinforcing agent in all these composites up to a certain filler loading under both tensile and flexural loading conditions. Lime sludge also improved the rigidity of the composites upon its addition by increasing the tensile and flexural modulus upon the application of tensile and bending loads. Due to the increase in the rigidity and strength of composites, the ductility decreased significantly upon rigid lime sludge addition. Characteristics such as filler-matrix interfacial adhesion, particle agglomeration at higher filler content, effective filler dispersion in the matrix and addition of stress generation locations by the rigid filler particles (leading to void creation upon loading) are important parameters affecting the mechanical properties of all these composites upon lime sludge addition. Additionally, it is observed that addition of 5 wt% MAPE as a compatibilizer showed to be an efficient agent in enhancing the filler-matrix interfacial adhesion, thereby improving the overall characteristics of the composites. However, MAPE increased the rigidity and strength of the composites which in turn decreased the ductility of the composites. Hence, industrial lime sludge waste proves to be an effective reinforcing agent in polymeric composites enhancing various properties as well as reducing the cost of the material; in addition to mitigating pollution, and increasing the versatility of an industrial waste for environmental sustainability.

Bibliography

1. Assessment of utilization of industrial solid wastes in cement manufacturing (2006) Technical report on programme objective series PROBES/103/2006–2007. Central Pollution Control Board (Govt. of India)
2. Wiegand PS, Unwin JP (1994) Alternative management of pulp and paper in-dustry solid wastes. Tappi J 77(4):91–97
3. Torkashvand AM, Haghighat N, Shadparvar V (2010) Effect of paper mill lime sludge as an acid soil amendment. Sci Res Essays 5(11):130–1306

4. Evanylo GK, Daniels WL (1999) Paper mill sludge composting and compost utilization. Compos Sci Utilization 7(2):30–39
5. Kwon S, Kim KJ, Kim H, Kundu PP, Kim TJ, Lee YK, Lee BH, Choe S (2002) Tensile property and interfacial dewetting in the calcite filled HDPE, LDPE, and LLDPE composites. Polymer 43(25):6901–6909
6. Bartczak Z, Argon A, Cohen R, Weinberg M (1999) Toughness mechanism in semi-crystalline polymer blends: II. High-density polyethylene toughened with calcium carbonate filler particles. Polymer 40(9):2347–2365
7. Zuiderduin W, Westzaan C, Huetink J, Gaymans R (2003) Toughening of polypropylene with calcium carbonate particles. Polymer 44(1):261–275
8. Kim KJ, White JL, Shim SE, Choe S (2004) Effects of stearic acid coated talc, $CaCO_3$, and mixed talc/$CaCO_3$ particles on the rheological properties of polypropylene compounds. J Appl Polym Sci 93(5):2105–2113
9. Kim HS, Lee BH, Choi SW, Kim S, Kim HJ (2007) The effect of types of maleic anhydride-grafted polypropylene (MAPP) on the interfacial adhesion properties of bio-flour-filled polypropylene composites. Compos A Appl Sci Manuf 38(6):1473–1482
10. Yang HS, Kim HJ, Park HJ, Lee BJ, Hwang TS (2007) Effect of compatibilizing agents on rice-husk flour reinforced polypropylene composites. Compos Struct 77(1):45–55
11. Kashyap S, Datta D (2017) Industrial Lime Sludge waste–HDPE composites— a study of their mechanical, thermal, and morphological properties. J Thermoplast Compos Mater. https://doi.org/10.1177/0892705717738289
12. Kashyap S, Datta D (2018) Evaluation of stearic acid modified industrial lime sludge waste as a filler in high density polyethylene composites. J Polym Eng 38(4):333–341
13. Acha BA, Aranguren MI, Marcovich NE, Reboredo MM (2003) Composites from PMMA modified thermosets and chemically treated wood flour. Polym Eng Sci 43(5):999–1010
14. Aziz SH, Ansell MP, Clarke SJ, Panteny SR (2005) Modified polyester resins for natural fibre composites. Compos Sci Technol 65(3):525–535
15. Wu CS (2005) Improving polylactide/starch biocomposites by grafting polylactide with acrylic acid–characterization and biodegradability assessment. Macromol Biosci 5(4):352–361
16. Martí-Ferrer F, Vilaplana F, Ribes-Greus A, Benedito-Borrás A, Sanz-Box C (2006) Flour rice husk as filler in block copolymer polypropylene: effect of different coupling agents. J Appl Polym Sci 99(4):1823–1831
17. Tserki V, Matzinos P, Panayiotou C (2006) Novel biodegradable composites based on treated lignocellulosic waste flour as filler. Part II. Development of biodegradable composites using treated and compatibilized waste flour. Compos A Appl Sci Manuf 37(9):1231–1238
18. Fan L, Dang Z, Nan CW, Li M (2002) Thermal, electrical and mechanical properties of plasticized polymer electrolytes based on PEO/P (VDF-HFP) blends. Electrochim Acta 48(2):205–209
19. Kim YD, Oh NL, Oh ST, Moon IH (2001) Thermal conductivity of W-Cu composites at various temperatures. Mater Lett 51(5):420–424
20. Gracia R, Evans RE, Palmer RJ, Johnson NJ (1987) Toughened composites. STP 937:397–412
21. Liau JY, Jang BZ, Hwang LR, Wilcox RC (1988) Toughening composites by matrix modification. Plast Eng 44(11):33
22. Bijwe J, Logani CM, Tewari US (1990) Influence of fillers and fibre reinforcement on abrasive wear resistance of some polymeric composites. Wear 138(1–2):77–92
23. Wang J, Gu M, Songhao B, Ge S (2003) Investigation of the influence of MoS2 filler on the tribological properties of carbon fiber reinforced nylon 1010 composites. Wear 255(1–6):774–779
24. Mir SS, Nafsin N, Hasan M, Hasan N, Hassan A (2013) Improvement of physico-mechanical properties of coir-polypropylene biocomposites by fiber chemical treatment. Mater Des 52:251–257
25. Nam TH, Ogihara S, Tung NH, Kobayashi S (2011) Effect of alkali treatment on interfacial and mechanical properties of coir fiber reinforced poly (butylene succinate) biodegradable composites. Compos B Eng 42(6):1648–1656

26. Salmah H, Ruzaidi CM, Supri AG (2009) Compatibilisation of polypropylene/ethylene propylene diene terpolymer/kaolin composites: the effect of maleic anhydride-grafted-polypropylene. J Phys Sci 20(1):99–107
27. Zhou Z, Xu M, Yang Z, Li X, Shao D (2014) Effect of maleic anhydride grafted polyethylene on the properties of chopped carbon fiber/wood plastic composites. J Reinf Plast Compos 33(13):1216–1225
28. Satyanarayana KG, Guimarães JL, Wypych F (2007) Studies on lignocellulosic fibers of Brazil. Part I: source, production, morphology, properties and applications. Compos Part A: Appl Sci Manuf 38(7):1694–1709
29. Jayabal S, Sathiyamurthy S, Loganathan KT, Kalyanasundaram S (2012) Effect of soaking time and concentration of NaOH solution on mechanical properties of coir–polyester composites. Bull Mater Sci 35(4):567–574
30. Morandim-Giannetti AA, Agnelli JAM, Lanças BZ, Magnabosco R, Casarin SA, Bettini SHP (2012) Lignin as additive in polypropylene/coir composites: Thermal, mechanical and morphological properties. Carbohydr Polym 87(4):2563–2568
31. Lei Y, Wu Q, Yao F, Xu Y (2007) Preparation and properties of recycled HDPE/natural fiber composites. Compos A Appl Sci Manuf 38(7):1664–1674
32. Yao F, Wu Q, Lei Y, Xu Y (2008) Rice straw fiber-reinforced high-density polyethylene composite: Effect of fiber type and loading. Ind Crops Prod 28(1):63–72
33. Ayrilmis N, Jarusombuti S, Fueangvivat V, Bauchongkol P, White RH (2011) Coir fiber reinforced polypropylene composite panel for automotive interior applications. Fibers Polym 12(7):919
34. Rozman HD, Tay GS, Kumar RN, Abubakar A, Ismail H, Ishak ZAM (1999) Polypropylene hybrid composites: a preliminary study on the use of glass and coconut fiber as reinforcements in polypropylene composites. Polym-Plas Technol Eng 38(5):997–1011
35. Bettini SHP, Bicudo ABLC, Augusto IS, Antunes LA, Morassi PL, Condotta R, Bonse BC (2010) Investigation on the use of coir fiber as alternative reinforcement in polypropylene. J Appl Polym Sci 118(5):2841–2848
36. Brahmakumar M, Pavithran C, Pillai RM (2005) Coconut fibre reinforced polyethylene composites: effect of natural waxy surface layer of the fibre on fibre/matrix interfacial bonding and strength of composites. Compos Sci Technol 65(3–4):563–569
37. Biswal M, Mohanty S, Nayak SK (2009) Influence of organically modified nanoclay on the performance of pineapple leaf fiber-reinforced polypropylene nanocomposites. J Appl Polym Sci 114(6):4091–4103
38. Nayak SK, Mohanty S, Samal SK (2010) Influence of interfacial adhesion on the structural and mechanical behavior of PP-banana/glass hybrid composites. Polym Compos 31(7):1247–1257
39. Satapathy S, Nando GB, Jose J, Nag A (2008) Mechanical properties and fracture behavior of short pet fiber-waste polyethylene composites. J Reinf Plast Compos 27(9):967–984
40. Satapathy S, Nando GB, Nag A, Raju KVSN (2013) HDPE-fly ash/nano fly ash Composites. J Appl Polym Sci 130(6):4558–4567
41. Satapathy S, Nag A, Nando GB (2012) Effect of electron beam irradiation on the mechanical, thermal, and dynamic mechanical properties of fly-ash and nanostructured fly ash waste polyethylene hybrid composites. Polym Compos 33(1):109–119
42. Pardo SG, Bernal C, Ares A, Abad MJ, Cano J (2010) Rheological, thermal, and mechanical characterization of fly ash-thermoplastic composites with different coupling agents. Polym Compos 31(10):1722–1730
43. Satapathy S, Kothapalli RVS (2018) Mechanical, dynamic mechanical and thermal properties of banana fiber/recycled high density polyethylene biocomposites filled with flyash cenospheres. J Polym Environ 26(1):200–213
44. Malkapuram R, Kumar V, Negi YS (2009) Recent development in natural fiber reinforced polypropylene composites. J Reinf Plast Compos 28(10):1169–1189
45. Ramprasath R, Jayabal S (2016) Particle swarm and simulated annealing based intuitive search optimization of flexural behaviors in bioparticles impregnated coir fiber–vinyl ester composites. Polym Compos 37(6):1765–1774

46. Rajamuneeswaran S, Jayabal S (2016) A lexicographic multi objective genetic algorithm for optimization of mechanical properties of crab carapace impregnated coir–polyester composites. Polym Compos 37(3):844–853
47. Matějka V, Fu Z, Kukutschová J, Qi S, Jiang S, Zhang X, Yun R, Vaculík M, Heliová M, Lu Y (2013) Jute fibers and powderized hazelnut shells as natural fillers in non-asbestos organic non-metallic friction composites. Mater Des 51:847–853
48. Aldousiri B, Alajmi M, Shalwan A (2013) Mechanical properties of palm fibre reinforced recycled HDPE. Adv Mater Sci Eng 2013:1–7
49. Yao Z, Xia M, Ge L, Chen T, Li H, Ye Y, Zheng H (2014) Mechanical and thermal properties of polypropylene (PP) composites filled with CaCO3 and shell waste derived bio-fillers. Fibers Polym 15(6):1278–1287
50. Muthu J, Priscilla J, Odeshi A, Kuppen N (2017) Characterisation of coir fibre hybrid composites reinforced with clay particles and glass spheres. J Compos Mater 0:1–15. https://doi.org/10.1177/0021998317712568
51. Khademieslam H, Kalagar M (2016) Evaluation of the bending strength, impact strength, and morphological properties of wheat straw fiber/paper mill sludge/polypropylene composites. BioResources 11(2):3914–3922
52. Knight GW (1996) Polyethylene. In: Polymer toughening, Marcel! Dekker Inc, Monticello, NY 12701-5185, USA, pp 189–235
53. Leong Y, Bakar A, Ishak Z, Ariffin A, Pukanszky B (2004) Comparison of the mechanical properties and interfacial interactions between talc, kaolin, and calcium carbonate filled polypropylene composites. J Appl Polym Sci 91(5):3315–3326

Electrochemical Discharge Drilling of Polymer Matrix Composites

Parvesh Antil, Sarbjit Singh, Alakesh Manna and Chander Prakash

Abstract The applications of nonconductive fibrous composites are increasing significantly over the last few years in numerous industries such as aerospace and marine application due to the unique combination of mechanical properties, i.e., lightweight and high strength. The components of aerospace and marine structures which are made of glass fibers require highly precise machining tasks like drilling for assembly in various parts of automobile and aerospace shuttles. Apparently, microdrilling of these nonconductive materials is still a challenge and critical aspect in the advancement of manufacturing industries. Recently, the utilization of electrochemical discharge drilling (ECDD) has emerged as the potential technique for the effective and precise microdrilling of such type of nonconductive materials. But, the reinforcement of abrasive particles deteriorates the drilling behavior of composites and results in high tool wear, increased cutting forces, and poor surface roughness of drilled hole. To avoid these complications, unconventional machining method like ECDD could provide a better platform for drilling of these types of materials. Keeping this in mind, the overview of electrochemical discharge drilling (ECDD) process including development and parametric optimization of the process parameters for effectual application in fibrous composites has been presented in this chapter. Moreover, an experimental investigation and optimization of ECDD process parameters have been carried out for the drilling of glass fiber reinforced polymer matrix composites.

P. Antil (✉)
Northern India Engineering College, New Delhi, India
e-mail: parveshantil.pec@gmail.com

S. Singh · A. Manna
Punjab Engineering College, Chandigarh, India
e-mail: sarb1234@gmail.com

A. Manna
e-mail: kgpmanna@rediffmail.com

C. Prakash
Lovely Professional University, Phagwara, India
e-mail: chander.mechengg@gmail.com

S. S. Sidhu et al. (eds.), *Futuristic Composites*, Materials Horizons: From Nature to Nanomaterials, https://doi.org/10.1007/978-981-13-2417-8_11

Keywords Electrochemical discharge drilling · Microdrilling
Polymer matrix composites · Taguchi's methodology

1 Introduction

Polymer matrix composites (PMCs) are newly developed nonconductive materials which are rapidly increasing their significance among the fraternity of advanced materials. The improved mechanical and tribological properties of PMCs have outclassed other materials for various industrial applications. Apart from these advantages, machining of these materials becomes a challenging feature for manufacturing industries to enhance adaptability in various areas. The aerospace industries use various components of composite materials require precise machining for the effective performance of designed component [1]. The presence of abrasive particles such as glass fibers, carbon fibers, SiC particulates, etc., deteriorate drilling behavior and restrict their widespread use in aerospace or other industry. The deteriorate quality characteristics are high tool wear, increased cutting forces, and the higher surface roughness of drilled hole wall [2]. The aerospace industries which use various components of composite materials require precise machining for effective performance of designed component [3]. The presence of abrasive particles such as glass fibers, carbon fibers, SiC particulates, etc., deteriorates drilling behavior and restricts their widespread use in aerospace or other industry [4]. These problems associated with conventional machining can be eliminated by unconventional machining method such as Electrochemical Discharge Drilling (ECDD), which can provide a better platform for machining of these types of materials. The ECDD process is an advanced and a hybrid machining route, where the machining mechanism of two well-known nonconventional machining processes has been superimposed, i.e., electrochemical machining process and electric discharge machining process. In ECDD process, material is removed from the workpiece surface due to chemical attack owing to electrochemical machining and electric sparks owing to electro discharge machining [5–8].

Even though the phenomenon of electrochemical discharge (ECD) machining was detected in mid of twentieth century, the potential of using this technique to machine nonconducting materials was explored by Karafuji and Suda [5] many years later. An additional analysis of material removal during electrochemical discharge machining and detailed characteristics of ECD process was explored by Allesu [9]. An electrochemical discharge drilling (ECDD) experimental setup consists of two electrodes, tool electrode and an auxiliary electrode which acts as cathode and anode, respectively. During experimentation, the material to be machined is placed normally below the tool electrode and immersed in an electrolyte, while the auxiliary electrode is placed at a particular distance from cathode electrode. A DC power supply source is used for initiation of the electrolysis process. When the applied voltage is lower than critical voltage, i.e., puncture strength of the gas film, the electrolysis process starts, and hydrogen bubbles are generated on the cathode tip. With the increase

in current density at cathode electrode, the size of hydrogen bubbles increases and coalescence to form a gas film. This gas film acts as an insulating layer between the tool electrode and electrolyte. As the applied voltage is higher than puncture strength of the gas film, the spark is initiated. The spark produced in the close vicinity of tool electrode results in melting, vaporizing, and thermally eroding of the workpiece due to discharge energy [10].

Various research studies advocated the different views on the ECDD mechanism. Ghosh [11] claimed that the electrical spark is produced due to switching phenomenon, instead of the breakdown of the insulating gas layer. Jalali [12] described this phenomenon as a hybrid mechanism based on a combination of local heating and chemical etching. The reactions which generally follows the electrochemical effect are of two types:

(i) Electrochemical responses at the electrode.
(ii) Chemical responses in the solution.

At the metal electrolyte boundary layers, the effect of electrochemical response at the electrode occurs and by dispersion, the relocation of ions in the electrolyte concentration takes place. As the appropriate potential is reached between IEG of machining zone, the reaction at tool and workpiece starts. The traditional types of reaction at the tool are:

(i) Cladding of metal ions

$$M^+ + e^- \rightarrow M$$

(ii) Progression of hydrogen gas

$$2H^+ + 2e^- \rightarrow H(\text{in acidic solution})$$
$$2H_2O + 2e^- \rightarrow 2(OH)^- + H_2(\text{alkaline sol.})$$

The reactions at anode are:

(i) Termination of metal ions in the electrolyte

$$M^- \rightarrow M^+ + e$$

(ii) Oxygen gas progression at the auxiliary electrode

$$2H_2O \rightarrow O_2 + 4H^+ + 4e^-(\text{acidic electrolyte})$$
$$4(OH)^- \rightarrow 2H_2O + O_2 + 4e^-(\text{alkaline electrolyte})$$

Basically, the material removal over workpiece surface includes the following main steps:

- electrochemical discharges initiate melting and vaporization,
- chemical etching at high temperature,

- unplanned thermal stresses and microcracking,
- expanding gases and electrolytic effect gives mechanical blow.

The performance of machining processes depends upon various prospects like the type of material to be machined, type of electrolytes used for the chemical action and most importantly, the type of tool electrode selected. The obtained observation from the available literature reveals that machining of superalloy and steel plates had also been attempted during ECDD process but mostly this process has been used for machining of nonconducting materials as shown in Fig. 1. In the domain of nonconductive materials, more than 60% research work has been carried out on materials made up of glass and quartz. As far as composites are concerned, nearly 5% research work has been carried out for the machining of composites. The machining of these materials is very difficult because of their fibrous structure and nonconductive nature. The selection of electrolyte for the ECDD process is a crucial aspect and needs to be addressed appropriately. From the available literature, it is confirmed that NaOH has attained popularity in comparison with other electrolytes due to high material removal rate as shown in Fig. 2. Nearly, 62% researchers worked on ECDD machining of materials have employed NaOH as electrolyte. The application of other electrolytes like NaCl and $NaNO_3$ are limited due to low MRR and generation of chlorine-based harmful gases. Additionally, the tool electrode of stainless steel and tungsten carbide are mostly used due to their chemical inertness, high temperature and wear resistance. The stainless steel is leading the chart with more than 30% of its share in tool electrodes, as shown in Fig. 3.

2 Literature Review

The electrochemical discharge drilling process has capabilities to machine hard, brittle as well as nonconductive materials. Various researchers have worked on electrochemical discharge phenomenon to machine various nonconductive materials. Basak and Ghosh [13] enlightened the process of the spark creation in the electrochemical discharge machining and effects of process parameters on the machining of electrically nonconductive materials. Bhattacharyya et al. [14] obtained best operating range of parametric combinations to achieve comparatively better machining rate and precision. Kulkarni et al. [15] put forward the role of spark generation and found that the perfect control of the spark initiations in the electrochemical discharge machining process has been a thought-provoking problem. Bhattacharyya and Munda [16] concluded that much precise shape with less overcut at sensible material removal rate can be produced (Fig. 4) by keeping the value of electrolyte concentration low, using higher voltage for machining and having a moderate value of pulse-on time. Sarkar et al. [17] highlighted the role of the interelectrode gap and witnessed that the increase in interelectrode gap decreases the heat-affected zone due to space between electrodes which increases the interelectrode gap resistance. Kumagai et al. [18] worked on the possibilities of increasing machining speed of electric discharge

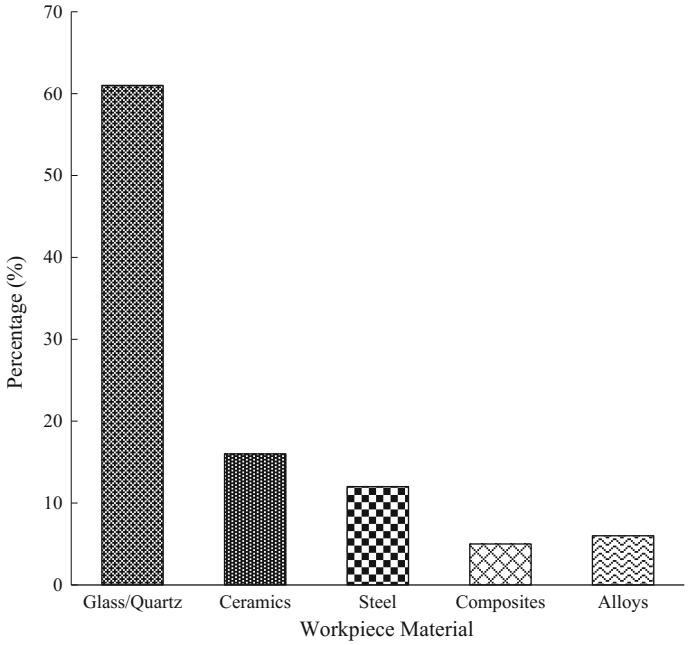

Fig. 1 Workpiece materials used in the ECDD process

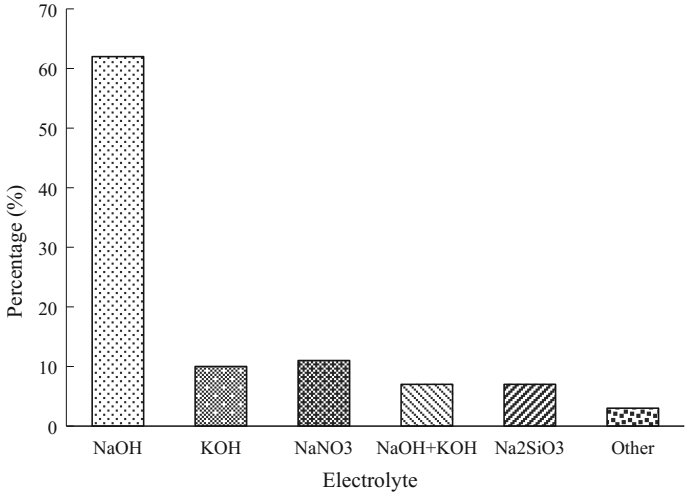

Fig. 2 Electrolytes used in the ECDD process

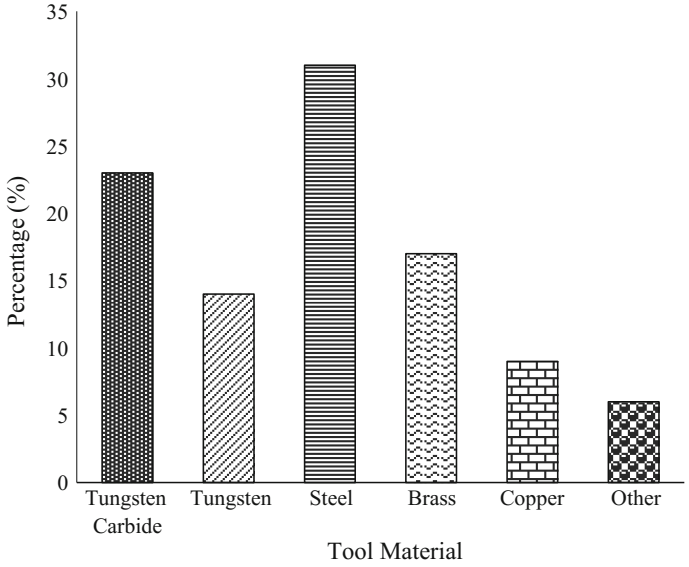

Fig. 3 Tool electrodes used in the ECDD process

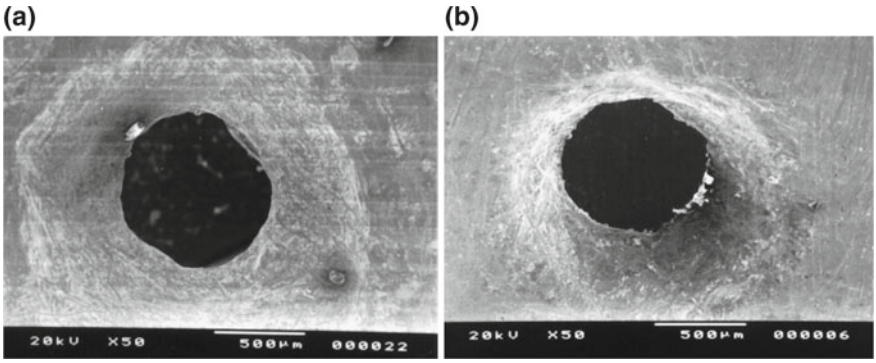

Fig. 4 SEM micrograph of machined hole at **a** 10 V, 25 g/L and 15 ms **b** 10 V, 20 g/L and 15 ms [16]

machining process and found that though abrupt electrode wear was experienced, yet speed of machining enhanced twofolds. Kim et al. [19] investigated that for a precise hole with the minor quantity of heating damage, it is compulsory to keep frequency higher and duty ratio minor, but it adversely affects the MRR.

Yang et al. [20] concluded that dielectric strength of the gas film is reduced by the presence of a conductive particle. Bhattacharyya et al. [21] witnessed the improvement in the machining accuracy during operation with tool vibrations as compared to machining with normal tool. The effect of heating in the machining zone was put forward by Mousa et al. [22] and explained that it affects the precise machining of the

workpiece material. Cheng et al. [23] worked on the improvement of surface roughness and explained that the rate of electrolysis affects the machined surface which improves with improving the electrolytic concentration. Liu et al. [24] concluded that the rate of gas bubbles generation accelerates with the acceleration in functional voltage, which generates a better quality of sparks in the sparking region and exaggerates the MRR. Han et al. [25] found that the stable cutting of glass is possible with the utilization of surface textured tool, which decreases the minimum voltage by 10 VDC with enhanced spark frequency. Manna and Narang [26] used specially designed square cross section with centrally micro-hole brass tool and round shape micro tool made of IS 3748 steel having different diameter for micro ESCM. The observations revealed that maximum MRR can be attained at operating parameters of voltage of 70 V; electrolyte concentration of 80 g/L; and interelectrode gap of 180 mm. Ziki et al. [27] concluded that the viscosity of the electrolyte can influence the fabrication of the microchannels. Bhuyan and Yadava [28] worked on modeling and optimization of travel wire electrochemical discharge machining process and revealed that electrolyte concentration is the most significant process parameter in travel wire ECDM followed by voltage, wire feed rate, and workpiece thickness. Malik et al. [29] worked on slicing of E-glass fiber epoxy composite by using hybrid wire electrochemical spark machining and found that improper and insufficient flow rate of electrolyte during machining produces many fins and scattered along the workpiece surface causing irregularity on the surface. Laio et al. [30] worked on the improvement of drilling quality in electrochemical discharge machining process. The authors concluded that the electrolyte mixed with Sodium Dodecyl Sulfate provides an increase in current density and gas bubbles around the electrode, which enables more stable pulse current. Kuo et al. [31] machined quartz glass with titrated electrolyte flow using wire ECDM. They revealed that quartz glass with straight and long slits with lesser mean width was obtained along with little electrolyte consumption when processed with wire ECDM. Jui et al. [32] worked on high aspect micromachining of glass by ECDM process and observed that the wear rate of electrode is deeply affected by nature of electrolyte. Huang et al. [33] analyzed the influence of process parameters like voltage, tool rotation, and diameter of tool electrode on the tool wear rate during ECDM of stainless steel. Chavoshi and Amir [34] presented a technical note on the significant process parameter which influences the drilling in hard to machine materials using electrochemical discharge machining process. Krötz and Konrad [35] employed electrochemical micromachining to find the possibilities for micro drilling in electrically conductive materials using electrochemical discharge phenomenon. The authors (Fig. 5) concluded that at higher electrical conductivity of electrolyte and longer machining time, there has been an impact on the shape of the hole entrance as well as the geometry as bigger the diameter, entrance will be more rounded and hole will be more cone shaped.

Baoyang et al. [36] analyzed the gas film using analytical modeling which involves gas film formation, electrolysis phenomenon, and gas bubble growth during ECDM. Dong et al. [37] used high-speed electrochemical discharge drilling to produce micro holes in the copper alloy plate using de-ionized water. The SEM analysis (Fig. 6) of micro holes confirms that the hole quality produced by high-speed electrochem-

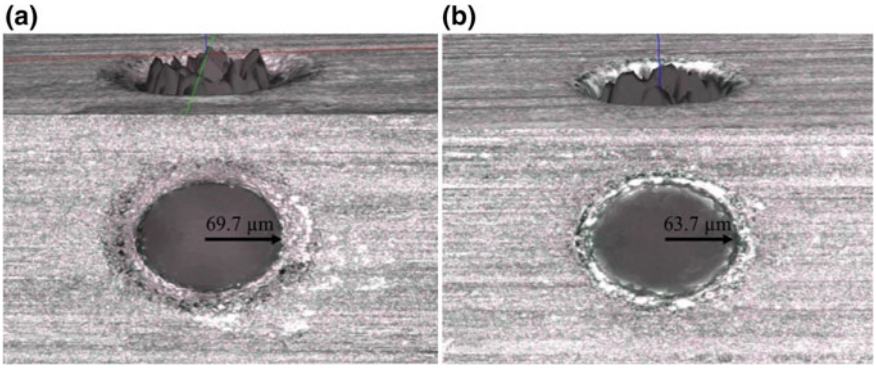

Fig. 5 Shape and diameter of the hole entrance of a micro hole drilled in sodium nitrate with **a** 30 ms/cm **b** 15 ms/cm [35]

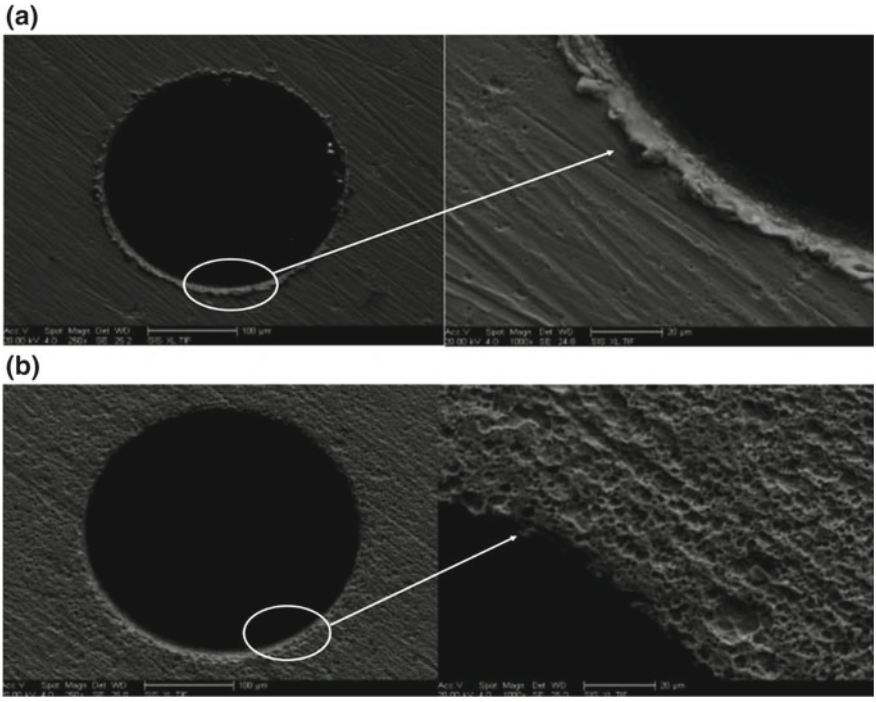

Fig. 6 SEM of hole drilled by **a** EDM **b** high-speed ECDD [37]

ical discharge drilling of C17200 beryllium copper alloy produces much uniform diameter in comparison with electric discharge machining.

Antil et al. [38] optimized electrochemical discharge drilling process during micro drilling in hybrid glass fiber SiC reinforced polymer matrix composites using gray

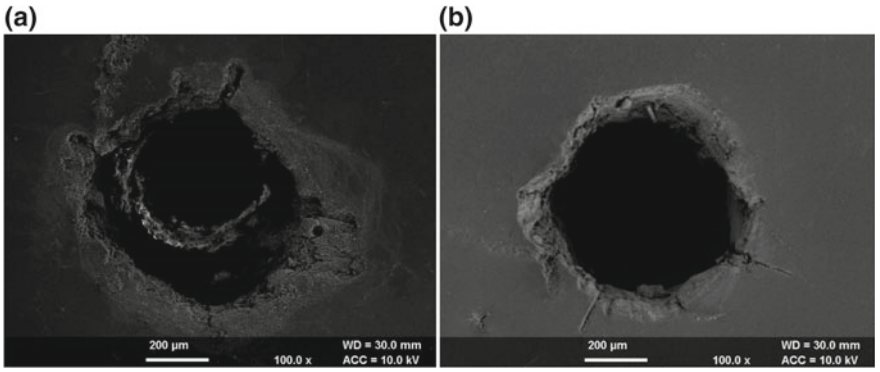

Fig. 7 SEM of hole drilled in experimentation by **a** Taguchi's OA **b** gray relational analysis [38]

relational analysis. The results revealed that among the machining parameters, inter-electrode gap and voltage were found as most significant parameters affecting MRR, overcut, and taper during ECDD. The SEM images as shown in Fig. 7 indicates the effect of heat zone on the surface of drilled hole boundary. The morphology indicates that tearing and cracking of a matrix induced over hole boundary can be controlled effectively by using the gray relational optimization approach.

3 Experimental Investigation

An experimental electrochemical discharge drilling setup has been designed and fabricated to be used for experimental analysis.

3.1 Experimental Setup: Design and Fabrication

The fabricated ECDD setup consists of four main components, i.e., (i) electrodes (ii) DC power supply (iii) machining chamber, and (iv) tool feed mechanism. Copper-plate was connected to positive terminal to function as auxiliary electrode, whereas hardened stainless steel needle of 0.4 mm diameter was used as tool electrode to serve as cathode. A voltage rectifier (i.e., converter cum regulator) was used to convert single phase 220 V, AC supply into DC supply voltage range of 20–200 V. An Acrylic Container was used to contain the required amount of electrolyte (aqueous solution of NaOH, KOH). During experimentation, the material which is to be machined is placed normally below the tool electrode and immersed in an electrolyte. The tool electrode is immersed in the electrolyte while the auxiliary electrode is placed away from cathode electrode. Gravity feed mechanism and constant velocity feed were

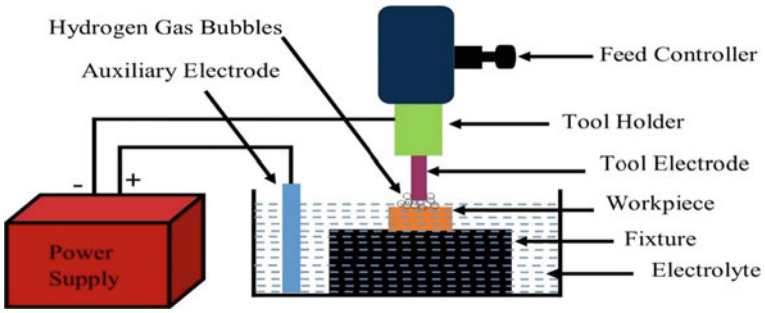

Fig. 8 Schematic representation of ECDD setup

provided to cathode for the entire experimentation. The schematic representation of fabricated ECDD setup is shown in Fig. 8. A DC power supply source is used for initiation of the electrolysis process. The machining zone of the ECDD process is shown in Fig. 9. The spark is produced over workpiece surface which is kept inside electrolyte chamber. The movement of the tool electrode is controlled by the feed controller. The variation in voltage is provided by the DC power supply unit. The variation in voltage affects the spark intensity as shown in Fig. 10. When the voltage was kept constant at 45 V, a low-intensity spark was produced but when the voltage was increased to 60 V and then 75 V, the spark intensity was comparatively higher.

3.2 Experimental Planning

The micro drilling of the glass fiber reinforced polymer matrix composite was performed on the electrochemical discharge drilling setup. Polymer matrix composite comprises of SiC particles of 400 mesh size and glass fibers as reinforcement along with epoxy resin as matrix was used as workpiece material. Six process parameters named as electrolyte, electrolyte concentration, voltage, interelectrode gap, pulse-on, and pulse-off were used as input parameters.

Table 1 represents the detail of various components like Electrochemical Discharge Drilling Setup (ECDD), electrolyte, electrolyte concentration workpiece, and tool material used during experimentation. The experimentation for micro drilling on the composite was designed through Taguchi's experimental design employing L_{18} orthogonal array. The performance of ECDD process depends on various input and output process parameters. An intricate interrelationship is presented between process parameters and output quality characteristics (QC), as shown in Fig. 11.

The material removal rate, overcut, and taper were measured as response characteristics. The material removal rate was measured as milligram per minute, whereas overcut and taper were measured in millimeter. The weight loss during micro drilling was measured by Denver SI 234 electronic weighing machine having least count of

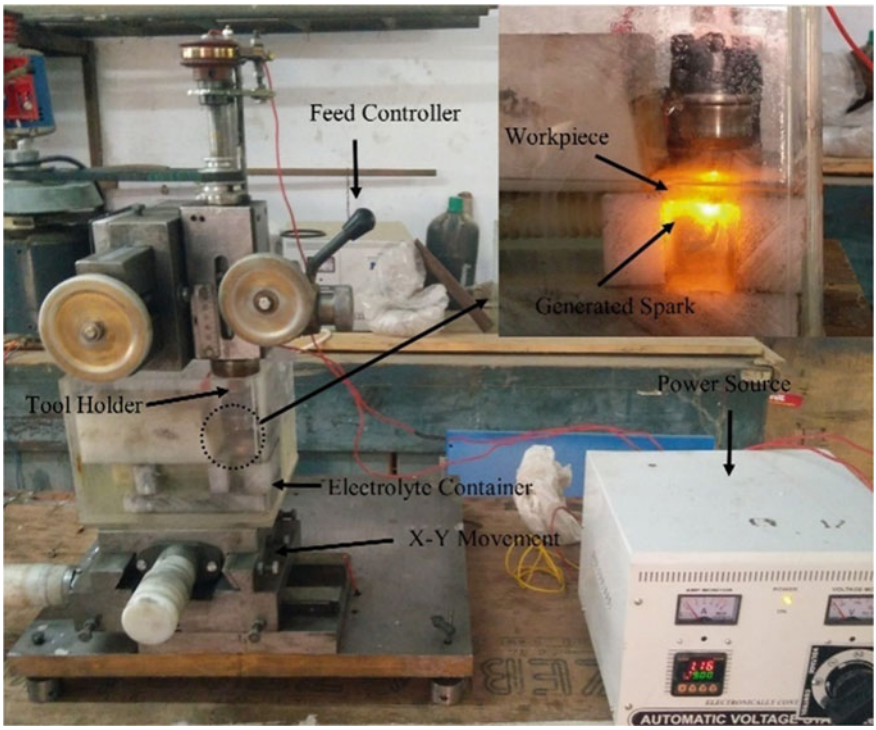

Fig. 9 ECDD setup

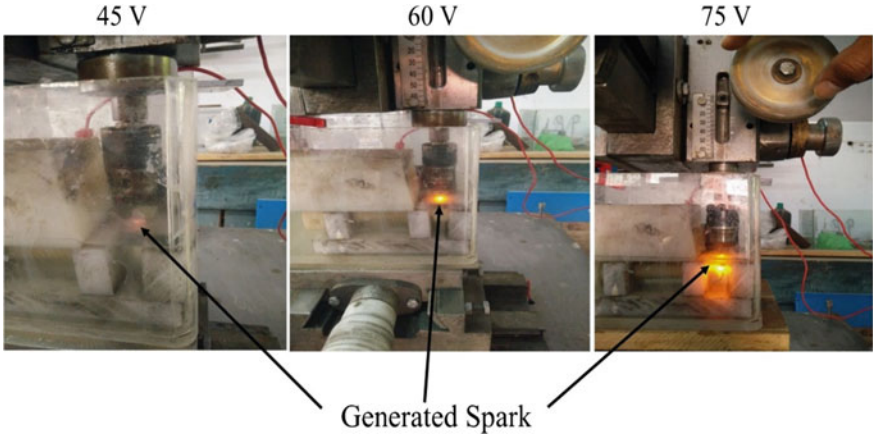

Fig. 10 Spark generation at different voltage

0.0001 g. The various machining parameters and levels used in experimentation are shown in Table 2.

Table 1 Experimentation details

Machine	Electrochemical discharge drilling setup
Electrolyte	NaOH, KOH
Electrolyte concentration	90; 100; 110 gm/L
Workpiece material	Glass fiber reinforced polymer matrix composite
Tool electrode	Hardened Stainless Steel Needle (0.3 mm)

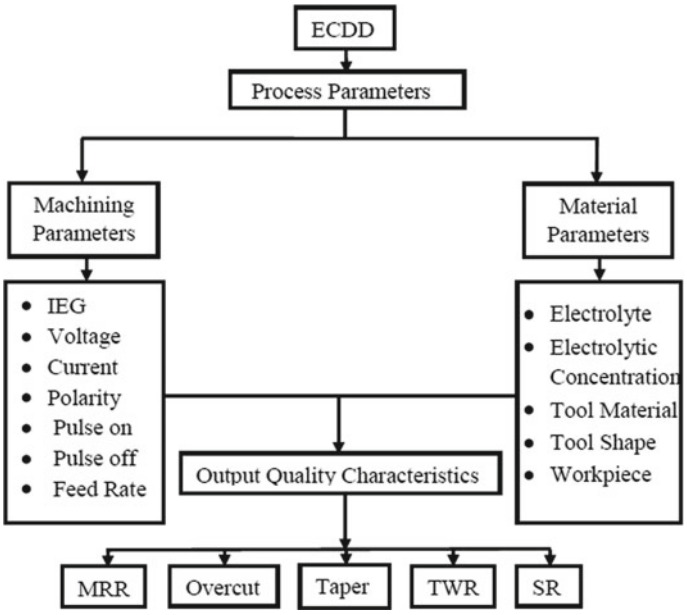

Fig. 11 Relation between input parameters and OQC

3.3 Results and Discussion

A number of experiments have been carried out with variation in parametric combination and obtained output was utilized for further analysis. Various plots have been drawn to examine the numerous parametric effects on the different machining characteristics of fabricated ECDD process. The obtained results for *S*/*N* ratio of material removal rate are plotted in Fig. 12. The greater value of *S*/*N* ratio corresponds to better quality characteristics because quality signal dominates the noise. Therefore, for higher material removal rate, the optimal combination of process parameters is the combination where *S*/*N* ratio is maximum. The optimal conditions for maximum material removal rate are electrolyte at level 2, electrolyte concentration at level 3, pulse-on at level 3, pulse-off at level 3, interelectrode gap at level 1, and voltage at level 3. In numeric values, the optimal values are electrolyte; NaOH; electrolyte

Table 2 Machining parameters and their levels

Symbol	Machining parameters	Level 1	Level 2	Level 3
A	Electrolyte	KOH	NaOH	–
B	Electrolyte concentration (gm/L)	90	100	110
C	Pulse-on (s)	6	8	10
D	Pulse-off (s)	0.5	1	1.5
E	Interelectrode gap (mm)	50	75	100
F	Voltage (V)	45	60	75

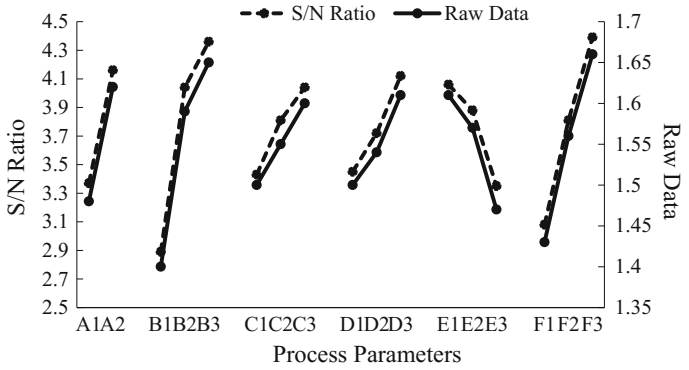

Fig. 12 Variation in MRR at different process parameters

concentration, 110 gm/L; pulse-on of 10 s; pulse-off of 1.5 s; interelectrode gap of 50 mm; and voltage of 75 V.

Figure 12 depicts that MRR increases with the change in the type of electrolyte from KOH (level A1) to NaOH (level A2). It is because NaOH generates higher amount of hydrogen gas bubbles and results in high spark intensity. When the electrolyte concentration changes from level B1 to level B2, there is a significant increase in MRR. However, MRR increases at slow rate from level B2 to level B3. The main reason for this behavior at higher concentration is the incremental degree of dissolution efficiency at high concentration is lesser as compared to low concentration [14]. When the pulse-on parameters changes from level C1 to level C2, there is steep increase in MRR, however, when the parameter changes from level C2 to level C3, the MRR increases at slow rate. During levels C1–C2, the spark is produced at workpiece surface for longer duration and causes higher amount of material removal. However, at level C3, the removed material is not completely flushed out and reduces the rate of material removal from workpiece surface. Whereas, for pulse-off, shown as parameters *D*, the MRR increases with increase in each level. This is because, at

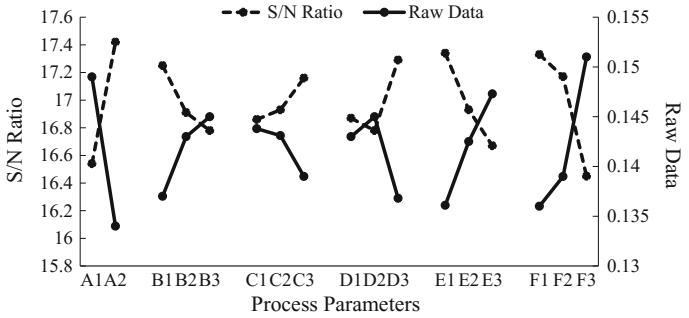

Fig. 13 Variation in overcut at different process parameters

higher pulse-off time, the electrolyte between workpiece surface and electrolyte is flushed away efficiently. The higher pulse-off time helps in effective removal of such particles from machined surface and increases MRR [28]. The effect of variation in MRR with the levels of interelectrode gap shows that the MRR decreases with increase in interelectrode gap from levels E1–E2 and then from E2 to E3. The reason behind this trend is because of variation in spark-affected zone (SAZ). The increase in interelectrode gap decreases the SAZ due to increased space between electrodes which further increases interelectrode gap resistance [13]. The voltage also has significant effect on material removal rate. The observed trends show that with increase in level of voltage, the MRR keeps increasing. The increase in voltage increase the MRR, it is because increase in voltage increases the rate of spark generation in spark zone [39]. The obtained observations for the MRR with variation in process parameters clearly indicate that voltage and electrolyte concentrations are most significant parameters for the MRR.

The obtained results for *S/N* ratio of overcut are plotted in Fig. 13. The optimal conditions for minimum overcut are electrolyte at level 2, electrolyte concentration at level 1, pulse-on at level 3, pulse-off at level 3, interelectrode gap at level 1, and voltage at level 1. In numeric values, the optimal values are electrolyte; NaOH; electrolyte concentration of 90 gm/L; pulse-on being 10 s; pulse-off at 1.5 s; interelectrode gap of 50 mm; and voltage of 45 V.

The graph shows a decrease in overcut with the change in type of electrolyte from KOH (level A1) to NaOH (level A2). When the electrolyte changes from KOH to NaOH, the steep decrease in overcut is observed because NaOH strengthens the spark intensity which helps in focused material removal form workpiece surface. The trend observed for the electrolyte concentration represents that the overcut produced during machining increases significantly with increase in electrolyte concentration, i.e., from B1 to B3. It is because at higher concentrations, the conductivity of the solution increases and results in increase in electrochemical reaction as well as circuit current [26]. The variation in pulse-on parameter shows that the overcut can be reduced if the machining of the composite is done at higher level of pulse-on parameter. When the pulse-on parameter varies from level C1 to level C2, the slow

decrease in overcut is observed, however, with further change from level C2 to C3, the overcut sharply decreases. The reason behind this trend is that the long spark duration enables effective digging of hole entrance, whereas comparatively lower spark duration increases fuzzing of matrix and results in high overcut. The observed trends for pulse-off shows that overcut increases with change in level D1 to level D3 but from level D2 to level D3, there is sharp decrease in overcut. At higher pulse-off time, the taper decreases because it provides effective time duration for removal of engraved material through electrolyte action [29]. The observed trends for interelectrode gap shows that overcut increases with the change in levels E1–E2 and similarly from E2 to E3. The reason behind this trend is that, with increase in interelectrode gap, the produced spark is not properly concentrated at specified machining zone but scattered all over at machined surface [40]. Similar to MRR, overcut is also significantly affected by the change in voltage. The overcut produced during machining is directly proportional to the applied voltage. With increase in voltage from level F1 to level F2, the overcut increases at slow rate. However, from levels F2 to F3, the overcut increases at high rate because high current density is generated at high voltage and results in increased overcut.

The obtained results for *S*/*N* ratio of taper are plotted in Fig. 14. The optimal conditions for minimum taper are electrolyte at level 2, electrolyte concentration at level 1, pulse-on at level 3, pulse-off at level 3, interelectrode gap at level 1, and voltage at level 1. In numeric values, the optimal values are electrolyte; NaOH; electrolyte concentration as 90 gm/L; pulse-on as 10 s; pulse-off as 1.5 s; interelectrode gap as 50 mm; and voltage as 45 V. The graph shows that taper produced during machining decreases with change in electrolyte from KOH (level A1) to NaOH (level A2), because KOH is less exothermic with water as compared to NaOH. Also, the KOH produces comparatively less amount of gas bubble during machining of through hole. The trend observed for the electrolyte concentration represents that from levels B1 to B2, the taper produced during machining increases significantly but at higher concentration, i.e., at level B3, slow increase in taper is observed. This is so because at low concentration, the entrance diameter is enlarged over a longer period due to insufficient flushing and material removal. However, at high concentration, the strong spark intensity removes material at comparatively uniform rate [41]. When the pulse-on parameter varies from levels C1 to level C2, the slow decrease in taper is observed. However, with further change from levels C2 to C3, the taper significantly decreases. The taper decreases at higher level of pulse-on time because extra machining time enables the spark and electrolyte to remove the wreckage produced during machining effectively. The observed trends for pulse-off shows that taper slightly increases with change in level D1 to level D2 but from level D2 to level D3, there is sharp increase in overcut.

The reason for pulse-off trend is somehow correlated with pulse-on time parameter. The higher pulse-on time enables the process to remove material in comparatively high amount and results in the requirement of high pulse-off time for flushing of machined material. The high pulse-off time provides better flushing of material through electrolyte and results in uniform machining of hole. The observed trends for interelectrode gap shows that taper increases with increase in level of interelec-

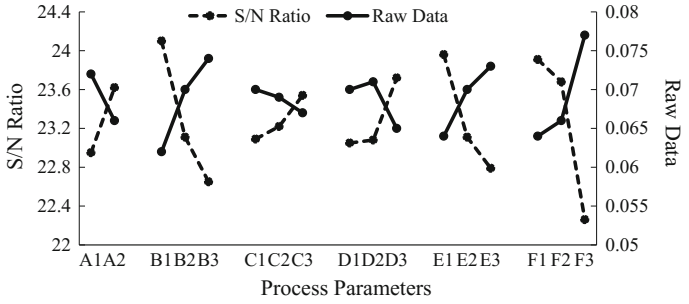

Fig. 14 Variation in taper at different process parameters

trode gap (level E). The taper produced during machining increases with increase in level from level E1 to level E2 and from level E2 to level E3 because number of spark generated during process decreases with increase in interelectrode gap. Lesser number of spark reduces the engraving action of the process and produces taper at hole exit [42]. With increase in voltage from level F1 to level F2 and further from level F2 to F3, the taper increases because high voltage increases the generation of gas bubbles at sparking zone which creates more stray sparking at side walls.

3.4 Morphological Inspection

The morphological analysis of the composite surfaces was done to analyze the state of surface after machining. The SEM image of composite micro machined at supply voltage of 45 V is shown in Fig. 15. The other process parameters were kept at constant having value of electrolyte concentration as 100 gm/L; pulse-on of 8 s; pulse-off at 1 s; and interelectrode gap of 50 mm. NaOH was used as electrolyte for the analysis. The spark intensity at applied voltage of 45 V is comparatively low because of the low energy density supplied in machining zone. The matrix cracking and nonuniformity in diameter are observed over composite surface. The fiber residual which produced during through hole machining is clearly visible inside hole boundary. These fiber residuals affect the machining process by blocking the electrolyte flow which decreases the material removal rate. The irregular flow of electrolyte affects the spark produced inside the machined hole and reduces the material removal phenomenon.

The SEM image of composite micro machined at supply voltage of 60 V is shown in Fig. 16. The other process parameters were kept at constant as discussed earlier. The SEM images show that the hole machined at 60 V has comparatively better finish at surface and absence of fiber residuals helps in generating required sparking effect. The increase in supply voltage increases the number of spark discharges which effectively removes the excessive fiber existence inside hole boundary during

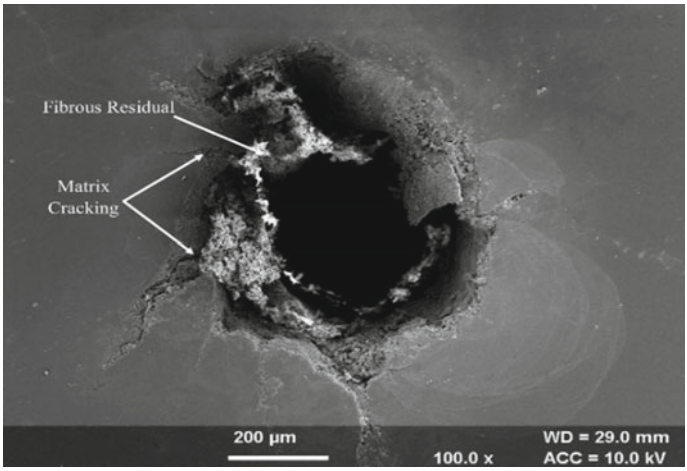

Fig. 15 SEM of hole at 45 V

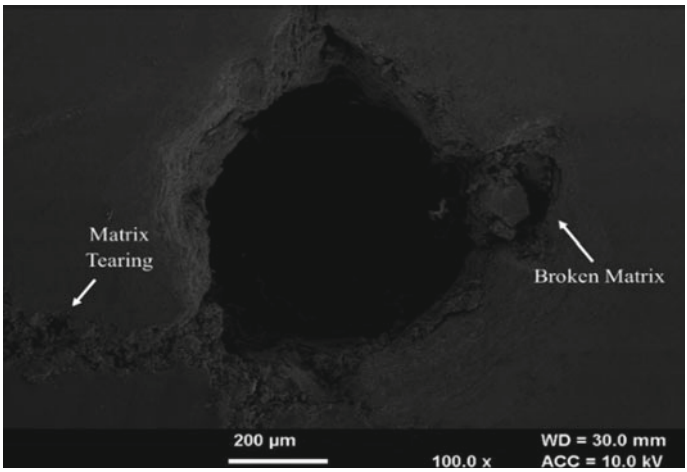

Fig. 16 SEM of hole at 60 V

machining. The hole produced during machining at 60 V has comparatively better uniformity in diameter at compared with earlier. Although, the matrix cracking and fiber matrix de-bonding are visible over composite surface but still the uniformity in hole diameter is achieved at this voltage.

The SEM image of composite micro machined at supply voltage of 75 V is shown in Fig. 17. The SEM image reveals that the surface at the entrance of hole is highly affected by the spark produced during machining. The high energy density produced at high voltage increases the overcut at the entrance of the hole. The fibers are visible at hole boundary wall because high intensity of spark deboned the fiber matrix bonding.

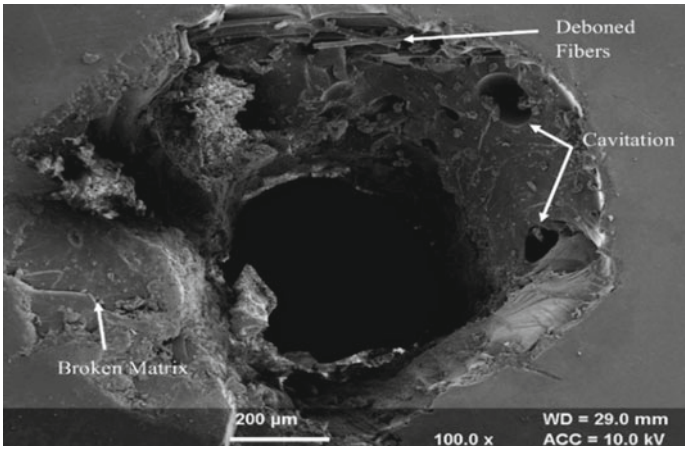

Fig. 17 SEM of hole at 75 V

The de-bonding of matrix and fibers also loses the secondary reinforcement which causes the cavitation over hole surface. The scattered spark increases the spark-affected zone which initiates the matrix breakage and increases the overcut.

4 Conclusions and Future Scope

Polymer matrix composites (PMCs) are newly developed nonconductive materials which are rapidly increasing their significance among fraternity of advanced materials. The improved mechanical and tribological properties of PMCs have outclassed other materials for various industrial applications. Apart from these advantages, drilling of these materials becomes a problematic feature for manufacturing industries to enhance adaptability in various areas. These problems associated with conventional machining can be eliminated by unconventional machining method such as Electrochemical Discharge Drilling (ECDD), which can provide better platform for machining of these types of materials. This chapter discusses the previously published research articles related to electrochemical discharge phenomenon which strengthen the fact that this process can be effectively used for the drilling of brittle and nonconductive composite materials. This chapter also presents the brief about the design and development of the electrochemical discharge drilling machine. This developed machine is utilized for drilling in nonconductive materials (i.e., polymer matrix composite). By analyzing various experimental results during drilling of workpiece on fabricated ECDD setup, it is believed that the electrochemical discharge drilling machine can be effectively use to drill nonconductive materials. However, during experimentation, it is identified that material removal rate as well as overcut was significantly affected by voltage. MRR increases with increase in voltage

and maximum MRR was observed in range of 60–70 V during electrochemical discharge drilling of polymer matrix composites. Interelectrode gap is proved to be the most significant parameter for overcut. The reduction in overcut during machining can be attained by keeping parametric setting of minimum interelectrode gap and electrolytic concentration of 100 gm/L. As far as taper is concerned, voltage is the most significant parameter followed by electrolyte concentration, interelectrode gap and electrolyte. The entire experimentation revealed that electrochemical discharge drilling can be effectively used for the machining of hard to machine composite materials. The optimized parameter of ECDD process can provide improved hole quality. As some research work has been done on possibilities of using electrochemical discharge phenomenon for the drilling purpose in conductive materials, this process can be precisely and intelligently used for drilling hard to cut materials.

References

1. Antil P, Singh S, Manna A (2017) Glass fibers/SiCp reinforced epoxy composites: effect of environmental conditions. J Compos Mater 52(9):1253–1264
2. Antil P, Singh S, Manna A (2017) Effect of reinforced SiC particulates of different grit size on mechanical and tribological properties of hybrid PMCs. Mater Today Proc 5(2):8073–8079
3. Rahamathullah I, Shunmugam MS (2014) Mechanistic approach for prediction of forces in micro-drilling of plain and glass-reinforced epoxy sheets. Int J Adv Manuf Technol 75(5):1177–1187
4. Singh S (2016) Effect of modified drill point geometry on drilling quality characteristics of metal matrix composite (MMCs). J Mech Sci Technol 30(6):2691–2698
5. Karafuji H, Suda K (1968) Electrical discharge drilling of glass. Ann CIRP 16:415–419
6. Prakash C, Uddin MS (2017) Surface modification of β-phase Ti implant by hydroaxyapatite mixed electric discharge machining to enhance the corrosion resistance and in-vitro bioactivity. Surf Coat Technol 326:134–145
7. Prakash C, Kansal HK, Pabla BS, Puri S (2017) Experimental investigations in powder mixed electric discharge machining of Ti–35Nb–7Ta–5Zrβ-titanium alloy. Mater Manuf Processes 32(3):274–285
8. Prakash C, Kansal HK, Pabla BS, Puri S, Aggarwal A (2016) Electric discharge machining a potential choice for surface modification of metallic implants for orthopedics applications: a review. Proc Inst Mech Eng, Part B: J Eng Manuf 30(2):331–353
9. Allesu K (1988) Electrochemical discharge phenomenon in manufacturing processes. Ph.D. thesis, Indian Institute of Technology, Kanpur
10. Razfar MR, Behroozfar A, Ni J (2014) Study of the effects of tool longitudinal oscillation on the machining speed of electrochemical discharge drilling of glass. Precis Eng 38(4):885–892
11. Ghosh A (1997) Electrochemical discharge machining: principle and possibilities. Sadhana J 22(3):435–447
12. Jalali M, Maillard P, Wuthrich R (2009) Toward a better understanding of glass gravity-feed micro-hole drilling with electrochemical discharges. J Micromech Micro Eng 19(4):1–8
13. Basak I, Ghosh A (1996) Mechanism of spark generation during electrochemical discharge machining: a theoretical model and experimental verification. J Mater Process Technol 62(1):46–53
14. Bhattacharyya B, Doloi BN, Sorkhel SK (1999) Experimental investigations into electrochemical discharge machining (ECDM) of non-conductive ceramic materials. J Mater Process Technol 95(1):145–154

15. Kulkarni A, Sharan R, Lal GK (2002) An experimental study of discharge mechanism in electro-chemical discharge machining. Int J Mach Tools Manuf 42(10):1121–1127
16. Bhattacharyya B, Munda J (2003) Experimental investigation on the influence of electrochemical machining parameters on machining rate and accuracy in micromachining domain. Int J Mach Tools Manuf 43(13):1301–1310
17. Sarkar BR, Doloi B, Bhattacharyya B (2006) Parametric analysis on electrochemical discharge machining of silicon nitride ceramic. Int J Adv Manuf Technol 28(9):873–881
18. Kumagai S, Sato N, Takeda K (2006) Combination of capacitance and conductive working fluid to speed up the fabrication of a narrow deep hole in electrical discharge machining using a dielectric-encased wire electrode. Int J Mach Tools Manuf 46(12):1536–1546
19. Kim DJ, Yoomin A, Seoung-Hwan L, Yong-Kweon K (2006) Voltage pulse frequency and duty ratio effects in an electrochemical discharge micro drilling process of Pyrex glass. Int J Mach Tools Manuf 46(10):1064–1067
20. Yang CT, Song SL, Yan BH, Huang FY (2006) Improving machining performance of wire electrochemical discharge machining by adding SiC abrasive to electrolyte. Int J Mach Tools Manuf 46(15):2044–2050
21. Bhattacharyya B, Malapati M, Munda J, Sarkar A (2007) Influence of tool vibration on machining performance in electrochemical micro-machining of copper. Int J Mach Tools Manuf 47(2):335–342
22. Mousa M, Allagui A, Ng HD, Wuthrich R (2009) The effect of thermal conductivity of the tool electrode in spark-assisted chemical engraving gravity-feed micro-drilling. J Micromech Micro Eng 19:1–7
23. Cheng C-P, Wu K-L, Mai C-C, Yang C-K, Hsu Y-S, Yan B-H (2010) Study of gas film quality in electrochemical discharge machining. Int J Mach Tools Manuf 50(8):689–697
24. Liu JW, Yue TM, Guo ZN (2010) An analysis of the discharge mechanism in electrochemical discharge machining of particulate reinforced metal matrix composites. Int J Mach Tools Manuf 50(1):86–96
25. Han MS, Min BK, Lee SJ (2011) Micro-electrochemical discharge cutting of glass using a surface-textured tool. CIRP J Manuf Sci Technol 4(4):362–369
26. Manna A, Narang V (2012) A study on micro machining of E-glass epoxy composite by ECSM process. Int J Adv Manuf Technol 61:1191–1197
27. Ziki JDA, Didar TF, Wüthrich R (2012) Micro-texturing channel surfaces on glass with spark assisted chemical engraving. Int J Mach Tools Manuf 57:66–72
28. Bhuyan BK, Yadava V (2013) Experimental modeling and multi-objective optimization of traveling wire electrochemical spark machining (TW-ECSM) process. J Mech Sci Technol 27(8):2467–2476
29. Malik A, Samir S, Manna A (2013) A study on hybrid WECSM setup during cutting of e glass fiber epoxy composite. In: International conference on advancements and futuristic trends in mechanical and materials engineering
30. Laio YS, Wu LC, Peng WY (2013) A study improve drilling quality of electrochemical discharge machining (ECDM) process. Proc CIRP 6:609–614
31. Kuo K-Y, Wu K-L, Yang C-K, Yan B-H (2013) Wire electro chemical discharge machining (WECDM) of quartz glass with titrated electrolyte flow. Int J Mach Tools Manuf 72:50–57
32. Jui SK, Kamaraj AB, Sundaram MM (2013) High aspect ratio micromachining of glass by electrochemical discharge machining (ECDM). J Manuf Process 15:460–466
33. Huang SF, Liu Y, Li J, Hu HX, Sun LY (2014) Electrochemical discharge machining micro-hole in stainless steel with tool electrode high-speed rotating. Mater Manuf Processes 29:634–637
34. Chavoshi SZ, Amir MB (2014) A note on influential control parameters for drilling of hard-to-machine steel by electrochemical discharge machining. Int J Adv Manuf Technol 71:1883–1887
35. Krötz H, Konrad W (2015) Spark assisted electrochemical machining: a novel possibility for micro drilling into electrical conductive materials using the electrochemical discharge phenomenon. Int J Adv Manuf Technol. https://doi.org/10.1007/s00170-015-6913-9
36. Baoyang J, Shuhuai L, Kevin W, Jun N (2015) Modeling and experimental investigation of gas film in micro electrochemical discharge machining process. Int J Mach Tools Manuf 90:8–15

37. Dong S, Wang Z, Wang Y (2016) High-speed electrochemical discharge drilling (HSECDD) for micro-holes on C17200 beryllium copper alloy in deionized water. Int J Adv Manuf Technol 88(1):827–835
38. Antil P, Singh S, Manna A (2017) Electrochemical discharge drilling of SiC reinforced polymer matrix composite using taguchi's grey relational analysis. Arab J Sci Eng 43(3):1257–1266
39. Malik A, Manna A (2016) An experimental investigation on developed WECSM during micro slicing of e-glass fibre epoxy composite. Int J Adv Manuf Technol 85(9):2097–2106
40. Antil P, Singh S, Manna A (2014) A study on input parameters affecting material removal rate and surface roughness in electrochemical discharge machining process. Int J Adv Res Sci Technol 3(12):400–405
41. Mallick B, Sarkar BR, Doloi B, Bhattacharyya B (2013) Parametric analysis of travelling wire electrochemical discharge machining process reason. Tech J 12(1):93–101
42. Manna A, Narang V (2012) An experimental investigation during micro machining of E glass fibre epoxy composite on developed electrochemical spark machining setup. Int J Manuf Mater Mech Eng (IJMMME) 2(2):10–15

Fabrication of Metal Matrix Composites by Friction Stir Processing

Vikas Upadhyay and Chaitanya Sharma

Abstract Friction stir processing (FSP) is gaining wide attention as an alternative route for the fabrication of metal matrix composites. This chapter commences with a general introduction to various aspects of metal matrix composites and various processing routes for their fabrication. It then provides basics of friction stir processing and briefs about multiple methods of secondary phase/reinforcement incorporation in the matrix. In the subsequent section, the effect of different FSP parameters on the mechanical properties and wear behavior of the composite material are discussed in detail. The chapter finally presents the summary of the significant aspects of composite fabrication by FSP and scope for future work.

Keywords Friction stir processing · Metal matrix composites · Fabrication

1 Introduction

The constant strive to produce lightweight materials with a tailor-made property to suit the pressing need of energy efficiency and sustainability led to the development of composite materials. Composites are composed of two or more materials which remain distinct and identifiable in the resulting material but complement each other to provide desirable properties superior than individual components. Metal matrix composites (MMCs) is an influential class of composite materials which incorporates secondary phase reinforcements in a relatively lightweight metal matrix. Reinforcements are usually in the form of particulates, whiskers, or fibers (continuous or short) to act as the primary load-bearing component of composites. The commonly used reinforcements in MMCs are oxides, carbides, ceramics, nanotubes such as SiC, Al_2O_3, B_4C, TiC, SiO_2, TiN, carbon nanotubes, to name a few. Nearly, all MMCs in

V. Upadhyay (✉)
Mechanical Engineering Department, National Institute of Technology Patna, Patna 800005, India
e-mail: vikasupadhyay.agra@gmail.com

C. Sharma
Rustamji Institute of Technology, Border Security Force, Tekanpur, Gwalior 475005, India

S. S. Sidhu et al. (eds.), *Futuristic Composites*, Materials Horizons: From Nature to Nanomaterials, https://doi.org/10.1007/978-981-13-2417-8_12

commercial use utilize discontinuous reinforcements, however, MMCs with continuous graphite, SiC, and Al_2O_3 fibers also exist [1]. The main reasons for enormous use of discontinuous reinforcements are their isotropic properties, competitive levels of specific strength and stiffness, easy fabrication by conventional techniques, and cost-effectiveness, i.e., they are comparatively less expensive [1, 2].

The size, shape, volume fraction, orientation, distribution, and type of reinforcement all affect the composite properties to a significant extent. So far as the reinforcement size is concerned, they can be broadly divided into nano size and micron size. Nano-size reinforcements require less quantity (volume fraction $<2\%$) to achieve desirable composite properties in comparison to conventional composites (volume fraction $\gg 10\%$) as the interface to volume ratio is significantly higher in nanocomposites. However, to get the desired properties, good distribution of reinforcement within the matrix is also necessary which in turn depends on the production process [2].

Many production techniques were used to develop MMCs and they can be broadly classified as the liquid state, solid state, and semisolid state processes depending on the state of the matrix material or as ex situ and in situ process by the method of reinforcement particle incorporation in the matrix material. Liquid state process is economical and amenable to industrial use but has serious concerns regarding wettability of reinforcement with matrix metal and adverse matrix reinforcement reactions due to high temperature involved in the process. Low wettability results in agglomeration of reinforcement in the matrix and leads to deterioration of composite properties. To overcome these problems, various approaches were attempted but the most promising is pre-coating of the reinforcement [3]. Whereas in the solid-state process, the processing temperatures were low enough for any undesirable interface reaction to occur but the bonding of reinforcement with matrix material is not adequate and porosity is high, often requiring secondary processes. The main advantages of solid-state processes are that high volume fraction of reinforcements can be incorporated and reinforcement/matrix combinations not possible by liquid casting process can be produced [3, 4]. In semisolid casting processes, partial solid mixture with small near-globular grains at solid fractions between 20 and 60% were shaped to get the composite. The basic advantages of the processes are low shrinkage and porosity, nonturbulent filling, and lower processing temperatures [4].

In ex situ method of composite production, reinforcements were produced/prepared separately and then dispersed into matrix by a suitable production process. Larger grain size, porosity, poor bonding, agglomeration of reinforcements, and adverse interface reactions are some of the problems related with ex situ processing [5]. Whereas in an in situ method, the reinforcement particles were produced during the process leading to clean particle–matrix interface, better bonding, and thermodynamically stable and finer particles [6].

Apart from these, some other techniques such as Equal Channel Angular Pressing (ECAP), Accumulative Roll Bonding (ARB), and Friction Stir Processing (FSP) were also utilized to produce composites. ECAP, ARB, and FSP are solid-state processes relying on severe plastic deformation and differ in the way of producing plastic deformation and mixing to develop composites [2]. ECAP and ARB are used to

produce bulk composites, whereas FSP is most suitable for surface composites [7]. Friction stir processing which is an adaptation of Friction Stir Welding (FSW), works on the same principle and is used either to improve composite properties or to produce composites by ex situ or in situ method.

The focus of this work is to summarize the various methods which is used to produce metal matrix composites, and then to discuss the FSP technique for production of surface composites in general and surface nanocomposites in particular. The basics of FSP and effect of various FSP parameters on composite were discussed in the subsequent sections.

2 Basics of Friction Stir Processing

FSP was introduced by Mishra et al. [8] as an adaptation to FSW process in which the single workpiece is stirred instead of two workpieces. The fabrication of surface composite by microstructure modification using FSP was also first reported by Mishra et al. [9]. It has gained a worldwide recognition as an alternative route for the fabrication of composites. In FSP, a nonconsumable rotating tool that consists of shoulder and pin, is inserted in the workpiece and is allowed to traverse in the required direction. This rotating and traversing motion of the tool increases the heat and deforms the workpiece material in the vicinity of shoulder and pin. The temperature in FSP is below the melting temperature of the matrix material, but this temperature is high enough to produce good bonding between reinforcement and matrix during stirring, but lower enough to minimize the formation of detrimental phase constituents within the microstructure. The heat generation, weld thermal cycle, peak temperature, material flow, etc., are mainly controlled by the tool and pin design and dimensions, welding speed, rotary speed, the axial force on tool, and tool tilt. The utmost care during the selection of the tool is required as it influences the generation of heat and material flow. Though during plunging of rotating tool into substrate material plate, the friction between pin and substrate plate generates heat, it is the friction between the shoulder and upper surface of the substrate plate which generates most of the heat in the later stage of FSP. Besides generation of heat, tool shoulder is important as it confines the heated and plasticized material and establishes material flow using strong coupling due to sticking friction between them [10].

Almost every type of composites can be developed using FSP technique by simply controlling the tool profile and geometry. The method of reinforcement/secondary phase incorporation is the specific feature of FSP which differs it from FSW. Surface coating, groove filling method, hole filling method, sandwich method, and direct friction stir processing tool method were used for reinforcement incorporation in the matrix. In the surface coating method, secondary phase particles were coated on the matrix material, whereas in groove and hole filling methods, secondary phase particles were incorporated in the narrow groove(s) and tiny holes, respectively. These grooves or holes can be closed by means of a pin-less tool before FSP to

prevent the escaping of particles during the process. The secondary phase particles were sandwiched between the sheets or plates in the sandwich method. In direct friction stir processing tool method, reinforcement particles were introduced on the surface of base metal through the hole drilled along the longitudinal axes of the tool [11].

3 Effect of FSP Parameters on the Mechanical Behavior of Composites

The development of sound surface composites by friction stir processing depends on thermomechanical deformation of the solid-state substrate to achieve homogeneous distribution of added strengthening particles of micron or nano size. The thermomechanical deformation of the substrate material is influenced by various parameters as listed in Fig. 1.

The various parameters were grouped under major heads of tool geometry variables, machine variables, material variables, and other variables. The variable related to tool and pin geometry, FSP machine, and properties of substrate material and reinforcing powder are principal independent variables and their combination affects dependent variables significantly which, in turn, govern the quality and properties of developed surface composites. Forthcoming sections discuss the influence of various parameters on the microstructure, mechanical, and wear behavior of composites fabricated by FSP with various kinds of reinforcements.

3.1 Effect of Tool and Pin Geometry

In general, the generation of heat increases with increase in shoulder diameter, however, its effect on material flow is different. The tool workpiece interface area increases with increase in shoulder diameter, leading to increase in the sliding torque, and decrease in sticking torque beyond the peak value. Therefore, for a given set of process parameter and workpiece, the optimum shoulder diameter should yield maximum sticking torque to have greatest coupling of the plasticized material with shoulder to result in effective material flow [12]. The friction stir welding/processing is highly efficient process as about 95% of the generated heat is utilized in softening of the workpiece/substrate materials [13].

The shoulder may be without pin or with pin and has flat, concave, or convex surface with or without spirals. Some of the basic shoulder designs are presented in Fig. 2.

Pin-less flat shoulder tool is generally employed to close the groove filled with reinforcing particles [14]. The concave shoulder surface is found to affect the microstructure and failure mode of FSW joints than flat surface [15, 16] while with

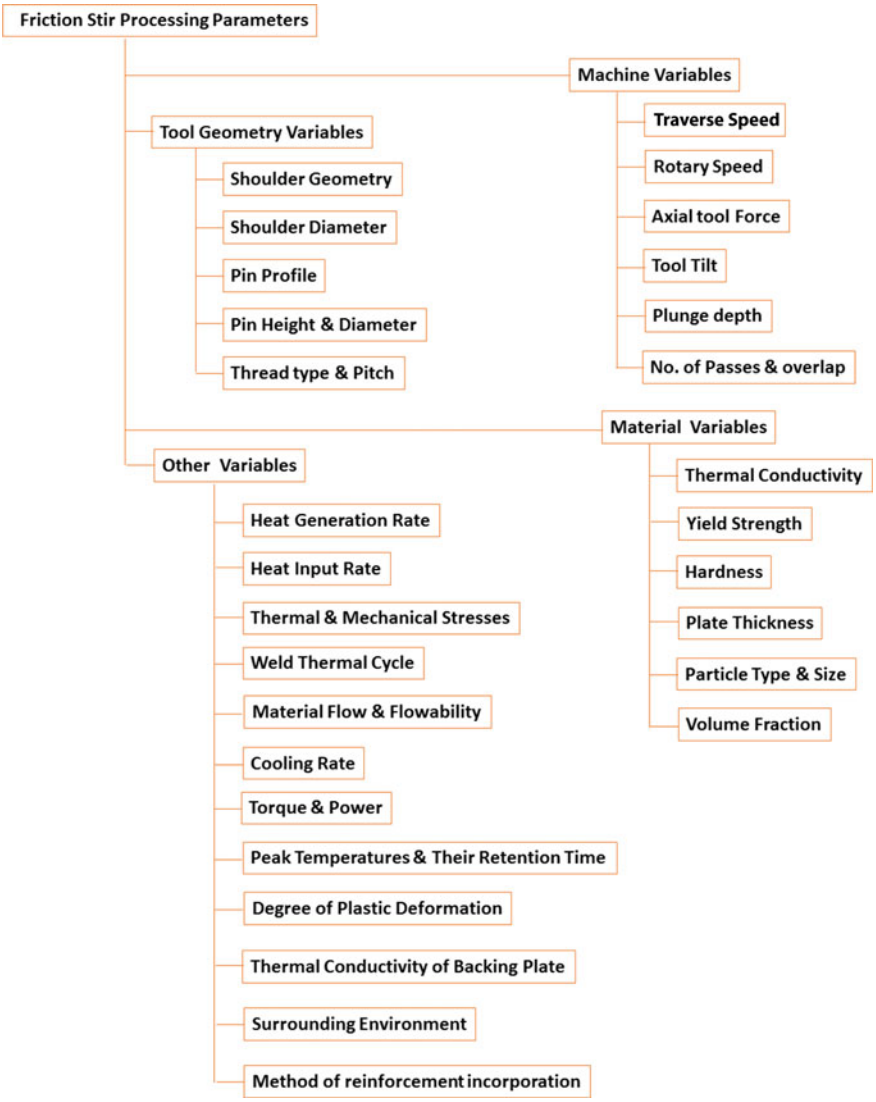

Fig. 1 Various parameters for friction stir processing

convex scroll shoulder, process was found to be more stable because greater area of shoulder–workpiece interface reduces axial force on increase in plunge depth from preset value and vice versa. The shoulder design significantly affects the generation of flash and thinning of workpiece/substrate plates just beneath the shoulder. The flat shoulder generates maximum flash followed by concave and convex scroll shoulder as shoulder is unable to completely confine the escaping plasticized material from stirred region [17]. The Whorl^{TM}, MX Triflute^{TM} displaces 60 and 70% less material

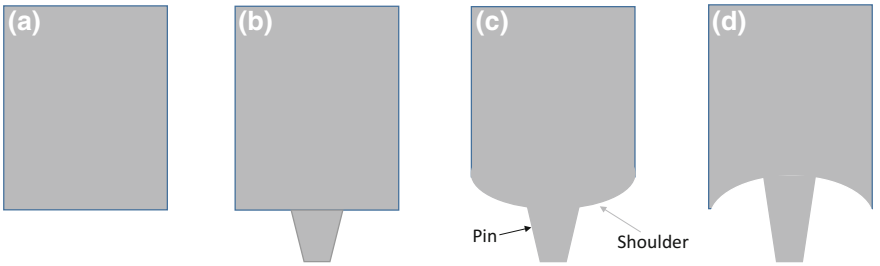

Fig. 2 Tool shoulder designs **a** flat shoulder without pin **b** flat shoulder with pin **c** convex and **d** concave

volume as opposed to cylindrical tool of same root diameters because of higher ratio of swept volume to volume of pin [18]. Though, bulk of material flow is enabled by tool shoulder, pin geometry also affects the flow of plasticized material and transport it from top to bottom of stir zone layer by layer [19].

The tapered pin design is supposed to offer smoother plunging than straight pin and fewer chances of pin breaking due to lower forces. Addition of features like flutes, thread, and their orientation on pin, increases the interfacial area resulting in higher heat generation, improved material flow and reduced axial, and transverse force on tool pin [20, 21]. Rotating truncated conical pin results in helical motion pushing the material downward and upwards in front and rear side of the tool to establish circular motion pattern which enhances the material flow and yields uniform material properties. Therefore, taper pin tools are favored as opposed to straight pin tool [22]. The traversing spherical pin end has line contact than surface contact in flat pin end and is believed to eliminate the occurrence of wormhole at the root of stirred zone. The square pin provided better distribution of reinforcing SiC particles in comparison to other tools, viz. circular without thread, circular with thread and triangular in Al–SiC metal matrix composite made by friction stir processing, regardless of rotary speed, whereas circular tool experienced much less wear than the flat-faced square and triangular tools [23]. The pin profile influences the occurrence of defects, distribution of reinforcing particles, grain size, and hardness of Al7075T651/TiN nanocomposite fabricated by friction stir processing (Fig. 3).

The square and triangular pin produced tunnel and pin hole defects while no such defect was observed in case of threaded taper pin. The stirred zone had dark and bright regions owing to varying density of TiN particles. The dark region with low TiN density was more in case of square and triangular pins than threaded taper pin. Threaded taper pin spreaded the bright region from the top to root of the stirred zone than other pins as threads facilitated downward movement of TiN particles leading to more uniform distribution. Similarly, threaded taper pin produced finer grains than triangular and square pin. However, the same do not exhibit any discernible effect on the hardness of the composites [14]. The threaded taper, square, and triangular pin caused particle agglomeration, tunnel defect, and pin hole in two-pass Al/TiN dispersion strengthened surface composites. The increase in number of passes from

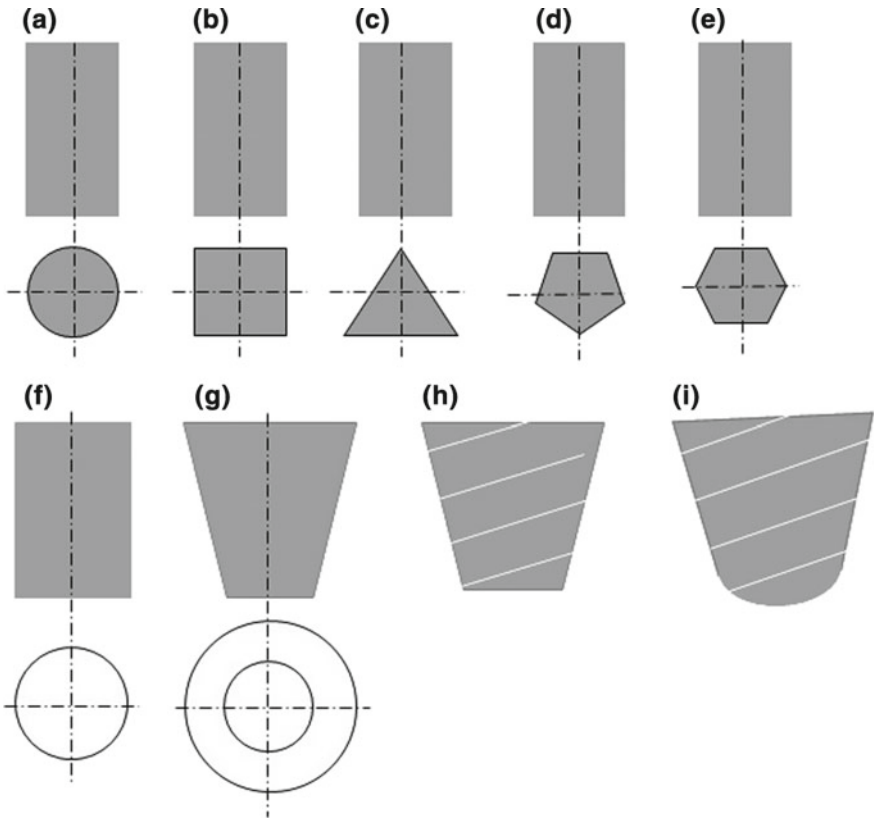

Fig. 3 The pin geometries **a** cylindrical **b** square **c** triangular **d** pentagonal **e** hexagonal and pin designs **f** straight **g** tapered or truncated conical **h** flat end with threads and **i** spherical/curved end with threads

two to four tends to make sound and denser composites as increasing number of passes enhances stirring and material flow resulting in more uniform particle distribution. The threaded tool pin causes better distribution of reinforcing particles than non-threaded tools. Threaded taper pin created uniform dispersion of TiN particles throughout the stirred zone as evident from white appearance of the stirred zone while other stirred zone were black at the bottom owing to the absence of TiN particle in the bottom region of stirred zone [24].

3.2 Effect of Rotary and Welding Speed

The tool rotary speed and welding speed governs the heat generation and heat input in per unit processing length and thus affects the composite properties. The

microstructure of AZ31/Al_2O_3 nano composites was influenced by rotational speed but the tool rotary speed did not influence the formation of cavities using non-threaded straight cylindrical tool. The cavities became smaller with the increase of rotary speed from 800 to 1200 rpm. At low rotary speed of 800 rpm, fluted pin stuck in the substrate material. The three flutes on the cylindrical pin reduced the threaded region largely reducing the heat generation and flowability of the material. The retarded flowability in case of pin with smaller threaded area lowered the downward movement of the material which in turn caused tunnel defect and heterogeneously stirred region as the level of breaking and dispersion of Al_2O_3 particles is reduced. The increase in rotary speed and number of passes produced more symmetric and uniform stirred zone. The size of Al_2O_3 particles and that of aluminum matrix decreased with increase in rotary speed from 800 to 1200 rpm, however, later is found to increase with further increase in rotary speed from 1000 to 1200 rpm. The hardness of AZ31/Al_2O_3 nano composites was found to decrease with increase in rotary speed. The increase in rotary speed exhibited improved distribution of Al_2O_3 nanoparticles and more homogeneous microstructure as increase in rotary speed was supposed to intense the stirring which in turn increased the heat generation and flowability resulting in smaller cluster size, improved distribution of reinforcement, and breaking of previously formed onion rings [25].

The microhardness of AZ31/Al_2O_3 nanocomposites increased with decrease in particle size from 1000 to 35 nm. The highest microhardness with finest size reinforcement (35 nm) is because of severe grain boundary pinning produced by uniformly distributed nano-size Al_2O_3 particles [25]. The ultimate tensile strength and hardness of multi-walled carbon nanotubes aluminum matrix (MWCNTs/Al) composites increased with increase in the volume (0–6%) of MWCNTs and elongation decreased with the same. The average microhardness and ultimate tensile strength with 6% volume of MWCNTs were found 2.2 and 2.05 times that of the friction stir processed aluminum alloy without MWCNTs. The significant improvement of microhardness and ultimate tensile strength can be attributed to grain refinement and strengthening by MWCNTs because of strong interface bonding. There was no significant change in grain size which indicates that improvement of hardness and ultimate tensile strength were due to improved load transfer capacity of the matrix with increase in the content of MWCNTs. The elongation of friction stir processed aluminum alloy without MWCNTs decreased from 26 to 9.6% due to increase in the content of MWCNTs from 0 to 6 vol%. This suggests that when MWCNTs content increases the MWCNTs/Al composite becomes brittle. The MWCNTs/Al composite with highest contents of MWCNTs exhibited insignificant necking and cleavage fracture contrary to composites without MWCNTs [26].

3.3 Effect of FSP Passes

In friction stir processing, multiple passes were generally employed to improve the distribution of reinforcing particles, homogenization of stir zone, and to improve the

mechanical and wear behavior of composites. With increase in number of passes, the grain size of Al7075T651/TiN nanocomposites decreased and hardness increased. The increase in number of passes from two to four leads to the disappearance of any defect in Al7075T651/TiN nanocomposites and better distribution of TiN particles assisted by altering metal flow caused by change of tool rotation from anticlockwise to clockwise and vice versa between successive passes [14]. The increase in number of passes from two to four tends to make Al/TiN dispersion strengthened surface composites sound and denser. The average microhardness increased with increase in number of passes while average grain size of matrix, average friction coefficient, and mass loss in wear decreased with the same. The uniform dispersion of TiN particles and finer matrix grains increased the microhardness which in turn lowered the friction coefficient [24]. No discernible effect of FSP passes was observed on the uniformity and formation of defects in the stir zone of AZ31/Al_2O_3 nanocomposites. The size of Al_2O_3 particles and that of aluminum matrix decreased with increase in number of passes from two to four while hardness of AZ31/Al_2O_3 nanocomposites increased with increase in number of passes. The increase in number of passes and rotary speed exhibited improved distribution of Al_2O_3 nanoparticles and more homogeneous microstructure [25]. The increase in number of passes from one to eight decreased the size and dispersed SiC particles more uniformly in the copper matrix while single pass yielded in partial agglomeration of SiC particles. The severe fragmentation of SiC particles was noticed during the second pass and same was less discernible in higher passes. The mechanical properties (microhardness, yield strength, ultimate tensile strength, and ductility) increased with the number of passes. The microhardness in stirred zone was found significantly higher than the base matrix of copper alloy. Moreover, uniform dispersion of SiC particles was believed to produce less fluctuation in microhardness of eight- and four-pass samples than single-pass sample [27]. The multi-pass FSP was applied on the Al 6061 aluminum plates reinforced with Cr_2O_3 particles by plasma spray. During FSP, aluminum reduced the Cr_2O_3 particles to form pure Cr and Al_2O_3 particles upto three passes beyond which formation of intermetallic compounds of Al–Cr occurred due to reaction between Al and Cr [28].

It is well known that FSP is similar to hot working of metals and involves extreme thermomechanical deformation for the modification of microstructure and improvement of mechanical and wear behavior. The effect of multiple passes during friction stir processing of reinforced composites is summarized below: The increase in number of passes during FSP increases the mechanical stirring and promotes the breaking of reinforcing particles. The reinforcing particles becomes finer and finer with increase in number of FSP passes. Same is also expected to reduce the tendency of clustering and breaking of previously formed onion rings [25]. Due to intense mechanical stirring, higher is the heat generation and greater is the flowability of plasticized material in stir zone. Finer reinforcing particles are expected to offer lower resistance to flow in plasticized state. The combined effect of these factors improve the material flow leading to better dispersion of finer reinforcing particles throughout the matrix of substrate material which in turn homogenizes the microstructure. The homogeneous dispersion of finer reinforcing particles offers increased pinning

effect and suppression of grain boundaries causing finer matrix grains. Fine grain structure of substrate matrix strengthened by uniform dispersion of finer reinforcing particles in the substrate matrix are believed to enhance hardness and other mechanical properties. Moreover, uniform dispersion of particles is believed to produce less fluctuation in microhardness [27].

4 Effect of FSP Parameters on the Wear Behavior of Composites

Wear is the progressive loss of the material in the form of debris from solid surfaces having relative motion and direct surface contact. Abrasion and adhesion are the two main forms of wear. The abrasion occurs when hard particles or projections are forced and moved against solid surface and may be two-body or three-body depending on the type of contact. The two-body abrasion was held responsible for the wear of as-received and friction stir processed materials and involves two moving surfaces. In general, the composites undergo three-body wear as reinforcing hard particles, i.e., abrasives were entrapped between the two moving surfaces. At microscopic level, abrasion is caused by plowing, cutting and brittle fracture. The actual contact between mating surfaces occurs at some high asperities. Adhesion wear is due to the separation of micro-junctions formed at opposing high asperities on moving solid surfaces. The micro joints, i.e., adhered region forms because of deformation and adhering of asperities on account of high applied forces. When the surfaces in contact moves, these micro-junctions are separated resulting in adhesion wear with wide range of wear rates. The presence of reinforcing particles, e.g., SiC, Al_2O_3, TiN, ceramic, etc., are believed to cause stress concentration between substrate matrix and reinforcing particles and provoke the nucleation and propagation of cracks resulting in material loss in the form of flakes or tiny sheets separated by delamination. The friction stir processed samples without any reinforcement has higher weight loss than Al6061-T6 alloy. The nano Al–Cr composite had lower weight loss than friction stir processed and as-received Al6061-T6 alloy. The friction stir processed sample had highest weight loss than other two samples suggesting that FSP without reinforcement reduces the wear resistance of Al6061-T6 alloy because of softening owing to loss of hardening precipitates. On the other hand, the presence of nano-sized particles enhances the hardness and resistance of material against plastic deformation which in turn diminishes the adhesion between sliding parts resulting in lowest weight loss. Parallel deep grooves were observed on the wear surface of unprocessed and friction stir processed Al6061-T6 samples and shallow grooves were seen on the worn surface of Al–Cr nano composites. The fracture and pull out of Al–Cr particles resulted in light edges on worn surfaces. The Al–Cr nano composites showed mono-layered smaller debris as opposed to as-received Al6061-T6 samples which exhibited layered shaped larger debris. Wear mechanism was the combination of adhesion and abrasion for as-received and friction stir processed Al6061-T6 samples [28].

The average friction coefficient and mass loss due to wear of Al/TiN dispersion strengthened surface composites decreased with the increase in number of FSP passes from two to four. The uniform dispersion of TiN particles and finer matrix grains increased the microhardness which in turn lowered the friction coefficient. The Al/TiN dispersion strengthened surface composites processed with threaded taper pin and four passes had coefficient of friction 45% lower than the parent metal and remained lowest and stable throughout the test run so, the composite should exhibit longer service life. The composite sample processed with threaded tool and four passes with 20% volume of reinforcing TiN particles underwent 60% lower mass loss during pin-disk wear test. The wear mechanism was the abrasion and adhesion as confirmed from the striation marks on composites surface and processed material on counter disks. The presence of Al_2O_3 and Fe_3O_4 films prevented the direct contact between sliding surfaces and reduced the wear of composites by changing the wear system from two-body to three-body [24].

The increased wear resistance of composites reinforced with several kinds of micro and nanoparticles is because of several factors: (a) The FSP is supposed to fragment the reinforcing particles and cause the uniform dispersion of finer reinforcing particles. This is facilitated by intense stirring on account of higher FSP passes and rotary speed. (b) The better dispersion promotes strong bonding of uniformly distributed finer reinforcing particles with the matrix of substrate material and improves the microhardness and resistance against the plastic deformation. (c) The hard reinforcing particles protect the soft matrix of the composites against the wear [29], and (d) The formation of Al_2O_3 and Fe_3O_4 films prevents the direct contact and changed the wear system from two body to three body [24]. The combined effect of all these factors may be responsible for the improved wear behavior of nano composites made by FSP.

5 Summary

Friction stir processing has emerged as one of the most promising methods to fabricate composites with favorable microstructure, excellent wear resistance, and desired mechanical properties. Microstructure as well as properties of composites are highly dependent on the selection of suitable tool geometry and FSP parameters. The threaded tool, multiple passes, high rotation are critical for effective material flow, fragmentation, and uniform dispersion of reinforcing particles. The homogeneous microstructure, smaller grains of substrate matrix, and uniform dispersion of finer reinforcing particles improves the mechanical properties and wear resistance. The properties of MMCs were generally better than the monolithic materials which can be further optimized by appropriate selection of processing techniques, FSP parameters, and reinforcements. Further, research also need to be directed to develop wear resistant tools for a sensible tool life and cost-effectiveness to establish the FSP suitability for making different parts, components or assemblies to be used in space,

defense, aviation, automotive, and other industries to meet the challenging needs of the future.

References

1. Miracle DB (2005) Metal matrix composites—from science to technological significance. Compos Sci Technol 65:2526–2540
2. Jayalakshmi S, Gupta M (2015) Metallic amorphous alloy reinforcements in light metal matrices. Springer Briefs in Materials. ISBN 978-3-319-15015-4
3. Matthews FL, Rawlings RD (2005) Composite materials: engineering and Science. Woodhead Publishing Ltd. and CRC Press LLC
4. Ceschini L, Dahle A, Gupta M, Jarfors AEW, Jayalakshmi S, Morri A, Rotundo F, Toschi S, Singh RA (2017) Aluminum and magnesium metal matrix nanocomposites. Springer Nature Singapore Pte Ltd
5. Gangil N, Siddique AN, Maheshwari S (2017) Aluminium based in-situ composite fabrication through friction stir processing: a review. J Alloy Compd 715:91–104
6. Bauri R, Yadav D (2018) Metal matrix composites by friction stir processing. Butterworth-Heinemann, Elsevier. ISBN: 978-0-12-813729-1
7. Sharma V, Prakash U, Kumar BVM (2015) Surface composites by friction stir processing: a review. J Mater Process Technol 224:117–134
8. Mishra RS, Mahoney MW, McFadden SX, Mara NA, Mukherjee AK (1999) High strain rate superplasticity in a friction stir processed 7075 Al alloy. Scr Mater 42:163–168
9. Mishra RS, Ma ZY, Charit I (2003) Friction stir processing: a novel technique for fabrication of surface composite. Mater Sci Eng A 341(1–2):307–310
10. Elangovan K, Balasubramanian V (2008) Influences of tool pin profile and tool shoulder diameter on the formation of friction stir processing zone in AA6061 aluminum alloy. Mater Des 29(2):362–373
11. Ratna SB (2016) Different strategies of secondary phase incorporation into metallic sheets by friction stir processing in developing surface composites. Int J Mech Mater Eng 11:12
12. Arora A, De A, DebRoy T (2011) Toward optimum friction stir welding tool shoulder diameter. Scr Mater 64(1):9–12
13. Chao YJ, Qi X, Tang W (2003) Heat transfer in friction stir welding—experimental and numerical studies. J Manuf Sci Eng 125:138–145
14. Al-Ghamdi KA, Hussain G, Hashemi R (2017) Fabrication of metal-matrix AL7075T651/TiN nano composite employing friction stir process. Proc IMechE Part B: J Eng Manuf 231(8):1319–1331
15. Lin PC, Pan J, Pan T (2008) Failure modes and fatigue life estimations of spot friction welds in lap-shear specimens of aluminum 6111-T4 sheets. Part 1: welds made by a concave tool. Int J Fatigue 30(1):74–89
16. Lin PC, Pan J, Pan T (2008) Failure modes and fatigue life estimations of spot friction welds in lap-shear specimens of aluminum 6111-T4 sheets. Part 2: welds made by a flat tool. Int J Fatigue 30(1):90–105
17. Cederqvist L, Sorensen CD, Reynolds AP, Oberg T (2009) Improved process stability during friction stir welding of 5 cm thick copper canisters through shoulder geometry and parameter studies. Sci Technol Weld Joining 14(2):178–184
18. Thomas WM, Nicholas ED, Smith SD, Das SK, Kaufman JG, Lienert TJ (2001) Aluminum 2001—proceedings of the TMS 2001 aluminum automotive and joining sessions, TMS, p 213
19. Kumar K, Kailas SV (2008) The role of friction stir welding tool on material flow and weld formation. Mater Sci Eng A A485(1–2):367–374
20. Zhao YH, Lin SB, Wu L, Qu FX (2005) The influence of pin geometry on bonding and mechanical properties in friction stir weld 2014 Al alloy. Mater Lett 59(23):2948–2952

21. Chowdhury SM, Chen DL, Bhole SD, Cao X (2010) Tensile properties of a friction stir welded magnesium alloy: effect of pin tool thread orientation and weld pitch. Mater Sci Eng A A527(21–22):6064–6075
22. Buffa G, Hua J, Shivpuri R, Fratini L (2006) Design of the friction stir welding tool using the continuum based FEM model. Mater Sci Eng A A419(1–2):381–388
23. Mahmoud ERI, Takahashi M, Shibayanagi T, Ikeuchi K (2009) Effect of friction stir processing tool probe on fabrication of SiC particle reinforced composite on aluminum surface. Sci Technol Weld Joining 14(5):413–425
24. Hashemi R, Hussain G (2015) Wear performance of Al/TiN dispersion strengthened surface composite produced through friction stir process: a comparison of tool geometries and number of passes. Wear 324. https://doi.org/10.1016/j.wear.2014.11.024
25. Azizieh M, Kokabi AH, Abachi P (2011) Effect of rotational speed and probe profile on microstructure and hardness of AZ31/Al2O3 nanocomposites fabricated by friction stir processing. Mater Des 32:2034–2041
26. Liu Q, Ke L, Liu F, Huang C, Xing L (2013) Microstructure and mechanical property of multi-walled carbon nanotubes reinforced aluminum matrix composites fabricated by friction stir processing. Mater Des 45:343–348
27. Barmouz M, Givi MKB (2011) Fabrication of in situ Cu/SiC composites using multi-pass friction stir processing: evaluation of microstructural, porosity, mechanical and electrical behavior. Compos Part A: Appl S 42:1445–1453
28. Anvari SR, Karimzadeh F, Enayati MH (2013) Wear characteristics of Al–Cr–O surface nanocomposite layer fabricated on Al6061 plate by friction stir processing. Wear 304:144–151
29. Hassan AM, Mayyas AT, Alrashdan A, Hayajneh MT (2008) Wear behavior of Al–Cu and Al–Cu/SiC components produced by powder metallurgy. J Mater Sci 43(15):5368–5375

Synthesis and Characterization of Oxide Dispersion Strengthened W-based Nanocomposite

A. Patra, S. K. Karak and T. Laha

Abstract The chapter involves fabrication and characterization of novel oxide dispersion strengthened (ODS) tungsten (W)-based nanocomposites used for kinetic energy penetrator (KEP) for defense and plasma facing materials (PCM) for nuclear reactor application. The chapter will discuss the benefits and challenges for using W-based alloys for high-temperature structural application. Synthesis of oxide-dispersed W-based nanocomposite (79W–10Mo–10Ni–1Y_2O_3) by mechanical alloying followed by consolidation through conventional pressureless sintering and advanced spark plasma sintering is carried out. The phase evolution, microstructure for milled powder, and sintered product have been investigated by X-ray diffraction (XRD), scanning electron microscopy (SEM), and transmission electron microscopy (TEM). The densification, hardness, and strengthening behavior of the alloy in two sintering mode are illustrated. The microstructure–mechanical properties are correlated to understand the operative densification and strengthening mechanism. Heterogeneous composition and bimodal grain size distribution of the alloy offers appreciable strength–ductility for structural applications. The chapter will provide a roadmap for design of novel alloys for similar applications.

Keywords W-based nanocomposites · Sintering · Oxide dispersion strengthened Strengthening mechanism

---

The original version of this chapter was revised: The reference sequence has been corrected. The correction to this chapter is available at https://doi.org/10.1007/978-981-13-2417-8_17

A. Patra (✉) · S. K. Karak
Nanomaterials Research Group, Metallurgical and Materials Engineering, National Institute of Technology Rourkela, Rourkela, Odisha 769008, India
e-mail: anspat.met@gmail.com

S. K. Karak
e-mail: skkarak@gmail.com

T. Laha
Metallurgical and Materials Engineering, Indian Institute of Technology, Kharagpur, West Bengal 721302, India
e-mail: laha.tapas@gmail.com

S. S. Sidhu et al. (eds.), *Futuristic Composites*, Materials Horizons: From Nature to Nanomaterials, https://doi.org/10.1007/978-981-13-2417-8_13

1 Introduction

W is an attractive contender for defense, fusion reactor, aviation counterweight application due to unique properties such as maximum density and melting point, superior hardness, strength, and minimum yield during sputtering [1, 2]. However, enhanced ductile–brittle transition temperature (DBTT) (200–500 °C) [2], radiation-based brittleness [3], and higher oxidation at and above 1000 °C temperature [2] are serious issues of W. Formation of porous and volatile WO_3 oxide at elevated temperature warrant suitable protective coating of W. W/W boundary is quite weak and exhibits interfacial de-cohesion. Several investigations have been carried out on W-based alloy such as W–Ni–Fe [4], W–Ni–Cu [5], W–Mo [6], W–Cr [7], and W–Cr–Nb [8] to enhance the physical (density), strength–ductility combination, and oxidation resistance. The desired properties for W-based alloys to be used in kinetic energy penetrator is ~6–8% elongation and elevated temperature strength owing to interaction with almost 2000 °C temperature atmosphere high hydrostatic pressure (2–6 GPa) [9]. Mo shows extensive liquid and solid solubility in W primarily due to the identical crystal structure. Ni is an effective addition in W with respect to improvement of ductility by reducing the barrier for dislocation motion [10]. Sintering of W is challenging as elevated temperature (over 2700 °C) fabrication leads to increase the processing cost and also depreciates the mechanical properties owing to excessive grain growth. Nanostructuring is a powerful technique to reduce the particle size (<100 nm at least in one dimension) and consequently the sintering temperature. Mechanical alloying has evolved as a nonequilibrium method for synthesis of nanostructured materials. The method facilitates enhancement of solubility of solute elements in matrix as compared to traditional melting–casting. The oxide dispersion technique in W was started in 1910 as W–ThO_2 alloy to enhance the mechanical properties of W at elevated temperature. However, Y_2O_3 surpasses ThO_2 as oxide dispersion in recent times owing to radioactive concerns of the latter [11]. Several literature evidences also suggest that Y_2O_3 dispersion results in strengthening by dispersion strengthening mechanism [12, 13]. Moreover, oxide dispersion refines the grain size and enhances the grain boundary area per unit volume which can act as a sink for radiation-based defects.

This chapter presents fabrication of W–Ni–Mo–Y_2O_3 alloy by both conventional and spark plasma sintering processes followed by characterization which will provide a comprehensive understanding of the effectiveness of both the processing method.

2 Synthesis of Nanostructured Materials by Mechanical Alloying

Mechanical alloying proves to be effective in terms of particle size reduction as compared to rapid quenching [14, 15], severe plastic deformation (SPD), high-pressure torsion, and multi-pass coin forge [16, 17]. Mechanical alloying involves processing

of commercial micron sized powders in solid state to nanostructured powders by rotating grinding jar along with grinding balls in a high energy ball mill. The ball mill comprises either two stations or four stations depending of number of grinding jars. The jar is filled with process control agent (PCA) such as toluene, stearic acid, methanol, benzene, ethanol, paraffin, and ethyl acetate (1–5 wt% of entire powder weight) [14]. Contamination from grinding ball to the powder blend during mechanical alloying is a serious concern. The process control agent hinders direct grinding ball to powder contact during rotation and minimizes the clustering and contamination of powders [14]. Several parameters, such as milling media, milling atmosphere, rotational speed of the mill, ball-to-powder weight ratio, diameter of grinding balls, level of PCA inside the jar, and milling duration, significantly influence the mechanical alloying process [14, 15]. Level of PCA addition is quite important which ensures the proper movement and collision between grinding balls and powder particles inside the grinding jar. During mechanical alloying, the powder particles are extended/ruptured depending on the nature of initial powder (ductile/brittle). The extended particles are fragmented into a smaller size with continued milling [15]. Several synthesis methods of both ODS and non-ODS W alloy powder by mechanical alloying have been reported in recent literatures [13, 18–24]. Further improvement can be achieved by handling of powders and alloying under vacuum or inert gas-filled (argon, helium) glove box to inhibit the contamination problem from atmosphere [14, 15]. A schematic mechanical alloying process is provided in Fig. 1. Nano-oxide dispersion in W-based alloys significantly reduces the particle size of W as compared to non ODS W-based alloys which is attributed to the improved deformation contributed by the enhanced surface energy of the nano-oxides [13]. Mechanical alloying is a preferred W alloy synthesis technique as compared to melting and casting method owing to high melting point of W and fabrication cost. Moreover, mechanical alloying enhances the solubility of solute elements in solvent matrix which is difficult to achieve in melting–casting route.

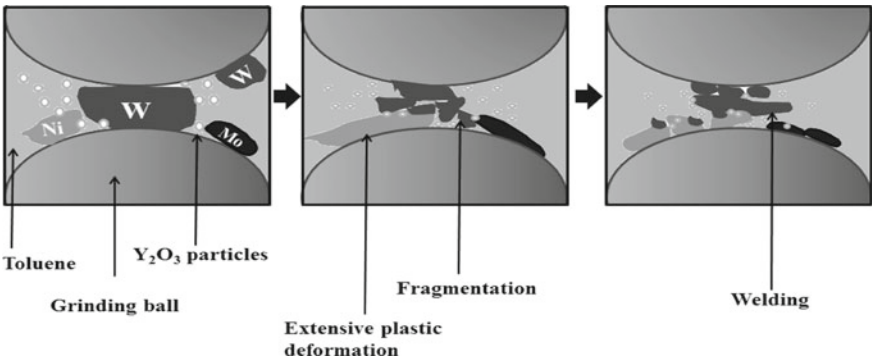

Fig. 1 Schematic of ball-powder impact mechanism during mechanical alloying process [25]

3 Consolidation Techniques

Several consolidation techniques such as conventional sintering (in absence of pressure), pressure-based sintering (spark plasma sintering, hot pressing, hot isostatic pressing, ultrahigh-pressure sintering, and hydrostatic extrusion) has been used by the researcher to fabricate bulk components from mechanically alloyed nanostructured powder. However, conventional sintering and spark plasma sintering of W-based alloys is discussed in subsequent sections with respect to the objective of the present paper.

3.1 Conventional Sintering

Prior to conventional sintering of W-based ODS alloys, the mechanically alloyed powders are compacted into pellets in a uniaxial hydraulic press by applying a pressure with 0.5–1.0 GPa and dwell time of almost 5 min for homogeneous pressure distribution. The applied pressure, load rate, and particle size distribution of mechanically alloyed powder influences the density of the compacted pellets. Consolidation of nanostructured materials is possible at low sintering temperature without application of sintering additives. Grain shape rearrangement during liquid-phase aided conventional sintering also leads to shrinkage [26]. The capillary pressure of liquid based stress (σ) and grain size (G) influences the shrinkage rate $\left(\frac{\mathrm{d}(\Delta L/L_O)}{\mathrm{d}t}\right)$ as [27]:

$$\frac{\mathrm{d}(\Delta L/L_O)}{\mathrm{d}t} = B\sigma^n \exp\left(\frac{-Q}{KT}\right)/G^3 \tag{1}$$

B: material constant, Q: activation energy for diffusion, T: temperature, stress factor $n \sim 1$.

During pressureless conventional sintering of W-based alloys, inert (argon), hydrogen atmosphere is quite effective with respect to the high propensity of oxidation of W. However, recent report shows that argon is more fruitful in the context of enhancement of sintered density of W alloys as compared to hydrogen [28]. The heating rate in conventional sintering is normally within 5–10 °C/min which allows a subsequent increase in grain size. Higher heating time may also leads to increase of dispersed particles at the interface which reduces the grain boundary pinning pressure followed by grain coarsening. Figure 2 shows the uniaxial hydraulic press for powder compaction.

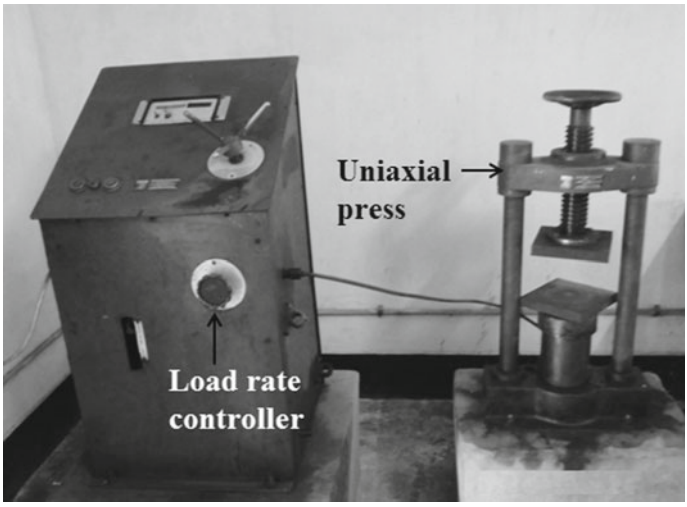

Fig. 2 Uniaxial hydraulic press used for powder compaction [25]

3.2 Spark Plasma Sintering

Spark plasma sintering (SPS) is an advanced sintering technique which involves high heating rate (50–300 °C/min) and application of pressure (15–100 MPa). Fast heating rate leads to refine the grain size as compared to conventional sintering. Generation of plasma and joule heating between powder particles leads to significantly enhance the particle bonding and sintered density [29]. The powders are filled in graphite die coated with carbon cloth and placed inside SPS chamber along with punch setup. Pressure application during spark plasma sintering is more beneficial as compared to pressure application before sintering with respect to increased particle bonding. Disruption of oxide film on the surface during SPS also leads to superior particle contact and densification. Application of external pressure is associated with surface-free energy of the liquid–vapor (γ_{lv}), particle radius (R), and liquid–solid contact angle (θ). The relationship is described below [30]:

$$P = 2\sqrt{2}\,\pi\left(\frac{\gamma_{lv}}{R}\right)\cos\theta \tag{2}$$

It is evident from above relationship that increased pressure can be effective with respect to particle rearrangement in case the initial particle size is finer [31]. Spark plasma sintering is also advantageous is terms of retaining the dimensional precision of the sample without any excessive shrinkage.

Table 1 Ball milling process parameter

Parameters	Value/material used
Process control agent (PCA)	Toluene
Rotational speed of the mill	300 rpm
Ball-to-powder weight ratio	10:1
Ball diameter	10 mm
Ball material	Hardened chrome steel

4 Experimental Method

The commercial micron-sized W, Ni, Mo, Nb (purity 99.5%), and nano Y_2O_3 (<50 nm) are mechanically alloyed for 20 h for synthesis of nanostructured powders. The weight percents of the initial elements are W: 79 wt%, Mo: 10 wt%, Ni: 10 wt%, and Y_2O_3: 1 wt%. The following ball milling parameters has been retained (Table 1). After every 30 min of milling, a pause time of 30 min is provided for cooling. To investigate the phases and microstructure by X-ray diffraction (XRD) and scanning electron microscopy (SEM), respectively, the powder is collected at 5, 10, 15, and 20 h of milling.

Williamson–Hall relationship has been used to determine the crystallize size and lattice strain induced in the milled powder during mechanical alloying as below [32]:

$$\beta \cos\theta = \frac{0.94\lambda}{D} + 4\eta \sin\theta \tag{3}$$

β: full width at half maxima (FWHM), D: crystallite size, η: lattice strain.

The intercept and slope between the linear fit of $\sin\theta$ and $\beta\cos\theta$ will yield the value of crystallite size and lattice strain, respectively [13].

The 20 h mechanically alloyed powders are compacted in a uniaxial hydraulic press at various pressures (0.5, 0.75, 1.0 GPa) to produce cylindrical compacts of 10 mm diameter and thickness ranging between 1.5 and 2.0 mm. The compacts are conventionally sintered in a tunnel furnace at 1500 °C and 2 h of soaking with continuous argon purging at the rate of 100 ml/min [6, 13]. Figure 3 displays the furnace used conventional sintering of the samples.

For spark plasma sintering, the 20 h mechanically alloyed powders are filled in a 10-mm-diameter graphite die and placed inside SPS chamber. The SPS is carried out under vacuum at various temperatures (1000, 1200, 1400 °C for 5 min with a heating rate of 50–100 °C and pressure of 75 MPa) to understand the temperature effect on densification and mechanical properties [33].

The sintered samples (both conventional and SPS) are subjected to phase and microstructure study (by XRD and SEM), densification (Archimedes' principle), microhardness, compressive strength evaluation, and high temperature oxidation study at 1000 °C for different time of exposure. The principle of characterization and process parameters are according to recent literature [6, 33].

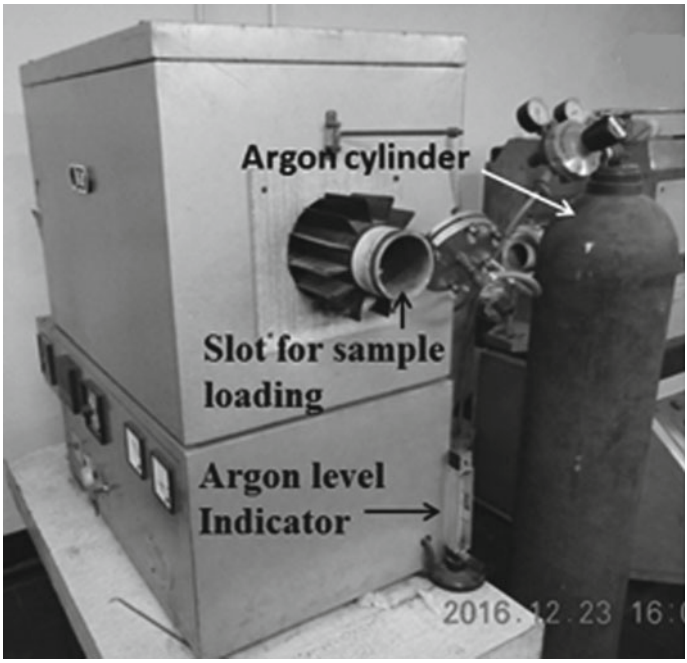

Fig. 3 Conventional sintering furnace [25]

5 Results and Discussion

5.1 Phases and Microstructure of Milled Powder

Various phase formations and microstructures of the powders during mechanical alloying have been studied by XRD and SEM, respectively. Figure 4 shows the XRD pattern of the alloy at various periods of milling. The scan range of 20–100°, step size of 0.05°, and scan rate of 20°/min have been used for XRD study. It is quite evident that no significant change in the intensity of Ni (111) peak occurs even at higher milling time (20 h) as compared to Mo. W diffraction peaks are broadened with increase in milling time which is related with the decrease in the size of W particles and enhancement of lattice strain [13]. It is also noticeable that Y_2O_3 peak also experiences reduction in intensity and broadening which implies encapsulation of Y_2O_3 particles inside W matrix. The dissolution of solute elements in W lattice leads to the formation of the solid solution at 20 h of milling. Minimum crystallite size and highest lattice strain of W matrix at 20 h of milling as evaluated from Williamson–Hall relationship is 29.4 nm and 0.51% [13]. Nano Y_2O_3 addition contributes additional energy required for powder deformation and substantially reduces the crystallite size and increases the lattice strain which is advantageous with respect to improving the sintering kinetics.

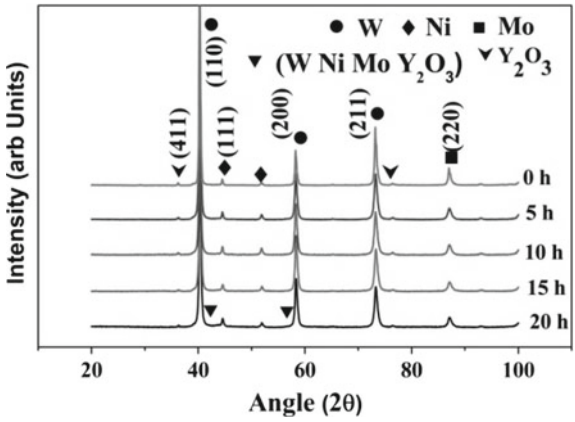

Fig. 4 XRD pattern of the alloy at a different time of milling. Reprinted from [13], p. 133. Copyright (2016) with permission from Elsevier

To understand the change in particle morphology with increase in milling time, it is quite necessary to investigate the powders under SEM. The powder particles indirectly collide with the grinding ball as the balls are covered with toluene. Therefore, the particle size reduces and the solute particles start dissolving inside the solvent lattice. The ductile constituents such as Ni and Mo are extensively deformed prior to fracturing contrary to brittle W. Figure 5a–d exhibits the variation of particle morphology with the increase in milling time. Particles with larger aspect ratio (stretched) are observed in the interim period (10 h) which suggest larger accommodation of deformation strain prior to particle rupturing. Both coarser and finer particles are observed in the 20 h milled alloy (Fig. 5d). This type of particle bimodality is of immense significance with respect to powder compaction. The elemental composition of the 20 h milled alloy evaluated by EDS analysis is 73.44% W, 16.86% Ni, 8.35% Mo, 0.70% Y, and 0.65% O which is different from starting power composition which indicates that mechanical alloying is a powder synthesis method with nonhomogeneous composition.

5.2 Phase and Microstructure of Conventionally Sintered Alloy

The phases formed during conventional sintering of 79W–10Mo–10Ni–1Y_2O_3 alloy are studied by XRD (Fig. 6) and evaluated by X'PERT HIGH SCORE (PHILIPS ANALYTICAL) software after mapping the JCPDS data with the software. Warping of W network by the solute addition (Mo, Ni) and dissolution of Y_2O_3 particles is reflected from the change in W (110) diffraction angle (40.36° in milled powder→40.57° in sintered alloy) [13]. MoNi intermetallic phase formation is also revealed from Fig. 6 which is ascribed to liquid-phase sintering mechanism. The intermetallic phase significantly enhances the strength of W/W interface but with

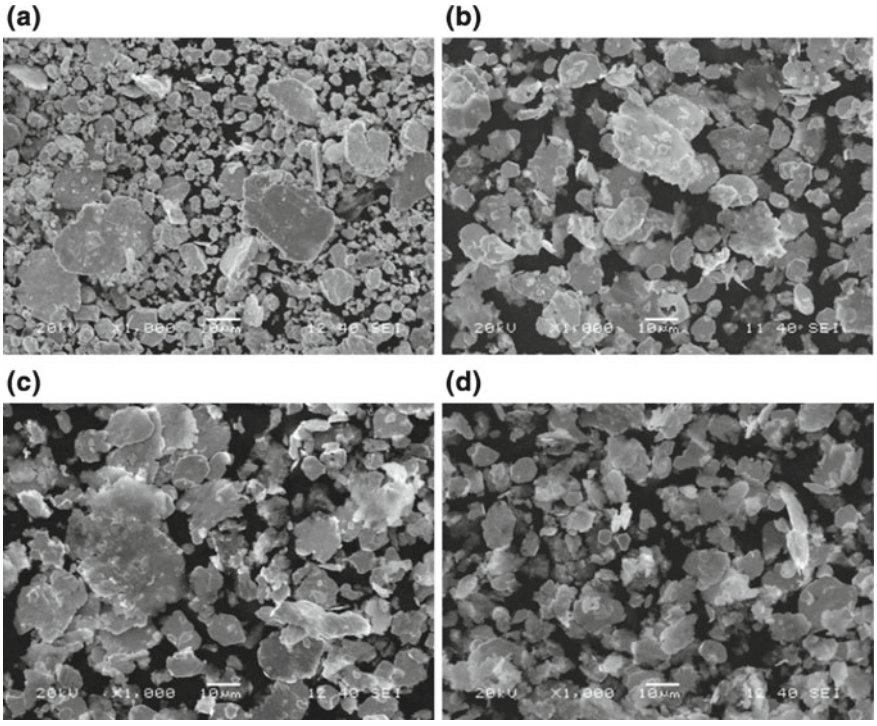

Fig. 5 SEM image represents the variation of powder particle morphology with change in milling time **a** 0 h, **b** 5 h, **c** 10 h, and **d** 20 h. Reprinted from [13], p. 133. Copyright (2016) with permission from Elsevier

compromised toughness. Therefore, volume fraction of intermetallic phases, location of precipitation, sintering temperature, and soaking time are important attributes to regulate the final desired microstructure with appreciable mechanical properties. During sintering, the accumulated lattice strain in the milled powder is relaxed; therefore, the broadening of the peak in the sintered alloy reduces such as W (110) peak with broadening of 0.2952° in 20 h milled powder reduces to 0.1968° in sintered alloy.

The W matrix size, MoNi intermetallic, and Y_2O_3 oxide particles are observed from the microstructure of the conventionally sintered alloy (Fig. 7). It is clearly evident that MoNi phases are mostly located at W/W boundary. Formation of liquid phase during heat treatment is a candidate method to improve the densification of the alloy by adding lower melting point element than the sintering temperature in an alloy. In the present study, Ni addition could facilitate both plastic flow property and improved density by infiltration of liquid in the pores. Recent report shows that enhanced presence of Mo increases the intermetallic phase formation rate [34]. The eutectic temperature in Mo–Ni phase diagram is 1317 °C, which is less as compared to transition temperature for MoNi phase formation (1362 °C). This feature in Mo–Ni

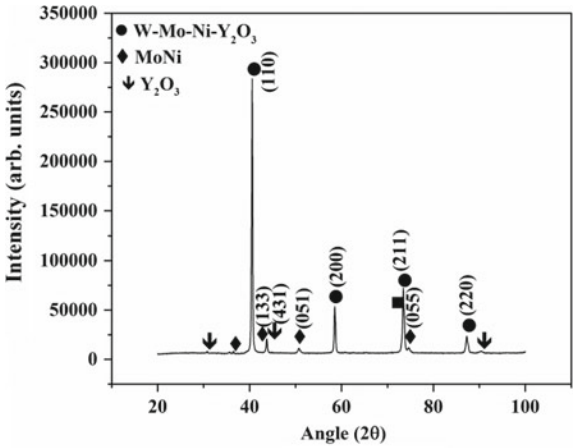

Fig. 6 XRD of conventionally sintered 79W–10Mo–10Ni–1Y_2O_3 alloy [13]

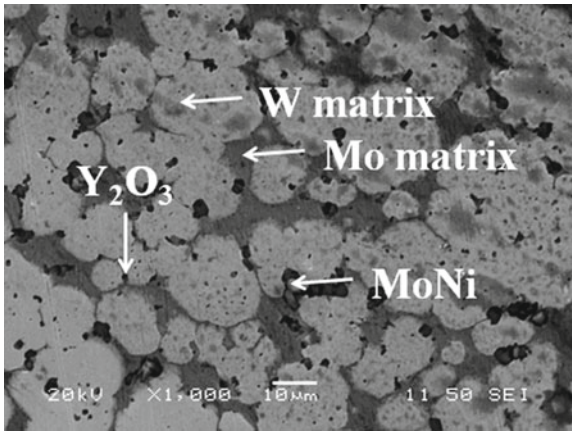

Fig. 7 Microstructure of conventionally sintered 79W–10Mo–10Ni–1Y_2O_3 alloy [13]

phase diagram activates the development of MoNi phase in the course of cooling [34]. The W matrix size is nonuniform in the sintered alloy which may be attributed to heterogeneous distribution of grain boundary pinning particles (Y_2O_3). Therefore, pinning pressure exerted on the boundary by the particles to inhibit grain growth is not identical throughout the microstructure.

The variation of grain size in the sintered alloy is displayed by the histogram in Fig. 8. Due to variation in the morphology, size of grains, and the capillary action of the pores, the formed liquid will favor wetting or filling of smaller size grains and pores, respectively [35]. Along with pores filling, the liquid dissolve the grains of solid W matrix followed by diffusion of solid and reprecipitation of solid in contact with solid surface possessing lesser energy which results in growth of coarser grain as compared to finer grains [35, 36].

High-resolution TEM (HRTEM) study in Fig. 9 shows the presence of Y_2O_3 dispersed particles and dislocation–particles interaction. The increase in stress on the

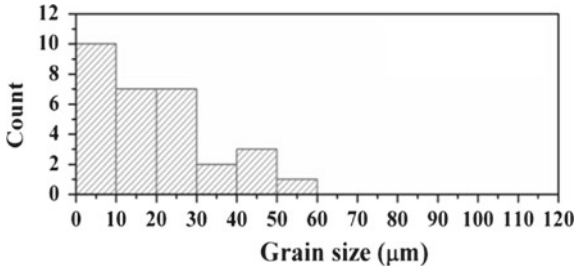

Fig. 8 Histogram of grain size in conventionally sintered 79W–10Mo–10Ni–1Y_2O_3 alloy [25]

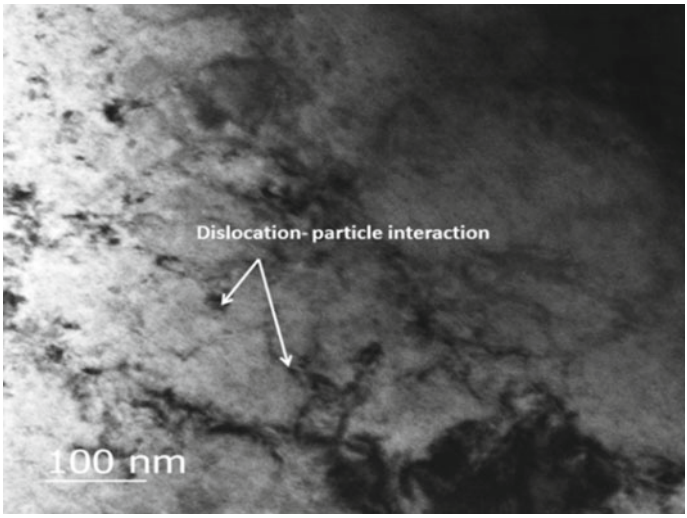

Fig. 9 HRTEM image represents the presence of dispersed particles and dislocation in conventionally sintered 79W–10Mo–10Ni–1Y_2O_3 alloy [13]

dislocation sources with dislocation–dispersoids interaction which needs to be surmounted for ease in dislocation motion. The mechanism leads to increase the strength of the matrix by dispersion strengthening [37, 38]. However, the size, shape, and volume fraction of the dispersed have a significant contribution on the strengthening. Coarsening of dispersed particles with prolonged heating time during conventional sintering may also reduce the population density followed by pinning force on the boundary and results in reduced strength of the matrix.

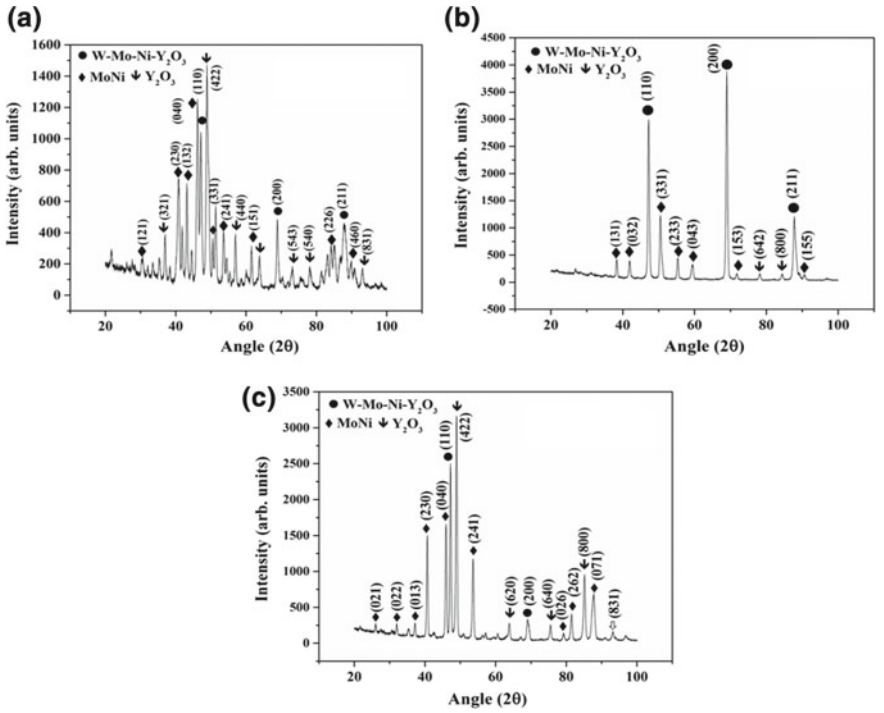

Fig. 10 Phase evolution in 79W–10Mo–10Ni–1Y_2O_3 alloy spark plasma sintered at **a** 1000 °C, **b** 1200 °C, **c** 1400 °C [33]

5.3 Phase and Microstructure of Spark Plasma Sintered Alloy

The evolved phases in spark plasma sintered alloy is at all temperatures is identical with the conventionally sintered alloy (Fig. 10). The number of MoNi peaks increases with increase in SPS temperature. This may be attributed to the improved atomic diffusion with temperature (decreased activation energy) [39]. The broadening of W matrix peak in the sintered alloy shows increasing and decreasing trend with an increase in temperature which may suggest coarsening of some W grain and retention of some grain size by Y_2O_3 (diverse grain sizes) dispersoids even with increasing temperature. Ni exhibits limited solubility in W matrix which resulted in MoNi intermetallic phase in the microstructure by the mechanism discussed in Sect. 5.2. The presence of MoNi intermetallic phases at 1000 °C suggests that liquid-phase sintering of W-based alloy is even possible at such low temperature.

The microstructure of 79W–10Mo–10Ni–1Y_2O_3 alloy spark plasma sintered at 1000, 1200, and 1400 °C is presented in Fig. 11a–c, respectively. The bright phase (arrow marked) indicates W matrix and the gray phase is Mo-rich (Mo matrix).

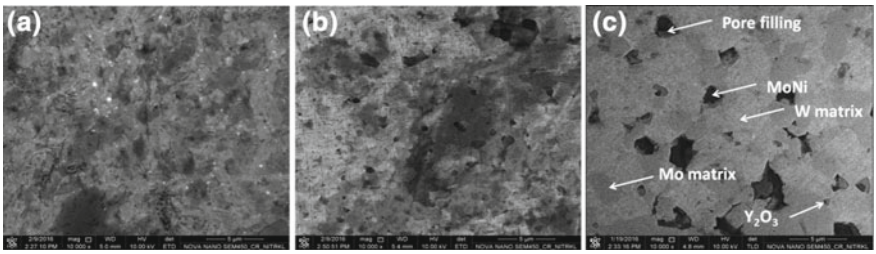

Fig. 11 FESEM micrograph of spark plasma sintered 79W–10Mo–10Ni–1Y_2O_3 alloy at **a** 1000 °C **b** 1200 °C and **c** 1400 °C. Reference for Fig. 11c: [33]

Coarsening of some grains with increase in SPS temperature from 1000 to 1400 °C is detected. Clear evidence of filling of pores is revealed in the microstructure. The densification during spark plasma sintering is contributed by partial liquid-phase sintering and faster atomic diffusion through particle neck [29]. The variation of temperature between powder particle surface and core increases with enhancement of sintering temperature. Faster grain coarsening occurs in case the SPS temperature exceeds 1000 °C [40]. The phases in the microstructure are identified by energy-dispersive spectroscopy (EDS) detector attached with field emission scanning electron microscopy (FESEM) through point EDS method (detection of phase at a specified area).

5.4 Densification of Compacted and Conventionally Sintered Alloy

Particle size distribution in the milled powder and the pressure application during compaction has significant influence on density of the compacted pellets (green density). According to literature evidence, the dependence of pressure on the density of the compacted pellets can be expressed as [41]

$$\ln\left(\frac{1}{1-D}\right) = A_0\sqrt{P} + B_0 \tag{4}$$

D: compacted pellet density (relative), P: pressure applied, A_0: plastic deformation assisted densification, and B_0: pressureless densification capacity of powders (tap density). The linear plot between $\ln\left(\frac{1}{1-D}\right)$ and $P^{1/2}$ for 90W–10Mo and 79W–10Mo–10Ni–1Y_2O_3 alloy in Fig. 12 suggests that the presence of both ductile Ni and dispersed Y_2O_3 particle decreases B_0 which suggest poor tap density owing to the variation of particle size as evident from SEM image of 20 h milled powder (Fig. 5d). However, A_0 value increases two manifolds in 79W–10Mo–10Ni–1Y_2O_3 alloy which indicates enhanced densification under compaction pressure. The het-

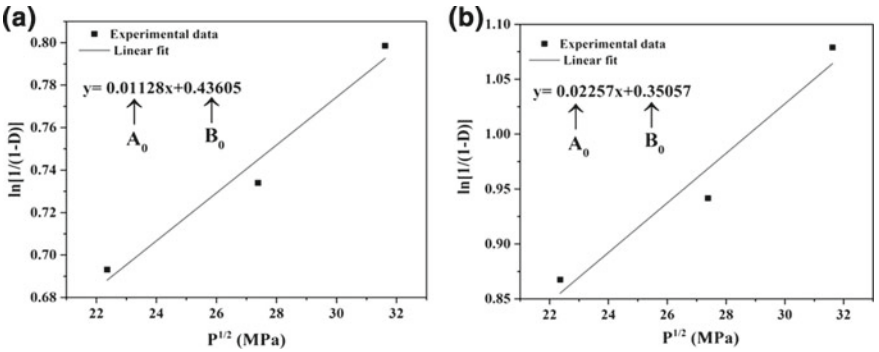

Fig. 12 Linear fit between $\ln\left(\frac{1}{1-D}\right)$ and $P^{1/2}$ of **a** 90W–10Mo (in wt%) and **b** present alloy (79W–10Mo–10Ni–1Y_2O_3) to understand the compaction behavior of the milled powder [25]

erogeneous particle size distribution as studied from SEM image (Fig. 5) improves the particle rearrangement, packing density during compaction, and improves the sintering kinetics.

The % relative sintered density (% of sintered density: theoretical density) also enhances from 90.8 to 95.2% with increase in compaction pressure from 0.50 to 1.00 GPa [26] in the alloy due to reduction of pore size in the compaction stage prior to sintering by improved particle rearrangement and packing. The relation between densification rate and pore radius is provided as [42, 43]

$$\frac{1}{\rho\,(1-\rho)}\frac{\mathrm{d}\rho}{\mathrm{d}t} \propto \frac{1}{d^n}\frac{1}{r}\exp\left(-\frac{Q}{RT}\right) \tag{5}$$

ρ designates density, n represents sintering mechanism-related constant, $n = 3$, 4 for lattice diffusion and grain boundary diffusion, respectively, where d is the particle size, Q is the activation energy for diffusion, $\mathrm{d}\rho/\mathrm{d}t$ is the rate of densification, r represents pore radius, and T is absolute sintering temperature. It is evident from above equation that rapid densification can be achieved throughout the sintering with smaller initial pore size and even distribution of pores. During liquid-phase sintering, the liquid flows to the smaller grain and pores which have enhanced the presence in the samples compacted at higher pressure and therefore enriches the densification. The lower the particle size in the final milled powder, the lesser is the sintering temperature required to achieve appreciable densification behavior by faster atomic diffusion through enhanced grain boundary area.

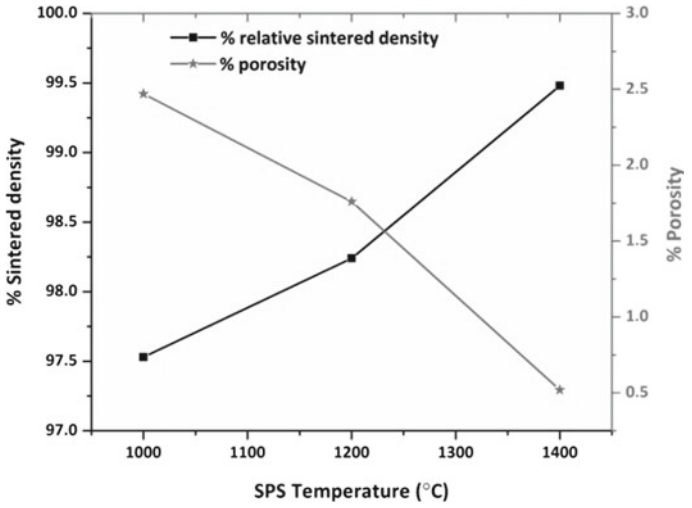

Fig. 13 Variation of % relative sintered density and % porosity with SPS temperature [33]

5.5 Densification of Spark Plasma Sintered Alloy

Spark plasma sintered alloy exhibits enriched densification as compared to conventionally sintered alloy. Generation of plasma by the application of electrical power leads to considerable improvement in atomic transport between the neck areas of powder particles supported by clearing of surface dirt through the pressure application along with sintering [29]. The soaking time in the present study is 5 min as compared to 2 h in conventionally sintered alloy. Such low soaking time and rapid heating rate (50–100 °C/min) results in substantial densification and minimal grain growth which is beneficial is fabricating bulk components with high hardness and strength. The sintered density of the present alloy improves from 97.53 to 99.48% with increase in SPS temperature from 1000 to 1400 °C, respectively [34] (Fig. 13). Therefore, it is obvious that SPS is a candidate method to fabricate product near to theoretical density. Spark plasma sintering is also beneficial in terms of controlling dimensional precession as due to rapid heating possibility of sample shrinkage can be eluded. However, in SPS one piece of sample can be sintered at a time as compared to conventional sintering in tube furnace where 5–6 samples can be loaded and sintered.

5.6 *Mechanical Properties of the Conventional and Spark Plasma Sintered Alloy*

Microstructure and grain size have immense importance with respect to controlling the mechanical properties (hardness, strength, etc.). Enhanced sintering time during conventional sintering leads to increase the grain size which results in reduced hardness as compared to spark plasma sintered alloy. The hardness is measured by microhardness tester at 50 gf load so that the hardness value is almost confined within the W matrix. The lesser the applied load, the smaller the deformed area on the sample, the higher will be the strain gradients and consequently the hardness will increase [44]. To adjust the proper measurement of the hardness of W matrix without much influence of second-phase particles or intermetallics at the grain boundary 50 gf has been selected for hardness study. Degree of porosity filling during liquid-phase sintering, concentration of solute elements in W matrix phase, compositional distribution of W in the matrix throughout the microstructure, and grain size significantly influence the hardness. Figure 14 shows the variation of hardness value for conventional and spark plasma sintered alloys. It is revealed from Fig. 14 that spark plasma sintered sample at 1400 °C exhibit maximum hardness as compared to lower SPS temperature and even higher conventional sintering temperature. Stress field generates due to variation of atomic size between solute elements Mo (0.190 nm), Ni (0.149 nm), and solvent W (0.193 nm) at different positions of W matrix that is nonuniform owing to heterogeneous composition. The more the stress field dislocation contact, the more the stress required for dislocation motion and results in improvement of hardness [37] as exhibited by the heterogeneous hardness distribution in Fig. 14. As discussed earlier, small pores are filled first by liquid during conventional sintering, however, closely spaced pores contact with each other to form open pores [45] which may not be filled during liquid-phase sintering leading to reduction in hardness. Spark plasma sintered alloys show comparatively less porosity, and therefore the effect of porosity on hardness is quite minimal.

Combination of strength–ductility is quite significant in terms of evaluation of material's fabricability. Enhancement of strength will adequate ductility in ODS alloys is challenging. The preferential site for oxide dispersion is grain boundary area. The dispersed oxides pin the grain boundary followed by grain size refinement and improve the strength. However, due to the difference in deformation characteristics between the oxides and matrix, it is difficult to achieve sufficient ductility. The ductility is less in fine-grained structure owing to inability to gather dislocations inside the smaller grains. Higher grain boundary area in fine-grained material hinders the dislocation motion and strengthens the material. Moreover, the dispersoids at the grain boundary grow in size during prolonged conventional sintering process. The large size oxides involve higher stress concentration and finally result in interfacial de-bonding during tensile or compressive loading [46]. The strategic for optimized strength–ductility in oxide-dispersed structural materials is by developing heterogeneous microstructure or bimodal grain size distribution and dispersing some portion of oxides inside the grains [46, 47]. Mechanical alloying technique is capable to pro-

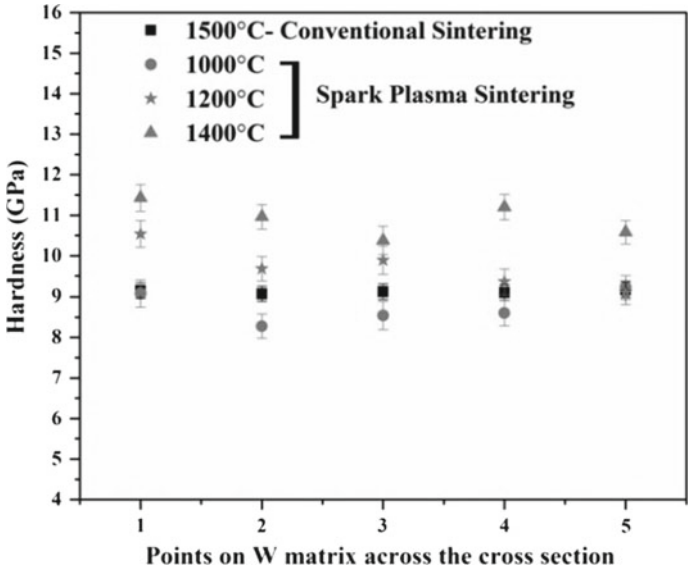

Fig. 14 Hardness on W matrix across the cross section for conventional and spark plasma sintered 79W–10Mo–10Ni–1Y_2O_3 alloy [13, 33]

duce nonhomogeneous microstructure owing to differential deformations between ball-powder particles arising from various natures of powders (ductile, brittle). The coarse grains are able to store and hinder the dislocations within the grains, increase the work hardening rate, and contribute in improvement of ductility, whereas the finer grains mostly contribute to strengthening.

W/W interface is very strong but very brittle in nature due to high DBTT. Alloying W with low DBTT material such as Mo will result in improvement of ductility (~8%) in minute amount [13]. Additionally, 10 wt% Ni addition in 90W–10Mo alloy enhances the plastic flow property as revealed from experimental and atomistic simulation-based study [6]. Generation of nanovoids and enhancement of nanotwins is responsible for the improvement of plastic flow behavior in W–Mo alloys by Ni addition [6]. Figure 9 shows that Y_2O_3 is encapsulated inside W matrix and the size of Y_2O_3 in conventional sintered 79W–10Mo–10Ni–1Y_2O_3 alloy is also nonuniform. Encapsulation of Y_2O_3 reduces the number density of dispersoids at the grain boundary, decreases the overall stress concentration at the interface, and improves the plasticity. The contact between dislocation–dislocation and dislocation–particle interaction is presented in Fig. 15a, b. The strengthening is achieved after the dislocations are discharged from coarser grains and gathered at the grain boundary of finer grains. Table 2 displays that the maximum compressive strength of 79W–10Mo–10Ni–1Y_2O_3 alloy increases with increase in SPS temperature which is attributed to increase in sintered density. The maximum compressive strength of the alloys is also superior even at 1000 °C as compared to conventional sintered

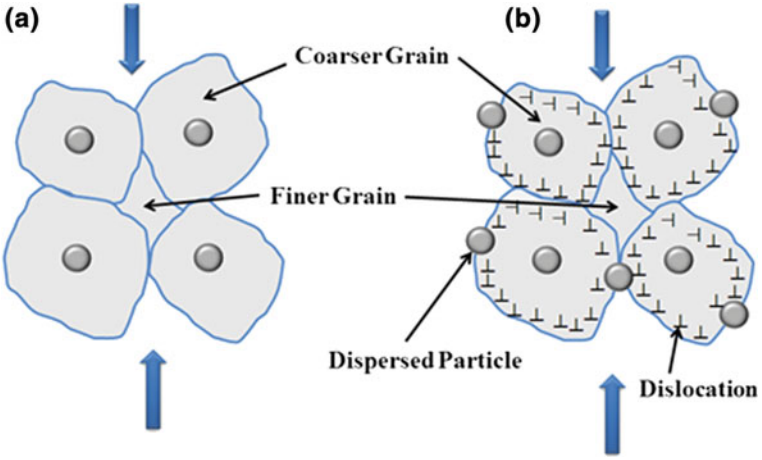

Fig. 15 **a** Coarse and finer grains with dispersed particle [48], **b** dislocation contact with dispersed particles [48]

Table 2 Strength and in 79W–10Mo–10Ni–1Y_2O_3 alloy with various sintering routes [13, 33]

Sintering route	Sintering temperature (°C)	Compressive strength (GPa)	% strain to failure
Conventional	1500	1.51	19.50
Spark plasma	1000 1200 1400	2.19 2.21 2.24	20.70 21.63 23.95

alloy at 1500 °C. It is quite exciting that at such low SPS temperature the density, hardness, strength, than conventional sintered sample. Therefore, at 1000 °C temperature, W can be successfully sintered with noticeable mechanical and physical (density) properties.

The morphology of the fracture surface is presented in Fig. 16a–d for conventional and spark plasma sintered alloy, respectively. W-based alloys exhibit various fracture morphologies such as fracture through W/W boundary by intergranular mode, through W-rich area, W matrix boundary [49]. Dispersion of Y_2O_3 particles at the interface leads to reduce the grain boundary cohesion and increase the chances of intergranular failure through W/W and W/matrix [50] followed by decrease in fracture toughness. The initiation of the cracks is from grain boundary porosity. Small porosities will grow and agglomerate to facilitate easy crack propagation. On the other hand, literature evidence illustrates that Y_2O_3 particles can alter the crack propagation; absorb energy to delay fracture which can improve the toughness [51]. Enhanced densification with reduced porosity in spark plasma sintered 79W–10Mo–10Ni–1Y_2O_3 alloy exhibits improved interfacial bonding as compared to conventionally sintered alloy. The presence of micro-voids in SPS sample (1400 °C) and superior grain boundary cohesion indicates improved plasticity

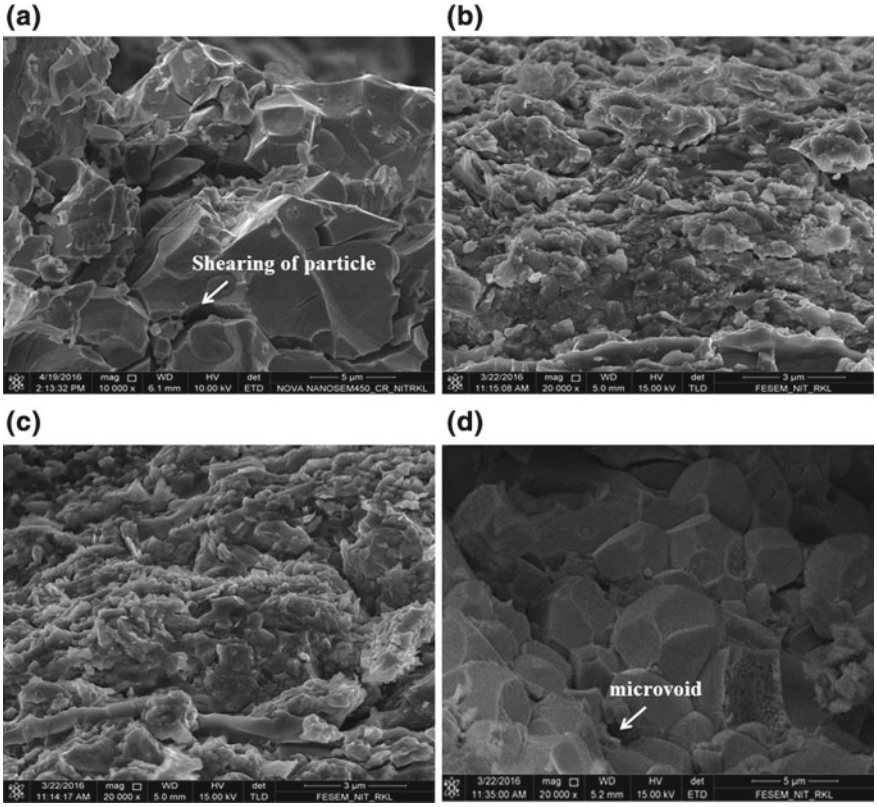

Fig. 16 Morphology of fracture surface for **a** conventionally sintered alloy [13], spark plasma sintered alloy at **b** 1000 °C, **c** 1200 °C, **d** 1400 °C. Reproduced, with permission from [52], © ASTM International

(Fig. 16d). The cohesion also improves and intergranular mode of fracture reduces with increase in SPS temperature which is in good co-relation with the strength values (Table 2). Encapsulation of Y_2O_3 particles inside W matrix also reduces overall stress concentration at the interface and contributes in improved bonding of W/W and W/matrix. Literature suggests that critical crack movement stress can be enhanced by decreasing the grain size [53]. Crack propagates between grains by the passage of grain boundary area which inhibits the crack movement. Consumption of excess energy takes place in case of fine grains in spark plasma sintered alloy (at 1400 °C) which enhances the strength of the alloy [54].

6 Conclusions and Future Prospects

The above investigation shows that mechanical alloying followed by conventional and spark plasma sintering is a promising alloy fabrication method. Spark plasma sintering route significantly improves the sintered density, hardness, strength of 79W–10Mo–10Ni–1Y_2O_3 alloy. The recent advancement of oxide dispersion strengthened W alloys competes with non-ODS W alloys such as W–Ni–Fe, W–Ni–Cu, W–Ni–Co, etc. with respect to enhance hardness, optimized strength, and ductility. Looking at the high-cost factor of nano Y_2O_3, dispersion also has to regulate properly. The appreciable strength and ductility in the alloy is attributed to bimodal particle and grain size distribution and heterogeneous microstructure. Encapsulation of Y_2O_3 inside W matrix is also the stimulating exploration of the prescribed work. The above study indicates that W-based Y_2O_3 nanocomposites could be sintered with substantial density and mechanical properties at 1000 °C SPS temperature which is quite challenging to achieve via melting and casting techniques. It could widen the research area on fabrication of bulk W-based ODS alloys at reduced temperature and power consumption for structural applications. Investigation of strength and ductility under tensile mode for ODS W samples and atomistic simulation to understand the dispersion strengthening effect by Y_2O_3 addition is limited and will be quite interesting to study. The fabrication of ODS–W alloys is a novel door step for studying identical materials to improve the penetration performance for armour and enhance the resistance to radiation for nuclear reactor application.

References

1. Lassner E, Schubert WD (1999) Tungsten-properties, chemistry, technology of the element, alloys, and chemical compounds. Kluwer Academic/Plenum Publishers, New York, pp 255–268
2. Johnson JL (2010) Sintering of refractory metals. In: Fang ZZ (ed) Sintering of advanced materials-fundamentals and processes. Woodhead Publishing, Cambridge (UK), pp 357–380
3. Norajitra P, Boccaccini LV, Gervash A, Giniyatulin R, Holstein N, Ihli T, Janeschitz G, Krauss W, Kruessmann R, Kuznetsov V, Makhankov A, Mazul I, Moeslang A, Ovchinnikov I, Rieth M, Zeep B (2007) Development of a helium-cooled divertor: material choice and technological studies. J Nucl Mater 367:1416–1421
4. Nicolas G (1990) Heavy tungsten–nickel–iron alloys with very high mechanical characteristics. US patent no. 4,960,563, Cime Bocuze, Courbevoie, FRX, 2 Oct 1990
5. Wang M, Li R, Yuan T, Chen C, Zhang M, Weng Q, Yuan J (2018) Selective laser melting of W-Ni-Cu composite powder: densification, microstructure evolution and nano-crystalline formation. Int J Refract Met Hard Mater 70:9–18
6. Patra A, Meraj Md, Pal S, Yedla N, Karak SK (2016) Experimental and atomistic simulation based study of W based alloys synthesized by mechanical alloying. Int J Refract Met Hard Mater 58:57–67
7. Telu S, Patra A, Sankaranarayana M, Mitra R, Pabi SK (2013) Microstructure and cyclic oxidation behavior of W-Cr alloys prepared by sintering of mechanically alloyed nanocrystalline powders. Int J Refract Met Hard Mater 36:195
8. Telu S, Mitra R, Pabi SK (2013) High temperature oxidation behavior of W-Cr–Nb alloys in the temperature range of 800–1200 °C. Int J Refract Met Hard Mater 38:47–59

9. Upadhyaya A (2001) Processing strategy for consolidating tungsten heavy alloys for ordnance applications. Mater Chem Phys 67:101–110
10. Wurster S, Baluc N, Battabyal M, Crosby T, Du J, García-Rosales C, Hasegawa A, Hoffmann A, Kimura A, Kurishita H, Kurtz RJ, Li H, Noh S, Reiser J, Riesch J, Rieth M, Setyawan W, Walter M, You JH, Pippan R (2013) Recent progress in R&D on tungsten alloys for divertor structural and plasma facing materials. J Nucl Mater 442:S181–S189
11. Benjamin JS (1970) Dispersion strengthened superalloys by mechanical alloying. Metall Trans A 1(10):2943–2951
12. Telu S, Mitra R, Pabi SK (2015) Effect of Y_2O_3 addition on oxidation behavior of W-Cr alloys. Metall Mater Trans A 46A:5909–5919
13. Patra A, Saxena R, Karak SK (2016) Combined effect of Ni and nano-Y_2O_3 addition on microstructure, mechanical and high temperature behavior of mechanically alloyed W-Mo. Int J Refract Met Hard Mater 60:131–146
14. Suryanarayana C (2001) Mechanical alloying and milling. Prog Mater Sci 46:1–184
15. Suryanarayana C (2004) Mechanical alloying and milling, vol 13. Marcel Dekker Inc, New York
16. Glieter H (1995) Nanostructured materials: state of the art and perspectives. Nanostruct Mater 6:3
17. Glieter H (2001) Nanostructured materials: basic concepts and microstructure. Acta Mater 48:1
18. Mondal A, Upadhyaya A, Agrawal D (2011) Effect of heating mode and sintering temperature on the consolidation of 90W–7Ni–3Fe alloys. J Alloy Compd 509(2):301–310
19. Das J, Rao GA, Pabi SK, Sankaranarayana M, Nandy TK (2014) Thermo-mechanical processing, microstructure and tensile properties of a tungsten heavy alloy. Mater Sci Eng A 613:48–59
20. Ruiz PL, Ordas N, Iturriza I, Walter M, Gaganidze E, Lindig S, Koch F, Rosales CG (2013) Powder metallurgical processing of self-passivating tungsten alloys for fusion first wall application. J Nucl Mater 442(1–3):S219–S224
21. Han Y, Fan J, Liu T, Cheng H, Tian J (2012) The effect of trace nickel additive and ball milling treatment on the near-full densification behavior of ultrafine tungsten powder. Int J Refract Met Hard Mater 34:18–26
22. Daoush WMR, Elsayed AHA, El Kady OAG, Sayed MA, Dawood OM (2016) Enhancement of physical and mechanical properties of oxide dispersion-strengthened tungsten heavy alloys. Metall Mater Trans A 47(5):2387–2395
23. Munoz A, Monge MA, Savoini B, Rabanal ME, Garces G, Pareja R (2011) La_2O_3-reinforced W and W–V alloys produced by hot isostatic pressing. J Nucl Mater 417(1–3):508–511
24. Lee KH, Cha SI, Ryu HJ, Hong SH (2007) Effect of oxide dispersoids addition on mechanical properties of tungsten heavy alloy fabricated by mechanical alloying process. Mater Sci Eng A 452–453:55–60
25. Patra A, Karak SK, Pal S (2017) Fabrication of nano-Y_2O_3 dispersed tungsten alloys by mechanical alloying followed by conventional and spark plasma sintering. PhD thesis, National Institute of Technology, Rourkela
26. Kang SJL, Kim KH, Yoon DN (1991) Densification and shrinkage during liquid-phase sintering. J Am Ceram Soc 74:425–427
27. Wang JG, Raj R (1984) Mechanisms of superplastic flow in a fine-grained ceramic containing some liquid phase. J Am Ceram Soc 67:399–409
28. Ren C, Koopman M, Fang ZZ, Zhang H (2016) The effects of atmosphere on the sintering of ultrafine-grained tungsten with Ti. JOM-J Min Met Mater S68(11):2864–2868
29. Basu B, Balani K (2011) Advanced structural ceramics. Wiley, New Jersey, p 116
30. Heady RB, Cahn JW (1970) An analysis of the capillary forces in liquid-phase sintering of spherical particles. Metall Trans B 1(1):185–189
31. Skandan G (1995) Processing of nanostructured zirconia ceramics. Nanostruct Mater 5(2):111–126
32. Jenkins R, Snyder RL (1996) Introduction to X-ray powder diffractometry. Wiley, New York

33. Patra A, Saxena R, Karak SK, Laha T, Sahoo SK (2017) Fabrication and characterization of nano-Y_2O_3 dispersed W-Ni-Mo and W-Ni-Ti-Nb alloys by mechanical alloying and spark plasma sintering. J Alloys Compd 707:245–250
34. Lin KH, Hsu C-S, Lin ST (2003) Precipitation of an intermetallic phase in Mo-alloyed tungsten heavy alloys. Mater Trans 44(3):358–366
35. German RM, Suri P, Park SJ (2009) Review: liquid phase sintering. J Mater Sci 44:1–39
36. Huppmann WJ, Riegger H, Kaysser WA, Smolej V, Pejovnik S (1979) The elementary mechanisms of liquid phase sintering, I rearrangements. Z Metallkd 70:707
37. Dieter G (1928) Mechanical metallurgy, SI Metric edn. McGraw-Hill Co, Singapore
38. Hull D, Bacon DJ (2001) Introduction to dislocations. Elsevier Press, UK
39. Alhamidi A, Edalati K, Iwaoka H, Horita Z (2014) Effect of temperature on solid-state formation of bulk nanograined intermetallic Al_3Ni during high-pressure torsion. Phil Mag 94(9):876–887
40. Li Z, Lu Z, Xie R, Lu C, Liu C (2016) Effect of spark plasma sintering temperature on microstructure and mechanical properties of 14Cr-ODS ferritic steels. Mater Sci Eng A 660:52–60
41. Panelli R, Filho FA (1998) Compaction equation and its use to describe powder consolidation behavior. Powder Metall 41(2):131–133
42. Mayo M (1996) Processing of nanocrystalline ceramics from ultrafine particles. Int Mater Rev 41(3):85–115
43. Groza JR (2007) Nanocrystalline powder consolidation methods. In: Koch Carl C (ed) Nanostructured materials: processing, properties and applications. William Andrew Publishing, Norwich, NY (USA), p 196
44. Nix WD, Gao H (1998) Indentation size effects in crystalline materials: a law for strain gradient plasticity. J Mech Phys Solids 46(3):411–425
45. Luo J, Stevens R (1999) Porosity-dependence of elastic moduli and hardness of 3Y-TZP ceramics. Ceram Int 25:281–286
46. Liu G, Zhang GJ, Jiang F, Ding XD, Sun YJ, Sun J, Ma E (2013) Nanostructured high strength molybdenum alloys with unprecedented tensile ductility. Nat Mater 12:344–350
47. Ma E, Zhu T (2017) Towards strength–ductility synergy through the design of heterogeneous nanostructures in metals. Mater Today 20(6):323–331
48. Karak SK, DuttaMajumdar J, Witczak Z, Lojkowski W, Manna I (2013) Microstructure and mechanical properties of nano-Y_2O_3 dispersed ferritic alloys synthesized by mechanical alloying and consolidated by hydrostatic extrusion. Mater Sci Eng A 580:231–241
49. Edmonds DV (1991) Structure property relationships in sintered heavy alloys. Int J Refract Met Hard Mater 11(5):15
50. Pan Y, Ding L, Li H, Xiang D (2017) Effects of Y_2O_3 on the microstructure and mechanical properties of spark plasma sintered fine-grained W-Ni-Mn alloy. J Rare Earths 35(11):1149–1155
51. Sun D, Liang C, Shang J, Yin J, Song Y, Li W, Liang T, Zhang X (2016) Effect of Y_2O_3 contents on oxidation resistance at 1150 °C and mechanical properties at room temperature of ODS Ni-20Cr-5Al alloy. Appl Surf Sci 385:587–596
52. Patra A, Saxena R, Sahoo RR, Karak SK, Laha T (2018) Evaluation of thermal, fracture and high temperature behavior of mechanically alloyed and spark plasma sintered nano-Y_2O_3 dispersed W-Ni-Mo and W-Ni-Ti-Nb alloys. Mater Perform Charact 7(1):515–531
53. Wang Y, Wang D, Liu H, Zhu W, Zan X (2012) Preparation and characterization of sintered molybdenum doped with $MoSi_2/La_2O_3/Y_2O_3$ composite particle. Mater Sci Eng A 558:497–501
54. Wang L (2007) Mechanical properties of materials. Northeastern University Press, Shenyang

Biocomposites for Hard Tissue Replacement and Repair

Marjan Bahraminasab and Kevin L. Edwards

Abstract Biomaterials with single composition suffer from shortcomings limiting their lifetime and sometimes restricting their applications. Therefore, biocomposites have been started to develop by combining two or more biomaterials with different characteristics to provide superior properties compared to each biomaterial alone. These materials can be flexibly tailored to provide material properties fitted with a given application. In their way to be designed, the principles exist in human body tissues that can be used as a guide. This helps in providing biomimetic materials. Over the recent past decades, research on composite materials for biomedical applications has been progressively increased. A large number of composites, therefore, have been developed and tested for hard tissue replacements and repair. This includes total joint replacements, devices used for fractured bone treatment, dental restorative materials, dental implants, and bone scaffolds. This chapter provides information on permanent and temporary implants and the essential material requirements for their applications. Furthermore, it specifically explains different types of composite biomaterials used in hard tissue replacements and repair. However, this chapter does not include ancillary implants or fasteners used to treat fractured bone.

Keywords Materials requirements · Biocomposites · Porous structure
Joint replacements · Scaffolds

1 Introduction

A biomaterial is a material that is able to interact with biological systems. Biomaterials are being extensively used to repair and substitute human body organs

M. Bahraminasab (✉)
Department of Tissue Engineering and Applied Cell Sciences, School of Medicine, Semnan University of Medical Sciences, Semnan, Iran
e-mail: m.bahraminasab@yahoo.com; m.bahraminasab@semums.ac.ir

K. L. Edwards
Institution of Engineering Designers, Courtleigh, Westbury Leigh, Wiltshire BE13 3TA, UK

S. S. Sidhu et al. (eds.), *Futuristic Composites*, Materials Horizons: From Nature to Nanomaterials, https://doi.org/10.1007/978-981-13-2417-8_14

damaged or diseased by traumatic or pathologic events to aid in the tissue healing process, to correct abnormalities, and to restore lost physical functions. Today, the medical industry benefits considerably from an abundance of mechanical devices and implants made from biomaterials. This includes bone plates, ligaments, joint replacements, dental implants, heart valves, biosensors, blood tubes, etc. However, despite the many successes achieved over previous decades, unfortunately some of the biomaterials used have failed during service. Biomaterials have to function inside the human body, which has complex conditions including an aggressive environment, site-specific properties, and activity-dependent loading. The biomaterials therefore need to simultaneously satisfy chemical, biological, mechanical, and physical requirements. The need to ideally have all of these characteristics in a material might make a homogeneous biomaterial compromise on certain requirements and therefore be unsuitable for some biomedical applications. This is more likely with the trend for material requirements becoming more demanding and the scope of applications increasing. This strongly encourages material researchers to direct their efforts more toward the design and manufacture of hybrid biomaterials such as composites [1].

Composite materials, or composites for short, are a group of hybrid materials comprising of a heterogeneous combination of two or more different materials (on a macroscopic scale), which usually have different compositions and characteristics. It is the unique ability of being able to tailor the properties of composites by altering their constituents (type, orientation, proportion, etc.) that make them highly desirable as biomaterials. Composites can be designed and manufactured to deliver specific properties for certain applications (i.e., flexible design and application-specific) that a single composition material might not be able to provide alone. Various composite biomaterials have already been developed and used successfully in some biomedical applications such as dental restorations, joint implants, bone fracture internal fixation devices, scaffolds (three-dimensional structures made from biodegradable fibers), artificial ligaments, and many others [2]. Composites are still widely under development to address the shortcomings of single composition material and to provide optimal characteristics for given applications. To achieve an optimal solution, the design of a new composite biomaterial should be done according to the biological structure of the tissue being substituted and such a material should ideally mimic the living tissue [3].

This chapter provides an overview of permanent (i.e., fixed) and temporary (i.e., resorbable) implants or prostheses and explains the essential material requirements considered to be necessary for their applications. It also specifically discusses composite biomaterials used in hard tissue (mineralized tissue with a firm intercellular matrix) replacements (permanent implants) and scaffolds (temporary implants) for bone tissue repair. This chapter does not include ancillary implants or fasteners used to treat fractured bone, e.g., plates, screws, pins, and intramedullary nails, although the essential material requirements are still applicable.

2 Hard Tissue Replacements

The replacement of damaged joints with prostheses has brought about a pain-free life with adequate functionality for many patients severely limited in their daily activities. Joint deterioration, which is the end stage of the articular cartilage destruction process, causes considerable pain, loss of motion, and sometimes an angular deformity. When cartilage experiences damage (e.g., injury or arthritis), it is permanent and usually progressive due to the limited repair capacity of cartilage. Therefore, in severe cases, the only treatment is total joint arthroplasty (TJR), although hemiarthroplasty may be done occasionally, based on the damage condition.

Total joint replacements (TJRs) are permanent implants and their fitting involves large removal of bone and cartilage. Total joint arthroplasty is usually carried out for hip, shoulder, knee, elbow, ankle, wrist, and finger. The prostheses used for these joint replacements comprise multiple components (see Fig. 1) for which every component should interact acceptably with the bony bed connected with and the adjacent tissues, and also with other components of the prosthetic implant. Therefore, their failure may happen due to a wide range of reasons. The failure of TJRs usually ends up with revision surgery, which has clinical outcomes that are less satisfactory and the most prevalent cause has been identified to be aseptic loosening [4–6]. The success of prostheses for joint replacements depends on many factors, most of which are related to the materials used for their fabrication. Traditionally, implants were designed with inadequate knowledge on biomaterials. Consequently, the clinical outcomes were not very promising. Nevertheless, expansion of research activities into biomaterials and the biomechanics of replacing joints has led to improved designs. Despite this, there is still a need for longer lasting in vivo performance, because of the younger patients involved in these surgeries and also due to increased life expectancy [7].

The material requirements must be determined based on the specific application. However, there are several characteristics that all materials for joint replacements must fulfill, which are described in the following subsection.

2.1 Materials Requirements

- **Mechanical strength**

The material strength is the prime factor in the success of every implant. Normally, implants comprise several components. Adequate strength is required for each material used in multiple component prostheses to prevent their failure, e.g., fracture. This can occur in the components of an implant, and at the interfaces (implant-cement and cement-bone) in cemented prostheses, and implant-bone in non-cemented prostheses. However, if the bone interface begins to fail, growth of a soft fibrous tissue at that interface allows "micro-motion" of the prosthesis component relative to the bone. This might influence the stability of the implant, cause aseptic loosening problem, and need for a subsequent revision procedure [8]. It is also important to consider

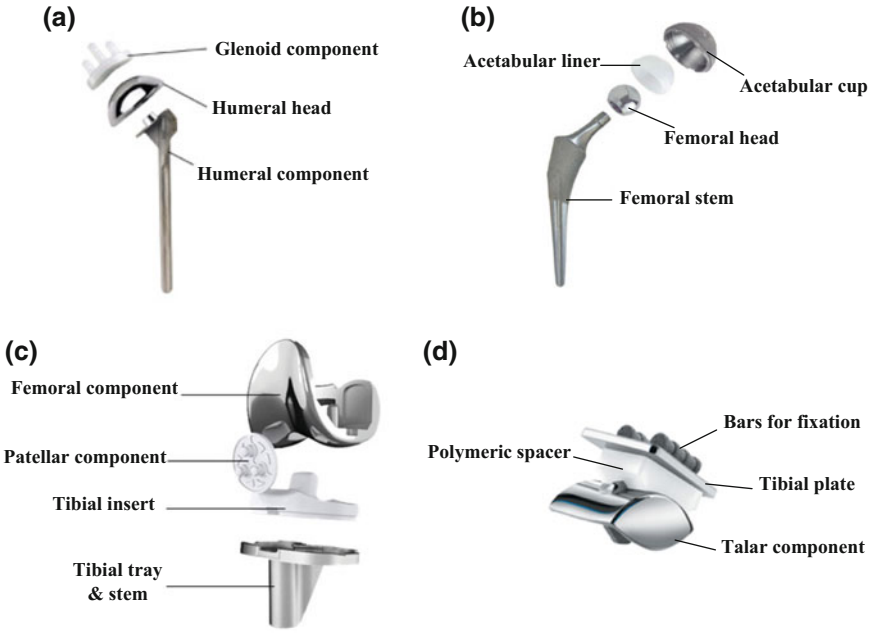

Fig. 1 Total joint replacements; **a** shoulder, **b** hip, **c** knee, and **d** ankle

the specific mechanical strength (strength/density), which should be as similar as possible to that of the replaced bone [9].

- **Modulus of elasticity**

The elastic modulus (or stiffness) of a material can contribute to an undesirable phenomenon known as the stress shielding effect. When the loading applied to a bone alters, a remodeling process takes place within the bone, changing its mineral density and structure to respond to the new loading conditions (add and remove bone tissue at locations experiencing high and low loading, correspondingly) [10]. Total joint replacements, as stated by "Wolff's Law", affect the load transfer naturally exist in the joints due to the presence of the prosthesis (different load transfers occur from the prosthesis to the neighboring bone). In fact, prostheses shield the load or stress from the bone and provide inadequate load transfer (stress shielding effect) leading to resorption of bone, deterioration of the implant-bone interface and final prosthesis loosening [11]. Stress shielding is attributed to large differences between the relatively high modulus of elasticity of the biomaterial and the adjoining bone [12]. In contrast, a lower elastic modulus causes the material to have higher damping capacity and impact energy absorption. This would be useful for reducing the high stresses between the bone and the articular prosthesis.

- **Ductility**

The ductility is the ability of a material to plastically deform without fracture. It is therefore important to prevent brittle failure of the prosthesis under applied loading.

- **Fatigue resistance**

Fatigue is the weakening of a material as a result of repeated applied loads (cyclic loading). Total joint replacements are subjected to cyclic loads during daily activity. Fatigue fracture is frequently reported for hip joint implants (in cast cobalt chrome femoral stem) [13] followed by major problems such as implant loosening. Furthermore, fatigue can generate wear debris which has adverse host tissue response. Fatigue wear can occur in cement and/or polymeric component of TJRs.

- **Creep resistance**

Creep (or cold flow) shows the propensity of a solid material to deform permanently under the effect of applied mechanical stresses. It possibly happens as a result of long-term exposure of a material to high stress values which are less than the material yield strength. Creep resistance is important in material selection/development of TJRs particularly for polymeric components which have a tendency to cause sinking of the prosthesis.

- **Wear resistance**

The articulating surfaces of a total joint replacement should operate with minimum friction under loading and produce the lowest volume of wear debris. The wear particles produced such as ultra-high-molecular-weight polyethylene (UHMWPE) debris cause osteolysis [14], which is a bone resorption process related to a foreign-body reaction to debris from a joint replacement and it is different from the bone resorption due to stress shielding. The process involves the phagocytosis by macrophages and the following secretion of bone-resorptive cytokines, leading to ultimate implant loosening, and hence the revision surgical procedure is needed [15].

- **Corrosion resistance**

The human body is a corrosive electrochemical environment. Therefore, the corrosion of metallic implants is inevitable. The metals and alloys used to fabricate prostheses release unfavorable metal ions, most of which are toxic and non-biocompatible. These ions either deposit in the nearby tissues or are transported to the other parts of the body. The metal traces, which have originated from orthopedic and dental prostheses, have been observed in blood, plasma, urine, serum, liver, lungs, and lymph nodes [16–18]. Also, corrosion can reduce the life of implants due to deterioration of the material structure and this may impose the need for revision surgery. Therefore, the implant material should have very high corrosion resistance.

- **Biocompatibility**

One of the prime requirements of a material to be used in the human body is biocompatibility. This is the ability of a material to interact with living tissues without

incurring an undesirable degree of harm. Biocompatibility covers all aspects related to the function of any bio-device (e.g., prosthesis), including its interaction with cells and tissues [19]. Material biocompatibility can be classified according to inducing cell or tissue death (i.e., cytotoxicity), cancer development (i.e., carcinogenicity), genetic damage (i.e., mutagenicity), immune reaction (i.e., pyrogenicity and allergenicity), or blood clotting (i.e., thrombogenicity) [20]. It should be born in mind though that a material used acceptably in an orthopedic application can be inappropriate for other uses such as cardiovascular applications because it might cause thrombogenicity.

- **Bioactivity (osseointegration ability)**

Bioactivity is a biomaterial property that shows the ability of a material to stimulate a favorable response from the body that is bonding to a host tissue (often bone). In bioactive materials, a close biomaterial–bone apposition is formed, which results in a strong bond and osseointegration. The inability of an implant material, i.e., inert material, to make bonding with the surrounding bone results in a non-adherent fibrous capsule formation around the implant a few weeks after implantation [21]. This can lead to micro-motion, promoting the loosening process. Osseointegration ability is of particular importance in non-cemented load-carrying prostheses where the surface of implant material directly contacts with the bony bed.

2.2 Composites for Total Joint Replacements

Composite biomaterials are promising for TJRs because it is possible to tailor the properties to suitably match with the biomechanical condition and physiological environment. Artificial joints have several components one of which is usually made of polymer and the others are often metal alloys, but sometimes ceramic. The main failure mode (aseptic loosening) of TJRs is attributed to stress shielding phenomenon, micro-motion of the prosthesis, and wear of the polymeric component. Furthermore, metallic materials in TJRs are subjected to corrosion in the physiological body environment. Therefore, composites for joint replacement applications should be designed in a way to improve these characteristics. For hip prostheses, composites have been mostly developed for the polymeric component. Nevertheless, they also have been made for the femoral stem and femoral head ball. The polymer component, which is usually fabricated from UHMWPE, suffers from wear, erosion, and creep deformation. Carbon and aramid (e.g., Kevlar) fibers have been used as reinforcement in different polymers to help reduce these problems. Carbon fibers have been added to UHMWPE, high-density polyethylene (HDP), polyether ether ketone (PEEK), polyether ketone ketone (PEKK), and epoxy resin to provide alternative materials to UHMWPE [22–27]. The PEEK matrix reinforced with 30 wt% carbon fibers has shown to reduce wear as compared to UHMWPE [25]. Carbon and Kevlar fibers have also been used to make composites with HDP, demonstrating that their wear behavior is promising [28]. Furthermore, it has been shown that composites comprising epoxy resin and carbon fibers and used as the bearing surface for acetabular cups against

alumina femoral heads provide minimum wear debris [27]. The wear rate was 5 and 30 times lower than UHMWPE articulating surface coupled with alumina and metal, correspondingly. However, the metal–epoxy composite wear was much higher. In addition to fibers, powders have also been used to reinforce UHMWPE where the hydroxyapatite (HA) is one of the most important reinforcements. Combinations of these two materials have been indicated to provide greater hardness, higher modulus of elasticity, and lower coefficient of friction and wear rate [29].

For metallic components, composite materials have been mostly used as coatings to enhance the cohesion between the prosthetic component and the adjoining bone, to reduce the corrosion and wear rates [30, 31]. The progress gained, however, detachment of the coating from the main body of the implant, which is still a recurring issue [32]. On the other hand, stress shielding is another problem associated with metal and ceramic components such as the femoral stem of a hip joint implant because their elastic modulus is greatly higher than that of human bone. The hip femoral stem is usually made of titanium with a stiffness of about 110 GPa. Therefore, composite femoral stems with elastic modulus close to that of natural bone are of potential. Several composites have been designed and/or fabricated including carbon fiber-reinforced polyamide 12, and carbon fiber-reinforced PEEK [33–35], and good results obtained in terms of load transfer. However, it should be noted that since these composites are more flexible, higher strains are produced inside the implants made of these materials. Meanwhile, reducing the femoral stem stiffness raises the shear stress at the proximal interface which is a risk to its failure. In order to have more uniform shear stress distribution at the interface and at the same time minimize the stress shielding, controlled stiffness composites should be designed. This can be done by combining a material of relatively high stiffness with a more flexible one in a way that by varying the layer composition, constituents' volume fractions and thickness, the stiffness gradually changes in the component (e.g., from the core to the surface). These types of "advanced" composites are called functionally graded materials (FGMs) [36]. FGMs are a group of composites designed to provide a gradient in composition and/or structure selectively in the component. This may vary, as an instance, from one side of the implant toward another side or from the component core toward its surface, based on the demanded application, which offers continuous variation in the properties of the material through thickness. Numerous FGMs have been created using finite element analysis and different manufacturing approaches including layered manufacturing techniques as one of the most recent approaches. HA–collagen, HA–bioglass–collagen, cellular graded Co–Cr alloy, Ti–HA, Ti–bioglass, Co–Cr alloy–Ti–HA, Co–Cr alloy–HA, and stainless steel–bioglass are few examples of FGMs suggested for the different components of a hip prosthesis [1].

The femoral head (ball) of a hip prosthesis is sometimes made of ceramic (e.g., alumina) material. It has been reported that pure alumina heads are quite safe and the risk of fracture is very low, but the reliability of heads with alumina matrix composite (AMC) is even superior [37]. Also, an AMC femoral head has shown extremely low volumetric wear as ceramic-on-ceramic (against alumina and AMC) in a hip joint simulator [38].

The components of total knee replacements also require new materials development. However, the complex knee geometry, loading condition, and kinematics make development of new hybrid materials for this application a complicated task. Fewer composite materials have been developed for knee joint replacement. The problems of creep deformation and subsequent sinking of prosthesis as well as wear also exist for tibial insert (made of UHMWPE) of knee prosthesis. Therefore, carbon fibers have been used to reinforce UHMWPE which improves the material properties including the tensile yield strength, creep resistance, stiffness, and fatigue strength. Nevertheless, contrary results have been gained regarding the wear behavior of carbon fiber–UHMWPE [2]. Carbon fibers have also been used to reinforce PEEK; however, the wear results were not promising and the wear rate was two orders of magnitude greater compared to that of UHMWPE under the same testing conditions [39]. Also, this composite has been investigated in a rotating hinge knee, but not as an alternative for UHMWPE insert [40]. AMC has also been examined for knee replacement and good wear results obtained [41]. Additionally, FGMs have been investigated for the femoral component and tibial tray of knee implants through finite element analysis such as alumina–titanium and Ti–HA, and Ti–collagen [1]. Other joint replacements such as shoulder and finger possess several components made of metal alloys, silicon rubber, HDP, or UHMWPE [42, 43]. Carbon fiber–UHMWPE, poly(-ethylene terephthalate) fabrics–silicon rubber, and carbon fiber–phenolic composites have been developed to improve the function of these prosthetic joints (e.g., higher strength, better creep resistance, and flexural properties).

Among the large number of different composite biomaterials developed for TJRs, only a few have found commercial use and distributed as approved medical implants. This is because the limitations still exist and occasionally, contradictory test results are obtained for some composites. To assure successful commercial application of these materials, further research and development is still required.

3 Scaffolds for Hard Tissue Repair

Tissue engineering applies engineering and biology principles to the design and manufacture of scaffolds using biomaterials, cells, and factors to repair defects in tissues. A scaffold acts as a templet for tissue regeneration and guides the new tissue growth. The usual prime strategy for tissue engineering involves mesenchymal stems cells (MSCs) isolation, ex vivo expansion, and seeding on a fabricated scaffold to form extracellular matrix (ECM), which is followed by inserting the acellular scaffold into the bony defect region [44]. Figure 2 represents schematically the usual process adopted in tissue engineering.

MSCs can be derived from bone marrow (BMSCs), which is a source of multipotent stem cells which can differentiate into fibroblastic, osteogenic, adipogenic, and reticular cells. In addition to bone marrow, other sources of osteogenic human cells can be adipose tissue stem cells (ASCs) and human embryonic stem cells (ESCs) [45–48]. Bone formation can be further controlled by adding osteoinductive growth

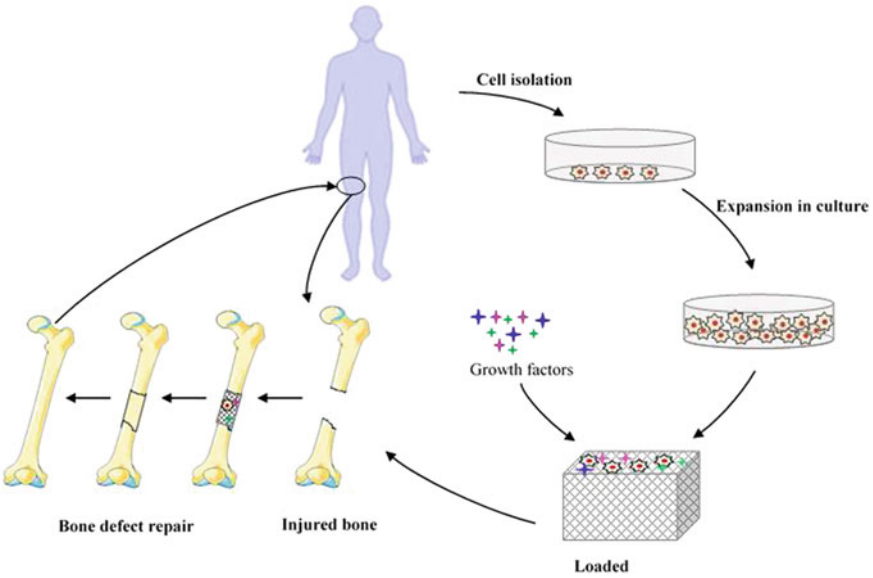

Fig. 2 Bone tissue repair using scaffold, cells, and growth factors

factors (endogenous factors, e.g., bone morphogenetic proteins (BMP) or exogenous factors, e.g., osteopromotive small phytomolecules) into the 3D scaffold [49, 50]. Incorporation of these factors into a scaffold provides a bioactive three-dimensional (3D) structure for interaction of cell–cell and cell-growth factor directing osteogenesis and angiogenesis. There is, however, a major challenge in the choice/design of scaffold material, and its structural design to achieve the optimal performance of a scaffold.

3.1 Materials Requirements

The properties needed for a tissue scaffold should be close to those of the neighboring tissues, as explained for the prosthetic materials in Sect. 2.1.

- **Mechanical strength**

Scaffolds are typically porous structures, which is needed to have adequate mechanical strength in order to preserve the integrity after implantation into the defect [51]. This is of particular importance in the regeneration of hard tissues and load-bearing applications, e.g., bones. The bone scaffolds, in fact, should withstand early loads (wound contraction forces and body loads) and have temporary mechanical stability while degrading over time, in a way that the bony defect could be entirely filled with new bone tissue without scaffold failure. When the degradation process is

slow, however, the scaffold (which is three dimensional) can maintain the structural integrity and mechanical stability. Sometimes, an external fixation is used to stabilize the bone, which is later removed when sufficient strength is gained in the newly formed bone.

- **Modulus of elasticity**

The modulus of elasticity (or stiffness) is another mechanical property that is essential for scaffold mechanical stability. For bone tissue repair, the scaffold should have higher stiffness, which is usually exhibited by materials based on metals, ceramics, and some polymers. Furthermore, appropriate stiffness is required for the remodeling of the bony tissue and not to cause stress shielding. Scaffolds for all other body tissues, however, require having fairly soft and pliable characteristics [52]. The modulus of elasticity also depends on the amount of porosity in the material structure.

- **Processability**

The processing of biomaterials is an important aspect that should be considered because the final geometry of the damaged tissue is required to be replicated by a scaffold. Easy processing of scaffold materials helps in attaining a diversity of internal configurations and overall shape.

- **Osteoconductivity**

For bone repair, an osteoconductive biomaterial, which is capable of having bone growth on its surface, is required to make scaffolds. This along with osteogenic cells and osteoinductive factors can be utilized for bone repair. Osteoinductive factors induce the osteogenesis process. This is done by the employment of immature cells and their stimulation to develop into preosteoblasts [53].

- **Biodegradability**

In addition to biocompatibility, it is important for a scaffold material to be biodegradable. Biodegradability is the ability of a material to decompose over time into nontoxic products due to its biological activity, while the products should be capable of getting metabolized and cleared from the body [54]. This is a critical factor in determining the move from using permanent implants to temporary scaffolds.

3.2 Structural Requirements

For tissue engineering typically, scaffolds should be three-dimensional porous structures to effectively carry out mass transport activities. Mass transport is one of the most challenging issues when designing a scaffold. Structures without porosity or wrongly designed scaffold structure can adversely affect the nourishment of cells, exchange of nutrients and wastes, and cell migration. These are key elements in the reconstruction of very metabolic organs (e.g., liver and pancreas), in particular [55].

Several factors related to porosity including pore size, pore shape, pore interconnectivity, and amount of porosity can influence the success of a designed bone scaffold [56]. One of the objectives in design of bone scaffold is to obtain a balance between the mechanical function and bio-factor delivery, which varies between a denser to a more porous bone scaffold [57]. This has encouraged material engineers to develop new materials, which are mostly aimed toward hybrid porous materials such as composites [58], and hierarchical/ functionally graded porous bone scaffolds [59] to gain both the required mechanical properties and mass transport characteristics, simultaneously.

3.3 Composite Materials Used

Ceramics, metals, and polymers have all been used to make bone scaffolds. However, metals and ceramics have been widely used for medical implantations with particular advances in orthopedic tissue replacements [5]. Nevertheless, most metallic and ceramic biomaterials are not biodegradable. The biodegradable materials using for bone repair and regeneration enthusiastically attract considerable interest in biomaterials research. The reason is that their biodegradable characteristic avoids the need for surgery for their removal, and additional cost and pain for patients. The exceptions for metals are magnesium (Mg), iron (Fe), and zinc (Zn), which has been employed in cardiovascular applications and hard tissue regeneration (mostly in combination with other materials) [60, 61]. From the ceramic biomaterials, tricalcium phosphate and hydroxyapatite are biodegradable [62]. This shortcoming (non-biodegradability) has made the polymeric materials with the ability of biodegradability to receive higher attention for making temporary scaffold in tissue engineering. There are a large number of biodegradable polymers including hydrolytically degradable and enzymatically degradable polymers [54]. Examples of the former polymer group are poly(α-esters) (e.g., polyglycolide, polylactides, poly(lactide-co-glycolide), polydioxanone), polyurethanes, poly(ester amide), poly(ortho esters), polyanhydrides, poly(anhydride-co-imide), cross-linked polyanhydrides, and many others. The latter polymer group includes proteins (e.g., collagen, elastin, albumin, and fibrin), poly(amino acids), and polysaccharides. Among these polymer groups, poly(α-esters), polyurethanes, poly(anhydride-co-imide), cross-linked polyanhydrides, and poly(propylene fumarate) have been used for load-bearing and orthopedic applications because these are relatively stiff. Nevertheless, their high stiffness may not be favorable for soft tissue or blood vessels due to biomechanical mismatch. Despite the progress achieved since the use of biodegradable polymers, some drawbacks still exist. For example, natural polymers suffer from poor mechanical properties and batch-to-batch variation due to isolation from biological tissues [55]. The synthetic polymers also have several limitations. The acidic products released from the biodegradation process of all polyesters, as an example, can unfavorably influence the biocompatibility [54]. The shortcomings exist in all group of biomaterials, and make them not to be optimally suited for the scaffolds serving in some particu-

lar applications which necessitates new biomaterials to be developed. This includes manipulation of the polymer chain and inter-chain bonding, and design of composite materials. For example, to make poly(propylene fumarate) or PPF mechanically favorable for orthopedic applications, cross-linking is a possible way forward [63]. However, another approach is to develop composites by incorporating ceramic materials such as tricalcium phosphate [64].

The ability to design composites gives the opportunity to achieve compromise properties in a single material system. This makes it possible to achieve a balance between the requirements by selecting the appropriate constituents and optimizing their volume fraction in the designing scaffold. This is of particular advantage when bioinspired design principles are taken into account because it can possibly lead to the material degradation rate coinciding the target tissue regeneration [65]. Usually, the combination of ductile polymers with stiff ceramics can overcome the main limitations of both groups, which is the insufficient rigidity caused mechanical instability, and brittleness of the ceramic constituent and the probability of fracture. However, other characteristics can also be amended. There have been several studies on ceramic–polymer composites, one of which developed polycaprolactone (PCL)–nanosize HA composites to achieve desirable mechanical properties and modify the drawbacks of PCL including hydrophobicity, low cell adhesion site, and little biological interactions [66]. Furthermore, glass–PLA composite scaffold was fabricated to improve flexural strength and avoid catastrophic failure [67]. Other ceramic–polymer scaffolds fabricated for bone regeneration include silica-poly(lactide-co-glycolide) or PLGA, poly(L-lactide) or PLLA–HA, PLA–ZnO, PLA–PCL–ZnO, β-tricalcium phosphate–PCL, silk fibroin–HA, etc. [68–72].

Polymers can also be combined with degradable metals to make composites controlling the rate of biodegradability and provide better strength and structural integrity. It has been indicated that the addition of Mg metal particles into poly-L-lactic acid (PLLA) can accelerate the slow degradation of PLLA scaffold by elevating the pH of the degradation medium due to the formation of alkaline product ($Mg(OH)_2$) [73]. This neutralizes the acidic products from degradation of PLLA, which promotes Mg degradation.

Polymer–polymer composites have also been investigated to provide scaffolds with improved properties. For example, scaffolds with polyethylene glycol (PEG)–PLA composites were manufactured with different weight ratios for bone tissue repair, and their biological properties including cell metabolic activity, bone matrix formation, and alkaline phosphatase activity were evaluated [74]. The results of this work showed superior mineralization of osteoblasts rather than scaffolds made of pure PLA. Numerous polymer–polymer composites have been developed; poly(3-hydroxybutyrate-co-3-hydroxyvalerate) or PHBV–gelatin, PLA–polyaniline (PANI), PLA–PCL, chitosan–collagen–hyaluronic acid, to name a few [75–77].

However, it should be noted that most of the composite biomaterials developed for bone scaffolds require more investigation to get the Food and Drug Administration (FDA) approval and hence transfer to clinical reality.

4 Conclusions

The development of biomaterials for bone replacement (prostheses) and bone repair (scaffolds) is a difficult task both from the engineering aspects and the biological perspective. A biomaterial should fulfill numerous requirements which necessitates the design of composite materials. Composites provide a tailor-based design methodology with more possibilities to orientate their properties than the single composition material. The implant structure and its interactions with the nearby tissues and cells can be improved by changing the constituents, the type of the reinforcing phase and its magnitude and distribution. For hard tissue replacement and repair, the research and development of composite biomaterials are being widely carried out; however, the use of these materials as industrially produced commercial medical devices still involves restrictions which demands a thorough understanding of the aims and limitations.

References

1. Bahraminasab M, Farahmand F (2017) State of the art review on design and manufacture of hybrid biomedical materials: hip and knee prostheses. Proc Inst Mech Eng Part H J Eng Med 0954411917705911
2. Salernitano E, Migliaresi C (2003) Composite materials for biomedical applications: a review. J Appl Biomater Biomech 1(1):3–18
3. Mano JF et al (2004) Bioinert, biodegradable and injectable polymeric matrix composites for hard tissue replacement: state of the art and recent developments. Compos Sci Technol 64(6):789–817
4. Sadoghi P et al (2013) Revision surgery after total joint arthroplasty: a complication-based analysis using worldwide arthroplasty registers. J Arthroplasty 28(8):1329–1332
5. Bahraminasab M et al (2012) Aseptic loosening of femoral components—a review of current and future trends in materials used. Mater Des 42:459–470
6. Luther C, Germann G, Sauerbier M (2010) Proximal interphalangeal joint replacement with surface replacement arthroplasty (SR–PIP): functional results and complications. Hand 5(3):233–240
7. Hernigou P et al (2004) Alternative femoral bearing surface options for knee replacement in young patients. Knee 11(3):169–172
8. Bahraminasab M et al (2013) Aseptic loosening of femoral components-materials engineering and design considerations. Mater Des 44:155–163
9. Farag MM (1997) Materials selection for engineering design. Prentice Hall
10. Christen P et al (2014) Bone remodelling in humans is load-driven but not lazy. Nat Commun 5:4855
11. Geetha M et al (2008) Ti based biomaterials, the ultimate choice for orthopaedic implants—a review. Prog Mater Sci 54(3):397–425
12. Denard PJ et al (2018) Stress shielding of the humerus in press-fit anatomic shoulder arthroplasty: review and recommendations for evaluation. J Shoulder Elbow Surg
13. Teoh SH (2000) Fatigue of biomaterials: a review. Int J Fatigue 22(10):825–837
14. Broomfield JA et al (2017) The relationship between polyethylene wear and periprosthetic osteolysis in total hip arthroplasty at 12 years in a randomized controlled trial cohort. J Arthroplasty 32(4):1186–1191

15. Ingham E, Fisher J (2005) The role of macrophages in osteolysis of total joint replacement. Biomaterials 26(11):1271–1286
16. Özcan M, Hämmerle C (2012) Titanium as a reconstruction and implant material in dentistry: advantages and pitfalls. Materials 5(9):1528–1545
17. Bahraminasab M, Hassan MR, Sahari BB (2010) Metallic biomaterials of knee and hip—a review. Trends Biomater Artif Organs 24(2):69–82
18. Okazaki Y, Gotoh E (2005) Comparison of metal release from various metallic biomaterials in vitro. Biomaterials 26(1):11–21
19. Williams DF (2009) On the nature of biomaterials. Biomaterials 30(30):5897–5909
20. Chen Q, Thouas GA (2015) Metallic implant biomaterials. Mater Sci Engi R Rep 87:1–57
21. Salinas AJ, Vallet-Regí M (2013) Bioactive ceramics: from bone grafts to tissue engineering. RSC Adv 3(28):11116–11131
22. Marques N, Davim JP (2002) Tribological comparative study of conventional and composite materials in biomedical applications, pp 487–490
23. Saha D et al (2007) Production and biocompatibility evaluation of carbon fiber reinforced polyethylene composite for acetabular cup. Sci Eng Compos Mater 14(1):47–55
24. Scholes SC, Unsworth A (2009) Wear studies on the likely performance of CFR-PEEK/CoCrMo for use as artificial joint bearing materials. J Mater Sci Mater Med 20(1):163–170
25. Marques N, Davim JP (2002) Tribological comparative study of conventional and composite materials in biomedical applications. Key Eng Mater 230:487–490
26. Geringer J, Tatkiewicz W, Rouchouse G (2011) Wear behavior of PAEK, poly(aryl-ether-ketone), under physiological conditions, outlooks for performing these materials in the field of hip prosthesis. Wear 271(11–12):2793–2803
27. Früh H-J, Willmann G (1998) Tribological investigations of the wear couple alumina–CFRP for total hip replacement. Biomaterials 19(13):1145–1150
28. Roy Chowdhury SK et al (2004) Wear characteristic and biocompatibility of some polymer composite acetabular cups. Wear 256(11–12):1026–1036
29. Liu JL et al (2008) Biotribological behavior of ultra high molecular weight polyethylene composites containing bovine bone hydroxyapatite. J China Univ Min Technol 18(4):606–612
30. Ghorbel HF et al (2017) Alumina-fluorapatite composite coating deposited by atmospheric plasma spraying: an agent of cohesion between bone and prostheses. Mater Sci Eng C 71:1090–1098
31. Qadir M et al (2017) Calcium phosphate-based composite coating by micro-arc oxidation (MAO) for biomedical application: a review. Crit Rev Solid State Mater Sci 1–25
32. Bartelstein MK et al (2017) Failure of a polyaryletheretherketone-cobalt-chromium composite femoral stem due to coating separation and subsidence: a case report. JBJS Case Connect 7(4):e83
33. Campbell M et al (2008) CF/PA12 composite femoral stems: manufacturing and properties. Compos Part A Appl Sci Manuf 39(5):796–804
34. Sridhar I, Adie PP, Ghista DN (2010) Optimal design of customised hip prosthesis using fiber reinforced polymer composites. Mater Des 31(6):2767–2775
35. Bougherara H et al (2007) Design of a biomimetic polymer-composite hip prosthesis. J Biomed Mater Res Part A 82(1):27–40
36. Sola A, Bellucci D, Cannillo V (2016) Functionally graded materials for orthopedic applications—an update on design and manufacturing. Biotechnol Adv 34(5):504–531
37. Lee G-C, Kim RH (2017) Incidence of modern alumina ceramic and alumina matrix composite femoral head failures in nearly 6 million hip implants. J Arthroplasty 32(2):546–551
38. Stewart TD et al (2003) Long-term wear of ceramic matrix composite materials for hip prostheses under severe swing phase microseparation. J Biomed Mater Res B Appl Biomater 66(2):567–573
39. Brockett CL et al (2017) PEEK and CFR-PEEK as alternative bearing materials to UHMWPE in a fixed bearing total knee replacement: an experimental wear study. Wear 374–375:86–91

40. Schierjott RA et al (2016) Analysis of carbon fiber reinforced PEEK hinge mechanism articulation components in a rotating hinge knee design: a comparison of in vitro and retrieval findings. BioMed Res Int 2016
41. Leyen S, Schwiesau J, Schmidt R (2002) Investigation of the wear behaviour of a ceramic knee concept with floating meniscal bearing. Key Eng Mater 585–586
42. Adkinson JM, Chung KC (2014) Advances in small joint arthroplasty of the hand. Plast Reconstr Surg 134(6):1260
43. Kim SS et al (2009) Development of the carbon/phenolic composite shoulder bearing. Compos Struct 88(1):26–32
44. Khan WS et al (2012) An osteoconductive, osteoinductive, and osteogenic tissue-engineered product for trauma and orthopaedic surgery: how far are we? Stem Cells Int 2012
45. Kern S et al (2006) Comparative analysis of mesenchymal stem cells from bone marrow, umbilical cord blood, or adipose tissue. Stem Cells 24(5):1294–1301
46. Smith LA et al (2010) The enhancement of human embryonic stem cell osteogenic differentiation with nano-fibrous scaffolding. Biomaterials 31(21):5526–5535
47. Kim S et al (2008) In vivo bone formation from human embryonic stem cell-derived osteogenic cells in poly(d, l-lactic-co-glycolic acid)/hydroxyapatite composite scaffolds. Biomaterials 29(8):1043–1053
48. Knippenberg M et al (2005) Adipose tissue-derived mesenchymal stem cells acquire bone cell-like responsiveness to fluid shear stress on osteogenic stimulation. Tissue Eng 11(11–12):1780–1788
49. Varkey M, Gittens SA, Uludag H (2004) Growth factor delivery for bone tissue repair: an update. Expert Opin Drug Deliv 1(1):19–36
50. Chen S-H et al (2012) Comparative study of osteogenic potential of a composite scaffold incorporating either endogenous bone morphogenetic protein-2 or exogenous phytomolecule icaritin: an in vitro efficacy study. Acta Biomater 8(8):3128–3137
51. Yang S et al (2002) The design of scaffolds for use in tissue engineering. Part II. rapid prototyping techniques. Tissue Eng 8(1):1–11
52. Kohn J (2004) New approaches to biomaterials design. Nat Mater 3(11):745–747
53. Albrektsson T, Johansson C (2001) Osteoinduction, osteoconduction and osseointegration. Eur Spine J 10(2):S96–S101
54. Nair LS, Laurencin CT (2007) Biodegradable polymers as biomaterials. Prog Polym Sci 32(8–9):762–798
55. Yang S et al (2001) The design of scaffolds for use in tissue engineering. Part I. Traditional factors. Tissue Eng 7(6):679–689
56. Adachi T et al (2006) Framework for optimal design of porous scaffold microstructure by computational simulation of bone regeneration. Biomaterials 27(21):3964–3972
57. Hollister SJ et al (2005) Engineering craniofacial scaffolds. Orthod Craniofac Res 8(3):162–173
58. Shavandi A et al (2015) Bio-mimetic composite scaffold from mussel shells, squid pen and crab chitosan for bone tissue engineering. Int J Biol Macromol 80:445–454
59. Hollister SJ (2005) Porous scaffold design for tissue engineering. Nat Mater 4(7):518–524
60. Liu YJ, Su WT, Chen PH (2018) Magnesium and zinc borate enhance osteoblastic differentiation of stem cells from human exfoliated deciduous teeth in vitro. J Biomater Appl 32(6):765–774
61. Qi Y et al (2018) Strategy of metal-polymer composite stent to accelerate biodegradation of iron-based biomaterials. ACS Appl Mater Interfaces 10(1):182–192
62. Sheikh Z et al (2015) Biodegradable materials for bone repair and tissue engineering applications. Materials 8(9):5744–5794
63. Zhao W et al (2005) Progress in researches on the synthesis of poly(propylene fumarate) and its crosslinking characteristics. Sheng wu yi xue gong cheng xue za zhi = J Biomed Eng = Shengwu yixue gongchengxue zazhi 22(2):381–384
64. Chu T-MG et al (2007) Segmental bone regeneration using a load-bearing biodegradable carrier of bone morphogenetic protein-2. Biomaterials 28(3):459–467

65. Jabbari E (2007) Bioinspired nanomaterials for bone regeneration. In: Nanopatterning and nanoscale devices for biological applications, p 329
66. Kim MH et al (2018) Quantitative analysis of the role of nanohydroxyapatite (nHA) on 3D-printed PCL/nHA composite scaffolds. Mater Lett 220:112–115
67. Mohammadkhah A, Day DE (2018) Mechanical properties of bioactive glass/polymer composite scaffolds for repairing load bearing bones. Int J Appl Glass Sci 9(2):188–197
68. Kaliaraj R et al (2018) A biomimetic mesoporous silica–polymer composite scaffold for bone tissue engineering. J Porous Mater 25(2):397–406
69. Szustakiewicz K et al (2018) Femtosecond laser-induced modification of PLLA/hydroxypatite composite. Polym Degrad Stab 149:152–161
70. Ivanovic J, Rezwan K, Kroll S (2018) Supercritical CO2 deposition and foaming process for fabrication of biopolyester–ZnO bone scaffolds. J Appl Polym Sci 135(7)
71. Huang B et al (2018) Polymer-ceramic composite scaffolds: the effect of hydroxyapatite and β-tri-calcium phosphate. Materials 11(1)
72. Farokhi M et al (2018) Silk fibroin/hydroxyapatite composites for bone tissue engineering. Biotechnol Adv 36(1):68–91
73. Shuai C et al (2018) Positive feedback effects of Mg on the hydrolysis of poly-*l*-lactic acid (PLLA): promoted degradation of PLLA scaffolds. Polym Testing 68:27–33
74. Bhaskar B et al (2018) Composite porous scaffold of PEG/PLA support improved bone matrix deposition in vitro compared to PLA-only scaffolds. J Biomed Mater Res Part A 106(5):1334–1340
75. Choi MO, Kim YJ (2018) Effect of poly(3-hydroxybutyrate-co-3-hydroxyvalerate)/gelatin ratios on the characteristics of biomimetic composite nanofibrous scaffolds. Colloid Polym Sci 1–10
76. Chen J et al (2018) Conductive nanofibrous composite scaffolds based on in-situ formed polyaniline nanoparticle and polylactide for bone regeneration. J Colloid Interface Sci 514:517–527
77. Kaczmarek B et al (2018) New composite materials prepared by calcium phosphate precipitation in chitosan/collagen/hyaluronic acid sponge cross-linked by EDC/NHS. Int J Biol Macromol 107(Part A):247–253

Evaluation of Elastomeric Composites Reinforced with Chicken Feathers

Carolina Castillo-Castillo, Beatriz Adriana Salazar-Cruz, José Luis Rivera-Armenta, María Yolanda Chávez-Cinco, María Leonor Méndez-Hernández, Ivan Alziri Estrada-Moreno and Tania Ernestina Lara Ceniceros

Abstract The use of reinforcements from natural or animal sources has recently taken relevance because it is a good way of obtaining improved polymers while reducing the environmental impact of the poultry industry, and at the same time, it allows to take advantage of the large amount of waste materials that is frequently considered useless. Styrene-butadiene copolymer (SBS) is used in a wide range of applications, for example, in shoes, adhesives, tires, plastic and asphalt modifiers, among others. However, SBS has limitations due to its mechanical and thermal properties; in some cases, it has been reinforced with particles in order to improve its thermomechanical behavior. Chicken feathers (CFs) represent a waste material from the poultry farming that has not been widely used in the polymer industry yet. Furthermore, in some cases, its final disposal management implies additional costs. CFs is mainly composed of keratin, a mix of proteins that have good mechanical and thermal properties. In the present work, CFs were milled and mixed with SBS with the aim of preparing SBS-CF composites. Composite materials were produced by means of a melt-mixing technique, and the effect of zinc oxide (ZnO) as coupling agent was evaluated. Three different concentrations of CFs at varying mixing speeds were tested with the aim of assessing their effect on the SBS-CF composites properties. The composites thermal properties were measured by means of differential scanning calorimetry (DSC), thermogravimetric analysis (TGA), and dynamic mechanical analysis (DMA), while their morphologic properties were evaluated by means of X-ray diffraction (XRD) and scanning electron microscopy (SEM).

C. Castillo-Castillo · B. A. Salazar-Cruz · J. L. Rivera-Armenta (✉) · M. Y. Chávez-Cinco
Petrochemical Research Center, National Technological of Mexico (TecNM), Technological Institute of Madero City, Madero City, Mexico
e-mail: jlriveraarmenta@yahoo.com

M. L. Méndez-Hernández
Superior Technological Institute of Tantoyuca, Tantoyuca, Mexico

I. A. Estrada-Moreno
CONACYT—Center for Research in Advanced Materials (CIMAV S.C.), Chihuahua, Mexico

T. E. Lara Ceniceros
Center for Research in Advanced Materials (CIMAV S.C.), Monterrey, Mexico

S. S. Sidhu et al. (eds.), *Futuristic Composites*, Materials Horizons: From Nature to Nanomaterials, https://doi.org/10.1007/978-981-13-2417-8_15

Keywords Keratin · Elastomer · Composites · Reinforcement · Thermal stability

1 Introduction

1.1 Composite Materials

Composite materials are defined as a combination of two or more materials that may be formed from a chemical or physical bonding resulting in a compound with improved properties that emerge from adding their individual characteristics. The composite components must not dissolve or melt in a complete way. Composites are heterogeneous materials and show anisotropic properties [1].

These materials can be classified according to their matrix in metallic, ceramic, and polymeric matrices. Regarding the shape of their reinforcement agents, they can also be classified into particles, which are subdivided in big and hardened by dispersion, fibers and finally in structural reinforcement, divided into laminar, sandwich, and non-laminar structures [2]. Composite materials offer high resistance, low density, flexibility including high dielectric resistance, corrosion resistance, enhanced fatigue behavior, and their use implies a reduction on maintenance costs. The polymer type is the mostly used matrix for preparing composite materials, and among them, thermoplastics, elastomers, and thermosets are the most commonly employed.

On the other hand, reinforcements are materials added to a matrix with the aim of improving its thermal, mechanical and/or optical properties. The reinforcement agents can be organic, inorganic, natural or synthetic. Polymers reinforcement is frequently selected to improve their mechanical resistance, wear, flow, and thermal behavior, as their properties are usually affected when the matrix is subjected to a transformation process.

1.2 Chicken Feathers (CFs) as Reinforcement

Nowadays, searching for new materials that have good mechanical properties, low cost, long durability, low weight, and that are environmentally friendly derivatives from natural or renewable sources, is not only a modern tendency but an urgent demand to reduce the use of synthetic materials presenting a low (or null) degradation rate when they are discarded to the environment. Options among these materials from renewable sources include natural plants and animal wastes. For instance, Chicken Feathers (CFs) are waste materials from the poultry industry that have been studied since 30 years ago. They are natural, renewable, with no cost (even some chicken farms use to pay for its disposal), and have a density that can range from 0.8 to 0.85 g/m^3.

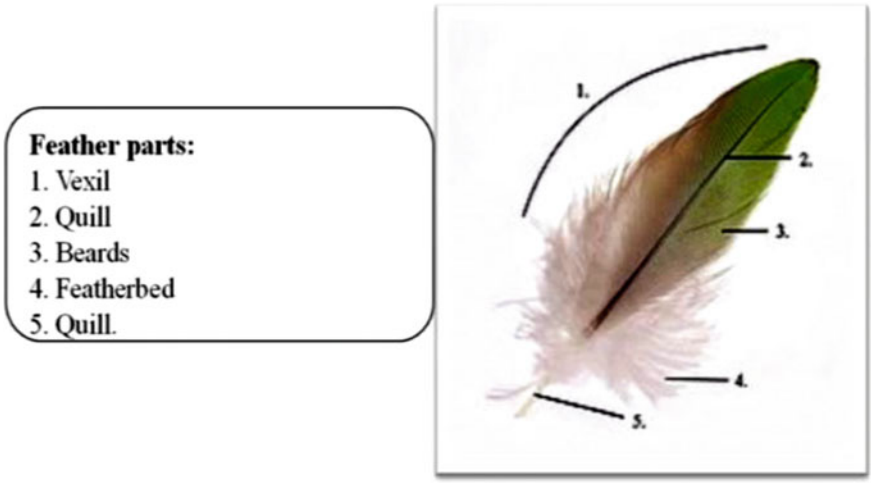

Fig. 1 Main parts of a chicken feather

The disposal of CFs is considered an environmental problem because it is difficult to locate the appropriate place that fulfills the legislations (Tesfaye et al. 2017). The CF is a chicken waste whose production is growing considerably day by day (Mollins et al. 2017).

The CFs' main component is keratin, around 90–95% by weight, and it is a material with good properties such as durability and insolubility, which is chemically nonreactive and flexible, with good mechanical and thermal properties attributed to the disulfide crosslinked bonds from cysteine and the nonhydrophilic aminoacids present in the chain sequence, which provide to keratin its hydrophobic character [3]. Because of these reasons, the keratin becomes an interesting material to be mixed with polymer. Figure 1 shows the bird feather parts.

The keratin has two main sheet structures: α and β (Fig. 2). The chemical composition of keratin includes several amino acids; among them, the cysteine is the most abundant. The α keratin is characterized by its high sulfur content as well as high glycine tyrosine proteins content [4]. The proposed secondary structure of CF changes according to the feather parts, quill β-sheet, the rachis 78% of β-sheet, and 18% helical from twisted sheet and barbs α-keratin (Martínez-Hernández and Velasco-Santos 2012).

An interesting way to improve the CF properties is its chemical modification; several reports of this methodology have been carried out (Tesfaye 2017; [5, 6]; Martínez-Hernández and Velasco-Santos 2012; Rivera-Armenta et al. 2012; [7]). The CF has been used also as reinforcement in several thermoplastic polymer matrices, for example, Polypropylene (PP) [8, 9]; polyethylene (PE) [10]; recycled high density polyethylene (RHDPE) [11, 12]; polymethyl methacrylate (PMMA) [13]; PVC [38]; Polylactic acid (PLA) ([14]; Baba and Ozmen 2015; [15, 16]); polyesthers [17]; epoxy [18]; polyurethane (PU) ([19, 20]; Mollins et al. 2017); and elastomer matrices

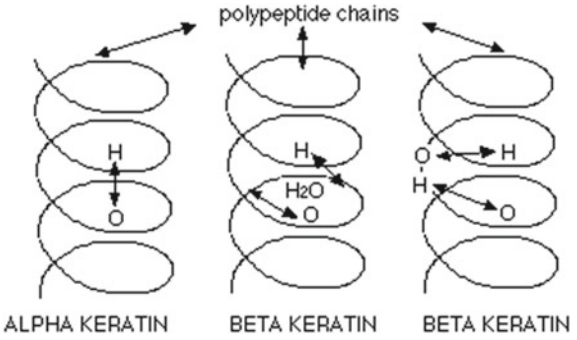

Fig. 2 Alpha and beta keratin structures

([21–24]; Jong et al. 2015). However, only few studies dealing with elastomers like styrene-butadiene copolymers (SBS) are available in the scientific literature [25, 26].

1.3 Elastomers

Elastomers are a kind of polymers that are characterized by their viscoelastic properties, which means that under certain conditions they can flow, and in some others, they can be deformed without suffering chemical and structural changes. The elastomers can be classified according to its properties and application areas in natural rubbers, synthetic rubbers, and thermoplastic elastomers (TPEs). The synthetic rubbers can be crosslinked to become thermoset polymers, for instance, styrene-butadiene rubber (SBR), chloroprene, nitrile rubber (NBR), and ethylene propylene diene monomer (EPDM).

The TPE family includes polyisoprene, polybutadiene (PB), polychloroprene, acrylonitrile-butadiene, silicones, and stryrene-butadiene copolymers (SBS). SBS is a common name for a group of materials that flow easily at processing temperatures, however, at higher temperatures, their mechanical properties decrease. The SBS have some wide application areas that include sealants, shoe soles, tires, adhesives, roofing, plastic modifiers, asphalt modifiers, and automotive parts. An important factor that impacts the SBS properties is its styrene content, because the higher the styrene content, the higher its plastic behavior, whereas the lower the content, the more similar its behavior to a vulcanized material.

In order to enhance the SBS attributes, its reinforcement with keratin fibers has been considered [25]. There are several studies on composite materials using styrene-butadiene rubber (SBR), nitrile-butadiene rubber (NBR), and keratin from chicken feathers that revealed the influence of different variables on the polymers' thermal and mechanical behavior, and the various valid tools for observing these variations [21, 23, 27, 28].

Some of the great characteristics of keratin from chicken feathers are its high mechanical and thermal resistance, which could improve the performance of syn-

Fig. 3 Procedure to obtaining of milled CF

thetic polymers and allows to obtain composite materials presenting comparable mechanical properties to those of the conventional material [6].

The aim of this work is to prepare composites materials using SBS as polymeric matrix and CF particles as reinforcement. The effect of composite preparation condition was evaluated changing the mixing speed, and the CF concentration in three levels (1, 3, and 5 phr). The properties of the SBS-CF composites were evaluated by means of thermogravimetric analysis (TGA), dynamic mechanical analysis (DMA), X-ray diffraction (XRD), and scanning electron microscopy (SEM).

2 Experimentation

2.1 Materials

Chicken feathers were obtained from a local slaughter house. The CFs were washed with water and rinsed with ethanol to disinfect them; process was repeated several times until a free-odor material was obtained, and subsequently, it was dried for 2 days under sunlight. CFs were milled using a domestic blender and the resulting pieces were sieved (No. 20) in order to obtain a homogeneous particle size of around 707 μm (Fig. 3).

Styrene-butadiene elastomer (SBS) of linear structure and a butadiene/styrene ratio of 69/31 were used as matrix. The main properties of SBS are hardness shore A 76, total styrene 31%, viscosity at 180 °C, 1600 cP, and penetration at 25 °C < 55

1/10 mm. The most common applications of this elastomer are asphalt modification, shoes soles, plastic modification, and adhesives.

Zinc oxide (ZnO) was employed as an agent for impeding the progress of the crosslinking process, and for improving the compatibility between CF and SBS. The particle size of ZnO was <5 μm with a purity of 99.9%.

2.2 Composites Preparation

The SBS-CF composites were prepared by a melt-mixing technique using an Intelli-Torque Brabender mixing chamber with roller blades; its operating conditions were determined by modifying the mixing velocity and the temperature in two levels for a total mixing time of 20 min. The ZnO was added as compatibilizing agent. The volume of the mixing chamber was 60 cm^3 and it was used at 70% of its capacity. Three levels of CFs concentration were tested: 1, 3, and 5 phr (parts per hundreds of resin). The composites codes were SBS-CF 1 phr, SBS-CF 3 phr, and SBS-CF 5 phr. The ZnO was added in the mixing chamber at a constant concentration of 1 phr and code for these materials were SBS-CF-X phr-ZnO, where X was 1, 3, and 5 phr.

After the mixing process, testing specimens were prepared using a Dake hydraulic press under the following procedure: first, a 0 T_{on} charge was applied during 20 min and 90 °C; subsequently, the pressure was increased to 5 T_{on} for 10 min and then 8 T_{on} were added during 8 min. The resulting testing specimens, of 1/8 inch thickness were used to obtain samples for Dynamic Mechanical Analysis (DMA).

2.3 Composites Characterization

The composites were characterized by means of different techniques:

2.3.1 Thermogravimetric Analysis (TGA)

The TGA was performed in order to evaluate the thermal stability of the prepared materials. The analysis was carried out in a TA Instrument model SDT Q600, using a nitrogen atmosphere with 100 mL/min flow, with a temperature range from room temperature to 600 °C with a heating rate of 10 °C/min and a weight sample of 10 ± 2 mg.

2.3.2 Dynamic Mechanical Analysis (DMA)

The DMA is a technique that involves a small deformation cycle in a sample and measure the resulting stress, or in equivalent way, a stress cycle to register the result-

ing deformation. The DMA was carried out in a TA Instrument equipment (model Q-800) with a dual cantilever clamp with sample size of $20 \times 10 \times 3$ mm, in a temperature range from −100 to 150 °C with 1 Hz frequency, 2 μm amplitude, and heating rate of 5 °C/min.

2.3.3 X-Ray Diffraction (XRD)

XRD is the most efficient technique for performing qualitative and quantitative analysis of crystalline phase materials. XRD determines the detailed structure to know the position of atoms, ions, or molecules in a crystalline material, and from the extent of this structural order; its physical and chemical properties can be deduced. In a crystal, the atoms or molecules are disposed in a regular form, and the term crystallinity refers to the structural order typical of solid materials. The crystalline region of a material is responsible for its hardness and brittleness, while its amorphous region provides tenacity, that is, the ability to bend without breaking. This technique was used to obtain the dispersion pattern of keratin in SBS-CF with and without ZnO. The analysis was carried out using Empyrean equipment in a range from 5 to 90° in 2θ scale at 25 °C.

2.3.4 Scanning Electron Microscopy (SEM)

SEM is a technique that uses an electron beam instead of a light beam to create an enlarged image from a surface. It is an instrument that allows the observation and superficial characterization of organic and inorganic solids, and it has a great depth of field, which allows it to focus at the same time a large part of the sample. The composites were analyzed in a SEM equipment Hitachi model TM-1000, operating at 15 kV with retro dispersed electrons.

3 Results and Discussion

3.1 Composites Preparation

In order to find the adequate conditions for mixing SBS with CF, the temperature was changed from low to high values. The first evaluated temperature was 230 °C; however, at this temperature, the material degraded and adopted a brown color. Consequently, the temperature was reduced to a milder value at which the materials did not degrade. The selected temperatures were 90 and 130 °C, while the mixing speeds were fixed at 50 and 70 rpm. The conditions selected to prepare SBS-CF composites in this study were different to those reported by Mendez-Hernández [26], who used 185 °C and 100 rpm, with a mixing time of 20 min. Another difference is the CF

particle size; in the cited research CF cut by scissors was used and, therefore, its particle size was bigger than the CF used in this work, which presented a homogeneous particle size of 200 μm that may favor its dispersion in the polymer matrix in comparison to larger particles. Another important variation was the styrene content in the SBS copolymer.

The composite materials showed excellent processing properties during the mixing at low temperatures, a good consistence, and flexibility and uniform blends with homogeneous color which became darker according with CF content in composites. The particle distribution in the composites had a determining role in the physical characterization of the final material, particularly onits mechanical properties. CF main component, keratin, has a hydrophobic behavior which is responsible to have a good dispersion in elastomeric matrix, reflected in a better compatibility when ZnO is added to composites. This behavior has been reported previously [9].

Figure 4 shows the torque behavior for SBS (a), composites SBS-CF with 1 (b) and 5 phr (c) and SBS-CF 5 phr-ZnO (d), prepared at 90 °C, 50 rpm, and 20 min. The maximum torque value for SBS was around 90 N m at 2 min, then decreased and at 8 min increased until a value of 30 N m that further decreased until the end of experiment. When CF was added to SBS, the time to reach the maximum torque was around 4 min and torque value increased compared to SBS pure due the presence of CF particles, however, the stable torque value was reached before comparing with SBS, indicating that a homogeneous material was obtained. The torque behavior

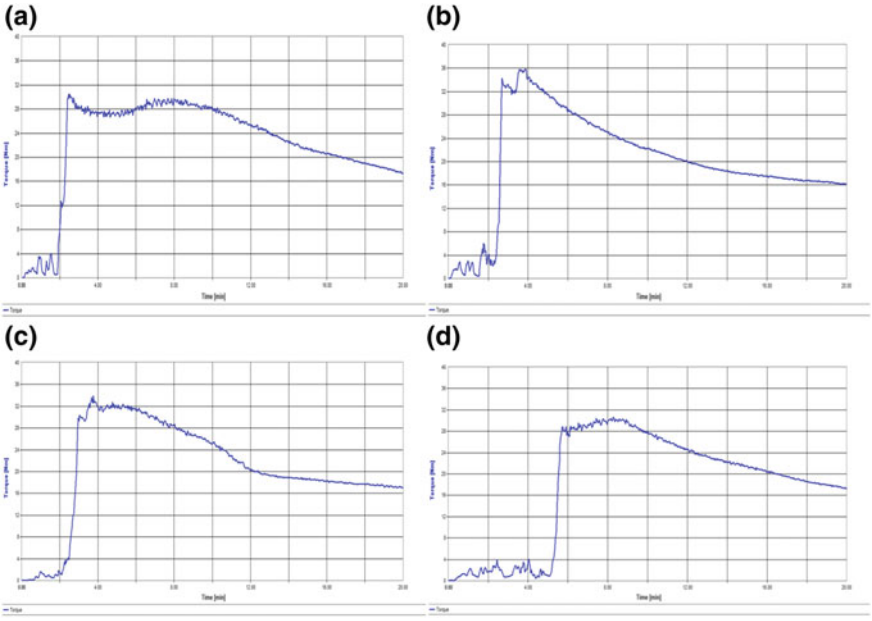

Fig. 4 Torque behavior for SBS (**a**), SBS-CF composites prepared with 1 phr (**b**), 5 phr (**c**) and 5 phr and ZnO (**d**) at 90 °C at 50 rpm and 20 min

for SBS-CF composite with ZnO (Fig. 4d) shows that maximum value has been reached at longer time compared with composites without ZnO, however, the torque at the end of experiment was quite similar for all materials, indicating that conditions for measurements were the adequate. The particle size played an important role in composites materials, and in most of cases, small particles improved the process ability of composites, which could be related with material´s properties as viscosity or melt flow index. There are reports that used CF in an irregular shape that improved the process ability and melt flow index in thermoplastic matrices [9, 38]. The addition of CF in SBR is favorable to reduce the viscosity and favors the crosslinking process reducing the vulcanization time [23].

3.2 Thermogravimetric Analysis (TGA)

The TGA analysis is a widely used technique for evaluating the thermal stability of a sample, which examines the final yielding, the composition, the processing and stability, as well as the decomposition behavior of materials.

Figure 5 shows thermograms of SBS-CF composites at different mixing speed and SBS and CF. The CF experiment showed two loss weight steps, first one around 100–220 °C, attributed to moisture loss and the second between 230 and 500 °C,

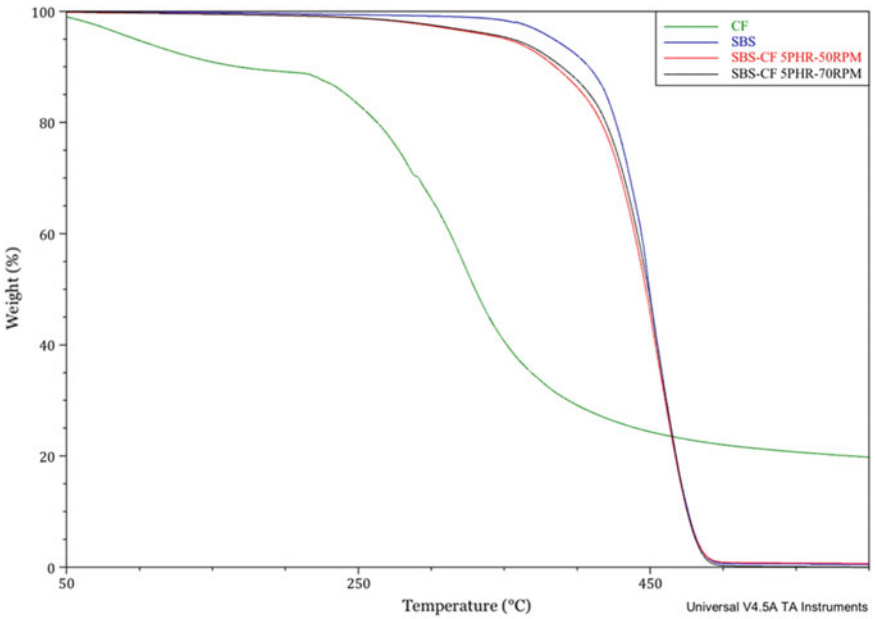

Fig. 5 Thermal curve TGA effect of preparation conditions of composites SBS-CF and CF

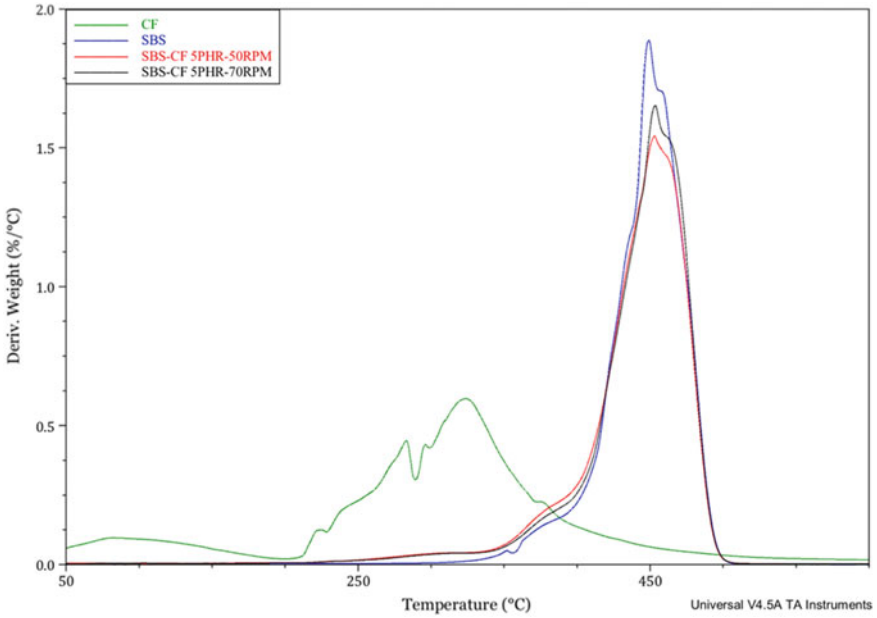

Fig. 6 DTA curve for SBS, SBS-CF composites prepared with 50 and 70 rpm speed mixing, 437 °C PS, PB 232

due the de-naturalization of proteins from keratin, mainly the β-protein structure (disulfide bonds and removal of H_2S), and rupture of C–C bonds from backbone. These values were higher to previous report under inert atmosphere [9, 15].

Figure 6 shows Differential Temperature Analysis (DTA) curves with the aim to identify in a better way the degradation steps in composites. It can be observed that CF shows a broad peak from 50 to 200 °C, attributed to water loss, which is important to identify if keratin, main component of CF, is within keratin as "free water" or if is "chemically bonded", the behavior that can contribute to the protein stability. Afterwards, the peaks around 290 °C and other at 310 °C were witnessed, which are attributed to breaking of disulfide bonds and H_2S elimination. The first peak attributed to denaturation of β-sheet of keratin, and the second one to pyrolysis of the chain linkages and skeletal degradation. This temperature can change depending on keratin source, Sánchez-Olivares et al. [16] report that main decomposition temperature of keratin from bovine skin hair is 304 °C, attributed to higher α keratin content, which is more stable than β keratin than keratin from CF.

The SBS copolymer shows one weight loss step starting around 350 °C, due to the rupture of the polymer backbone (Fig. 5). The SBS-CF composites have lower thermal stability compared to pure SBS; the composites present the weight loss on set close to 250 °C, and the decomposition is carried out in a single step. The SBS-CF composites prepared at 70 rpm are slightly more stable compared to the SBS-CF composite obtained at 50 rpm; also it is evident that SBS-CF composites are less

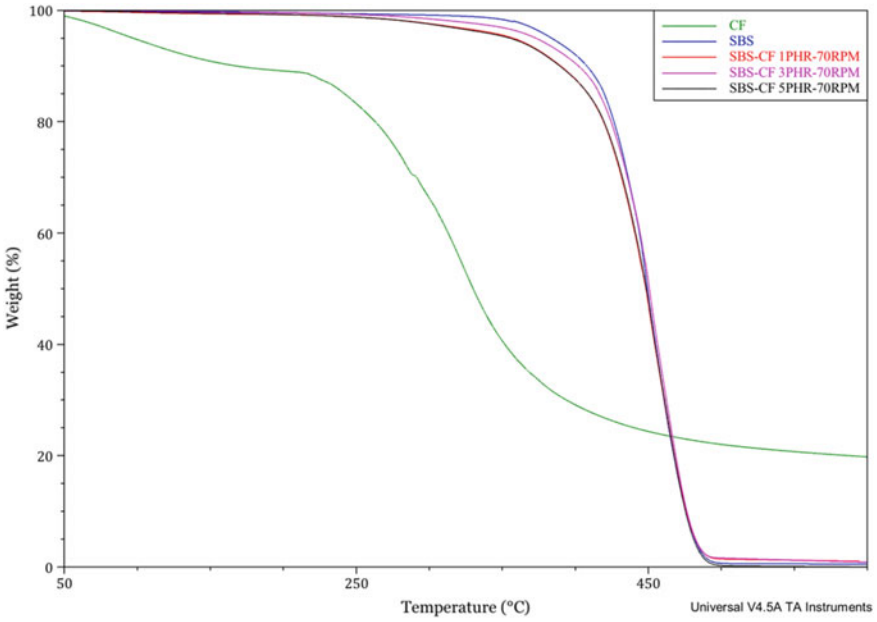

Fig. 7 Effect of CF amount in SBS-CF composite over thermal behavior (TGA)

thermal stable regarding pure SBS. To properly identify the decomposition behavior, DTA curves are presented in Fig. 6. It can be observed that SBS and SBS-CF have one weight loss step, with a peak around 448 °C, and a small shoulder around 458 °C. DTA curves show that the maximum peak of SBS diminish compared with SBS-CF composites, however, the peak that attributed to decomposition of composites displace slightly to lower temperature and the intensity of peak diminish indicative of a slower decomposition compared with pure SBS. These results are opposite to previous work that reported that elastomer-CF composites show a similar thermal stability comparted with an elastomeric matrix (Ntumba and Prochon 2016). The residue at the end of analysis is similar for SBS and SBS-CF composites, although not in a significant way, the mixing speed affects the thermal degradation of composites. An acceptable dispersion of CF in the polymer matrix acts as a barrier against the release of the gases generated from thermal degradation, and this provokes a delay in the composites decomposition [29].

The effect of the CF amount on the thermal behavior of SBS-CF composites (Fig. 7) shows that the thermal degradation of the composites is quite similar to that of pure SBS, and also, it shows that an increase from 1 to 3% of CF in the composite, produces an increasing at the beginning of the degradation temperature, but a CF content of 5% causes an opposite behavior. All the composites are thermally stable until 285 °C, and the compatibility between matrix and reinforcement plays an important role in thermal stability of composites, due to the miscibility of the keratin in the matrix.

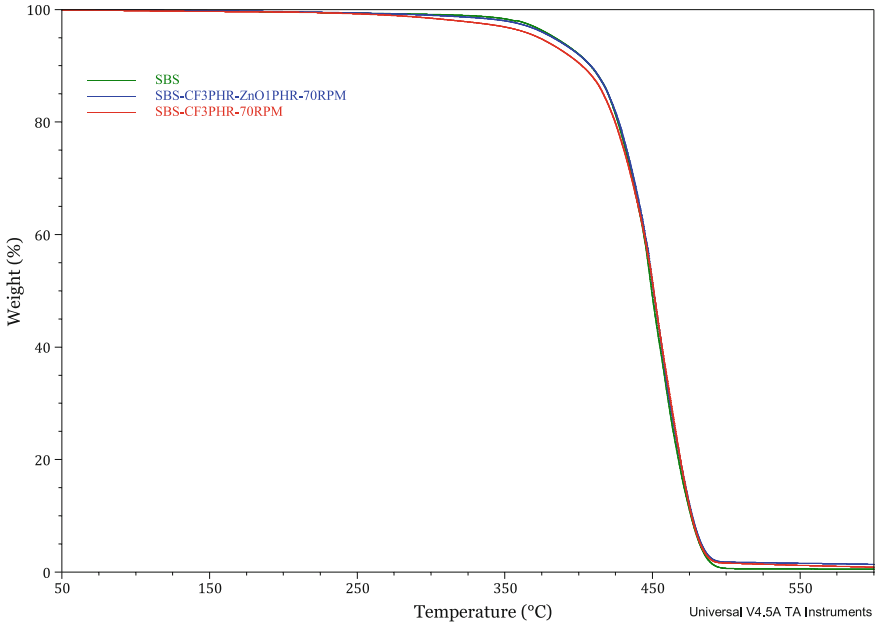

Fig. 8 Effect of addition of ZnO on TGA of SBS-CF composites

There are reports that chemical modification of CF can improve the thermal stability of composites with CF, increasing its behavior compared with styrene-butadiene elastomers [5, 30, 31]. The temperature decomposition for composites with CF can increase due to the miscibility of keratin with polymer matrix and affect the decomposition speed decomposition of matrix.

When ZnO was added to SBS-CF composites, the thermal stability increased slightly (Fig. 8) because of an induced enhancement in the compatibility between SBS and CF, and a similar behavior was noticed for pure SBS, which is an evidence for the advantage of using ZnO in comparison with the composites without ZnO. This behavior was reported earlier by Prochon et al. [23], who evaluated the effect of the addition of waste keratin to vulcanized SBR, and report a diminishing on the rate of thermo-oxidative decomposition of rubbers, at the time that affects the crosslinking process.

3.3 Dynamical Mechanical Analysis (DMA)

The viscoelastic behavior of SBS-CF composites was studied by means of DMA, which is a powerful technique that makes possible the identification of the reinforcement dispersion degree and its effect on the matrix modification. The storage

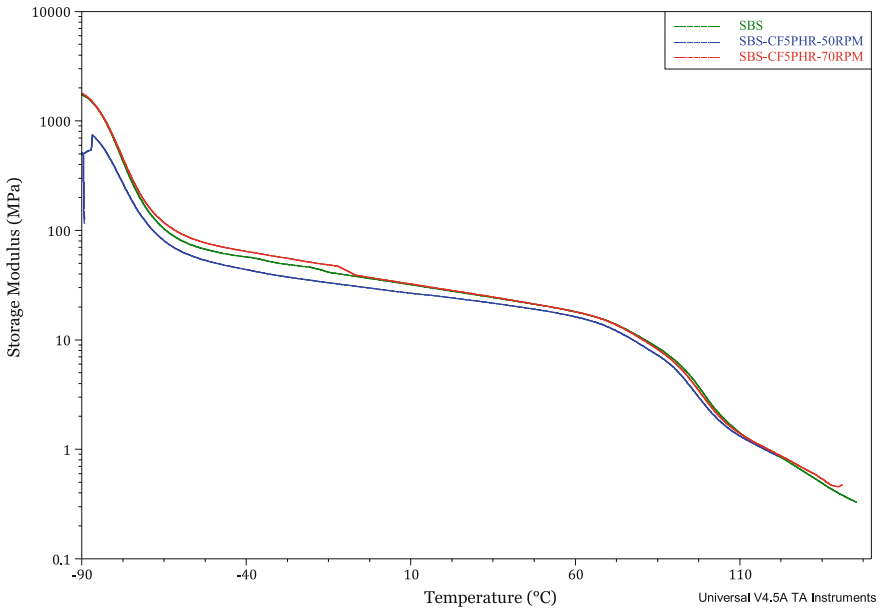

Fig. 9 DMA thermogram for SBS, SBS-CF 5 phr composites at 50 and 70 rpm mix speed

modulus measured through DMA provides information about the structural changes on the matrix backbone, and it allows to relate it to the molecular basis of the thermomechanical properties of the materials. The Tan δ can be related to the impact resistance, and it is also associated to dynamic percolating clusters in the region that is near to the glass transition. In addition, Tan δ peak decreasing indicates damping reduction.

The reinforcement level of the composite depends on the amount, shape, and particle size of the reinforcement agent. CFs has been used as reinforcement agents in several polymer matrices such as PMMA, PP, HDPE, PLA, PU, frequently in irregular shapes, or fibers. However, the use of a homogeneous particle size obtained by sieve has not been used that often. Some research works dealing with the addition of protein particles over synthetic elastomers and natural rubbers have been reported [22, 32].

Figure 9 shows the effect of the mixing speed on the storage modulus of SBS-CF composites and pure SBS. The SBS-CF composites prepared at 50 rpm shows the lowest storage modulus in the rubbery plateau region and above 100 °C, the modulus has a similar behavior to pure SBS. SBS-CF composites obtained at 70 rpm shows a higher storage modulus after the rubbery plateau, which implies that the higher the mixing speed, the better the reinforcement effect. A higher storage modulus indicates that the material stiffness is increasing, due to the free movement of the particles in the polymer backbone.

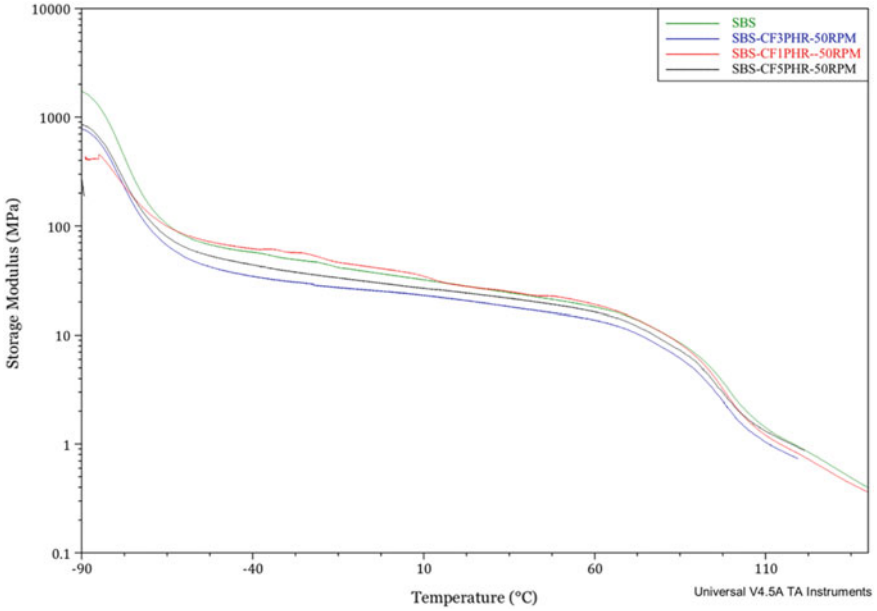

Fig. 10 Effect of CF amount in SBS-CF composites over storage modulus

Mendez-Hernández et al. [26] report that the increasing of CF amount in SBS-CF composites promotes the enlargement of storage modulus, and this improves the stiffness of elastomeric matrix. The difference between the storage modulus values and the previously reported was attributed to the use of CF particles cut into small pieces without homogeneous shape and size, which is quite different to our work. The theory indicates that a small and homogeneous particle size may result in a better dispersion of the particles in the polymer matrix. As previously stated, in this project, the CF particle size was 707 μm; furthermore, CF has lower stiffness compared to other materials such as fiberglass and natural fibers.

Figure 10 shows the storage modulus curves for SBS-CF composites with 1, 3, and 5 phr and pure SBS, when CF was added to SBS the modulus decrease for composites with 3 and 5 phr, and composite with 1 phr shows a similar behavior than pure SBS, indicating that the material stiffness decrease when CF content in composite increase.

Opposite results were reported for other polymer matrices. For instance, Jimenez Cervantes Amieva et al. [9], with PP, Villarreal-Lucio et al. [38] with PVC, Zhan and Wool [33], with fiberglass-CF composites, Özmen and Baba [15] with PLA-CF, and Pourjavaheri et al. [20], for TPU-CF fibers. In the case of this research, the presence of a two-block copolymer as the polymer matrix, one of them being the predominant phase, cause that one of the blocks is more affected than the other; in this case, the CF particles are more easily embedded within the PB structure than in the PS block,

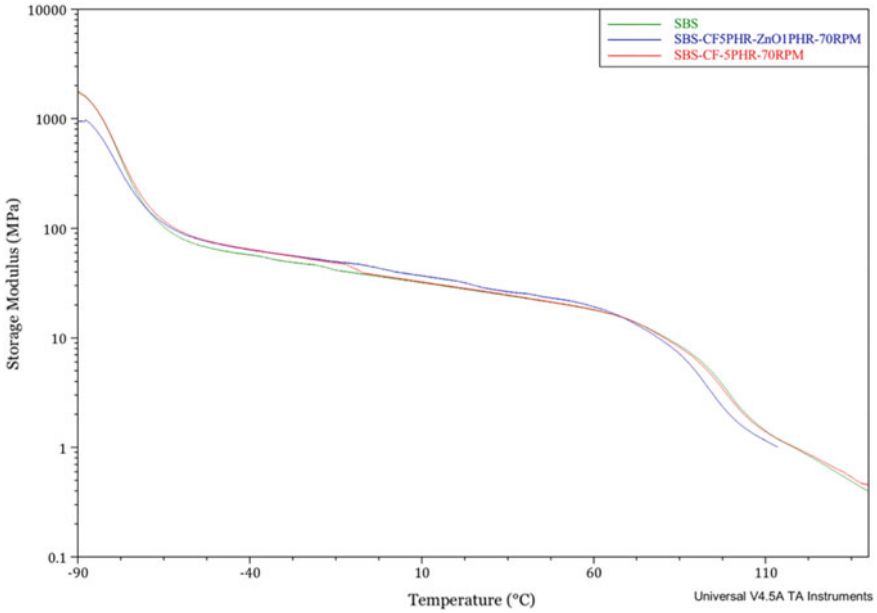

Fig. 11 Effect of addition of ZnO over storage modulus of SBS-CF composites

according to the storage modulus behavior. The same explanation can be inferred from the Tan δ behavior.

The effect of ZnO on the storage modulus can be observed in Fig. 11; the storage modulus curve for SBS-CF is also included for the preparation containing 5 phr with and without ZnO. The figure reveals that the composite without ZnO has a higher modulus at low temperatures and that this behavior prevails at high temperatures.

Figure 12 shows the Tan δ curves for SBS-CF composites with 5 phr and pure SBS. Tan δ damping represents the ratio between the loss and storage modulus and depends on the particle and matrix adhesion; therefore, Tan δ values can be related to the reinforcement dispersion level. It is evident that the elastomer shows the typical behavior for block copolymers with two peaks associated to a Tg for each copolymer block (at −75 °C for PB and 100 °C for PS). When CF particles were added to SBS, the maximum Tan δ peak decreased for both blocks PB and PS, which implies that the amount of stored potential energy is greater than the dissipated energy. This condition is a consequence of the restriction of the polymer chains mobility because of the presence of CF that hinders the movement of the matrix molecules [33]. The Tg value for each block did not show a significant change; however, a slightly decrease in Tan δ value was mainly observed for the PB block. A similar behavior was described by Cheng et al. [14] who added CF to a PLA matrix.

Méndez-Hernández et al. [26] reported no significant change in Tg value is determined using Tan δ signal in DMA in SBS-CF copolymers with different styrene

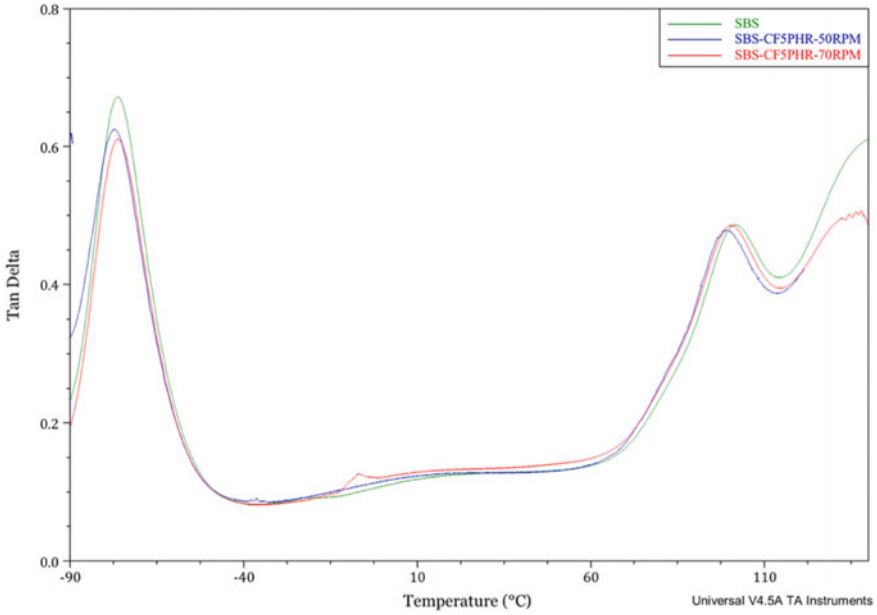

Fig. 12 Effect of mixing speed over Tan δ of SBS-CF composites with 5 phr

contents in SBS, and when styrene content was lower, the affectation over Tan δ value was more evident.

Figure 13 shows the effect of CF content in composites on Tan d, t can be seen that the greatest interaction between CF is with the blocks of PS (peak at 100 °C), due the maximum of the peak if higher than peak for pure SBS. For composites with higher CF content, a similar behavior is observed, and the maximum of peak for PB block is lower than peak of pure SBS, which can indicate that maximum interaction of CF with SBS is with PS block.

Figure 14 makes evident that the addition of ZnO affects the Tg value calculated through the Tan δ signal, with a Tg value of around −60 °C compared to pure SBS and SBS-CF composite with 5 phr. This is an obvious response to the presence of more particles in the polymer matrix that demand higher temperatures in order to increase the mobility of the polymer chains, thus CF can be considered as a promising material to improve the viscoelastic properties on composites.

Pourjavaheri et al. [20], reported that the value of Tg determined by DMA using Tan δ signal, decrease with the addition of CF fibers to TPU matrix, attributing this behavior to a poor bonding between filler and polymer matrix, which creates inefficient stress transfer, which means the molecules move easier and then Tg value diminish, which is contrary with results of this work.

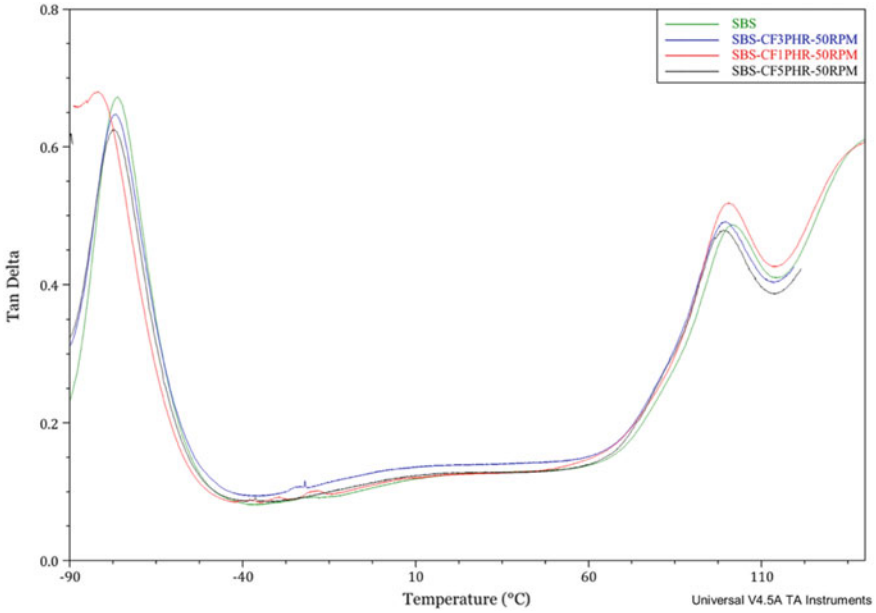

Fig. 13 Effect of CF content over Tan δ of SBS-CF composites

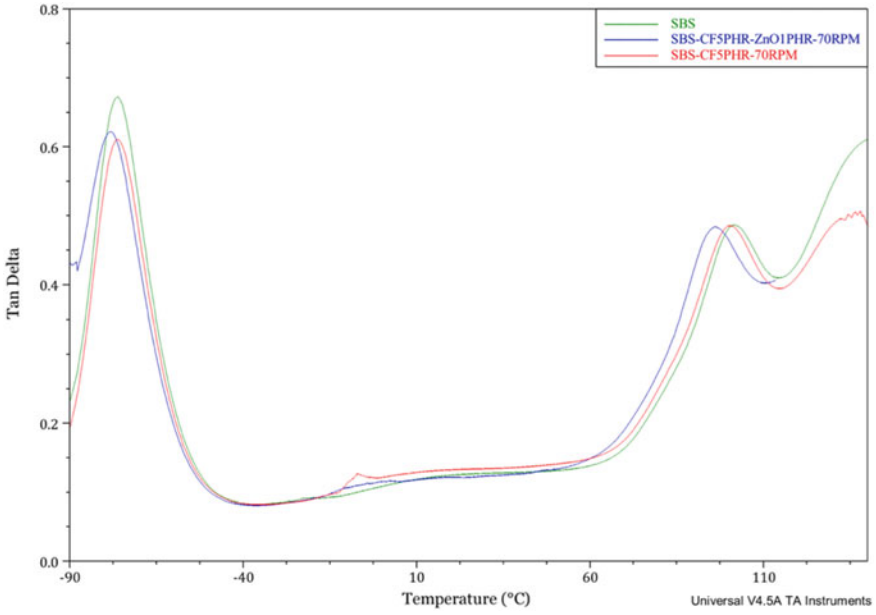

Fig. 14 Effect of ZnO over Tan δ of SBS-CF composites

3.4 X-Ray Diffraction (XRD)

X-ray diffraction is a technique used for identifying crystalline phases in solid materials. The crystallinity is related to the structural order in a solid. In a crystal, the atoms or molecules are disposed in a regular and periodic manner. Crystallinity makes the materials become stronger, but also brittle, while amorphous regions confer tenacity to the polymer.

The crystallinity of CF is crucial for understanding its physical, chemical, optical, and thermal properties. The CF is a macromolecular polymer with crystalline and amorphous regions. The crystalline CF fractions show a diffraction peak around $2\theta = 9°$ (α-helix) and a peak at $2\theta = 22°$. The XRD pattern for CF shows two characteristic peaks originated by two crystalline structures: α-helix and β-sheet.

Figure 15 shows the XRD patterns of SBS-CF with 1 and 5 phr composites. It can be observed that the composites present peaks in 2θ scale at: 9°, 20°, attributed to alpha and beta helix of keratin, the third one is due the crystalline content of keratin for both composites; however, the composites prepared with 5 phr of CF shows a small and broad peak around 42°, that can be related to the interplanar spacing of polymer matrix and the interfacial adhesion that can improve the compatibility between SBS matrix and CF particles [34]. Figure 16 presents the pattern for SBS-CF 5 phr composites with and without ZnO, the signals discussed previously at 9°, 19°, and 45° attributed to crystalline regions of CF particles, and others emerge, peaks at 34, 36, 37, 48, 57, and 65° are attributed to ZnO of hexagonal structure as reported in previous works [35, 36]. The peaks at 9° and 19° in 2θ scale, were reported previously by Oladele et al. [11], and also reported a peak around 45° attributed to crystalline regions for CF fibers. On the other hand, Belarmino et al. [3] report 3 signals for CF

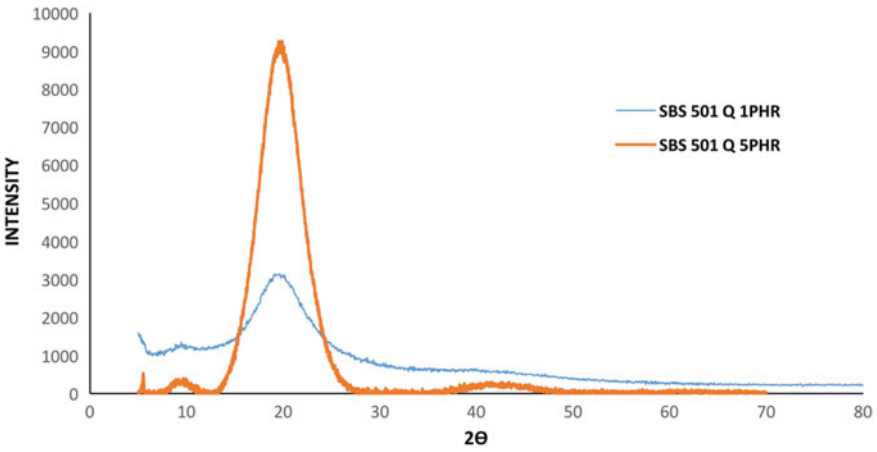

Fig. 15 XRD pattern for SBS-CF composites

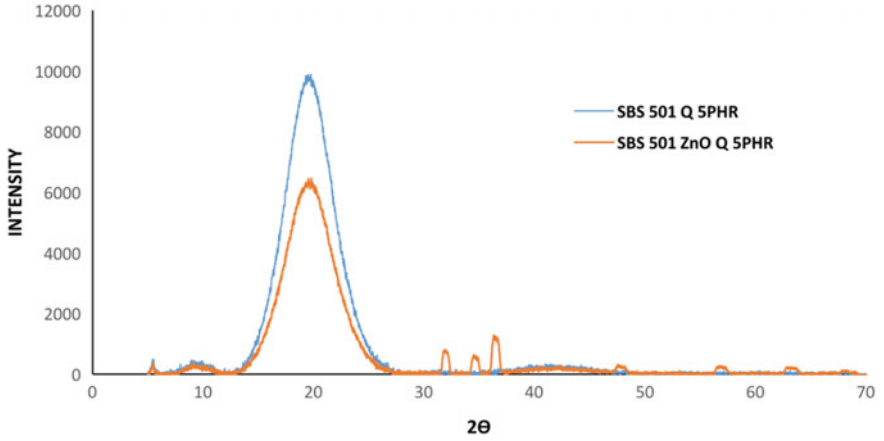

Fig. 16 XRD pattern for SBS-CF composites with ZnO

fibers around 38°, 64°, and 77°, which are not identified in our work, however, the difference is the particles shape due they use CF fibers.

3.5 Scanning Electron Microscopy (SEM)

Figure 17 shows SEM micrograph of SBS, SBS-CF 1 phr, 5 phr, and 5 phr-ZnO. It is observed that materials present a homogeneous, uniform surface with roughness on a micro level, attributed to a good dispersion of CF particles in the elastomeric matrix. The increasing of CF in composite did not generate changes in the composites morphology. These results are according to DMA in previous discussion, because a good compatibility between polymer matrix and CF particles is evident. In the figure, it is possible to identify the CF and ZnO particles in matrix.

Yazid et al. [12] reported that RHDPE/NR/CF composites presented high amount of holes attributed to detachment of keratin fibers on the surface. On the other hand, Ghani and Izzuddeen [37] studied the fracture surface of R-HDPE/NR/CF fibers identifying voids and fiber detachment due the poor adhesion between fibers and polymer matrix.

SEM micrographs indicate that matrix embed the particles when CF particles was added to elastomer, generating an improvement in mechanical properties due to a mechanical bonding between phases [24]. Other researches indicate that CF can be well dispersed if it is added in fibers to a polymer matrix such as PLA [16], PU [19, 20], PVC [38], and in SBS [26] acting as a mechanical reinforcement.

Jong [22] reported the presence of aggregates with globular structure and that protein particles added to an elastomeric matrix are embedded in matrix, this is due the particle size used in matrix.

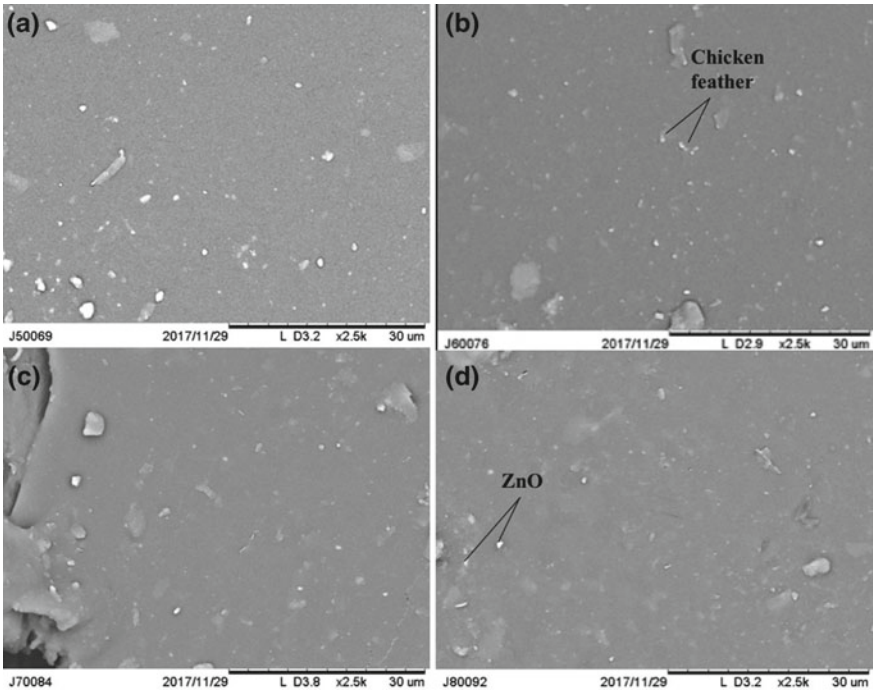

Fig. 17 SEM micrographs for SBS, SBS-CF with 1 and 5 phr and 5 phr and ZnO

4 Conclusion

According to the results discussed, preparing SBS-CF composites by means of a melt-mixing process is possible at low temperatures. After the evaluation of high temperatures (230 and 190 °C), the best conditions to obtain SBS-CF composites were set at 90 °C, 20 min, and two mixing speeds of 50 and 70 rpm. The operating conditions of the composites preparation proved to affect the SBS-CF final properties. Better thermal behavior was observed for the samples prepared at higher mixing speed. The CF amount has a negative effect on the thermal degradation behavior of SBS-CF, because degradation temperature decreased as the CF concentration augmented. The addition of CF caused a change in the viscoelastic properties of SBS-CF composites, as it was shown in Tan δ curves behavior. A diminish of Tan δ indicated that composites are more prone to store potential energy than to dissipate it. The addition of ZnO improves the viscoelastic behavior of the composites, but the Tg values were not affected. The XRD patterns allow to identify the main signal peaks attributed to keratin, and it also made possible to identify the hexagonal structure of ZnO when it was added to the composites. Finally, SEM micrographs suggest that homogeneous, uniform and rough surfaces were obtained.

Acknowledgments The authors wish to thank The National Council for Science and Technology of Mexico (CONACYT) for the support to IvánAlziri Estrada-Moreno (72016) through the Program of Cátedras-CONACYT (604). We also wish to thank the National Laboratory of Nanotechnology (Nanotech) for the facilities provided and to Karla Campos for its valuable collaboration during the present research.

References

1. muyinteresante.com/plumadepollo
2. Askeland D 3rd (ed) (1998) The science and engineering of materials. PWS Pub Co, Richmond
3. Belarmino DD, Ladchumananandasivam R, Belarmino LD, Pimental JRM, da Rocha BG, Galvao AO, Andrade SMB (2012) Physical and morphological structure of chicken feathers (keratin biofiber) in natural, chemically and thermally modified forms. Mater Sci Appl 3:887–893
4. Feughelman M (1994) A model for the mechanical properties of the α-keratin cortex. Text Res J 64:236–239
5. Reddy N, Hu C, Yan K, Yang Y (2011) Thermoplastic films from cyanoethylated chicken feathers. Mater Sci Eng C 31(8):1706–1710
6. Senoz E, Wool RP, McChalicher CW, Hong CK (2012) Physical and chemical changes in feather keratin during pyrolysis. Polym Degrad Stab 97(3):297–307
7. Khosa MA, Wu J, Ullah A (2013) Chemical modification, characterization and application of chicken feathers as novel bioabsorbents. R Soc Chem Adv 43:20800–20810
8. Huda S, Yang Y (2008) Composites from ground chicken quill and polypropylene. Compos Sci Technol 68:790–798
9. Jimenez Cervantes Amieva E, Velasco Santos C, Martínez Hernández AL, Rivera Armenta JL, Mendoza Martínez AM, Castaño VM (2015) Composites from chicken feathers quill and recycled polypropylene. J Compos Mater 49(3):275–283
10. Barone JR, Schmidt WF (2005) Polyethylene reinforced with keratin fibers obtained from chicken feathers. Comp Sci Technol 65:173–181
11. Oladele IO, Okoro AM, Omotoyinbo JA, Khoathane MC (2018) Evaluation of the mechanical properties of chemically modified chicken feather fibers reinforced high density polyethylene composites. J Taibah Univ Sci 12:56–63
12. Yazid MIM, Supri AG, Zainuddin F, Musa L (2013) Recycled high density polyethylene/natural rubber/chicken feather fibers (RHDPE/NR/CFF) composites: the effects of fiber loading and benzyl urea. Adv Mater Res 795:582–586
13. Martínez-Hernández AL, Santiago-Valtierra AL, Alvarez-Ponce MJ (2008) Chemical modification of keratin biofibers by graft polymerisation of methyl methacrylate using redox initiation. Mater Res Innov 12:184–191)
14. Cheng S, Lau KT, Liu T, Zhao Y, Lam PM, Yin Y (2009) Mechanical and thermal properties of chicken feather fiber/PLA green composites. Compos Part B Eng 40(7):650–654
15. Özmen U, Baba BO (2017) Thermal characterization of chicken feather/PLA biocomposites. J Thermal Anal Calorim 129:347–355
16. Sánchez-Olivares G, Sánchez-Solis A, Calderas F, Alongi J (2017) Keratin fibres derived from tannery industry wastes for flame retarded PLA composites. Polym Degrad Stab 140:42–54
17. Subramani T, Krishnan S, Ganesan SK, Nagarajan G (2014) Investigation of mechanical properties in polyester and phenyl-ester composites reinforced with chicken feather fiber. Int J Eng Res Appl 4:93–104
18. Mishra SC, Nayak NB (2010) An Investigation of dielectric properties of chicken feather reinforced epoxy matrix composite. J Reinf Plast Compos 29:2691–2697
19. Gokce O, Kasap M, Akpinar G, Ozkoc G (2017) Preparation, characterization, and in vitro evaluation of chicken feather fiber-thermoplastic polyurethane composites. J Appl Polym Sci 45338:1–9

20. Pourjavaheri F, Jones OAH, Mohaddes F, Sherkat F, Gupta A, Shanks RA (2016) Green plastics: utilizing chicken feather keratin in thermoplastic polyurethane composites to enhance thermomechanical properties. In: Society of Plastic Engineers annual technical conference (SPE-ANTEC), May 2016
21. Janowska G, Kucharsk-Jastrzabek A, Prochon M, Przepiorkowska A (2013) Thermal properties and combustibility of elastomer–protein composites. Part II, Composites NBR–keratin. J Therm Anal Calorim 113:933–938
22. Jong L (2006) Effect of soy protein concentrate in elastomer composites. Compos Part A Appl Sci Manuf 37:438–446
23. Prochon M, Janowska G, Przepiorkowska A, Kucharska-Jastrzabek A (2012) Thermal properties and combustibility of elastomer-protein composites. J Therm Anal Calorim 109:1563–1570
24. Sreenlvasan DP, Sujlth A, Rajesh C (2017) Cure, mechanical and swelling properties of biocomposites from chicken feather fiber and acrylonitrile butadiene rubber. J Polym Environ 1–10
25. Brebu M, Spiridon I (2011) Thermal degradation of keratin waste. J Anal Appl Pyrolysis 91(2):288–295
26. Méndez-Hernández ML, Salazar-Cruz BA, Rivera-Armenta JL, Estrada-Moreno IA, Chavez-Cinco MY (2018) Preparation and characterization of composites from copolymer styrene-butadiene and chicken feathers. Polimeros. Ciencia e Tecnologia (accepted to publish 2018)
27. Hill P, Brantley H, Van Dyke M (2010) Some properties of keratin biomaterials: kerateines. Biomaterials 31(4):585–593
28. Winandy JE, Muehl JH, Micales JA, Raina A, Schmidt W (2003) Potential of chicken feather fibre in wood MDF composites. Proc EcoComp 2003(20):1–6
29. Supri AG, Ismail H (2013) Recycled high density polyethylene/natural rubber/chicken feather fibers (RHDPE/NR/CFF) composites: the effect of fiber loading and benzyl urea. Polym Plast Tehcnol Eng 52:1316–1322
30. Prochoń M, Ntumba YHT (2015) Effects of biopolymer keratin waste sources in XNBR compounds. Rubber Chem Technol 88:258–275
31. Xiao-Chun Y, Fang-Ying L, Yu-Feng H, Wang Y, Rong-Min W (2013) Study on effective extraction of chicken feather keratins and their films for controlling drug release. Biomater Sci 1:528–536
32. Jong L (2015) Influence of protein hydrolysis on the mechanical properties of natural rubber composites reinforced with soy proteins particles. Ind Crops Prod 102–109
33. Zhan M, Wool RP (2016) Mechanical properties of composites with chicken feather and glass fibers. J Appl Polym Sci 133:1–15
34. Ghani SA, Ismail H, Azimi EA (2017) The effect of maleic anhydride on properties of recycled high density polyethylene/tyre dust/chicken feathers fibers (r-HDPE/TD/CFF) composites. Chiang mai J Sci 44:649–659
35. Díaz de León CL, Olivas-Armendariz I, Hernández Paz JF, Gómez-Esparza CD, Reyes-Blas H, Hernández-González M, Velasco-Santos C, Rivera-Armenta JL, Rodríguez-González CA (2017) Synthesis by sol-gel and cytotoxicity of zinc oxide nanoparticles using wasted alkaline batteries. Dig J Nanomater Biostruct 12:371–379
36. Salas G, Rosas N, Galeas S, Guerrero V, Debut A (2016) Synthesis de nanopartículas de ZnO por el método de Pechini. Revista Politécnica 38:1–5
37. Ghani SA, Izzuddeen M (2014) Tensile properties, swelling behavior, and morphology analysis of recycled high density polyethylene/natural rubber/chicken feather fibers (R-HDPE/NR/CFF) composites: the effect of caprolactam. Adv Mater Res 844:293–296
38. Villareal DS, Rivera JL, Rivas V, Diaz NP, Páramo U, Gallardo NV, Chávez MY (2017) Manufacturing of composites from chicken feathers and polyvinyl Chloride (PVC). Handb Compos Renew Mater 159–174

Perspective Composition Materials for Electrode-Tools Production

Nikita Ogleznev, Svetlana Oglezneva and Timur Ablyaz

Abstract This chapter reports the result of an experimental study to examine the physical, mechanical properties of electrode-tools made from copper-based composite materials with the addition of refractory metals, ceramic, graphite phases in the erosion of tool steel. Composite materials based on copper with different contents of the refractory phase were made by powder metallurgy. Electrodes' wear rate made from "copper–chromium" is lower than traditionally used compounds made from pure copper M1 and "copper–tungsten" material. Using methods of X-ray phase and Raman Effect, spectrum analysis investigated the formation of intercalated graphite with copper and sp^3 connections in graphite, sintered with copper. During the sintering of the "copper–titanium carbide" and "copper–titanium carbonitride" chemical interaction was not observed. However, in the copper–carbosilicate titanium system, dissociation of the compound was established such as de-siliconization from titanium carbosilicide grains, part of titanium carbosilicide grains was converted to carbon-based Titanium silicide Ti_5Si_3 (C) and small amounts of titanium carbide, silicon carbide, and titanium silicide $TiSi_2$. The lowest porosity (6%) was witnessed in materials containing titanium carbosilicide, regardless of its content. The flexural strength was 2 times higher in systems with titanium carbosilicide in comparison with carbide and titanium carbonitride. When investigating the relative wear of the electrode during the machining of tool steel, it was established that all the studied systems have better wear resistance than pure copper and copper–tungsten carbide material.

Keywords EDM · Electrode-tool · Composite material · Copper · Carbide Carbonitride · Titanium carbosilicide · Strength · Hardness · Electrical resistivity Erosion resistance

N. Ogleznev (✉) · S. Oglezneva · T. Ablyaz
Department of Materials, Technologies, and Design of Machines,
National Research Polytechnic University, Perm, Russia
e-mail: osa@pm.pstu.ac

S. S. Sidhu et al. (eds.), *Futuristic Composites*, Materials Horizons: From Nature to Nanomaterials, https://doi.org/10.1007/978-981-13-2417-8_16

Abbreviations

CNT	Carbon nanotubes
D	Interplanar distance (nm)
EDM	Electric discharge machining
ET	Electrode-tool
HB	Hardness (MPa)
I	Intensity (%)
P	Porosity (%)
R_a	Surface roughness (μm)
TEG	Thermally expanded graphite
σ_b	Flexural strength (MPa)

1 Introduction

Electrode-tools (ET) can be divided into two groups: a profile-volume electrode and noncore electrode wire [1]. When choosing electrode's material, it is necessary to take into consideration its erosive resistance, electric conductivity, workability (possibility to produce tools of required shape), price, resistance, corrosion resistance, lack of poisonous emissions under high temperatures during discharge [2, 3]. Construction of ET must be tough enough and resist mechanical and temperature deformations. Total deformation must not exceed 0.3% of basic dimension limits of the workpiece. Electrode's material [4–6] has a great influence on quality and productivity of the EDM process, and it has been chosen according to the qualities of processed material and requirements to the surface. The main materials for producing ET are carbon [1, 7–11], which is used nowadays for the rough working and for the finishing work, copper and its alloys and also composite materials on the basis of copper as shown in Table 1. Copper-based materials are the main part of the applied electrode materials whereas electrolyte copper M1 and M2 is used more often having high electrical and heat conductivity. Electrode's wear rate directly depends on the time of the process wherein borders are worn first of all.

Flat surface experiences maximum run out with increasing of broach deepness [1, 5–7, 10, 11]. Copper electrodes can contain small amounts of additives 0.3–0.7% Te, 1.8–2% Be, 0.5–0.9% Cr, 0.7–1% Cd, which make heat conductivity a little worse (except beryllium), but erosive resistance higher. There are different opinions about the wearability of copper-based electrode-tools, which were produced using the method of pressure molding and galvanoplastics. At one side, they have higher run out in comparison with ET made from rolled steel due to higher and irregular porosity, which is the reason of irregular run out of ET, however, it can be decreased using a so-called comb-like impulses, especially during finishing regimes [4, 7, 11]. Carbon and graphite ET are widely applied in EDM process due to their electro-conductivity and erosive resistance, low price, and good processibility. However,

Table 1 Specifications and fields of ET application

Material	Field of application
Carbon EEPG (Specs 48-20-29-77) MPG6, MPG7 (Specs 48-20-51-74)	Rough and semi-finishing of EDM process, die tooling, press forms and other shaped objects from steel, heatt-resistant and titanium alloys
Copper M1, M2 (GOST 859-78)	All types of EDM process (also in a regime with low wear rate) heat-resistant, tough and titanium alloys
Brass LS-59-1 (GOST 15337-70)	EDM process of through holes in details from steel of hard alloys; sizing details from hard alloys, cutting of workpieces
Aluminum alloy D-1 (GOST 4784-74)	Rough EDM process of molds for aluminum molding and other details from steel
Alloys on the zinc basis Zama K3, Zama K5	EDM process of through holes in details from steel of hard alloys; sizing details from hard alloys, cutting of workpieces
Tungsten BPH	Machining diameter less than 1 mm in steels
Molybdenum MPH	Machining diameter less than 1 mm in hot-resistant and hard alloys
Compositional material MNB-3 (Specs 063-52-78)	EDM process of hard alloys, during heighten criteria of resistance
Compositional material MBH-3 (Specs 215-13-84)	EDM process of hot resistance and titanium alloys
Composition copper–tungsten	EDM process of hard alloys of heat metals and alloys during heighten criteria of resistance

because of low mechanical resistance graphite ETs have limited use while machining holes with a small diameter and narrow gaps [5, 6, 11–15]. Another drawback of a graphite electrode is a tendency of extra carbon deposition while long-lasting short circuit and as a result cause damage to the instrument and the workpiece, especially when using coarse-grained graphite. Electrode wear rate while treating steel with copper electrodes directly depends on the time of machining [1, 7–11] and current intensity. There is another issue associated with the graphite electrodes; wear rate is increased until the definite point and then becomes stable (Fig. 1). Graphite's with copper infiltration (25–35% of copper) have higher electrical conductivity; it helps in increasing the current density as compared to graphite. Titanium alloy (Ti–6Al–4V) and copper–graphite electrodes (infiltrated) have the highest productivity rate in comparison to electrodes made from graphite, copper, aluminum, tungsten–copper, steel, and alloys (Fig. 2).

Graphite electrodes (EDM-3) characteristics were investigated in [20] with the density of 1.8 g/cm^3, copper–graphite (EDM-C3) with density 3.25 g/cm^3, produced by the method of powder metallurgy route (Poco Graphite Co, Ltd.). It was established that the graphite electrode has the highest productivity and better surface finish,

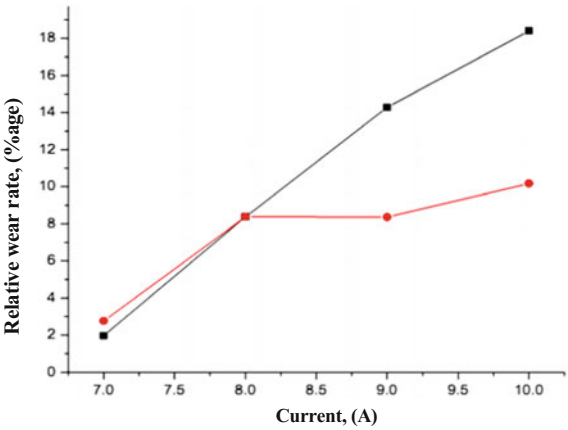

Fig. 1 Relative electrode's wear rate made from copper (filled square) and graphite (filled circle) while machining of steel

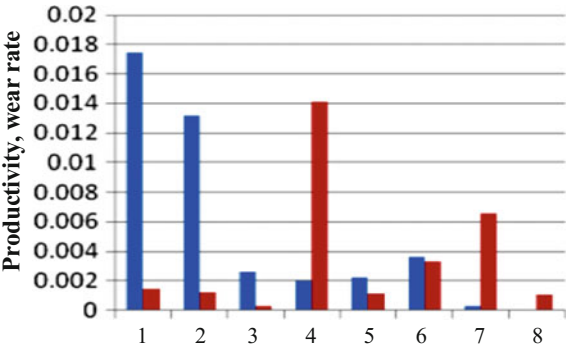

Fig. 2 Productivity (Blue bar, g/min) and wear rate (Red bar, g/min) electrodes while treating titanium alloy, 1 copper–graphite, 2 graphite, 3 copper, 4 copper–beryllium, 5 copper–tungsten, 6 brass, 7 aluminum, 8 steel EN24

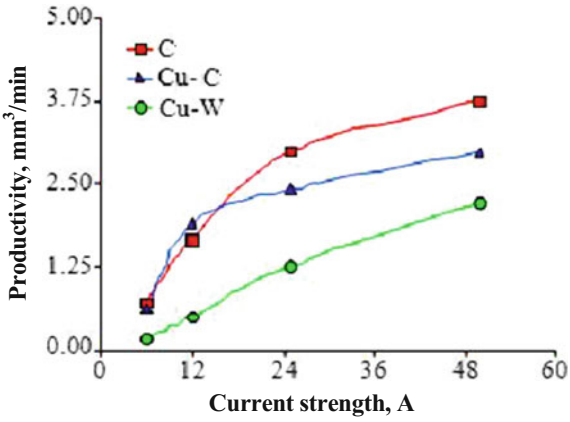

Fig. 3 Productivity of graphite electrodes, copper–graphite, and copper–tungsten while machining of hard alloy WC–Co

but it has a relative wear rate of graphite electrode in comparison with Poco EDM-C3 (copper–graphite) and copper–tungsten is shown in Fig. 3.

Furthermore, the electroconductivity of iron electrodes can be enhanced by increasing carbon content and creating the cell structure of graphite elements [4–7, 11].

The wear rate of the electrode tool can be decreased by using the materials, which have high erosive resistance. The erosive resistance of the materials for electrodes increasing in a way by using graphite, iron, brass, copper, tungsten, graphite materials [3, 7, 8, 12–15]. However, it is necessary taking into consideration the criteria of machining combinations. For instance, for machining stainless steel in various regimes, it is established that electrode-tool from molybdenum can be recommended while working with frequencies higher than 66 kHz, because rapid increase in wear rate of electrode-tool is happening at the same time with the decreasing of productivity (Fig. 4); copper electrode-tool has the highest wear rate on the frequency of 44 kHz, but at the same time it has high productivity; for every electrode-tool's material, excepting brass, an average machine's regime became optimal, as in frequency 66 kHz satisfied productivity of electrode tool is provided without significant changes in wear rate; Thus, due to the little wear rate and stable productivity for machining small holes it is desirable to use tungsten as a material for electrode-tool production.

Decreasing productivity can be connected with the difficulties of debris evacuation because the quantity of debris becomes higher with the increase of pulse energy.

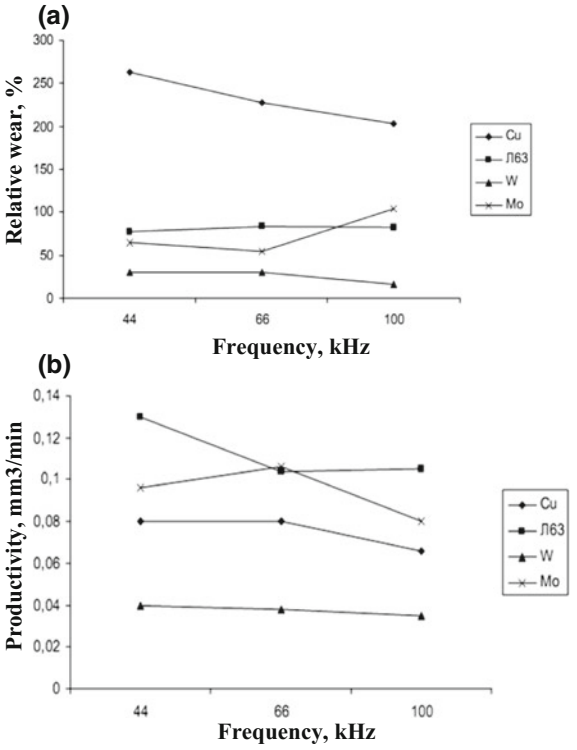

Fig. 4 **a** wears rate of electrode-tool and **b** productivity if machined stainless steel with different frequency and electrode-tools material

With the increasing of pulse energy, there is an opportunity for sintering of particles, thats why it is necessary to speed the removal process of by-products from the interelectrode gap.

2 Experimental Procedure

Powder of electrolytic copper PMS-1 (GOST 49-60-75), tungsten PV-0 (specs 48-19-101-84), chromium PH-1C (GOST 14-1-1474-75), molybdenum MPCH (specs 48-19-69-80) were used for the production of electrodes. Copper powder was mixed with chromium, tungsten and molybdenum powder in a stirred tank with the shifted spinning axis, samples were pressed and then these samples were annealed down in the vacuum oven and made second pressing, pressings were finally sintered down in the vacuum oven under the temperature of 1070 ± 10 °C, for 2 h.

In the second case, the electrodes were made using powder metallurgy from copper powder PMS-1 (GOST 49-60-75) and powder of refractory phases: carbothermic titanium carbide (specs 6-09-492-75), titanium carbonitride KNT-20-80 (specs MIHM-2009), VK-8 (8% cobalt and 92% tungsten carbide) (GOST 3882-74), titanium carbosilicide (synthesized by Institute KomiNC UrORANб using method of reaction sintering) [16]. Metals powder and refractory compounds were mixed in the stirred tank and then electrodes were pressed and further these samples were sintered in the vacuum oven with in-between repressing and finally sintered in the vacuum oven under the temperature of 1070 ± 10 °C, for 2 h.

In the third case, the electrolytic copper powder was used for producing electrodes from PMS-1 (GOST 49-60-75), tungsten PV-0 (specs 48-19-101-84), the compound of dry colloidal graphite C-1 (specs 113-08-48-63-90), expanded graphite produced by OAO "Novomet-Silur" and multilayered carbon nanotubes "Taunit MD".

Copper powder PMS-1 was mixed with powder graphite C-1, TRG, tungsten, were pressed, and then samples were let down in the vacuum oven under the temperature of 1070 ± 10 °C, for 2 h. Copper nanopowder PMVD-0 was mixed with (CNT) "Taunit MD", pressed in press forms under pressure 50–300 MPa, pressures were preliminarily restored in the atmosphere of dry up hydrogen under 380 °C and then sintered it in the vacuum under 1000 °C for 2 h.

The study of composite materials' microstructure after sintering was held on optical microscope "AXIOVERT 40 MAT" in zoom 50–500 and electronic scan microscope (TESCAN Vega 3 SEM), installed with energy dispersive spectrometer X-Max 50. The concentration of the carbon in composite materials was defined in accordance with GOST 12344-88 using the device (AUS-8144). The phase composition was investigated by X-ray phase analysis with the help of diffractometer (XRD-6000 Shimadzu) in Cu–Kα rays. Interpretations of diffractograms were made with the help of lookup tables [17]. Raman spectrum (spectrum of Raman effect) of the samples were made in multifunctional dispersive spectrometer of light Raman effect (Senterra). Length of excitation laser wave is 532 nm.

The testing of electrodes' properties were made during electro-erosive machining of steel sheet (H12F) with the depth 5.5 mm on the Electronica Smart CNC machine during rough working regimes E81 (impulse time 100 μs, pause 32 μs, current strength 15 A) and E93 (impulse duration time 150 μs, pause 32 μs, current strength 20 A). EDM oil—IPOL SEO 450 was used as the dielectric medium.

Relative electrode wear has defined the depth of the broached hole made in steel (material removal rate) to the linear wear rate of the electrode [15]. The density of materials was defined according to a standard method (GOST 18898-89). Electrical resistance was measured using the digital programmed milliohm meter GOM-802. The hardness of the sintered samples was measured with the help of Brinell tester according to GOST 9012-59. The three-point bending of the samples without split was used to measure strength using machine FP 10/1 according to GOST 18227-85.

Productivity was defined as the relation of working hours of the tool to the volume of produced material, mm^3/min. The roughness surface was measured using profilometer (Mahr Perthometer S2) according to GOST 2789-73.

3 Results and Discussion

3.1 The System "Copper and Refractory Metals"

The material's porosity has been increased with an increase in the concentration of refractory phase as there is lack of chemical influence during the process of sintering of copper with metal refractory phases [18] and the surface of metallic contact is reduced. Thus, increasing porosity reduces the strength of materials, as shown in Table 2.

Table 2 Physical and mechanical properties of the composite materials

System	Content of the refractory phase, (vol%)	Porosity after sintering, (%)	Flexural strength, (MPa)	Hardness, HB, (MPa)
Cu–Cr	25	4	400 ± 40	720 ± 30
	35	8	400 ± 40	710 ± 30
	50	7	400 ± 40	810 ± 30
Cu–Mo	25	11	110 ± 10	590 ± 20
	35	12	–	650 ± 20
	50	16	–	790 ± 30
	80	24	90 ± 20	850 ± 30
Cu–W	25	15	200 ± 20	340 ± 15
	35	11	120 ± 20	450 ± 20
	50	13	150 ± 30	510 ± 20
	80	22	50 ± 10	620 ± 20

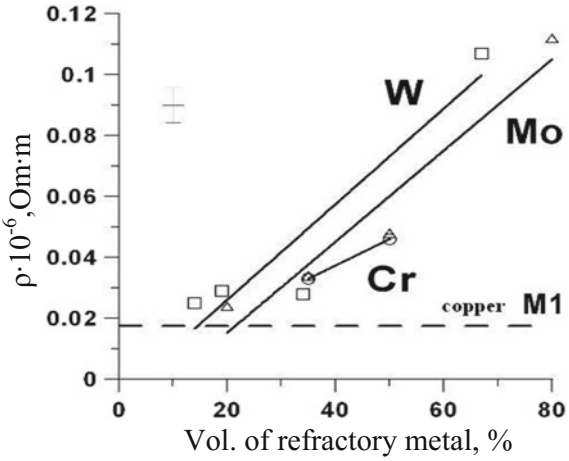

Fig. 5 Comparison of electrical resistivity of the composite materials: copper—refractory and electrolytic copper

Table 3 Regimes EDM process

	Regime E81	Regime E92
Voltage, B	50	50
Current strength, A	15	20
Pulse ratio	1.32	1.82
Frequency, Hz	10	6.67

It was observed that the lowest strength is reported in the systems, containing molybdenum and tungsten because they don't interact with copper or lack of intermetallic phase. Slight solvability of the chromium in copper (approx. 1%) provides formation of the durable inter-particle contact [18], thus demonstrated higher density and strength.

While increasing the additives quantity (chromium, tungsten, and molybdenum) leads to the growth of porosity thus increases of electrical resistivity (electrical resistibility of chromium, molybdenum, tungsten is accordingly 1.3×10^{-7}, 5.2×10^{-8}, and 5.5×10^{-8} Ωm) [19] (Fig. 5).

Relative wear of the electrode from pure copper while machining (machining) in regimes E81 and E92. The process parameters of regimes are given in Table 3. Figure 6a, b, shows the relative wear of the electrodes. The lowest figures for wear rate were in the systems "copper–chromium" and "copper–tungsten".

The relative wear of the systems, containing molybdenum was the highest; probably because of its oxidation (molybdenum oxide appears under 600 °C and can vaporize [20]). Unlike molybdenum, the interaction of chromium and oxygen is very active and further quickly slows due to appearing of oxide membrane on the metal surface, which is being destroyed under 1200 °C [16]. While making investigations about ET wear rate in different regimes, the electrode of Cu–Cr system had demonstrated high wear resistance rate during both regimes (E81 and E92). The relative wear is shown in Fig. 6 and Table 4.

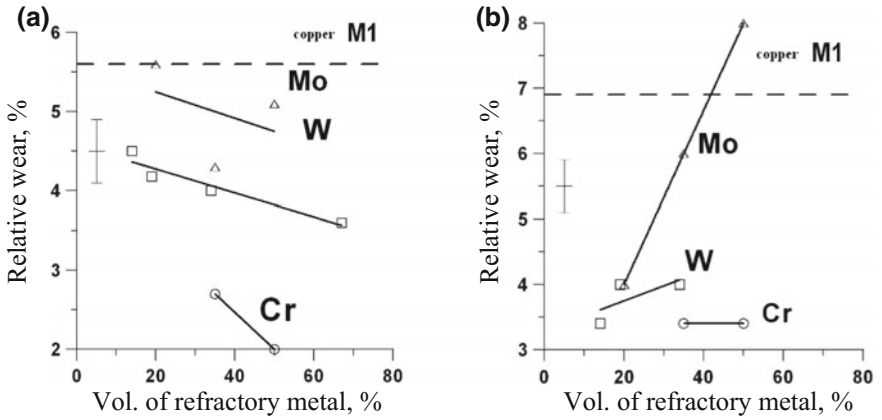

Fig. 6 Electrode relative wear of copper–refractory metal **a** during regime E81 **b** during regime E92

Table 4 Electrodes' productivity on the basis of copper while machining (machining) steel H12F

Refractory phase	Quantity of refractory phases, (vol%)	Relative ET wear rate, (%)		Productivity, (mm^3/min)	
		Regime E81	Regime E92	Regime E81	Regime E92
Cr	35	2.7	3.4	27.6	36.2
	50	2.0	3.4	26.1	33.5
W	25	3.6	3.4	15.6	63.18
	35	4.1	4.0	38.1	42.8
	50	4.0	4.0	33.6	36.6
	80	3.6	–	–	–
Mo	25	5.6	4.0	27.6	43.5
	35	4.3	5.9	34.8	29.3
	50	5.1	8.0	10	11.3
M1 without additives	0	5.6	6.9	34.7	49.7

Taking into the consideration of high erosive resistance of the electrodes. These electrodes provide the higher precision of the process, and have a good complex-shaped machining utilization properties.

3.2 *The Systems "Copper and Carbide, Carbonitride, Titanium Carbosilicide"*

The composite materials which contain a mixture of electrically conductive and refractory phases are the most preferable components in terms of electro-erosive resistance properties. During the melting process in these systems, liquid metal alloy stays in the capillary of sponge system of the refractory structure with the help of Laplace surface tension force. Refractory phase enhances the mechanical strength and the low melting phase in the system (Cu) has to wet out refractory phase. However, the refractory and low melting phases do not have to interact with each other at the boundaries [21]. While crystallization of composite material, low melting phase (Cu) crystallizes on the surface of the refractory phase. The presence of electroconductive qualities which refractory phase increases the operating properties of the composite materials for electrode-tools.

Data from X-ray phase analysis showed that composite materials, containing carbide or titanium carbonitride, the copper matrix demonstrates lack of interaction in the systems during sintering. It was noted that composite material of copper with titanium carbosilicide contains copper phases, titanium carbosilicide (Ti_3SiC_2), titanium silicides (Ti_5Si_3) and ($TiSi_2$), titanium and silicium carbides TiC and SiC, accordingly. These facts do not contradict data [21–25], which reported the partial decomposition of titanium carbosilicide. In the structure of sintered composite materials, a copper matrix and ceramic refractory particles are represented in Fig. 7. After sintering the carbide and titanium carbonitride, hasn't changed, however, the presence of carbon in materials decreased up to 5% in comparison with origin in materials which contain titanium carbosilicide, Table 5. Micro-hardness practically did not depend on the quantity of refractory additive in sintered composite materials (Table 5). This is due to the fact that there is the lack of interaction (inter-metallic compounds) between copper and ceramic particles. Micro-hardness of the copper-containing titanium carbide has been increased while decreasing of titanium carbide concentration, Table 5. Micro-hardness of the copper-containing titanium carbosilicide was significantly higher than in pseudo alloy with carbide and titanium carbonitride, but it did not depend on the concentration of the titanium carbosilicide.

There was enhanced micro-hardness of material containing carbosilicide particles concentration. The porosity of sintered composite materials has increased with the growth of refractory particles concentration because the quantity of metal contacts while sintering has been decreased. That's why systems containing tungsten and titanium carbides, titanium carbonitride which do not interact with copper have rather high porosity [26], and the lowest porosity was in materials containing titanium carbosilicide, which have physical and chemical interaction, Table 6.

In accordance with the rule of additives of composite materials', increasing in the ceramic phase content, possessing high electrical resistivity and porosity, Fig. 8.

It was observed that the electrical resistance was lower in materials with tungsten and titanium carbide, and also titanium carbonitride as compared to the materials containing titanium carbosilicide. In systems where there is the chemical interaction

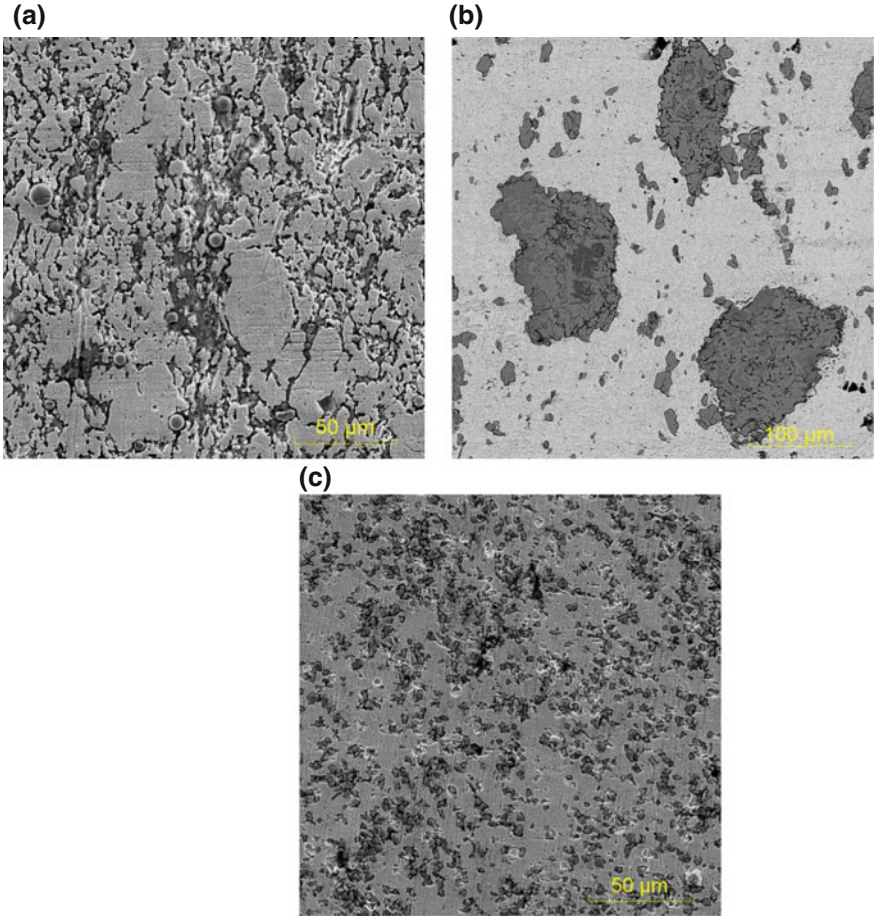

Fig. 7 Microstructure of sintered powder composite materials on the basis of copper, containing 37.5 vol%, **a** titanium carbonitride **b** titanium carbosilicide **c** titanium carbide

of ceramic particles of titanium carbosilicide with copper, the formation of solid liquids and nonconductive phases also had an influence on the electrical resistance of the composite material, and it fits the data in [27, 28]. As shown in Table 6, the hardness of sintered composite materials has increased proportionally to the density and concentration of refractory and solid ceramic particles, especially in case of material containing titanium carbosilicide and tungsten carbide. This is due to the fact that systems "copper–tungsten carbide" and "copper–titanium carbosilicide" has the formation of solid liquids and infiltrations [25, 26, 29, 30], moreover, the flexural strength of these materials was the highest, (please refer Table 6). On the other hand, the systems of copper and carbide or titanium carbonitride had not possessed interphase formation [26]. Thus, there were high porosity and low flexural strength,

Table 5 Carbon content and micro-hardness of composite materials after sintering

Concentration of refractory phase, (vol%)	Carbon concentration, (mass%)	Micro-hardness, HV, (MPa)
12.5 TiCN	1.02	970 ± 50
25 TiCN	2.15	940 ± 40
37.5 TiCN		940 ± 40
12.5 Ti_3SiC_2	0.67	1070 ± 50 (copper) 4870 ± 100 (Ti_3SiC_2)
37.5 Ti_3SiC_2	2.4	1070 ± 40 (copper) 5850 ± 100 (Ti_3SiC_2)
12.5 TiC	1.25	1340 ± 55
25 TiC	2.6	1110 ± 50
37.5 TiC	4.35	1010 ± 40

Table 6 Physical and mechanical properties of composite materials

Concentration of refractory phase, (vol%)	Porosity after sintering, (%)	Hardness, HB, (MPa)	Flexural strength, (MPa)
12.5 TiC	6	590 ± 20	150 ± 30
25 TiC	8	650 ± 20	150 ± 30
37.5 TiC	14	650 ± 20	160 ± 30
12.5 Ti_3SiC_2	3	620 ± 20	250 ± 20
37.5 Ti_3SiC_2	6	750 ± 30	300 ± 30
12.5 TiCN	12	650 ± 20	–
25 TiCN	13	790 ± 30	150 ± 30
37.5 TiCN	14	–	110 ± 10
12.5 WC	11		–
25 WC	13	770 ± 40	250 ± 20
37.5 WC	22	880 ± 60	300 ± 30

(Table 6). Relative wear of developed electrode from composite material is lower in comparison with the relative wear of electrode-tool from pure copper M1, in both regimes of machining as shown in Fig. 9a, b.

However, tendencies of ET wear during both regimes are the same, but according to absolute value, wear rate is higher during regime E92. Electrodes' wear decreased in the system of copper–tungsten carbide with increasing tungsten carbide concentration in copper matrix from 12.5 to 25% on both regimes of EDM process (Fig. 9). The composite materials containing small amounts of titanium carbide and carbonitride particles (12.5 vol%), relative wear of ET was twice lower than in pure copper, it is connected with the centers of crystallization of liquid copper on the ceramic particles. It is noted that the electrode tool containing Ti_3SiC_2 have good utilization properties, during both regimes of testing. Relative wear of these compounds was lower than in ET from copper, especially during regime E81, Fig. 9. The improvement of tool

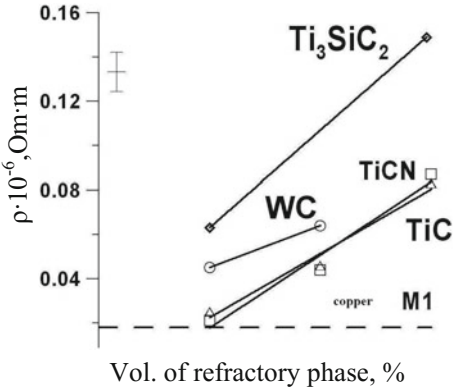

Fig. 8 Electrical resistivity of composite materials, containing titanium carbosilicide, titanium carbonitride, tungsten carbide

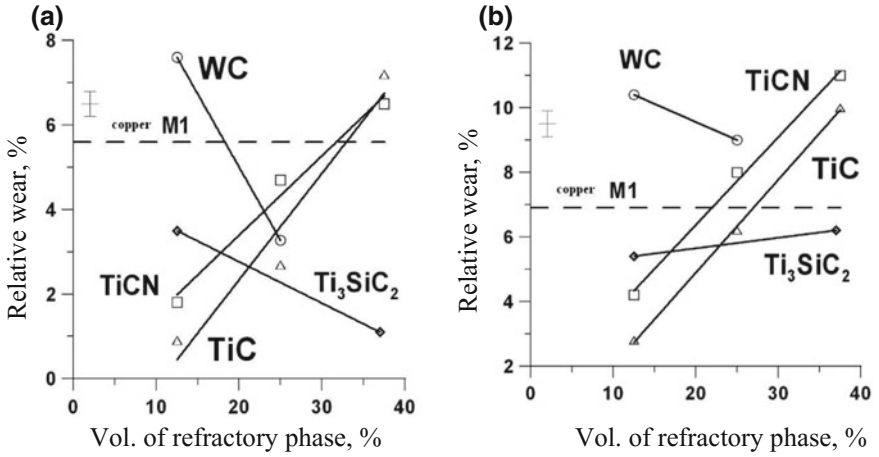

Fig. 9 Relative wear of electrodes of "copper–titanium compounds" depending on refractory phase content, **a** regime E81, **b** regime E92

properties was due to low electrode's porosity and banded nanostructure of titanium carbosilicide which act as capillaries for holding melted copper. Besides this, lower wear rate may be connected with the high conductivity of the carbosilicide during the EDM process. The productivity of ET treatment with titanium carbosilicide was significantly lower than pure copper. The productivity of ET containing low concentrations of ceramic refractory particles was matched with the productivity from pure copper (compounds with titanium carbide and carbonitride) (Please refer to Table 7). The precision of machining and finished surface while machining steel H12F using regime E81 was worse during EDM process with the copper electrode, however,

Table 7 Precision of treatment, surface finish, electrodes' productivity on the basis of copper and during electro-erosive machining of steel H12F

Quantity of refractory additive to copper, (vol%)	R_a, (μm)	Productivity, (mm^3/min)	
		E81	E92
12.5 TiC	12	45	37.7
25 TiC	Not defined	33	Not defined
37.5 TiC	Not defined	11	12.3
12.5 TiCN	16.5	32	48
25 TiCN	15.5	28	14
37.5 TiCN	11.5	12	10
12 Ti_3 SiC_2	Not defined	18	11
25 Ti_3 SiC_2	5	Not defined	Not defined
37.5 Ti_3 SiC_2		6	8
12.5 WC	15	Not defined	Not defined
25 WC	11.5	Not defined	Not defined
No additives	14	34.7	49.7

Table 8 Productivity and relative wear of electrodes during erosive machining of alloy BT5

Electrodes composition	Productivity, (mm^3/min)	Relative wear, (%)
Cu + 12.5% TiC	1.8	66
Copper M1	1.5	100

higher precision was reached in compounds with titanium carbonitride and titanium carbosilicide, (Table 7).

The highest surface finish R_a of the hole was obtained after using the electrode tool, containing titanium carbosilicide, (Table 8). It is known that precision of treatment directly depends on the wearability of electrodes; ET compounds containing titanium carbosilicide have suitable operating properties. In another case, electrode systems "copper–titanium carbide" were tested during machining (machining) of titanium alloy (BT5) is shown in Table 8.

3.3 The Systems "Copper–Carbonic Phases"

Despite the number of developed composite materials with improved properties, still, copper and graphite are the basic materials used for machining. Production of copper–graphite materials is considered to be a difficult task, because copper doesn't interact with graphite chemically [31]. Due to the variety of carbonic structures nowadays there is a necessity of investigating their structure, properties, and applications for producing different functional materials. Colloidal graphite is pro-

duced by grinding of natural or artificial flaked graphite up to the size of less than 4 nm and then treated with sulphuric or hydrogen acid for formation of graphite oxides [32]. As a result of chemical treatment, graphite intercalates appear, containing molecules or acid ions between graphene layers [33]. Thermally expanded graphite can be produced by the treatment of natural or artificial graphite in sulphuric acid which formed intercalated residuals of compounds [33]. Multilayer cylindrical carbonic nanotubes (CNT) "Taunit MD" were produced using CVD method on the catalyzator Fe/Co/Mg/Al. In the volume of synthesized material separate nanotubes are situated parallel to each other and make a bank of tubes [34, 35]. The structure of the sintered materials system "copper–carbonic phases" consists of a copper, sponges and dispersive particles of carbonic phases. The particles of carbonic phases are uniformly dispersed in the copper phase, as shown in Fig. 10. The flaked colloid

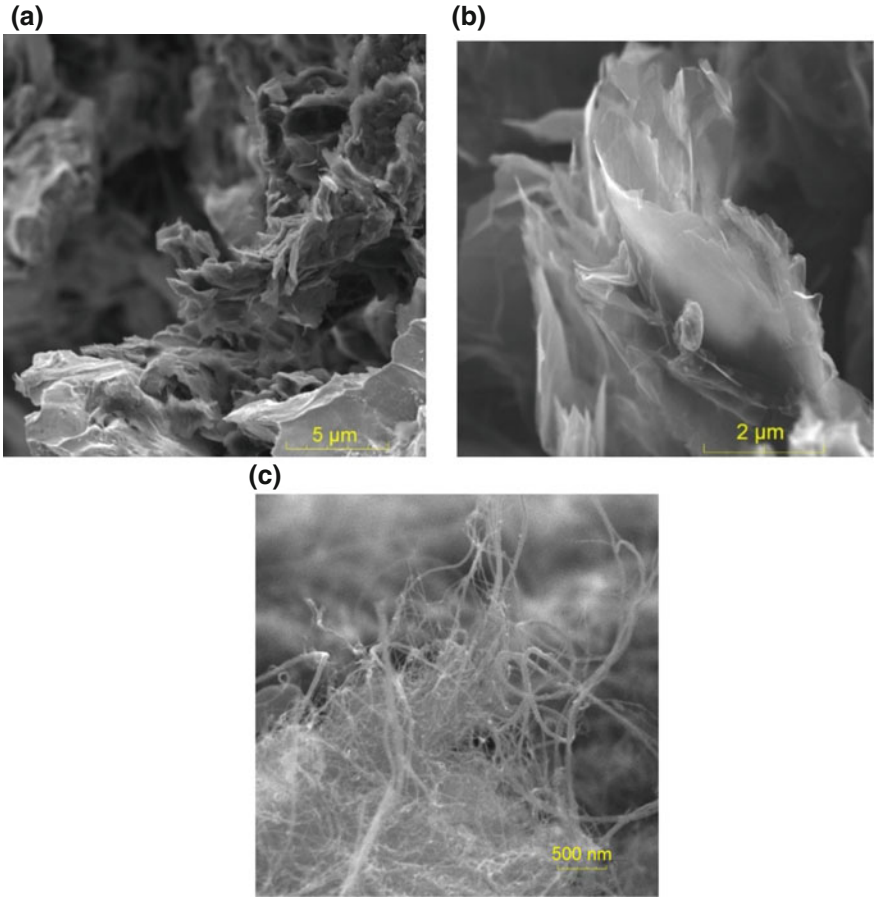

Fig. 10 Fractogramms of sintered materials **a** copper–colloid graphite **b** copper–thermal expanded graphite **c** copper–carbonic nanotubes

graphite are seen in the materials containing graphite, (Fig. 10a). And you can see the flakes of thermally expanded graphite with well defined "curly" graphene surfaces, (Fig. 10b).

Carbon threads retain its initial form and size are well seen in Fig. 10c. Diffractogram of colloid graphite powder C-1 shows reflexes which are related to the graphite and carbon silicide, which can be impurities of natural graphite, the base material for C-1, Fig. 11a, Table 9. Interplanar spacing of sintered powder (copper—20 vol% graphite C-1) is shown in Table 10.

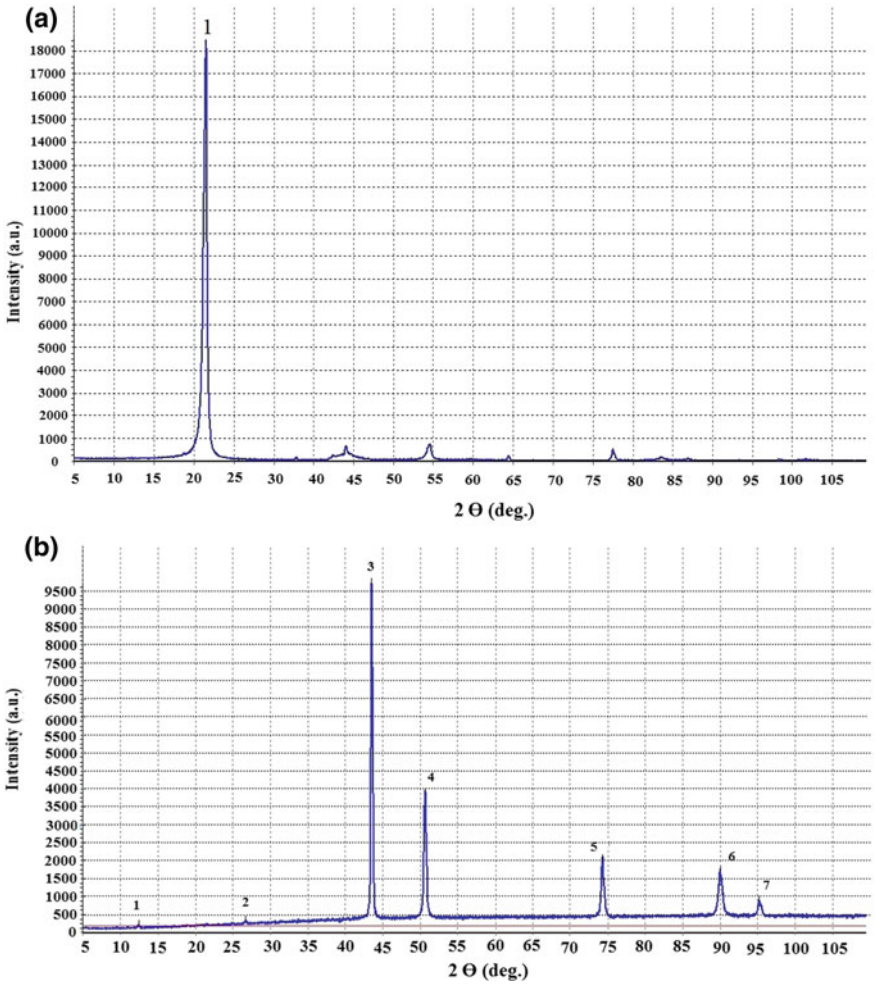

Fig. 11 Diffractograms of **a** graphite's powder C-1 **b** and sintered powder material (copper—20 vol% graphite C-1)

Table 9 Interplanar spaces in the powder colloid graphite C-1

№	Graphite's reflexes C-1			Graphite's reflexes			SiC reflexes	
	2θ, (°)	d, (Å)	Density, (%)	d, (Å)	Density, (%)	Indices of plane hkl	d, (Å)	Density, (%)
1	26.46	3.37	100.000	3.3700	100	002		
2	37.80	2.38	0.862				2.3970	15
3	42.40	2.13	1.246	2.1320	2	100		
4	44.02	2.06	3.514				2.0550	100
5	44.62	2.03	1.653	2.0360	3	101		
6	54.54	1.68	3.965	1.6820	8	004		
7	59.86	1.55	0.379	1.5410	2	103		
8	64.38	1.45	1.104				1.4460	41
9	77.46	1.23	2.663	1.2320	6	110	1.2320	18
10	83.60	1.16	0.763	1.1550	6	112		
11	86.86	1.12	0.357	1.1200	2	006		
12	98.26	1.02	0.434				1.0180	7
13	101.80	0.99	0.291	0.988				

Table 10 Interplanar spaces of sintered powder (copper—20 vol% graphite C-1)

Reflex	2θ	d, (nm)		Intensively relatively, (%)
		Graphite	Copper	
1	12.40	7.14		0.450
2	26.70	3.34		1.558
3	43.50		2.08	100.000
4	50.62		1.80	38.835
5	74.30		1.28	19.517
6	90.00		1.09	16.138
7	95.20		1.04	7.374

Standard diffractogram was made using Cu–Kα rays scan and the speed 2 grad/min, Fig. 11b shows the presence of the most intensive graphite in the system of Cu—20 vol% colloid graphite. A weak line of graphite at an angle $2\theta = 12.4°$ is also identified. It can be identified as a reflex 001 from derated graphite's lattice.

While surveying at a pitch of 0.02°, weak reflexes are confidently identified and it corresponds to line 001 of the graphite, Fig. 12a and also line $2\theta = 25°$, Fig. 12b which corresponds to the split line 002 together with the line $2\theta = 26.5°$.

Also, the line at $2\theta = 29.4$, which is absent in diffractogram of the base graphite. Authors [36] have established the formation of intercalated compounds of graphite and melted copper, as a result, there is a corrugating of graphene surfaces with the formation of sp^3 connections (app. 5%), Taking into consideration the method of graphite preliminary treatment with acids and high pressure of copper vapor, the

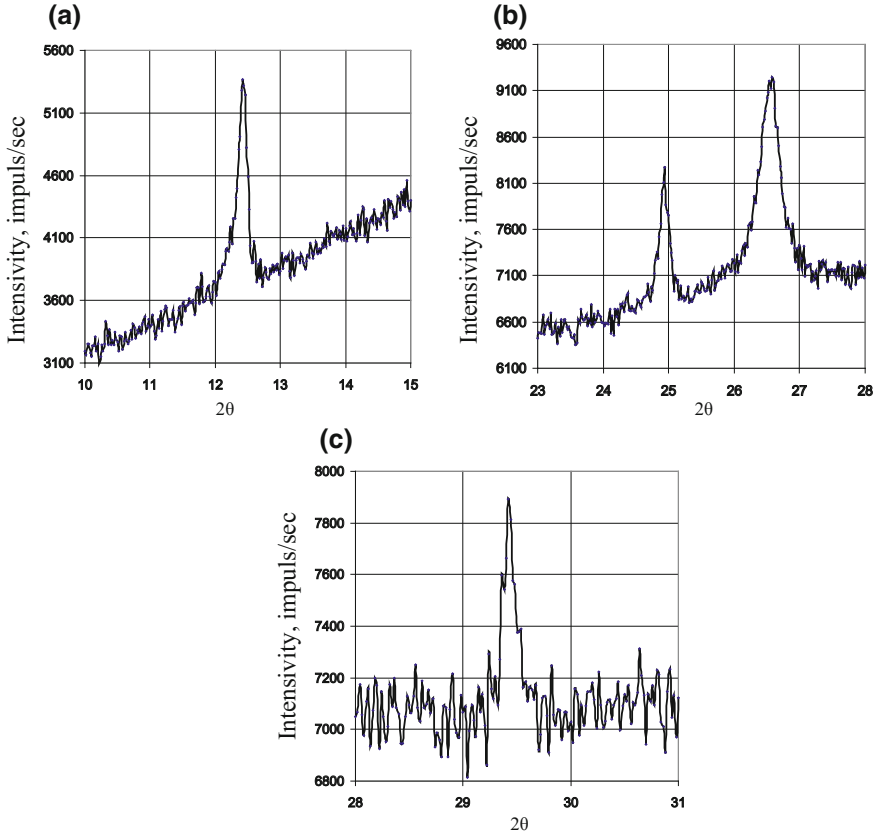

Fig. 12 Diffractogram of sintered material (copper—20 vol% colloid graphite) in the intervals 2θ (Cu–Kα), **a** 10°–15° **b** 23°–28° **c** 28°–31°

formation of intercalated compounds with copper under pre-melting temperature is probably possible. Moreover, there were no formation characteristics of sp^3 connections as evident from X-ray phase analysis while surveying with a low speed in the base colloid graphite.

Table 11 shows the interplanar spacing of thermally expanded graphite powder and composite powder (copper—20 vol% TEG).

Diffractogram of sintered material "copper–5 mass% TEG" is similar to diffractogram obtained for the colloid graphite in many ways in terms of structure and methods of obtaining similarity, Table 12, however technology of obtaining TEG depicted distractions in the crystal makeup of graphite and many reflexes were not found or displaced. The intercalated compounds of oxidized graphite are non-stable and are easily eliminated from interlayer space [37–40]. The peaks were found in spectrums of Raman effect investigated carbonic materials; they are typical for carbonic phases *G*, *D*1, 288, 860, and 2450 s m^{-1} [41, 42], (Please refer Fig. 13 and

Table 11 Interplanar spacing of thermally expanded graphite (TEG) powder and composite powder (copper—20 vol% TEG)

	Thermally expanded graphite		Copper—20 vol% TEG		*hkl*
1	*d*, (nm)	Intensity, (a.u.)	*d*, (nm)	Intensity, (a.u.)	
2	0.3572	100	0.3380	20.10	002
3	0.21094	9.30	0.20963	33.63 (Total intensity with copper reflex)	100
4	0.16798	4.71	0.16132	11.72 (Peak split)	004
5	0.112	1.98	Not found		006

Table 12 Spectrums of Raman effect of carbonic forms' powders and sintered composite materials "copper-carbon", (s m^{-1})

Material	*G*	2*D*	*D*1	*D*2	*D*4	*i*TA	*D*3	LA	*G**	oTO	IFM$^-$
Graphite C-1	1580_6	2682_{weak}	1352_4	–	–	265_6	1510_{weak}	–	2438_2	863_3	675_1
Copper–5 mass% graphite C-1	1582_6	2682_1	1349_8	1620_2	1233_2	284_6	1510_{weak}	–	2429_2	885_5	653_2
TEG	1581_{10}	2691_1	1351_6	–	1212	290	1510	–	2449_3	856_5	759_2
Copper–5 mass% TEG	1582_7	2700	1360_6	1620	1218_1	268_2	1516_1	496_2	2440_3	864_5	665
Taunit	1582_5	2688_2	1348_6	–	1206_1	267_5	–	485_1	2439_1	855_4	656_2
Copper–0.1 mass% Taunit	1588_2	–	1332_2	–	1206_1	274_5	–	–	2446_2	874_5	674_1

Table 12). Strong lines *G* and *D*1 are in spectrums of colloid graphite samples C-1 (base and sintered with copper), identifying sp^2 connections, the very weak peak 2D, pointing out on disorder along graphite axis *c* [41]. Peak 2D in both cases is not clearly asymmetric and has little intensity, as a result, there is strong ordering in structure [41], both spectrums have weak peaks 3D, peculiar to nanocarbon and showing the presence of interlayer space [41]. Peaks *G* and *D*1 are becoming wider in the structure of graphite, sintered with copper, that proves graphite's disorder. "Arm" *D*2 appears on the peak *G*, the so-called "defect's arm", which shows the defects together with the peak *D*1 on the edges and inside the graphene surfaces. Moreover, weak peak *D*4 is appearing, which shows the presence of sp^3 connections. The low intensity of reflexes is connected with the small concentration of graphite in copper and probably with the small number of corrugated surfaces. The relations between peaks' intensities *D*1/*G* in graphite after sintering with copper is increasing, that's why it is possible to make a conclusion about decreasing of crystal sizes.

TEG spectrum and TEG sintered with copper practically have no differences. There are no peaks of "defect arm" in the basic TEG spectrum; it shows the lack of disorder inside the graphene surfaces. There is reflex *D*4 which shows the presence of sp^3 connections which is due to the TEG producing (oxidation by functional groups)

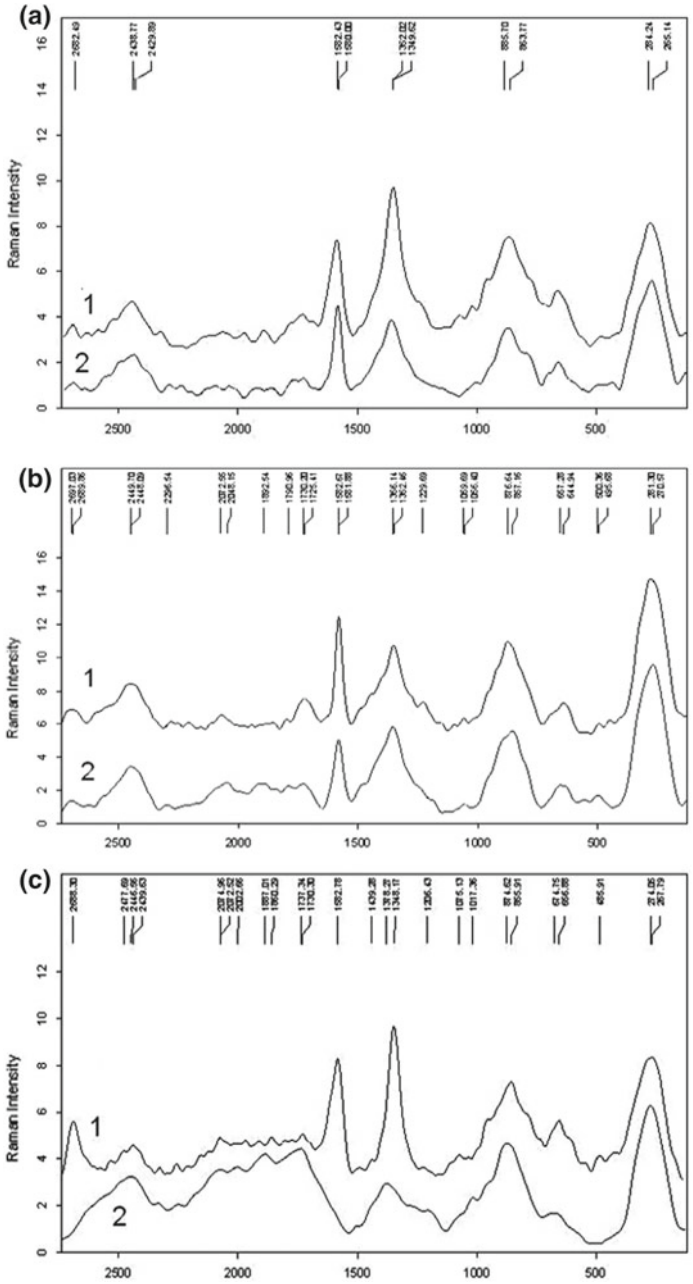

Fig. 13 Raman effect spectrums, **a** sintered material "copper—20 vol% colloid graphite C-1 (1) and graphite's powder C-1 (2) **b** powder of thermally expanded graphite (1) and sintered material "copper—20 vol% thermal expanded graphite (2) **c** spectrums (Taunit MD) (1) and sintered material "copper—2 vol% Taunit (2)

[33, 40], there is no peak of amorphous carbon. There is a disorder in graphene surfaces and the weak peak of amorphous carbon in spectrum TEG sintered with copper; the intensity of line *D*1 becomes higher than of line *G*. The reflex *D*4 shows the presence of sp^3 connections and corrugated surfaces.

Peaks *G*, 2*D*, *D*1, *D*4 are in Raman effect spectrums of taunite, which are typical for carbonic structures. Peaks *G* and *D*1 are not very wide as a result it is possible to define the structure. Small peak *D*4 shows the presence of sp^3 connections, which are formed by atoms on the closed semispherical ends of the CNT (carbon nanotube) and possible defects in forms of 5 and 7 atoms' rings on the graphene surfaces. Peak with wave number 485 s m^{-1} shows the presence of amorphous phase in CNT content. The relation of peaks *G*/*D*1 intensity is less than 2, which is the sign of multiwall CNT [43]. The intensity of *D*4 peak, responsible for sp^3 connections, does not decrease, after sintering with copper in taunite's spectrum. The relation of peaks' *G*/*D*1 intensity is less than 2, which shows saved multiwall CNT after sintering [43]. However, peaks' *G* and *D*1 intensity are significantly decreased after sintering and peaks become very wide, as a result, defects' "arm" *D*2 and was impossible to identify clearly. Besides, the spectrum had new lines at 1726 and 1399 s m^{-1}, it shows the formation of oxygen-containing groups. Investigations of CNT established that [44], oxygen connections appear at first at the ends of CNT, that's why peak *D*4 saving is possible and it is connected with the fact that new defects appear on the graphene surfaces. The significant decreasing of intensity and widening of peak G and also crossover of some peaks in the interval of wave numbers 1600–1800 s m^{-1} are similar to the spectrums of disordered graphene after bombardment by argon ions [42]; this result might be the consequence of defects' formation inside graphene layers of CNT. Thus, the signs of forming intercalated of copper compounds and graphite were found in the colloid graphite after the sintering process. The possibility of intrusion of copper ions without melting into interlayer spaces of graphite is explained by preliminary chemical treatment of graphite and the process of intercalates formation can be presented as residual in graphene layers, and are eliminating while refactoring in the vapor phase, copper ions get into extended interlayer spaces of graphite, The process of intercalating is similar to the process of catalytic synthesis of diamond which establishing special electrons' configurations between ions of catalytic metal and graphite. However, it was considered that pure copper cannot be a catalytic metal for diamond synthesizing [45, 46]. The role of acid residuals has been increased in interlayer graphite's space because strong delocalization of graphite electrons can cause only metals traps for metal cations. The deformation of graphene layers during the intercalating process and after formation of diamond, connections is proved by Raman effect spectrums, which are responsible for defects inside and on the edges of graphene surfaces.

Metal ions which have not left the interlayer spaces of graphite after sintering, affect the conducting properties of composite material "copper–graphite": the electrical conductivity of copper–graphite material does not decrease in comparison with pure non-sponge copper or high residual porosity structure.

Intercalating of CNT by copper was developed while mixing of CNT with copper acetates hydrate in infrared rays up to 400 °C [34]. While doing this the possible

Table 13 Electrical resistivity of sintered composite materials on the copper base

Additive	Quantity, (vol%)	ρ, (Om m)
C-1	0.4	0.013
	4	0.021
	20	0.044
TEG	0.4	0.015
	4	0.018
CNT	0.8	0.021
	2.4	0.017

process was called solid-phase reaction of copper salt restoration with carbon on the surface of CNT. Visually intercalates were found with the help of translucidus electronic microscopic images from inside and on the edges of CNT. Adding graphite to copper made better electrical conductivity of composite materials, it is due to the low electrical resistance of graphite and probably intercalating graphite with copper, Table 13.

There was a slight increase of electrical resistivity while increasing of colloid graphite volume up to 20%, probably it was connected with the formation of additional porosity during decreasing of metal contact while sintering, worsening conductivity properties in comparison with pure copper. The electrical resistivity of "copper–CNT" while CNT varies from 0.8 and 2.4 vol% became low 0.021 and 0.017 Ωm, due to the presence of porosity. The improvement of conductive properties by intercalated metals in carbonic structures has already being used for development of electro-technical materials [47].

Relative wear of electrode from pure copper while machining on E81 and E92 regimes are 5.6 and 6.9%, respectively. Figure 14a, b, represents the relative wear rate of electrodes. As a comparison, there is data depicted that relative wear of electrode of composite materials (copper–tungsten), are significantly lower than copper. The improvement of operating properties in the systems "copper–carbonic phases" was achieved due to the low electrical resistivity of composite materials even in high porosity (up to 13%). This enhancement of properties is due to the formation of the three-dimensioned net form phase as well as the presence of smaller size cells (capillary effect). The relative wear of ET from the sintered powder of pure copper was 15 times higher than in composite materials "copper–graphite", Fig. 14a, b.

The electrodes' relative wear for 0.8 and 2.4 vol% of CNT was 2.9 and 8.5% during E81 regime, respectively, and during E92 regime material wear with 0.8 vol% of CNT was 9.4%. Higher material wear rate is due to higher material porosity and on the other hand low wear rate is probably due to capillary effect. The processes of composite materials structure open new possibilities for creating materials for electrode-tools with improved properties using the method of powder metallurgy.

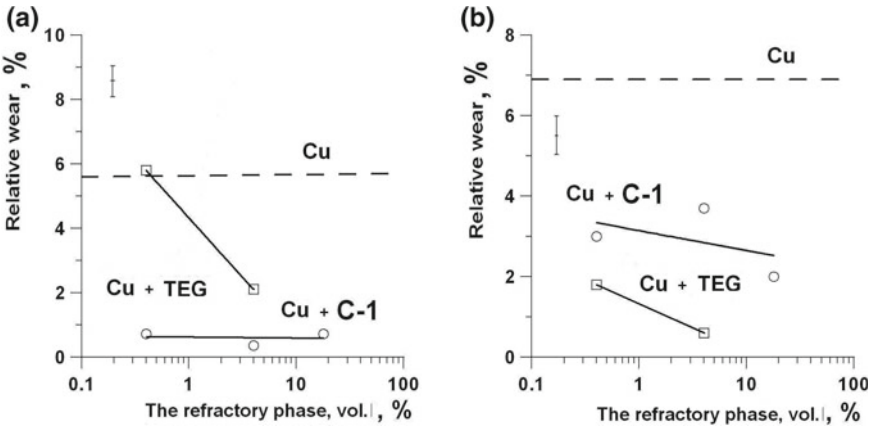

Fig. 14 Electrode wear from refractory phase content in the systems of copper–chromium, copper–tungsten, copper–molybdenum, copper–graphite during EDM of steel **a** during regime E81 **b** during regime E92

4 Conclusions

Strength and hardness were recorded to be 1.2 times higher in systems containing copper with chromium additives and "copper–tungsten or molybdenum". The electrical resistivity of "copper–chromium" was 1.5 times lower than in the systems with tungsten and copper. While investigating relative electrode tool wear rate during machining of tool steel on the rough working regimes, it was established that the best wear resistibility has the systems of Cu–Cr due to the chemical interaction with copper and much higher refractory resistance of chromium. Electrodes wear rate reported from "copper–chromium" is lower than traditionally used compounds made from pure copper M1 and "copper–tungsten" material. Using chromium instead of tungsten or molybdenum as a refractory additive to the electrode-tools material of copper is advantageous because of the higher wear resistivity and significantly lower price.

There is no chemical interaction between phases while sintering of the systems of "copper–titanium carbide" and "copper–titanium carbonitride". Porosity was the lowest in the system of "copper–titanium carbosilicide" due to chemical interaction with copper. The strength was 2 times higher in systems with titanium carbosilicide in comparison with carbide and titanium carbonitride. It was established that the systems with the copper base containing titanium carbide, titanium carbonitride and titanium carbosilicide have better wearability during machining of instrumental steel on rough working regimes than pure copper and material "copper–tungsten carbide". Using methods of X-ray phase and Raman Effect spectrum analysis was investigated the formation of intercalated graphite with copper and sp^3 connections in graphite phase sintered with copper. Sintered materials "copper–carbonic phases" have an electrical resistivity is in the level of copper, probably because of intercalated

structures formation. While machining tool steel on rough working regimes it was established that erosive wear rate of the electrode-tools system such as “copper—colloid graphite” 8–15 times lower than copper and system of “copper–tungsten”. Based on high electrical conductivity and capillary properties of intercalated structures, the increase of electrode-tools wear resistance of “copper–carbonic phases” was suggested.

References

1. Serebrenitsky PP (2007) Modern erosion technologies and equipment: training, allowance. Baltimore State Technologies University. St. Petersburg, Russia
2. Panov DO, Ablyaz TR, Abrosimova AA (2013) Metallographic analysis of the surface of 65G steel after electro erosion treatment. Mod Probl Sci Educ [Electron Resour] (5):232. Access mode: http://www.science-education.ru/pdf/2013/5/232.pdf. Version from the screen
3. Nemilov EF (1983) Electroerosive processing of materials: a textbook for vocational school. Machine building, Leningrad. Department, Leningrad, Russia
4. Matvienko EV, Varaksin MA, Blinov TA (2011) Influence of electrode tool material on the choice of erosion control modes. Sb. doc. In: International scientific-practical conference of students, graduate students and young scientists “Youth and scientific and technological progress”. Part 1, Gubkin: OOO Aikyu, Moscow, pp 134–137
5. Bates CH (2004) Effect on the performance of the electrode material electroerosion machining. Am Machinist 148(2):56–57
6. Dubois D (2002) Copper or graphite—the choice of materials for electrodes duplicating machine tools machining (2002). TraMetal (66):57–58
7. Zhurin AV (2005) Methods for calculating process parameters and tool electrodes for electroerosion processing. Abstract of Ph.D. dissertation, Tula state. University, Tula, Russia
8. Eliseev YuS, Saushkin BP (2010) Electroerosive processing of aerospace products. Izd-vo MSTU him NE, Bauman, Moscow, Russia
9. Kovalenko VS (2000) Non-traditional methods of processing materials in Japan. Electron Mater Process (3):4–12
10. Zolotykh BN (2003) On the discovery and development of electroerosive material processing. Electron Process Mater (3):4–9
11. Nemilov EF (1983) Electroerosive processing of materials: a textbook for vocational schools. Machine building, Leningrad department-e, Leningrad, Russia
12. Zolotykh BN (1956) Influence of duration of a working impulse on electric erosion of metals. Electricity (8):19–31
13. Sijanov SY (2002) Technological support of quality of a surface layer of details at electroerosive processing. Abstract of Ph.D. dissertation, BSTU, Bryansk, Russia
14. Levinson EM and others (1971) Electroerosive treatment of metals. Mechanical Engineering, Leningrad, Russia
15. Foteev NK (1980) The technology of electroerosive processing. Mechanical Engineering, Moscow, Russia
16. Nadutkin AV (2007) The study of the synthesis of TI3SIC2 and the formation of structural ceramics on its basis. Abstract of Ph.D. dissertation, PSTU, Perm, Russia
17. International Center for Diffraction Data—PDF-2 (The Powder Diffraction Files (2001), no. licenz 81200030 [Elektronnyi resurs]
18. Shukhardin SV (1979) Double and multicomponent copper systems. Science, Moscow, Russia
19. Shmatko YA, Mustache YV (1987) Electrical and magnetic properties of metals and alloys. Naukova Dumka, Kiev, USSR

20. Ivenson VA (1985) Phenomenology of sintering and some questions of theory. Metallurgy, Moscow, Russia
21. Avramov IS, Shliapin AD (1999) New composite materials based on immiscible components: production, structure, properties. MGIU, Moscow, Russia
22. Mirkin LI (1961) Handbook of X-ray diffraction analysis of polycrystals. Fizmatlit, Moscow, Russia
23. Kero I (2007) Ti3SiC2 synthesis by powder metallurgical methods. Abstract of Ph.D. dissertation, Luleå University of Technology, Department of Applied Physics and Mechanical Engineering, Luleå, Sweden
24. Oglezneva CA, Kacheniuk MN, Ogleznev ND (2016) Study of the formation of the structure and properties of materials in the system "copper-carbolicidal titanium". Izvestiia vuzov. Poroshkovaia metallurgiia i funktsional'nye pokrytiia (4):60–67
25. Zhou Y, Gu W (2004) Chemical reaction and stability of Ti3SiC2 in Cu during high-temperature processing of Cu/Ti3SiC2 composites. Zeitschrift für Metallkunde 95(1):50–56
26. Karpinos DM (1985) Composite materials: reference book. Naukova dumka, Kiev, USSR
27. Ngai Tungwai L, Zheng Wei, Li Yuanyuan (2013) Effect of sintering temperature on the preparation of Cu-Ti3SiC2 metal matrix composite. Prog Nat Sci: Mater Int 23(1):70–76
28. Dudina DV, Ulianitsky VY, Batraev IS, Korchagin MA, Mali VI, Anisimov AG, Lomovsky OI (2013) Interparticle interactions during consolidation of Ti3SiC2-Cu powders influenced by preliminary mechanical milling. Met Mater Int 19(6):1235–1241
29. Kosolapova TI (1968) Carbids. Metallurgiia, Moscow, Russia
30. Ngai TL, Zheng W, Li Y (2013) Effect of sintering temperature on the preparation of Cu-Ti3SiC2 metal matrix composite. Prog Nat Sci: Mater Int 23(1):70–76
31. Efimov, AI and others (1983) Properties of inorganic compounds. Reference, Chemistry, Leningrad, Russia
32. Oglezneva SA, Grevnov LM, Zhigalova IV and others (1998) Forms of existence of carbon. Their receipt and application. Perm State Technologies University. Perm, Russia
33. Belova MY (2008) From the "black chalk" to the seals from the TRG. Armature 1(52):42–49
34. Mishchenko SV, Tkachev AG (1998) Carbon nanomaterials: production, properties, application. Mechanical Engineering, Moscow, Russia
35. Tkachev AG, Melezhik AV, Smykov MA et al (2010) Synthesis of beams of multi-walled carbon nanotubes on the catalyst FeCoMo/Al2O3. Chem Technol 11(12):725–732
36. Andreeva VD, Stepanova TR (2002) Influence of copper atoms on the graphite structure. Lett ZhTF 18(28):18–23
37. Kalbus K (2012) Copper intercalation into graphite theses and dissertations. Abstract of Ph.D., The University of Wisconsin-Milwaukee, Wisconsin, United States
38. Bin X et al (2008) Preparation and structural investigation of CuCl2 graphite intercalation compounds. Acta Geol Sin Russ Edn 82(5):1056–1060
39. Amsler M, Flores-Livas JA, Lehtovaara L, Balima F, Ghasemi SA, Machon D, Pailhes S, Willand A, Caliste D, Botti S, San Miguel A, Goedecker S, Marques MAL (2012) Crystal structure of cold compressed graphite. Phys Rev Lett 108(6):065501-1–065501-4
40. Dunaev AV, Archangelsky IV, Avdeev VV (2007) Creation of nanocarbons with metal nanoparticles from GIC for different applications in catalysis. In: 8th biennial international workshop "Fullerenes and atomic clusters", St Petersburg, Russia, p 266
41. Biske NS, Kolodey VS (2014) Spectroscopy of Raman scattering of graphite from deposits and ore occurrences in the Ladoga area. Geol Miner Karelia 17:103–109
42. Jorio A (2012) Raman spectroscopy in graphene-based systems: prototypes for nanoscience and nanometrology. Rev Art Int Sch Res Netw. ISRN Nanotechnol 2012:1–16
43. Tikhomirov SV, Kimstach TB (2011) Raman spectroscopy is a promising method for studying carbon nanomaterials. Analytics (11):28–33
44. Gorsky SY (2014) Development of the process of functionalization of carbon nanotubes in nitrogen acid and hydrogen peroxide. Abstract of Ph.D. dissertation, TSTU, Tambov, Russia

45. Kostikov VI, Shipov NN, Kalashnikov YL and others (1991) Graphitization and diamond formation. Metallurgy, Moscow, Russia
46. Ermolaev AA, Laptev AI, Polyakov VP (2000) Influence of the composition of the alloy-catalyst on the mechanism of synthesis and composition of phases of polycrystalline diamond carbonado. Izv. Universities. Non-ferrous Metall (2):62–65
47. Liu J et al (1998) Fullerene pipes. Science 280:1253

Correction to: Synthesis and Characterization of Oxide Dispersion Strengthened W-based Nanocomposite

A. Patra, S. K. Karak and T. Laha

Correction to:
Chapter "Synthesis and Characterization of Oxide Dispersion Strengthened W-based Nanocomposite" in: S. S. Sidhu et al. (eds.), *Futuristic Composites,* Materials Horizons: From Nature to Nanomaterials, https://doi.org/10.1007/978-981-13-2417-8_13

In the original version of this chapter, the reference sequence was incorrect. This has now been rectified and the reference sequence has been updated.

The updated original online version of this chapter can be found at https://doi.org/10.1007/978-981-13-2417-8_13

S. S. Sidhu et al. (eds.), *Futuristic Composites*, Materials Horizons: From Nature to Nanomaterials, https://doi.org/10.1007/978-981-13-2417-8_17